QUASI-ELASTIC ELECTRON SCATTERING FROM A HIGH-MOMENTUM NUCLEON IN DEUTERIUM

A Dissertation

Presented to

The Faculty of the Department of Physics

The College of William and Mary in Virginia

In Partial Fulfillment

Of the Requirements for the Degree of

Doctor of Philosophy

by

Cornel Butuceanu

2006

APPROVAL SHEET

This dissertation is submitted in partial fulfillment of
the requirements for the degree of

Doctor of Philosophy

Cornel Butuceanu

Approved, January 2006

Dr. Keith A. Griffioen, Chair

Dr. John M. Finn

Dr. Charles F. Perdrisat

Dr. John D. Walecka

Dr. Mahbub Khandaker, Norfolk State University

Dr. Sebastian Kuhn, Old Dominion University

This work is dedicated to my sons, Nicolae Alexandru and Cristian Joseph

CONTENTS

ACKNOWLEDGEMENTS

Albert Einstein once said, “In the middle of difficulty lies opportunity.” I look back upon my life (that of Communism, revolution, little hope and uncertainty) and am in awe that opportunity found its way to my door. It needed knock only once, for I was waiting. During the wait, I read that, “To accomplish great things, we must not only act, but also dream; not only plan, but also believe.” As I see this work in its final form, I realize that my actions, my dreams, my plans and my beliefs have been molded, created and brought to fruition by many people. I would like to acknowledge those individuals who have helped me to dream, to plan, to believe, and to seize such an incredible opportunity.

First, let me thank my advisor, Professor Keith Griffioen, whose patience, guidance and advice helped me stay focused on this long and arduous journey. Many thanks are deserved by my thesis committee members, Michael Finn, Todd Averett, and Dirk Walecka, who rallied behind me and supported my efforts. A special thank you goes out to Sebastian Kuhn, Charles Perdrisat and Mahbub Khandaker who agreed to serve on my committee for the final step of this road. A major contribution into my appreciation of physics was made by, perhaps, the greatest teacher I’ve known, Professor Walecka. To have been his pupil was a priviledge and a gift, for he increased my desire to learn and made physics seem like magic. Tremendous gratitude goes to Professor Marc Sher, who convinced the Admissions Committee to take a chance on a Romanian science teacher who had been out of circulation for several years. He instilled in me the strength and courage to tackle the Ph.D. program, stood behind me through the qualifying exam, and served as my cheerleader throughout my studies.

I am forever grateful to a few key individuals who helped me to understand and adjust to the rigors of what lay before me when I entered the doors of Small Hall and the Jefferson Laboratory. First, I would like to thank Zoltan Batiz, a former colleague from my undergraduate studies in Romania whom I found again at William and Mary upon my admission to the program. If it were not for Zoli, I would never have made it through my first two years of graduate school. Zoli, one of two angels I believe came into my life for a purpose, tutored me tirelessly and helped me to find my way back into the world of physics. Special thanks go to Ioana and Gabriel Niculescu, also Romanian friends and colleagues, whom I met at Jefferson Lab. Gabi was always just a phone call or e-mail away, filled with information and an uncanny ability to comprehend and explain the most intricate of things in the most basic of terms.

I would like to acknowledge the assistance provided by the Jefferson Laboratory staff and the CLAS Collaboration. My first steps into the world of CLAS at Jlab were directed by Hovanes Egiyan, Harut Avakian, Stepan Stepanyan, Rustam Niyazov, and I thank them for their great support. A special thank you goes to my fellow colleague and friend, Alexei V. Klimenko, who worked closely with me and helped me through the difficult stages of this project. I would like to thank Kim Egiyan for fruitfull discussions and assistance with my analysis.

I would like to pay tribute to my parents for the sacrifices they made in their lives-for doing without so that I could one day fulfill my dreams. I would especially like to thank my mother, Niculina, who left my father's side to come to the U.S. for eight months to care for our twin sons soon after their birth. This sacrifice and gesture of compassion enabled me to continue my thesis work and be assured that my sons were in loving hands.

And, finally, I owe everything to my other angel–my wife, Kathryn Butuceanu. She helped me to believe in myself and in things I had thought impossible. Kathy brought me to this country, introduced me to the Physics Department at William and Mary, and convinced me that I had the potential to become a scholar. Her contributions to my success are endless, and her love and support through the years are unmatched. Thank you, Kathy, for always being there for me and for showing me that life is filled with "opportunity".

LIST OF TABLES

LIST OF FIGURES

ABSTRACT

I present an analysis of data from experiment E94-019 using the CEBAF Large Acceptance Spectrometer (CLAS) at the Thomas Jefferson National Accelerator Facility (TJNAF). The experiment ran in the spring of 2002 over the course of two months with 5.765 GeV unpolarized electron beam on a liquid deuterium target and collected a total of 4.5×10^9 triggers. These data cover a wide kinematic range from the quasielastic peak up to an invariant mass $W \approx 3$ GeV of the final hadronic system for four-momentum transfer Q^2 from 1.5 to 6.0 GeV^2. Using CLAS we tagged spectator protons released in quasielastic scattering from high-momentum neutrons in deuterium at large emission angles with respect to the momentum transfer direction. Using these data one can test the physics of small-sized wavepacket expansion inside the nucleus. The absorption of a high-momentum virtual photon on a nucleon leads to the production of a small-sized wavepacket (due to the supression of long-range pion and gluon fields) which evolves rapidly in time until it reaches the nucleon size. We can investigate how such a wavepacket moves within a nucleus and how long-range fields are restored. This study could provide information about the quark-gluon degrees of freedom, internucleon forces in nuclei, and color coherents effects such as color screening (CS) and color transparency (CT). Color screening would allow a small-sized object to escape from the nucleus without further interaction. Measuring the evolution of FSIs with the momentum transfer Q^2 could reveal whether or not nuclear transparency may occur in quasielastic reactions such as d(e,e′p)n. We computed the ratio of the experimental cross section for d(e,e′p)n measured for kinematics dominated by rescattering effects to the cross section measured for the kinematics dominated by screening effects (suppression of FSIs). I present a study of the acceptance of CLAS for the inclusive d(e,e′) reaction at high x and for the exclusive d(e,e′p)n reaction in the quasielastic region. We have extracted absolute cross sections for the inclusive d(e,e′) channel and they are presented in two-dimension kinematic bins with $\mathrm{Q}^2 = 1.7 - 6.7$ GeV^2 and $x = 0.7 - 1.9$. By mapping these cross sections we can extract the probabilities of finding short range nucleon-nucleon correlation (SRC) state in nucleus. Absolute cross section for the exclusive d(e,e′p)n channel are presented for spectator momenta p_s from 250 to 1000 MeV/c and four-momentum transfers $Q^2 = 2 - 6$ GeV^2. Experimental measurements suggest a strong contribution from meson exchange and Δ-isobar currents which dominate FSIs. This makes it difficult to observe color coherent effects. This picture is corroborated by new theoretical developments.

QUASI-ELASTIC ELECTRON SCATTERING FROM A HIGH-MOMENTUM NUCLEON IN DEUTERIUM

CHAPTER 1

Physics Overview

1.1 Introduction

> **"I often say that when you can measure what you are speaking about, and express it in numbers, you know something about it; but when you cannot measure it, when you cannot express it in numbers, your knowledge is of meager and unsatisfactory kind"**
>
> William Thompson, 1st Baron Lord Kelvin

A little less than a century ago, a series of table-top experiments conducted by Rutherford changed the way we understand the structure of matter. It opened the door to smaller and smaller distances inside the matter. Figure 1.1 shows a flow chart with the building blocks of matter and corresponding sizes. The main building block, the atom, has a size of $\approx 10^{-10}$ m. Most of its mass is carried by the nuclear core which is about 10000 times smaller than the atom itself. A cloud of electrons surrounds the nucleus, giving the atom its size, and correspondingly anything made of atoms,. The nucleus consists of nucleons (neutrons and protons) with radii of $\approx 10^{-15}$ m. The number of positively charged protons is equal to the number of negatively charged electrons in atom. Neutrons are neutral particles, thus the atom is electrically neutral. A natural question arises: How do all protons (with positive charge) stay together inside the nucleus without flying apart? The nuclear

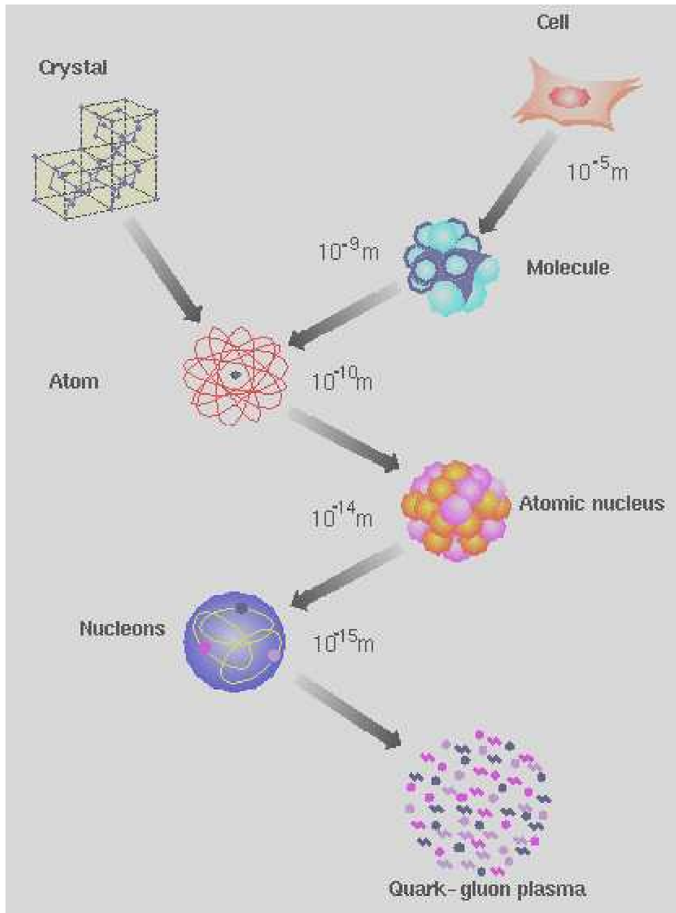

FIG. 1.1: Flow chart with the building blocks of matter and corresponding sizes.

strong force is responsible for binding the nucleons together inside the nucleus. The strong force inside the nucleus can be described by the well potential as shown in Figure 1.2. The force on the nucleon is $\vec{F} = 0$ inside the well. The force at the surface is very large thus, the particle is kicked back being trapped inside the well. Quantum Mechanics and the Uncertainty Principle allow though a particle to "tunnel" through the potential barrier and escape (i.e. positively charged α

particles). By studying the rate of such emissions and its associated energy spectra from different large nuclei we can obtain the shape of the force field these particles have to travel through. The strong potential is roughly constant inside the nucleus, while the electrical Coulomb potential increases with the number of protons in the nucleus, eventually leading to unstable heavy nuclei. The strong force between

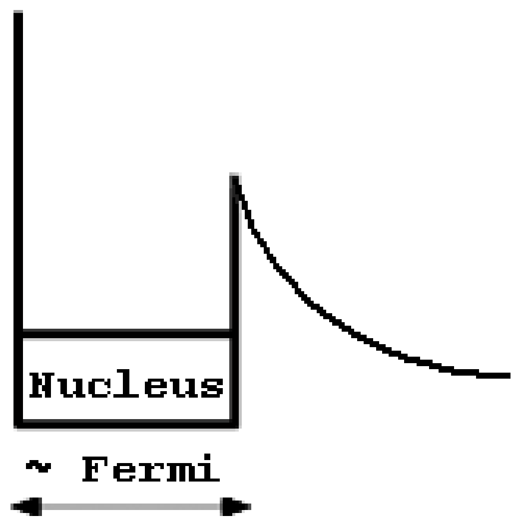

FIG. 1.2: Well potential. It describes the strong force inside the nucleus.

nucleons has a short range, commensurate with the nucleon size, while the electrical repulsion obeys a $\frac{1}{r^2}$ force law. During early attempts to understand how the strong force binds the nucleons it was hypothesized that the proton and the neutron are exchanging some particle (which today is called pion) between them. The theoretical prediction of Yukawa (1935) [1] and the experimental discovery (1947) [2] of the pion led to the discovery of many more strongly interacting particles (such as Δ^{++},K^{+}). The simple pion-exchange mechanism which only accounts for the long-range part of the interaction was not able to explain the strong interaction between nucleons and all the newly discovered particles.

Experiments carried at SLAC (1968) [3] proved the existence of internal spin $\frac{1}{2}$

constituents, the quarks. Today we know that the pion is a composite particle made up of quarks, as are the proton and the neutron, and that the strong force describes the interaction between these quarks. Quarks interacts by exchanging strong force carriers called gluons. The theory that describes strong interactions between quarks and gluons is called Quantum Chromodynamics (QCD). The strong interaction is responsible for binding quarks together into baryons and mesons (three and two quark states, respectively), and also for binding the nucleons together into a nucleus. In order to respect Pauli's exclusion principle which states that **no two particles**

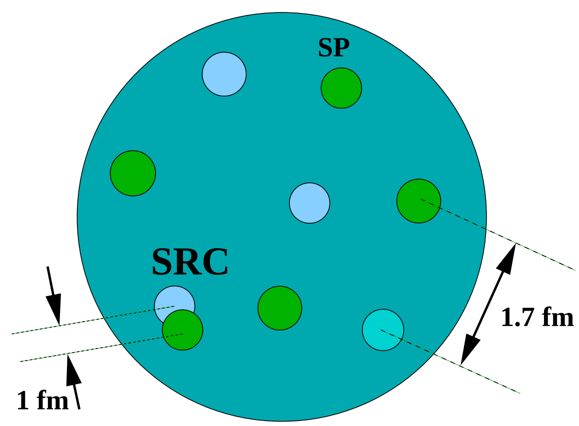

FIG. 1.3: Schematic picture of a nucleus. Single nucleons primarily moving in an average field (SP) and short-ranged nucleon-nucleon correlations (SRC).

with half-integer spin can share the same quantum state, a "color" degree of freedom was introduced (characterized by a quantum number called **color charge**) to label the quarks. The color degrees of freedom are labeled red (R), blue (B) and green (G) in analogy with the visible light. Each nucleon is composed of three quarks of different color such that the nucleon (and any particle) is a color neutral object. Just as the combination of RBG produces white light, 3 quarks of 3 colors produces a color neutral object. This is a characteristic of strong force analog to the atom being charge neutral. Color neutrality of all particles found in Nature and color confinement of quarks (no free quarks) are the foundations of QCD. An important feature of QCD theory is that the "up" quark (abbreviated as u) and the "down" quark (abbreviated d) are nearly massless particles (≈ 5 MeV). In this limit the chiral symmetry (left-right symmetry) is spontaneously broken in the ground state of QCD. The proton electromagnetic radius is ~ 0.86 fm (1 fm= 10^{-15} m), and the average distance between nearby nucleons (center-to-center) is ~ 1.7 fm. Thus, under normal conditions nucleons are closely packed and nearly overlap as they move in an average field created by all the other nucleons. The nucleus is a quantum system and its wave functions contains components with nucleons separated center-to-center by 1 fm or less. In these configurations there is a significant region of overlap of the two nucleons, in which short range correlations (SRC) are dominant. These high-density fluctuations may modify the configuration of the underlying quarks inside the nucleons. In these regions the physics of confinement, which defines the limit of QCD, may no longer be aplicable and the chiral symmetry may be (partially) restored.

A few questions are worth emphasizing here: What happens during the brief intervals when two or more nucleons overlap in space? Can we account for the interactions using meson exchanges, or do we instead need to consider explicitly quark aspects such as quark exchanges between nucleons and mixing of nucleon constituents into six- or nine-quark bags? At high densities, can we detect the presence of superfast quarks?

Color degree of freedom is another avenue to test QCD as the underlying theory of the strong interaction. The availability of high-energy beams provides the opportunity to observe features of nuclear structure at small-distance scales such as color-singlet fluctuations of a hadron into an object with small spatial extent, namely, point-like configurations (PLC), which evolves with time. These configurations are possible due to the suppression of long-range pion and gluon fields when

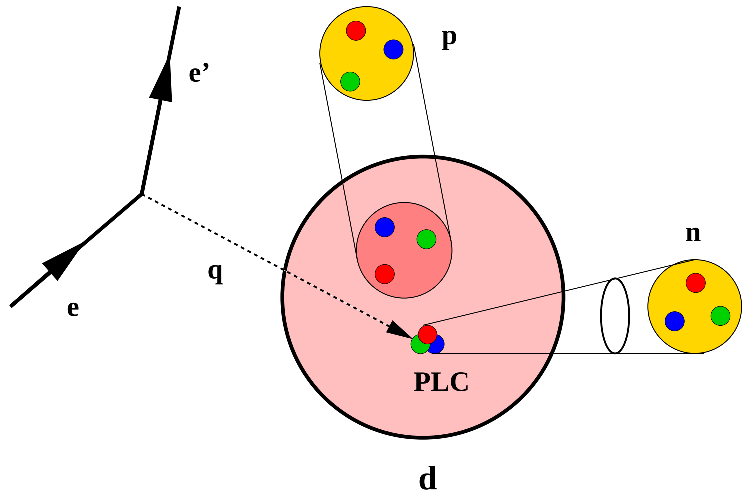

FIG. 1.4: Schematic picture of hard quasi-elastic electron scattering from a deuterium target. The high momentum virtual photon could probe point-like constituents (PLCs) - nucleonic states in which the long-range soft pion and gluon fields are suppressed.

the 3 valence quarks are close to each other. Figure 1.4 shows schematically how a high-momentum transfer virtual photon can probe a PLC inside the nucleus (in this case the deuterium). Since the cross section is proportional with the transverse size of the PLC it means that its cross section will be reduced. If the PLC is still small after propagating about 1.5 fm through the nuclear matter, the final state interactions are suppressed. The result is that significant color coherent effects, which can either enhance or suppress computed cross sections, are predicted [23] to occur for momentum transfer $Q^2 = 4 - 10$ GeV^2. The phenomenon of color transparency means that for a short period of time a nucleon can be viewed as a PLC. In this configuration, the nucleon can tunnel through the nuclear matter with reduced interactions.

These subjects (dense nuclear matter, superfast quarks and color coherence) could expand our understanding of exotic phenomena in nuclei. Studies of the local high-density fluctuations are important for understanding the equation of state of cold, dense matter which is crucial to untangle the problem of the phase transition of neutron stars to "quark stars", whose experimental existence was suggested in Ref. [4]. Color transparency could provide a mechanism for a phase transition to a new form of matter in a sufficiently dense nuclear system, such as in the core of neutron star. In QCD, transitions to new phases of matter are possible in different regimes of density and temperature.

Such studies are therefore of great interest for understanding important issues of QCD, such as the existence of chiral restoration and deconfinement, the onset of quark-gluon degrees of freedom and the structure of the phase transition from hadronic to quark-gluon states of matter.

1.2 Lepton-Hadron Scattering Formalism

Lepton scattering is one of the main tools for studying the internal structure of the nucleus. Quantum Electrodynamics (QED) describes well the electromagnetic interaction between an electron and a hadron target, with an exchange of a virtual photon. In order to observe the internal structure of a hadron, a probe with a wave length smaller than the size of a hadron constituent needs to be used. Since the wave length is inversely proportional to the energy, a higher energy probe will allow us to identify smaller hadron constituents. The virtual photon exchanged in hard reactions between the incident lepton and a hadron constituent inside the nucleus is an excellent probe for studying nuclear structure. The energy and momentum transfers of the virtual photon (which are the energy and momentum of the scattered electron) are setting the resolution of this "microscope". At low energy transfer the electron scatters elastically from the nucleus as a whole leaving it in its ground state or in an excited nuclear state. At higher energy and momentum transfers, scattering is dominated by quasi-elastic (QE) processes, where the photon interacts with a single nucleon (proton or neutron). With increasing energy and momentum transfer, the exchanged virtual photon probes the quark degrees of freedom in the nucleon. At high enough energy and momentum transfer, the interaction can be approximated well by the elastic scattering from a "free" quark.

1.2.1 Elastic Electron-Proton Scattering

Elastic electron-nucleon scattering is dominated by single photon exchange. The proton is an extended structure and cannot be considered as a point-like particle. We need to find the "wavefunctions" that describe a proton in terms of its constituents quarks and gluons. The Feynman diagram for elastic electron-proton scattering is shown in Figure 1.5. The incident electron has the four-momentum $k(E,\vec{k})$ with the incident energy $E = E_{beam}$ and the scattered electron has four-momentum $k'(E',\vec{k'})$ with emerging energy E$'$. The proton target has the four-momentum $p(E_p,\vec{p})$ with the energy E_p and the knocked-out proton has four-momentum $p'(E'_p,\vec{p'})$ with the energy E'_p. A virtual photon with four-momentum $q(\nu,\vec{q})$ is exchanged between the incident electron and the proton target with the energy $\nu = E - E'$. The scattering amplitude for this process can be written as a product of current densities for the electron and the proton, and the photon propagator:

$$\mathcal{M}_\gamma = j_l^\mu \frac{1}{Q^2} j_\mu^h, \tag{1.1}$$

where j_l^μ is the current density of the incident lepton (electron or muon), j_μ^h is the current density of the nucleon target, and $Q^2 = -q^2 = 4EE'\sin(\theta/2)$ is the Lorentz invariant square of the four-vector momentum transfer. The electron current density can be expressed in terms of Dirac spinors (u and $\bar{u}$), γ-matrices and the electron

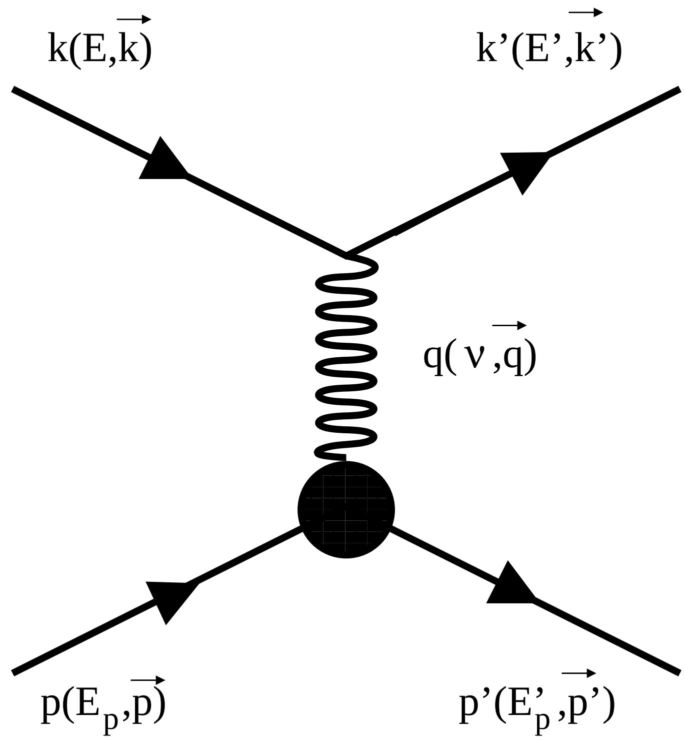

FIG. 1.5: Feynmann diagram for elastic electron-proton scattering.

charge (e) as:

$$j^{\mu} = -e\bar{u}\gamma^{\mu}u \tag{1.2}$$

Since the proton is not a point-like particle, we can describe the hadronic current density as a general Lorentz covariant quantity that satisfies parity, time-reversal invariance and current conservation, all of which are obeyed by the electromagnetic interaction:

$$j_{\mu} = e\bar{u}\left[F_1(Q^2)\gamma^{\mu} + \frac{\kappa}{2M_p}F_2(Q^2)i\sigma^{\mu\nu}q_{\nu}\right]u, \tag{1.3}$$

where the "form factors" F_1 and F_2 depend only on Q^2, M_p is the proton mass, and $\kappa = 1.79$ is the anomalous magnetic moment of the struck nucleon. F_1 and F_2 are experimentally measurable quantities that describe the deviation from point-like scattering and characterize the structure of the proton. Proton structure is determined primarily by strong-force interactions between its constituents. The scattering of a unpolarized "spinless" lepton from a "spinless" and infinitely heavy point-like target particle is expressed by the differential Rutherford cross section:

$$\left(\frac{d\sigma}{d\Omega}\right)_{Rutherford} = \frac{4(Ze)^2\alpha_{EM}E'^2}{Q^4} = \frac{(Ze)^2\alpha_{EM}}{4E^2\sin^4\left(\theta_{el}/2\right)}, \tag{1.4}$$

where $\alpha_{EM} = \frac{1}{137}$ is the fine structure constant of electromagnetic interaction and Ze is the electric charge of the point-like hadronic target. For electron scattering we introduce a factor $\left(1 - \beta^2 \sin^2 \frac{\theta}{2}\right)$ due to the spin of the electron and a factor $\frac{E'}{E}$ due to the recoiling of nucleus. Here $\beta = \frac{v_{el}}{c}$ and c is the speed of light. In the limit $\beta \to 1$ the differential cross-section becomes the Mott cross-section:

$$\left(\frac{d\sigma}{d\Omega}\right)_{Mott} = \frac{E'}{E} \cdot \cos^2\frac{\theta_{el}}{2} \cdot \left(\frac{d\sigma}{d\Omega}\right)_{Rutherford} \tag{1.5}$$

We need to take into consideration not only the interaction of the electron with the nuclear charge, but also we have to consider the interaction between the current of the electron and the nucleon's magnetic moment. Thus, the magnetic interaction introduces a factor $\sin^2\frac{\theta}{2}$ into the interaction and we obtain for the cross section of a charged, spin 1/2 particle with a point-like target:

$$\frac{d\sigma}{d\Omega} = \left(\frac{d\sigma}{d\Omega}\right)_{Mott} \cdot \left[1 + \frac{Q^2}{2M_P^2}\tan^2\frac{\theta_{el}}{2}\right]. \tag{1.6}$$

Introducing the nucleon structure functions F_1 and F_2 the total differential cross section can be expressed as:

$$\frac{d\sigma}{d\Omega} = \left(\frac{d\sigma}{d\Omega}\right)_{Mott}\left(\left[F_1^2 + \frac{\kappa Q^2}{4M_p^2}F_2^2\right] + \frac{Q^2}{2M_p^2}\left[F_1 + kF_2\right]^2\tan^2\frac{\theta_{el}}{2}\right) \tag{1.7}$$

A linear combination of F_1 and F_2 leads to a more convenient expression of the above equation so called the *Rosenbluth formula*:

$$\frac{d\sigma}{d\Omega} = \sigma_{Mott}\left(\left[\frac{G_E^2(Q^2) + G_M^2(Q^2)}{1+\tau}\right] + 2\tau G_M^2(Q^2)\tan^2\frac{\theta_{el}}{2}\right), \tag{1.8}$$

where $G_E = F_1 - \tau\kappa F_2$ and $G_M = F_1 + \kappa F_2$ are the Sachs electric and magnetic form factors., and $\tau = Q^2/4M_p^2$. The measured Q^2-dependence of the Sachs form factors gives information about the radial charge and magnetic moments. In the limit $Q^2 \to 0$ the Sachs form factors are the Fourier transform of the charge and magnetic moment distributions within the nucleon [5], and

$$\lim_{Q^2 \to 0} G_E = 1, \qquad \lim_{Q^2 \to 0} G_M = 1 + \kappa = \mu_p, \tag{1.9}$$

where the magnetic moment of the proton is defined as $\mu_p = e\hbar/2M_P = 2.7929\mu_N$, with $\mu_N = 3.1525 \times 10^{-14}$ MeV$\cdot$T^{-1} the nuclear magnetic moment. At $Q^2 = 0$ the Sachs form factors for proton and neutron take the values:

$$\begin{aligned} G_E^p &= 1, \qquad G_M^p = 2.79\mu_N, \\ G_E^n &= 0, \qquad G_M^n = -1.91\mu_N \end{aligned} \tag{1.10}$$

At low momentum transfer , the slope of $G_{E,M}^p$ gives us the mean square charge and magnetic radii, $\langle r^2, \rangle_{E,M}^{p,n}$, of the proton:

$$\langle r^2 \rangle_{E,M}^{p,n} = 6 \cdot \lim_{Q^2 \to 0} \frac{dG_{E,M}^{p,n}(Q^2)}{dQ^2} \tag{1.11}$$

The charge and magnetic radii of the proton are both ≈ 0.81 fm [5], which corresponds to an energy scale of about 200 MeV, comparable to its mass. In order to independently determine $\mathrm{G}_E^p(\mathrm{Q}^2)$ and $\mathrm{G}_M^p(\mathrm{Q}^2)$ the cross-sections must be measured at fixed values of Q^2, for various scattering angles θ and different beam energies E.

1.2.2 Inelastic Electron-Proton Scattering

With sufficient energy transfer inelastic scattering becomes possible and the nucleon is excited into a resonant state or into the continuum. As in the elastic case, single photon exchange is the dominant mechanism. The current density given by Eq. 1.3 cannot be expressed anymore in terms of Dirac spinors since the proton is a composite object made up of quarks and gluons. The inelastic cross section is generalized to:

$$d\sigma \sim L^{e}_{\mu\nu} W^{\mu\nu}, \tag{1.12}$$

where $L_{\mu\nu}$ represents the symmetric lepton tensor which describes the emission of the virtual photon, and $W^{\mu\nu}$ is the hadronic tensor which describes the absorption of the virtual photon by the nucleon. The leptonic tensor can be written as a sum of symmetric and antisymmetric parts:

$$L^{e}_{\mu\nu} = \sum_{spins} |\bar{u}\gamma^{\mu}u||\bar{u}\gamma^{\nu}u| = \frac{1}{2}Tr\left((k' + m)\gamma^{\mu}(k + m)\gamma^{\nu}\right), \tag{1.13}$$

where m is the electron mass. The most general hadronic tensor $W^{\mu\nu}$ can be written as:

$$W_{\mu\nu} = -W_1 g^{\mu\nu} + \frac{W_2}{M_p^2} p^{\mu}p^{\nu} + \frac{W_4}{M_p^2} q^{\mu}q^{\nu} + \frac{W_5}{M_p^2}(p^{\mu}q^{\nu} + q^{\mu}p^{\nu}), \tag{1.14}$$

in which $g^{\mu\nu} = (1, -1, -1, -1)$ is the metric tensor. Eq. 1.16 can be further simplified due to current conservation $q_{\mu}W^{\mu\nu} = 0$. The inclusive differential electron-proton cross section ($ep \rightarrow eX$), in the laboratory frame (target rest frame) becomes:

$$\begin{aligned} \left|\frac{d^2\sigma}{dE'd\Omega}\right|_{lab} &= \frac{\alpha^2}{4E^2 \sin^4 \frac{\theta}{2}} \left[W_2(\nu, Q^2)\cos^2\frac{\theta}{2} + 2W_1(\nu, Q^2)\sin^2\frac{\theta}{2}\right] \\ &= \left(\frac{d\sigma}{d\Omega}\right)_{Mott} \left[2W_1 \tan^2\frac{\theta}{2} + W_2\right] \end{aligned} \tag{1.15}$$

In the case of elastic scattering, the energy transfer ν and the four-momentum transfer Q^2 are related by the expression $\nu = Q^2/2M_p$. In inelastic scattering these variables become independent. From conservation of energy and momentum at the hadron vertex (see Figure 1.5):

$$W = p + q, \qquad W^2 = p^2 + 2p \cdot q + q^2 \tag{1.16}$$

Here W is the invariant mass of the hadronic system. In the lab frame $p \cdot q = M_p\nu$ and the invariant mass squared can be written as $W^2 = M_p + 2M_p\nu - Q^2$ and depends on two independent scalar variables, Q^2 and ν. Structure functions are measurable quantities that describe the photon-nucleon interaction. For values of $Q^2 < 1$ GeV^2 they are dependent on both ν and Q^2. At high momentum transfer, when the virtual

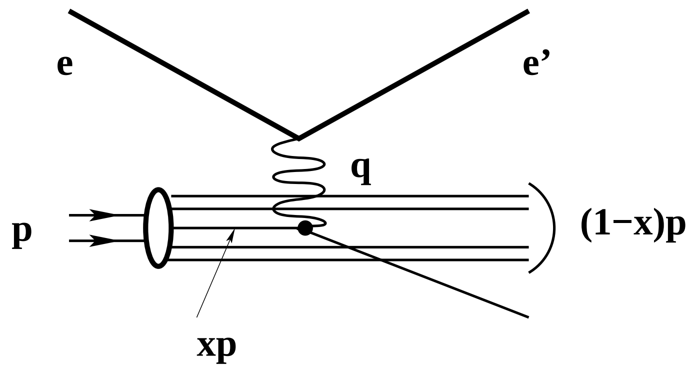

FIG. 1.6: Deep inelastic e-p scattering in the parton model.

photon probes the nucleon constituents (quarks), it is more convenient to express them as functions of $x = \frac{p \cdot q}{p \cdot k}$, the so called Bjorken scaling variable. In the limits $Q^2 \to \infty$ and $\nu \to \infty$, with x fixed, the structure functions W_1 and W_2 scale as:

$$M_p W_1(\nu, Q^2) \to F_1(x), \tag{1.17}$$

$$\nu W_2(\nu, Q^2) \to F_2(x). \tag{1.18}$$

Data from SLAC [3] support the scaling behavior in which x becomes the fraction of the nucleon momentum carried by the struck quark. The scattering process in the deep-inelastic region can be visualized as in Figure 1.6. The virtual photon is absorbed by a quark which carries a fraction x of the momentum of the proton. In this picture the struck quark i has momentum $p_i = xp$ and a mass $m_i \approx xM$ before absorbing the virtual photon, where p is the four-momentum of the proton and M_p is the nucleon mass. Because the quarks are point-like particles of spin $\frac{1}{2}$, the electron-muon formalism could be applied here. The differential cross-section for elastic scattering of an electron by a quark of flavor i becomes [6]:

$$\frac{d^2\sigma_i}{d\Omega dE'} = \frac{4\alpha^2 E'^2}{Q^4}\left[e_i^2\cos^2\left(\frac{\theta}{2}\right) + e_i^2\frac{Q^2}{2m_i^2}\sin^2\left(\frac{\theta}{2}\right)\right]\delta\left(\nu - \frac{Q^2}{2m_i}\right). \tag{1.19}$$

in which e_i is the fraction of electron charge carried by the quark of flavor i. Comparing the above expression with Eq. 1.17, and using the $m_i = xM$, we obtain:

$$W_1^i = e_i^2\frac{Q^2}{4M_p^2x^2}\delta\left(\nu - \frac{Q^2}{2Mx}\right), \quad W_2^i = e_i^2\delta\left(\nu - \frac{Q^2}{2Mx}\right). \tag{1.20}$$

With the probability that a parton of flavor i has momentum fraction x, and considering that the contributions of individual quarks to the inelastic e-p differential cross section add incoherently, we obtain:

$$M_pW_1(\nu, Q^2) = \sum_i \frac{e_i^2}{2}f_i(x) \equiv F_1(x), \tag{1.21}$$

$$\nu W_2(\nu, Q^2) = \sum_i e_i^2 x f_i(x) \equiv F_2(x), \tag{1.22}$$

where $f_i(x)$ is the probability that a quark of flavor i has momentum fraction x. As a result we obtain the Callan-Gross relation $2xF_1(x) = F_2(x)$, which is a consequence of quarks having spin 1/2 and basically states that in order for a photon to be absorbed by a parton (quark) with momentum fraction x, it must have the right values of Q^2 and ν such that $x = x_{Bjorken} = \frac{Q^2}{2M\nu}$, which is in fact the elastic electron-quark scattering constraint. This explains the observed scaling behavior in the deep-inelastic scattering regime, and proves the existence of point-like spin 1/2 constituents inside of nucleon. QCD, however violates this scaling law.

1.3 d(e,e′N)N Exclusive Reactions Formalism

One of the primary goals, in the study of d(e,e'N)N exclusive reactions, is the determination of the high momentum component of the deuteron wave function, which is believed to be dominated by short-range nucleonic correlations (SRC). The precise description of the coupling between the electron and the virtual photon, using QED, and the exclusivity of this reaction allows us to obtain a deeper understanding of the dynamics of the reaction as well as to gain information about the microscopic structure of SRCs. The combination of three factors: high energy, high momentum transfer and exclusiveness could lead to nuclear color transparency (CT), in which point-like quark configurations could pass nearly undisturbed through the nuclear medium. During the last decade a dozen experiments were dedicated to semi-exclusive nuclear reactions at large momentum transfer ($> few$ GeV/c), in the quest for nuclear color transparency [7] [8] [9] [10] [11]. Theoretical descriptions of semi-exclusive reactions have been successful in medium-energy nuclear physics [12] and lately they have been applied to hadronic interactions with large transferred energy and momentum. The main challenge for theoretical descriptions consists of describing the strong re-interaction of final-state hadrons in nuclear matter, which seem to be the dominant feature of these reactions. For small energies of produced hadrons ($E_N < 1$ GeV) final state interactions (FSIs) in semi-exclusive reactions are usually evaluated in terms of an effective potential for the interaction in the residual system using the optical model [13]. For large energies the description of FSIs becomes more complicated due to the increasing number of partial waves with energy, and due to the predominantly inelastic nucleon-nucleon (NN) interactions for $E_N > 1$ GeV. Final state interactions in hadron-induced nuclear reactions at higher energies ($1 < E_N < 4$ GeV) were often described within the Glauber approximation [14]. The formalism for calculating cross sections for semi-exclusive processes (e.g. the exclusive d(e,e′p)n reaction) was developed by Glauber based on the assumption that the interactions of the incident particle (electron, π) with the nucleons (protons or neutrons) inside nuclei could be individually treated by the general methods of diffraction theory. The nucleons were considered frozen in their instantaneous positions during the incident particle's passage through nuclear matter. The interactions of incident particles were assumed to be described by two-body forces and as a consequence the total phase change of the emerging wave was approximated by the sum of the phase changes produced by the individual nucleons. This approximation works well for stationary scatterers but it cannot be applied to the class of eA reactions in which bound nucleon momenta and excitation energies of the residual nuclei are large enough such that short-range multi-nucleon correlations are dominant in the nuclear wave function [15].

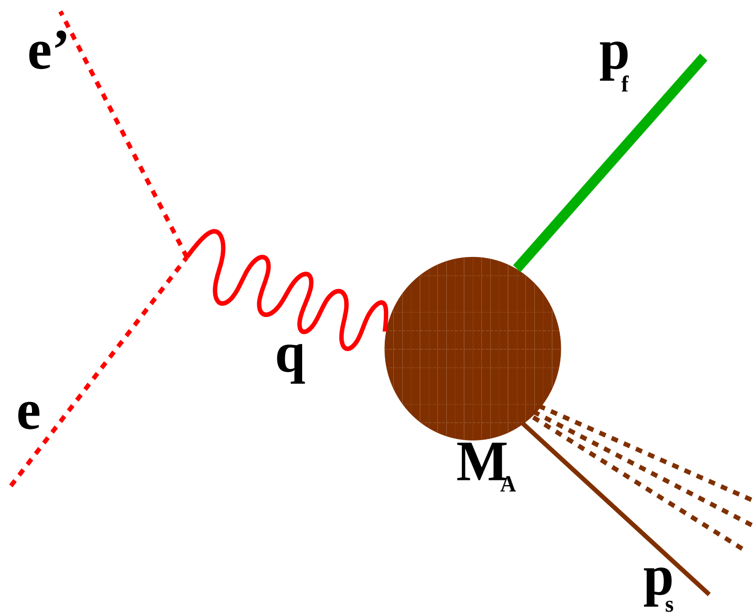

FIG. 1.7: First order Feynman diagram for the lepton-nucleus interaction.

1.3.1 Features of Exclusive Electronuclear Reactions

The general type of these reactions can be diagrammatically represented as in Figure 1.7. A large momentum $\mathbf{q} \equiv (\nu, \overrightarrow{q})$ is transferred to the nucleus and the observed final hadronic state carries almost the entire momentum of the virtual photon (fast hadrons with momentum $p_f \approx q$), while the residual hadrons (spectator hadrons with momentum p_s) carry a relatively low momentum $<$ 1 GeV/c. The general kinematic requirements are:

$$
\begin{aligned}
Q^2 &> 1\,GeV^2, \quad p_f \approx q, \quad p_f \gg p_m \\
p_s &< 1\,GeV/c, \quad E_f \gg E_m = E_f - \nu,
\end{aligned}
\tag{1.23}
$$

where $p_m = p_f - q$ is the missing momentum of the reaction, $E_f = \sqrt{M^2 + p_f^2}$ and E_m is the missing energy characterizing the excitation of the residual nuclear system, and M is the mass of the nucleon. We can construct light-cone momenta as:

$$
p_\pm = p_0 \pm p_z \tag{1.24}
$$

where the z axis is chosen along the direction of the virtual photon momentum q. For the kinematic constraints in Eq. 1.23:

$$
\frac{q_-}{q_+} \approx \frac{mx}{2q} \ll 1, \quad \frac{p_{f-}}{p_{f+}} \approx \frac{m^2}{4p_f^2} \ll 1, \tag{1.25}
$$

where x is the Bjorken scaling variable mentioned earlier. These **small parameters** are one of the important features of high-energy scattering as compared to the low-intermediate energy reactions, as will be shown later in the text. Four main processes contribute to semi-exclusive electronuclear reactions in which at least one energetic nucleon is observed in the final state, as shown in the Fig. 1.8. Fig. 1.8 (a) shows the impulse approximation (IA) amplitude, in which the virtual photon knocks out a bound nucleon which propagates without further interactions. Fig. 1.8 (b) shows the FSI amplitude, in which the knocked-out nucleon re-interacts with the residual hadronic system. Fig. 1.8 (c) shows the amplitude due to meson exchange currents (MEC), in which the virtual photon interacts with the mesons exchanged between two nucleons in the nucleus. Fig. 1.8 (d) shows the isobar current amplitude (IC), in which the virtual photon produces a Δ-isobar that re-interacts with the residual nuclear system producing a nucleon in the final state.

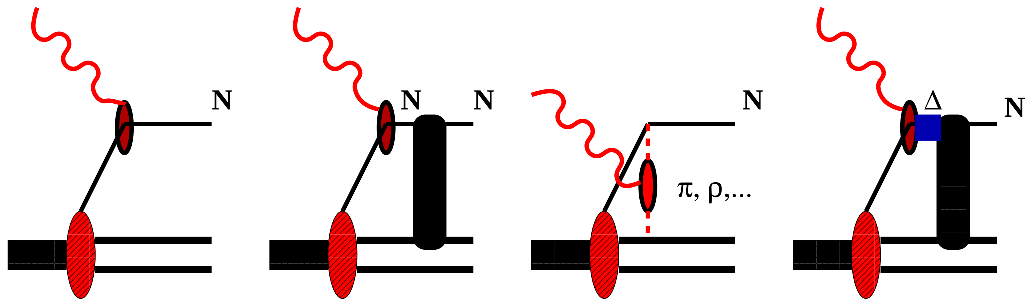

FIG. 1.8: Diagrams for the A(e,e′N) reaction in the impulse approximation (a), with final state interactions (b), with meson exchange currents (c), and with Δ-isobar (d) contributions to the scattering amplitude.

For the kinematics of large missing momentum p_m and missing energy E_m, and small $Q^2(\ll 1\ \mathrm{GeV}^2)$ the FSI, MEC and IC diagrams dominate the cross-section. While at large p_m and E_m the IA amplitude is defined by the nuclear wave function at short inter-nucleon distances, the FSI, MEC and IC amplitudes are defined by the nuclear wave function of average configurations [15]. As shown in Figure 1.9, in semi-exclusive A(e,e'N) reactions, for small $Q^2(< 1\ \mathrm{GeV}^2)$, only $x = \frac{Q^2}{2m\nu} < 1$ is appropriate for detection of large $p_{mz} \geqslant 300$ MeV/c. At small Q^2 FSIs are dominated by S-wave scattering and have broad angular distribution, making it difficult to isolate or suppress them with respect to the impulse approximation amplitude. Therefore, it is impossible to probe small time-space intervals in the nucleus using probes of larger size (1/q $\geqslant$ 1 fm). Measurements [16] of MEC and IC contributions to the d(e,e'p)n cross section at large missing momenta and low Q^2 are shown in Figure 1.10. In the kinematic region of these experiments theoretical calculations [12] show that for large p_m ($> 300MeV/c$), MEC and IC (see Fig. 1.10 full curve) dominate the PWIA (see Fig. 1.10 dashed curve) contribution. For large energy and momentum transfers the wavelength of the probe becomes much smaller

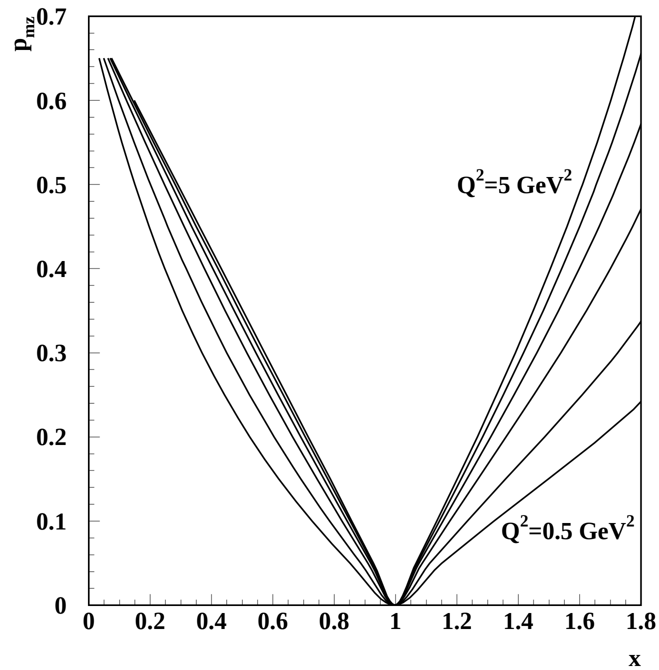

FIG. 1.9: The z component of the missing momentum p_{mz} as a function of x, for different values of Q^2 ($Q^2 = 0.5, 1, 2, 3, 4, 5$ GeV^2), for quasi-elastic A(e,e$'$N) reaction at large missing momenta and low Q^2, in the impulse approximation.

than the sizes of the interacting particles, and we can see more clearly inside the nucleus. Quantitatively, with increasing energies, the small parameters given in Eq. 1.23, become available and they play an important role in the calculations of these reactions. In the following section I will discuss the basic features of all four amplitudes in Figure 1.8 at large values of Q^2.

1.3.2 Plane Wave Impulse Approximation

The impulse approximation diagram for electro-disintegration of the deuteron is shown in Figure 1.11 (a). We consider the reaction e + d $\rightarrow$ e$'$ + p + n in which the recoiling nucleon has momentum $p_s < 1$ GeV/c and the virtual photon is exchanged with a bound (off-shell) nucleon with Fermi momentum $-p_s$. A description of the electromagnetic interaction with off-shell nucleons [15] presents many uncertainties

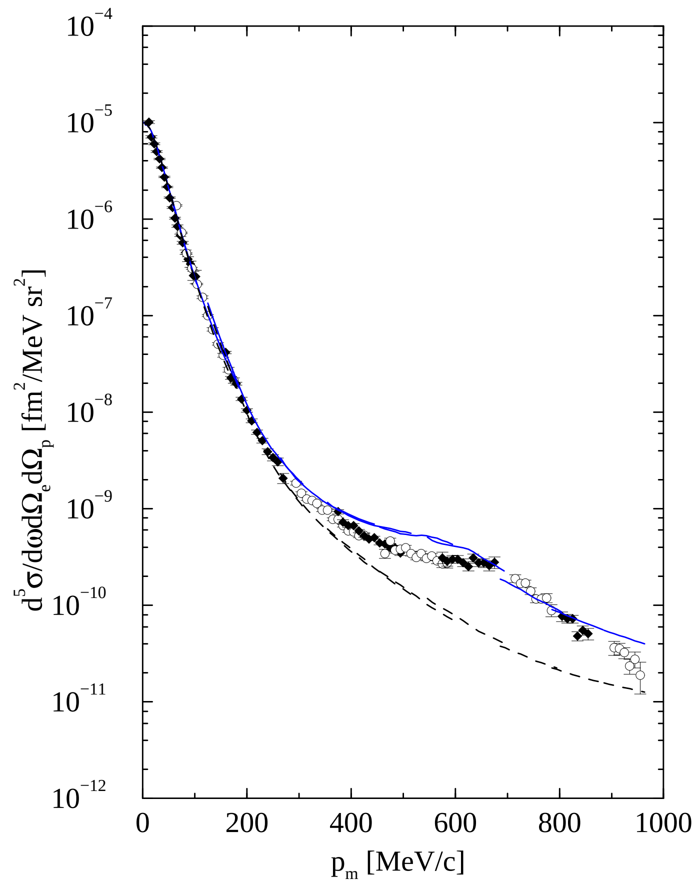

FIG. 1.10: The p_m dependence of the differential cross sections of d(e,e′N) reaction for $Q^2 = 0.13 - 0.33$ GeV^2. The data are from Ref. [16]. Solid and dashed curves correspond to theoretical calculations [12] with and without MEC and IC, respectively.

due to the absence of a self-consistent theory of the strong interaction that describes the binding of the nucleon. In the case of low energy transfer the off-shell effects are characterized by the modifications of the nucleons properties due to the in-medium nuclear potential [17]. At high energy transfer the virtual photon interacts with nucleons in a rather large phase volume, thus the off-shell effects are mostly related to the non-nucleon degrees of freedom [15]. The covariant Feynman amplitude corresponding to the diagram of Fig. 1.11 (a) can be written as [18]:

$$A_0^\mu = -\frac{\bar{u}(p_s)\bar{u}(p_f)\Gamma^\mu_{\gamma^* N}\left[\hat{p}_D - \hat{p}_s + m\right]\Gamma_{DNN}}{(p_D - p_s)^2 - m^2 + i\epsilon}, \tag{1.26}$$

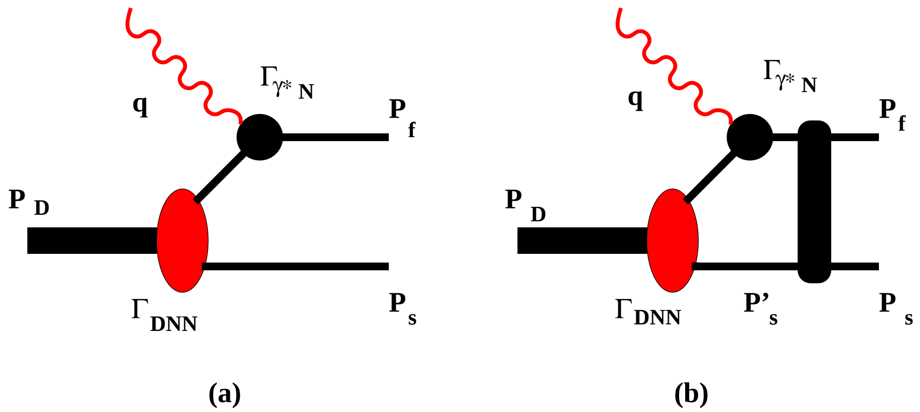

FIG. 1.11: Diagrams for the e + d → e' + p + n reaction. (a) the PWIA contribution, (b) the single re-scattering contribution.

in which $\hat{p} \equiv p_\nu \gamma^\nu$, μ are the indices corresponding to the light cone components ($+$ and $-$) of the electromagnetic current , Γ_{DNN} represents the covariant D $\rightarrow$ NN transition vertex and $\Gamma^\mu_{\gamma^* N}$ is the covariant electromagnetic vertex of the $\gamma^* N_{bound} \rightarrow N$ transition. The spin indices of the deuteron are suppressed for simplicity. Both Γ_{DNN} and $\Gamma^\mu_{\gamma^* N}$ are covariant vertices, and in the time-ordered expansion they contain both the impulse approximation and vacuum fluctuation diagrams (e.g. Γ_{DNN} may represent $\bar{N}D \rightarrow N$ and $\Gamma^\mu_{\gamma^* N}$ may represent $\gamma^* \rightarrow \bar{N}N$). For the "$\mu = -$" component of the electromagnetic current the vacuum component of the $D \rightarrow NN$ vertex is negligible if one uses the reference frame in which the target (deuteron) has a very large ($\frac{q_-}{q_+} \ll 1$) momentum, called the infinite momentum frame [19]. In this case, for the "$-$" component, the amplitude of $\gamma^* \rightarrow N\bar{N}$ with subsequent $\bar{N}d \rightarrow N$ is strongly suppressed, and only the contribution in which γ^* interacts with the bound nucleon survives. In the case of other components of electromagnetic currents this is not true. In general a complete description of the off-shell nucleon currents requires the negative energy state contribution with additional invariant form-factors as compared to the on-shell nucleon [20]. The off-shell part of the "$-$" IA amplitude decreases with increasing transferred energy.

Thus, in the high energy limit one can identify the "good" component ("$-$") of the electromagnetic current which is insensitive to the off-shellness of the bound nucleon spinor [18]. We introduce the electromagnetic current for a bound nucleon as:

$$j^{\mu} = \bar{u}(p_f)\Gamma^{\mu}_{\gamma^* N} u(p_D - p_s). \tag{1.27}$$

This current still has an ambiguity related to the off-shellness of the bound nucleon. However this effect is rather small for the kinematics of Eq. 1.23. Using the approximation $\hat{p}_D - \hat{p}_s + m \approx \sum_{\lambda} u_{\lambda}(p_D - p_s)\bar{u}_{\lambda}(p_D - p_s)$ and inserting j^{μ} into Eq. 1.26, we obtain for the scattering amplitude:

$$A_0^{\mu} = \frac{j^{\mu}\bar{u}(p_s)\bar{u}(p_D - p_s)\Gamma_{DNN}}{(p_D - p_s)^2 - m^2 + i\epsilon} \tag{1.28}$$

Since we neglect negative energy contributions we can express the $D \longrightarrow NN$ vertex using the non-relativistic deuteron wave function [21, 22]:

$$\psi_D(p_s) = \frac{\bar{u}(p_s)\bar{u}(p_D - p_s)\Gamma_{DNN}}{[m^2 - (p_D - p_s)^2]\sqrt{(2\pi)^3 2m}} \tag{1.29}$$

Inserting Eq. 1.29 into Eq. 1.28 for the scattering amplitude within IA we obtain:

$$A_0^{\mu} = \sqrt{(2\pi)^3 2E_s}\,\psi_D(p_s) j^{\mu}(p_s, q). \tag{1.30}$$

1.3.3 Single Re-scattering Amplitude

Figure 1.11 (b) represents the single re-scattering amplitude. Using the Feynman rules (see Appendix A) and the kinematic restrictions mentioned earlier in the section we can express this amplitude as [18]:

$$A_1^{\mu} = -\frac{(2\pi)^{\frac{2}{3}}\sqrt{2E_s}}{4i}\int \frac{d^2k_t}{(2\pi)^2} f_{pn}(k_t)\cdot j^{\mu}_{\gamma^* N}(p_D - \tilde{p}_s + q, p_D - \tilde{p}_s)\cdot[\psi_D(\tilde{p}_s) - i\psi'_D(\tilde{p}_s)], \tag{1.31}$$

where $k_t = p'_{s\perp} - p_{s\perp}$ is the transverse component of the momentum transferred during NN re-scattering, $\tilde{p}_s(\tilde{p}_{sz}, \tilde{p}_{s\perp}) \equiv \mathbf{\tilde{p}_s}(p_{sz} - \Delta, p_{s\perp} - k_{\perp})$, ψ_D is the deuteron wave function defined in Eq. B1, and ψ'_D is defined in Eq. B7 (see Appendix B). The scattering amplitude $f_{pn}(k_t)$, which enters with ψ_D, and $f'_{pn}(k_t)$ which enters with ψ'_D, are generally different, since in the later case $f'_{pn}(k_t)$ corresponds to the off-shell amplitude. The off-shell contribution from ψ'_D is small and the off-shell effects in $f_{pn}(k_t)$ can be neglected. Using the Fourier transform of the deuteron wave function:

$$\psi_D(p) = \frac{1}{(2\pi)^2}\int d^3r\phi_D(r)e^{-ipr}, \tag{1.32}$$

and the coordinate space representation of the nucleon propagator:

$$\frac{1}{[p'_{sz} - p_{sz} + \Delta + i\epsilon]} = -i\int dz^0\Theta(z^0)e^{i(p'_{sz}-p_{sz}+\Delta)z^0}, \tag{1.33}$$

one can obtain a formula for the re-scattering amplitude which can be reduced to the Glauber approximation (GA) in the limit of zero longitudinal momentum transfer Δ as follows [18]:

$$A_1^\mu = -j^\mu(p_s+q,p_s)\frac{\sqrt{2E_s}}{2i}\int d^3r\psi(r)\theta(-z)\Gamma^{pn}(\Delta,-z,-b)e^{ip_sr}, \tag{1.34}$$

where $\vec{r} = \vec{r}_p - \vec{r}_n$ and the generalized profile function Γ^{pn} is defined as [18]:

$$\Gamma^{pn}(\Delta,z,b) = \frac{1}{2i}e^{-i\Delta z}\int f^{pn}(k_t)e^{-ik_\perp b}\frac{d^2k_\perp}{(2\pi)^2}. \tag{1.35}$$

Glauber theory was derived [14] in the approximation of stationary nucleons, i.e. for zero momentum of spectator nucleons in the target. The dependence of the profile function Γ^{pn} on the longitudinal momentum transfer Δ originates from the non-zero momentum of the recoiling nucleon, p_s. In conclusion, in the limit of single re-scattering, the generalization of GA, so called generalized eikonal approximation (GEA), requires the addition of a phase factor $e^{i\Delta z}$ in the Glauber profile function $\Gamma^{pn}(\Delta,z,b)$ [23] which accounts for the geometry of high-energy processes related to the longitudinal momentum transfer in the rescattering. This factor arises from excitations in the residual nuclear system. This result is analogous to the account of finite coherence length effects in the diffractive vector meson photoproduction from nuclei in the eikonal approximation [24]. In this case GEA reflects final longitudinal distances ($\leq R_A$ - nuclear radius) for photoproduction processes at intermediate energies.

1.3.4 Final State Interactions

When a fast nucleon propagates through the nuclear medium it reinteracts with the residual hadronic system and as a result some information about the preexisting momentum distribution of the bound (off-shell) nucleons is lost. Due to FSIs the reconstructed recoil momentum does not coincide with the actual momentum of the bound nucleon in the nucleus. Thus FSIs hinder the extraction of reliable information not only on nuclear structure, but also on fundamental hadronic properties in the medium. With increasing energy the soft (small angle) NN interaction is simplified in several ways. As seen in Figure 1.12 both pp and pn total cross sections become nearly energy-independent at lab momenta greater than a few GeV/c. This simplifies the description of FSIs because at small scattering angles the NN scattering amplitude is proportional to σ_{NN}^{total}, and is predominantly imaginary, which will conserve the helicity of the interacting particles. Another consequence of high energies is the onset of a new (approximate) conservation law in which the light-cone variable $\alpha_i = \frac{p_{i-}}{m}, i = 1, 2$, of the bound nucleon is conserved, and $p_- = p_0 - p_z$. The uniqueness of high-energy rescattering lies in the fact that although both energy and momentum of the bound nucleon are distorted due to re-scattering, the combination $p_0 - p_z$ is not. This can be seen from Figure 1.13, where α was calculated [18] as a function of the scattered nucleon momentum. The smaller the transferred momentum during re-scattering, the better the accuracy of the conservation law. Since the α distribution of bound nucleons is largely preserved, even in the pres-

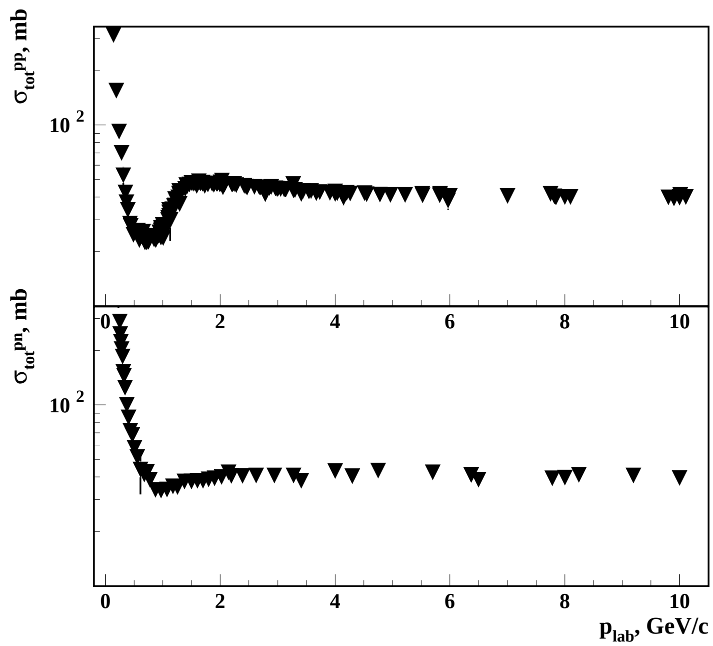

FIG. 1.12: Proton-proton and proton-neutron total cross sections as a function of the incoming momentum in the laboratory frame. Data is from Ref. [25].

ence of FSIs, we can effectively investigate the short-range properties of nuclei in semi-exclusive reactions. At electron scatterin small angles the momentum transfer is practically transverse and the NN scattering amplitude can be parameterized as $f_{NN} \approx is\sigma_{tot}e^{-\frac{\beta}{2}p_{\perp}^2}$, in which β is a slope parameter related to the angular distribution of NN scattering at forward angles and $p_{\perp}$ is the transverse component of the nucleon momentum. And one last feature of high momentum transfer exclusive reactions is summarized in the so called **Reduction Theorem** which basically states that **high energy particles propagating in the nuclear medium cannot interact with the same bound nucleon a second time**. As a consequence of this theorem, in the limits where the virtuality of a bound nucleon (which is interacting with the propagating, energetic nucleon) can be neglected, the sum of the interaction amplitudes for a given nucleon can be replaced by the invariant phenomenological NN scattering amplitude f_{NN} (see Figure 1.14), which can be extracted from the

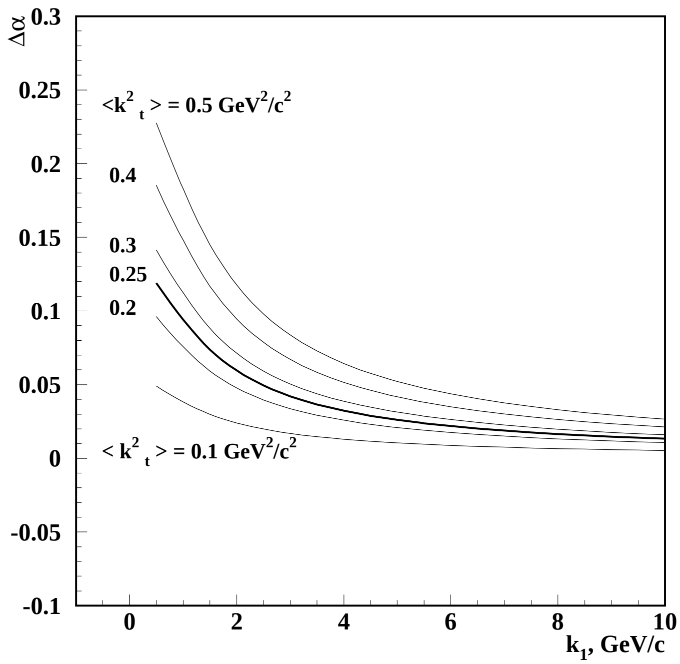

FIG. 1.13: Conservation of $\alpha = \frac{p_{i-}}{m}, i = 1, 2$ as a function of the propagating nucleon momentum, k_1, at different values of average momentum transfer $\langle k_t^2 \rangle$ [18].

NN scattering data [23]. This is the basic ingredient of the generalized eikonal approximation (GEA). The major difference from the conventional semi-classical approach (Glauber approximation) is that the GEA does not require the spectator nucleons to be stationary scatterers [14]. Using the reduction theorem a new set of Feynman diagram rules were derived for the scattering amplitude of a knocked-out nucleon undergoing n scatters off the (A - 1) residual system [15]. According to these rules (see Appendix C) the n-fold rescattering amplitude can be represented by n vertex amplitudes in which each vertex corresponds to one NN scattering. The NN scattering amplitude could be written as:

$$f^{NN} = \sigma_{tot}^{NN}(i + \alpha)e^{-\frac{\beta}{2}(p_3 - p_1)_\perp^2}, \tag{1.36}$$

where σ_{tot}^{NN} is the total NN cros section, α (not to be confused with the light-cone fraction) is the absorptive part of F_{NN}, and β is the slope of the variation of NN

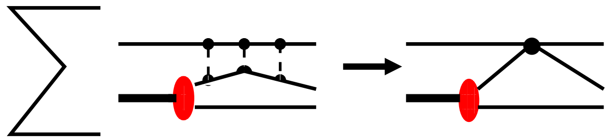

FIG. 1.14: The sum of the scattering vertices is replaced by the NN scattering amplitude in GEA.

scattering angular distribution (forward angle) with energy. These parameters can be extracted from experimental NN scattering data. Using these new Feynmann rules one can express the intermediate spectator states in the diagram of Figure A.1 in terms of nucleons but not nuclear fragments because we can use closure over various nuclear excitations in the intermediate state. Because the typical average scale for high energy reactions is significantly larger than for nuclear excitations, one can use closure, and after the evaluation of the intermediate-state nucleon propagators, the covariant amplitude will be reduced to a set of time ordered non-covariant diagrams. This establishes the connection between the nuclear vertex functions and the nuclear wave functions:

$$\psi_A(p_1, p_2, ...p_A) = \frac{1}{\left(\sqrt{(2\pi)^3 2m}\right)^{A-1}} \frac{\Gamma_A(p_1, p_2, ...p_A)}{D(p_1)}, \tag{1.37}$$

where $\Gamma_A(p_1, p_2, ...p_A)$ are the vertex functions which describes the transitions between a nucleus A and A nucleons with momenta $p_1, p_2, ...p_A$, and $D(p_1) = -(p_1 - m - i\epsilon)$ is the intermediate nucleon propagator. Here the wave functions ψ_A are normalized such that:

$$\int |\psi_A(p_1, p_2, ...p_A)|^2 \, d^3p_1 d^3p_2 ... d^3p_A = 1. \tag{1.38}$$

1.3.5 Meson Exchange Currents and Δ-Isobar Contributions

Estimates of contributions from meson exchange currents corresponding to diagrams similar to Fig. 1.15 (a) are rather controversial at large Q^2 since these terms are very sensitive to the assumed t-dependence of the meson-nucleon vertex form factors. These form factors are obtained from a fit to the experimental data. Experimental results at low Q^2 for d(e,e'N)N shows that meson exchanged

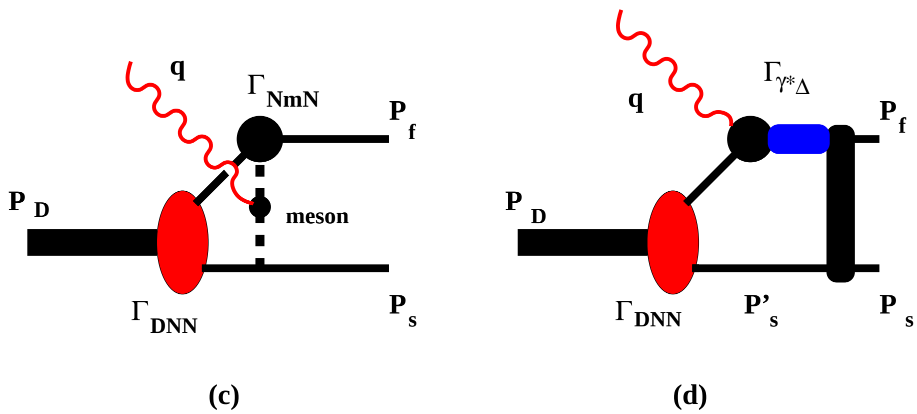

FIG. 1.15: Meson Exchange Currents (a) and the Δ-isobar contribution (b) for the e + d → N + N reaction.

currents (MEC) and Δ-isobar contributions (IC) to the NN scattering amplitude become dominant for higher momenta p_s. The virtuality of the exchange mesons grows with Q^2 for $Q^2 \gg m^2_{meson}$, where m_{meson} is the meson mass. One expects that the contributions of meson exchange currents will decrease with increasing virtuality Q^2. The overall Q^2 dependence of the MEC amplitude can be estimated as [18]:

$$\begin{aligned} A^{\mu}_{MEC} &\sim \int d^3p \cdot \psi(p) \frac{J^{\mu}_m(Q^2)}{(Q^2 + m^2_{meson})} \Gamma_{MNN}(Q^2) \\ &\propto \int d^3p \cdot \psi(p) \left(\frac{1}{(Q^2 + m^2_{meson})(1 + Q^2/\Lambda^2)^2} \right) \end{aligned} \tag{1.39}$$

where $J^{\mu}_m \sim 1/(Q^2 + m^2_{meson})$ is the meson electromagnetic current proportional to the elastic form factor of the meson, and $m^2_{meson} \approx 0.71$ GeV^2. For the meson-nucleon vertices, the meson form factor $\Gamma_{MNN} \sim (1 + Q^2/\Lambda^2)^{-2}$ with $\Lambda \sim 0.8 - 1.$ GeV^2. For large Q^2 quark counting rule lead to $\Gamma_{MNN} \sim \frac{1}{Q^6}$. Thus we expect that MEC will be strongly suppressed for $Q^2 \geq (m^2_{meson}, \Lambda) \sim 1$ GeV^2. SLAC experi-

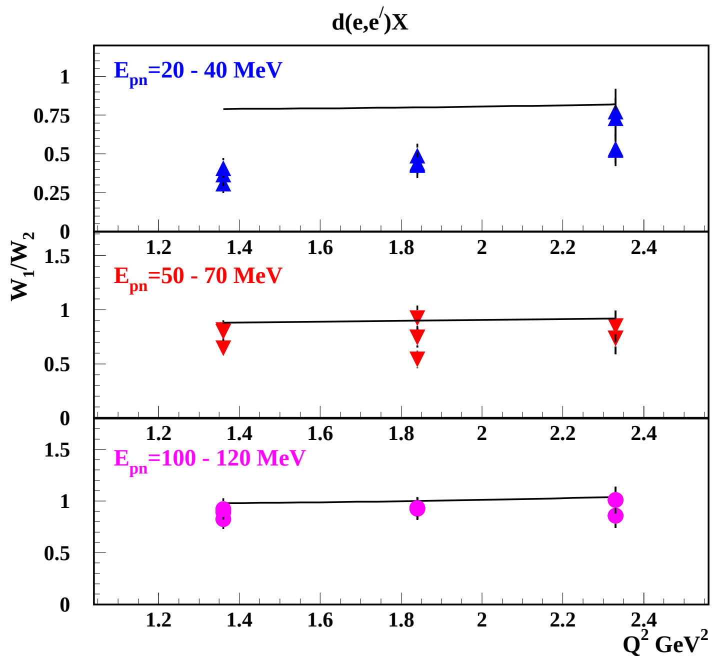

FIG. 1.16: The Q^2-dependence of W_1/W_2 for the inclusive d(e,e')X reaction. The data are from Ref. [26]. $E_{pn} = W_{pn} - m_D - \epsilon_d^{bound}$, where $W^2_{pn} = W^2_{\gamma^* D} = (q^\mu + p^\mu_D)^2$ is the CM energy of the proton and neutron in the final state of the reaction. Solid lines are PWIA predictions within light cone dynamics in the collinear approach [18].

ment [26] results as shown in Figure 1.16 indicate such suppression. The experiment measured the ratio of structure functions W_1/W_2 at the deuteron threshold $x \rightarrow 2$. Particularly the Q^2-dependence of this ratio at fixed relative energy of the final pn system is sensitive to the Q^2-dependence of MEC contributions. Fig. 1.16 indicates that MEC contribution decreases with the increase of Q^2 and become negligible for $Q^2 \geq 1.5$ GeV^2 and $E_{pn} \geq 50$ MeV.

For the case of IC contributions, the virtual photon produces the Δ-isobar in the intermediate state which subsequently re-scatters off the spectator nucleon through

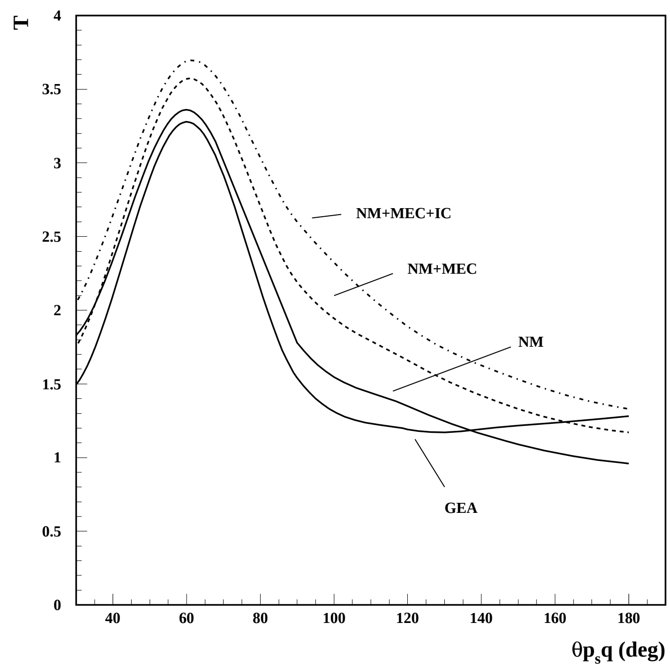

FIG. 1.17: The θ_n dependence of ratio T at $Q^2 = 1$ GeV^2. The curve marked by "NM" corresponds to the cross section including final state interactions calculated in Ref. [12]. The curves with "NM+MEC" and "NM+MEC+IC" correspond to the calculations of Ref. [12] including meson exchange and Δ-isobar contributions respectively. The curve marked by "GEA" corresponds to the cross section calculations of Ref. [18] using the generalized eikonal approximation.

the $\Delta N \to NN$ channel, as is shown diagrammatically in the Figure 1.15 (b). The Δ-isobar current contribution can be estimated as [18]:

$$A^{\mu}_{IC} \sim i \int \psi_D \left(p_{mt} - k_t, p_{mz} - \frac{m^2_{\Delta} - m^2}{2q} \right) J_{\gamma^* N\Delta}(Q^2) A_{\Delta,N\to NN}(k_t) d^2k_t, \quad (1.40)$$

where $J_{\gamma^* N\Delta}(Q^2)$ and $A_{\Delta,N\to NN}$ are the electromagnetic $N \to \Delta$ and hadronic $N\Delta \to NN$ transition amplitudes, respectively. There are several factors that contribute to the suppression of IC contributions at high Q^2 as compared to the IA contributions. The main factors are the energy dependence of $A_{\Delta,N\to NN}$ amplitude and the Q^2-dependence of the electromagnetic $\gamma^* N\Delta$ transition form factors, as compared with the elastic $NN \to NN$ amplitude and the $\gamma^* N$ form factor, respectively. The $N \to NN$ amplitude is known to be dominated by the pion

Reggeon exchange with the ρ-Reggeon which dominates at very high energies, thus being a small correction up to energies of $\sqrt{s} \sim 30$ GeV [27]. The scattering amplitude of an interaction depends on the spin, J, of the exchanged particle as: $A \sim s^J$, in which s is the square of the center of mass energy of final the NN system ($s \approx (\frac{2}{x} - 1)Q^2 + 2m^2$). Using the spin dependence of scattering amplitude the $\Delta N \to NN$ transition amplitude is being suppressed at least by a factor $\propto 1/Q^2$ (at $Q^2 \geq 2$ GeV^2), as compared with the elastic $NN \to NN$ amplitude, leading to a similar suppression of IC contributions. There is an experimental indication that the electromagnetic $\gamma^* N\Delta$ transition form factor decreases even faster with Q^2 as compared to the elastic $\gamma^* NN$ transition amplitude [28]. In Figure 1.17 are shown the results of the model of Ref. [12]. The ratio between the full cross section (containing all the contributions of Figure 1.11) to the PWIA cross section, T, is plotted versus the nucleon polar scattering angle. Calculations have been performed in the kinematics $Q^2 = 1$ GeV^2, $q_0 \sim 400 - 500$ MeV/c for the spectator momentum $p_n = 400$ MeV/c. Within this model the contributions of meson and isobar currents, in the kinematics where NN soft re-scattering is dominant, are small ($\sim 6\%$ for MEC and $\sim 4\%$ for IC contributions).

1.3.6 d(e,e′N)N Cross Section

The cross section of d(e,e′N)N can be written in terms of leptonic and hadronic tensors as follows:

$$\frac{d\sigma}{dE' d\Omega' d^3p_f/2E_f d^3p_s/2E_s} = \frac{E'_e}{E_e}\frac{\alpha^2}{q^4}\eta_{\mu\nu}T_D^{\mu\nu}\delta^4(p_D + q - p_f - p_s) \tag{1.41}$$

where $\eta_{\mu\nu} = \frac{1}{2}Tr(\hat{k_2}\gamma_\mu\hat{k_1}\gamma_\nu)$, $k_1 \equiv (E_e, \vec{k}_1)$, and $k_2 \equiv (E'_e, \vec{k}_2)$ are the four-momenta of the incident and scattered electrons, respectively. The electromagnetic tensor $T_D^{\mu\nu}$

of the deuteron is:

$$T_D^{\mu\nu} = \sum_{spin} (A_0 + A_1)^\mu (A_0 + A_1)^\nu \tag{1.42}$$

where A_0 and A_1 correspond to impulse approximation and single re-scattering amplitudes calculated earlier in Eqs. 1.30 and 1.34. Using the fact that in soft NN re-scattering $< k_t^2 >_{rms} \sim 250\ MeV^2/c^2 \ll |\mathbf{q}|^2$ the bound nucleon electromagnetic current can be factorized out of the integral in Eq. 1.31. The distorted wave impulse approximation (DWIA), in which the scattering cross section is represented as a product of the off-shell eN scattering cross section σ_{eN} and the distorted spectral function $S_D(p_f, p_s)$ replaces PWIA in this case:

$$\frac{\sigma}{dE' d\Omega' dp_f} = p_f^2 \sigma_{eN} S_D(p_f, p_s). \tag{1.43}$$

Here the distorted spectral function can be represented as follows:

$$S_D(p_f, p_s) = \left| \psi_D(p_s) - \frac{1}{4i} \int \frac{d^2 k_t}{(2\pi)^2} f_{pn}(k_t) \cdot [\psi_D(\tilde{p}_s) - i\psi'_D(\tilde{p}_s)] \right|^2 \tag{1.44}$$

The off-shell cross section σ_{eN} contains ambiguity in the spinor part related to the fact that the knocked-out nucleon is bound. The above calculations using the factorization theorem are assuming that the contributions from MEC and IC currents are small in the kinematics where NN rescattering is dominant. In contrast with these earlier theoretical predictions, a recent theoretical development [29] supports a major contribution due to IC and MEC currents to the scattering amplitude in the same kinematical region mentioned above. These calculations are discussed in the next section.

1.3.7 New Theoretical Developments

A new theoretical approach [29] uses kinematics where re-scattering takes place on a propagating on-shell nucleon. In this picture the electron scatters on a proton at rest which propagates on-shell and re-scatters on the neutron which is also at rest. In the Lab frame, the soft neutron recoils at 90° with respect to the fast proton which is emitted in the forward direction. The angle between the soft neutron momentum and the momentum transfer direction is defined as θ_R. Two body kinematics imposes that the angle θ_R of the re-scattering peak moves with the recoil momentum (see Figure 1.18). The same occurs, in a different part of the phase space, when the electron interacts with a neutron (the case of this analysis). The

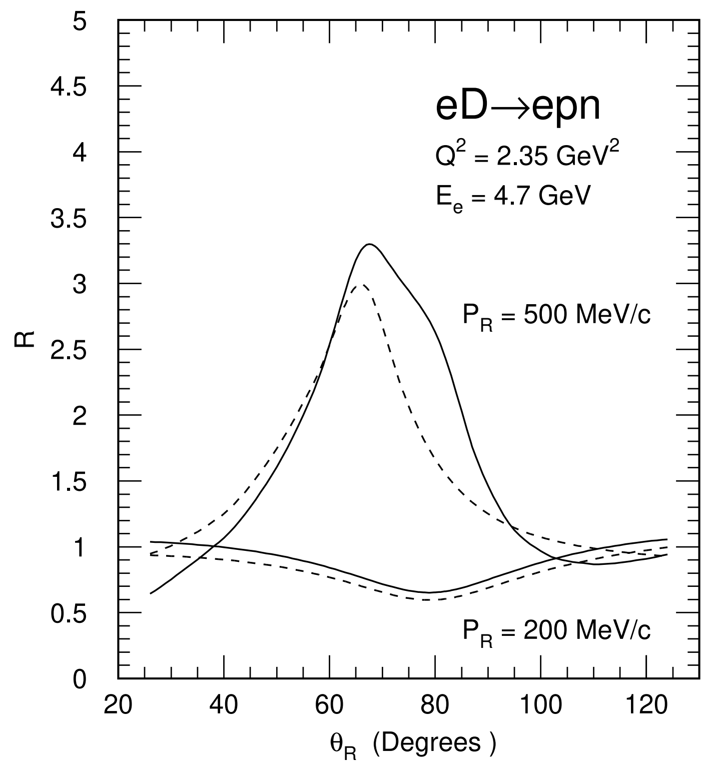

FIG. 1.18: The ratio $R = \frac{\sigma^{FULL}}{\sigma^{PWIA}}$ versus the angle between the recoil nucleon (neutron) and the virtual photon momentum $\vec{q}$ direction. FSI (dashed lines) and MEC+IC (full lines) for two fixed values of recoil momenta are shown [29].

model involves on-shell elementary matrix elements and they are maximized in the quasi-elastic kinematics, when the re-scattering takes place on a nucleon at rest, and $x = \frac{Q^2}{2m_p\nu} = 1$, where x is the Bjorken scaling variable, ν is the energy of the exchanged virtual photon, and m_p is the mass of the nucleon. In these kinematics the singular part of the FSI and MEC amplitudes does not depend on Q^2, beyond the momentum dependence of the momentum operators. Thus, one expects that with increasing Q^2 the FSI, MEC, and IC contributions will dominate the total cross section. By choosing these kinematics we could study exotic components of the nuclear wave function via color transparency or color screening. Figure 1.18 shows the features of quasi-elastic on-shell re-scattering effects. It shows the dependence of the ratio between the full cross section of the d(e,e′p)n reaction and the quasi-free (PWIA) contribution versus the angle θ_R between the recoiling nucleon and the virtual photon, for constant recoil momentum. Near $\theta_{p_s,q} = 70^o$ (where $x = 1$) FSIs are maximized, and on-shell rescattering is dominant.

At low values of the recoil momentum ($p_s = 200$ MeV/c), the on-shell nucleon cross section is reduced by screening, while at high values of the recoil momentum ($p_s = 500$ MeV/c) the quasi-free contribution is suppressed due to re-scattering effects. Similarly, the meson exchange currents (MEC) and Δ-isobar (IC) contributions induce "singularities" at large recoil angles and shift the NN re-scattering peak (Figure 1.18 - full lines). Other virtual nucleon resonances can be excited and propagate, widening the peak even further toward large re-scattering angles. In the range of recoil momenta of a *few hundred* MeV/c the Δ-isobar contribution is larger than that of higher mass resonances. This approach uses relativistic propagators to estimate the PWIA and FSI contributions, and no angular approximation is made in evaluating the integral loops [30]. The PWIA and FSI scattering amplitudes for d(e,e′p)n are computed using the following descriptions:

$$\begin{aligned} T_{PWIA} &= \frac{1}{\sqrt{4\pi}}\left[\sum_{m_1}\langle m_1|J_p(q^2)|m_p\rangle\langle\frac{1}{2}m_p\frac{1}{2}m_2|1M_J\rangle U_0(\vec{p}_2)+\right. \\ &+ \left.\sum_{m_2}\langle m_1|J_n(q^2)|m_n\rangle\langle\frac{1}{2}m_n\frac{1}{2}m_1|1M_J\rangle U_0(\vec{p}_1)\right] + D\ Wave, \end{aligned} \tag{1.45}$$

$$
\begin{aligned}
T_{FSI} &= \sum_{\lambda_p,\lambda_n,m_l,m_s} \int \frac{d^3\vec{n}}{(2\pi)^3} \frac{m}{E_p(p^0 - E_p + i\epsilon)} \\
& \quad \big\{ (\lambda_p|J_p(q^2)|m_s - \lambda_s)(\vec{p}_1 m_2 \vec{p}_2 m_1|T_{NN}|\vec{p}\lambda_p\vec{n}\lambda_n) \\
&+ \quad (\lambda_p|J_p(q^2)|m_s - \lambda_s)(\vec{p}_2 m_2 \vec{p}_1 m_1|T_{NN}|\vec{p}\lambda_p\vec{n}\lambda_n) \big\} \\
&\times \quad (\frac{1}{2}\lambda_p \frac{1}{2}(m_s - \lambda_n)|1 m_s) \left\{ \frac{1}{\sqrt{4\pi}} U_0(|\vec{n}|)\delta_{M_J m_s}\delta_{m_l 0} \right. \\
&+ \quad \left. U_2(|\vec{n}|)(2 m_l m_s|1 M_J) Y_2^{m_l}(\hat{\vec{n}}) \right\}, \qquad (1.46)
\end{aligned}
$$

where $E_p = \sqrt{m^2 + (\vec{k} - \vec{n})^2}$ and $p_0 = M_D + \nu - \sqrt{m^2 + \vec{n}^2}$. The momenta and magnetic quantum numbers of the outgoing proton and neutron are respectively $\vec{p}_1$, $\vec{p}_2$, m_1 and m_2, while the magnetic quantum number of the deuteron target is M_J. The S and D parts of the deuteron wave function are respectively U_0 and U_2. In this model [29] the dipole expression is used for the magnetic form factors of the proton and the neutron. The Galster parameterization [31] was used for the neutron electric form factor, while the latest JLab experimental values [32] were used for the proton electric form factor. Because the energy of the virtual photon is larger than the sum of the masses of the two nucleons, the knocked out nucleon $(\vec{p}, \lambda_p)$ can propagate on-shell. Due to the dominance of the S-state in the deuteron wave function, the corresponding singular part of the integral is maximum when the scattering of the electron on a nucleon at rest takes place in quasi-free kinematics. In Figure 1.19 the width of the on-shell (dot-dashed line) peak reflects the Fermi motion inside the target nucleon, while the off-shell part of the cross section is suppressed at $x = 1$. The classical Glauber approximation uses a linearization of the nucleon propagator and neglects recoil effects. Thus, the re-scattering peak is fixed at 90^o. GEA takes into account the higher order recoil terms in the nucleon propagator of Eq. 1.46, and neglects only terms on the order of $p_\perp^2/m_p^2$. Laget's diagrammatic approach, which takes into account the full kinematics, predicts the FSI peak (see Figure 1.19 - full

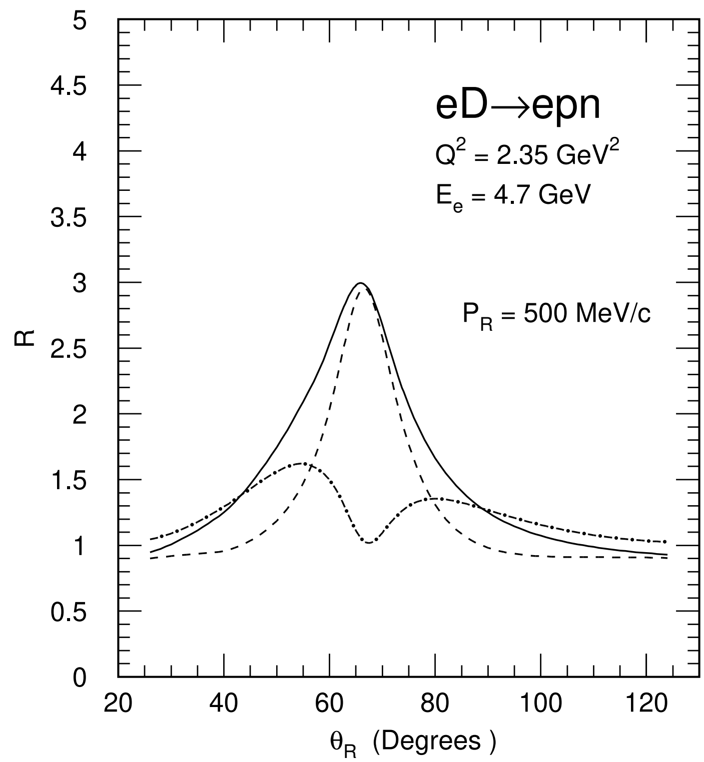

FIG. 1.19: Angular dependence of the ratio of the FSI to the PWIA cross sections for the on-shell (dot-dashed line) and respectively for the off-shell (dashed line) propagating nucleon.

line) at the same place as the GEA predictions. This model uses a parametrization of NN scattering amplitude of the form:

$$T_{NN} = \alpha + i\gamma(\vec{\sigma}_1 + \vec{\sigma}_2) \cdot \vec{k}_\perp + (\text{spin} - \text{spin}) \ \text{ terms}, \tag{1.47}$$

in which $\vec{k}_\perp$ is the unit vector perpendicular to the scattering plane. This parameterization takes into account the fact that for higher kinetic energies of the outgoing fragments, more inelastic partial waves make it difficult to compute the NN cross section from a potential. Above 500 MeV, the central part α of the NN scattering amplitude is dominant, is mostly absorptive, and can be expressed as:

$$\alpha = -\frac{W p_{CM}}{2m^2}(\epsilon + i)\sigma_{NN} e^{-\frac{\beta}{2}t} \tag{1.48}$$

In the forward direction its imaginary part is related to the total cross section σ_{NN}, while the slope parameter β is related to the angular distribution of the NN scattering amplitude at forward angles. Both quantities are extracted from experimental

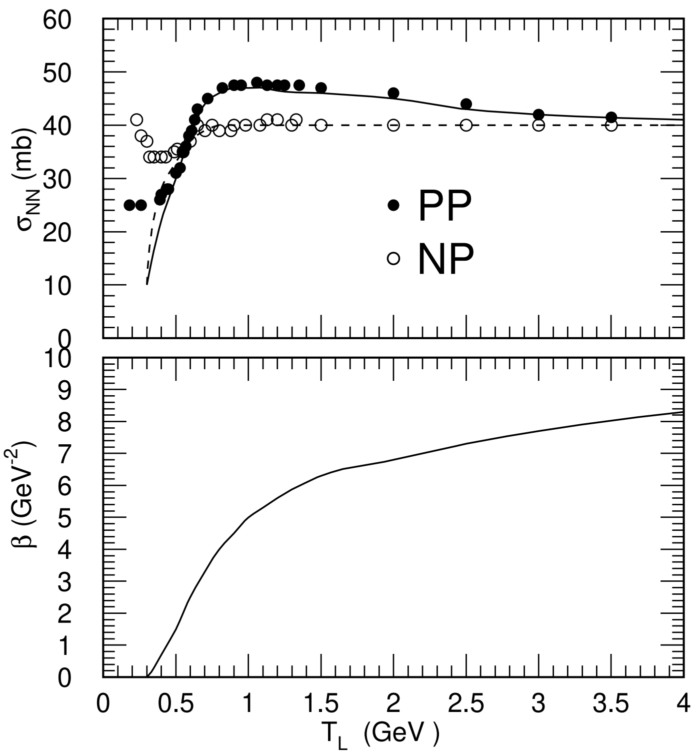

FIG. 1.20: The experimental NN cross section σ_{NN} and β variation with energy used in the parameterization described in the text [29].

results from Los Alamos, COSY, and Saturne (see Figure 1.20). This parameterization also includes the low energy regime by expanding the amplitude in terms of SPD waves of the Paris potential (with a small contribution for recoil momenta T_L above 500 MeV/c). The Δ-isobar and MEC amplitude contributions contain both π and ρ meson exchanges and are computed according to Eqs. (C1) and (C2) of Ref. [33]. The author of Ref. [29] implemented the full relativistic description of the πNN vertex, instead of the classical description in Eq. (C2), with a small final effect on the overall estimation of MEC contributions. For the $N \to \Delta$ form factor a general fit to the latest experimental values [34] was used: $F_{\gamma N\Delta} = F_{dip}(Q^2)(1 - Q^2/9)$,

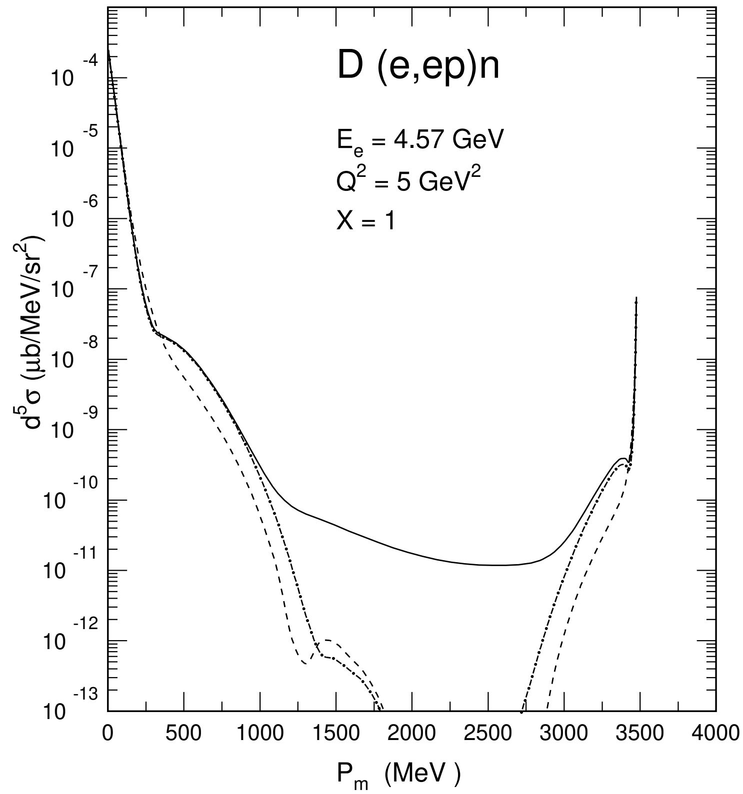

FIG. 1.21: The momentum distribution in the d(e,e′p)n reaction at $x = 1$ and $Q^2 = 5$ GeV^2. Dashed line PW. Dash-dotted line: with FSI. Full line: MEC and Δ included [29].

as shown in Figure 1.22. The Δ formation amplitude is suppressed at high Q^2 (see Fig. 1.22) due to its steep fall-off compared with the nucleon dipole form factor F_{dip}. Also in quasi-free kinematics the singularities associated with Δ propagation are weaker than the FSI amplitude, due to the fact that the Δ pole is off from the energy axis by its half width. Figure 1.21 shows the full angular distribution of the d(e,e′p)n reaction for $Q^2 = 5$ GeV^2, at $x = 1$. The Δ formation term has a small contribution up to $p_n \approx 800$ MeV/c, but is predominant for the higher momentum range. At large scattering angles of the recoil nucleon FSI, MEC and IC contributions dominate the interaction between the electron and the nucleon. Preliminary experimental results [35,36] of the electro-disintegration of ^{3}He and ^{4}He show a good

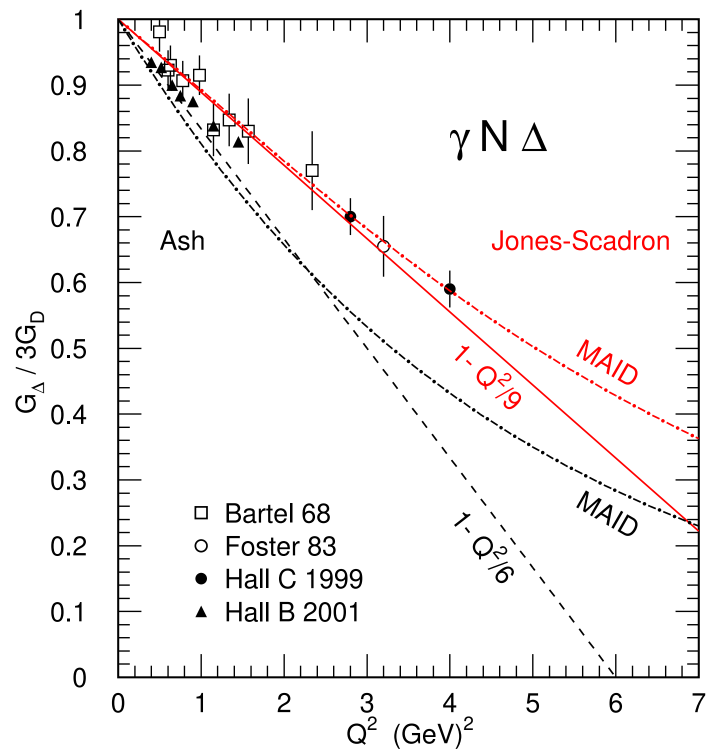

FIG. 1.22: The Δ form factor G_M^* is plotted as a function of Q^2. Experimental values for different data sets are shown together with several theoretical prediction from MAID.

agreement with the diagrammatic method [29] described above and are presented in Figure 1.23.

1.3.8 Nuclear Transparency T and Re-scattering Effects

The ratio T, called nuclear transparency, of the cross section σ^{IA+FSI}, given by the distorted plane wave approximation of Eq. 1.44, to the cross section σ^{IA}, calculated with only the IA amplitude A_0 included, is an effective measure of re-scattering effects in nuclei. The nuclear transparency T is then:

$$T = \frac{\sigma^{IA+FSI}}{\sigma^{IA}} = \frac{S(p_f, p_s)}{|\psi_D(p_s)|^2} \tag{1.49}$$

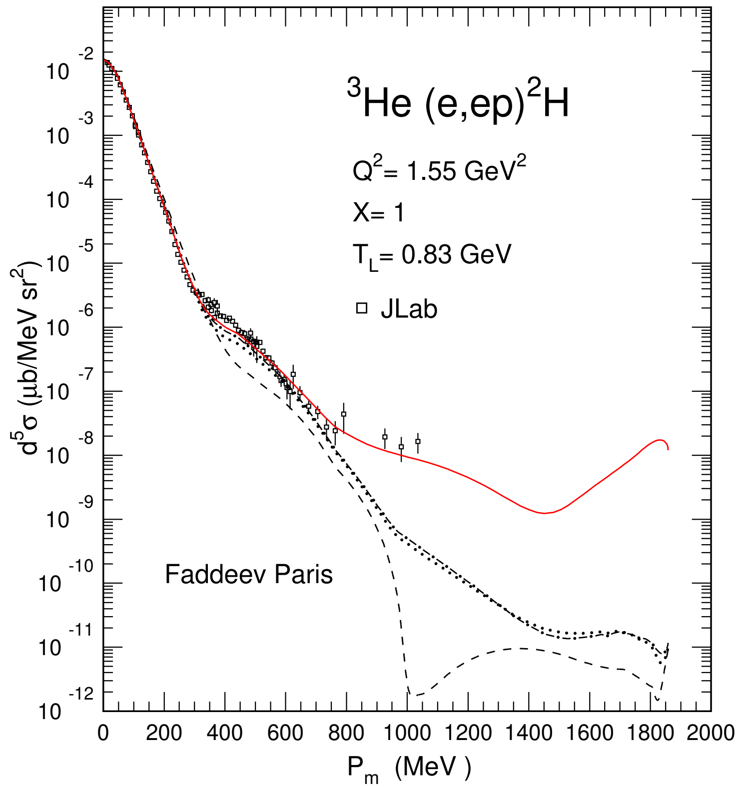

FIG. 1.23: The momentum distribution in the ^{3} He(e,e'p)d reaction at $x = 1$ and $Q^2 = 1.55$ GeV^2. Dashed line: PW. Dotted line: with FSI. Dash-dotted line: 2 body MEC and Δ included. Full line: 3 body mechanism included [29].

By calculating T as a function of the recoil nucleon angle with respect to $\vec{q}$ for different values of nucleon momenta (see Figure 1.24), we can clearly see the consequences of re-scattering effects on the total cross section. At recoil momenta $p_s \leq 300$ MeV/c, T has a minimum and generally $T < 1$ while at recoil momenta $p_s \geq 300$ MeV/c, T has a distinctive maximum and $T > 1$. These effects could easily be explained if we recall the fact that for soft NN re-scattering the amplitude is mainly imaginary $f_{pn} = \sigma_{tot}(i + \alpha)e^{-\frac{B}{2}k_\perp^2}$ with $\alpha \ll 1$. Within the theoretical frame described earlier by Strikman and Frankfurt (Eqs. 1.43 and 1.44), Eq. 1.44

inserted into Eq. 1.49 yields:

$$T \approx 1 - \frac{1}{2}\left|\frac{\psi_D(p_s)\cdot\int\frac{d^2k_\perp}{(2\pi)^2}f_{pn}(k_\perp)\cdot[\psi_D(\tilde{p}_s) - i\psi'_D(\tilde{p}_s)]}{\psi_D^2(p_s)}\right| + \frac{1}{4}\frac{\left|\int\frac{d^2k_\perp}{(2\pi)^2}f_{pn}(k_\perp)\cdot[\psi_D(\tilde{p}_s) - i\psi'_D(\tilde{p}_s)]\right|^2}{\psi_D^2(p_s)}. \quad (1.50)$$

Here ψ_D and ψ'_D are the on-shell and off-shell deuteron wave functions, respectively. In Eq. 1.50 we can observe that the second term, called the interference term,

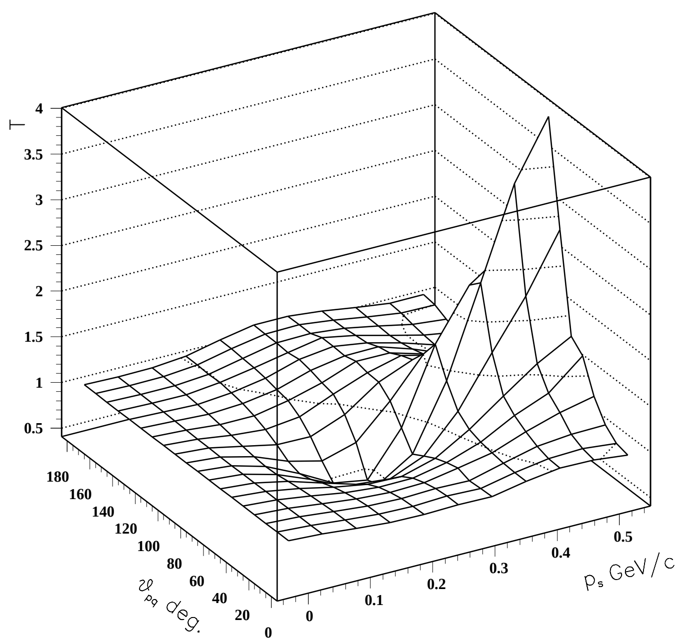

FIG. 1.24: The dependence of the transparency T on the angle θ_{sq} and the momentum p_s of the recoil nucleon. The angle is defined with respect to $\vec{q}$.

has a negative sign and is proportional to $\frac{\psi_D(p_{sz},p_{s\perp})\psi_D(p_{sz}-\Delta,p_{s\perp}-k_\perp)}{\psi_D^2(p_{sz},p_{s\perp})}$. Thus, in the kinematics where the interference term is dominant there is screening of the overall cross section. The maximal screening is found at $p_{s\perp} \approx 200$ MeV/c, at which the square of the third term, called the re-scattering term, is small, resulting in $T \leq 1$. A further increase of p_s suppresses the relative contribution of the interference term as compared to the square of the re-scattering term which results in $T > 1$. The dominance of the re-scattering term as compared to the interference term,

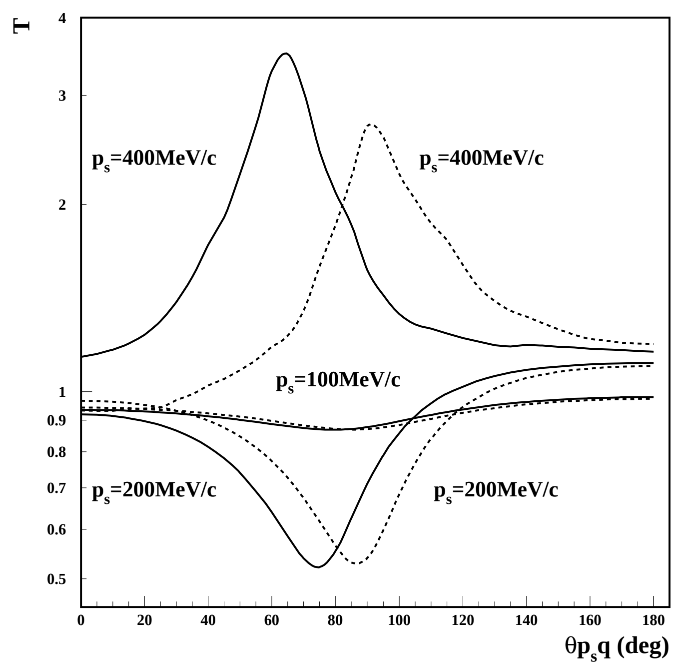

FIG. 1.25: The $\theta_{p_s q}$ dependence of T at different values of p_s. Solid lines are obtained within GEA, and dashed lines are obtained within Glauber approximation [62].

with increasing p_s, is explained by the fact that the interference term grows as $\sim \frac{1}{|\psi_D(p_s)|}$ while the re-scattering term grows as $\sim \frac{1}{|\psi_D(p_s)|^2}$. Predictions of T calculated within GEA and in the Glauber approximations are rather close when the recoil nucleon momenta are small (see Figure 1.25). Glauber theory assumes that the target nucleons are stationary scatterers and therefore neglects their Fermi motion. At large Fermi momenta predictions of both approaches differ considerably. In the case of $p_s = 400$ MeV/c the GEA and Glauber approximation predictions for the angular dependence of the maximal contribution of the re-scattering amplitude (i.e. the position of the maximum of T in Figure 1.25) differ by as much as 30^o. Such a difference is quite dramatic and is one of the motivations behind this analysis.

As mentioned earlier one of the important features of high energy scattering is the

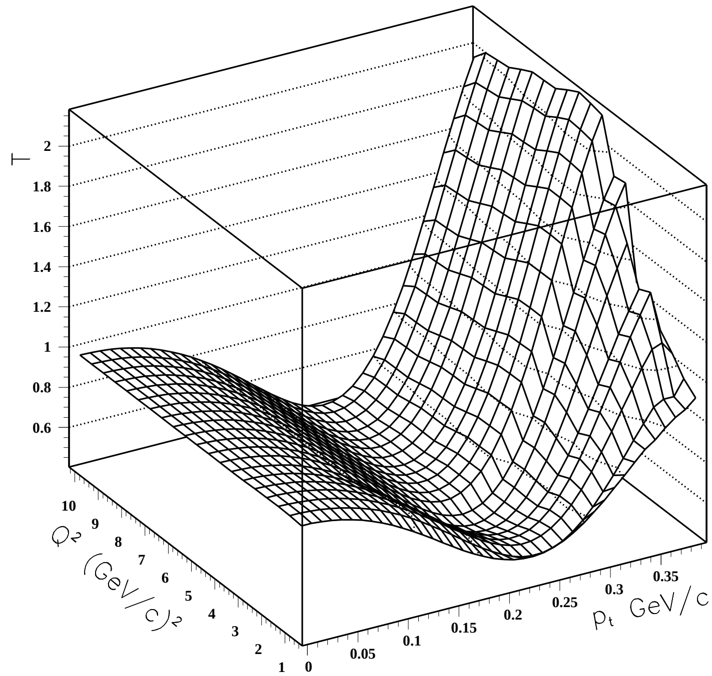

FIG. 1.26: T as a function of Q^2 and p_{st} at $\alpha = \frac{E_s - p_{sz}}{m} = 1$.

energy independence of the NN soft scattering cross section (e.g. Figure 1.20), which enters into the re-scattering amplitude of the d(e,e'N)N reaction as shown diagrammatically in Figure 1.11 (b). This feature bring us to the dependence of T upon Q^2. As Figure 1.26 shows, with increase of Q^2, T becomes practically independent of Q^2 at a given value of p_s. Within GEA the Q^2 independence of T can be used as a baseline to study the onset of the color coherent regime in high Q^2 exclusive reactions off nuclei.

The elastic $\gamma^* N$ interaction, at high $Q^2 \geq Q_0^2$ ($Q_0^2 \approx 6 - 8$ GeV^2), is dominated by the contribution of the minimal Fock component of the quark-gluon wave function of the nucleon, which corresponds to a point-like configuration (PLC). Thus for $Q^2 \geq Q_0^2$ in the QCD picture it is expected that hard elastic scattering will favor PLCs from the wave function of the nucleon. This feature is characteristic of both the perturbative [38, 46] and non-perturbative [23] regime of QCD. If PLCs are produced in high Q^2 exclusive reactions, then because of the color screening effect we expect that they will propagate through the nuclear medium largely undisturbed, without final state interactions. This phenomena is called Color Transparency (CT) and is believed to be responsible for specific upward and downward changes in the hard quasi-elastic d(e,e'N)N cross section, depending on the kinematics which control the relative size of the screening and re-scattering terms mentioned earlier in the section. This phenomenon was observed at FNAL in high energy regime when perturbative QCD is valid [39, 40].

In non-perturbative QCD, observation of color coherent phenomena is obstructed by the fact that at finite energies PLCs will evolve to the normal hadronic states during their propagation through the nucleus. As a result FSI will not be negligible at the later stages of the interaction. The rapid expansion of PLCs, is believed to be the major reason that prevented the observation of the onset of color transparency in A(e,e'p)X reactions for the range of Q^2 up to 8 GeV^2 [7, 8]. Thus the major issue in the studies of color coherence phenomena in the non-perturbative regime is the suppression of the expansion of PLCs which can be achieved [41, 42] in exclusive d(e,e'N)N reactions with large values of momentum transfer.

There are several non-perturbative models which allow an estimate of color coherence by incorporating PLC expansion (see e.g. [43, 44]). One of the models developed is the Quantum Diffusion Model (QDM) of Ref. [43]. Basically this model introduces the dependence of the scattering amplitude on the transverse size of the PLC. The expansion of PLC is included in the QDM model by allowing the re-scattering amplitude to depend on the distance from the photon absorption point. The calculation of the deuteron electro-disintegration cross section within the QDM model is performed by rewriting the amplitude of Eq. 1.31 in coordinate representation and using a new scattering amplitude for the PLC–N re-interaction $f^{PLC,N}$

to replace the amplitude of NN scattering f_{pn}. Within QDM:

$$f^{PLC,N}(z,k_t,Q^2) = i\sigma_{tot}(z,Q^2)\cdot e^{\frac{b}{2}t}\cdot \frac{G_N(t\cdot \sigma_{tot}(z,Q^2)/\sigma_{tot}}{G_N(t)}, \tag{1.51}$$

where $b/2$ is the slope of the elastic NN amplitude, $G_N(t) \approx (1-t/0.71)^2$ is the Sachs form factor, $t = -k_t^2$, and $\sigma_{tot}(l,Q^2)$ is the effective total cross section of the interaction of PLCs at a distance l from the interaction point. In QDM $\sigma_{tot}(l,Q^2)$ takes the following form:

$$\sigma_{tot}(l,Q^2) = \sigma_{tot}\left[\left(\frac{l}{l_h} + \frac{\langle r_t^2(Q^2)\rangle}{\langle r_t^2\rangle}(1-\frac{l}{l_h})\right)\Theta(l_h - l) + \theta(l - l_h)\right], \tag{1.52}$$

in which $l_h = 2p_f/\Delta M^2$, with $\Delta M^2 = 0.7 - 1.1$ GeV^2. Here $\langle r_t^2(Q^2)\rangle$ is the average transverse size squared of the configuration produced at the interaction point. Other non-perturbative models are incorporating the production and expansion of PLCs using the fact that with an increase of energies the contribution from the inelastic transitions with intermediate baryonic resonances of the same spin as the nucleon (as N^* and N^{**}) are no longer suppressed. As a consequence the intermediate hadronic state (after the γ^*N vertex as shown in the diagram of Figure 1.11 (b)) can be represented as a superposition of nucleonic, baryonic excitation and continuum states. The three-state model uses the assumption that the intermediate state is a superposition of three resonance states (N,N*, and N**):

$$|PLC\rangle = \sum_{m=N,n^*,N^{**}} F_{m,N}(Q^2)|m\rangle, \tag{1.53}$$

where $F_{m,N}(Q^2)$ are elastic ($m = N$) and inelastic transition form factors. Color transparency is introduced in this model as the condition of lack of FSI at the interaction point (where PLCs are produced): $T_S|PLC\rangle = 0$, where T_S is the 3×3 Hermitian matrix representing the small angle final-state interactions. The cross section in this model is obtained from Eq. 1.43 replacing the scattering amplitude f_{pn} with T_S. Detailed numerical calculations were done in Ref. [41], and they demonstrated that both models, the QDM model and the three-states model, predict similar magnitudes for the color transparency phenomena, as a suppression of final state re-scatterings. In order to observe a color coherent effect, we need to identify the

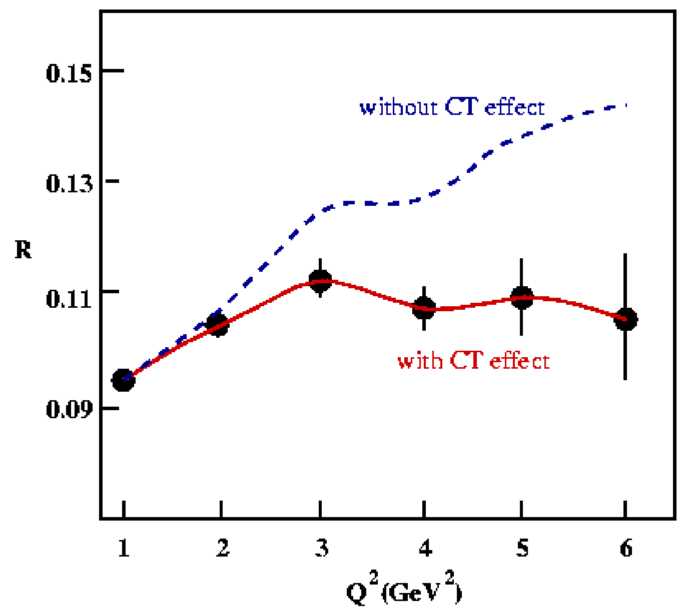

FIG. 1.27: Theoretical predictions for the Q^2 dependence of the ratio R for the exclusive d(e,e'p)n reaction with CT effects (solid line) and without CT effects (dashed line) together with projected data points and error bars for the experiment E94-019 [45] at TJANF.

quantity most sensitive to the suppression of FSIs with increasing Q^2. As it was shown in Figure 1.24, within GEA, FSI are dominant in the transverse kinematics ($\theta_{p,q} \approx 90^o$), corresponding to $\alpha = \frac{E_s - psz}{m} = 1$. From Figures 1.24 and 1.25 we can see that for $p_s \lesssim 300$ MeV/c the screening term of Eq. 1.42 is dominant, resulting in $T < 1$. At $p_s \gtrsim 350$ MeV/c the dominant contributions arises from the re-scattering term in Eq. 1.42 and as a result $T > 1$. Based on these observations a ratio of cross section, measured at kinematics where double scattering is dominant, to the cross section measured at kinematics where the screening effects are the main contributors, becomes a very sensitive tool in studying the suppression of FSIs with increasing Q^2:

$$R = \frac{\sigma(p \approx 400MeV/c)}{\sigma(p \approx 200MeV/c)} \tag{1.54}$$

A prediction for the ratio R evolution with Q^2 for actual experiment is presented in the Figure 1.27. It can be seen here that color coherent effects will suppress FSIs and consequently will reduce the transparency T with increasing momentum transfer Q^2.

1.4 Overview of Existent Data

To observe color coherent effects we need processes that are dominated by scattering from PLCs and that can be computed using perturbative quantum chromodynamics (pQCD). Several such processes have been suggested in the literature, and corresponding pQCD factorization theorems have been proven for them. These processes include diffractive pion dissociation into two high transverse momentum jets [23] and exclusive vector meson production [46, 47]. Recent experiments at HERA which focused on exclusive vector meson production in deep inelastic scattering (DIS) have confirmed the basic pQCD predictions – a rather fast increase of the cross section with energy at large Q^2, a dominance of the longitudinal photon cross section, and a weaker t-dependence of the ρ-meson production at large Q^2 relative to J/ψ photo-production. Di-jet and vector meson production processes have a very particular characteristic: in the region of small shadowing (for values of $x \geq 0.02$) the interaction of a $q\bar{q}$ pair with a nuclear target does not suffer attenuation through nuclear matter, thus the pair $q\bar{q}$ becomes "color coherent". As a result, the amplitude of this process at $t = 0$, and the cross section of quasi-elastic processes are each proportional to the nucleon number A. At Fermi laboratory, E791 experiment observed color transparency in the exclusive coherent production of two jets in the process $\pi + A \rightarrow 2 \;\; jets + A$ at pion energies of $E_\pi = 500$ GeV.

As predicted [23], the A-dependence of the process [40] led to a seven times larger platinum/carbon ratio than soft physics would have predicted. Evidence for color transparency effects was reported also in incoherent vector meson production in DIS scattering of muons [48]. It can be concluded that CT concept has been established experimentally as well as theoretically using high energy processes.

The first electron-proton scattering A(e,e'p) experiment looking for color transparency was NE18 performed at SLAC [7, 8]. The maximum value of the momentum transfer of the virtual photon Q^2 was ≈ 7 GeV^2, corresponding to a formation length $l_c \sim \frac{1}{\Delta M}\frac{p_h}{m_h} \leq 2$ fm, where p_h and m_h are the momentum and the mass of the interacting hadron, and ΔM is the characteristic excitation energy defined by $\Delta M^2 = (m_{ex}^2 - m_h^2)$ with m_{ex} being the invariant mass of the closest exited state. Predictions of color coherent effects in this kinematical range were rather small and they were consistent with the NE18 data. Recent Jefferson Lab experiments [9,10], have been performed in the kinematical range up to $Q^2 = 8$ GeV^2 and no color transparency effects have been observed. However, the accuracy of these experiments and the effects of expansion in the realistic models are not sufficient to rule out color transparency. Another experiment was performed at BNL [49], which measured the color transparency of nuclei measured in the A(p,2p) quasi-elastic scattering process near 90^o in the pp center of mass. The incident momenta varied from 5.9 to 14.4 GeV/c, corresponding to $4.8 < Q^2 < 12.7$ GeV^2. In these experiments the angular dependence of the nuclear transparency near 90^o, and the nuclear transparency for deuterons was studied. They found that the nuclear transparency for A(p,2p), unlike that for A(e,e'p), is not a constant versus energy as predicted by Glauber calculations. The nuclear transparency for carbon and aluminum showed an increase by a factor of two between 5.9 and 9.5 GeV/c incident proton momentum. At higher energies, surprisingly, the nuclear transparency was observed to fall back to values compatible with the constant A(e,e'p) nuclear transparency, supported by the Glauber calculations. This oscillating behavior, as shown in Figure 1.28, was

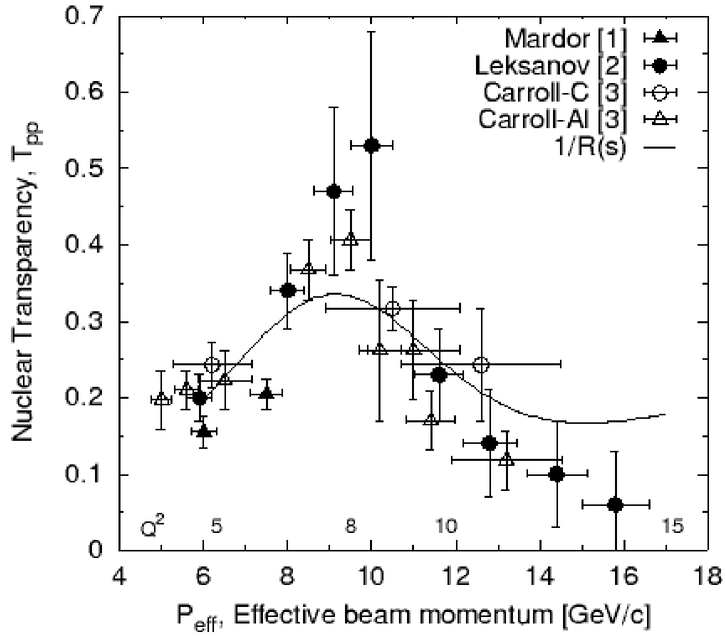

FIG. 1.28: The nuclear transparency T_{pp} values for carbon and for aluminum (scaled) are plotted versus their p_{eff} values [49]. The solid curve represents the inverse of $R(s) = \frac{d\sigma}{dt_{pp}}(\theta = 90°|_{c.m.}) \times s^{10}$. The scale s of Q^2 is included at the bottom of the figure in GeV^2.

explained as an interplay between two components of the pN scattering amplitude; one short range and perturbative, and the other long range and strongly absorbed in the nuclear medium. Studies of the A-dependence of nuclear transparency conclude that the effective cross section varies with incident momentum and is considerably smaller than the free pN cross section. The first data from a new (p,2p) experiment, EVA [50], at $p_{inc} = 6 - 7.5$ GeV/c confirmed the findings of the first experiment [51] and more recently EVA has reported measurements in a wider momentum range up to 14 GeV/c. The data appear to confirm both the increase of transparency between 6 and 9 GeV/c and a drop of transparency at 12 and 14 GeV/c [52]. As suggested in [53, 54] the drop in the transparency could be understood as a peculiarity in the high momentum transfer *pp* scattering amplitudes. The recent Jefferson Lab data [10] studied the (e,e'p) reaction on targets of deuterium, carbon, and iron up to $Q^2 = 8.1$ GeV^2. The nuclear transparency was determined by comparing the data to calculations of quasi-free cross sections in the Plane-Wave Impulse Approximation (PWIA). The dependence of the nuclear transparency on Q^2 (see Figure 1.29) as well as on the atomic number A was investigated in a search for the onset of the Color Transparency (CT). None was found in this kinematical range. However

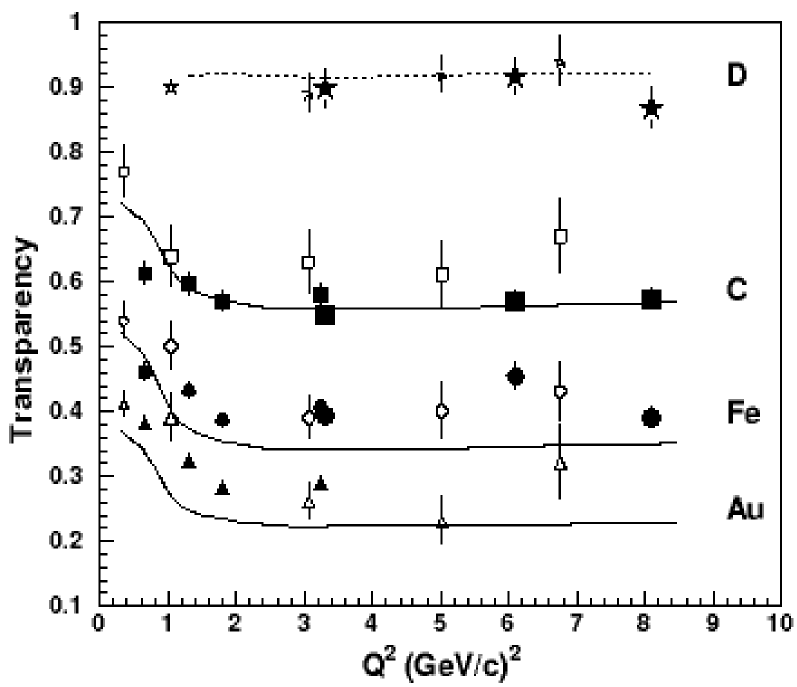

FIG. 1.29: Transparency T_p for (e,e'p) quasi-elastic scattering from D (stars), C (squares), Fe (circles), and Au (triangles). Solid large and small symbols are from JLab data Refs. [9] and [10], respectively. Solid large open symbols are SLAC data from Refs. [7,8]. Small open symbols correspond to Bates data from Ref. [55]. Solid curves represents the Glauber calculations from Ref. [56] and in the case of deuterium (D), the dashed curve corresponds to calculations from Ref. [41]

these data allow constraints on the parameters defining the onset of CT. From an analysis [18] done within the QDM of nuclear transparency for the range of the expansion parameter ΔM^2 (with $\Delta M^2 = 0.7$ GeV^2 shown in Fig. 1.30-(a) and with $\Delta M = 1.1$ GeV^2 shown in Fig. 1.30 (b)) it was determined that the lower limit for the formation of point-like constituents (PLCs) is at $Q^2 \approx 4$ GeV^2. The upgrade

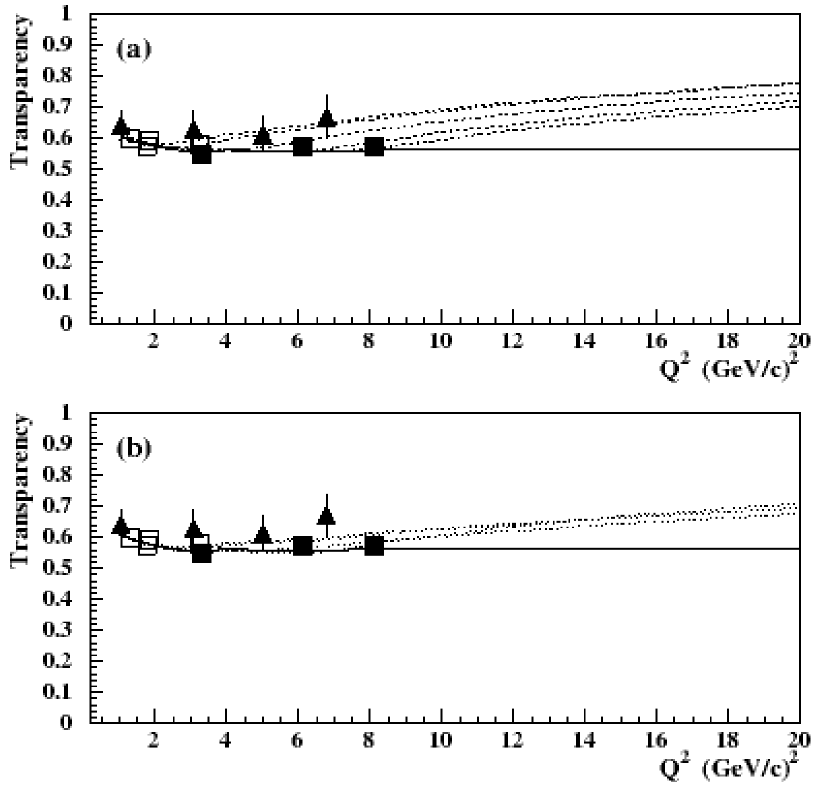

FIG. 1.30: The Q^2-dependence of T. The solid line is the prediction of the Glauber approximation (GA). In (a) dashed curves correspond to the CT prediction with $\Delta M^2 = 0.7$ GeV^2 and with $Q^2 = 1, 2, 4, 6$ and 8 GeV^2. In (b) dotted curves correspond to the CT prediction with $\Delta M^2 = 1.1$ GeV^2 and with $Q^2 = 1, 2, 4$ and 6 GeV^2. All calculations are normalized to the data at $Q^2 = 2$ GeV^2 [18]. Data shown here are from Bates, SLAC, and JLab as mentioned in Fig. 1.29.

of Jefferson Lab to 12 GeV would allow measurements of T to higher Q^2 where the color transparency predictions for (e,e$'$) diverge from conventional calculations (e.g. Glauber approximation). Experimental results from EVA have indicated in a model-independent way that for nucleon momenta ≥ 7.5 GeV/c, expansion effects are not large enough to mask the increase of nuclear transparency. Hence measurements at $Q^2 \geq 14$ GeV^2, corresponding to momenta of the ejectile nucleon up to 14 GeV, would clearly answer the question whether nucleon form factors in these kinematics are dominated by small or large size configurations.

1.5 Analysis Objectives

To obtain more detailed knowledge of the interaction of PLCs with nuclei, we can select processes in which the ejectile interacts a second time during its propagation through the nucleus (double scattering) [57–59]. This can be done by studying recoil nucleons with transverse (with respect to virtual photon momentum $\vec{q}$ direction) momenta $p_{s,\perp} \geq 200$ MeV/c. At low Q^2, the majority of high momentum nucleons are produced from re-scattering with the spectator nucleon in the nucleus. The onset of CT would reduce the probability of re-scattering, thus the number of such nucleons will decrease. The wave functions for the lightest nuclei (D, ^{3}He, ^{4}He) are known fairly well; therefore double scattering reactions can be modeled accurately in terms of FSIs, based on new theoretical developments [29, 59] (e.g. GEA model). Another advantage of double scattering is that the inter-nucleon distances probed ($1-2$ fm) are not large. These distances are comparable to the formation length for Q^2 as low as $4-6$ GeV^2 (accessible to this experiment), and may provide evidence for color coherent phenomena in the transitional Q^2 region.

Ultimately, the double scattering measurements of this experiment will allow us to determine whether the lack of an observed signature of CT in A(e,e$'$p) reactions for $Q^2 \leq 8$ GeV^2 is related to the rapid expansion of PLCs, or if it is because PLCs are not produced at all in this kinematical range. This experiment has measured the ratio of the cross section at kinematics for which double scattering is dominant, to the cross section measured at kinematics where screening effects have a larger contribution to the total cross section, as given in Eq. 1.58. To enhance the effect of the final state interaction in both regions, the light cone momentum fraction α of the recoiling nucleon was taken close to one ($\alpha = \frac{E_s - p_{s,z}}{m} \approx 1$), where E_s and m are the energy and the mass of the recoiling nucleon in the final state, and $p_{s,z}$ is the component of momentum in the direction of $\vec{q}$. Another aim of a double scattering experiment is to compute the ratio between the neutron and proton quasi-elastic cross sections at the same values of incident energy, Q^2, ν, E_{inc} and $\vec{p_i}$:

$$R_N \equiv \left| \frac{\sigma^n_{eN}}{\sigma^p_{eN}} \right|_{exp} \tag{1.55}$$

This ratio should be independent of the spectral function, if this function is similar for both the neutron and the proton. Predictions [60, 61] shows a strong difference between several theoretical calculations. The main difference arises from the Q^2-dependence of R_N. Since the difference in spectral functions is related to the evolution of the FSIs, the information gained from how this ratio evolves with the energy will shed light on the general picture of nuclear dynamics.

Another objective of this analysis is to extract inelastic cross sections for the inclusive d(e,e$'$) reaction at high x. When scattering electrons off a nucleon (proton or neutron), the range of $x \leq 1$. For scattering off a nucleus, it is possible for x to be larger than unity. The Bjorken scaling variable x is a measure of the fraction of the longitudinal momentum carried by the struck quark. Hence, $x > 1$ indicates that the electron scatters off a super-fast quark that carries more momentum than the nucleon. Using kinematics in which the virtual photon will knock out a nucleon while the correlated nucleon will be detected in the fragmentation region we obtain information about the structure of two-nucleons pre-existing at very small distances, so called short-range correlations (SRC). Ratios of A(e,e$'$) for different nuclei, normalized by A show a scaling behavior in the $x > 1.5$ region. It was suggested [92,93] that the ratio between A+1 and A cross sections in the $x > 1.5$ region will be proportional with the probability of finding SRCs in nucleus. Previous results from

Jlab-CLAS used ^{3}He cross section as the normalization to extract SRC probabilities for ^{4}He, ^{12}C and ^{56}Fe. The inclusive d(e,e$'$) cross sections for $x > 1.5$ can be used now as the normalization in extracting SRC probabilities for ^{4}He, ^{12}C and ^{56}Fe.

CHAPTER 2

Experimental Apparatus

2.1 Accelerator

The Continuous Electron Beam Accelerator Facility (CEBAF) at the Department of Energy's Thomas Jefferson National Accelerator Facility (TJNAF) is the home of a recirculating linear accelerator which supplies a very low noise, high duty-factor, continuous polarized electron beam ($\approx$70%) to three experimental halls (Hall A, B, C) simultaneously. A 45 MeV electron beam is delivered to the accelerator by a superconducting RF injector, and then accelerated through two identical linear accelerators (North and South LINAC) connected by two 180° arcs. The beam is recirculated up to five times as shown in Figure 2.1. Acceleration in the linac is achieved by 20 cryomodules, each one containing eight superconducting radiofrequency cavities (SRF), made of niobium, whose average gradient is 10 MeV/m. The SRF cavities are kept at 2 K using liquid helium produced by a refrigerator. At the end of each circulating pass through the machine the beam can be extracted using an RF chopper operating at 499 MHz. The beam is sent to the experimental halls in bunches separated by 2.0039 ns intervals at beam currents ranging from

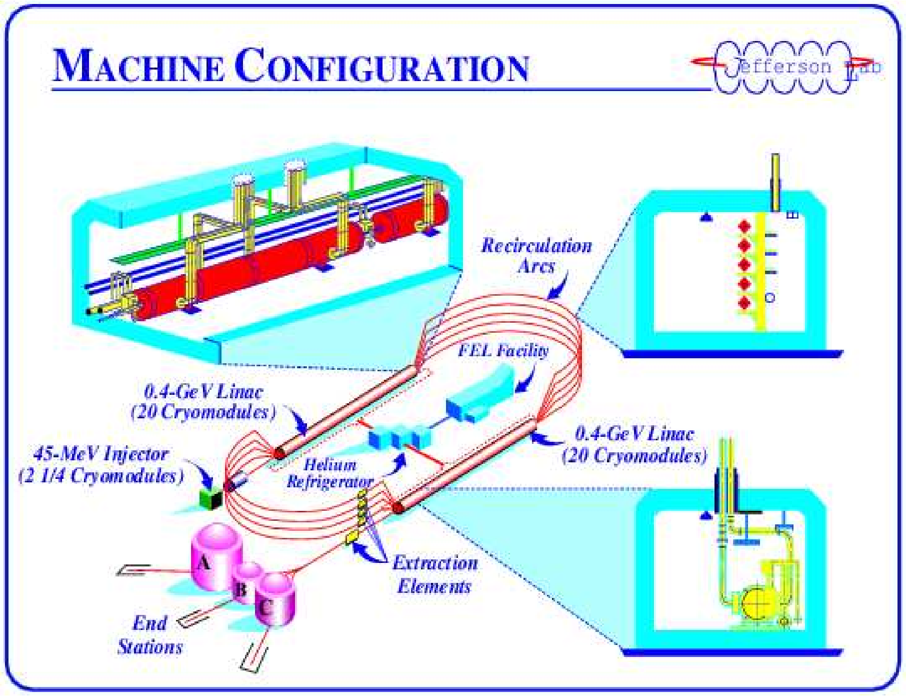

FIG. 2.1: The CEBAF machine configuration. In the upper corner one can see a blowup of the north linac showing one of the cryomodules. A vertical cross section of a cryomodule is shown in the lower right corner of the diagram. In the upper right corner a cross section of the five recirculating arcs is shown. The two linear accelerators and the bending arcs are shown in the center of the picture. The electron beam starts at the injector and terminates at the experimental halls (Hall A, B, C).

100 pA to 180 μA. The accelerator can deliver beam currents sufficient to achieve luminosities of several times 10^{38} cm^{-2}s^{-1} to Halls A and C. The beam delivered to Hall B is four orders of magnitude less intense because the maximum luminosity of a large-acceptance detector such as CLAS is limited by detector rates. The beam energies available to the experimental halls range from 1.1 GeV (one pass) to $\approx$5.6 GeV (5 passes). The maximum energy can be delivered with an energy resolution of less than 0.01 % and a beam spot size at the target of less than < 0.5 mm.

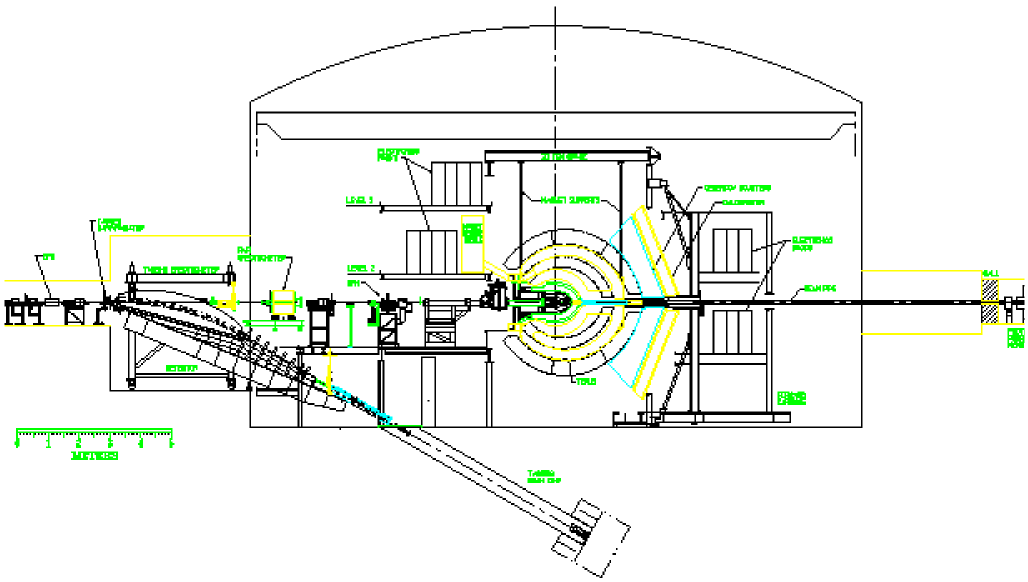

FIG. 2.2: Side view of the experimental setup in Hall B with the beam-line, CLAS detector in the center, and associated equipment.

2.2 General Description of the CLAS Detector

The CEBAF Large Acceptance Calorimeter (CLAS) shown in Figure 2.2 is the main experimental setup in Hall B. The CLAS detector has nearly 4π solid angle coverage, and allows the detection of charge particles with polar angles from $8°$ to $140°$, and neutral particles from $8°$ to $75°$. The large acceptance of CLAS and the continuous beam provided by CEBAF are well suited for experiments that require the detection of two and more particles in the final state with a very small accidental background to signal ratio of less than 10^{-3} over a large angular range in the laboratory frame for luminosities up to 10^{34} cm^{-2}sec^{-1}. Besides the actual detection of charged particles, CLAS is designed to measure their momentum, time of flight, and trajectory with good accuracy. From these measurements and the curvature of the track, the mass and charge of each particle can be inferred. In order to make these precise measurements, several sets of detectors have been assembled in CLAS as shown in Figure 2.3. The target is located at the center of CLAS. Charged particles are bent by a toroidal (azimuthal) magnetic field, with a maximum intensity of 2 Tesla in the forward direction. A mini-torus is used to curl up the Moller electrons that then exit into the beam dump. Three layers of Drift Chambers (DC), from 8° to 140°, allow us to map out the trajectory of a charged particle through the known magnetic field, and to determine its momentum. A Cherenkov counter (CC), from 8° to 45° provides discrimination between electrons and pions. A system of scintillator counters, from 8° to 140°, measures the time of flight (TOF) of charged particles. Finally the electromagnetic calorimeter (EC), located in the forward direction (8° to 45°), is used for identifying electrons and neutral particles. A pair of Large-Angle Calorimeters (LAC) was designed to detect charged particles scattered from 45° to 75°.

2.2.1 Main Torus Magnet

The magnetic field for CLAS is provided by six superconducting coils arranged in a toroidal geometry around the electron beam line as is shown in Figure 2.4 (left). The field points primarily in the ϕ-direction with a magnitude as is shown in Figure 2.4 (right). This design allows a measurement of charged particles with good momentum resolution at high energy and small scattering angles where the magnetic field is strong and at low energies and larger scattering angles where the magnetic field is weaker (see Fig. 2.4, right). This design provides a wide geometrical coverage for charged particles at large scattering angles as well. The magnet is approximately 5 m in diameter and 5 m in length. At the maximum design current of 3860 A, the integrated magnetic field reaches 2.5 Tesla·meter in the forward direction, dropping to 0.6 Tesla·meter at a scattering angle of 90°.

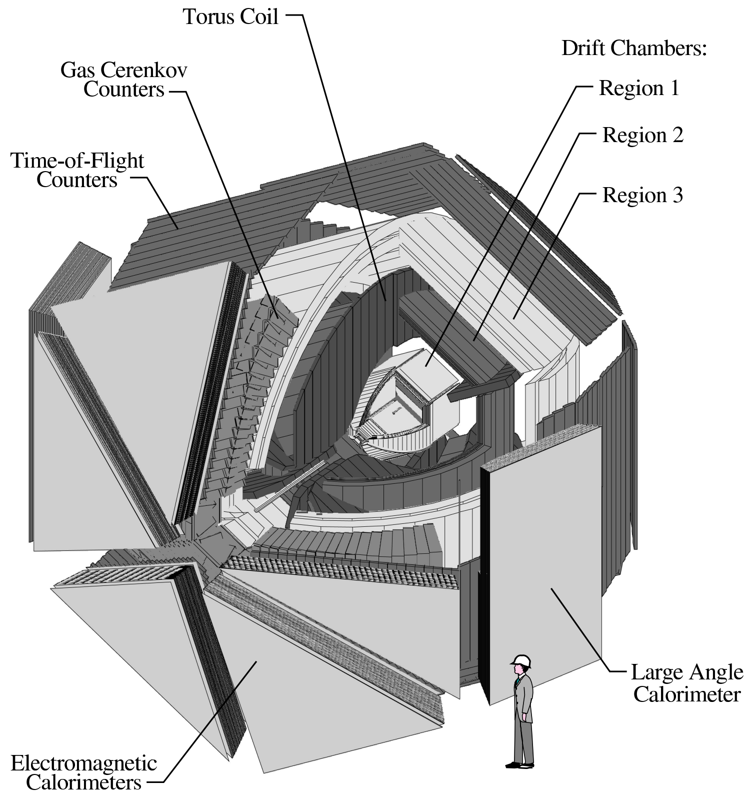

FIG. 2.3: 3D representation of CLAS with the detector sub-systems.

2.2.2 Drift Chambers

Determination of charged particle trajectories in CLAS is done using multi-wire drift chambers that are designed to track particles with momenta greater than 200 MeV/c. The drift chambers cover a range from 8° to 140° in polar angle for 80% of the 2π azimuth. Each of the six sectors of CLAS has three separate radial chambers called regions R1, R2, R3, as shown in Figure 2.5. The first region is the innermost and the smallest section of the drift chambers and is located in a nearly field free volume around the target. The second region is located inside the magnetic field and is actually mounted onto the cryostats containing the coils of the magnet. The third region is the biggest section and is located outside of the volume with magnetic field. A schematic representation of a sector wire chamber

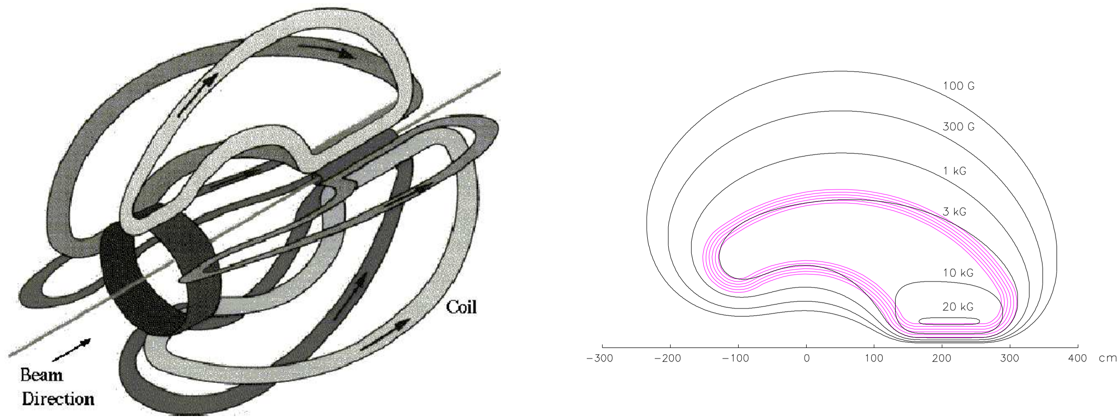

FIG. 2.4: Left: The main superconducting magnet composed of six toroidal-shaped coils. Right: Contours of constant absolute magnetic field for the CLAS toroid in the mid-plane between two coils.

with all the components is shown in Figure 2.6 (left). Each region of the drift chambers consists of two super-layers of wires : one axial super-layer, where all the wires are strung parallel to the direction of the magnetic field, and one stereo super-layer, in which the wires are strung at $6°$ with respect to the axial wires. These two sets of wires allow us to determine the azimuthal angle ϕ of the particle. Each super-layer is made up of 6 layers of sense wires plus field wires making up cells of hexagonal shape, as illustrated in Figure 2.6 (right). In addition, there is a layer of guard wires surrounding the perimeter of each super-layer to reproduce the electric-field configuration of an infinite grid of hexagonal cells. All three regions of the drift chambers are filled with 90% argon, 10% CO_2 non-flammable gas mixture. This provides a drift velocity of at least 4 cm/μs and an operating voltage plateau of several hundreds volts before breakdown. The average layer efficiency is $\geq 98\%$ [64]. Most of the inefficiency comes from tracks passing very close to the sense wire which give rise to signals with low pulse heights and long durations. The tracking, that is the reconstruction of the momentum and angles of the tracks, is done in two stages. First, the hits in a superlayer are combined to form a “track segment”. Then the

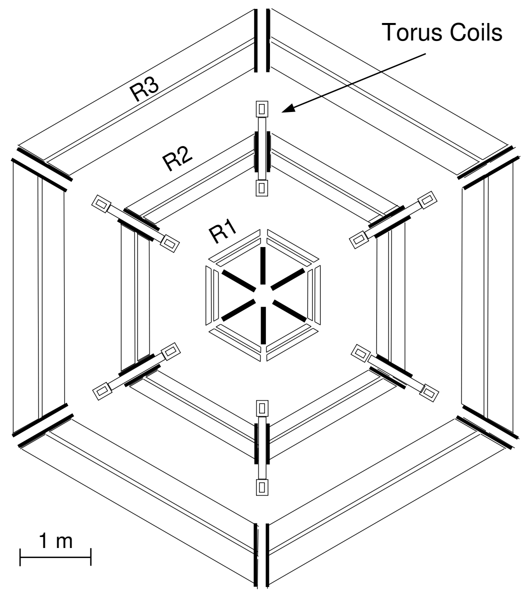

FIG. 2.5: Vertical cut through the drift chambers transverse to the beam at the target location.

"track segments" from different superlayers are linked to form a track. At this point the reconstructed momentum is within 3% to 5% of the true value of the momentum of the particle. In the second stage, the start time information from the scintillation counters is used to obtain the drift time, and then, to convert it into distance from the center of the cell. In overall average, the tracking efficiency remains greater than 95%, the chamber hit occupancy is up to 4% and the momentum resolution is better than 0.4% [64].

2.2.3 Cherenkov Counters

Cherenkov Counters (CC) detect electrons and pions and distinguish them by measuring the electromagnetic shock wave emitted by a medium when a charged particle travels faster than the speed of light in that medium. The CLAS Cherenkov detector system uses perfluorobutane gas (C_4F_{10}), at 0.2% above atmospheric pressure as the medium. This gas is easily purified, ten times heavier than air, and

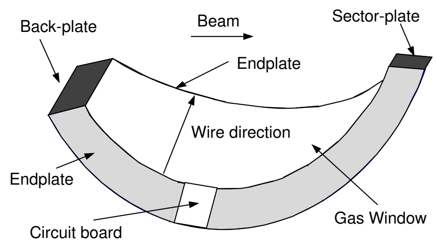

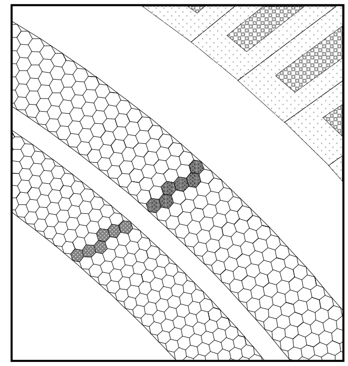

FIG. 2.6: Left: Schematic representation of radial chamber corresponding to one sector. Right: Layout of super-layer in Region 3. The sense wires are located in the center of each cell, while the field wires are located in the vertices of the hexagons. The shadowed hexagons represent the cells containing the sense wires which produced a signal for a representative track.

has excellent light (UV) transmission properties. The CC consists of six nominally identical counters, one per sector. Each counter covers the polar angular range $8° \leq \theta \leq 45°$, with nearly full coverage in the azimuthal angle ϕ. Cherenkov light is collected by covering as much space as possible with mirrors, and placing the phototubes in the regions of ϕ that are obscured by the torus magnet coils. Cherenkov light, emitted by the particles passing through each counter, is collected by the optical elements of each of the 216 light collection modules. The array of modules in one sector is shown in Figure 2.7. The optical elements of each module consist of two focusing mirrors, a Winston light collection cone, and a cylindrical mirror at the base of the cone as shown in Figure 2.8). A Phillips photomultiplier tube (PMT) is mounted at the base of the Winston cone for detection of Cherenkov light. The trajectory of the light produced by a typical electron passing through the Cherenkov detector is illustrated in Figure 2.8. The calibration of the Cherenkov detector re-

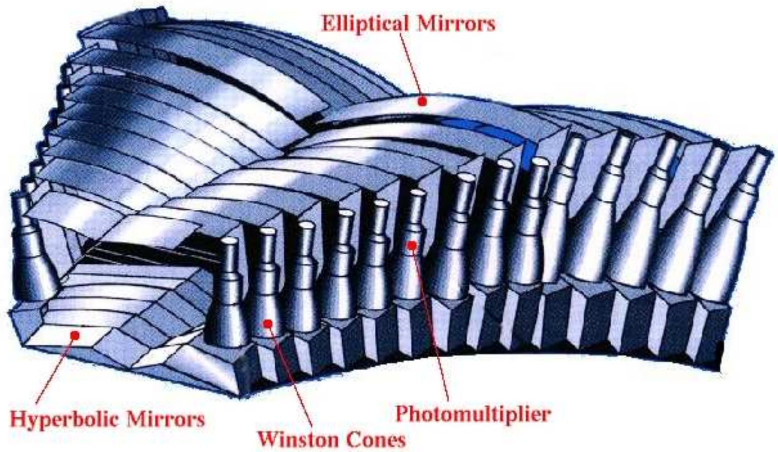

FIG. 2.7: The 3-dimensional structure of the Cherenkov counter in one of six sectors in CLAS.

quires equalizing the gains of the phototubes and setting the hardware thresholds. Since the CC threshold is included in our trigger, the calibration of this system is especially important. Due to the shape of CLAS, the Cherenkov counters can be triggered by electrons at the edges of the mirrors, beyond which the optical efficiency for the detected light drops rapidly. In order to avoid large efficiency corrections, a fiducial cut is applied in the analysis software.

2.2.4 Time-of-Flight Detector System

In CLAS, hadron identification relies mostly on the combination of measured charged-particle momenta and the flight time from the target to the respective scintillator counters of the time-of-flight detector system (TOF). The vertex time is determined by the accelerator RF, modulo 2 ns. The identification of the RF beam bucket in which the interaction occurred is accomplished using the time of flight (TOF) of the scattered electron, tracked back to the interaction point. A good timing resolution of the TOF detectors allows clear selection of the correct beam bucket. Thus, the vertex time is determined with the precision with which the beam bucket

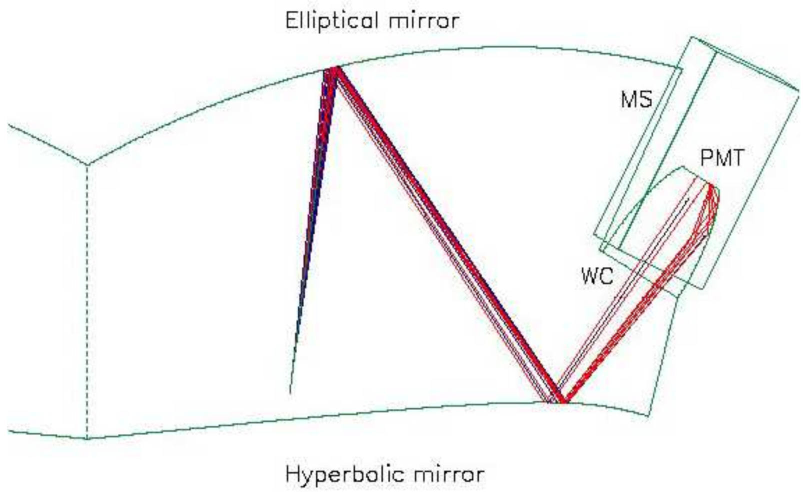

FIG. 2.8: Optical arrangement of one of the 216 optical modules of the CLAS Cherenkov counter, showing the optical and light collection components.

time is recorded. The calibration of this system affects the extracted flight time and thus the extracted particle mass. The scintillator counters (paddles) are located between the Cherenkov counters and the electromagnetic calorimeters as shown in Figure 2.9 (left). The TOF system has an excellent timing resolution ($\sigma \approx 120$ ps at forward angles, and $\sigma \approx 250$ ps at angles above $90°$) and good segmentation for flexible triggering and prescaling. In the final analysis particle identification is achieved by combining time measurements with pulse-height information for time-walk corrections. The TOF system in CLAS covers an area of 206 m^2 and is composed of 5.08 cm thick and 15 or 22 cm wide scintillation counters, covering a range of θ between $8°$ and $142°$. The lengths of the counters vary from 32 cm at the most forward angle to 450 cm at larger angles (Figure 2.9, right). Bicron BC-408 was selected as the scintillator material since it yields a single attenuation length of 500 cm and it is possible to fabricate scintillator pieces as long as 450 cm. [65] The system has been designed to optimize the time resolution, which varies from about 80 ps for the short counters to 160 ps for the longer ones. This resolution is needed to allow separation

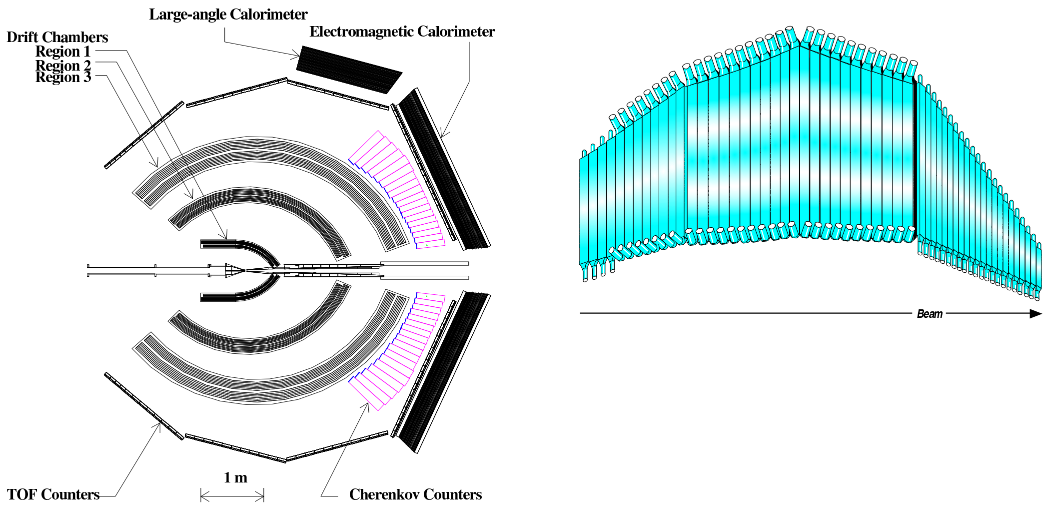

FIG. 2.9: Left: Schematic cross section of CLAS, showing 3 layers of drift chambers, time of flight walls, Cherenkov counters and calorimeters. The upper and lower cross sections correspond to two of the six sectors of CLAS. Right: View of TOF counters in one sector showing the grouping into four panels.

of pions and kaons up to 2 GeV. A good particle identification is ensured by a good resolution of the time-of-flight measured by TOF detector subsystem together with a good momentum and position resolution obtained from the DC.

2.2.5 Electromagnetic Shower Calorimeter

The forward electromagnetic shower calorimeter (EC) covers polar angles from $\theta = 8°$ to $45°$ with ϕ coverage matched to that of the drift chambers. It is designed to detect electrons above a given threshold, as well as neutral particles (photons and neutrons). An electromagnetic shower is produced in the lead by the electrons passing through the calorimeter. The electrons produced in the shower are then converted by the scintillator strips into light, which is collected by photo-multipliers. A typical electron trigger in CLAS requires a signal based on the total energy deposited in the electromagnetic calorimeter in coincidence with a CC signal in the same sector. Detection of neutrons, and their discrimination from photons, is achieved using time-of-flight measurements. Each sector of CLAS contains a triangular-shaped

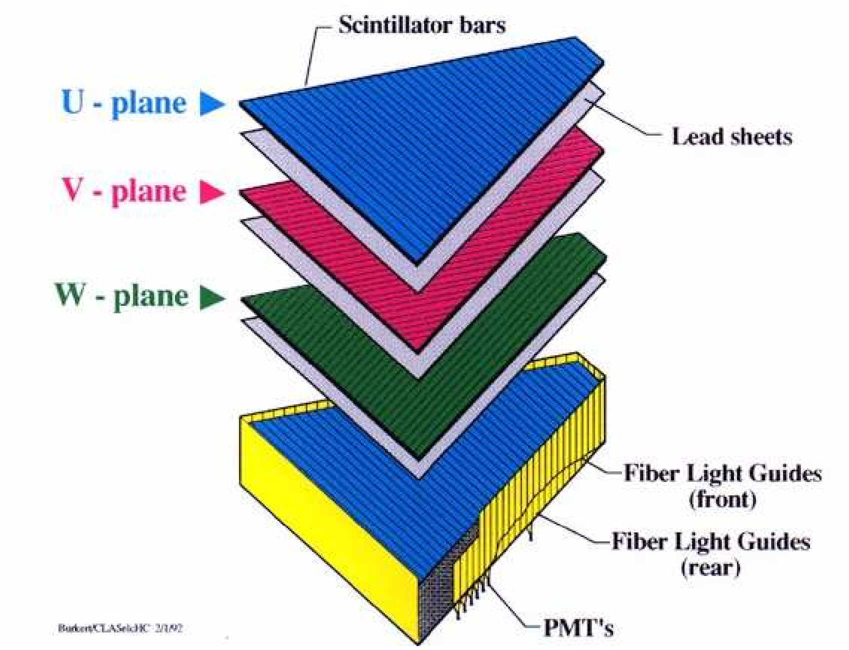

FIG. 2.10: Expanded view of one of the six EC modules used in CLAS.

electromagnetic calorimeter that is longitudinally segmented into inner and outer components [66]. Each calorimeter is made of alternating layers of scintillator strips (39 layers of 10 mm thickness) and lead sheets (2.2 mm thickness) resulting in a total thickness of 16 radiation lengths (see Figure 2.10). The ratio between lead and scintillator thicknesses is 0.2, thus approximately 1/3 of the energy in an electromagnetic shower is deposited in the scintillator. Each layer of scintillators is laid parallel to one of the three sides of the triangular container and the width of the strips increases through the stack. Each scintillator layer is further segmented into 36 strips approximately 10 cm wide with single sided readout in one of three views. The three views are oriented approximately in the direction 0°, 120° and 240° around the normal to the target. This provides good granularity and a redundant position measurement for multiple-hit reconstruction. Each of the three orientations (labeled U,V and W) contain 13 layers that provide stereo information on the location of the energy deposition [66]. Each orientation is further subdivided (*i.e.*, separate

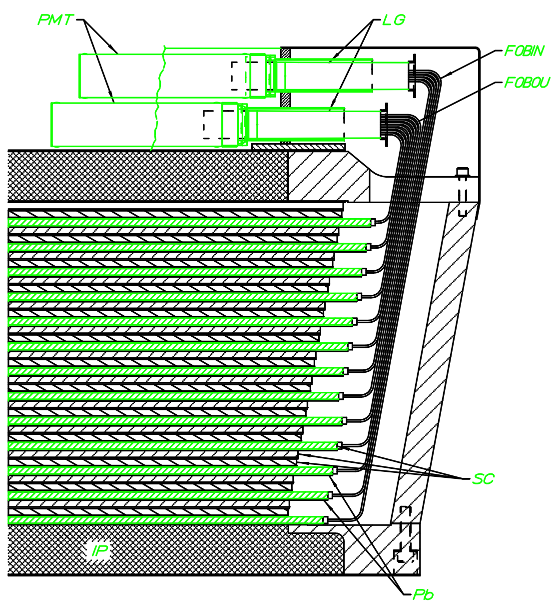

FIG. 2.11: Schematic side view of the fiber-optics readout unit for a single inner and outer stack of the calorimeter module.

readouts) into 5 inner and 8 outer stacks, which provides longitudinal sampling of the shower for better hadron identification. The optical readout of the EC is built from plastic fibers attached to the PMTs in flight-path-compensating geometry as is shown in Figure 2.11. The total energy deposited in the calorimeter is available at the trigger level to reject minimum ionizing particles or to select a particular range of scattered electron energies. Pions are largely suppressed by including an EC total energy threshold in the CLAS hardware trigger. With an overall position resolution of σ=2.3 cm, and time resolution of τ=3 ns, the EC functions are close to its initial specifications.

2.3 Cryogenic Target

The E6 target (Figure 2.12) was positioned in the center of CLAS to allow for the detection of protons of large scattering angles (greater than 90°). As little material as possible was used in the back of the target to minimize energy loss of backward-going protons. This unique new target design was expressly built for this

FIG. 2.12: The E6 target features a very small size target cell and a low amount of material in the back of the target for easy detection of the backward-going particles.

experiment. The target cell, made of kapton (7.2 mg/cm^2) had a diameter of 1.2 cm upstream and 0.7 cm downstream. A conical shape was chosen in order to allow the bubbles formed in the target material, due to electron beam heating, to escape out the back of the cell more efficiently. The entrance and the exit windows were made out of aluminum with a thickness of 15 μm and a diameter of 4 mm. The target cell was 5 cm long and thermally insulated by 5 layers of combined aluminized mylar and cerex. The target cell was installed in a scattering chamber which was placed under vacuum. The scattering chamber was made of polyurethane foam (64 mg/cm^2) covered with a nylon safety sock (see Figure 2.13). The exit tube was made of carbon fiber and was connected to the scattering chamber with epoxy. The scattering chamber exit window was a 71 μm thick aluminum foil. The target cell

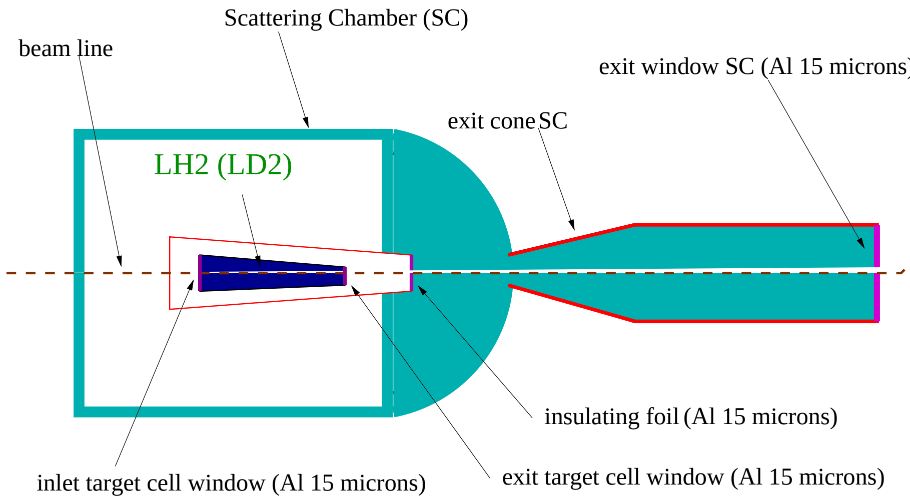

FIG. 2.13: Schematic view of the scattering chamber, and the liquid hidrogen/deuterium target.

was filled with either liquid hydrogen or liquid deuterium. The nominal parameters for hydrogen (deuterium) were 20 (22) K temperature, 1100 (1315) mbar pressure, and 0.0711 (0.162) g/cm^3 density.

2.4 Event Trigger and Data Acquisition

The data for this experiment were collected during a six week period, as part of the E6 group run, from January 30th through March 16th, 2002. We used a polarized electron beam with an energy of 5.765 GeV and an average current of 8 nA. Under these conditions, the luminosity of the liquid deuterium target was 1.1 $\times\ 10^{34}$ cm$^{-2}\cdot$ s^{-1}. Two configurations of the main torus magnetic field were used: in-bending (negatively charged particles are bent toward the axis of CLAS) and out-bending (negatively charged particles are bent away from the axis of CLAS). For the analysis of this thesis we used only the in-bending data because we were interested in high Q^2 with good statistics. Data were selected for the analysis using the Level-2 trigger and the downscaled trigger bits 7+8 for later calibrations. The Level-2 trigger

Trigger Bit	Prescaled	CC [mV]	EC_{inner} [mV]	EC_{tot} [mV]	Level 2
1-6	1	100	72	72	yes
7	10	20	72	172	no
8	100	0	0	80	no

TABLE 2.1: The E6 trigger setup. Trigger bits 1 through 6 corresponds to each sector of CLAS and required a minimum 1 photo-electron (equivalent of 100 mV) threshold for the CC, and a threshold in the EC (shown in column three and four). Trigger bits 7 and 8 were prescaled as shown in column two, and were added for CC and trigger efficiencies studies.

Target	Torus Current [A]	Data [mC]	Data [mil. trigg.]
LD_2	2250	9.4855	4055.43
LD_2	-2250	0.7793	452.87
LH_2	2250	0.6622	209.31
LH_2	-2250	0.2436	66.14
Empty	2250	0.9387	77.83
Empty	-2250	0.4703	77.51
Total LD_2	-	10.2448	4508.3
Total LH_2	-	0.9058	275.45

TABLE 2.2: Summary of E94-016 experiment data taking. The settings of the torus magnetic field are shown in the second column for liquid hydrogen target (LH_2), liquid deuterium target (LD_2), and empty targets (Empty). The accumulated charge and the number of triggers are shown in columns three and four, respectively.

requires a minimum of 500 MeV energy deposited in the electromagnetic calorimeters (EC), more than one photo-electron observed in the Cerenkov counters (CC), and at least two track segments (out of 5 possible super-layers) observed in the same sector. If any of the six sectors of CLAS sees this trigger, the corresponding trigger bit (1 through 6) is set. For efficiency studies of the CC, another auxiliary trigger bit (trigger bit 7) was used, with low threshold and no track segments required. Finally, we had one more trigger bit (trigger bit 8) that simply requires a signal above 250 MeV in the EC. This trigger was used to give us an unbiased sample of

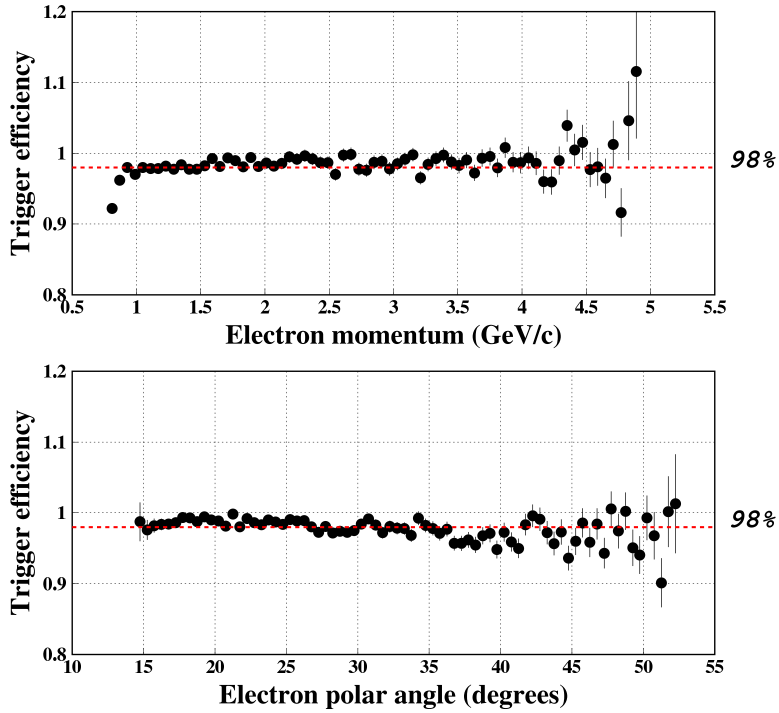

FIG. 2.14: The upper plot shows the Trigger Level 2 efficiency as a function of electron momentum. The lower plot shows the Trigger Level 2 efficiency as a function of electron polar scattering angle.

all particles, including pions. Trigger bits 7 and 8 were heavily prescaled, by factors of 10 and 100, respectively. A summary of all the settings for our trigger is presented in Table 2.1. The efficiency of our trigger was defined as the ratio of data with the first six trigger bits set to data with just trigger bit 8 set for the momentum and polar angular distributions of the detected electron. An efficiency of 98% was found for our trigger (see Figure 2.14). During the experimental run we have collected approximately 4.5×10^9 triggers and accumulated a total charge of 11.1 mC, using two magnetic field configurations and two target materials: liquid hydrogen (LH_2) and liquid deuterium (LD_2). Table 2.2 presents a summary of the accumulated data during the E6 run period.

CHAPTER 3

Data Processing

3.1 Detector Calibrations

The raw data for every event accepted by our trigger was recorded on magnetic tapes using the Hall B CODA Data Acquisition System (DAQ). Data was stored in runs broken up into approximately 30 files. During the experiment specific runs were taken for calibration purposes. Careful calibration of each detector system is crucial for good detector resolution and particle identification. Each detector system has his own calibration procedure developed by the CLAS collaboration over the past seven years of operation. The calibration data were processed with the CLAS event reconstruction software RECSIS and then stored in BOS format. After calibration of each subsystem of CLAS new calibration constants were extracted and saved in an interactive MySQL database used further by the reconstruction software to identify the tracks and the event information. The calibration of each detector was a time-consuming procedure performed by A. Klimenko for the DC system, L. Kramer for the EC system, A. Vlassov for CC detector system, and C. Butuceanu for the TOF system. These procedures are described briefly in this chapter.

3.1.1 Drift Chamber Calibration

The Drift Chambers (DC) measure the momentum of a charged particle by tracing its trajectory through the magnetic field. When a particle travels through the DC, each of its 34 wire layers should produce a signal (called a “hit”). Due to inefficiencies or dead wires in the DC, an average of 30 hits per track are obtained. The raw DC data is a collection of TDC measured drift times corresponding to each hit in a drift cell. The drift times are converted into a distance of closest approach

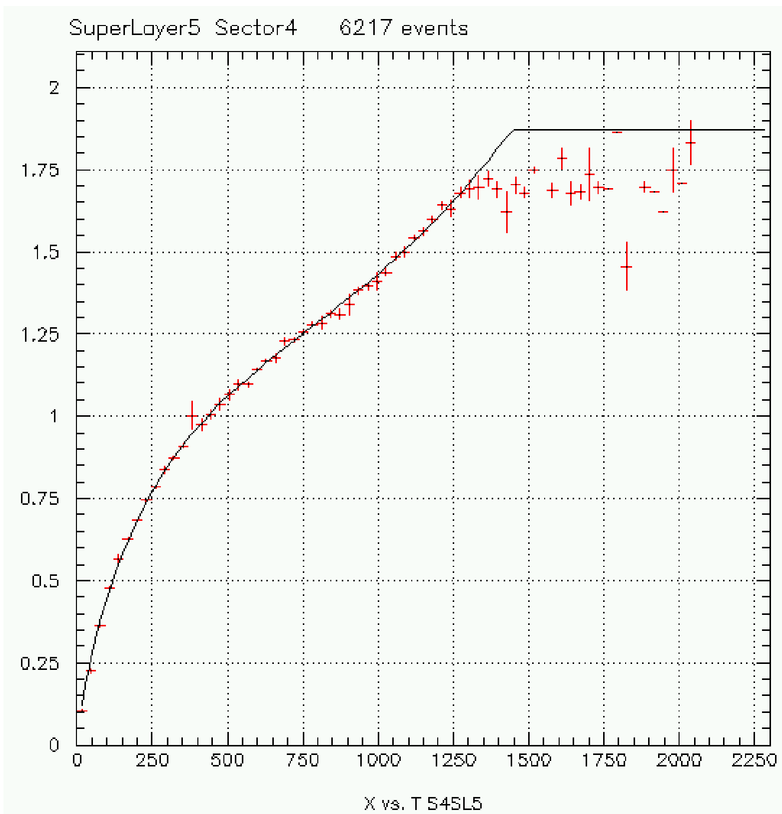

FIG. 3.1: Hit position versus drift time for Super-layer 5, Sector 4. The vertical axis is defined by the distance (cm) from the track to the sense wire, and the horizontal axis is defined by the drift time (ns). Reconstructed data using a previous parametrization is represented here by the points. The fit function is used for the final reconstruction.

(DOCA) defined as the shortest distance from a track to a sense wire using the drift velocity. The DC calibration parameterizes the drift distance as a function of drift time for each super-layer in each sector [67]:

$$x(t) = v_0 t + \mu \left(\frac{t}{t_{max}}\right)^q + \kappa \left(\frac{t}{t_{max}}\right)^p \tag{3.1}$$

where t_{max} is the drift time of the electron along the longest path from the farthest corner of the cell, v_0 is the value of the saturated drift velocity near $t = 0$, μ and κ, q and p are parameters determined from the fit shown in the Figure 3.1. This function relates the time it takes from the moment the track passed through the drift chamber (estimated initially from the β obtained from hit-based-tracking system described below and the path length from the track's origin to the drift cell) to the moment when the sense-wire fired, calculated from the TDC, to the distance the hit occured from the wire. The conversion from the drift time to the distance of closest approach

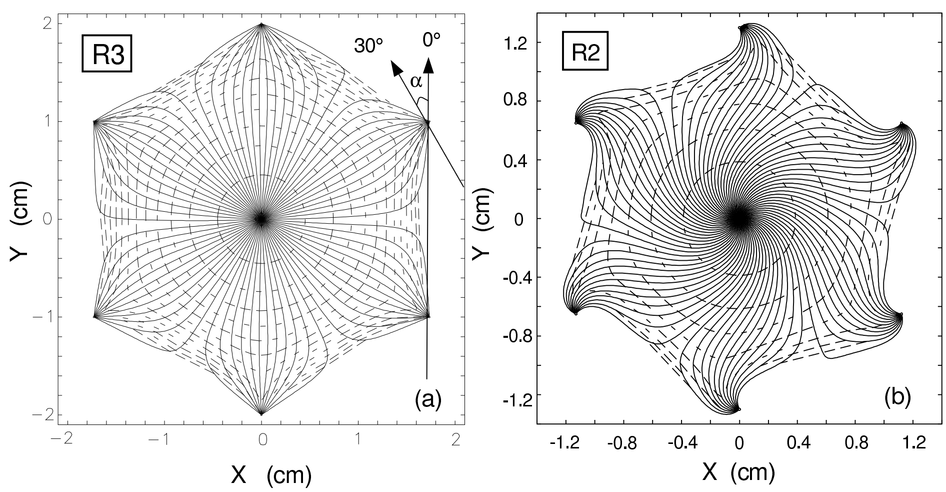

FIG. 3.2: The field configuration inside Region 3 (left panel) and inside Region 2 (right panel) of the DC, is shown with solid lines. Dashed lines represents track positions with the same drift time, so-called isochrones. Region 2 field lines are distorted due to their location within a toroidal mixed electro-magnetic field. The plots are from Ref. [64].

is complicated due to the strongly varying electric fields in each drift cell. Fig. 3.2 shows the field lines (solid-lines) and isochrones (dashed-lines), points of equal drift time, for cells in Region 3 (left) and Region 2 (right). Due to the location of Region

2 in the toroidal mixed electro-magnetic field, the effective field lines are distorted as shown in Fig. 3.2 (right). The tracking process requires that hits be adjacent to one another and that there be at most one layer missing from within the super-layer. Segments of adjacent hits are then compared sector by sector against a previously

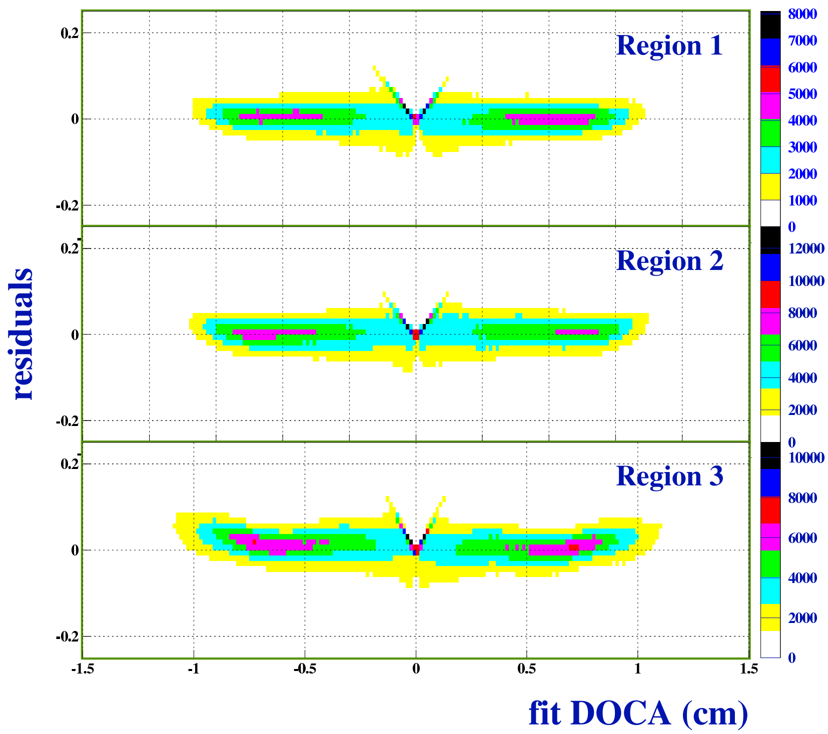

FIG. 3.3: Drift Chamber residuals plotted as a function of the calculated fit DOCA, for Sector 1, Run no. 31956.

generated map of linked segments associated with simulated tracks. At least five of the six super-layers of the DC, must contain a segment for a track to be fit. After an initial guess, the so-called Hit-Based-Tracking (HBT) procedure is performed. HBT uses each hit to determine a particle's track via a least squares fit that minimizes the sum of the squares of the closest distance between each hit wire and the track [64]:

$$\chi^2 = \sum_i \frac{(d^i_{\mathrm{DOCA}})^2}{\sigma^2_{\mathrm{HBT}}} \tag{3.2}$$

where d_{DOCA} is the distance of closest approach of the track to the closest sense wire in the i-th layer of the DC and σ_{HBT} is set to the size of the drift cell. The results of the hit-based-tracking is then passed on to the time-based-tracking (TBT) routine which performs a similar fit to the tracks, but now χ^2 is defined as:

$$\chi^2 = \sum_i \frac{|x^i_{\mathrm{driftDOCA}} - x^i_{\mathrm{fitDOCA}}|^2}{\sigma_i^2}, \tag{3.3}$$

where $x^i_{\mathrm{driftDOCA}}$ is the drift distance corresponding to the drift time for the i-th wire hit, x^i_{fitDOCA} is the distance of closest approach of the trial trajectory for the i-th wire and σ_i is the uncertainty in $x^i_{\mathrm{driftDOCA}}$. The distance calculated from the track

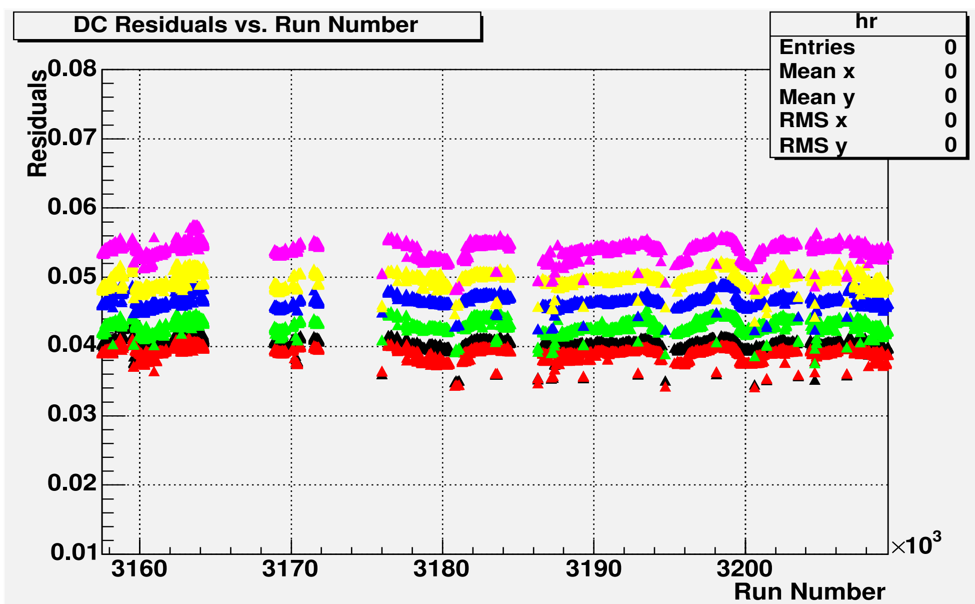

FIG. 3.4: DC residual resolutions plotted as a function of run number. Different colors correspond to each of six super-layers of the DC.

fit to each sense-wire is called the fit DOCA. The difference between the absolute value of the calculated DOCA and the absolute value of the fit DOCA is defined as the residual for each cell and is the primary unit of measuring the resolution of DC detector system. A properly calibration of DC system should result in a flat dependence of residuals on drift time and the calculated distance. An example of residual versus calculated DOCA is shown in Fig. 3.3 for Sector 1, Run no. 31956. For this data set a good resolution in DC was achieved as shown in Fig. 3.4.

3.1.2 Time-of-Flight System (TOF) Calibration

Particle identification relies heavily on measured charged-particle momenta from the drift chambers and the flight time determined using the TOF counters. Good timing resolution is therefore crucial for determining hadron masses, and a good calibration of the TOF system is required. The calibration procedure requires several steps described below:

- Amplitude-to-Digital Converter (ADC) thresholds were determined using a dedicated DAQ configuration. The measured pulse heights were calibrated using the minimum ionizing particles peak (MIPs), and then used to reconstruct the energy deposited in the scintillators (see Figure 3.7). The constants for each ADC pedestal were saved in the calibration database.

- Time-to-Digital Converter (TDC) calibration was realized by measuring the response of each TDC channel for different delays between the start and stop signals and converting them into time (ns) using a quadratic function [65]:

$$t = c_0 + c_1 T + c_2 T^2 \tag{3.4}$$

  where typical values of $c_0 \sim 1$ ns, $c_1 \sim 0.0495$ ns per channel, and $c_2 \sim 5 \times 10^{-8}$ ns per channel^2. The constants were constrained such that the average of the 64 channels for each FASTBUS card was zero.

- Time-walk corrections account for the dependence of leading-edge discriminator timing on signal pulse height. The correction constants were obtained with laser systems which delivered a light pulse to the center of each counter. The dependence of pulse timing on the pulse height is shown in Figure 3.5. This de-

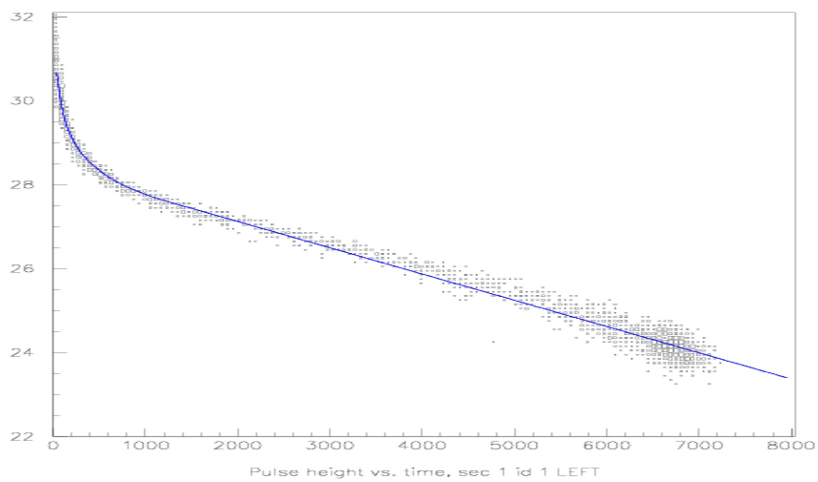

FIG. 3.5: Pulse height as a function of time-walk (solid boxes) and the fitting function (solid line) for Sector 1, Paddle 1, left PMT. Data were obtained from the laser calibration data.

pendence was obtained using a filter which varied the amount of light delivered to each counter. The measured time corresponds to when a photomultiplier (PMT) pulse crossing a fixed (leading-edge) voltage threshold. To correct for time-walk, we performed software corrections of the form:

$$T_{\mathrm{w}} = t - f_{\mathrm{w}}\left(\frac{A-P}{V_{\mathrm{T}}}\right) + f_w\left(\frac{600}{V_{\mathrm{T}}}\right) \tag{3.5}$$

where A is the ADC pulse height corrected by subtracting the ADC pedestal P threshold, V_T is the leading-edge discriminator threshold (20 mV) which corresponds to $\approx$ 35 ADC counts, and f_w is the time-walk-correction function. The peak of the energy loss of MIPs is nominally set to 600 ADC counts by adjusting the PMT high voltage. This form will result in $t_w = t$ for MIPs pulses. The procedure basically extracts four constants for each PMT: w_0, w_1, w_2, w_3 which adjust the time-walk correction function f_W to the required dynamic range [69]:

$$f_{\rm w}(x) = w_1 + \frac{w_2}{x^{w_3}} \text{ if } x = \frac{A-P}{V_{\rm T}} < w_0,$$

$$f_{\rm w}(x) = w_1 + \frac{w_2}{w_0^{w_3}}(1+w_3) - \frac{w_2 w_3}{w_0^{w_3+1}}x \text{ if } x > w_0. \quad (3.6)$$

The four fit parameters are then updated in the CLAS calibration database to be used for time-walk corrections during the final particle ID reconstruction.

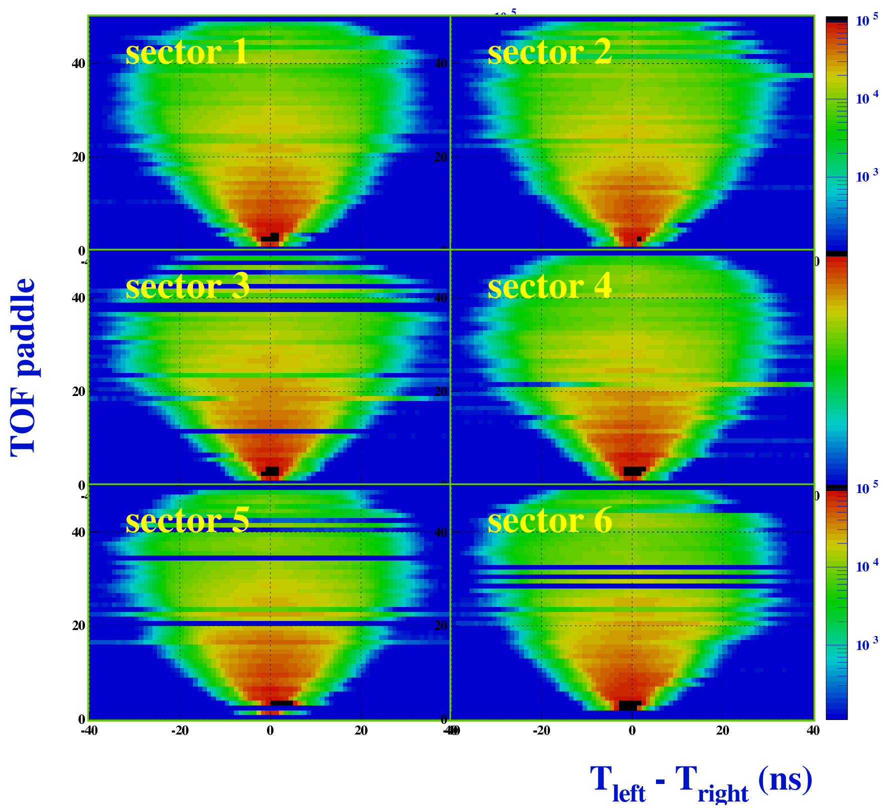

FIG. 3.6: The time difference between the response of the left and right PMTs located on the ends of each TOF counter plotted versus scintillator number (1 - 48), for each sector of CLAS, after left-right alignment calibration. The empty spaces represents the malfunctioning TOF scintillators excluded from the analysis.

- The left-right alignment corrects for different time delays of the signals from the left and right PMTs located at opposite ends of each scintillator. A good calibration of these timing responses is crucial for determining the hit position along the scintillator and reconstructing the correct final time of flight. In Figure 3.6 the time difference after left-right calibration between the left and right PMTs is plotted versus scintillator number . We can see that some of the TOF counters give no signal (empty spaces) which means that they malfunctioned during the experiment and were counted as "dead" in the calibration database. In addition we can see that a few TOF counters were miscalibrated (distributions are shifted left or right) because one of the PMTs (left or right) did not function properly during the experiment. Those TOF counters were excluded from final data analysis.

- The energy is estimated by evaluating the geometric mean of pulse height from right and left PMTs. The calibrated *ADC* pulse height is used to reconstruct the energy deposited in each of the scintillators. The energy loss of protons increases linearly at low momentum until they begin penetrating the scintillators, at which point the energy loss can be estimated with the Bethe-Bloch formula. As we can see in Figure 3.7 the pions and protons which produce different *ADC* pulse heights are clearly distinguished for momenta between 0.3 and 1 GeV/c. A weak deuteron band can be seen in the plot as well.

- Light traveling through a scintillator is attenuated. Thus, the attenuation length for each side (λ_L, λ_R) of the TOF counter can be determined using the pedestal corrected ADC values (A_L, A_R) in units of MeV (E_L, E_R) and the y position along the paddle relative to the center of the paddle from time of flight [65]:

$$\begin{aligned} A_{\mathrm{L}} - P &= \frac{M0_{\mathrm{L}}}{k} \cdot E_{\mathrm{L}} e^{-y/\lambda_{\mathrm{L}}}, \quad y = \frac{v_{\mathrm{L}} v_{\mathrm{R}} (T_{\mathrm{L}} - T_{\mathrm{R}})}{v_{\mathrm{L}} + v_{\mathrm{R}}}, \\ A_{\mathrm{R}} - P &= \frac{M0_{\mathrm{R}}}{k} \cdot E_{\mathrm{R}} e^{-y/\lambda_{\mathrm{R}}}, \end{aligned} \tag{3.7}$$

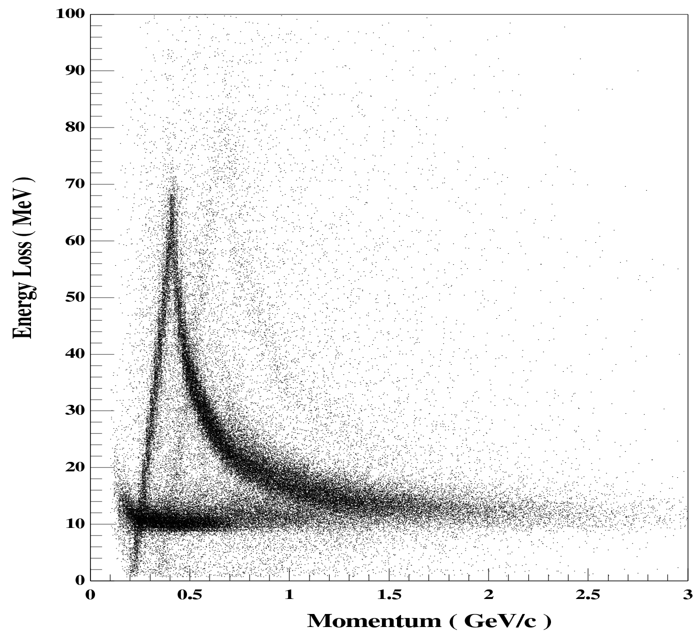

FIG. 3.7: Energy deposited in a TOF scintillator as a function of particle momentum for an empty target. Protons and pions can be distinguished, as well as a faint deuteron band.

where k = 10 MeV correspond to the MIP peak value in units of MeV at the center of each paddle, $M0_L$ ($M0_R$) is the pulse height normalization, T_L (T_R) is the walk-corrected time in ns for left (right) tube and v_L (v_R) is the speed of light propagation towards the left (right) end of the TOF paddle. There are cases when both left and right signals are present for a paddle, when just signals from one side are presents and when only one TDC was functioning. The calibration software tries to accommodate all these cases using information from left and right PMTs for each TOF counter whenever possible. The status of each PMT and counter is reported in the calibration database and taken in consideration in the final particle ID reconstruction.

- The effective velocity v_{eff} of scintillator light for each counter was defined as:

$$\begin{aligned} t_{\mathrm{L}} &= t_0 + y/v_{\mathrm{eff}}, \\ t_{\mathrm{R}} &= t_0 - y/v_{\mathrm{eff}}, \end{aligned} \tag{3.8}$$

  where t_0 is the time at the center of the counter, t_L (t_R) is the time recorded in the left (right) PMT and y is the position of the hit along the length of the scintillator determined from tracking. We used a fit to the time difference between right and left tubes plotted as a function of hit position y to extract the effective velocity v_{eff} for each scintillator counter.

- RF Offset Calibration: The Radio Frequency (RF) signal from the accelerator is used to adjust the time delay for individual scintillators with respect to each other. As previously mentioned, the beam is delivered to Hall-B in bunches with a frequency of 499 Hz, which corresponds to a time interval (ΔT) of $\approx$ 2 ns between two separate bunches of electrons. The reaction $ep \to e\pi X$ was used to determine the time delay between the 288 counters by comparing the time from a TOF counter to the RF beam time. The difference between the vertex time of pions or electrons reconstructed from the TOF measurements and the time of the RF bunch was calculated and then was divided by 2.004 and the reminder was taken as the RF offset correction to the TOF time:

$$T_{\mathrm{RF}}^{\mathrm{offset}} = \mathrm{mod}\left(\frac{\mathrm{T_{sc}} - \mathrm{T_{flight}} - \mathrm{T_{rf}} + 100 \cdot \Delta\mathrm{T}}{\Delta\mathrm{T}}\right) - \frac{\Delta\mathrm{T}}{2}, \tag{3.9}$$

  where $\Delta T = \frac{3}{\nu_{\mathrm{acc}}}$ is the RF beam time interval, T_{sc} is the time in nanoseconds measured by the TOF scintillator, $T_{\mathrm{flight}} = l_{\mathrm{el}}/\beta_{\mathrm{el}} \cdot c$ is the calculated flight time for the scattered electron from the vertex to the TOF scintillator, and T_{rf} is the RF beam time for a particular bunch. The calibration of each individual TOF counter depends on the RF signal itself. Figure 3.8 shows the RF offset plotted as a function of RF beam time before (upper plot) and after (lower plot) a proper calibration.

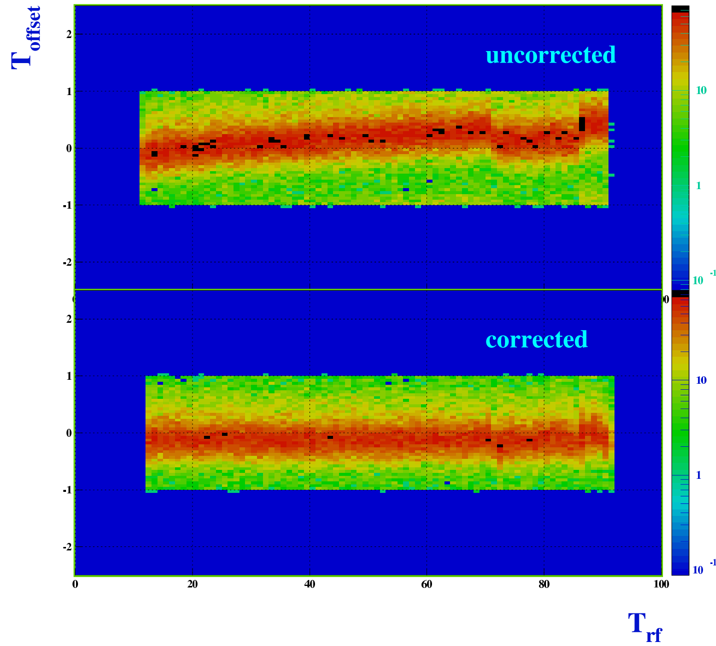

FIG. 3.8: The RF offset plotted as a function of RF beam time before (upper plot) and after (lower plot) corrections.

- Paddle-to-Paddle Corrections: After RF offset corrections there is still 2.0004 ambiguities since the actual beam bunch, which caused the recorded event, was unknown. In order to correct for these ambiguities, electron-pion coincidence events were used. The calibration constants for each paddle were determined, modulo 2.004 ns, by requiring that the two reconstructed tracks have a common vertex time. These constants were updated in the calibration database, and the procedure was repeated several times, thereby improving as much as possible the quality of this calibration and the TOF detector resolution. Once all aspects of the TOF calibration have been resolved, the RF offset distribution should be peaked at zero and should have a sigma in the range of 150 to 200 ps (see Fig 3.9). The resolution of the RF offset peak for each individual counter sets the resolution for that counter. Knowing the trajectory and the momentum of a particle (using DC information) we can compute the mass by knowing the correct time of flight.

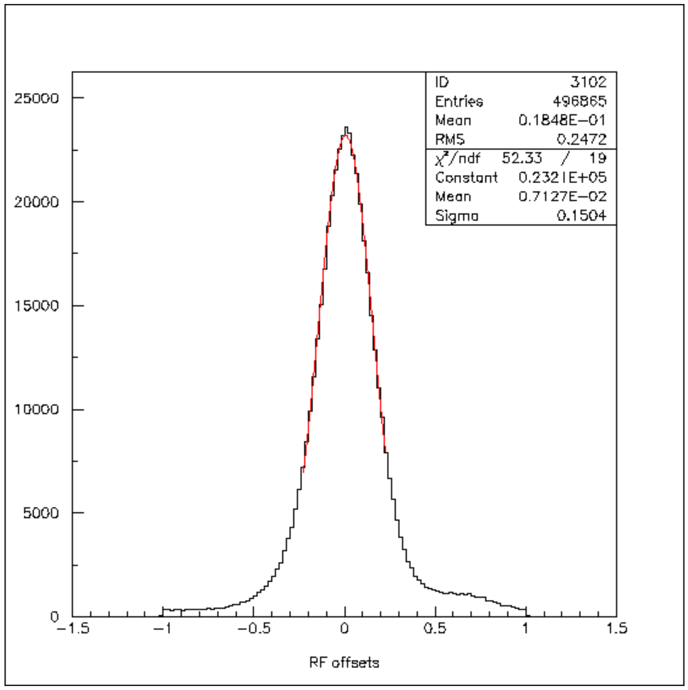

FIG. 3.9: The RF offset (black histogram) for Run no. 31935, after corrections, fitted with a Gaussian function (red curve). Data were taken at a beam energy of 5.764 GeV.

The quality of the TOF calibration is reflected in the reconstruction of detected particles (momentum, mass, velocity). As is shown in Figure 3.10 an average resolution of 160 ps was obtained for this data set.

3.1.3 Electromagnetic Calorimeter Calibration

A good calibration of the Electromagnetic Calorimeter (EC) is very important in the detection of electrons and discrimination of neutral particles (photons and neutrons). To calculate the energy of neutral particles we use their time of flight. In this procedure we use the electron arrival time measured by both the EC and the Scintillator Counters (SC), and match the two measurements under the assumption

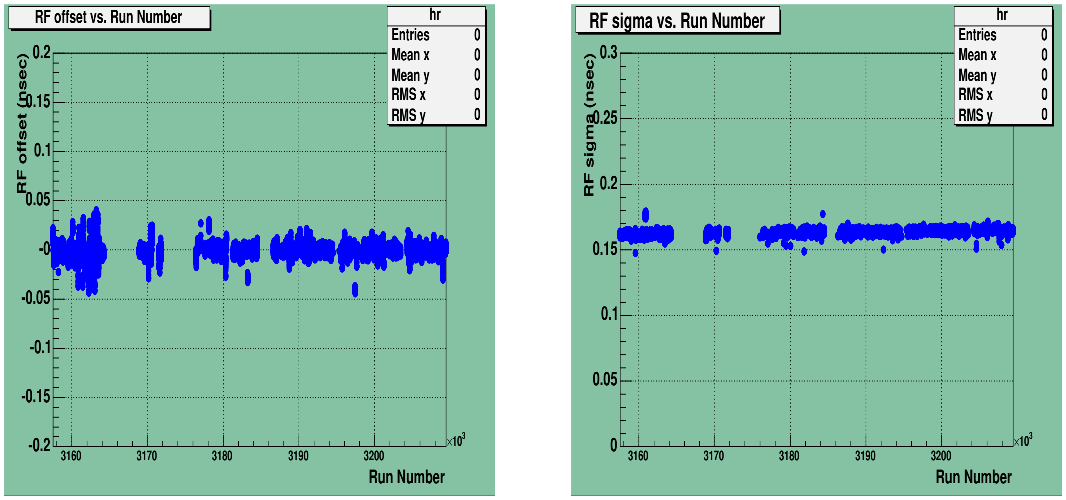

FIG. 3.10: The mean (left) and sigma (right) of the RF offset distribution after TOF calibration versus run number. An overall TOF resolution of 160 ps was obtained.

that the time of flight is accurately measured. EC time is given by:

$$t_{\mathrm{EC}} = t_{\mathrm{TOF}} + \frac{d_{\mathrm{SC-EC}}}{v \cdot \cos(\alpha)}, \tag{3.10}$$

in which t_{TOF} is the arrival time of the electron measured by the TOF detector system, $d_{\mathrm{SC-EC}}$ is the distance between SC and EC layers, v is the electron velocity which is close to the speed of light, and α is the impact angle to the EC plane (see Figure 3.11). The calibration involves fitting the reconstructed particle arrival time measured by the EC:

$$t_{\mathrm{EC}} = a_1 + a_2 \cdot \mathrm{TDC} + \frac{a_3}{\sqrt{\mathrm{ADC}}} + a_4 \cdot l^2 + a_5 \cdot l^3 - \frac{l}{v_{\mathrm{eff}}}, \tag{3.11}$$

in which a_i are five fit parameters, TDC and ADC are the TDC and ADC channels, l is the length from the hit point to the readout edge, and v_{eff} is the effective velocity of the light passing through the scintillator material. The first two terms (a_1 + a_2 $\cdot$ TDC) represent the linear TDC response; the third term ($a_3/\sqrt{\mathrm{ADC}}$) is the correction for time-walk; the fourth and fifth terms ($a_4 \cdot l^2 + a_5 \cdot l^3$) are small corrections due to the difference between the arrival times at the readout edge for

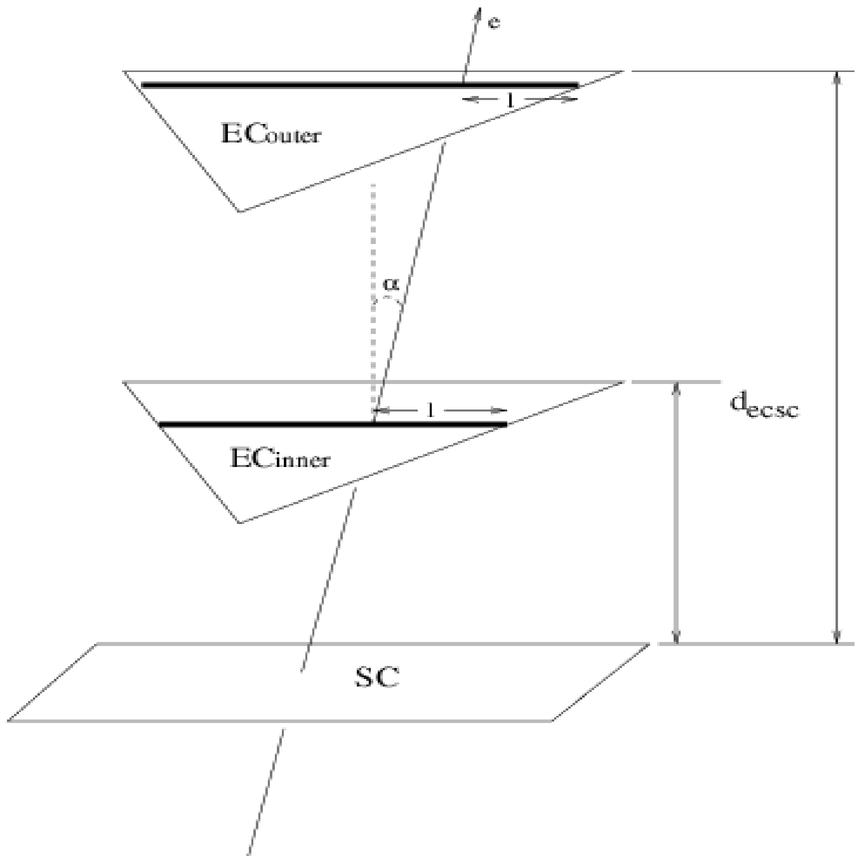

FIG. 3.11: Schematic of EC/SC timing. Using the corrected TOF time we extrapolated the EC arrival time. Here $\mathrm{d}_{\mathrm{EC-SC}}$ is the distance between the EC layer (inner or outer) and the TOF counter, α is the angle of impact of the electron with the EC plane and l is the length from the hit point to the readout edge along the scintillator bar.

the scintillator bars that are connected to the same PMT; and the last term $(\frac{l}{v_{\mathrm{eff}}})$ is compensation for transit time through the scintillator material from the hit position to the readout edge. The difference between the electron arrival time reconstructed using Eq. 3.10 and the time extrapolated from the SC time using Eq. 3.11 is shown in the Figure 3.12 for Run no. 31567 for each sector of CLAS. The EC time resolution shown in Fig. 3.12 remained $\approx$ 400 ps for the entire run period.

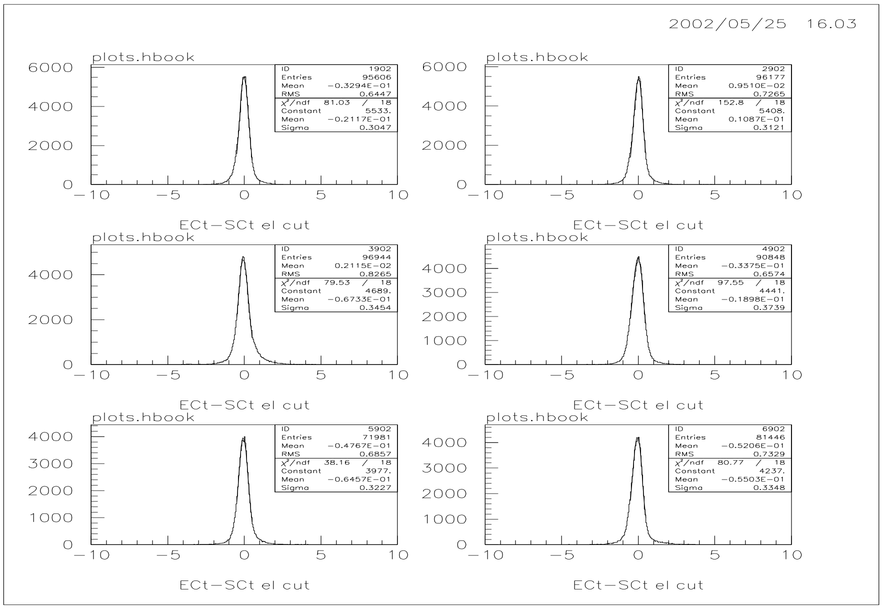

FIG. 3.12: After EC calibration the distribution of time difference between EC time and SC had a width of ≈ 400 ps. Here is shown the EC - SC time distribution for Run no. 31567.

3.2 Data Selection

The raw data is stored on magnetic tapes in a mass storage system called the SILO. The data are divided in runs of approximately 30 files and consecutively numbered in such a way that they can be identified with a specific time period during the experimental run. The CLAS detector is a complicated system and perfect operation is almost impossible. During a run of several months the conditions can change and thus the quality of the recorded data may change. The first step of analysis was to run the entire data set through the reconstruction code RECSIS which turns raw detector signals into physical variables (momentum, charge, scattering angle) for each detected particle and puts this information into BOS format files. In order to study the quality of our data we performed several checks over the entire experiment. The first check was to monitor the electron rate dividing the number

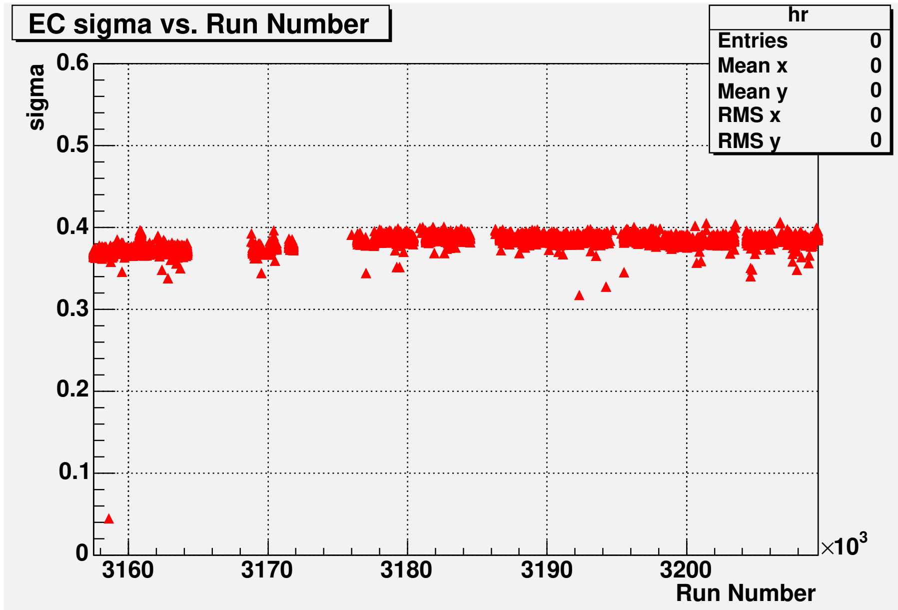

FIG. 3.13: The sigma of EC timing plotted as a function of the run number each of CLAS. The resolution was typically below 400 ps through the entire E94-019 experiment.

of electrons N_{el} by the accumulated beam charge, for each sector and file:

$$N = \frac{N_{\rm el}}{Q_{\rm FCG}}, \tag{3.12}$$

in which $Q_{\rm FCG}$ is the charge read from the live-time gated Faraday Cup. Live-time gating means that the signal is only integrated during the time the data acquisition system is live. In this way, the charge is already corrected for the data acquisition system (DAQ) dead-time. The fact that the electronics read the accumulated charge on the Faraday Cup only every 10 seconds contributes 0.4 % to the systematic error. Figure 3.14 shows the evolution of the electron rate as a function of run number separately for each sector, over the entire run period. This ratio was stable during to whole experiment with the exception of Run no. 31970– 32094 where the efficiency of Sector 6 dropped significantly due to dead wires in Region 1 of the DC. The data corresponding to Sector 6 for these runs were excluded from the analysis and an

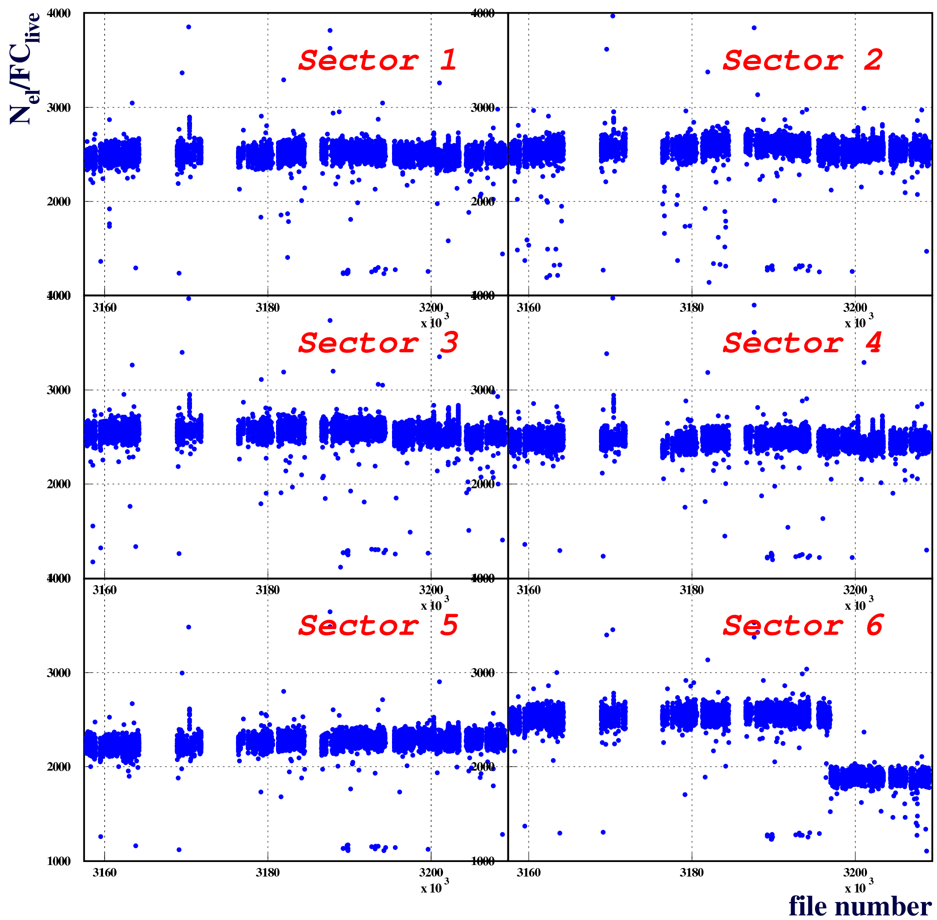

FIG. 3.14: The number of electrons that passed the ID cuts, normalized to the charge accumulated by the Faraday Cup "live-gated" and plotted as a function of the file number, for each of the six sectors of CLAS over the entire run period.

appropriate correction was made to the cross section normalization. Runs with N less than 2000 for Sectors 1, 2, 3, 4, and 6, were excluded from the analysis. Due to the lower efficiency of the DC in Sector 5, runs with N less than 1800 in this sector were excluded from the analysis. The second qualitative check that we performed was to monitor histograms generated by the reconstruction software RECSIS for each data file. These histograms were designed to monitor the quality of detector calibrations (CC, EC, DC, TOF) and reconstructions of physical observables (invariant mass, momentum, energy, β, missing mass) for different particles (electrons,

Range of Runs	Golden Runs	Silver Runs	Poor Runs
31575 – 31969	3761.56μC	256.739μC	2059.93muC
31970 – 32094	2626.96μC	82.7461μC	366.835μC

TABLE 3.1: Accumulated charge in deuterium in-bending runs. These runs were divided into golden, silver, and poor runs according to their data quality. Accumulated charges for each category are listed.

protons, neutral particles, pions). We checked the quality of these histograms for each data file. Data were selected in three categories: "golden" runs which had no negative comments in the experiment log book and at least 10^6 events (20 files), "silver" runs which had no negative records associated with it in the electronic log book, but had less than 20 files per run, and "poor" runs which had problems mentioned in the log book or low and high voltage trips in DC and TOF systems. Poor runs were not used for calibrations, but were included in the data analysis if they passed all the quality requirements mentioned here. The accumulated charge for different run ranges and quality are shown in Table 3.1.

3.3 Electron Identification

The hardware trigger, Level 2 was formed from a coincidence of signals in the electromagnetic calorimeter (EC) and the Cherenkov counters (CC), together with a good track candidate in the DC. The reconstruction software RECSIS has a more rigorous definition of an electron candidate, and rejects $\approx 50\%$ of the events that passed the hardware thresholds. In this case a "good" electron is a negatively charged particle that satisfies the following criteria:

- it has a good reconstructed track in the DC.
- it gives a hit in the CC and EC in the same sector.

- it passes the cut on the minimum energy deposited in the EC calorimeter.
- it passes the sampling fraction E/p cut.
- it satisfies the Cherenkov photo-electron cut.
- It is contained within the vertex cut.

A detailed description of the EC and CC cuts, applied in identification and selection of the electrons, is described in the following subsections.

3.3.1 Fiducial Cuts

Fiducial cuts are applied to eliminate inefficient regions of the CLAS detector systems. A good separation of electrons from pions relies heavily on a good efficiency of the CC. In order to reduce the pion contamination of the recorded raw data set, a threshold of 100 mV was set for the signal in the Cherenkov Counters. This signal corresponds on average to one photo-electron registered by the PMT. A set of cuts on polar and azimuthal scattering angles for different particle momenta and magnetic field settings was made to eliminate the inefficient edges of the Cherenkov detector [70]. The efficiency for a given bin in θ and ϕ can be written in terms of the expected average number of photo-electrons (μ) and the minimum CC threshold in photo-electrons (N_{cut}) as,

$$\epsilon_{\rm CC} = 1 - \sum_{n=0}^{n<N_{\rm cut}} \frac{\mu^n e^{-\mu}}{n!} \tag{3.13}$$

For electron momenta below 3.0 GeV/c, a software threshold was set at 2.5 photo-electrons. At this threshold the CC efficiency is greater than 80%. Using Eq. 3.13 we required an average expected signal of 5.4 photo-electrons. This number was extracted from A. Vlassov's simulation [64] which was calibrated using real data. The average number of expected photo-electrons was plotted in the θ_{el} -$\phi_{\rm el}$ plane for

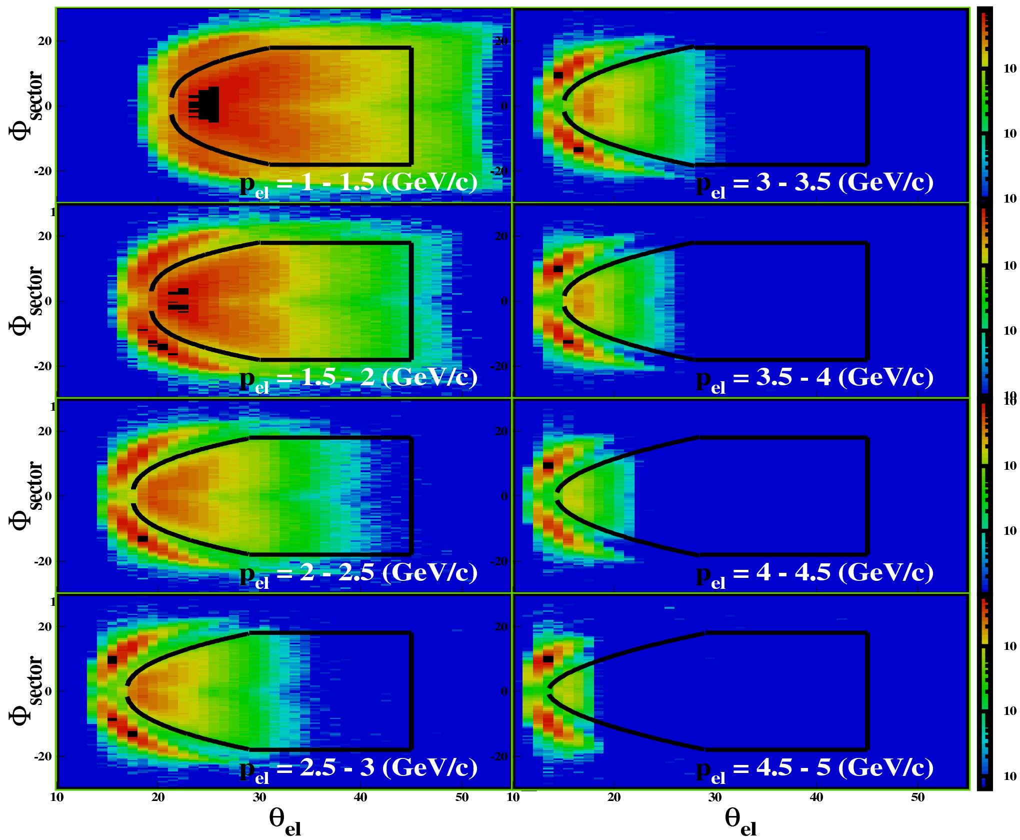

FIG. 3.15: The polar angle versus the azimuthal angle for scattered electrons from the regions where the Cherenkov counter efficiency was greater than 80%. The boundaries of the geometrical fiducial cut applied for 8 momentum bins from 0. to 5. GeV/c for Sector 1 are outlined with solid lines. Events inside these boundaries were accepted.

each of six momentum bins between 0. and 3. GeV/c (as shown in the Figure 3.15, left) and inefficient regions of the Cherenkov counter were identified.

The fiducial cut was designed as the geometrical boundary of the high efficiency region of the Cherenkov counter and was defined on a sector-by-sector basis as follows:

$$18^\circ - \Delta\phi < \phi_{\text{sect}} < 18^\circ + \Delta\phi \quad \text{and} \quad \theta_{\text{cut}} < 45^\circ, \tag{3.14}$$

where ϕ_{sect} is the electron azimuthal angle in sector coordinates (from 0° to 30°)

and

$$\theta_{\rm cut}(P_{\rm el}) = a_1 + \frac{a_2 \cdot I_{\rm torus}}{3375 \cdot (P_{el} + a_3)},$$
$$\Delta\phi(\theta_{\rm el}, P_{\rm el}) = a_4 \cdot \sin(\theta_{\rm el} - \theta_{\rm cut})^{\eta},$$
$$\eta = 0.33 \cdot \left(P_{\rm el} \frac{3375}{I_{\rm torus}} \right)^{0.33}. \tag{3.15}$$

Here a_1, a_2, a_3, a_4 are parameterization constants, I_{torus} is the torus current, P_{el} is the reconstructed electron momentum, θ_{el} is the polar angle of the detected electron (in radians), and θ_{cut} is the edge of the cut in polar angle (in radians) of the detected electron.

$\mathbf{P_{el}}$ **(GeV/c)**	$\mathbf{a_1}$	$\mathbf{a_2}$	$\mathbf{a_3}$	$\mathbf{a_4}$
$\mathbf{p_{el} < 3.0}$	12.0	25.0	0.22	35.0
$\mathbf{p_{el} > 3.0}$	11.5	22.5	0.17	42.0

TABLE 3.2: Coefficients a_1, a_2, a_3, a_4 from Eq.Eq. 3.15 for low momentum ($P_{el} <$ 3.0 GeV/c) and high momentum ($P_{el} >$ 3.0 GeV/c).

For the high momentum particles ($P_{el} >$ 3.0 GeV/c) a software cut of 1 photo-electron was used. Using Eq. 3.13, at this threshold we required an average signal of 3.3 photo-electrons, to obtain an efficiency greater than 80%. The same procedure as mentioned above was used to obtain the geometrical fiducial cut parameters as shown in Figure 3.15 (right). The parameters for both cases are summarized in Table 3.2. Additional cuts were applied to the electron polar scattering angle to account for unstable regions of CLAS observed in the actual data sample. These additional "holes" are due to TOF paddles or DC regions that malfunctioned during the data taking. They are summarized in Table 3.3.

Sector 3	$\frac{11}{0.15+P_{\rm el}\cdot I_{max}/I}+20.2<\theta_{el}<\frac{11}{0.15+P_{\rm el}\cdot I_{max}/I}+22.2$
Sector 5	$\frac{7}{0.9+P_{\rm el}\cdot I_{max}/I}+16.7<\theta_{el}<\frac{7}{0.9+P_{\rm el}\cdot I_{max}/I}+20.9$ $\frac{7}{1.5+P_{\rm el}\cdot I_{max}/I}+23.5<\theta_{el}<\frac{10}{1.5+P_{\rm el}\cdot I_{max}/I}+26.2$ $\frac{10}{0.9+P_{\rm el}\cdot I_{max}/I}+29<\theta_{el}<\frac{10}{0.9+P_{\rm el}\cdot I_{max}/I}+30.5$
Sector 6	$\frac{13}{0.1+P_{\rm el}\cdot I_{max}/I}+18.5<\theta_{el}<\frac{12}{0.1+P_{\rm el}\cdot I_{max}/I}+23$ $\frac{12}{0.15+P_{\rm el}\cdot I_{max}/I}+24.2<\theta_{el}<\frac{10}{0.15+P_{\rm el}\cdot I_{max}/I}+28.7$ $\frac{10}{0.19+P_{\rm el}\cdot I_{max}/I}+29.8<\theta_{el}<\frac{10}{0.19+P_{\rm el}\cdot I_{max}/I}+31.7$ $\frac{7}{0.35+P_{\rm el}\cdot I_{max}/I}+41<\theta_{el}<\frac{7}{0.35+P_{\rm el}\cdot I_{max}/I}+43$ $\frac{70}{1.5+P_{\rm el}\cdot I_{max}/I}-15<\theta_{el}$

TABLE 3.3: Excluded angular regions for Sectors 3, 5 and 6. Here θ_{el} is the electron polar scattering angle in degrees; $I_{\rm max} = 3375A$ is the maximum value of the torus current; $I = 2250A$ is the actual torus current for this experiment, and $P_{\rm el}$ is the electron momentum.

3.3.2 Electromagnetic Calorimeter Cuts

Pions can produce more than 2.5 photo-electrons in the most efficient region of the Cherenkov detector, by Cherenkov radiation for $P > 2.5$ GeV/c or by electron knock-out for $P < 2.5$ GeV/c. Cuts applied on the sampling fraction (defined as the ratio between E and P) in the Electromagnetic Calorimeter can reduce drastically the negatively charged pion contamination (π^-) of our main trigger (electron).

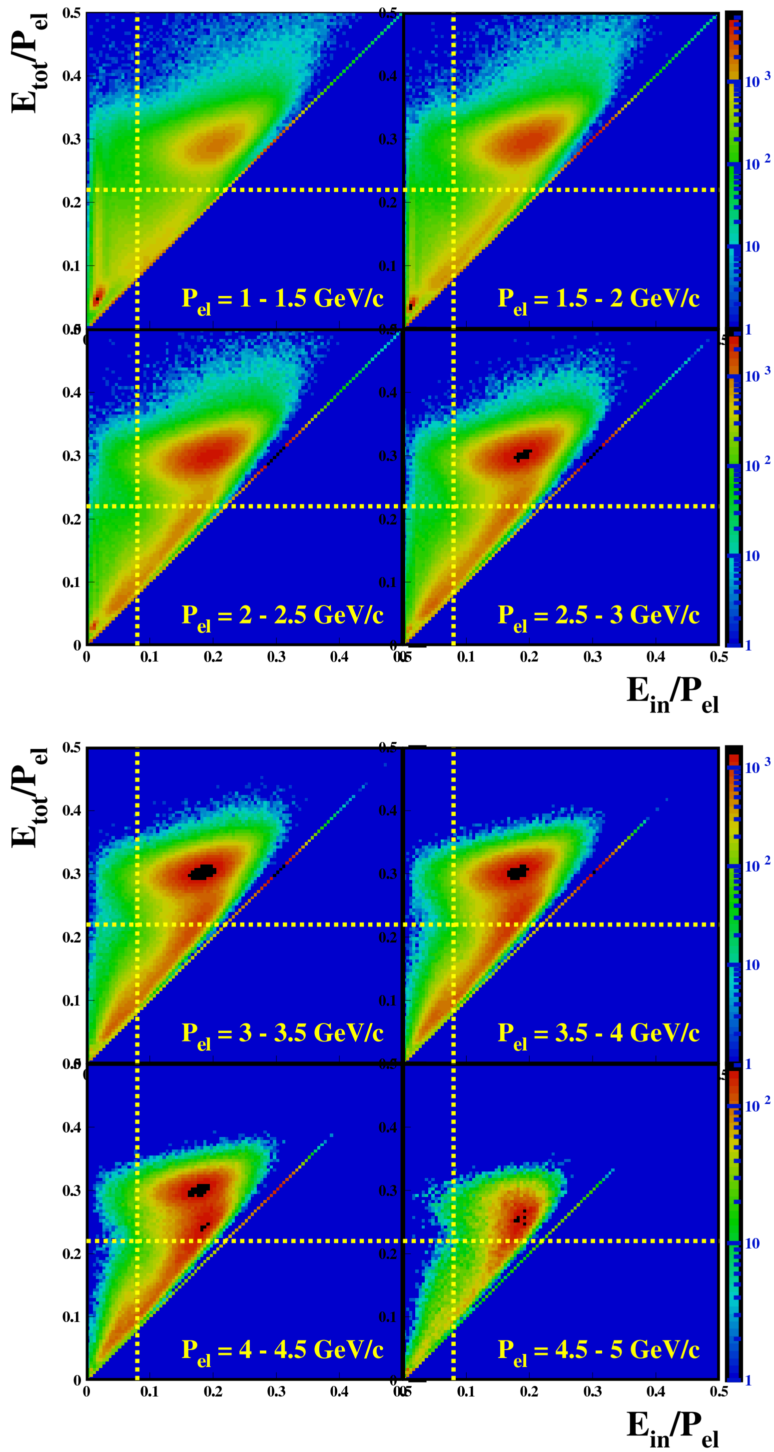

FIG. 3.16: Sampling fraction of the total energy deposited in the EC plotted as a function of sampling fraction of the energy deposited in the inner layer of the EC for momentum range from 1 GeV/c to 5 GeV/c. The EC cut on the sampling fraction is represented by dotted lines.

We plotted the total energy deposited by the first particle reconstructed in each event ($E_{\rm tot}$) as a function of the energy deposited in the inner layer of EC ($E_{\rm inner}$), both normalized to the momentum of the detected particle measured by the DC. As a result, we obtained a good separation of the detected electrons from the pion background due to the fact that pions (electrons) have a small (large) sampling fraction. Several momentum bins have been selected to reflect both low (see Figure 3.16, upper panel) and high (see Figure 3.16, lower panel) electron momenta. We can see in Fig. 3.16 the pion tail located at lower sampling fraction values ($E_{\rm inner}/P < 0.1$) while the electron sample peak can be seen at larger sampling fraction values ($E_{\rm inner}/P > 0.1$). For our data we applied the cuts $E_{\rm tot}/P > 0.22$ and $E_{\rm inner}/P > 0.08$ for good electrons.

3.3.3 Pion Contamination

Cherenkov counters can distinguish between electrons and pions because of the higher momentum threshold for pions (2.7 GeV/c) compared with electrons (9 MeV/c). Inefficient regions in the Cherenkov counters were removed by the fiducial cuts described earlier. Therefore, particles that produce a small signal in the CC were assumed to be pions misidentified as electrons. Two cuts on the number of photoelectrons detected in the CC were applied depending on the scattered electron's momentum:

- For $P_{el} < 3$ GeV/c, events with $N_{phel} > 2.5$ were accepted.
- For $P_{el} > 3$ GeV/c, events with $N_{phel} > 1$ were accepted.

By using these cuts as part of the particle identification we rejected some of the electrons that did not have a high enough signal to pass the EC and CC ID cuts. A fraction of pions, on the other hand, did pass the ID cuts and they contaminate the data sample. Both cases need to be considered for the final counting. By simulating a pure sample of electrons and obtaining the CC response in the region where the CC cut was applied we can estimate the loss of good electrons due to those cuts (see Figure 3.17 left and right). An efficiency of $\approx 90\%$ was obtained for the CC

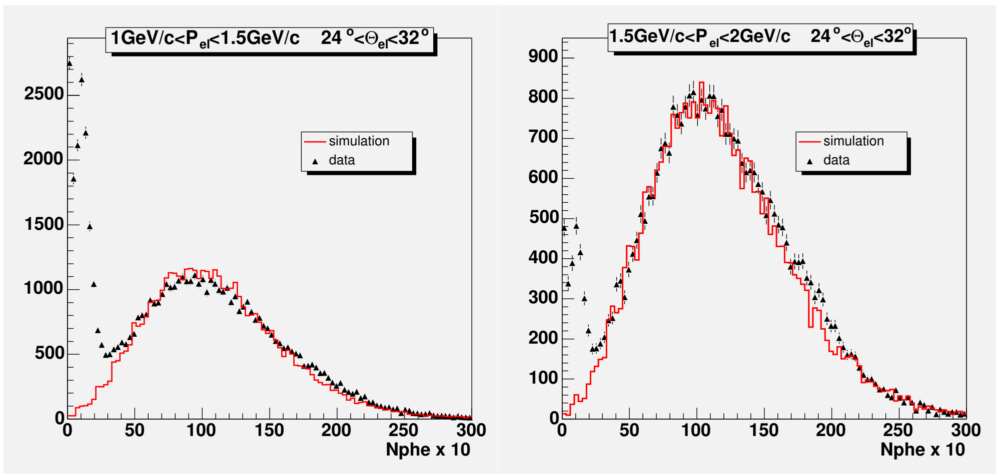

FIG. 3.17: The Cherenkov response to a simulated electron data sample (solid line) together with the measured Cherenkov response to real data (solid triangles) for two electron momentum ranges $1 < p_{el} < 1.5$ GeV/c (left panel) and $1.5 < p_{el} < 2$ GeV/c (right panel).

photoelectron cuts above. Using a selected sample of pions we obtained the pion contamination rate of our sample. The Cherenkov photoelectron spectrum for measured electrons was fitted using the sum of the simulated CC response distribution for pure pion sample (scaled by a factor A) and the simulated CC response distribution for ideal electrons with no pion contamination (scaled by a factor B) as shown in the Figure 3.18. The pion spectrum, normalized to the measured CC spectrum, was integrated above the CC cuts (2.5 and 1 photo-electrons corresponding to different momenta ranges) and used to estimate the pion contamination rate of the measured data sample after applying all ID cuts. The total fraction of pions to electrons was estimated for the electron momentum range $1 - 2.6$ GeV/c, and was fitted with the function $\frac{N_\phi}{N_{\rm el}} = ae^{bP_{\rm el}}$ (see Figure 3.19). The same functional form

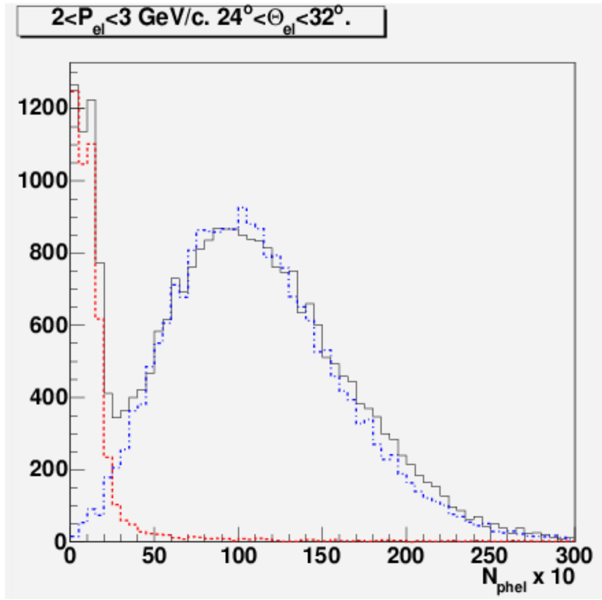

FIG. 3.18: The Cherenkov counters response to measured electrons (solid line) compared to a simulation for pions (dashed line) and electrons (dash-dotted line).

was used for determining the pion contamination for $P_{el} > 3.0$ GeV/c. In parallel a study of EC cuts efficiency was performed [70]. An efficiency of $\approx 95\%$ for the sampling fraction cuts was found.

3.3.4 Contamination from e^+e^- Pair Production

Pair-symmetric leptons (e^+e^-) in CLAS come largely from $\pi^0 \to \gamma e^+e^-$ processes (Dalitz decay), from bremsstrahlung photons generated in the target or by $\gamma\gamma$ decays with one of the photons converting to e^+e^-. Following the procedure described in Ref. [71] we evaluated the level of contamination due to electron-positron pair production in our electron data sample by analyzing runs taken with identical beam energies but opposite torus polarity. In this way the detector acceptance canceled out in the ratio of rates of positrons with negative torus polarity and electrons with positive torus polarity, and similarly for positrons with positive torus polarity to rates of electrons with negative torus polarity. The rates were determined using

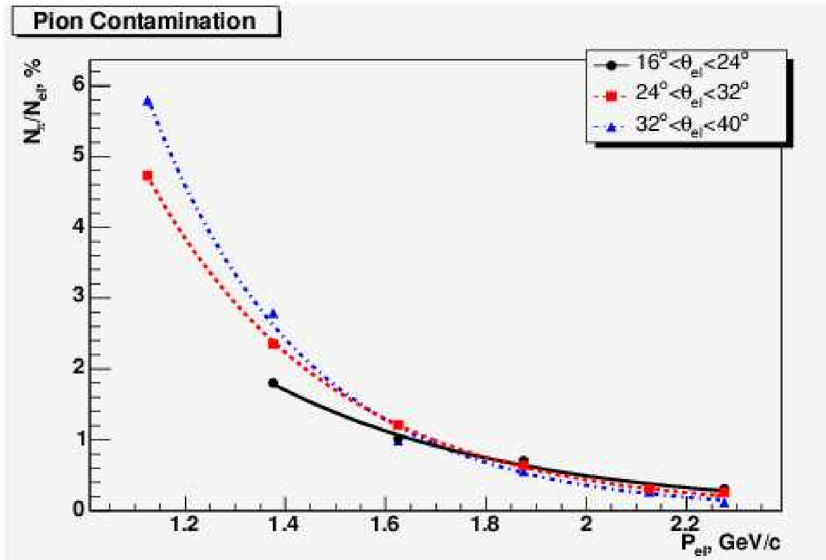

FIG. 3.19: Fit to measure π/e ratios after the CC cut. The curves correspond to different electron polar angles. The plot is from Ref. [70].

the ratio of events passing our electron ID and fiducial cuts, divided by the live-time corrected Faraday Cup readings. Three types of particle identification were used: A) electrons using the ID cuts described earlier in the section, B) pions using the CC photo-electron cut ($0.3 < N_{phel} < 1.5$), and C) electrons using a hard cut $N_{phel} > 6$. The out-bending data were used to produce the same plots for positrons as in the electron case. For these data the "positron trigger" required the first particle in each event to have a positive charge and hits in both the CC and EC detector systems. Histograms obtained using ID setting A were fitted with the sum of B and C histograms (see Figures 3.20, left and right). The integral of histograms obtained using ID setting B for the positrons were then used as a number of electrons coming from e^+e^- pair production. The same sets of histograms for the electron were used as denominator in the e^+e^- ratio. This study is explained in more detail in Ref. [70]. The ratios obtained were fitted as a function of the electron scattering angle and momentum, resulting in a parameterization over all momentum and angular ranges.

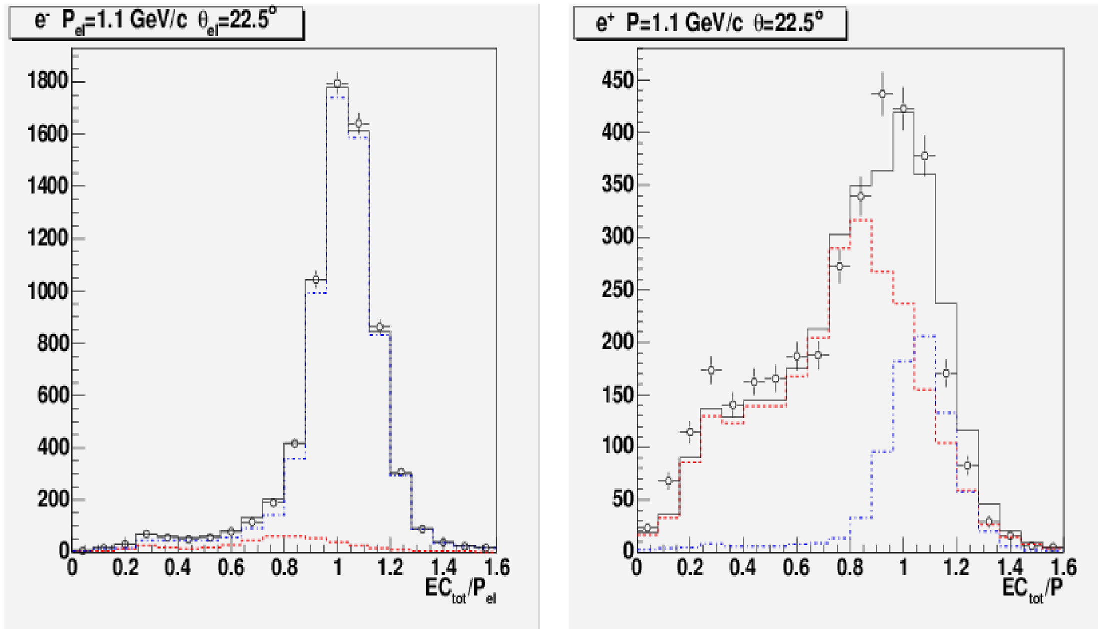

FIG. 3.20: Electron (left) and positron (right) histograms of $\mathrm{EC}_{total}/\mathrm{P}_{el}$. Black circles, dot-dashedlines, dashed lines and black solid lines correspond to ID cuts A, B, C and B+C, respectively. Plots are from Ref. [70].

The ratio was fit to $\frac{e^+}{e^-} = ae^{-bP_{el}}$ (see Figure 3.21). Parameters a and b were then fit with 3rd and 5th order polynomials in scattering angle. The extracted correction function was applied event by event to the data.

3.3.5 Electron Vertex Correction

Due to a possible beam offset there is an azimuthal angular dependence of the reconstructed electron vertex Z_{el}. This dependence is a result of the tracking reconstruction code which calculates the vertex of the particle by extrapolating the track to the nominal beam axis. In order to apply the same sets of vertex cuts for all six sectors, we performed a geometrical correction to align the reconstructed vertices:

$$Z_{\mathrm{corr}} = Z_{\mathrm{rec}} + \frac{r}{\tan(\theta)} \cos(\phi - \phi_{\mathrm{beam}}) \tag{3.16}$$

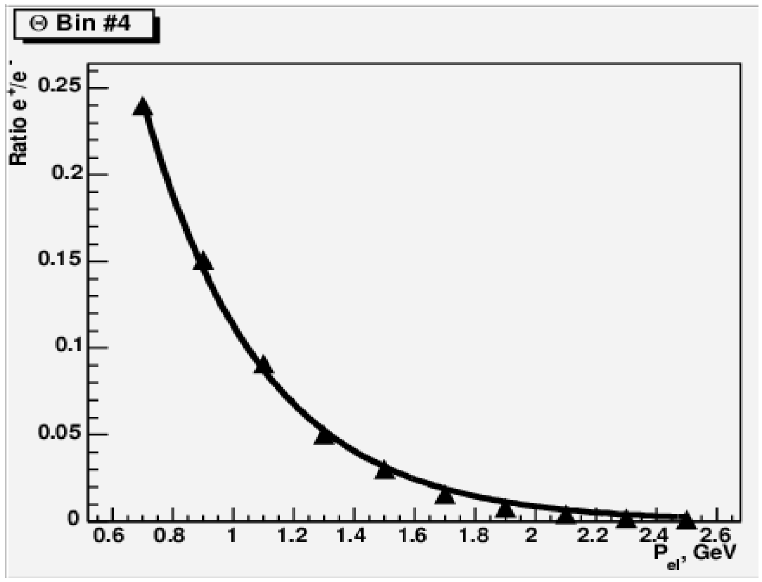

FIG. 3.21: The fit of the momentum dependence of the positron to electron ratio, for one of several bins in electron scattering angle. This result is from Ref. [70].

where $Z_{\rm corr}$ is the real vertex position along the target axis from where the detected electron have originated, $Z_{\rm rec}$ is the initial reconstructed electron vertex, θ and ϕ are the polar and the azimuthal electron scattering angles, and r is the distance from the axis, along the target, to the actual beam line. The beam offset, defined by $\phi_{\rm beam}$ and r, is obtained from the fit to the distribution of the average vertex position over all sectors. The electron vertex distribution before and after vertex corrections is shown in Figure 3.22.

3.3.6 Electron Vertex Cut

An electron vertex cut is required in order to remove events that came from the target walls, the scattering chamber or the entrance and exit foils. An electron vertex cut from -2.0 to 1.5 cm relative to the center of CLAS was applied as shown in Figure 3.23. An additional cut of minimum scattered electron momenta of 1 GeV/c was applied in order to reject the sample of data with high levels of pion and

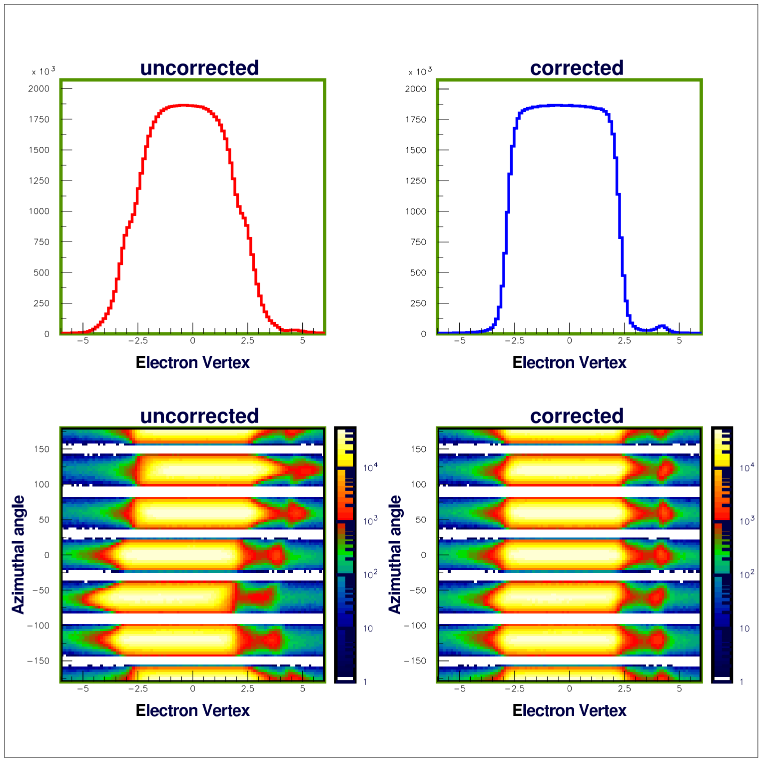

FIG. 3.22: The electron Z vertex distribution before (left) and after (right) corrections. The upper panel shows histograms of Z, whereas the lower panels show the azimuthal angular distributions of the Z.

e^+e^- contamination.

3.4 Proton Identification

3.4.1 Time-of-Flight Back-Paddle Correction

In this analysis we are focusing on protons at large scattering angles ($> 50°$), and the accuracy of detecting them relies heavily on the accuracy of the TOF detector system. Due to the geometry of CLAS, at larger scattering angles the resolution of the TOF system degrades as the lengths of the scintillators increases. Moreover the large-angle paddles (no. 40 to 48) are composed of two scintillators coupled (glued) together and the time response of each half is different (Figure 3.24). This

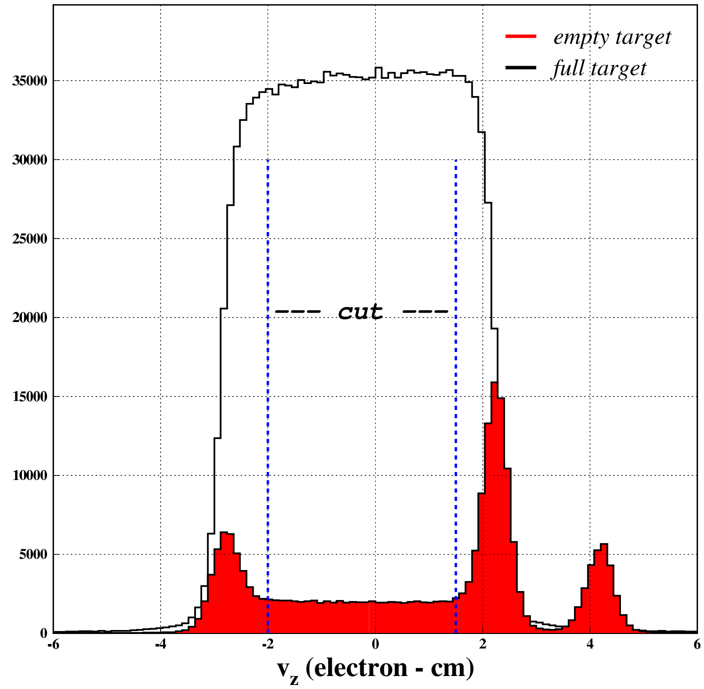

FIG. 3.23: The electron vertex cut. A vertex cut $-2 < v_z < 1.5$ cm is required to eliminate the target wall contribution.

feature, and the fact that the number of backward going particles used to calibrate the coupled paddles is extremely low, makes an accurate calibration difficult. For this analysis a special effort was made to calibrate the coupled paddles in the TOF detector system, corresponding to backward-going protons. This task require: identification and exclusion of the inefficient paddles, and correction of the overall time offset for efficient paddles on a sector-by-sector basis. In order to determine the time offset (Δt_{pr}) between the expected and recorded time of flight (computed from the DC path length, momentum and energy), for each scintillator within coupled paddle, we defined:

$$\Delta t_{\mathrm{pr}} = t_{\mathrm{sc}} - t_{\mathrm{start}} - \frac{r_{\mathrm{sc}}}{P_{\mathrm{pr}}/E_{\mathrm{pr}}} \tag{3.17}$$

in which t_{sc} is the time recorded by the scintillator counters, t_{start} is the event start time, r_{sc} represents the path-length of the particle from the target to the scintillator plane, and P_{pr} and E_{pr} are respectively the momentum and the energy of the detected

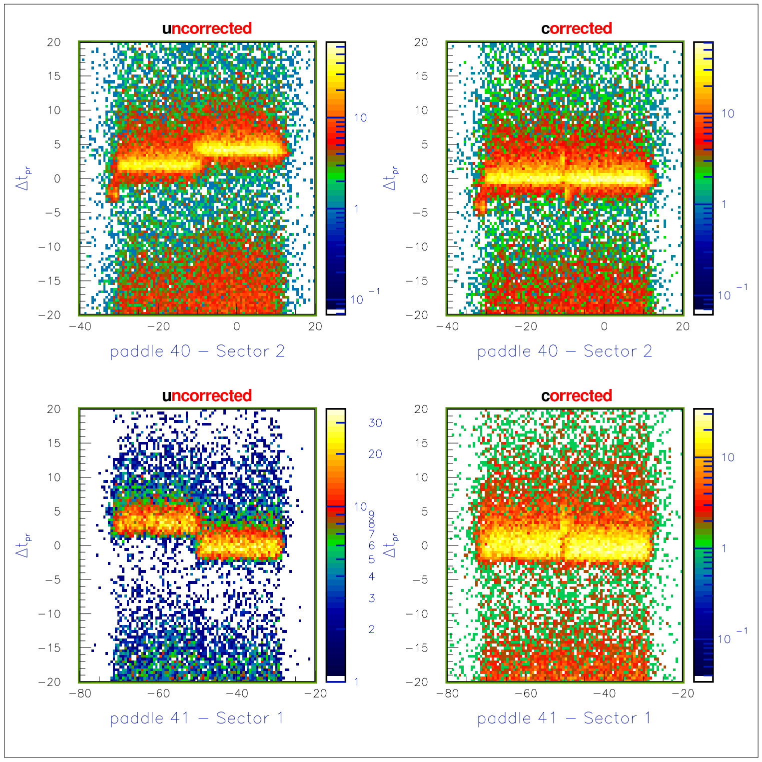

FIG. 3.24: Time offsets for Paddle no. 40 in Sector 2 and Paddle no. 41 in Sector 1 before (left) and after (right) corrections. Here the proton time vertex is plotted versus the scintillator mid plane coordinate.

charged particle (in this case we used large-angle protons). The actual time of flight recorded is corrected by this offset, ultimately improving the time resolution and identification of backward protons. An example of this procedure is shown in Figure 3.25, where the difference between recorded time of flight and expected time of flight is shown as a function of counter mid plane Z coordinate for TOF paddles of Sector 1. We placed protons in the secondary position in each event following the electron. Protons detected in the scintillator counters had to fall within a 12 ns window: from -5.0 to 7.0 ns from the expected arrival time as shown in Figure 3.26.

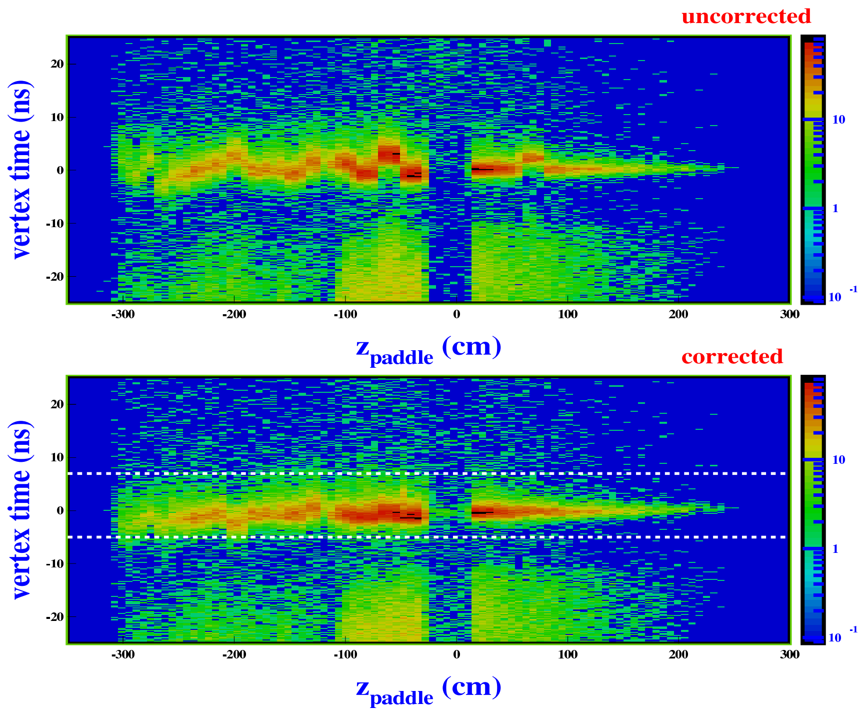

FIG. 3.25: The differences between expected and recorded times of flight for protons versus the scintillator counter mid plane coordinate Z, before (upper) and after (lower) correction. The time window required for proton ID is shown with dashed-lines in the lower plot.

3.4.2 Proton Vertex Correction

As in the electron case there is an azimuthal angular dependence of the reconstructed proton vertex Z_{pr} due to the beam offset. This dependence results from RECSIS calculating the proton vertex by extrapolating the track to the central axis of CLAS rather than the actual beam axis. Using the same correction function as in the electron case, we found the position of the beam, defined by ϕ_{beam} and r, using the fit to the distribution of average vertex positions for all 6 sectors in CLAS. An offset of $r = \pm 1.8$ mm and $\phi_{\text{beam}} = -58°$ (toward Sector 6) was observed. The proton Z vertex distribution and the azimuthal angle ϕ, plotted as a function of Z for the proton vertex before and after corrections, are shown in Figure 3.27.

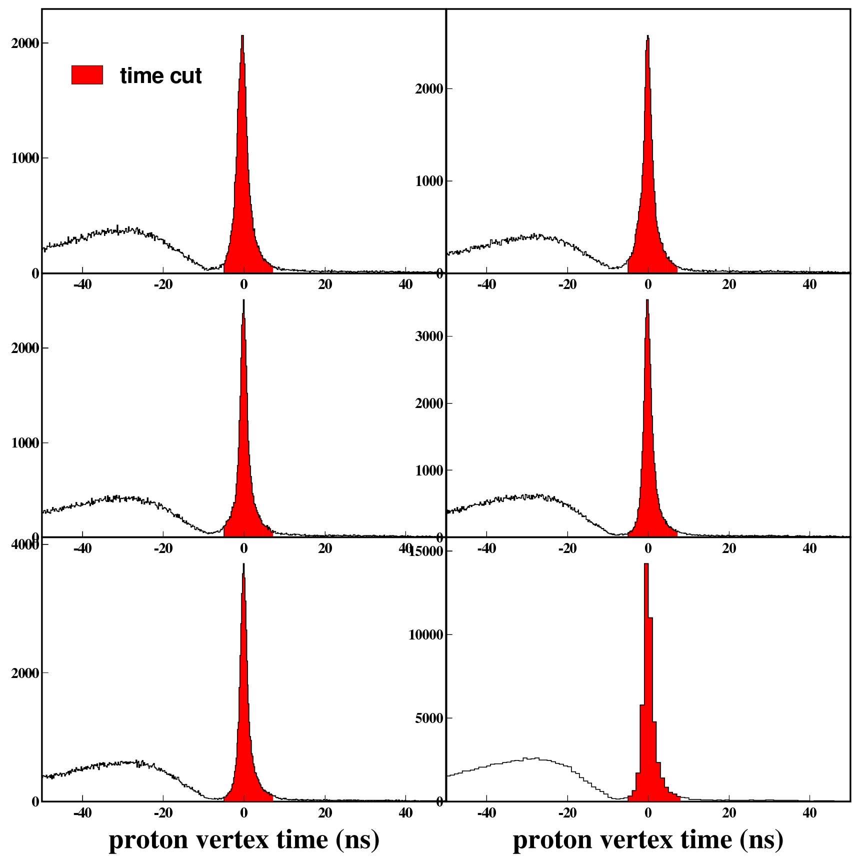

FIG. 3.26: The time cut window from -5.0 to 7.0 ns (full area) for each sector in CLAS. All the positively charged particles (protons) detected in this time window were selected for this analysis.

3.4.3 Proton Vertex Cut

Detected protons can come from different sources. They could be produced by the target entrance and exit windows, which are made of thin aluminum foil, by the target support structure, or by the target cell walls. In order to select just the protons coming from within the target cell, a proper vertex cut needs to be applied. For slow-moving protons (large scattering angles) the detector resolution is lower than for the fast electrons case, thus a wider vertex cut is required. We applied the proton vertex cut on the Z_{pr} axis of the target, along the beam direction, such

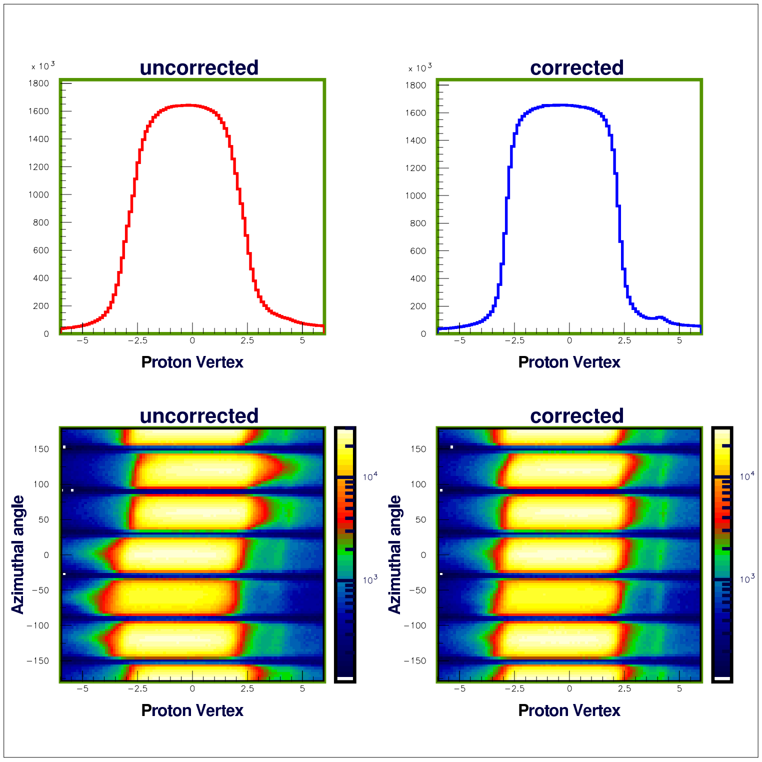

FIG. 3.27: Proton vertex corrections. Upper plots show the uncorrected (left) and corrected (right) Z position of the proton vertex. Lower plots shows the uncorrected (left) and corrected (right) azimuthal angular dependence of the proton vertex.

that $-2.0 < Z_{pr} < 1.5$ cm as shown in Figure 3.28 (left). The physical re-scattering target is reconstructed from the electron vertex plotted versus the proton vertex and is shown in Fig. 3.28 (right). Another cut was applied such that the difference between proton and electron vertices was between -2.0 and 2.0 cm.

3.4.4 Energy Loss Correction

Protons lose energy as they pass through the target material. To correct for energy loss we used GSIM, a simulation of the CLAS detector based on the GEANT Monte Carlo package. We generated a flat distribution of protons over the entire

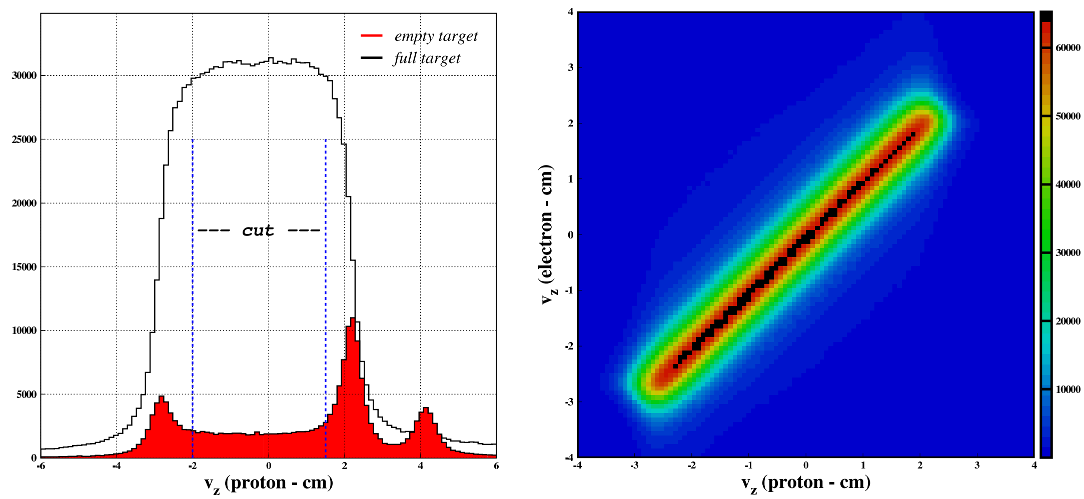

FIG. 3.28: Proton vertex (left) for full (empty histogram) and empty target (filled histogram), and electron vertex versus proton vertex (right). A proton vertex cut $-2 < Z_{Pr} < 1.5$ cm was applied to eliminate the target walls contribution.

azimuthal range (0° - 360°), with a momentum range up to 5 GeV/c and a polar angular range between 10° and 140°. We used GSIM to simulate the CLAS detector and the target, and produced a set of files analogous to our raw data. The GSIM post processor (GPP) was used to remove dead wires in the DC and dead PMTs in the TOF, as in the analysis of the experimental data. GPP also smeared the Monte Carlo data to account for the spatial resolution of the DC and the timing resolution of the TOF detectors. The smearing was adjusted such that simulated distributions agreed with the experimental data. This procedure is explained in more detail in the Section 5.3.1. In the reconstruction of the simulated events the same analysis package RECSIS was used as for the real data. We constructed momentum distributions of generated and reconstructed protons for 15 bins in the polar scattering angle. Figure 3.29 shows the difference between the generated and reconstructed proton momenta, $p_0 - p$, normalized to the reconstructed momentum, versus reconstructed momentum (upper plot), and the proton momentum corrected for energy loss as a function of the uncorrected proton momentum (lower plot). We

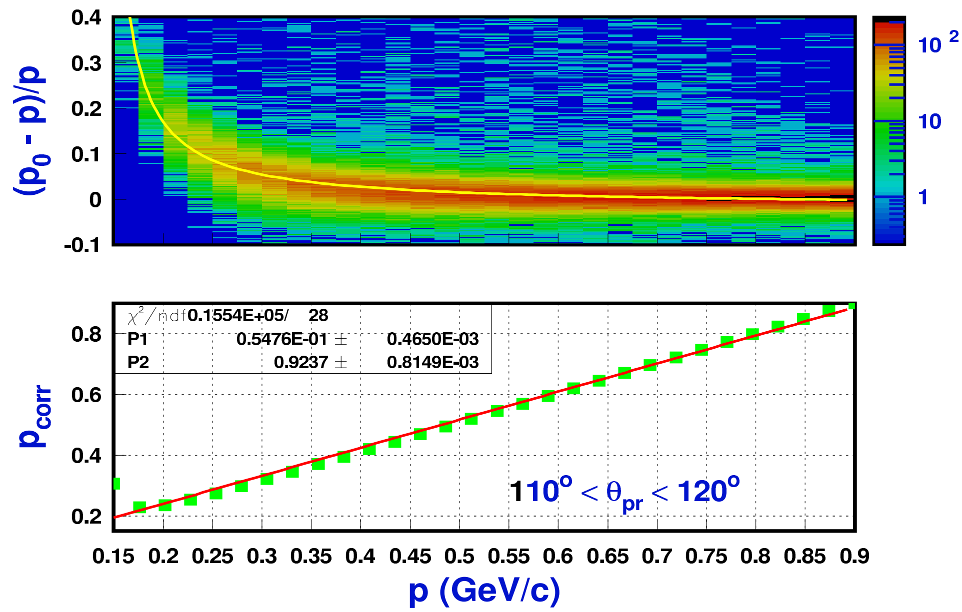

FIG. 3.29: Energy loss correction for recoil protons. Upper plot shows the difference between the generated and reconstructed proton momenta $(p_0 - p)/p$, normalized to the reconstructed momentum, versus reconstructed momentum (p). Corrected momentum versus reconstructed momentum is shown in the lower plot for the polar angle $110° < \theta < 120°$.

fitted the above distributions with a hyperbolic type function of the form:

$$P_{\mathrm{corr}} = P_{\mathrm{rec}} \left(1 + p_1 + \frac{p_2}{P_{\mathrm{rec}} - p_3} \right), \qquad (3.18)$$

where P_{corr} is the proton momentum corrected for energy loss, P_{rec} is the initial reconstructed proton momentum, and p_1, p_2, and p_3 are fit parameters given in Table 3.4. This correction was applied event-by-event in the final analysis.

3.4.5 Momentum and Angular Corrections

Due to inaccuracies in the magnetic field map and in the drift chamber alignment, the reconstructed momenta of detected charged particles deviate from their "true" values. For semi-inclusive data (e.g. d(e,e′p)), the mean value of the missing mass peak deviates from the expected mass of the neutron $M_{\mathrm{neutron}} = 0.939565$ GeV

θ_p (deg.)	p_1	p_2	p_3
10. – **20**.	−0.00489	0.00448	0.16164
20. – **30**.	−0.00670	0.00537	0.14818
30. – **40**.	−0.00704	0.00545	0.14537
40. – **45**.	−0.00499	0.00448	0.14759
45. – **50**.	−0.00583	0.00490	0.14362
50. – **55**.	−0.00638	0.00530	0.14111
55. – **60**.	−0.00599	0.00481	0.14451
60. – **70**.	−0.00501	0.00438	0.14775
70. – **80**.	−0.00702	0.00548	0.13975
80. – **90**.	−0.00927	0.00682	0.12483
90. – **100**.	−0.00701	0.00550	0.14232
100. – **110**.	−0.00950	0.00674	0.12601
110. – **120**.	−0.00693	0.00559	0.12857
120. – **130**.	−0.00353	0.00428	0.14702
130. – **140**.	0.00150	0.00124	0.24677

TABLE 3.4: The fitted coefficients p_1, p_2, and p_3 of Eq. 3.18 for 15 bins of the proton polar scattering angle.

with a significantly broadened width (see Figure 3.30, upper panel). The correction procedure was developed by A. Klimenko and S. Kuhn and reported in Ref [72]. This procedure was developed using completely exclusive reactions, where the kinematics were over-determined. Deviations of measured values from expected ones, $d\theta$ in the polar scattering angle, and dp in the momentum for a detected particle, and $d\phi$ in the azimuthal angle were fit using 14 free parameters for each sector by minimizing the sum of the squared differences of initial and final four-momenta in the following reactions:

$$\begin{aligned} e+p &\rightarrow e'+p' \\ e+p &\rightarrow e'+p'+\pi^+\pi^- \\ e+d &\rightarrow e'+p'+p''+\pi^- \end{aligned} \tag{3.19}$$

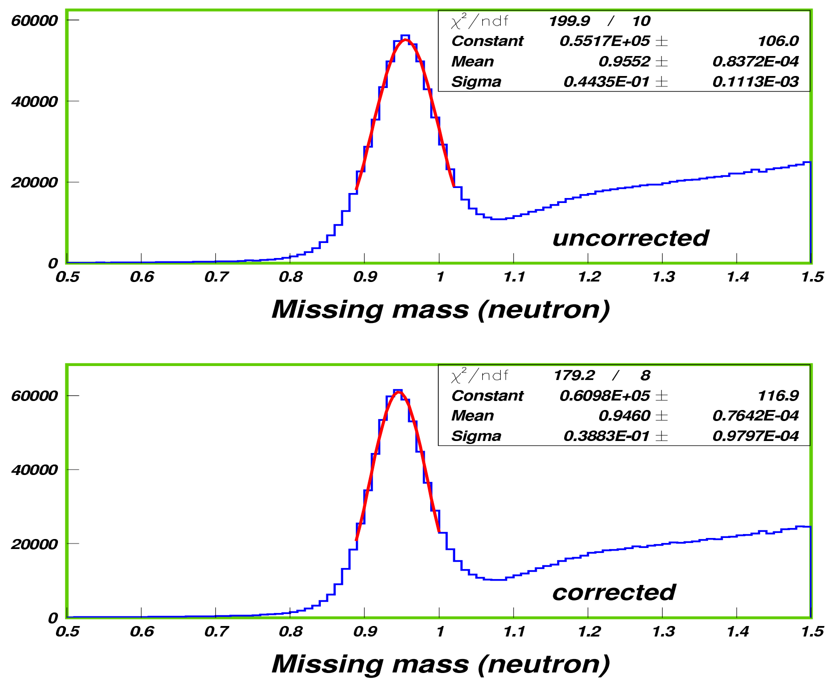

FIG. 3.30: Uncorrected (left) and corrected (right) missing mass distributions for the exclusive d(e,e'p)n channel. An overall momentum resolution of 40 MeV/c was obtained for this data set.

During the fitting procedure hadron momenta were corrected for the energy losses inside the target. The functional form used for the polar angle is:

$$\begin{aligned} d\theta &= (c_1 + c_2\phi_{\rm rec})\frac{\cos\theta_{\rm rec}}{\cos\phi_{\rm rec}} + (c_3 + c_4\phi_{\rm rec})\sin\theta_{\rm rec} \\ \theta_{\rm corr} &= \theta_{\rm rec} + d\theta \end{aligned} \tag{3.20}$$

where c_1, c_2, c_3, and c_4 are fit parameters, θ_{rec} and ϕ_{rec} are the polar and the azimuthal scattering angles of the detected particle as reconstructed by the tracking software (RECSIS), and θ_{corr} is the corrected polar scattering angle. The functional form used for the momentum is:

$$
\begin{aligned}
dp &= \left[(c_5 \sin\theta_{\mathrm{rec}} + c_6\phi_{\mathrm{rec}})\frac{\cos\theta_{\mathrm{corr}}}{\cos\phi_{\mathrm{rec}}} + (c_7 + c_8\phi_{\mathrm{rec}})\sin\theta_{\mathrm{corr}}\right]\frac{p_{\mathrm{rec}}}{qB_{\mathrm{torus}}} \\
&+ \quad c_9 + c_{10}\phi_{\mathrm{rec}} + c_{11}\phi_{\mathrm{rec}}^2 + (c_{12} + c_{13}\phi_{rec} + c_{14}\phi_{\mathrm{rec}}^2)\sin\theta_{\mathrm{corr}} \\
p_{\mathrm{corr}} &= p_{\mathrm{rec}} + dp
\end{aligned}
\tag{3.21}
$$

where p_{rec} is the reconstructed momentum of the particle and q is its charge in units of the elementary charge e. The parameterization of the integral $\int B \cdot dl$ along the path of the track is given by:

$$
\begin{aligned}
B_{\mathrm{torus}} &= 0.76\frac{I_{\mathrm{torus}}\mathrm{sin}^2 4\theta}{3375\theta(\mathrm{rad})}, \quad \text{for} \quad \theta < \frac{\phi}{8} \\
B_{\mathrm{torus}} &= 0.76\frac{I_{\mathrm{torus}}}{3375\theta(\mathrm{rad})}, \quad \text{for} \quad \theta \geq \frac{\phi}{8}
\end{aligned}
\tag{3.22}
$$

Corrections for drift chamber displacements are parameterized by the coefficients c_1 to c_8, and the corrections for errors in the magnetic field map are parameterized by the coefficients c_9 to c_{14}. The parameters are determined by minimizing the χ^2 of the fit using the CERNLIB routine MINUIT. After applying these corrections, the width σ of the invariant mass distribution was improved by ≈ 10 MeV/c , resulting in an overall momentum resolution of ≈ 40 MeV/c. The momentum dependence of the electron polar θ_{el} and azimuthal ϕ_{el} scattering angles was minimized significantly as well, as shown in Figure 3.31.

3.4.6 Accidentals Protons

After cuts were applied to the electron and proton vertices, and to the difference between them, there was still the possibility of accidental coincidences. These accidental coincidences are coming from an electron detected in coincidence with a proton produced by the photo-disintegration process of deuterium or by proton

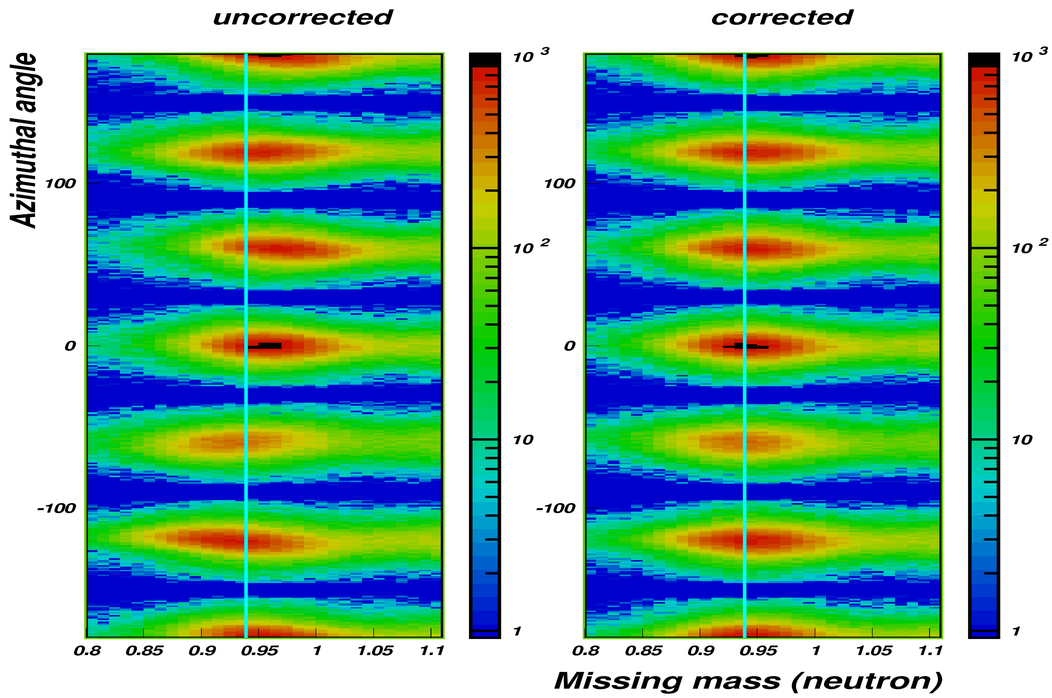

FIG. 3.31: Uncorrected (right) and corrected (left) missing mass distributions versus azimuthal electron scattering angle for the exclusive d(e,e$'$p)n channel, in CLAS.

re-interaction with another deuterium nucleus. At the same time these cuts could be rejecting "good" protons, and the fraction of rejected protons needs to be estimated as well. An accidental proton was defined as a positively charged particle having a time-of-flight measured to be at least 12 ns longer than that expected for a proton with the same momentum (see Eq. 3.17). The time windows for true and accidental protons were taken to have the same width of 12 ns. The window for accidental protons was chosen at least 5 ns below the peak of good coincidence deuterons to avoid an overlap as shown in Figure 3.32. An average background of 7% was estimated by comparison between the rate of accidental electron-proton coincidences in the time window described above with the unbiased data sample of coincidences using the particle identification procedures and cuts described earlier. However, the further the proton time deviates from the start time ($\approx$ 20 ns), the worse is the tracking

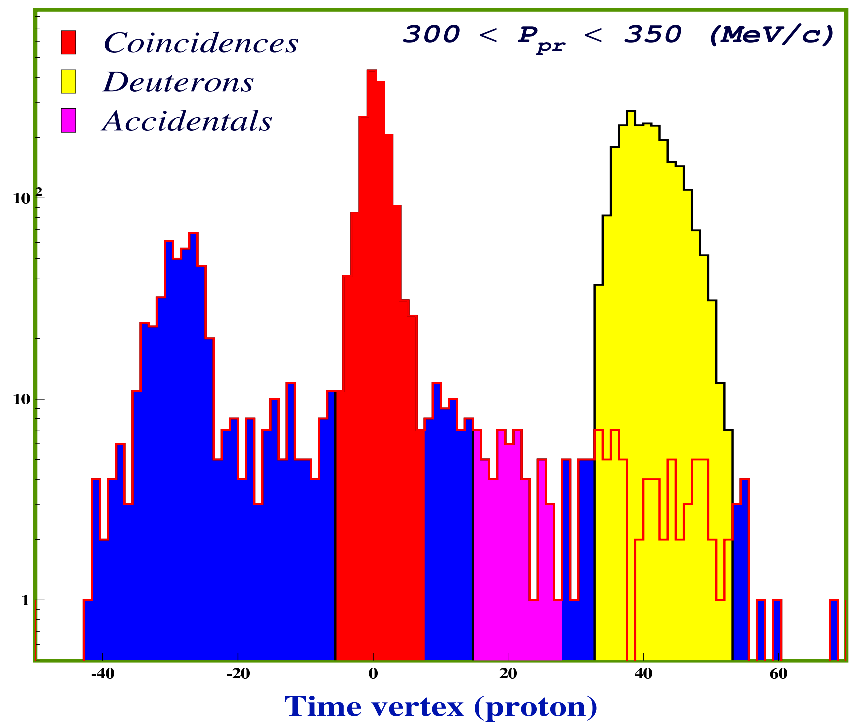

FIG. 3.32: Relative electron-proton timing at the target vertex. The accidental coincidence window (magenta) was taken to be 12 ns, above the expected arrival time of good coincidence protons (red), and 5 ns below the expected arrival time of coincident deuterons (yellow).

efficiency. As a result, accidentals are underestimated. The data sample contains two-step process accidentals, where a scattered electron reinteracts further along the target cell and knocks out a proton which arrives with "good" TOF. Protons produced in such a way enhance the positive side of the vertex difference $Z_{pr} - Z_{el}$. To account for two-step accidental coincidences we selected a data sample of good protons in coincidence with electrons detected outside of our vertex difference cut $|\Delta Z| > 2.$ cm which was subtracted from "good" coincidences. The correction factor and the systematic uncertainties associated with these selections are presented in Section 4.4.

CHAPTER 4

Physics Analysis

4.1 Event Selection and Kinematic cuts

The first task of this analysis was to reduce the data sample, by selecting events with an electron and a proton. The next step was to select quasi-elastic events with a cut on *ep* missing mass (MM) centered on the neutron mass. This missing mass spectrum is shown in Figure 4.1 plotted versus the momentum (< 1 GeV/c) of the proton. We were able to detect protons with a momentum as low as 250 MeV/c. The band centered at the neutron mass ($m_n \approx 0.939$ GeV) clearly separates the quasi-elastic events from the inelastic events at missing mass greater than 1.1 GeV. The relatively large momentum resolution ($\sigma \approx 40$ MeV/c) of the CLAS detector for electrons is responsible for the broad quasi-elastic missing mass peak. In ideal conditions the missing mass distribution should present a narrow peak because the Fermi motion in quasi-elastic scattering is taken into account. We applied a cut to this missing mass spectrum around the known neutron mass. Thus, this cut eliminated some good events while failing to exclude some inelastic background. We performed a simple study to estimate the ratio of the signal (quasi-

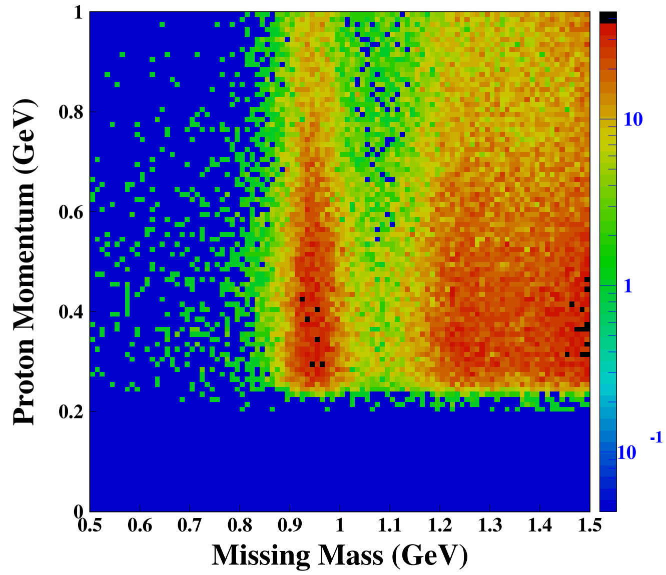

FIG. 4.1: Missing mass distribution for electron plus proton coincidence events as a function of the scattered proton momentum. The band centered at the neutron mass clearly identifies the quasi-elastic events. The inelastic events have missing mass greater than 1.1 GeV.

elastic peak) to the background (inelastic contribution) by varying the MM cuts and looking at the Bjorken scaling variable x distribution. To select a clean inelastic sample we accepted events far from the quasi-elastic peak with $1.2 < MM < 1.3$ GeV. A clean quasi-elastic sample was obtained by selecting events with $MM <$ 0.9 GeV (see Fig. 4.1), where the inelastic contribution is insignificant. The x spectrum obtained by applying different missing mass cuts is presented in Figure 4.2 (left). We can see that the x distribution, symmetric about $x = 1$ for elastic scattering, is enhanced on the low site by the inelastic background. With more restrictive MM cuts the x distribution becomes more symmetric as the inelastic events are eliminated. Figure 4.2 (right) shows that the integral of the quasi-elastic x distribution increases until $MM = 1.05$ GeV and then reaches a plateau as all quasi-elastic events are accounted for. At the same time the inelastic background increases more dramatically with increasing missing mass. The cut $MM = 1.05$ GeV maximizes the quasi-elastic signal while minimizing the inelastic background.

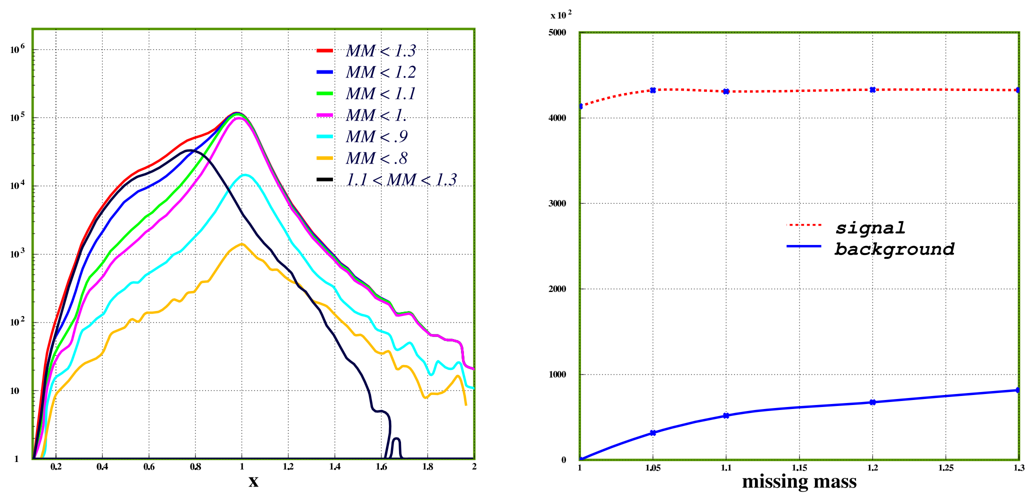

FIG. 4.2: Left: x distribution evolution for several cuts on the missing mass (MM) quasi-elastic peak. The integral of the black curve represents the contribution from the inelastic background while the integral of the blue curve is the contribution from clean quasi-elastic events. To maximize the ratio of the signal (quasi-elastic peak of MM distribution) to the inelastic background we have chosen the missing mass cut as: $MM < 1.05$ GeV/c. Right: The quasi-elastic signal and respectively the inelastic background evolution with the missing mass cut.

The curves in Fig. 4.2 (right) provide the correction factors for background and quasi-elastic events.

A more rigorous way to determine the best missing mass cut, and the uncertainties associated with this cut, consists of a fit of the MM spectra for 50 MeV/c wide bins in the scattered proton momentum p_s between 0.25 GeV/c and 1 GeV/c at $Q^2 = 2.5, 3.5, 4.5,$ and 5.5 GeV^2 as shown in Figure 4.3. Each MM spectrum for 50 MeV/c bins in p_S and 1 GeV^2 bins in Q^2 was fit with two Gaussians, one for the signal (quasi-elastic peak) and one for the background (inelastic contribution). Figs. 4.5 – 4.7 show these fits. The dotted curves show each Gaussian individually, and the solid curve shows the sum. The integral of the first Gaussian function was used to determine the total number of quasi-elastic events. This number could then be compared with the number extracted from the analysis with different cuts on the MM peak. Five different cuts presented in Table 4.1 were used.

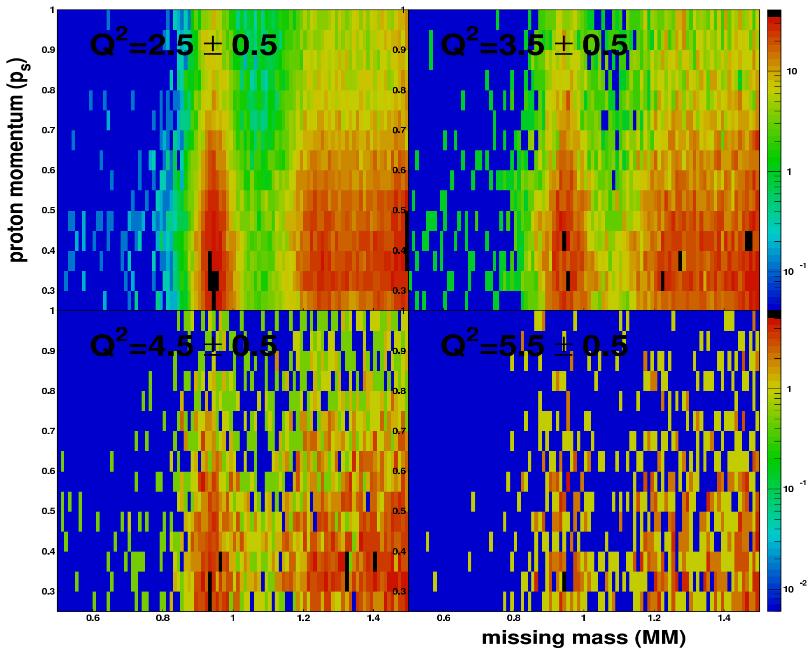

FIG. 4.3: Missing mass distribution as a function of momentum of the scattered proton p_s for $Q^2 = 2.5, 3.5, 4.5,$ and 5.5 GeV^2.

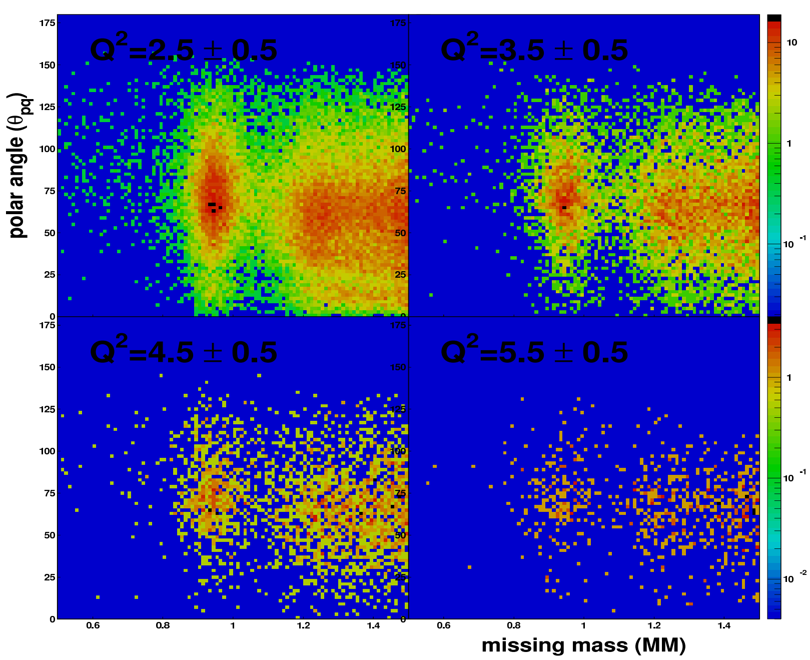

FIG. 4.4: Missing-mass distribution as a function of proton scattering angle with respect to the direction of momentum transfer θ_{pq} for $Q^2 = 2.5, 3.5, 4.5,$ and 5.5 GeV^2.

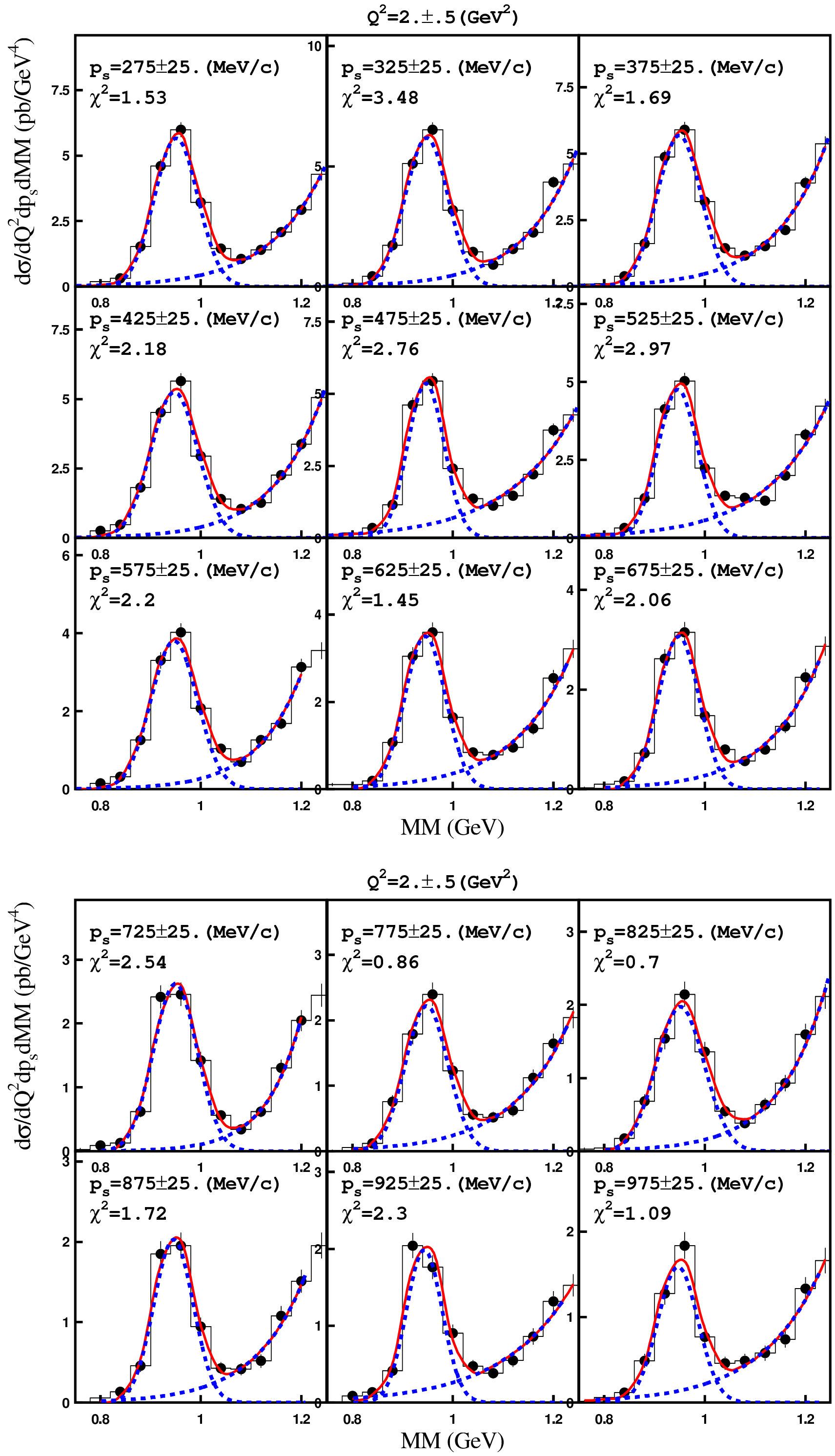

FIG. 4.5: Missing-mass spectra corresponding to 15 bins in p_s, and to $Q^2 = 2.5$ GeV^2 fitted with two Gaussians (solid curve). The dotted curves show the individual Gaussians used to fit the quasi-elastic signal and the inelastic background. The integral of the first Gaussian was used to estimate the quasi-elastic cross section.

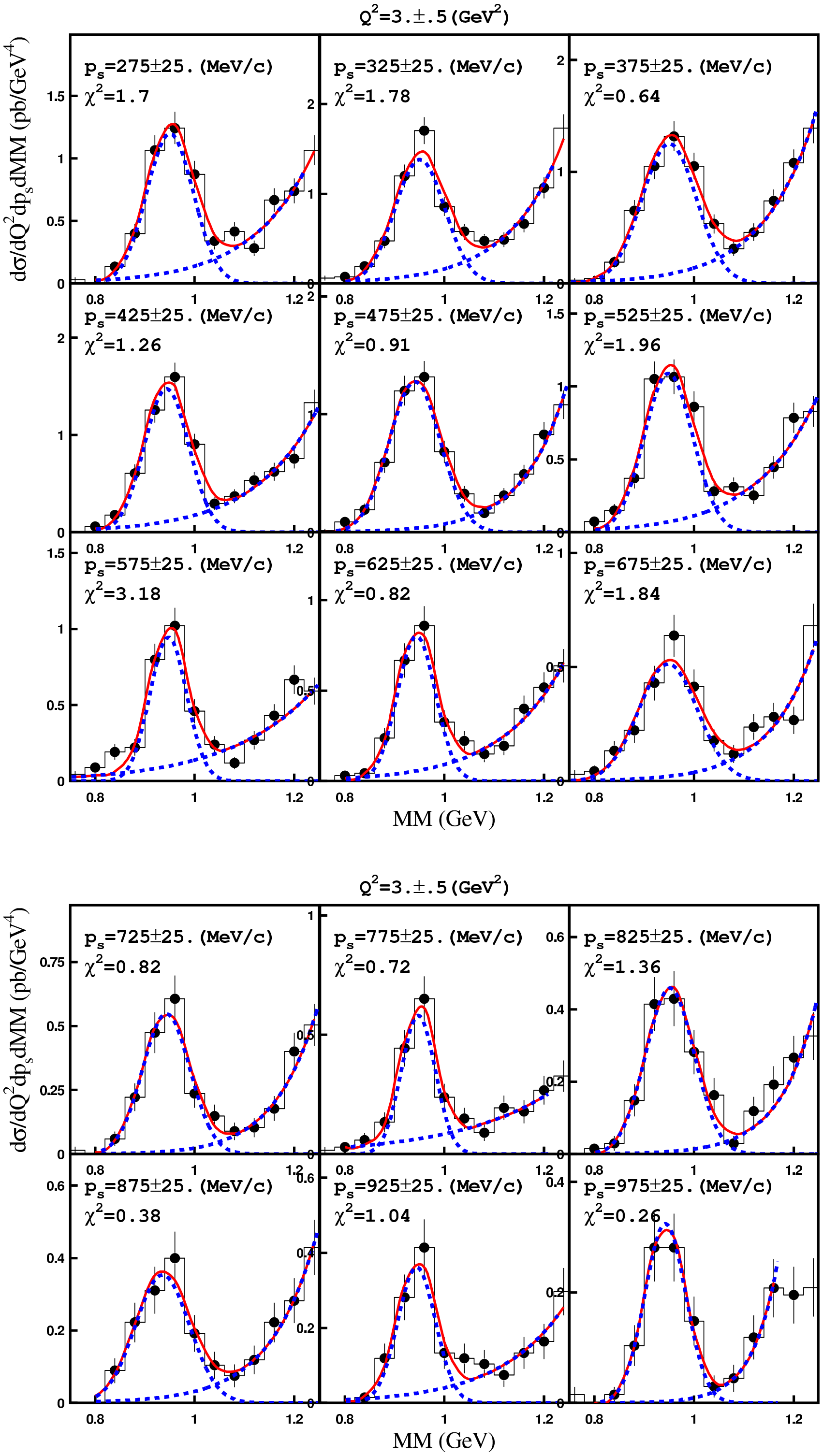

FIG. 4.6: Same as in Fig. 4.5 except for $Q^2 = 3.5$ GeV^2.

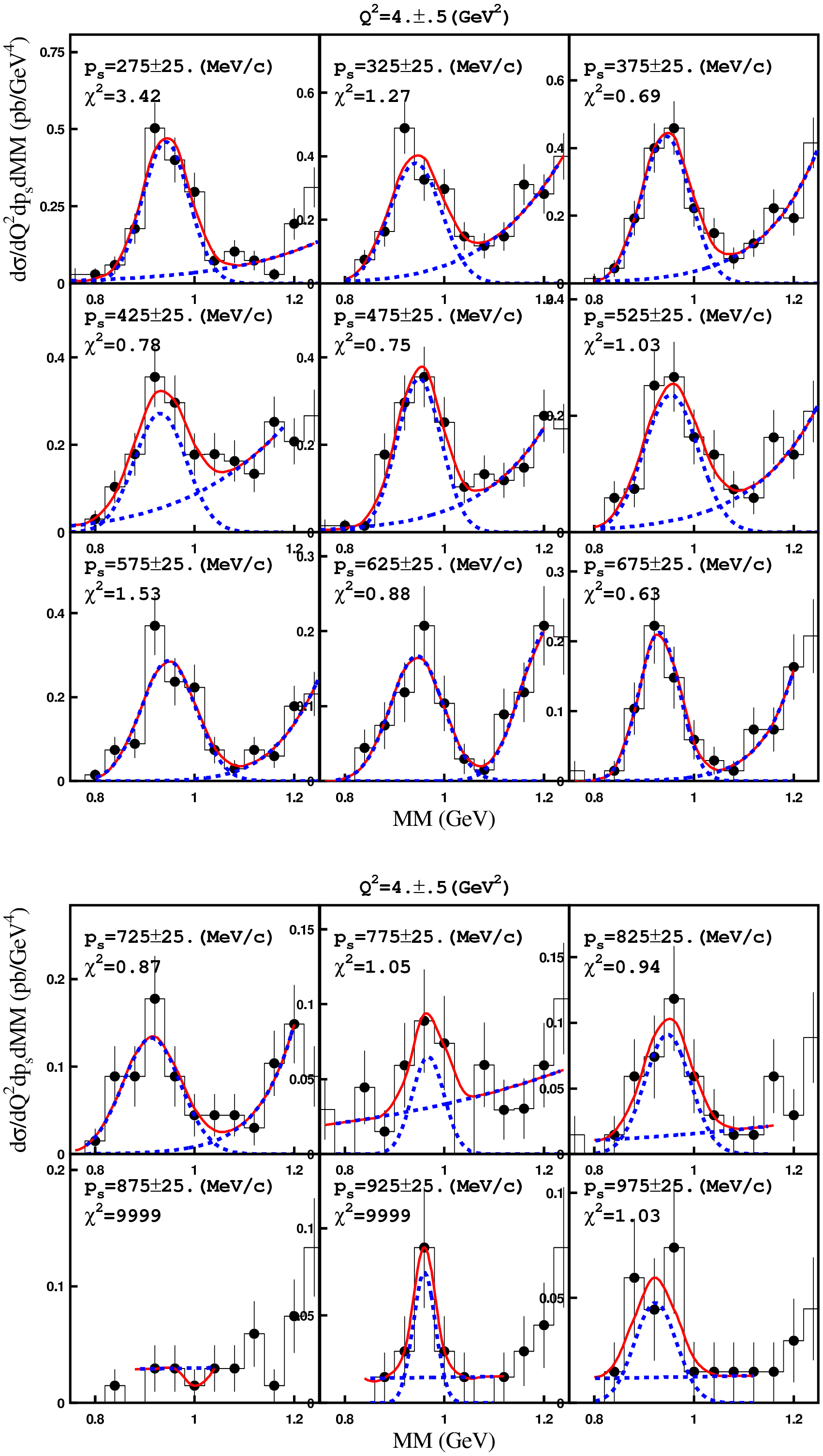

FIG. 4.7: Same as in Fig. 4.5 except for $Q^2 = 4.5$ GeV^2.

MM cut	1	2	3	4	5
[GeV/c]	.8<MM<1.	.85<MM<1.05	.85<MM<1.	.8<MM<1.05	MM<1.

TABLE 4.1: Estimation of the systematic error associated with the missing mass cut. Five different cuts around the quasi-elastic missing-mass peak were used to estimate the systematic errors associated with the missing mass cut in the main analysis.

The systematic uncertainty associated with the missing mass cut was defined as the standard deviation $\sigma = \frac{1}{N}\sqrt{\sum(\mu - r_i)^2}$ of the ratio of the yield obtained from the fitting procedure to the yield obtained by applying the MM cut for each kinematic bin. Here μ was the mean of five trial values of the ratio (corresponding to five different MM cuts) mentioned above and r_i was their deviation obout the mean μ. We extracted the uncertainties for 60 kinematic bins; 15 momentum bins and 4 momentum transfer bins $Q^2 = 2.5, 3.5, 4.5$ and 5.5 GeV^2.

p_s [MeV/c]	$Q^2 = 2.5$ GeV^2 SysErr [%]	$Q^2 = 3.5$ GeV^2 SysErr [%]	$Q^2 = 4.5$ GeV^2 SysErr [%]	$Q^2 = 5.5$ GeV^2 SysErr [%]
275	3.25	3.49	3.39	3.38
325	2.88	3.87	3.43	3.39
375	2.94	4.17	3.11	3.41
425	3.52	2.35	3.63	3.17
475	2.36	2.43	3.57	2.79
525	2.52	4.24	4.11	3.63
575	3.00	4.68	3.79	3.82
625	2.93	2.53	3.28	2.91
675	2.72	3.90	1.86	2.83
725	2.55	3.40	1.59	2.51
775	2.65	1.89	1.76	2.10
825	3.48	4.78	1.76	3.34
875	2.09	2.44	4.31	2.95
925	2.55	3.35	2.54	2.81
975	2.26	1.56	1.22	1.68

TABLE 4.2: Systematic errors associated with the missing mass cut, for $Q^2 = 2.5, 3.5, 4.5$, and 5.5 GeV^2 and for 15 proton momentum p_s bins.

For $Q^2 = 5.5 \pm 0.5$ GeV^2, statistics did not allowed us to perform a reasonable fit to the missing mass spectra. Therefore the systematic errors for $Q^2 = 5.5$ GeV^2 were calculated from the average of the other three bins in Q^2. Figs. 4.8 and 4.9 show the effect of applying different MM cuts around the quasi-elastic peak. The optimal choice for this cut obtained from this study and used in the main analysis was $0.8 < MM < 1.0$ GeV. We could see that the simple method described in the begin of the sections agrees quite well with the later result. This cut minimizes the inelastic background while maximizing the elastic signal. The systematic errors associated with this cut for each kinematic bin (bin in proton momentum p_s and in momentum transfer Q^2) are summarized in Table 4.2.

The same procedure was performed by fitting MM spectra in kinematic bins defined by the proton scattering angle with respect to the direction of momentum transfer and Q^2 (see Fig. 4.4). The missing mass spectra corresponding to these bins, and the corresponding double-Gaussian fits, are shown in Fig. 4.10 for Q$^2 = 2.5 \pm 0.5$ GeV^2, in Fig. 4.11 for Q$^2 = 3.5 \pm 0.5$ GeV^2, and in Fig. 4.12 for Q$^2 = 4.5 \pm 0.5$ GeV^2. The extracted yields using the fitting procedure and the missing mass cut procedure in the kinematic bins defined above are shown in the Figs. 4.13 and 4.14 (upper plots). The ratio of the yield obtained from the fitting method to the yield obtained from the cut method are shown in the Fig. 4.13 and 4.14 (lower plots).

The uncertainties associated with the missing-mass cut for each kinematic bin were defined as the standard deviation of the ratios mentioned above for each θ_{pq} bin and they are summarized in Table. 4.3. The systematic errors for Q$^2 = 5.5 \pm 0.5$ GeV^2 were obtained by averaging the errors obtained for the other three Q^2 bins. The systematic uncertainties were added in quadrature to determine the final errors for each kinematic bin.

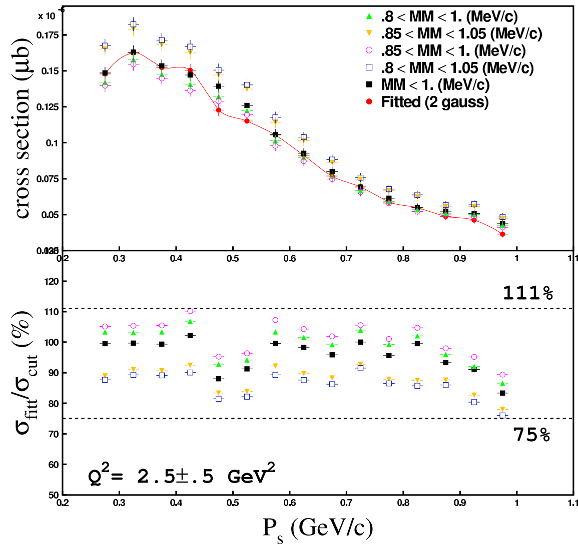

FIG. 4.8: Cross sections (upper plot) as a function of proton momentum extracted by applying five different MM cuts (different color markers) and by the fitting procedure (black bullets) for $Q^2 = 2.5$ GeV^2. The ratio of the cross section obtained from the fitting to that obtained by using different cuts (lower plot) shows how too strict cuts give a ratio above unity whereas too generous cuts give a ratio below 1.

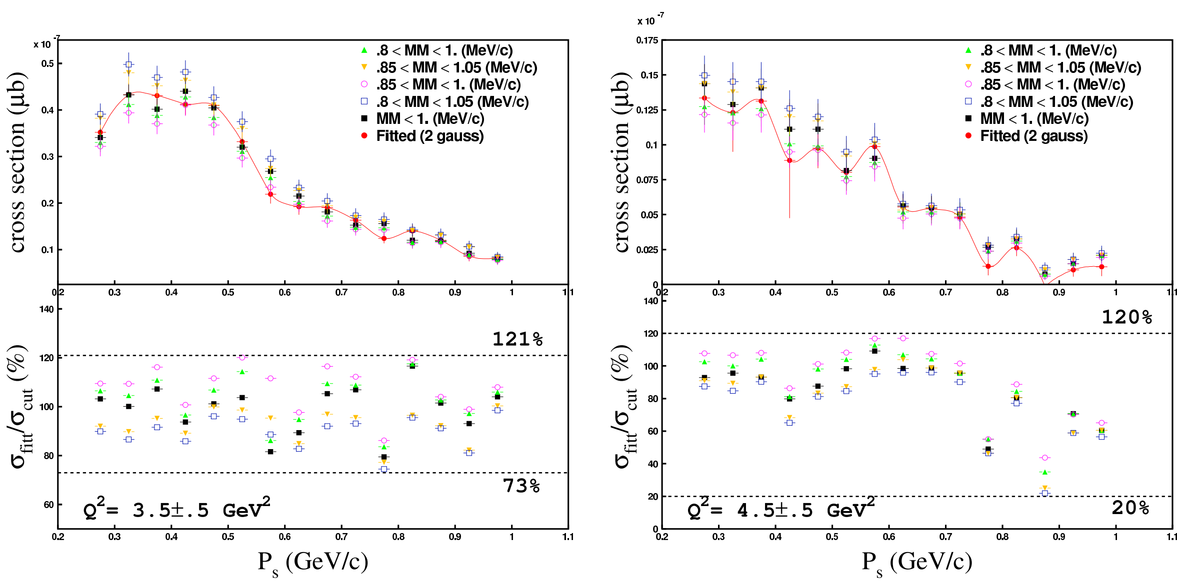

FIG. 4.9: Same as in Fig. 4.8 except for $Q^2 = 3.5$ GeV^2 (left) and $Q^2 = 4.5$ GeV^2 (right).

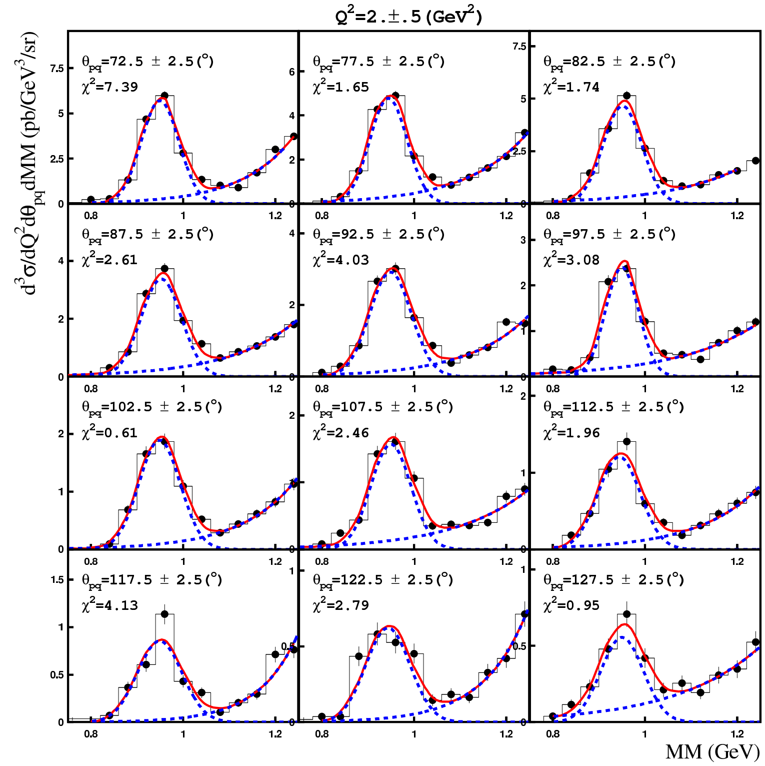

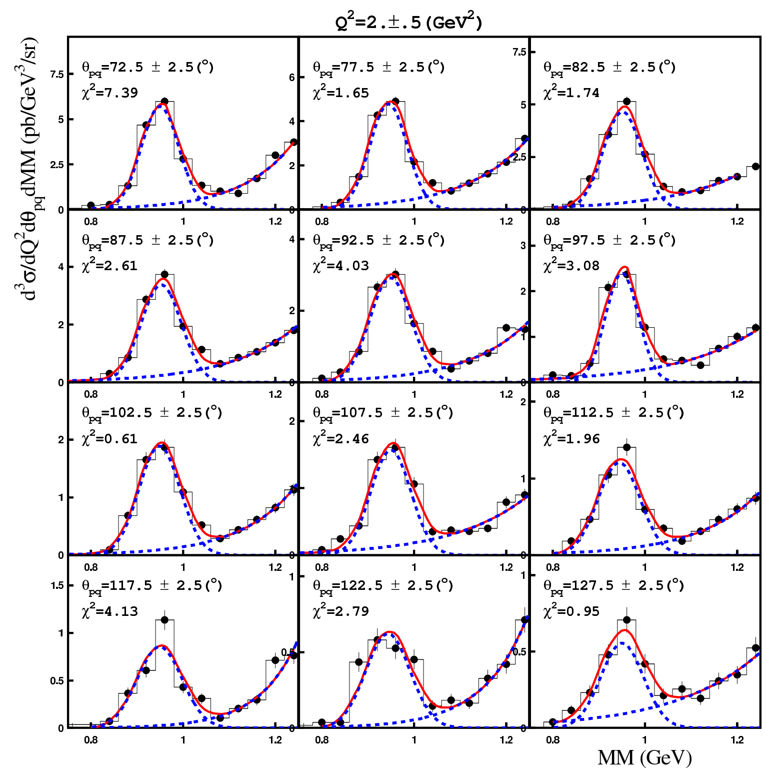

FIG. 4.10: Missing-mass spectra corresponding to 24 bins in θ_{pq}, and to $Q^2 = 2.5$ GeV^2 fitted with two Gaussians (solid curve). The integral of the first Gausian was used to estimate the yield of quasi-elastic events. Dashed curves correspond to the individual Gaussians.

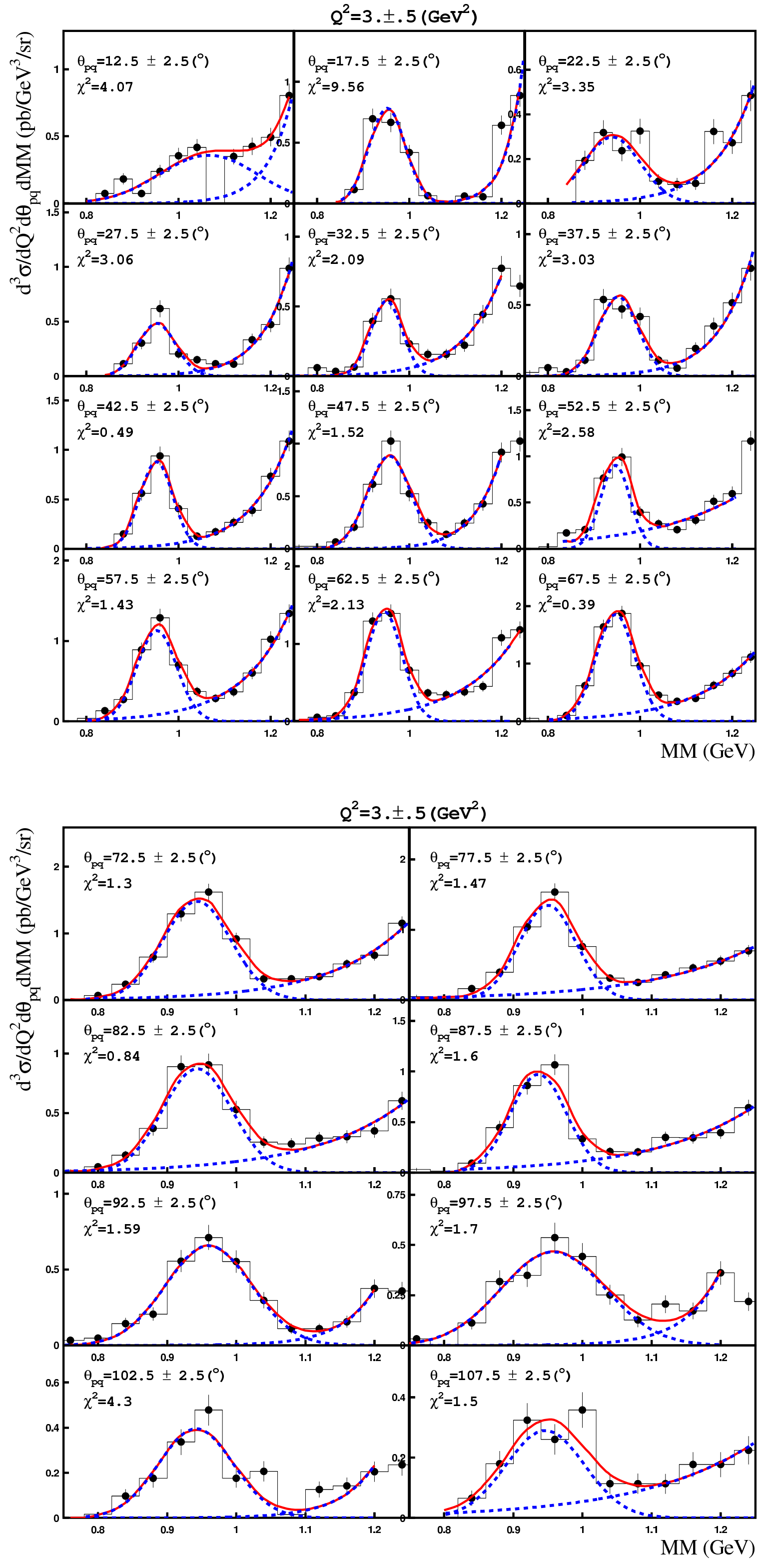

FIG. 4.11: Same as in Fig. 4.10 except for $Q^2 = 3.5$ GeV^2.

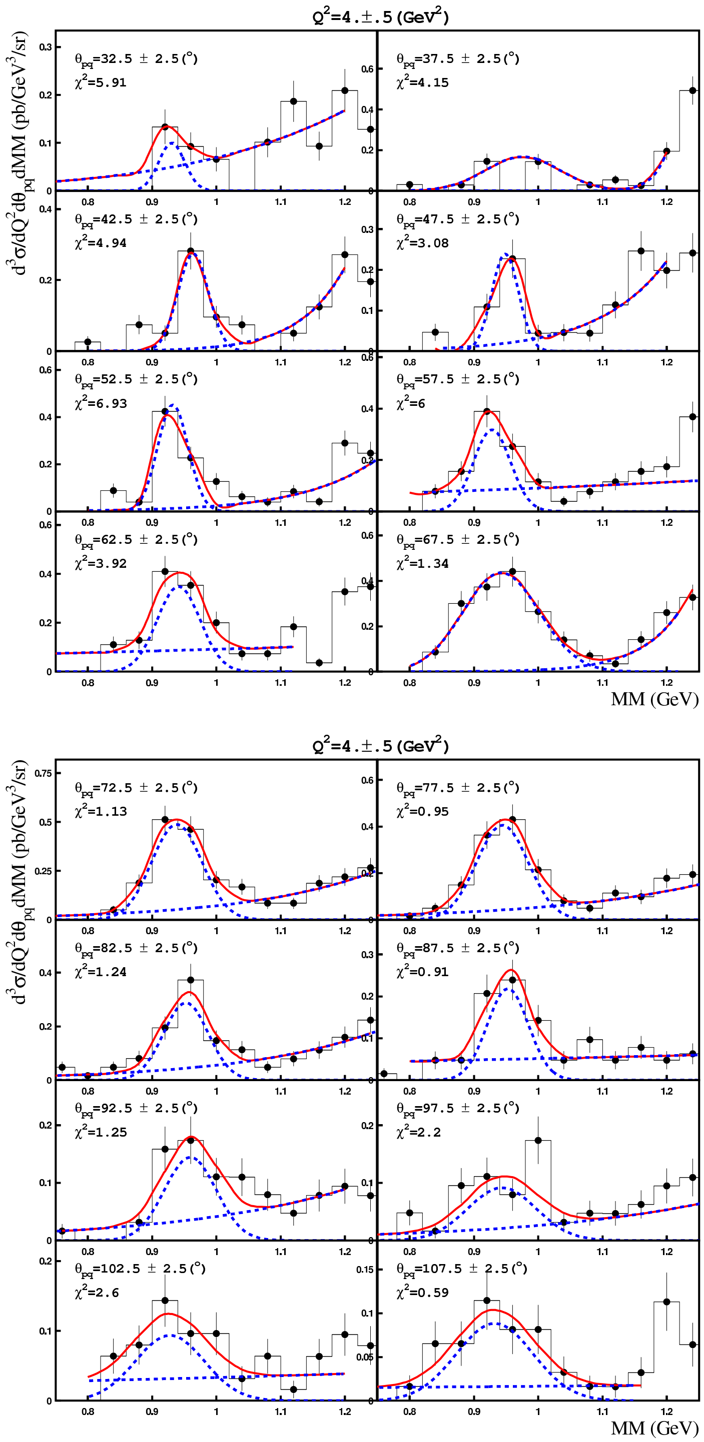

FIG. 4.12: Same as in Fig. 4.10 except for $Q^2 = 4.5$ GeV^2.

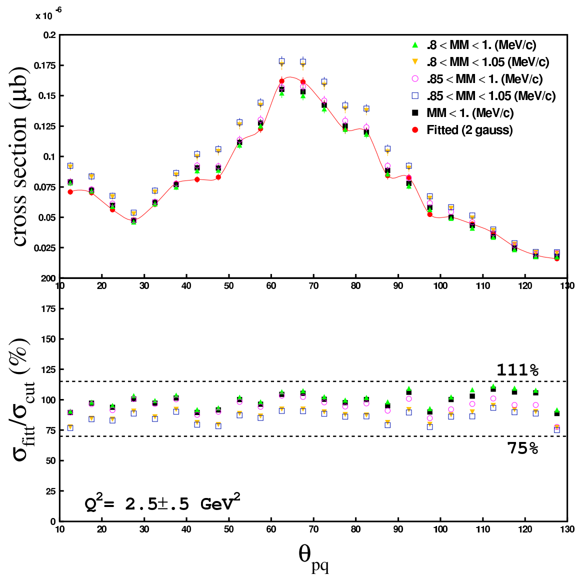

FIG. 4.13: Cross sections versus proton scattering angle θ_{pq} (upper plot) extracted by applying five different MM cuts (different color markers) and by using the fitting procedure (black bullets) for $\mathrm{Q}^2 = 2.5$ GeV^2. The ratio of the cross section obtained by fitting to that obtained by using different cuts (lower plot), show similar effects as in Fig. 4.8.

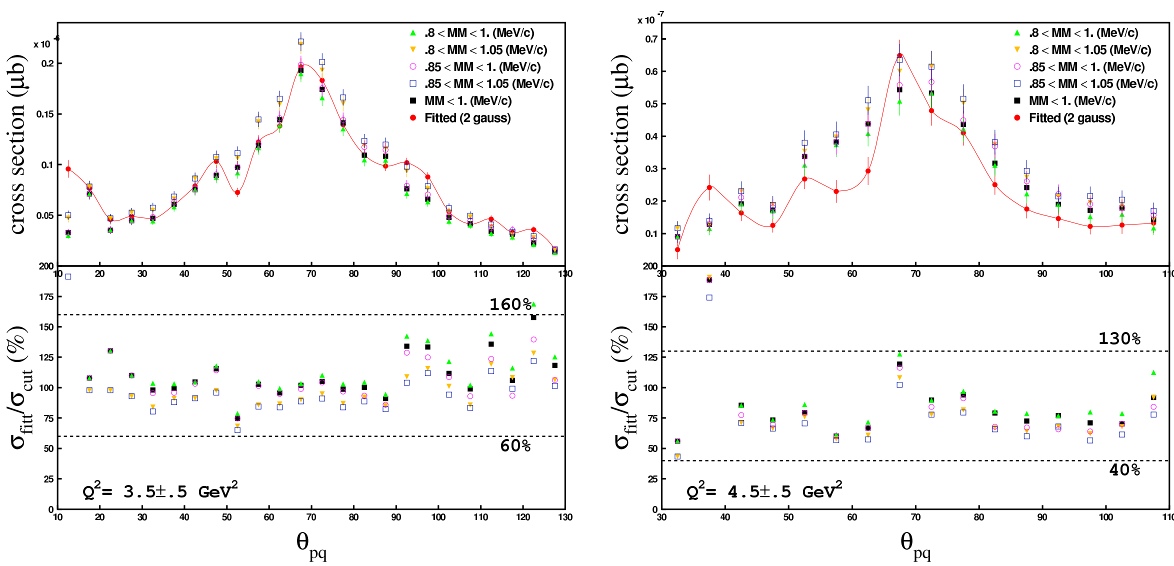

FIG. 4.14: Same as in Fig. 4.13 except for $Q^2 = 3.5 \pm 0.5$ GeV^2 (left) and $Q^2 = 4.5 \pm 0.5$ GeV^2 (right).

θ_{pq} [°]	$Q^2 = 2.5$ GeV^2 SysErr [%]	$Q^2 = 3.5$ GeV^2 SysErr [%]	$Q^2 = 4.5$ GeV^2 SysErr [%]	$Q^2 = 5.5$ GeV^2 SysErr [%]
12.5	2.78	3.08	-	-
17.5	2.85	2.22	-	-
22.5	2.27	7.09	-	-
27.5	2.66	3.70	-	-
32.5	2.80	3.91	2.76	3.16
37.5	2.42	2.44	4.86	3.24
42.5	2.12	2.83	2.90	2.61
47.5	2.85	4.22	1.41	2.83
52.5	2.73	2.19	2.27	2.40
57.5	2.36	3.94	0.76	2.35
62.5	2.92	2.62	2.25	2.60
67.5	3.08	2.74	2.94	2.92
72.5	2.52	3.17	2.38	2.69
77.5	2.41	3.24	3.00	2.88
82.5	2.87	2.57	2.88	2.77
87.5	3.38	1.94	2.92	2.75
92.5	3.45	6.59	2.16	4.06
97.5	2.59	4.54	3.63	3.58
102.5	2.92	4.16	2.48	3.19
107.5	3.61	3.26	5.21	4.03
112.5	3.18	5.00	-	-
117.5	3.51	3.49	-	-
122.5	3.51	7.88	-	-
127.5	3.01	3.95	-	-

TABLE 4.3: Systematic errors associated with the missing mass cut, for $Q^2 = 2.5, 3.5, 4.5,$ and 5.5 GeV^2 and 24 bins in θ_{pq}.

4.2 CLAS Acceptance Calculations

4.2.1 Detector Simulation

In order to relate experimental yields to the cross sections we need to extract the geometrical acceptance and the efficiency of all detector subsystems of CLAS. The procedure for determining the geometrical acceptance and the detector efficiencies requires several steps: first, we need to simulate the response of CLAS to the propagation of charged particles through its component subsystems; second, we need a realistic generator that will reproduce distributions of particles emitted in the reaction that we are studying; and third, we need a consistent reconstruction and analysis procedures for both simulated and real data. The procedure is schematically shown in Figure 4.15. Based on the GEANT simulation software package, from CERN, GSIM models the response of CLAS to the propagation of different charged particles through the spectrometer. GSIM is a stand-alone software package that can be tailored for the various experimental runs with CLAS by simply changing a configuration file that contains information about detector thresholds and about the target, and an input file that contains the output of the event generator. Specific to each experimental group is the model of the target. For the E6 run period, N. Dashian from the Yerevan Group set up the target model. GSIM simulates a realistic response of CLAS to charged particles traveling through. In order to account for CLAS detector responses a post processor (GPP) program turns the trails of deposited energy created by GSIM into raw detector signals. GPP reads from a MySQL database that contains information about dead regions in the DC and malfunctioning TOF paddles at the actual time of data taking and excludes them from the simulated data. After this step the simulated data are passed through the same particle reconstruction code (RECSIS) as the real data. In order to calibrate the simulation to the real data we checked the TOF scintillator efficiencies sector by sector. We plotted the electron vertex time, defined as the difference between the time of flight measured by CLAS and the expected time of flight computed using electron momentum and velocity, versus the TOF scintillator paddle number. In this way we could identify the malfunctioning TOF paddles and exclude them from the analyses, of both simulated and real data as shown in Figure 4.16.

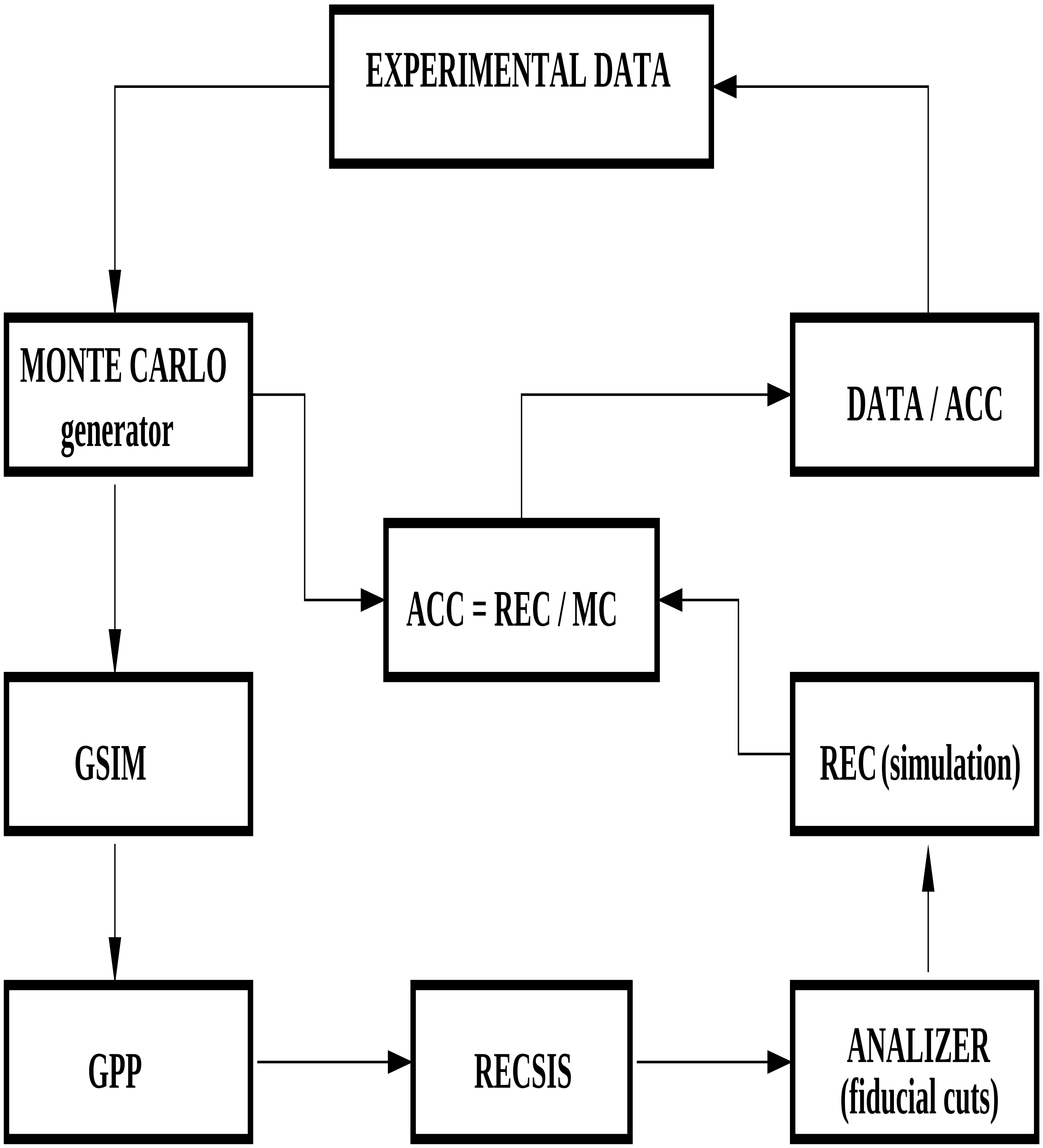

FIG. 4.15: Flow chart for acceptance calculations. Using the Monte Carlo technique we generate events that closely resemble the real experimental data, we pass them through GSIM, and then we generate raw signals in the DC and TOF detectors using GPP, which simulates the resolution of the actual data. As the next step we use the RECSIS package for particle reconstruction in the same way as for the real data. We analyze the simulated data in the same way as the real data, including all cuts. The acceptance for a particular kinematic bin is obtained by dividing the reconstructed simulated events (REC) by the initial thrown events (Monte Carlo). Experimental data are corrected for detector acceptance. This process can be iterated by fitting the corrected experimental data to improve the input model and repeating the process.

In Fig. 4.16 (left) Sector 1 has one miscalibrated paddle #16, Sector 2 has one miscalibrated paddle #6, Sector 3 has two inefficient paddles #11 and #16, Sector 5 has one inefficient paddle #21, and Sector 6 has an overall good TOF scintillator efficiency. Some of these paddles have been identified by "paddle-to-paddle" software (P2P) as inefficient and they were labeled in the MySQL database as bad paddles, and thereafter this information was used by the GSIM package. Others were not implemented properly in the simulation. In Fig. 4.16 (right) we can see that the simulation could not reproduce perfectly the bad paddles seen in real data. Therefore these paddles were excluded from the final analysis. A detailed description of the procedure of identifying and correcting for inefficient regions of the DC and dead scintillator paddles in the TOF wall can be found in Ref. [70].

External radiation of the scattered electrons in the target is calculated by GSIM. GPP smears the spatial position of the DC hits and the times of flight, such that the simulated data have the same resolution as the experimental data. The smearing is controlled by three coefficients corresponding to the three regions of DC (a, b, c) and one coefficient for the TOF (f). To obtain these coefficients we simply compared real data step-by-step with simulated data for different sets of smearing coefficients. The invariant mass W distribution for the inclusive d(e,e$'$) reaction and the missing mass MM distribution for the exclusive d(e,e$'$p)n reaction obtained from real data were used to determine whether the smearing coefficients used by GPP were reasonable. Fig. 4.17 shows the W distributions obtained from real data for each sector in CLAS compared with the simulated data (left) and the ratios of the real to the simulated W spectra. Details about the simulations of the inclusive and exclusive channels are given in Sections 4.2.2 and 4.2.3. The coefficients for DC smearing obtained from this study were: $a = 1.58$, $b = 1.58$, $c = 1.58$. The time resolution of TOF described in GSIM was found to be in good agreement with the experimental data.

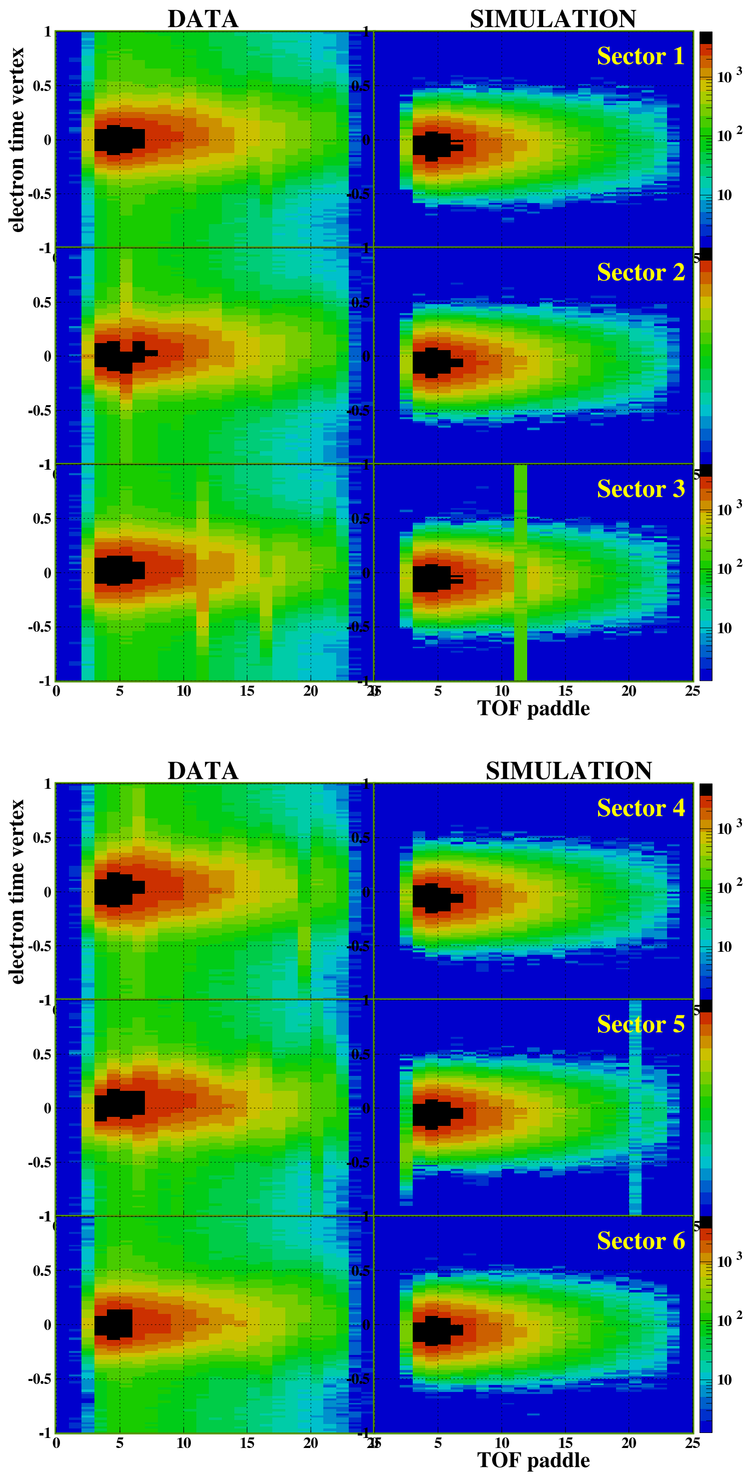

FIG. 4.16: Electron time vertex versus TOF scintillator paddle number for real (right) and simulated (left) data, for each sector of CLAS.

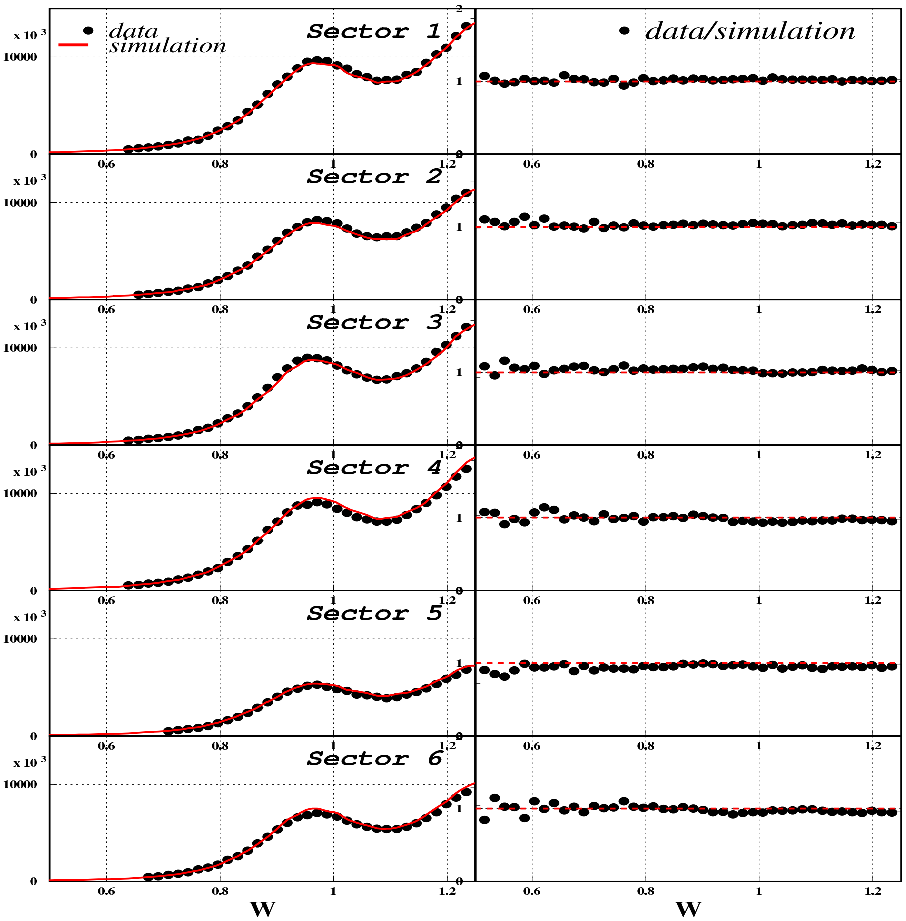

FIG. 4.17: Invariant mass W distributions (left) for real (solid bullets) and simulated (solid line) data and ratios (right) of data to simulation for the six sectors of CLAS.

Fig. 4.18 shows the electron time vertex spectra for data (upper panel) and simulation (lower panel), fitted with a Gaussian in each case. The electron time vertex was defined as the difference between the measured time of flight using the RF signal, and the computed time of flight using electron momentum and velocity. We can see that the means and widths of each distribution are similar. Thus, the coefficient f corresponding to TOF smearing in GPP was chosen to be 1. These coefficients were used in simulations for both inclusive d(e,e$'$) and exclusive d(e,e$'$p)n channels.

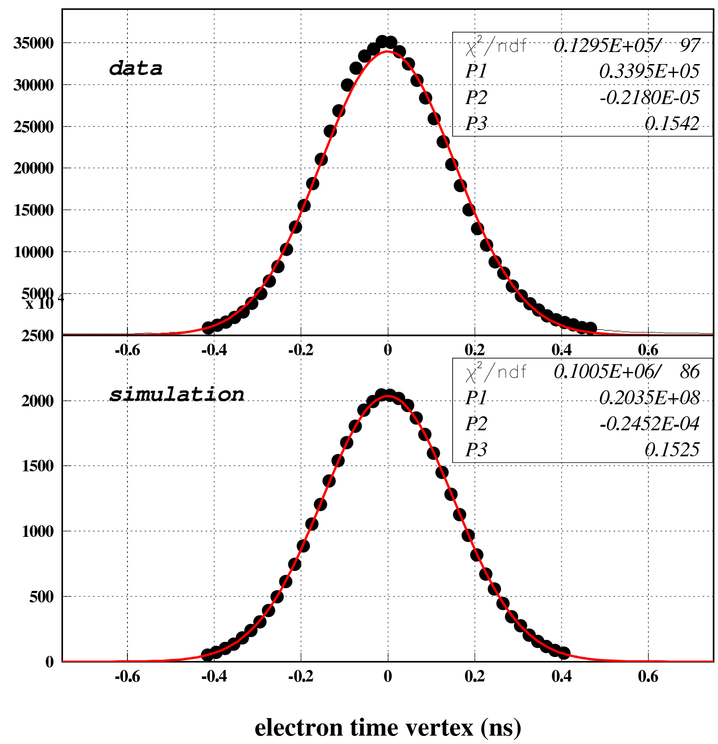

FIG. 4.18: Electron time vertex for real (upper plot) and simulated (lower plot) data. Malfunctioning scintillator paddles were excluded.

4.2.2 Inclusive d(e,e′) Simulation

Acceptances for the inclusive d(e,e′) reaction were calculated and applied to the experimental data in order to extract absolute cross sections. Existent world data for d(e,e′) from SLAC [78, 80] and from Jefferson Laboratory [73] were used for comparison with our results. In Figure 4.19 we present the kinematic coverage of E6 and the existent inclusive d(e,e′) experiments. As mentioned earlier in the text we needed to model the experimental data in order to extract acceptances. Our d(e,e′) simulation was based on a theoretical model constructed by Misak Sargsian as described in Ref. [81]. This model computes the cross sections of the inclusive d(e,e′) reaction using two different approaches: the Virtual Nucleon Impulse Approximation [60, 78] and the Impulse Approximation based on Light Cone Dynamics [82].

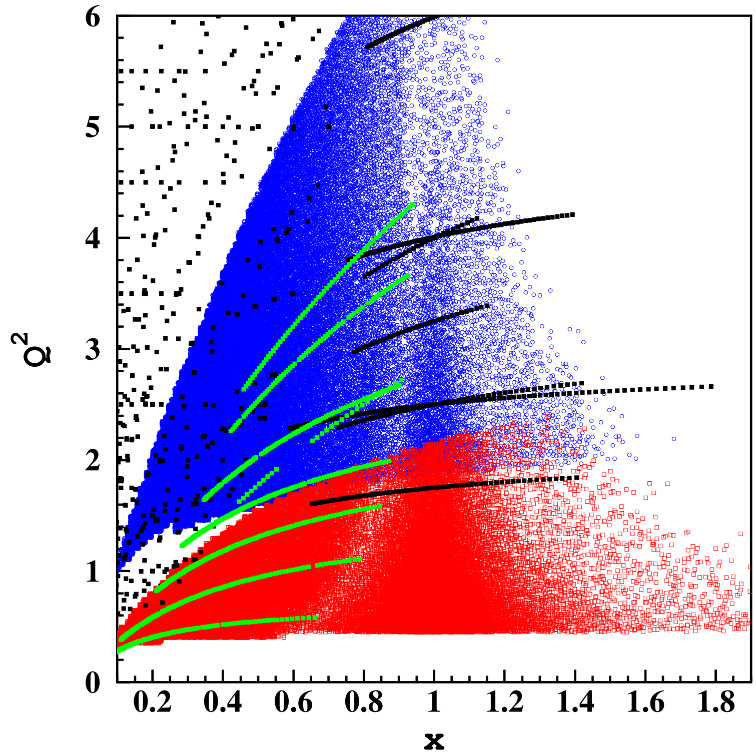

FIG. 4.19: Kinematic regions covered by d(e,e′) experiments that extend to $x_B > 1$: red area - E1d run period (CLAS) $E = 2.474$ GeV; blue area - E6a run period (CLAS) $E = 6.764$ GeV^2; green points are from Hall C [73] and black points are from SLAC [74–78]. The plot is from Ref. [79].

For this simulation we used the cross sections calculated in the Relativistic Light Cone Impulse Approximation where the high momentum components of the nuclear spectral function are described in the framework of the Glauber approximation. It is assumed here that the few-nucleon short range correlations (SRC) account for the high momentum components of the nuclear wave function. This allows us to describe the electron-nucleus cross section at $x > 1$ in terms of the absorption of virtual photons on individual few-nucleons correlations. This model describes electron scattering where the momenta of the struck nucleon exceeds the Fermi momentum and relativity and off-shell effects become more important. This model uses the deuteron wave function derived from the Paris potential. For quasi-elastic scattering the dipole nucleon form factor has been used, and for the inelastic part of the inclu-

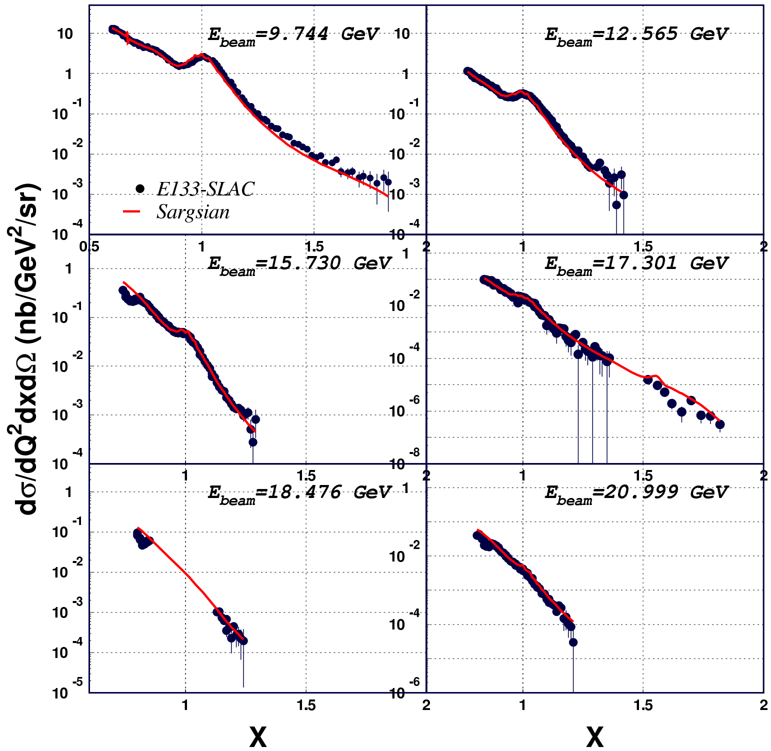

FIG. 4.20: Experimental cross sections $d\sigma/dQ^2dx$ from Ref. [78] (solid bullets) and the model from Ref. [81] (solid curves) for six different beam energies: E_{beam} = 9.744, 12.565, 15.730, 17.301, 18.476, and 20.999 GeV.

sive d(e,e′) cross section only Δ-isobars are considered. For the parametrization of inelastic form factors Ref. [74] has been used. The spectral function is constructed using the simple Fermi step distribution for nucleon momenta with contributions above the Fermi surface coming from two-nucleon short-range correlations.

In this analysis we focused on quasi-elastic inclusive electron scattering for $Q^2 = 1 - 7$ GeV^2 and $x = \frac{Q^2}{2m_p\nu} = 0.7 - 2.0$. Reasonable agreement between this model and data from SLAC [78] and Jefferson Lab [73] is shown in Figs. 4.20 and 4.21, respectively. This model agrees well enough (within 10-15%) with the data to be used as an input generator in our acceptances calculations for d(e,e′). We generated Monte Carlo events with a distribution corresponding to the model cross section. We passed simulated data through GSIM and GPP (using the smearing coefficients adjusted to reproduce the quasi-elastic peak width), reconstructed the

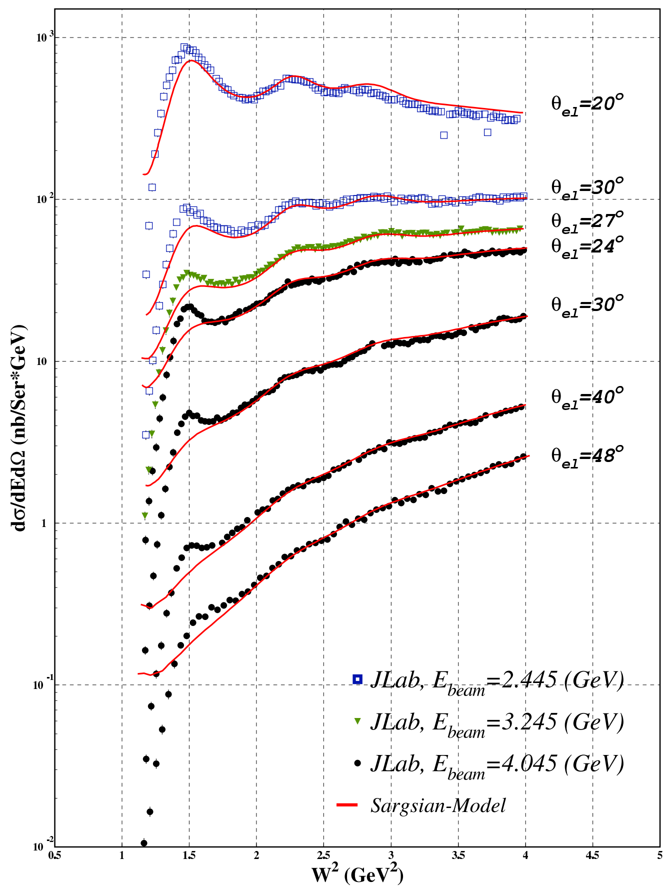

FIG. 4.21: Experimental cross sections $d\sigma/dE'd\Omega$ from Ref. [73] (bullets) together with the model from Ref. [81] (solid curves) for three different beam energies: $E_{beam} = 2.445$ (squares), 3.245 (triangles), and 4.045 (bullets) GeV and several electron scattering angles. Only the inelastic region ($x < 1$) is covered by these data.

particles with RECSIS, and collected the reconstructed events in Ntuple-10 format (CLAS) just as we did with the experimental data. Wherever possible the number of Monte Carlo events was chosen to be much larger than the corresponding number of real events in order to avoid statistical uncertainties in the simulation being a significant error. The ntuples containing Monte Carlo events were analyzed with the same analysis software package as for the real data. Cross sections were obtained by normalizing experimental yields (obtained within our fiducial cuts and corrected for

e^+e^--pairs, pion backgrounds, and internal radiative effects) to the total live-time gated charge accumulated by the Faraday Cup, the target density and the detector acceptance. Comparisons between experimental raw cross sections (no acceptance applied) and simulations, on a sector by sector basis are presented in Fig. 4.22 versus Q^2, in Fig. 4.23 versus electron momentum distributions, in Fig. 4.24 versus electron polar scattering angle, and in Fig. 4.25 versus electron azimuthal scattering angle. With the exception of regions of low acceptance (at the edge of CLAS) the agreement between the simulation and real data was found to be within 10%, which is comparable with the accuracy of the model. We extracted acceptances (as shown schematically in Fig. 4.15) in each kinematic bin as the ratio of the number of reconstructed events N_{rec} (obtained within our fiducial cuts) over the number of events generated N_{gen} (generated in full phase space):

$$F_{\mathrm{acc}} = \frac{N_{\mathrm{rec}}}{N_{\mathrm{gen}}}, \tag{4.1}$$

where F_{acc} is the acceptance factor which was used to normalize the experimental yields. A sample of F_{acc} for several Q^2 bins is presented in Fig. 4.26. The detection efficiency of CLAS defined as the ratio of the number of reconstructed to generated events within E6 fiducial cuts mentioned in Section 3.3.1 (geometrical contour of regions of high detection efficiency in CLAS) was obtained from simulations. In Figure 4.27 we can see the increase in efficiency with Q^2. An overall efficiency of $\approx$ 91 % was observed. The fluctuations from unity are due to the kinematic smearing simulated by GPP. For distributions with sharp peaks or steep slopes shapes of generated and reconstructed spectra may well be different. This introduces a non-trivial kinematic dependence into the efficiency. Two sources of systematic uncertainties could be identified from the acceptance calculations.

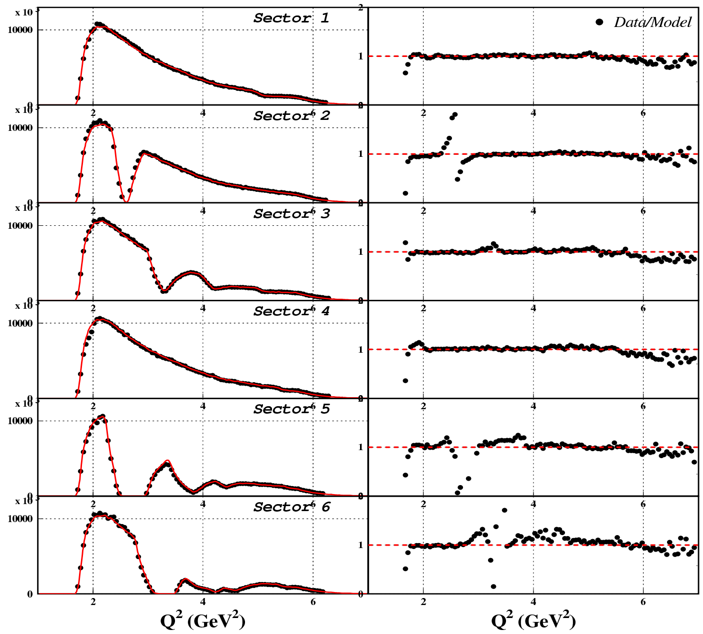

FIG. 4.22: Q^2 distributions (left) for real (solid bullets) and simulated data (solid line), and ratios (right) of data to simulation for the six sectors of CLAS. The acceptance in Q^2 is reasonably flat with deviations arising from the mismatch between actual and simulated detector dead regions.

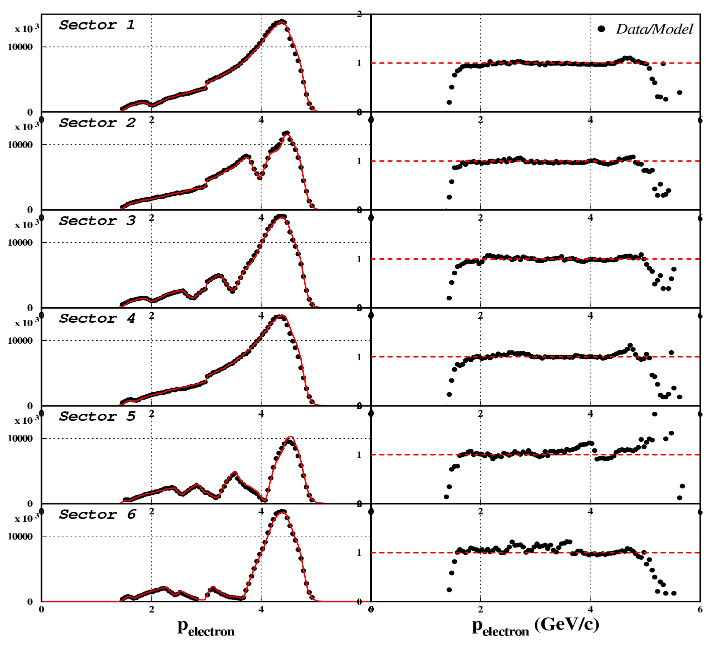

FIG. 4.23: Electron momentum $p_{electron}$ distributions (left) for real (solid bullets) and simulated data (solid line), and ratios (right) of data to simulation for the six sectors of CLAS. The acceptance in $p_{electron}$ is relatively flat but falls off rapidly at low and high momentum.

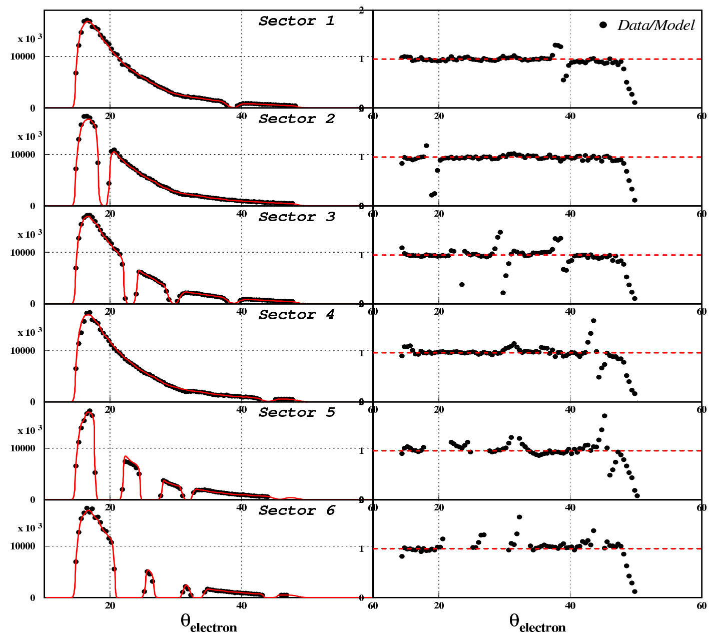

FIG. 4.24: Distributions of electron scattering angle $\theta_{electron}$ (left) for real (solid bullets) and simulated (solid line) data, and ratios (right) of data to simulation for the six sectors of CLAS. The acceptance versus $\theta_{electron}$ is relatively flat and falls precipitously above about 50°.

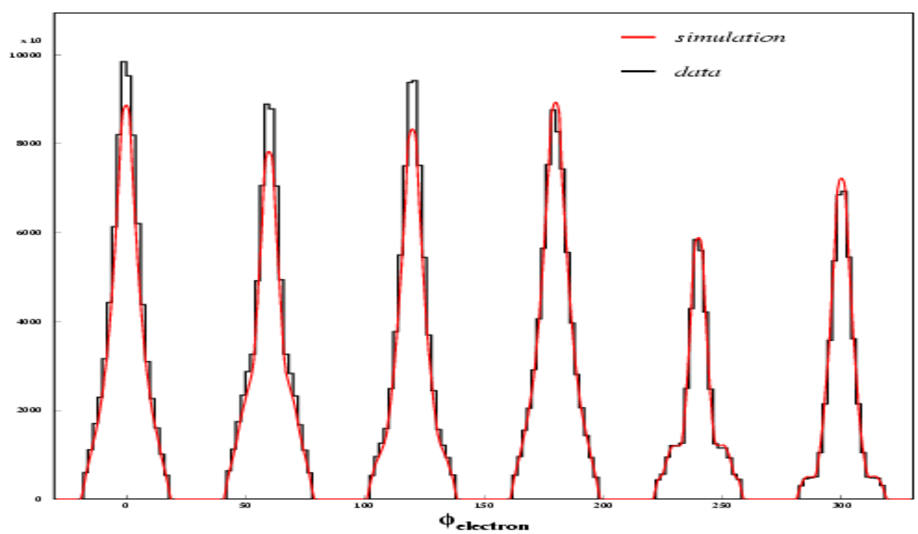

FIG. 4.25: Distributions of electron azimuthal scattering angle $\phi_{electron}$ for real (solid histogram) and simulated (solid line) data for the six sectors of CLAS.

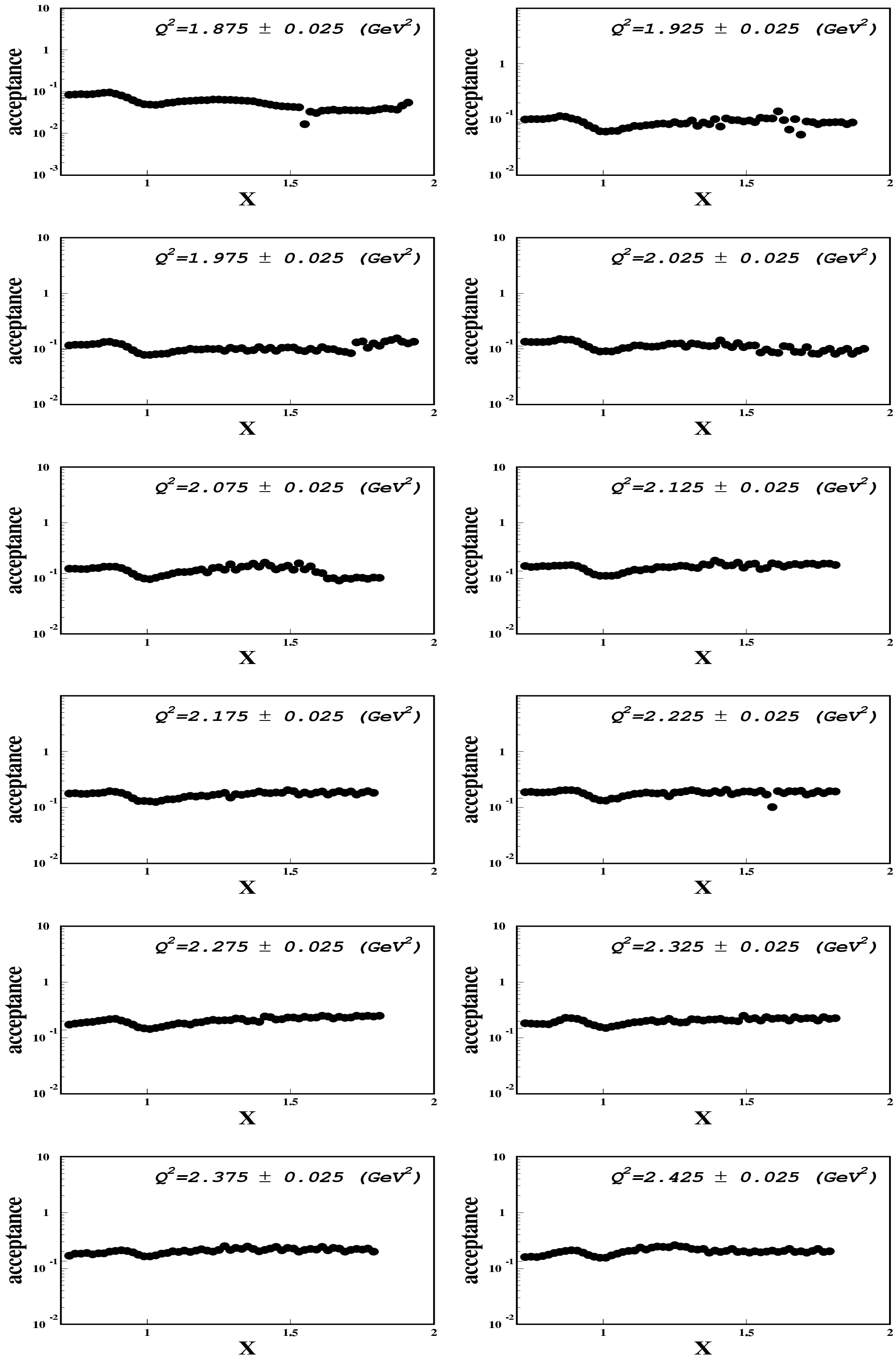

FIG. 4.26: Acceptances versus x for several bins in Q^2 from 1.8 to 2.4 GeV^2. The acceptance rises with increasing Q^2 and ranges from less than 10 % to as much as 30 %.

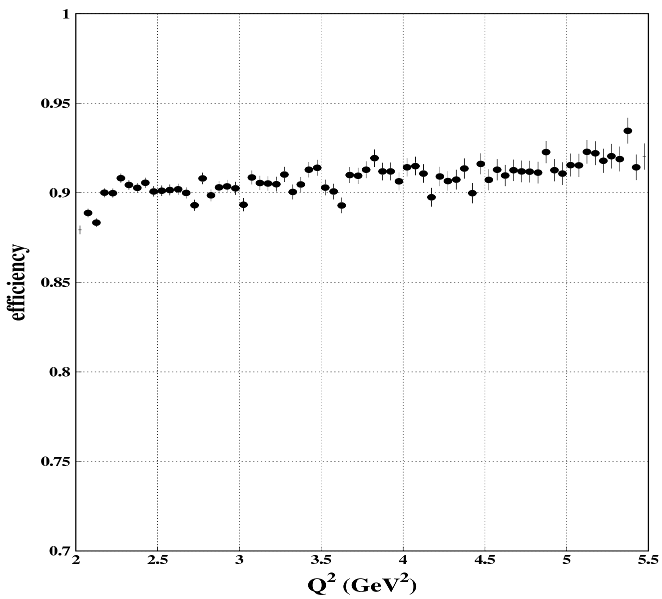

FIG. 4.27: Efficiency obtained from GSIM simulations. The efficiency was defined as the ratio of the number of reconstructed events to the number of generated events within our geometrical fiducial cuts. Here the efficiency increases with Q^2.

The first one is due to the model used in the simulation. A wrong cross section model used in the event generator could lead to a deviation of the absolute GSIM simulated cross sections from the measured ones. We used a wrong model by modifying the distributions given by the model of Ref. [81] and extracted a new set of acceptances. The difference in the acceptances obtained using two different models, for each kinematic bin, was taken as an estimate of the systematic uncertainty. A uniform systematic uncertainty of 1.5% due to model dependence of the acceptance calculations was added in quadrature to the total systematic error. The second source of uncertainty comes GSIM's inability to reproduce a realistic response to electron tracks at different momenta and scattering angles. We calculated the GSIM systematic errors as:

$$\delta_{\mathrm{GSIM}} = \sqrt{(\bar{\delta}_{\mathrm{GSIM}})^2 - (\delta^{\mathrm{stat}}_{\mathrm{GSIM}})^2} \tag{4.2}$$

Here $\bar{\delta}_{\mathrm{GSIM}}$ is the weighted root mean square deviation of the difference between measured and simulated raw cross sections for all six sectors of CLAS:

$$\bar{\delta}_{\mathrm{GSIM}} = \delta^{\mathrm{stat}}_{\mathrm{GSIM}} \sqrt{\sum_{i=1}^{6} \frac{\left|(\sigma_i^{\mathrm{exp}} - \sigma_i^{\mathrm{GSIM}}) - \bar{\Delta}_\sigma\right|^2}{(\delta^{\mathrm{stat}}_{\mathrm{exp}})^2 + (\delta^{\mathrm{stat}}_{\mathrm{GSIM}})^2}}, \tag{4.3}$$

where $\bar{\Delta}_\sigma$ is the weighted average of the difference $(\sigma_i^{\mathrm{exp}} - \sigma_i^{\mathrm{GSIM}})$. The statistical component of the deviation is given by:

$$\delta^{\mathrm{stat}}_{\mathrm{GSIM}} = \left(\sum_{i=1}^{6} \frac{1}{(\delta^{\mathrm{stat}}_{\mathrm{exp}})^2 + (\delta^{\mathrm{stat}}_{\mathrm{GSIM}})^2} \right)^{-1/2} \tag{4.4}$$

The resulting systematic errors, averaged over W and plotted as a function of Q^2, are shown in Figure 4.28. Systematic deviations from sector to sector ranged from 1 to 3% and depended mostly on the electron polar scattering angle. All systematic errors were added in quadrature.

Absolute normalizations, error analysis and extraction of absolute cross sections for the inclusive d(e,e′) channel are presented in Section 4.2.4.

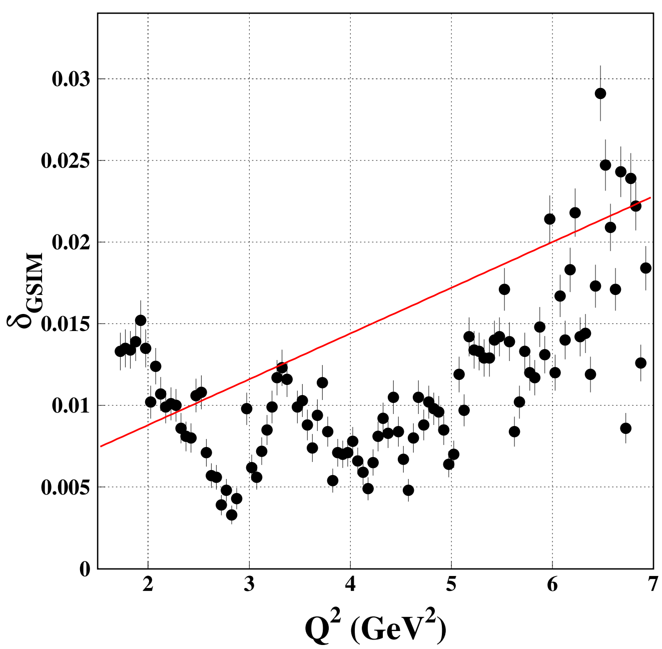

FIG. 4.28: GSIM systematic errors δ_{GSIM} as a function of Q^2. The solid line show the parameterization used in calculating acceptance uncertainties.

4.2.3 Exclusive d(e,e$'$p$_s$)n Simulation

For the simulation of the exclusive d(e,e$'$p$_s$)n channel we began by building an event generator based on realistic distributions extracted from E6 data. We fit data distributions in spectator proton momentum p_s, Bjorken scaling variable x, momentum transfer Q^2 and proton scattering azimuthal angle with respect to the momentum transfer direction ϕ_{pq}, all distributions being integrated over all other variables. Then we generated p_s, x, Q^2, and ϕ_{pq} according to these fits and calculated the proton polar angle with respect to $\vec{q}$, θ_{pq}, from the constrained tagged quasi-elastic kinematics. This assumed factorization of probability distributions for the coincidence data.

The kinematics of d(e,e$'$p$_s$)n are presented in Figure 4.30. The leptonic plane is defined by the incident k(E$_{beam}$,$\vec{k}$) and scattered k'(E$'$,$\vec{k}'$) electron momenta. Momenta of the spectator proton p(E$_p$,$\vec{p}_s$) and the struck neutron n(E$_n$,$\vec{n}$) form the hadronic plane. Here E_{beam}, E_p and E_n are the beam, spectator proton and struck neutron energies, respectively. The virtual photon four-momentum is $q(\nu,\vec{q})$ where $\nu = E_{beam} - E'$. The angle between these two planes is ϕ_{pq}. The proton polar angle with respect to the momentum transfer direction $\vec{q}$ is defined as θ_{pq}. The advantage of an exclusive process is that we can account for all reaction products by applying conservation laws. Applying conservation of energy for d(e,e$'$p$_s$)n we obtain:

$$\begin{aligned} \nu + M_d &= E_p + E_n, \\ E_n^2 &= {M_n}^2 + n^2, \\ E_p^2 &= M_p^2 + p_s^2, \end{aligned} \tag{4.5}$$

where $M_d \approx 2M_p$, M_p and M_n are the deuteron, spectator proton and on-shell neutron masses, respectively. From momentum conservation we obtain:

$$\begin{aligned} \vec{q} - \vec{p}_s &= \vec{n}, \\ q^2 + p_s^2 - 2qp_s\cos\theta_{pq} &= n^2, \end{aligned} \tag{4.6}$$

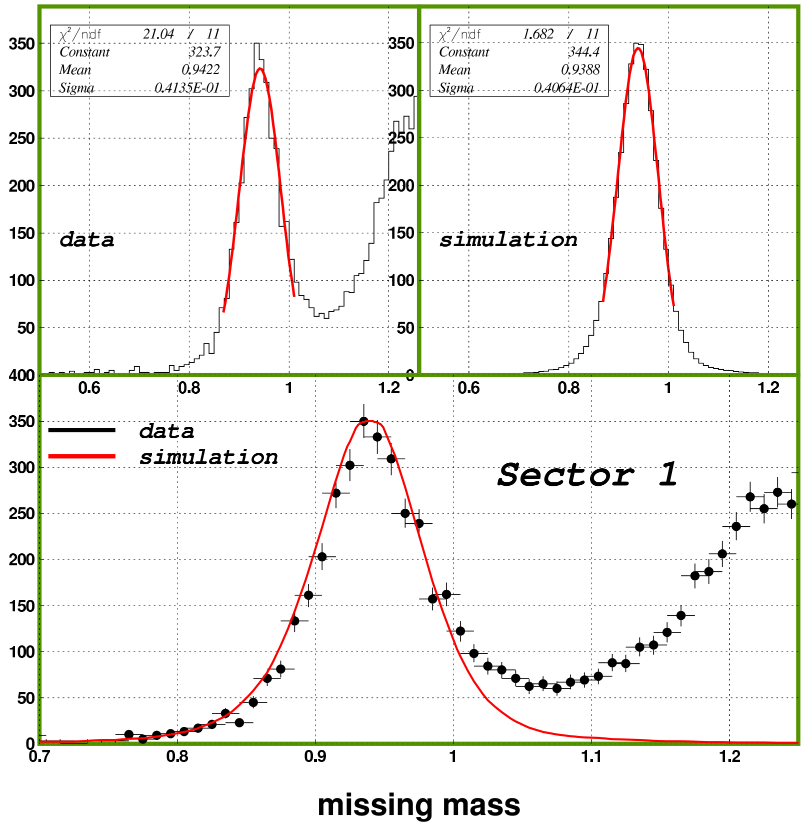

FIG. 4.29: Missing mass (MM) spectra obtained from real (upper-left panel) and simulated (upper-right panel) data each fitted with a Gaussian. The real (solid bullets) and simulated (solid curve) MM spectra for Sector 1 are shown in the lower panel.

where $q^2 = q_x^2 + q_y^2 + q_z^2$, $p_s^2 = p_x^2 + p_y^2 + p_z^2$, and $n^2 = n_x^2 + n_y^2 + n_z^2$. Introducing Eq. 4.5 into Eq. 4.6 we obtain:

$$(\nu + M_d - E_p)^2 = {M_n}^2 + q^2 + p_s^2 - 2qp_s \cos\theta_{pq} \tag{4.7}$$

Rearranging assuming $M_d = M_p + M_n$ and $M_p \simeq M_n$ and $Q^2 = q^2 - \nu^2$ yields:

$$\cos\theta_{pq} = \frac{Q^2 - 4(M_p + \nu)M_p + 2(\nu + 2M_p)E_p}{2qp_s} \tag{4.8}$$

This is the main constraint we applied to our kinematics. Our event generator picks the set (p_s, Q^2, ϕ_{pq} and x) using the distributions fit to the experimental data and calculates θ_{pq} using Eq. 4.7. From the first iteration using this model we extracted

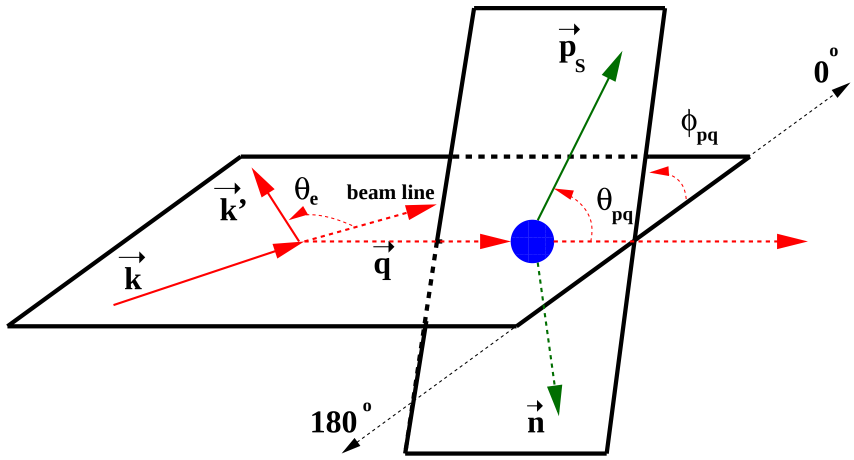

FIG. 4.30: Kinematics of the d(e,e$'$p$_s$)n reaction.

preliminary acceptances and corrected the data. We performed another set of fits to the acceptance corrected data and extracted a new set of constants for the parameterizations used in the event generator. Several iterations were needed to adjust the model to the data. The parameterizations of p_s, Q^2, ϕ_{pq} and x distributions used in our final input model are presented in Appendix F. Figure 4.31 shows good agreement between the simulated and experimental plots of ϕ_{pq} versus θ_{pq}. Distributions for spectator proton momentum p_s (upper panel), momentum transfer Q^2 (middle panel), and x (lower panel) obtained from experimental (solid bullets) and simulated data (solid curves) are shown in Figure 4.32 (left). The corresponding ratios of real to simulated data are shown in Figure 4.32 (right), for each distribution. The proton polar angular distributions for real (solid bullets) and simulated data (solid curve) are shown in Figure 4.33 (left), and the corresponding ratio between them is shown in Figure 4.33 (right). For each iteration we passed the generated events through GSIM using the FFREAD card input (presented in Appendix D) which contains setting of CC, EC, DC, SC cuts, target characteristics and beam energy. These settings were chosen to bring the simulations as close as possible to the real

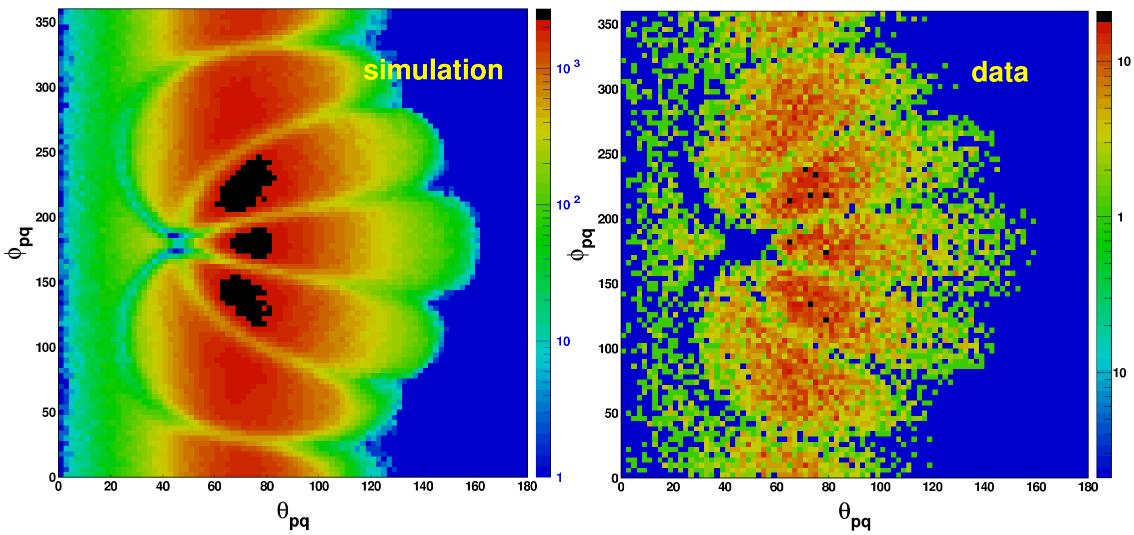

FIG. 4.31: Proton polar versus azimuthal angle with respect to the momentum transfer direction for simulated (left panel) and real data (right panel).

experimental conditions at the time of data taking. After this step we passed our simulated data through RECSIS and we stored the output in Ntuples 10-format just as was done for the real data. The simulated ntuples have information about the initial generated data (thrown Monte Carlo events) and about the reconstructed events which passed all the ID and fiducial cuts required in the main analysis. We ran the Monte Carlo simulation long enough such that the simulated data had far smaller statistical errors than the real data. The output from GSIM was fed into

Energy [GeV]	Region 1	Region 2	Region 3
5.645	1.58	1.58	1.58

TABLE 4.4: GPP smearing parameters for the three DC regions.

the Post Processing program GPP to generate the Monte Carlo raw data. Smearing parameters corresponding to different DC regions were adjusted until the missing mass spectrum (MM) obtained from simulated and real data agreed (see Fig. 4.29). These parameters are given in Table 4.4.

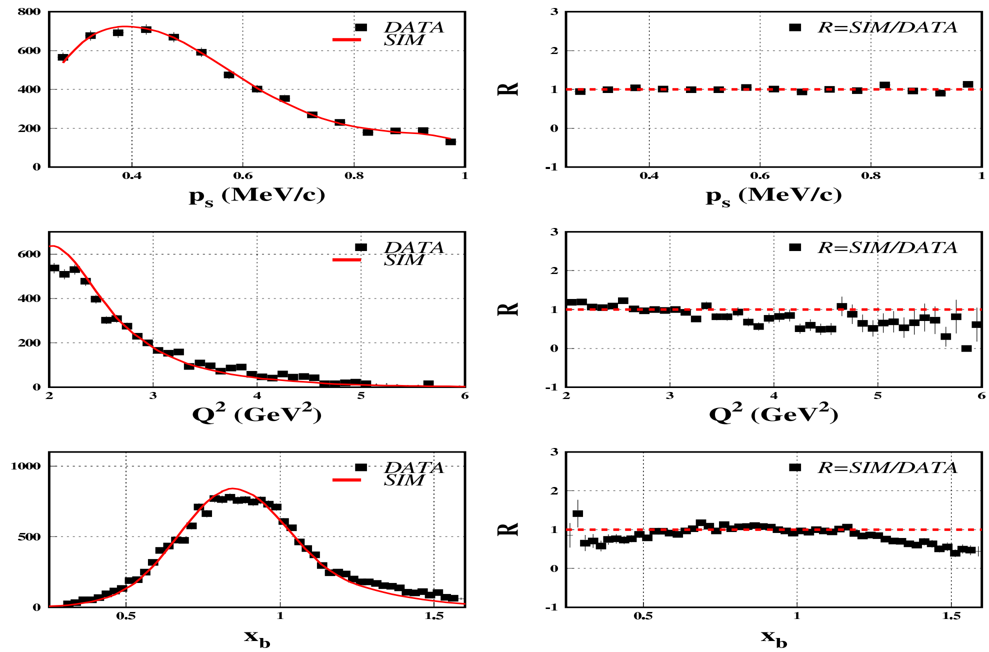

FIG. 4.32: Left: Proton momentum p_s (upper panel), momentum transfer Q^2 (middle panel) and Bjorken scaling variable x spectra for real (solid bullets) and simulated (solid lines) data. Right: The corresponding ratios of real to simulated data.

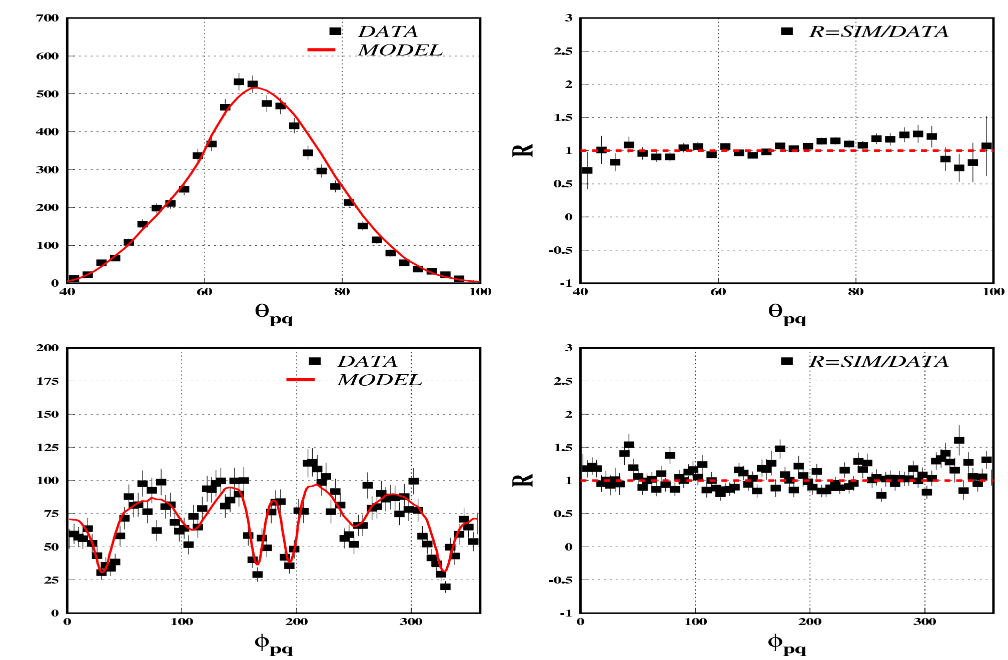

FIG. 4.33: Left: Proton scattering polar angle θ_{pq} (upper panel) and proton azimuthal scattering angle ϕ_{pq} (lower panel) with respect to $\vec{q}$ for real (solid bullets) and simulated (solid lines) data. Right: The corresponding ratios of real to simulated data.

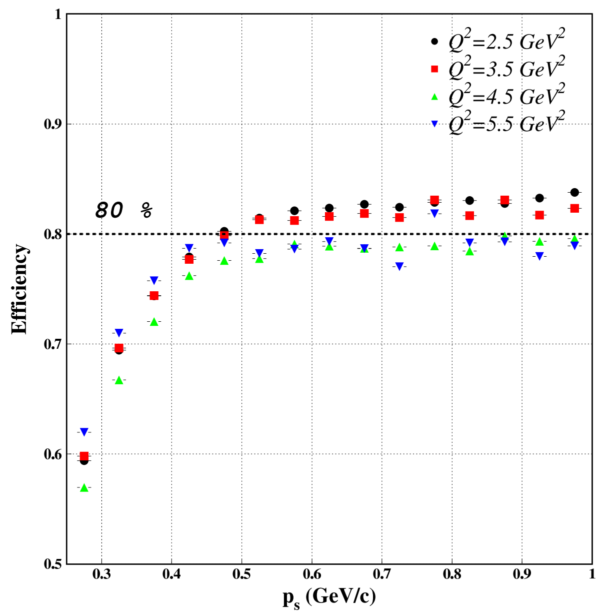

FIG. 4.34: Detection efficiency of d(e,e$'$p$_s$)n events in CLAS within E6 fiducial cuts for $Q^2 = 2.5, 3.5, 4.5$ and 5.5 GeV^2 (different colors and shapes markers). An efficiency of $\approx$ 80% was obtained.

As shown schematically in Figure 4.15 the last step in extracting the acceptance for each kinematic bin is to compute the ratio of the number of reconstructed events which passed all the ID and fiducial cuts as for real data to the number of events generated in the full phase space. The detection efficiency of d(e,e$'$p$_s$)n events in CLAS within our fiducial cuts was obtained from simulations with the same fiducial cuts as the experimental data. An efficiency of $\approx$ 80 % was obtained as shown in Figure 4.34. The TOF smearing parameter $f = 1$ gave a good agreement between data and simulation. Acceptance calculations should not depend strongly on the input model if buin migration is not significant. We used several trial models to adjust our simulation to be as close as possible to the real data and studied the model dependence of our acceptance calculations. Figs. 4.35 - 4.37 (upper panels) show p_s distributions for experimental data (solid bullets)) and various trial models (colored curves) for four kinematic bins $Q^2 = 2.5, 3.5, 4.5$ and 5.5 GeV^2.

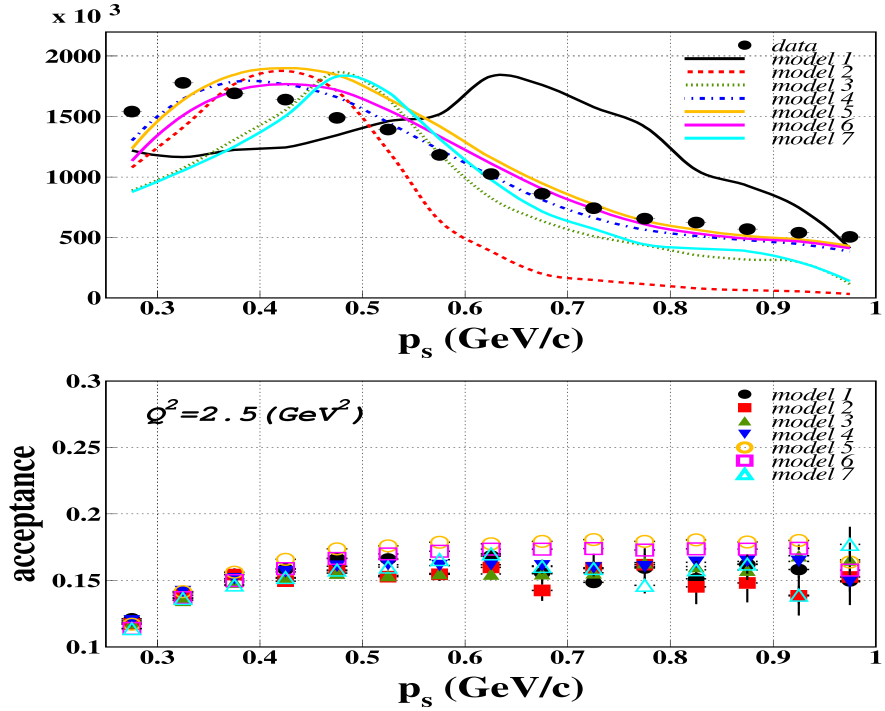

FIG. 4.35: Upper panel: Spectator proton momentum for real data (solid bullets) together with several simulation models (different color curves). Lower panel: Corresponding acceptances (different colors and shapes markers). Both plots correspond to $Q^2 = 2.5$ GeV^2.

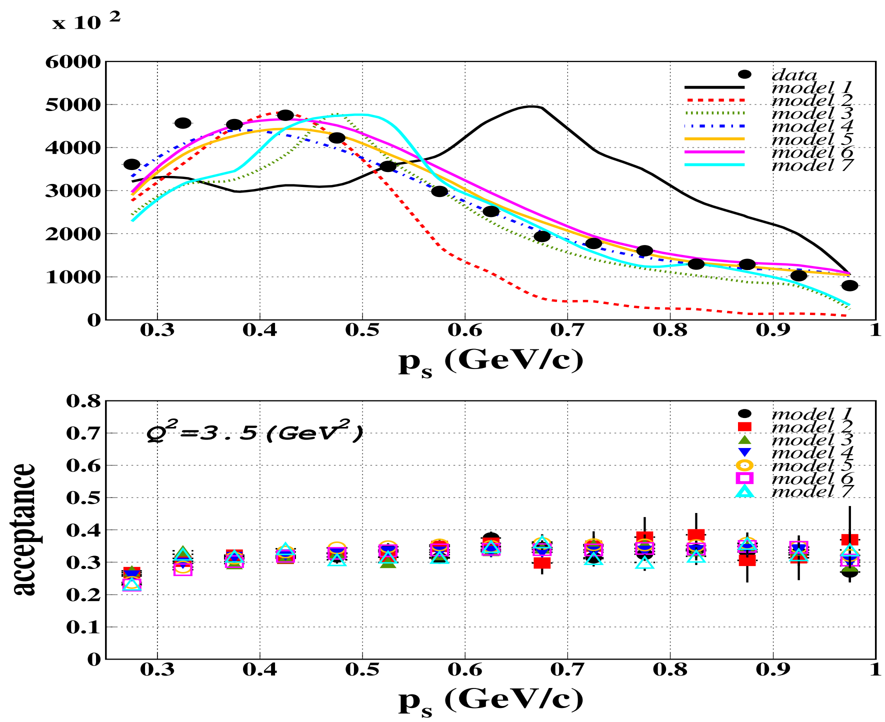

FIG. 4.36: Same as in Fig. 4.35, except for $Q^2 = 3.5$ GeV^2.

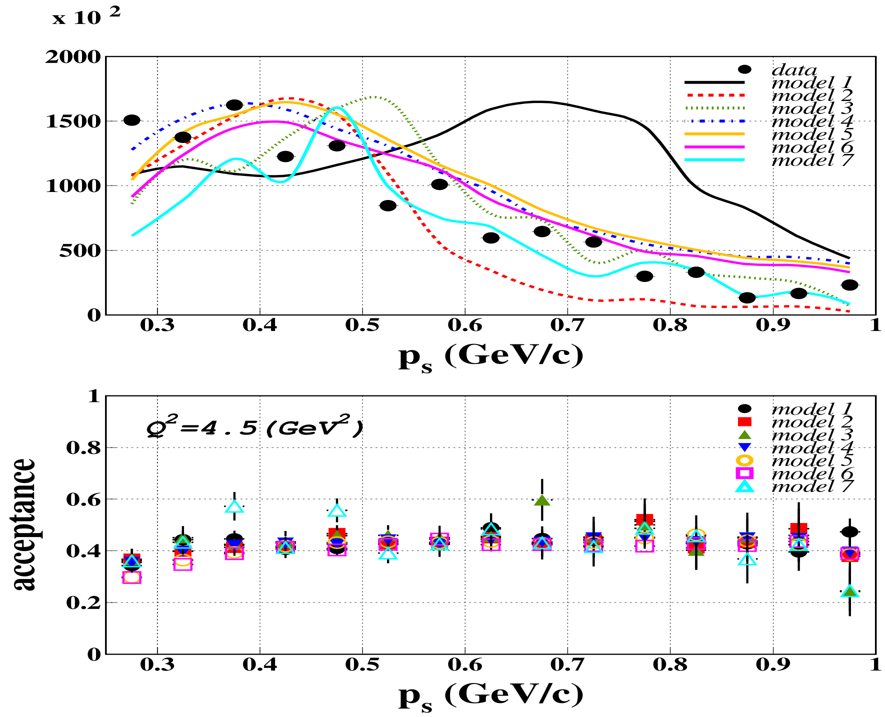

FIG. 4.37: Same as in Fig. 4.35, except for $Q^2 = 4.5$ GeV^2.

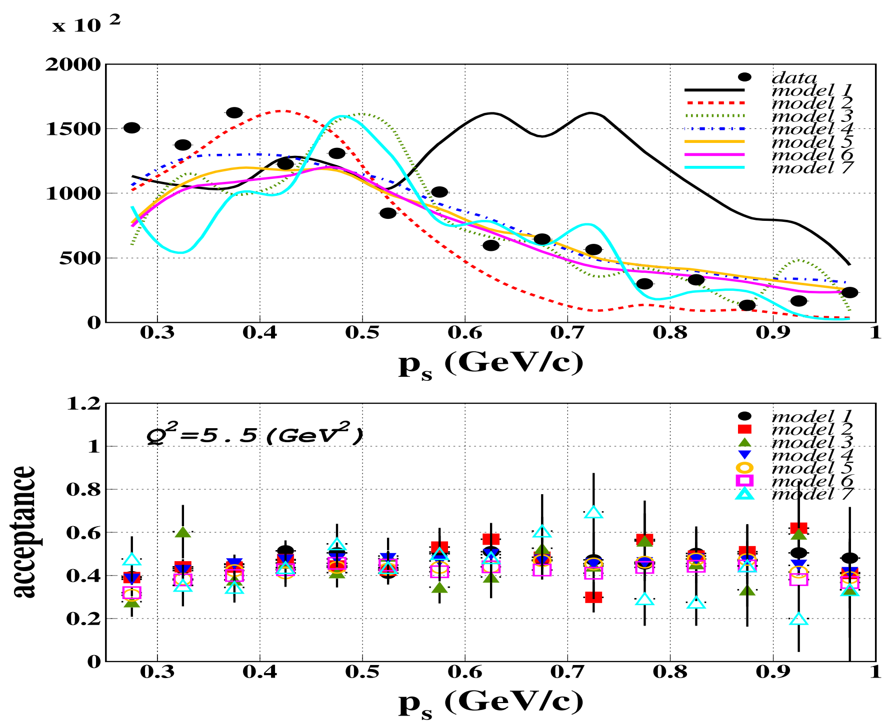

FIG. 4.38: Same as in Fig. 4.35, except for $Q^2 = 5.5$ GeV^2.

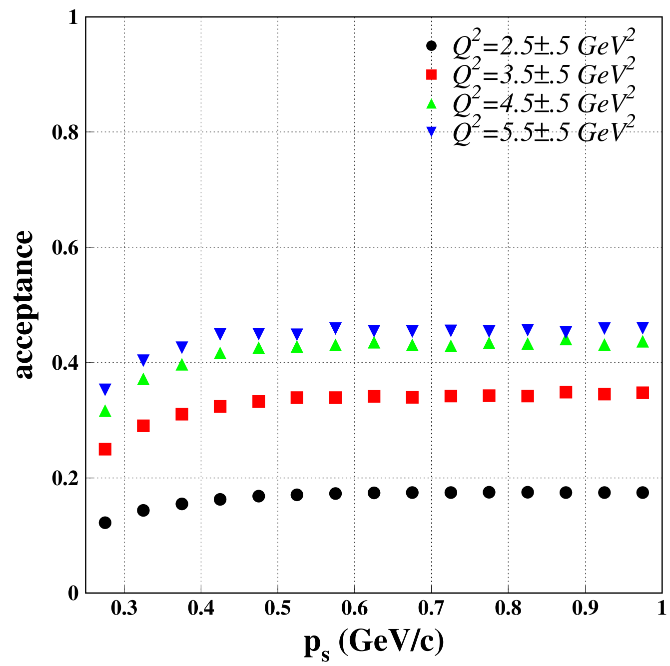

FIG. 4.39: Final spectator proton acceptances extracted from simulations for $Q^2 = 2.5, 3.5, 4.5$ and 5.5 GeV^2 and $p_s = 0.25 - 1.00$ GeV/c.

The corresponding acceptances extracted using different input models for the d(e,e$'$p$_s$)n simulations are shown in Figs. 4.35 - 4.37 (lower panels) by different colored and shaped markers. At low Q^2 the model dependence of the acceptance calculations is small, but it increases with momentum transfer Q^2. We conclude that a good simulation of the real data is crucial in order to obtained a realistic acceptance. The final acceptances as a function of p_s using the most realistic model are shown in Figure 4.39. They were used in extraction of absolute cross sections versus p_s in the d(e,e$'$p$_s$)n reaction presented in Section 5.2 and tabulated in Appendix D.

The acceptances range from 15% to 45% . The systematic uncertainties associated with the model dependence of the acceptance calculations were taken as the root mean square (RMS) deviation of the input models used in simulations for each kinematic bin. These uncertainties are given in Table 4.5. If the detector model implemented in GSIM were perfect, then we would obtain the perfect response of CLAS

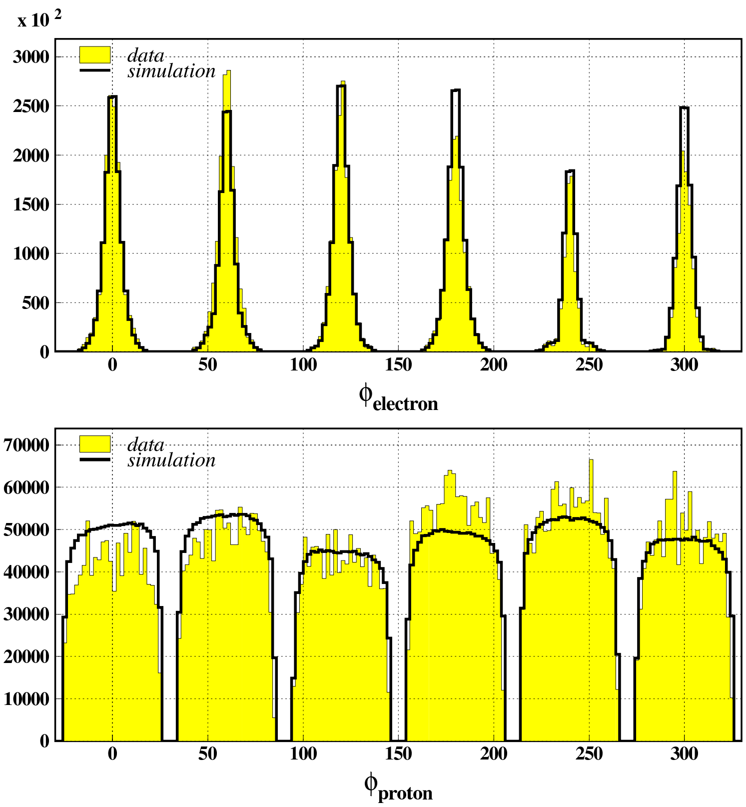

FIG. 4.40: Distributions in electron azimuthal angle (upper panel) and proton azimuthal angle (lower panel) for real (filled histogram) and simulated (solid histogram) data. Sectors 1,3, and 5 for electrons and Sectors 3, 5, and 6 for protons are well described by the simulations.

to detected charged particles. But in reality the GEANT simulation of CLAS does not reproduce all detector responses to charged particles. We can correct for this by comparing the data and the simulation on a sector-by-sector basis. Figure 4.40 shows the scattered electron azimuthal angle (upper panel) and the scattered proton azimuthal angle (lower panel) for real (filled histogram) and simulated data (solid histogram), corresponding to each of the six sectors of CLAS. For the electron case, Sectors 1,3, and 5 are well-described by the simulations, while for the other three sectors GSIM fails to reproduce perfectly the experimental data. For the proton case, Sectors 3, 5, and 6 are well-described by the simulations while Sectors 1, 2 and 4 are poorly reproduced. The uncertainties associated with this effect were computed with the same method described in Section 4.2.2, Eqs. 4.2 – 4.4. We corrected for the sector inefficiency by normalizing the yields of badly simulated sectors to the average of well simulated sectors. The correction factors associated and systematic uncertainties are presented in Section 4.4.

p_s [MeV/c]	$Q^2 = 2.5$ GeV^2 SysErr [%]	$Q^2 = 3.5$ GeV^2 SysErr [%]	$Q^2 = 4.5$ GeV^2 SysErr [%]	$Q^2 = 5.5$ GeV^2 SysErr [%]
275	0.09	0.62	1.07	2.34
325	0.09	0.73	1.37	2.88
375	0.12	0.31	2.19	1.41
425	0.19	0.37	0.35	1.20
475	0.23	0.40	1.82	1.58
525	0.29	0.58	0.73	1.02
575	0.33	0.55	0.34	2.23
625	0.28	0.51	0.84	1.99
675	0.42	0.74	2.19	2.02
725	0.38	0.63	0.49	2.50
775	0.36	0.88	1.33	3.20
825	0.42	0.72	0.76	2.70
875	0.35	0.64	0.99	2.05
925	0.57	0.64	1.00	2.96
975	0.35	1.15	2.95	1.80

TABLE 4.5: Systematic uncertainties associated with the model-dependence of acceptance calculations for different kinematic bins: $Q^2 = 2.5, 3.5, 4.5,$ and 5.5 GeV^2 and $p_s = 0.25 - 1.$ GeV/c.

4.3 Absolute Normalizations

4.3.1 Beam Charge

A Faraday cup was used to measure the accumulated charge of incident electrons. Computer dead time in the experiment was taken into account by gating the Faraday cup on the computer live time. The Faraday cup is digitized with 9136 counts per μC. The data acquisition system (DAQ) records data at a rate of ≈ 2

kHz. A second scaler records continuously the accumulated charge from the beginning to the end of each run. Because of a bug in the DAQ sofware some runs had a non-zero value at the beginning of the run. Therefore, instead of taking just the end value of accumulated charge for that run, we have to subtract the charge recorded exactly at the beginning. Taking this effect into account for each run, and summing over all runs, we obtained a total charge of 9.18722 $\times 10^{-3}$ Coulomb, which corresponds to 5.742 $\times 10^{16}$ electrons. The average beam current during the experiment was about 7 nA. Therefore the number of counts N_{counts} written to the data stream by the DAQ every 10 second interval counts is:

$$N_{counts} = \frac{7(nA) \cdot 10(sec)}{10^{-4}(\mu C)/(counts)} = 700 \;\; counts \tag{4.9}$$

Assuming that the calibration error for the Faraday cup is negligible, the uncertainty associated with the total charge comes from the digitization truncation of 700, or 0.14% for a file of x events. This error is small and can be neglected.

4.3.2 Empty Target contribution

In order to remove the contribution from scatterings on the target walls we analyzed the empty target data in the same way as the full target data. We normalized the integrated yields to the charge accumulated on the "live-gated" Faraday cup and subtracted from the full data:

$$N_{\mathrm{corr}}(x, Q^2) = N_{\mathrm{full}}(x, Q^2) - \frac{Q_{\mathrm{full}}^{\mathrm{tot}}}{Q_{\mathrm{empty}}^{\mathrm{tot}}} N_{\mathrm{empty}}(x, Q^2), \tag{4.10}$$

in which $N_{\mathrm{corr}}(x, Q^2)$ is the corrected yield, N_{full} is the number of events selected from the full target data, N_{empty} is the number of events selected from the empty target data, and Q_{full} and Q_{empty} are the FC charge accumulated for the fulland empty target data sets, respectively. A possible systematic error on the absolute normalization of the extracted cross section is related to the cold D_2 gas remaining

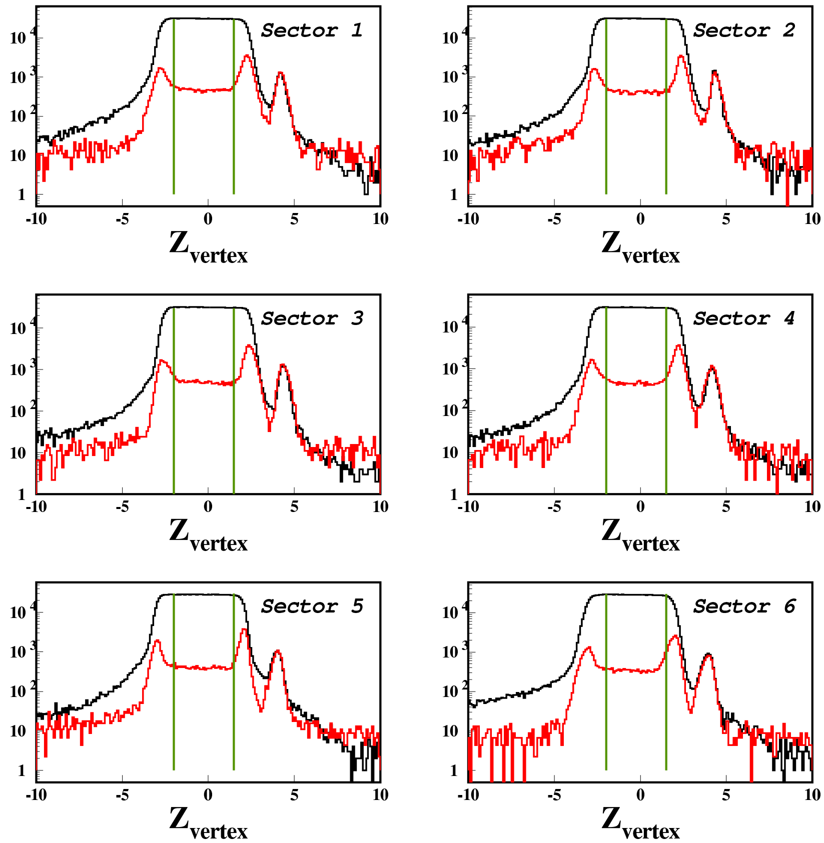

FIG. 4.41: Vertex distribution for each sector of CLAS for scattered electrons along the beam direction. The black histogram shows electron Z-vertex distribution for the full deuterium target while the red histogram corresponds to the empty target. Each distribution is normalized to the live-gated charge collected by the Faraday cup.

inside the target even after the target was emptied. This can be estimated by a comparison of the integrated yields of full and empty target runs within the target volume, excluding the target walls. We applied an electron vertex cut $-2. < Z_{el} < 1.5$ to both empty and full target data and estimated the ratio between them for each sector. The ratio appeared to be sector independent with an uncertainty of 0.1%. After target contribution subtraction the fraction of events remaining well outside of our vertex cut ($|Z_{el}| > 2.$) gave a fraction of 0.3%. These systematic errors were added in quadrature to the final systematic error.

4.3.3 Cross Section Calculation

The inclusive d(e,e′) cross section was evaluated using the following equation:

$$\frac{d^2\sigma}{dQ^2dx}(x,Q^2) = \frac{1}{\rho\frac{N_A}{M_A}lQ_{tot}}\frac{N_{LH}(x,Q^2)}{\Delta Q^2\Delta x}\times\mathbf{C.F.} \tag{4.11}$$

in which ρ is the density of liquid deuterium (D_2) in the target, N_A is Avogadro's number, M_A is the target particle's molar mass, l is the target length, Q_{tot} is total live-gated charge in Faraday cup, and $N_{LH}(x,Q^2)$ is the number of events obtained from Eq. 4.1.6. The corresponding bin sizes are ΔQ^2 and Δx. The correction factor **C.F.** accounts for the photo-electron cut in CC (F_{phe}), pair production and pion contaminations ($F_{e^+e^-}$), detector acceptance (F_{acc}), electron detection efficiency (μ_{el}), radiative effects (F_{rc}) and luminosity (L) and is given as:

$$\mathbf{C.F.} = \frac{1}{L\mu_{\rm el}}F_{\rm rc}F_{\rm acc}F_{\rm phe}F_{e^+e^-}. \tag{4.12}$$

The exclusive d(e,e′p$_s$)n cross section is presented in bins of Q^2, x, and p_s within the solid angle $d\Omega_{pq}$ defined by the azimuthal and polar angles with respect to the exchanged virtual photon momentum direction. The number of events detected in the kinematic bin dK ($dK = dQ^2dxdp_sd\Omega_{pq}$) can be computed as:

$$N_{\rm dK} = \frac{\int Idt}{e}\frac{\rho}{M_A}N_{\rm A}l\frac{d\sigma}{dK}dK. \tag{4.13}$$

The electron charge is $e = 1.602\times10^{-19}$ Coulomb and Avogadro's number is $N_A = 6.02\times10^{23}$ (per mole). The liquid deuterium target has a density of $\rho = 0.169$ g/cm^3 and the length of the target used in this analysis was 3.5 cm. The differential cross section for the kinematic bin defined by ΔQ^2, Δx, Δp_s and Δ_{pq} can be writen as:

$$\begin{aligned}\frac{d\sigma}{dK} &= \frac{N_{\rm dK}}{dK}\times\frac{e}{\int Idt}\times\frac{M_A}{\rho N_{\rm A}l}\\ &= \frac{N_{\rm dK}}{\Delta Q^2\Delta x\Delta p_{\rm s}\Delta\Omega_{\rm pq}}\times\mathbf{C.F.}\end{aligned} \tag{4.14}$$

The correction factor **C.F.** is defined in a similar way as one in Eq. 4.11 but taking into account the proton detection efficiency μ_{pr} and sector tracking inefficiency μ_{sect}:

$$\mathbf{C.F.} = \frac{1}{L\mu_{\rm el}\mu_{\rm pr}\mu_{\rm sect}} F_{\rm rc}F_{\rm acc}F_{\rm phe}F_{e^+e^-}. \tag{4.15}$$

The integrated luminosity is defined as $L = N_{el}N_d$ where N_{el} and N_d are the number of electrons corresponding to the total charge accumulated on the "live-gated" Faraday cup and the number of deuterons per unit target area, respectively:

$$\begin{aligned} N_{\rm el} &= \frac{\int Idt}{e} = 5.742 \times 10^{16} \text{ electrons} \\ N_d &= \frac{\rho N_{\rm A} l}{M_A} = 3.5({\rm cm}) \times 0.169({\rm g/cm^3}) \times \frac{6.022 \times 10^{23}(1/{\rm mol})}{2({\rm g/mol})} = 1.781 \times 10^{23}{\rm cm}^{-2} \end{aligned} \tag{4.16}$$

The integrated luminosity for this experiment was:

$$L = 5.742 \times 10^{16} \times 1.781 \times 10^{23}{\rm cm}^{-2} = 1.022 \times 10^{40}{\rm cm}^{-2} \tag{4.17}$$

All the correction factors included in the final absolute normalization are presented in Table 4.8.

4.3.4 Radiative Corrections

The electron may lose some of its energy before or after scattering by ionization of the target material or by bremsstrahlung. Internal bremsstrahlung occurs in the field of the nucleus involved in the reaction, and external bremsstrahlung occurs when the electron radiates in presence of another nucleus. The rate for internal bremsstrahlung is proportional to the target thickness, whereas the rate for the external bremsstrahlung is proportional to the square of the target thickness. Therefore, external radiative effects are reduced considerably in very thin targets, and internal bremsstrahlung dominates.

The first calculations of these radiative effects were done by Schwinger [83] and later improved by Mo and Tsai [84]. The Feynman diagrams of the lowest order radiative effects are shown in Figure 4.42. Although the Mo and Tsai recipe has been used for decades for inclusive elastic and inelastic electron scattering, for exclusive processes such as d(e,e′p)n this approach cannot be directly applied. For the inclusive d(e,e′) channel we extracted the radiative correction factor for each kinematic bin from the ratio of the model cross sections of Ref. [85] with and without radiative effects. Samples of the radiative correction factor N_{RC} extracted from this model and defined as the ratio of the full cross section to the Born cross section ($N_{RC} = \frac{\sigma Full}{\sigma^{Born}}$) are shown in Figure 4.43. The radiative effects were calculated in this code using the method developed by Mo and Tsai. The radiative tail from elastic and inelastic processes were evaluated in the peaking approximation which uses the fact that bremsstrahlung photons are mostly emitted in the direction of the incident and scattered electrons. In these calculations internal radiation as well as the external radiation together with ionizations effects were taken into account [86]. Under the elastic and quasi-elastic peaks the systematic errors can be neglected because in this region the Schwinger correction is dominant, known to a very good accuracy from QED, and model independent. In the quasi-elastic region ($x \geq 1$) the radiative correction N_{RC} is almost independent of momentum transfer Q^2 with a value of ≈ 0.70. For the exclusive d(e,e′p)n reaction a proton is detected in addition to the final electron, which modifies the phase space allowed for the final radiated electron. The exact formalism for the exclusive internal correction requires four structure functions associated with the additional angular dependence, instead of the two used by Mo and Tsai. The Mo and Tsai method requires an unphysical parameter for splitting the soft and hard regions of the radiated photon's phase space in order to cancel the infrared divergence. An essential step in this calculation is to integrate over an energy range ΔE that includes part of the elastic peak and part of the radiative tail. Another method proposed by Bardin and Shumeiko [87], uses a covariant procedure that uses an integration over a squared missing mass.

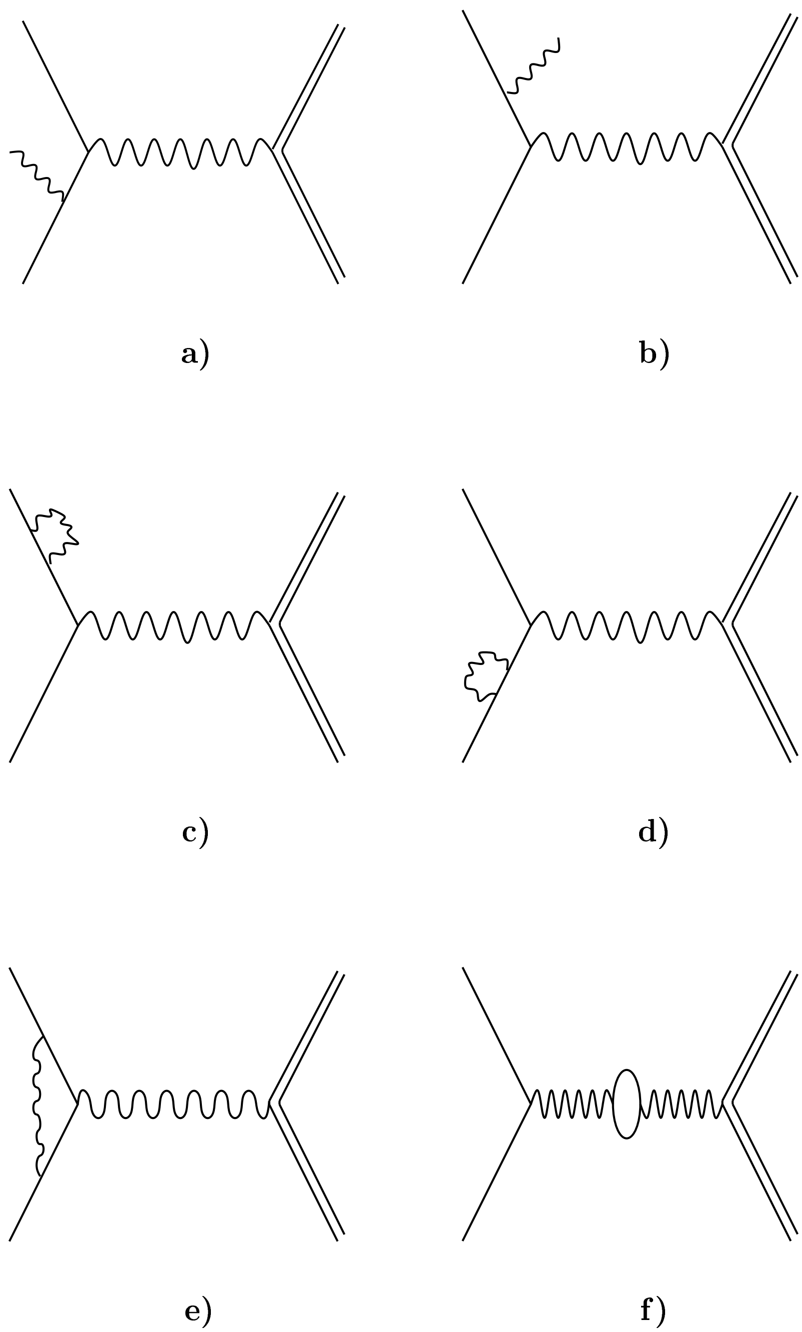

FIG. 4.42: Feynman diagrams for internal radiative processes: a) and b) represent bremsstrahlung before and after the interaction, c) and d) corresponds to the renormalization of the electron mass, e) represents the vertex correction, and f) results in the renormalization of the virtual photon due to vacuum polarization.

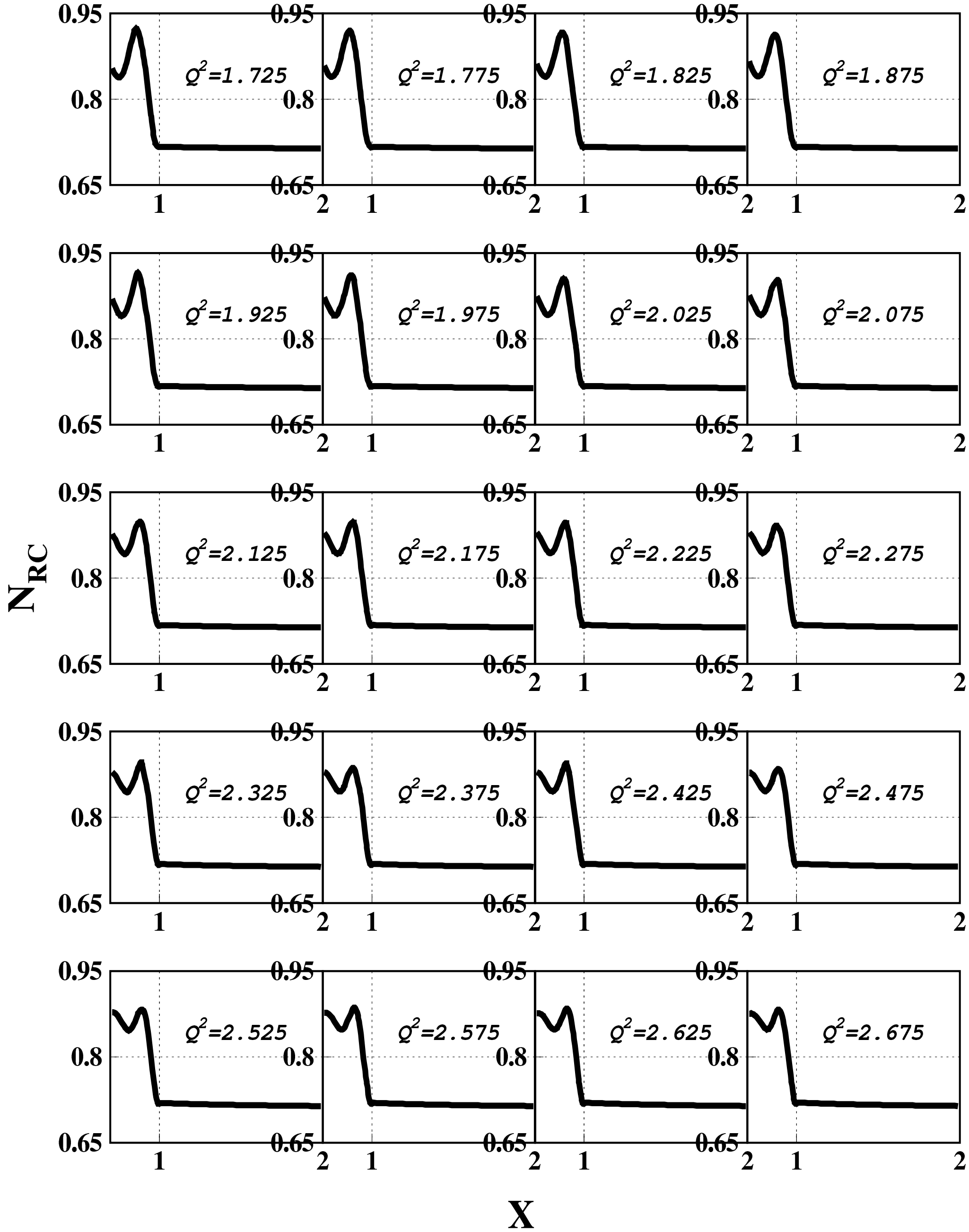

FIG. 4.43: Radiative correction factor $N_{RC} = \frac{\sigma^{Full}}{\sigma^{Born}}$, defined as the ratio of full to Born cross sections, for the inclusive d(e,e′) reaction for $Q^2 = 1.7 - 2.7$ GeV^2, and $x = 0.7 - 2$. The calculations were taken from the model described in Ref. [85].

The radiative cross section of the exclusive process d(e,e′p)n can be written as [88]:

$$d\sigma_r = \frac{(4\pi\alpha)^3 dQ^2 dW^2 d\Omega_h}{2(4\pi)^7 S^2 W^2} \int d\Omega_k dv \frac{v\sqrt{\lambda_W}}{f_W^2 Q^4} L_{\mu\nu}^{(R)} W_{\mu\nu}, \tag{4.18}$$

where $S \equiv 2E_i M_p$, $d\Omega_h$ is the solid angle of the detected proton, $v = \Delta^2 - m_u^2$ is the missing mass (or inelasticity) due to the emission of a bremsstrahlung photon, m_u is the mass of the undetected hadron (in this case neutron), $L_{\mu\nu}$ and $W_{\mu\nu}$ are the leptonic and the hadronic tensors. Here, factors λ_W and f_W are given by:

$$\begin{aligned} \lambda_{\mathrm{W}} &= (W^2 - m_h^2 - M_{\mathrm{miss}}^2)^2 - 4m_h^2 W^2, \\ f_W &= W - E_h + p_h[\cos\theta_h \cos\theta_k + \sin\theta_h \sin\theta_k \cos(\phi_h - \phi_k)], \end{aligned} \tag{4.19}$$

where $\theta_h, \phi_h, \theta_k$ and ϕ_k are the proton and radiated photon's polar and respectively azimuthal angles. We used a modified version of the program EXCLURAD, written by A. Afanasev [88] for exclusive pion electro-production p(e,e'π^+)n , and modified by G. Gilfoyle [89] for the d(e,e′p)n channel. The response functions for the deuteron were calculated by W. Van Orden and implemented into the code.

EXCLURAD uses as inputs the beam energy E_{beam}, the invariant mass of the struck neutron W, the squared virtual photon momentum Q^2, and the detected proton angles in the center-of-mass frame, and the inelasticity cutoff v, θ_p and ϕ_p, as shown in Figure 4.44. In our analysis we choose a cut on the missing mass at 1 GeV to select quasi-elastic events. Hence we obtain $v = 0.117$. The radiative corrections are strongly dependent on v. A tight cut on the missing mass eliminates contributions from the higher-energy part of the bremsstrahlung spectrum, thus leading to a larger magnitude radiative corrections. In order to apply radiative corrections to our data we transformed from the CM of the detected proton used by

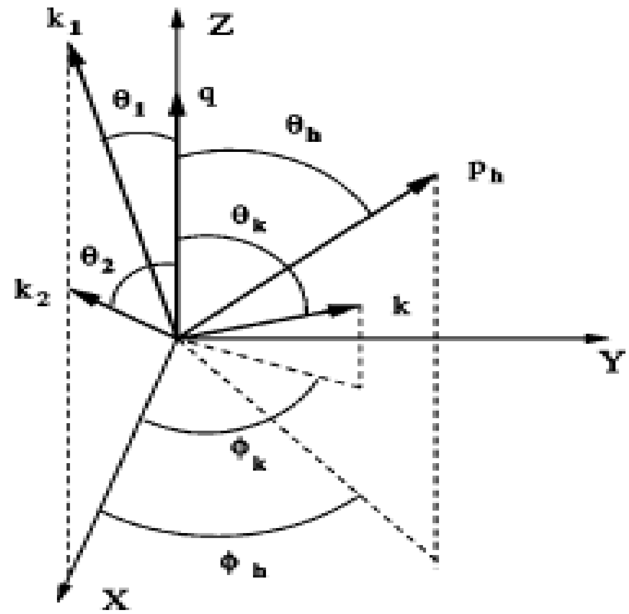

FIG. 4.44: Definition of momenta and angles in the center-of-mass of the detected proton for the d(e,e$'p_s$)n reaction.

EXCLURAD to the LAB frame using the Lorentz transformations defined as:

$$\begin{aligned}
\nu_{\mathrm{CM}} &= \gamma(\nu_{\mathrm{LAB}} - \beta q_{\mathrm{LAB}}), \\
q_{\mathrm{CM}} &= \gamma(q_{\mathrm{LAB}} - \beta \nu_{\mathrm{LAB}}),
\end{aligned} \tag{4.20}$$

where $\beta = \frac{q}{M_d+\nu}$ is the Lorentz boost from the LAB frame to the CM frame of scattered proton. The energy and momentum transfer in the CM are, respectively, ν_{CM} and q_{CM}, while the corresponding quantities in the LAB frame are ν_{LAB} and q_{LAB}. The orthogonal components of the spectator momentum $(p^{||}_{\mathrm{LAB}}, p^{\perp}_{\mathrm{LAB}})$ in the LAB frame are given by:

$$\begin{aligned}
p^{||}_{\mathrm{LAB}} &= p_s \theta^{\mathrm{LAB}}_{pq}, \\
p^{\perp}_{\mathrm{LAB}} &= p_s \sin\theta^{\mathrm{LAB}}_{pq},
\end{aligned} \tag{4.21}$$

where p_s is the momentum component of four-vector $p_s(\mathrm{E}_p,\vec{p}_s)$ and θ_{pq} is the proton scattering angle with respect to the momentum transfer direction. Using the Lorentz

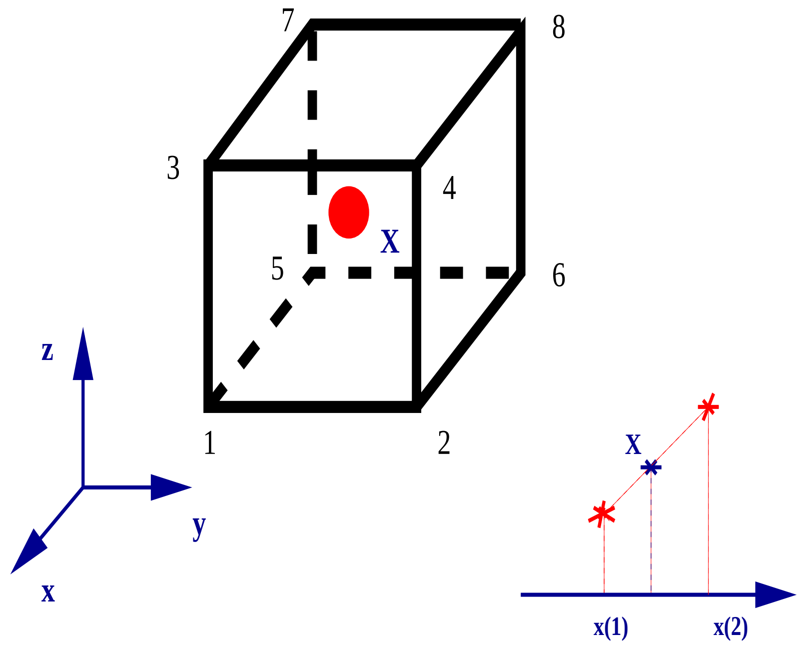

FIG. 4.45: Linear interpolation to compute probabilities t, u and v to find a particle with coordinates x, y, and z in a bin of known boundaries x_1, x_2, y_1, y_2, z_1, and z_2. The probabilities t, u and v are given in Eq. 4.22.

transformations of Eqs. 4.18 and the Eqs. 4.19 we can compute the orthogonal components of the spectator proton momentum in CM frame:

$$\begin{aligned} p^{||}_{\mathrm{CM}} &= \gamma(p^{||}_{\mathrm{LAB}} - \beta E_p), \\ p^{\perp}_{\mathrm{CM}} &= p^{\perp}_{\mathrm{LAB}}, \end{aligned} \tag{4.22}$$

where $p^{||}_{\mathrm{CM}}$ and $p^{\perp}_{\mathrm{CM}}$ correspond to the orthogonal components of the proton momentum in the CM frame and E_p is the energy of the scattered proton. Now we can compute the polar angle $\theta^{\mathrm{CM}}_{pq}$ between the virtual photon momentum $\vec{q}$ and the spectator proton momentum $\vec{p}_s$ in CM frame:

$$\cos\theta^{CM}_{pq} = \frac{p^{||}_{CM}}{\sqrt{(p^{||}_{CM})^2 + (p^{\perp}_{CM})^2}}. \tag{4.23}$$

Using EXCLURAD we generated radiative corrections corresponding to each kinematic bin in Q^2, x and p_s. The θ- and ϕ-dependence of the radiative corrections is

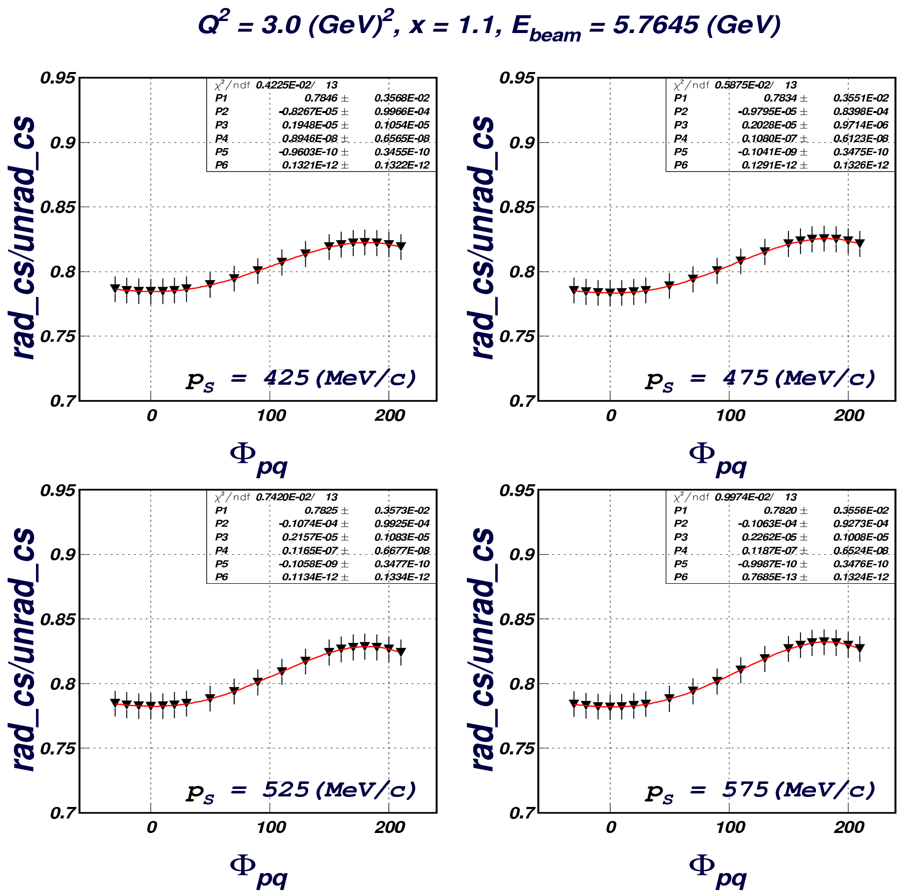

FIG. 4.46: Dependence of the radiative corrections on ϕ_{pq} for four values of the spectator momentum $p_s = 425, 475, 525$ and 575 MeV/c at $Q^2 = 3$ GeV^2 for $x = 1.1$, and the polinomial fit (solid curves) of this dependence.

significant for our analysis (see Figure 4.46). We parameterized the ϕ-dependence of the correction using a fifth-order polynomial (solid curves in Fig. 4.46) in the variables Q^2, x, and p_s. In the final analysis we found that a simple linear interpolation was sufficient for obtaining radiative corrections at specific values of x, Q^2, and p_s. The formula for a 3-way interpolation is:

$$\begin{aligned} \langle f \rangle &= f_5(1-t)(1-u)(1-v) + f_2 tu(1-v) + \\ &+ f_1 t(1-u)(1-v) + f_7(1-t)(1-u)v + \\ &+ f_6(1-t)u(1-v) + f_8(1-t)uv + \\ &+ f_3 t(1-u)v + f_4 tuv, \end{aligned} \tag{4.24}$$

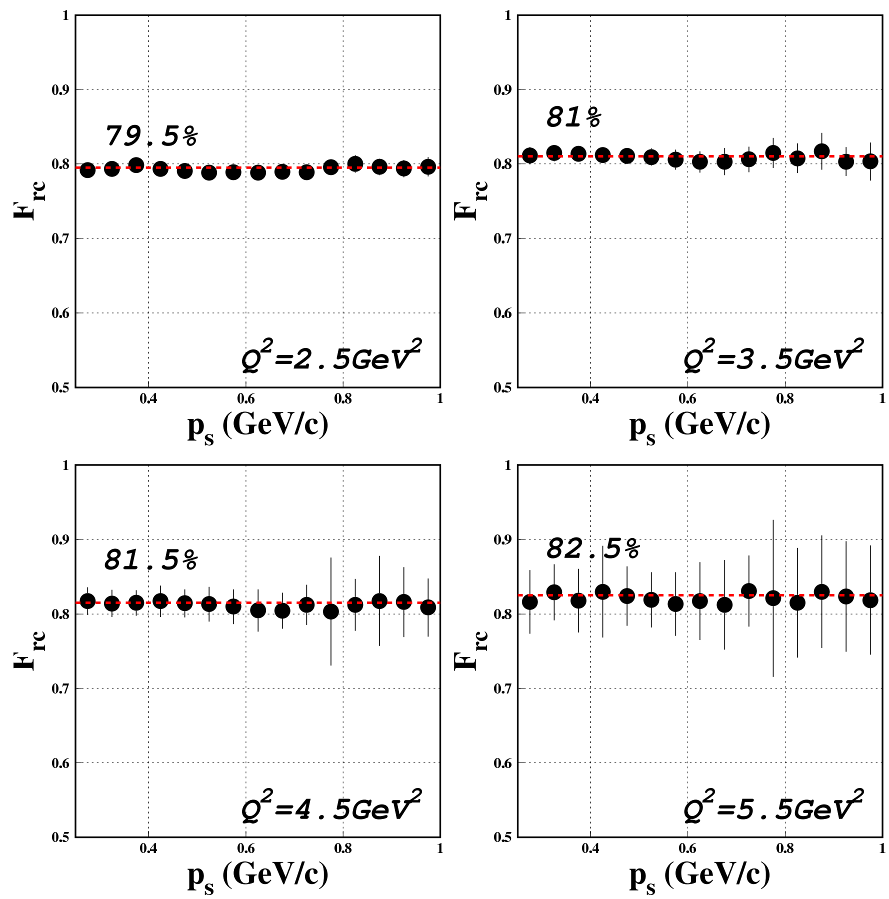

FIG. 4.47: Radiative correction factor F_{rc} as a function of p_s for $Q^2 = 2.5, 3.5, 4.5,$ and 5.5 GeV^2. F_{rc} is nearly independent of p_s and Q^2 and ranges from 79.5% to 82.5%.

where $\langle f \rangle$ is evaluated at the coordinates x, y, z within 3-dimensional bin of known boundaries x_1, x_2, y_1, y_2, z_1, z_2. Then:

$$t = \frac{x - x_1}{x_2 - x_1}, u = \frac{y - y_1}{y_2 - y_1}, v = \frac{z - z_1}{z_2 - z_1} \tag{4.25}$$

We generated a grid in Q^2, x, and p_s and used Eq. 4.24 to interpolate radiative correction factors for d(e,e′p)n. We applied these interpolated factors event-by-event as a weighting factor in the histograms of accumulated events as explained in Section 5.2.2. The radiative correction factor F_{rc} defined as the ratio of the radiated to unradiated cross sections versus p_s is shown in Figure 4.47 for Q^2 =

2.5, 3.5, 4.5, and 5.5 GeV^2. F_{rc} is nearly independent of p_s and Q^2 and ranges from 79.5% to 82.5%. The model used for calculating radiative corrections for d(e,e$'$p)n is based on $PWIA$, and does not include the meson exchange currents ρ and π (MEC) and Δ-isobar contributions. Although we know this to be naive,

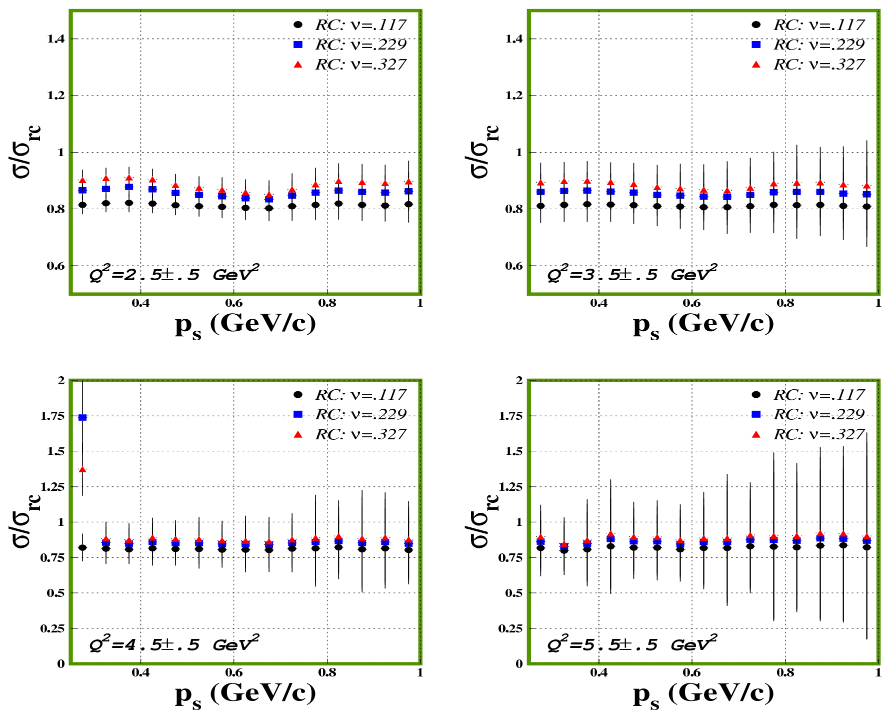

FIG. 4.48: The ratio of the unradiated to radiated cross sections for four different bins in Q^2 and for three different missing mass cuts corresponding to different inelasticity v marked by different symbol shapes.

the radiative corrections should depend primarily on the correct kinematics of the exclusive reaction (the inclusive and exclusive PWIA corrections differ by a factor of 2) we anticipate similar results when more sophisticated radiative corrections become available. To estimate the uncertainties associated with the missing-mass cut, which determines the inelasticity v, we extracted three sets of corrections for three different missing mass cuts: MM <1., MM <1.05 and MM <1.1 GeV (as shown in Figure 4.48). The systematic errors associated with the dependence of the radiative corrections on the choice of missing-mass cut are summarized in Table 4.6. The systematic errors for $Q^2 = 5.5$ GeV^2 were evaluated using the average value

p_s [MeV/c]	$Q^2 = 2.5$ GeV^2 SysErr [%]	$Q^2 = 3.5$ GeV^2 SysErr [%]	$Q^2 = 4.5$ GeV^2 SysErr [%]	$Q^2 = 5.5$ GeV^2 SysErr [%]
275	2.09	1.96	1.84	1.89
325	2.11	2.00	1.73	1.20
375	2.14	1.97	1.61	1.56
425	2.02	1.91	1.81	2.12
475	1.70	1.77	1.61	1.87
525	1.55	1.61	1.65	1.78
575	1.46	1.53	1.52	1.58
625	1.30	1.45	1.49	1.65
675	1.20	1.40	1.44	1.65
725	1.41	1.56	1.60	1.86
775	1.73	1.80	1.79	1.83
825	1.89	1.88	1.92	1.95
875	1.92	1.87	1.81	2.10
925	1.88	1.81	1.81	2.04
975	1.91	1.78	1.76	1.91

TABLE 4.6: Systematic errors associated with the dependence of radiative correction factor F_{rc} of the inelasticity $v = \Delta^2 - m_u^2$ for $Q^2 = 2.5, 3.5,$ and 4.5 GeV^2 and 15 spectator proton momentum p_s bins.

of errors corresponding to the lower Q^2 bins for each momentum bin. As shown in Table 4.6 this uncertainty is ≈ 2 %. In the near future we will evaluate the radiative corrections using Laget's model [29] which seems to agree with the experimental data. We expect that the uncertainties associated with the dependence of radiative corrections of the model to be no more than 5%, so we assigned an overall systematic error associated with the dependence of radiative corrections of the theoretical model and of the missing mass cut of 5%.

4.4 Corrections and Error Analysis

This section summarizes all the cuts and corrections applied to the experimental data and the uncertainties associated with them. First cuts were applied on the electromagnetic calorimeter (EC) and on Cherenkov photoelectrons. The EC sample

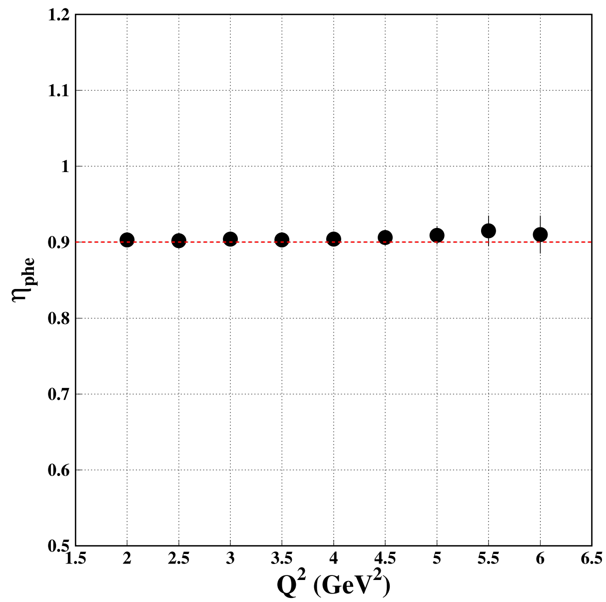

FIG. 4.49: The electron rejection factor due to the CC photo-electron cut plotted as a function of Q^2.

fraction cuts were $E_{total}/p > 0.22$ and $E_{inner}/p > 0.08$, where E_{total} and E_{inner} are the EC total energy (sum of energies in the inner and outer layers of the EC) for events with momentum p and the energy in the inner layer of EC, respectively. These cuts were designed to reduce the pion contamination in the electron sample. A 2% systematic error was obtained by varying these cuts by 50% and computing the RMS variations in the final data. The electron detection efficiency after the CC cut is almost independent of Q^2 as shown in Figure 4.49 and has a value of $\approx 90\%$. The data was multiplied by a factor of 1.111 to account for this inefficiency. A 1% systematic uncertainty was associated with this correction factor to account for the observed deviation of the cut efficiency from sector to sector. The electron rejection factor due to sampling fraction cut (EC cut) was estimated to be 5% and accordingly a correction factor of 1.05 was included in the data as well. A 2% systematic error was assigned to this factor due to uncertainty about the source of the deviation of efficiency of this cut in data and simulation. Despite the EC cut and an increased CC threshold we still have pion contamination in the electron sample used in our analysis. The π^- contamination of the electron sample was estimated to be small (see Figure 4.50), in a range from 0.6% to 2.4%. To correct for the pions misidentified as electrons we reduced our yields with a variable correction factor that ranged from 0.943 to 1. This factor is dependent on electron momentum and polar scattering

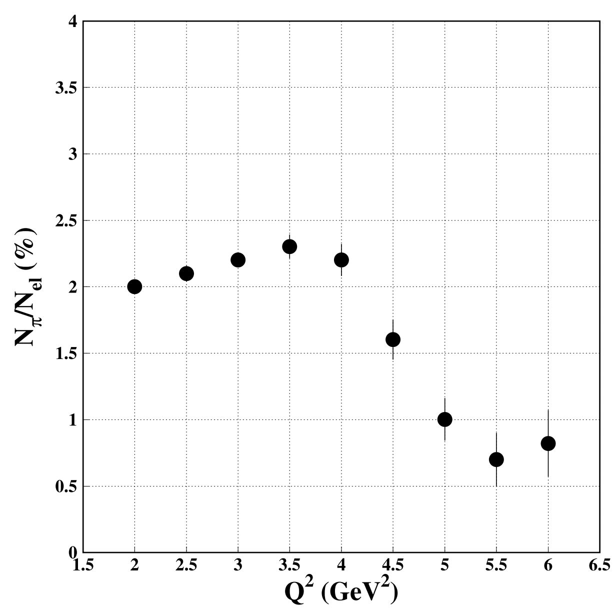

FIG. 4.50: The Q^2 dependence of the π^- contamination of the electron sample selected for this analysis.

angle. To account for electrons produced in e^+/e^- pair-production we reduced our yields by a correction factor ranging from 0.985 to 1. The systematic uncertainties corresponding to these corrections were obtained by varying these factors by 50%, then applying them to the data and observing the resulting changes in the final distributions (cross sections). Figure 2.14 of Section 2.4 shows that our trigger

Type of Cut	Applied to	Cut Boundaries	Purpose
Data Selection	$N_{run} = \frac{N_{el}}{q_{FC}}$	$N_{run} > 2000$ nC^{-1}	reject data with low electron efficiency
Electron Fiducial Cut	ϕ electron distribution	$\Delta\phi < \phi(\theta, p)$	select detector region with high electron detection efficiency
Electron Selection	electron vertex Z_{el}	$-2.0 < Z_{el} < 1.5$ (cm)	reject target walls contributions
Electron ID	energy accum. in EC	$E_{tot}/p > 0.22$ $E_{inner}/p > 0.08$	reduce pion π^- contamination
Electron ID	CC photo-electron spectrum	$N_{phel} > 2.5$ ($p < 3.0$ GeV/c) $N_{phel} > 1.0$ ($p > 3.0$ GeV/c)	reduce pion π^- contamination
Electron ID	momentum distribution	$p > 1.0$ GeV/c	exclude low-energy electrons
Proton Selection	proton vertex Z_{pr}	$-2.5 < Z_{pr} < 2.0$ (cm)	reject target walls contributions
Proton ID	TOF proton time vertex	$-2.0 < \Delta t < 7.0$ (ns)	proton identification
Coincidence Event Selection	vertex difference between electron and proton vertex	$-2.0 < \Delta Z < 2.0$ (cm)	reject accidental coincidences

TABLE 4.7: Cuts applied to the experimental data.

efficiency was $98 \pm 2\%$. A correction factor of 1.02 with 2% uncertainty was taken into account in the overall normalization for trigger inefficiency. A correction factor of 1.014 with 0.7% uncertainty was introduced into the overall normalization to account for the loss of electrons recorded by the reconstruction code (RECSIS) in the secondary position in the event data bank. In our main analysis we selected electrons as the first particle in each event, negatively charged and passing our cuts, neglecting the posibility that a good electron could has been recorded in the second position in our BOS-format events. A data sample containing coincidence events with an electron in the secondary position and a proton which passed all the ID and fiducial cuts. To reject coincidence events originating in the target walls, a cut on the Z component of the electron vertex, $-2. < Z_{el} < 1.5$ cm, proton vertex, $-2.5 < Z_{pr} < 2.$ cm and a cut on the difference between electron vertex and proton vertex, $-2.0 < \Delta Z < 2.0$ cm, were applied to the data. The correction factor to account for the electrons lost due to this cut was estimated to be 1.012 with 0.6% systematic error, computed with the method described above. For proton identification a cut

Type of Correction	Correction Factor	Purpose
EC ID Cut	1.052	correct for the inefficiency of the EC cut
CC ID Cut	1.111	correct for the inefficiency of the CC cut
Trigger Efficiency	1.020	correct for hardware trigger inefficiency
Secondary Electrons	1.014	correct for mistakenly identified electrons
Pion Contamination	$0.943 - 1.000$	correct for pion contamination
e^+/e^- Contamination	$0.985 - 1.$	correct for false electrons introduced from e^+/e^- pair production
Accidental Coincidences	$0.957 - 0.985$	correct for the contribution of accidental coincidences
Coincidences with Knock-out Proton	$0.8 - 1.0$	correct for the contribution of coincidences between an electron and knock-out proton
Difference Vertex Δv Cut Inefficiency	1.012	correct for difference vertex cut inefficiency
Radiative Corrections	$1.000 - 1.242$	correct for events lost due to radiative effects
Sector Tracking Inefficiency	1.098	correct for sector tracking inefficiency

TABLE 4.8: Correction factors applied to the experimental data.

was made on the proton vertex time, defined as the difference between recorded and expected time of flight. A constant normalization factor of 1.01 was introduced to correct for lost events due to this cut. A systematic error of 0.5% was evaluated with the method described earlier and applied to the overall normalization. To correct for the loss of events due to momentum dependence of these cuts we included in overall normalization a factor of 1.012 with 0.75% systematic error. Accidental coincidences

Source of Uncertainties	SystErr Range [%]
EC ID Cut	2
Trigger Efficiency	2
Secondary Electrons	0.7
Electron Vertex ID Cut	0.6
Proton Timing ID Cut	0.5
CC Efficiency	1
Pion Contamination	$0.5-3$
e^+/e^- Contamination	$0.-0.75$
Accidental Coincidences	$0.-\langle 1.2\rangle-4$
Coincidences with Knock-out Proton	$0.-\langle 2.3\rangle-6$
Vertex Difference Cut	$0.75-1.5$
Radiative Corrections	$0.-5$
Tracking Inneficiency	2
Luminosity	3
Bin Migration & Model-Dependence of Acceptance Calc.	$0.-\langle 1.5\rangle-4$
Total	$\langle 6.1\rangle$

TABLE 4.9: Relative systematic errors in percent. The range of the error as well as their average values (in brackets) are given.

were defined as coincidence events with an electron and an accidental proton, defined as a positively charged particle with the time of flight at least 12 ns longer than that expected for a proton of the same momentum (see Eq. 3.17). We subtracted the accidental coincidences from each bin of the final histograms. This subtraction resulted in a variable correction factor between 0.957 and 0.985 with uncertainty up to 3%. The same procedure of varying these factors by 50% and observe the resulting change in the final histograms was used to extract the systematic errors.

Another source of background is a proton originating from two-step proton knock-out from a recoiling deuteron. We subtracted this contribution from the data sample

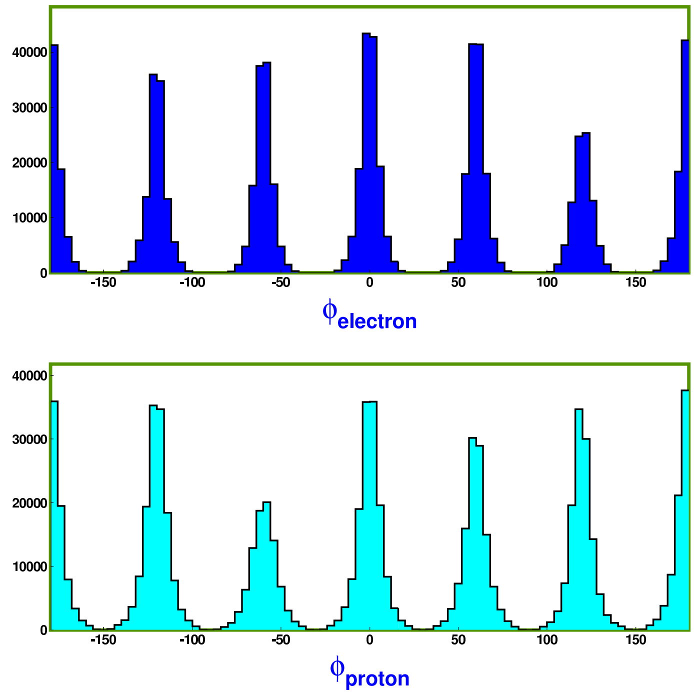

FIG. 4.51: Azimuthal angular distribution for d(e,e$'$p$_s$)n events. The electron azimuthal angular distribution (upper plot) shows a sector inefficiency for Sectors 3, 5, and 6 due to dead DC regions and miscalibrated or malfunctioning TOF scintillators. The corresponding proton azimuthal angular distribution shows an inefficiency for Sectors 2, 3, and 6. An appropriate correction factor was included in the overall normalization of the absolute d(e,e$'$p$_s$) cross sections.

in bin-by-bin basis which is equivalent with a variable correction factor up to 20% with an overall uncertainty of 2.3%. A summary of all the cuts and corrections is shown in Tables 4.7 and 4.8. The systematic errors associated with these cuts and corrections are summarized in Table 4.9.

Systematic errors associated with model-dependence of acceptance calculations and the bin migration are shown in the Table 4.5 for $Q^2 = 2.5, 3.5, 4.5,$ and 5.5 GeV^2, and $p_s = 0.25 - 1$ GeV/c. A correction related to sector-by-sector tracking inefficiency was also applied to the data. As seen from Figure 4.51 each sector's tracking efficiency is different. This effect is due to dead wires in the DC and miscalibrated or malfunctioning scintillators in the TOF system. We see that Sector 6 is the least efficient for proton detection, followed by Sector 2 and 3. Sectors 3, 5, and 6 are the least efficient for detecting electrons. We used the average number of events detected in the best three sectors as the measure to normalize the actual total number of events detected in CLAS. The correction due to sector tracking inefficiency is:

$$\mu_{sect} = \frac{\sum_{i=1}^{6} N_{Si}}{2 * (N_{S1} + N_{S4} + N_{S5})}, \tag{4.26}$$

where N_{Si} is the number of events detected within the boundaries of Sector i. We estimated that the correction due to the sector inefficiency is about 10%. The systematic error associated with this normalization factor is 2%.

CHAPTER 5

Results and Discussion

5.1 Inclusive d(e,e′) Absolute Cross Sections

We extracted absolute cross sections for the inclusive d(e,e') process in 2-dimensional kinematic bins with Q^2 from 1.7 to 6.7 GeV^2 and Bjorken scaling variable x from 0.7 to 1.9. The bin size for Q^2 was 0.05 GeV^2 which is comparable with the CLAS resolution, and the bin size for x is 0.02. Results are presented in Figs. 5.3 – 5.7 and tabulated in Appendix C. The cross sections are plotted versus x and each histogram corresponds to a different Q^2 bin. The solid bullets represent the absolute differential inclusive cross sections corrected for acceptance and radiative effects (as described in Sections 4.2.2 and 4.3.4). The solid triangles shows the cross sections prior to acceptance and radiative corrections. The solid curves are calculations of the model described in Refs. [85, 86].

Previous studies of inclusive lepton scattering represent a significant source of information about nuclear structure. Although the deep inelastic scattering (DIS) regime, which corresponds to large momentum transfer Q^2 and large missing mass W, is well studied, the intermediate kinematic region corresponding to $Q^2 \approx$ few

GeV^2 and $x > 1$ offers an opportunity to improve our understanding of short-range correlations (SRC) in nuclei. SRCs appear as a consequence of overlapping of nucleonic wave functions in nucleon-nucleon (NN) interactions and they seem to contribute significantly to the high-momentum component of the nuclear wave function. Scattering dominated by SRCs can provide information about deeply bound nucleons. High-energy inclusive electron scattering A(e,e$'$) provides a simple way to investigate SRCs. The main issue that these studies faced was selecting electron-SRC scattering events from a very large (several orders of magnitude) inelastic and/or quasi-elastic background. This problem was solved by selecting the kinematic region $x = \frac{Q^2}{2M_N\nu} > 1$ where contributions from inelastic scattering and meson exchange currents (at high Q^2) were significantly reduced. Theoretical predictions from Refs. [90, 91] suggested that at momenta higher than the Fermi momentum P_F, nucleon momentum distributions in light and heavier nuclei are similar. Based on these predictions a new technique was suggested by the authors of Refs. [92, 93] that the ratios of A(e,e$'$) cross sections for different nuclei, normalized by A, should scale, i.e., they should be independent of electron scattering variables, Q^2 and x. Due to the dominance of SRCs in the high momentum component of the nuclear wave function and the assumption that the shape of the distribution is universal, it was suggested that the ratio between A+1 and A (i.e. ^{3}He/^{2}D, ^{4}He/^{2}D) cross sections will be proportional to the SRC probability in NN interactions. Previous results from Jlab-Hall C [73, 78] concentrated on using the y scaling variable to deconvolute the nuclear wave function from the inclusive cross section. Although this technique leads to the extraction of momentum distributions in the nucleon, the extraction of SRC probabilities is affected by large uncertainties [94]. Data for deuterium from SLAC [78] and for heavier nuclei [95] were used in Ref. [93] to extract these ratios. The scaling behavior was confirmed at $Q^2 > 1$ GeV^2 and $x > 1.5$. The data sets were collected in different experimental environments, at different kinematics, and a complicated fitting procedure was performed to obtain these ratios at the same values of (Q^2, x). Since the cross sections varied strongly with angle, incident energy and Q^2, a simplification of this interpolations was performed by the authors [93]. They divided the experimental deuterium cross section by the theoretical calculation within the impulse approximation. This procedure may have affected the final extracted ratios. More recently analyses on the scaling

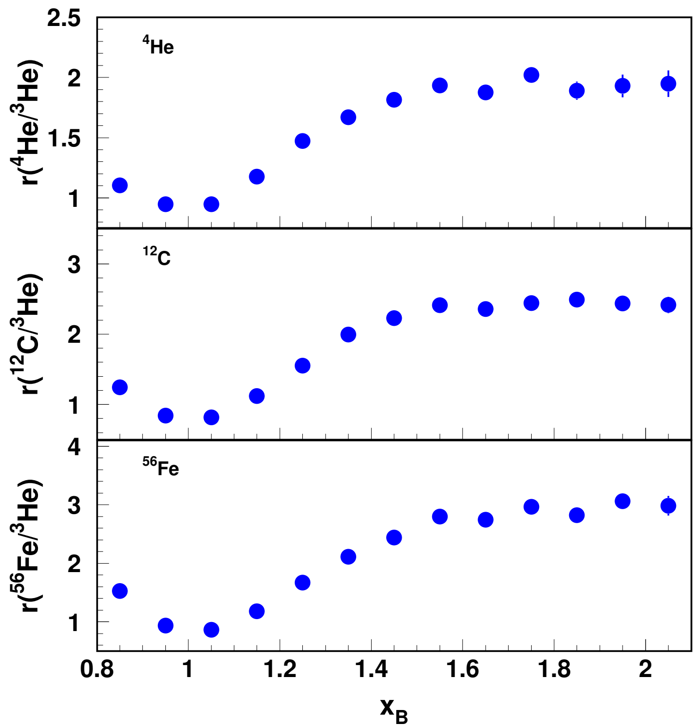

FIG. 5.1: Cross section ratios of ^{4}He (upper panel), ^{12}C (middle panel) and ^{56}Fe (lower panel) to ^{3}He as a function of x_B for $Q^2 > 1.4$ GeV^2. The scaling region ($x > 1.5$ were used to calculate the per-nucleon probabilities for 2-nucleon SRCs in nucleus A relative to ^{3}He. The plot is from Ref. [96].

behavior of these ratios and extraction of 2-nucleon and 3-nucleon SRC probabilities in nuclei were performed using CLAS data from Jlab, at 4.5 GeV beam energy (see Refs. [94, 96]). They extracted ratios of ^{4}He, ^{12}C, and ^{56}Fe to ^{3}He cross sections per nucleon (as shown in Fig. 5.1), for $1 < x < 2.$ and $Q^2 > 0.65$ GeV^2. Using the scaling behavior of these ratios, they extracted the relative probability of nucleon-nucleon SRCs in various nuclei. The inclusive deuterium data presented here were collected under the same conditions using the same detector, except a higher beam energy. The inclusive d(e,e$'$) absolute cross sections from this experiment (E94-019) can now be used instead of ^{3}He as the normalization in extracting SRC probabilities for ^{4}He, ^{12}C, and ^{56}Fe.

A parallel analysis presented in Ref. [97], which also extracted inclusive cross sections from the E6 data is in excellent agreement with our results. A point-by-point comparison of the two analyses shows an agreement within 10% with an average deviation of 4.5% for all kinematics. The two sets differ in event selection, acceptance calculations (different model simulations), radiative corrections, and binning. Figure 5.2 shows the cross section ratios for the two analyses as a function of Q^2. The weighted average of all point is 1.0 ± 0.013 indicating that the two analyses are consistent.

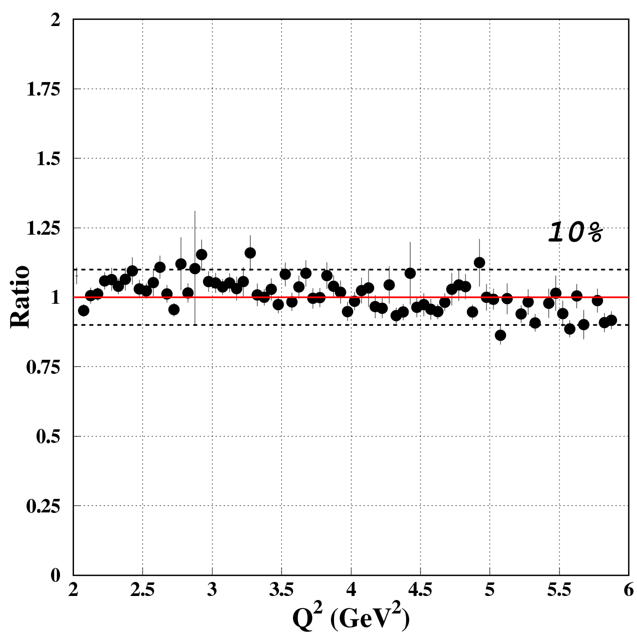

FIG. 5.2: Ratio of cross sections from Ref. [97] and cross sections extracted in this analysis as a function of Q^2.

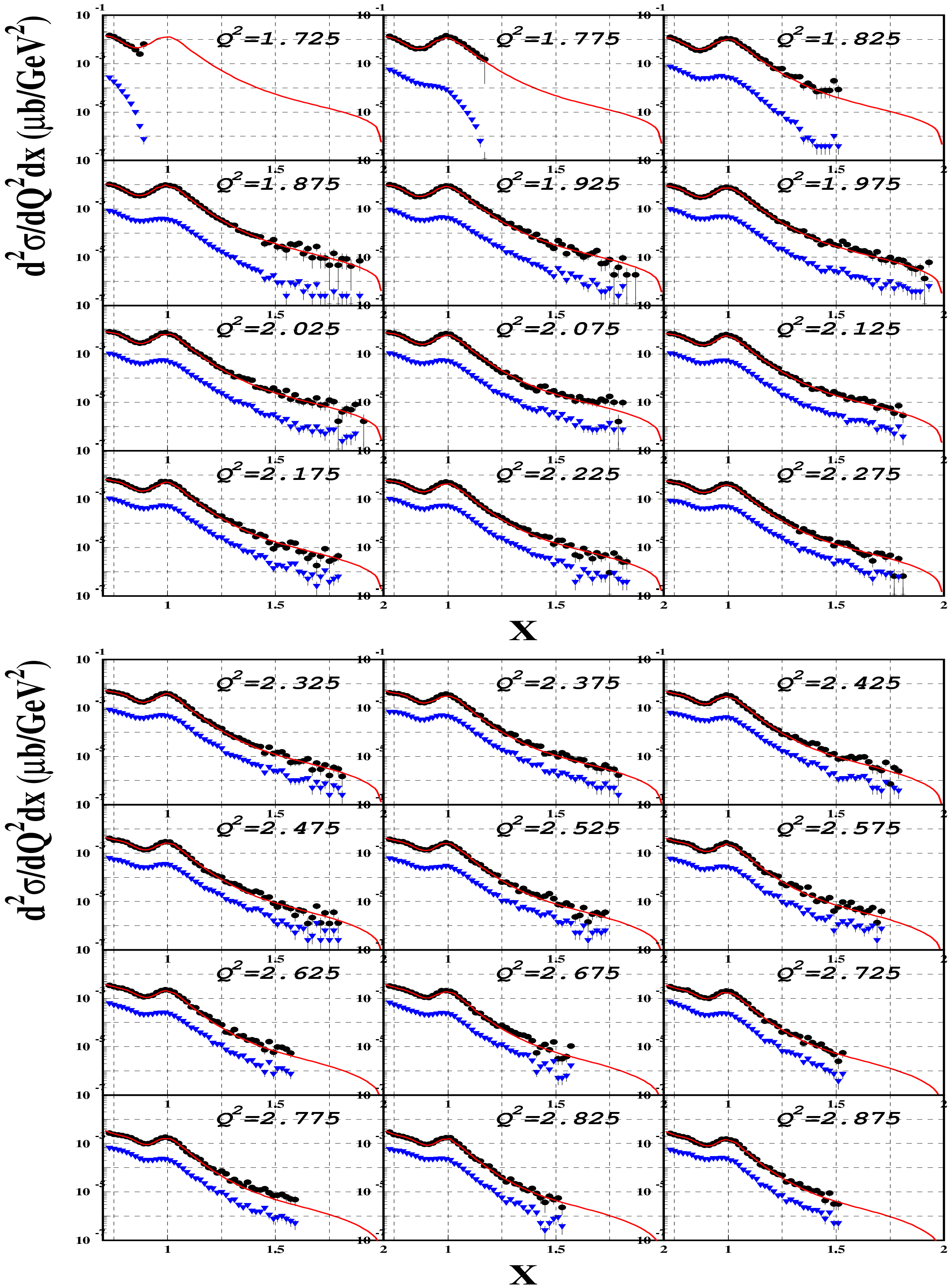

FIG. 5.3: Differential d(e,e′) cross sections $\frac{d\sigma}{dQ^2dx}$ versus x for $\mathrm{Q}^2 = 1.75 - 2.9$ GeV^2 before (triangles) and after (circles) acceptance and radiative corrections. The solid line is the model of Ref. [81].

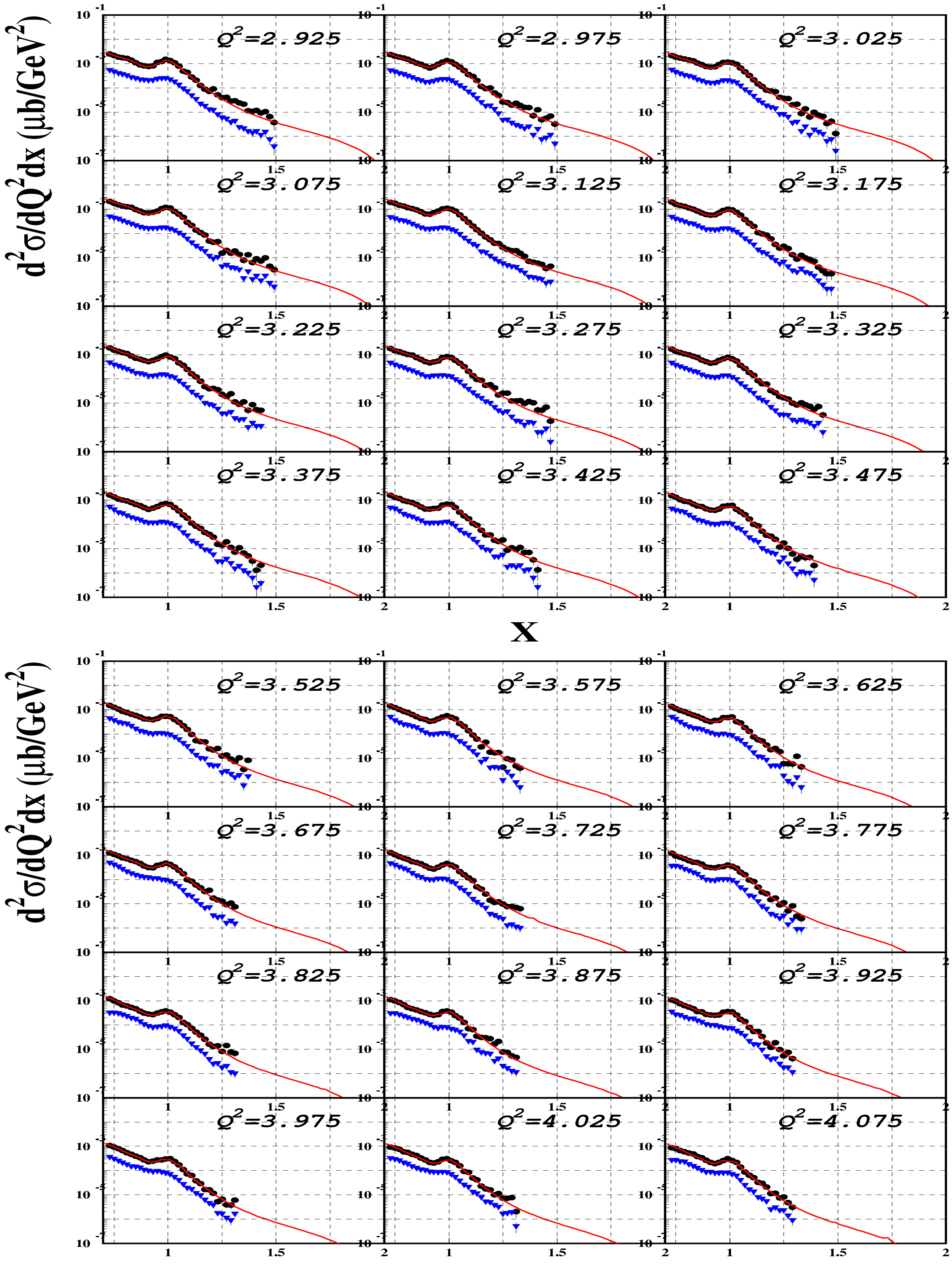

FIG. 5.4: Same as in Fig. 5.3 except for $Q^2 = 2.9 - 4.1$ GeV^2.

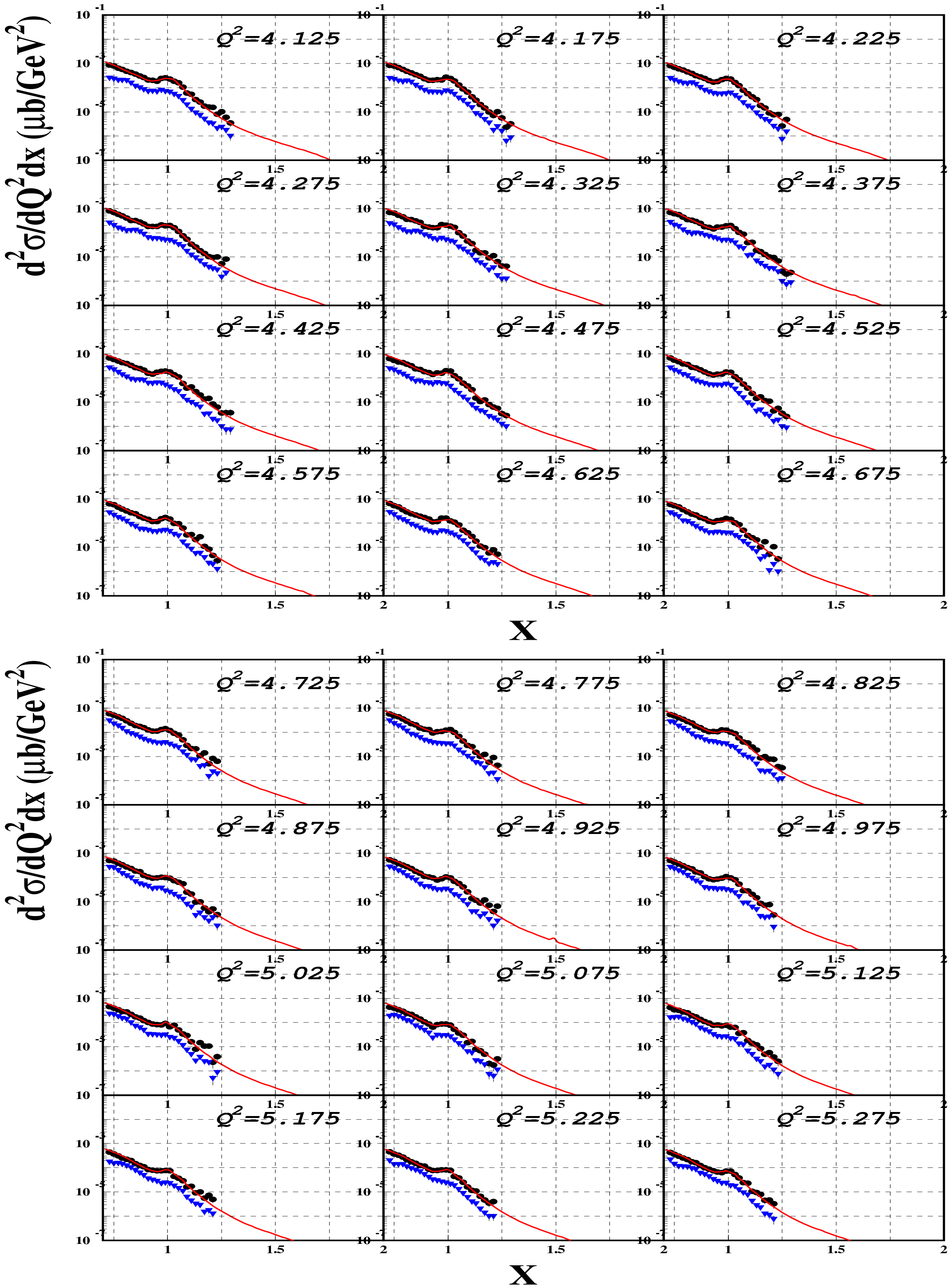

FIG. 5.5: Same as in Fig. 5.3 except for for $Q^2 = 4.1 - 5.3$ GeV^2.

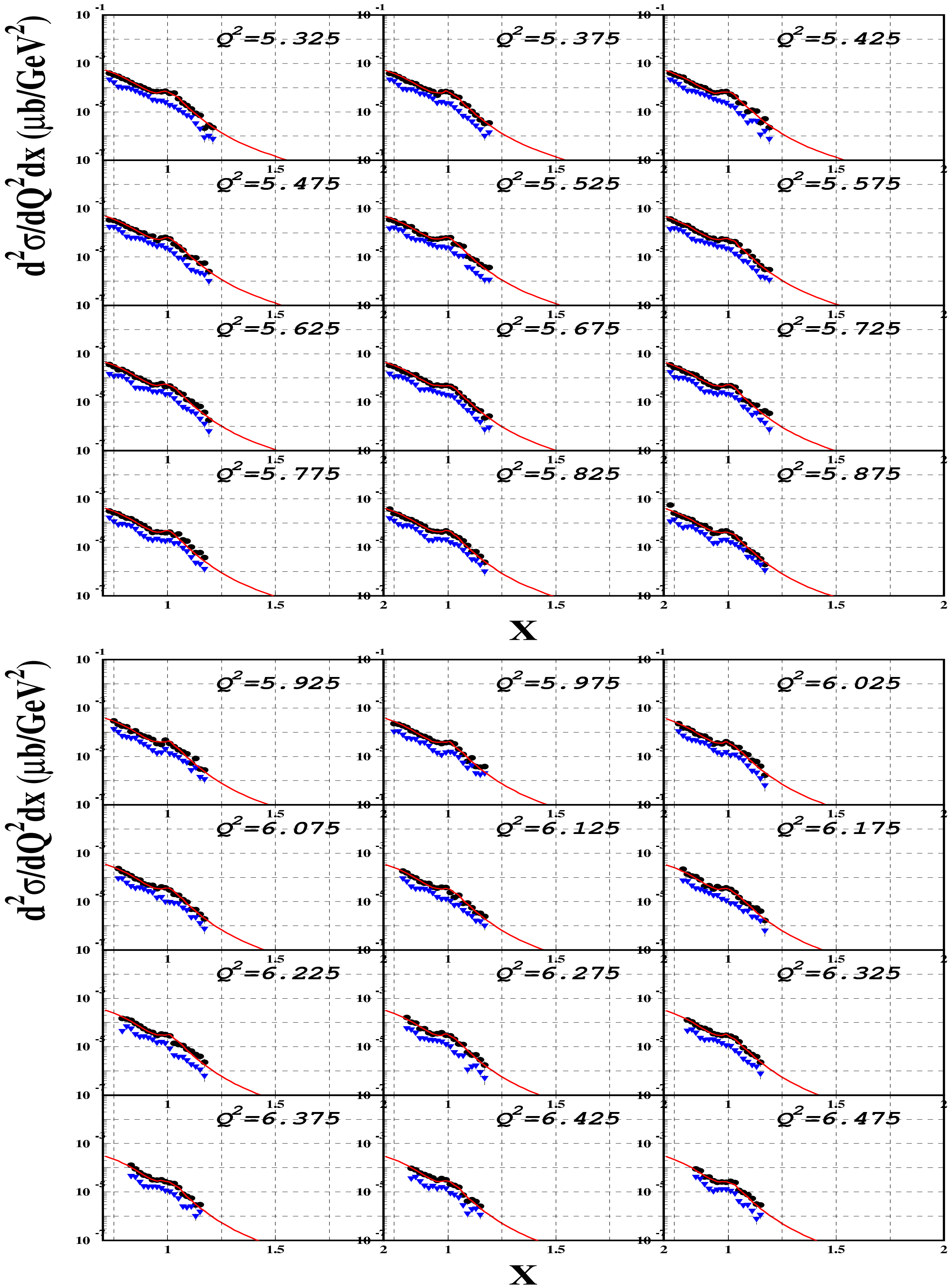

FIG. 5.6: Same as in Fig. 5.3 except for for $Q^2 = 5.3 - 6.5$ GeV^2.

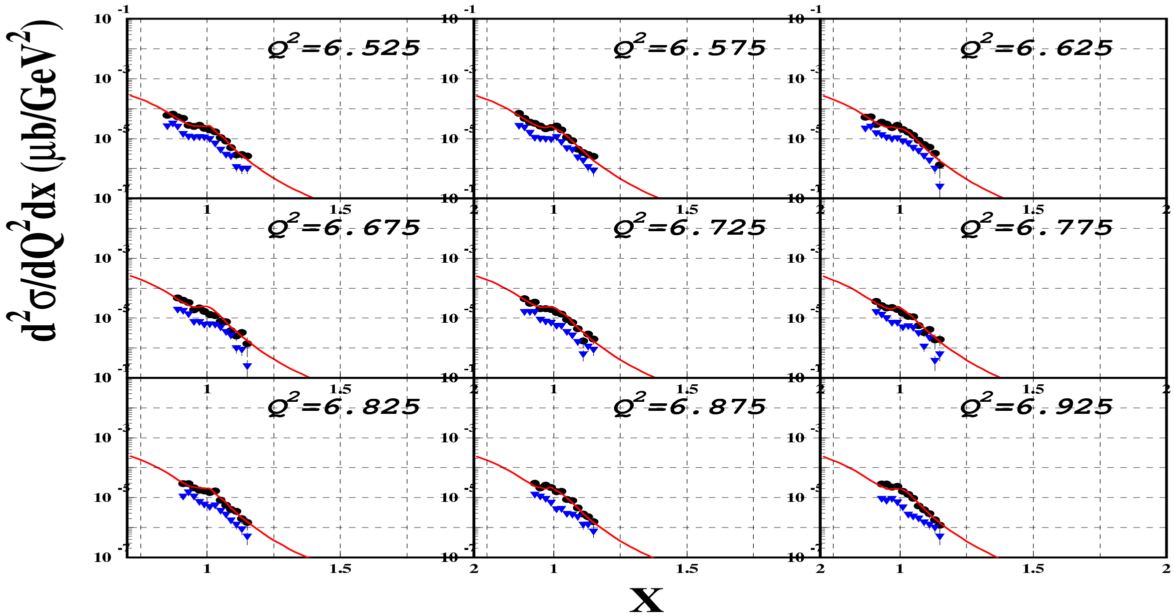

FIG. 5.7: Same as in Fig. 5.3 except for $Q^2 = 6.5 - 6.95$ GeV^2.

5.2 Exclusive d(e,e′p)n Absolute Cross Sections

We extracted cross sections for the quasi-elastic exclusive d(e,e′p)n reaction for spectator proton momenta $p_s = 250-1000$ MeV/c and $Q^2 = 2-6$ GeV^2. We present the data in several sets of one-dimensional histograms. The first set in Fig. 5.8 shows the cross section integrated over the full range of θ_{pq} (0°–180°), ϕ_{pq} (0°–360°) and x(0–2) plotted as a function of p_s (circles) for $Q^2 = 2.5, 3.5, 4.5,$ and 5.5 GeV^2. The second set in Figure 5.9 shows the cross section integrated over the full range of ϕ_{pq} and x, and $p_s = 0.250 - 1.0$ GeV/c as a function of θ_{pq} for the same Q^2 bins as in Fig. 5.8. The third set of histograms (Figure 5.10) shows cross sections as a function of x. The error bars for each data point are statistical only. The systematic errors are represented by the solid band at the bottom of each panel. Each experimental cross section is plotted with the theoretical calculations of Ref. [29]. Solid curves correspond to full calculations of the d(e,e′p)n scattering cross section including the plane-wave impulse approximation (PWIA), meson exchange (MEC), Δ-isobar currents (IC) and FSIs (PWIA+MEC+IC+FSI). Dot-dashed curves correspond to PWIA, and dashed curves include only the final state interactions (PWIA+FSI). Differential d(e,e′p_S)n cross sections $d^3\sigma/dQ^2dp_sd\theta_{pq}$ versus θ_{pq} for $Q^2 = 2.5, 3.5, 4.5,$ and 5.5 GeV^2 and $p_s = 375, 625,$ and 875 MeV/c are shown in Figs. 5.11 – 5.14. Differential cross section $d^3\sigma/dQ^2dp_sdx$ as a function of x for the same kinematic bins are shown in Figs. 5.15 – 5.18. Figs. 5.19 – 5.25 shows differential cross sections $d^3\sigma/dQ^2dxdp_s$ plotted versus proton momentum p_s for $Q^2 = 2.5, 3.5, 4.5,$ and 5.5 GeV^2) and $x = 0.4, 0.6, 0.8, 1, 1.2, 1.4,$ and 1.6. Figs. 5.26 – 5.32 shows differential cross sections $d^3\sigma/dQ^2dxd\theta_{pq}$ as a function of θ_{pq} for $Q^2 = 2.5, 3.5, 4.5$ and 5.5 GeV^2 and $x = 0.4, 0.6, 0.8, 1, 1.2, 1.4$ and 1.6.

All of the above cross sections as well as the calculations of Ref [29] are only within E6 fiducial cuts whereas the cross sections presented in Appendix D are integrated over all phase space and $p_s = [0.250 - 1] GeV/c$.

The model from Ref. [29] (see Section 1.2.7) predicts a large contribution of Δ-isobar currents to the d(e,e′p)n reaction in the low Q^2 and low spectator momentum region. This means that we have a fairly large probability for Δ-isobars to propagate on-shell after being produced on one nucleon (by exchanging a virtual photon with high momentum transfer) and having a further interaction (exchanging π and ρ mesons) with the second nucleon through the $\Delta N \rightarrow NN$ channel. There are two kinematic regions for d(e,e′p)n reaction, one in which a low momentum spectator proton recoils at large scattering angles while the fast moving neutron is emitted forward, and the other in which the fast moving struck proton is emerging in the forward direction with a spectator neutron recoiling at larger angles. Here we discuss only the first case, while the second case is the subject of another analysis done by the Yerevan Group [98]. In the calculations from Ref. [29] Δ formation and MEC amplitudes takes into account both ϕ and ρ exchanges. Early predictions [18] supported the strong suppression of MEC and Δ-isobar currents (IC) with increasing Q^2. However, the contributions of initial state interactions (π, ρ, Δ) seem to decrease with increasing Q^2 (as shown in Figs. 5.8 – 5.10) and are comparable in size to the final state interactions. The formation of a Δ-isobar strongly competes with the re-scattering (i.e. FSI) between an on-shell proton and on-shell neutron. These calculations are supported by the experimental results of this analysis to a level of 10 to 15 %. As shown in Fig. 5.9 the proton momentum is almost perpendicular ($\theta_{pq} \approx 70°$) to the momentum transfer direction. At high values of the recoil proton momentum (p_s = 500 MeV/c) the quasi-free contribution (PWIA) strongly decreases as the on-shell rescattering (MEC+FSI) takes over and dominates as shown in Figs. 5.19 – 5.25. At $\theta_{pq} \approx 70°$ the on-shell rescattering (ΔN or NN) is maximized. At low recoil momentum (p_s = 200 MeV/c) theoretical predictions [29] (see Fig.1.14) show a depletion due to on-shell nucleon rescattering that reduces the quasi-free contribution from unitarity (part of quasi-elastic channel is tranferred into inelastic ones). Due to geometrical acceptance of CLAS and due to kinematic restrictions imposed by the fiducial cuts we were able to detect spectator proton with momentum as low as 250 MeV/c. The experimental results presented here support the physical picture described by the calculations from Ref. [29]. In this picture the electron scatters on a neutron at rest, which propagates on-shell and rescatters on the proton which also is at rest (spectator). In the lab frame, the soft proton recoils at 90° with respect to the fast moving neutron emitted in the forward direction. Two body kinematics requires that the angle of the rescattering peak (or dip in the case of low momentum spectator protons) moves with increasing the spectator (recoil) proton momentum. This picture is supported reasonably well by experimental data. As shown in Figs. 5.11 – 5.14 the proton scattering angle θ_{pq} decreases to lower values with increasing spectator momenta. The competing rescattering effects (MEC, IC, and FSIs) in perpendicular kinematics obstruct our ability to isolate states with small coherent lengths, or electron-SRCs. This suggests that for determining the high momentum components of the deuteron wave function, believed to be dominated by SRCs, quasi-elastic kinematics are not well suited. Figure 1.18 shows the suppresion of on-shell rescattering for parallel or antiparallel kinematics. Although perpendicular kinematics offer a good starting point to study the evolution with Q^2 of the initial and final state nucleon-nucleon interactions in view of determining the structure of superdense matter at short distances, parallel or antiparallel kinematics are better-suited for obtaining a supression of on-shell nucleon rescattering.

We can point out several observations resulting from this study:

- At kinematics chosen here, PWIA is typically 1/3 to 1/2 of the total cross section.

- FSI, MEC and Δ-nucleonic exited states account for the rest of ≈ 50 % of the total cross section.

- Laget's model [29] supports the fact that the Δ-nucleonic excitations, Δ on-shell propagation through the nuclear matter and Δ-decay are major contributors to the d(e,e$'$p)n cross section at small Q^2.

- Sargsian's model [62] supports the idea of suppression of MEC and IC at large Q^2.

All of the above observations mask the actual high momentum distribution of the deuteron which at large p_s should have its origin in SRCs; these are not the right kinematics to observe SRCs. Parallel or antiparallel kinematics may be better suited.

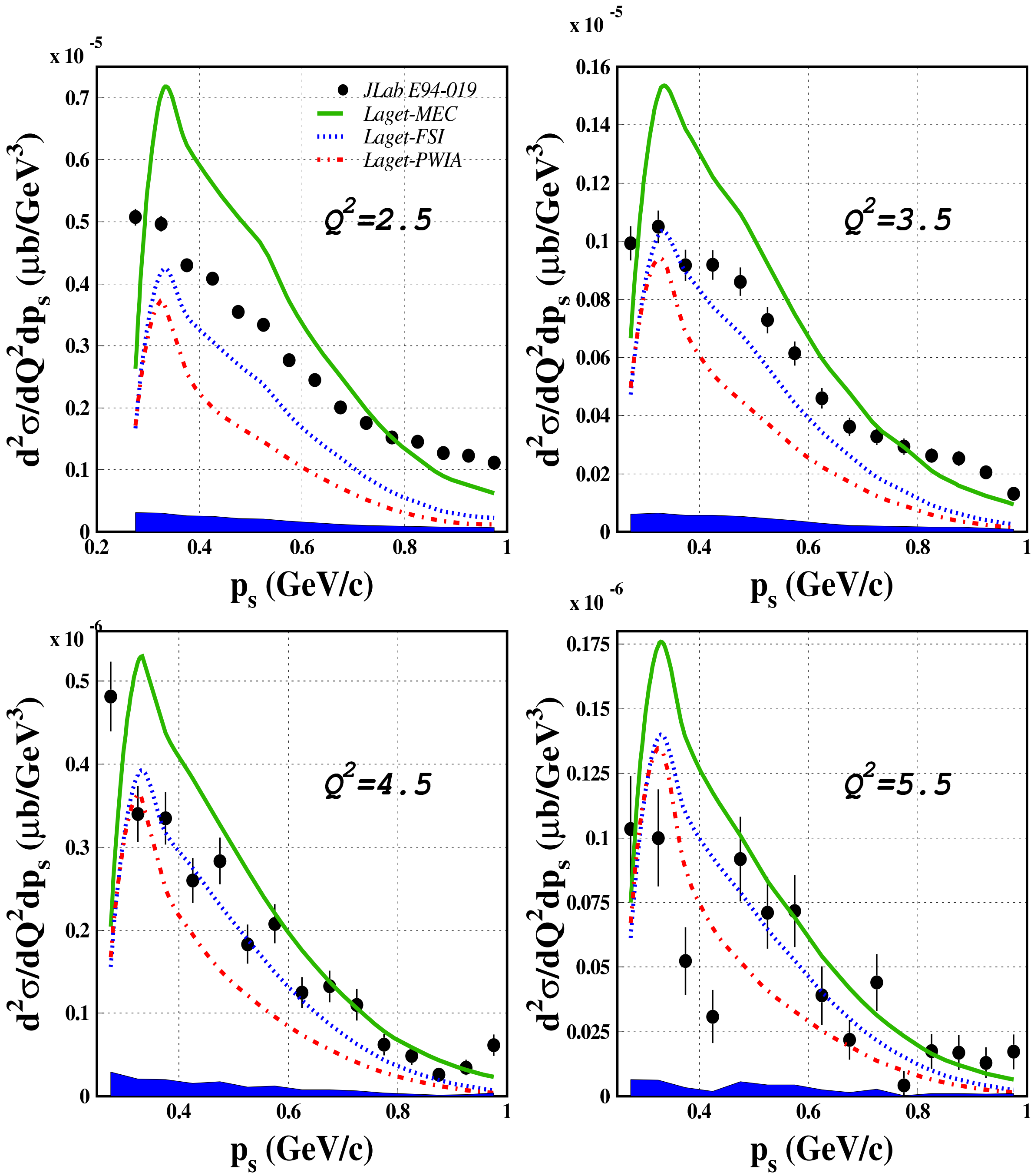

FIG. 5.8: Cross sections within the fiducial CLAS acceptance versus momentum p_s of the scattered proton (circles) for $Q^2 = 2.5, 3.5, 4.5$, and 5.5 GeV^2. The curves correspond to the model from Ref. [29]. Solid curves correspond to the full description of d(e,e′p)n scattering amplitude (PWIA+MEC+IC+FSI). Dot-dashed curves correspond to the PWIA and dashed curves correspond to FSIs only (PWIA+FSI). Systematic errors are represented by the solid area at the bottom of each plot.

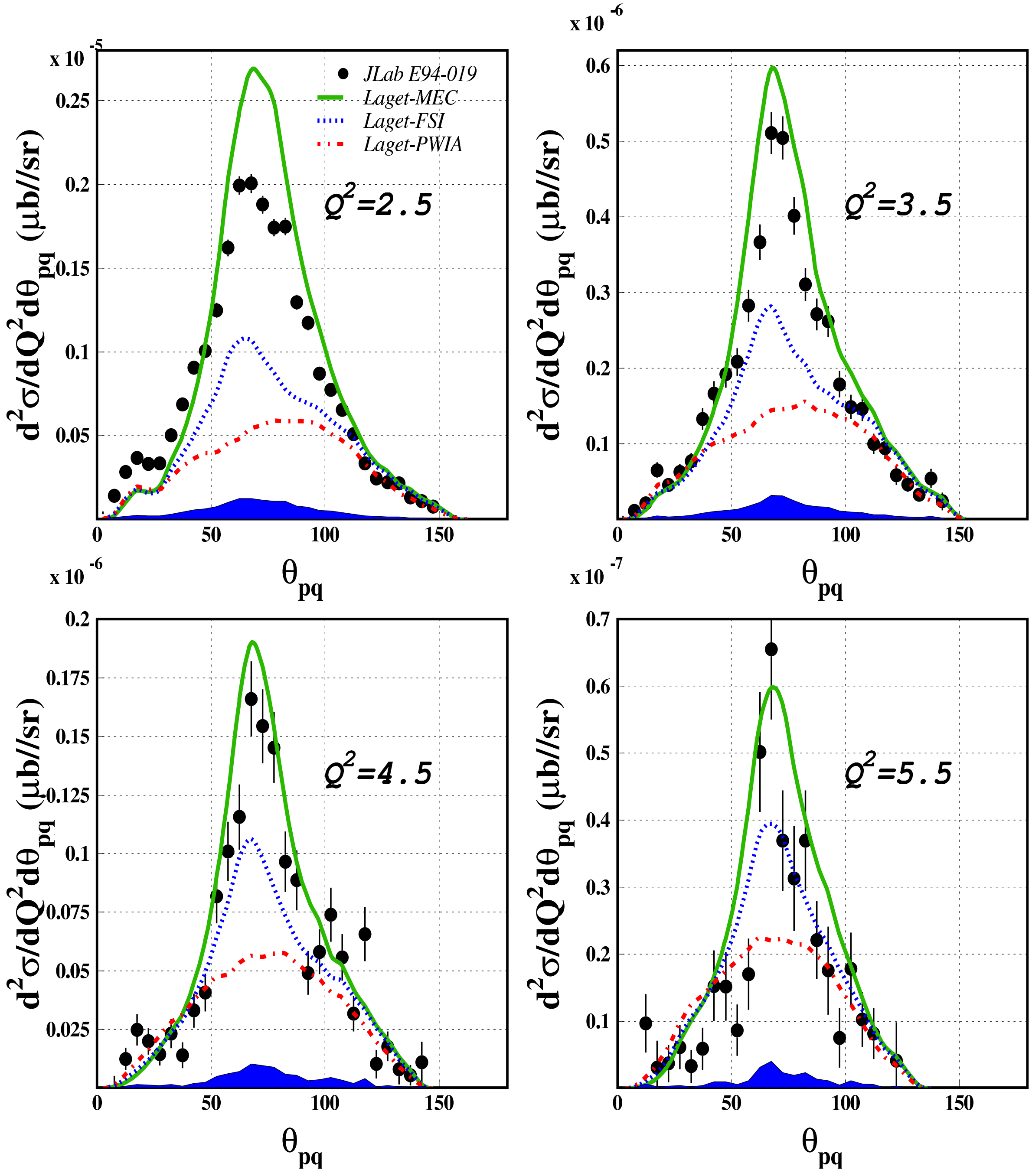

FIG. 5.9: Same as in Fig. 5.8 except with cross sections versus proton scattering angle with respect to the momentum transfer direction θ_{pq}.

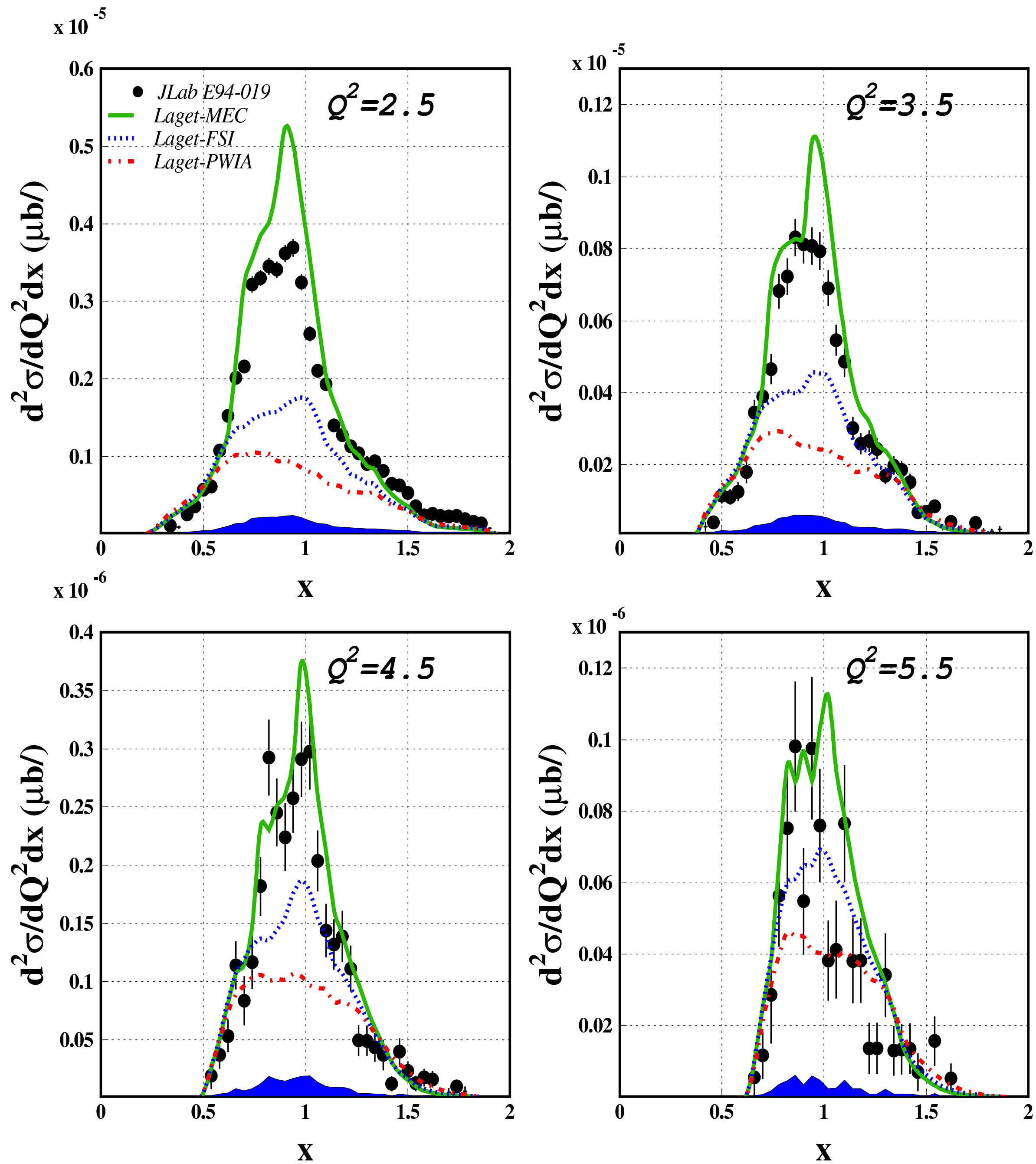

FIG. 5.10: Same as in Fig. 5.8 except with cross sections versus Bjorken scaling variable x.

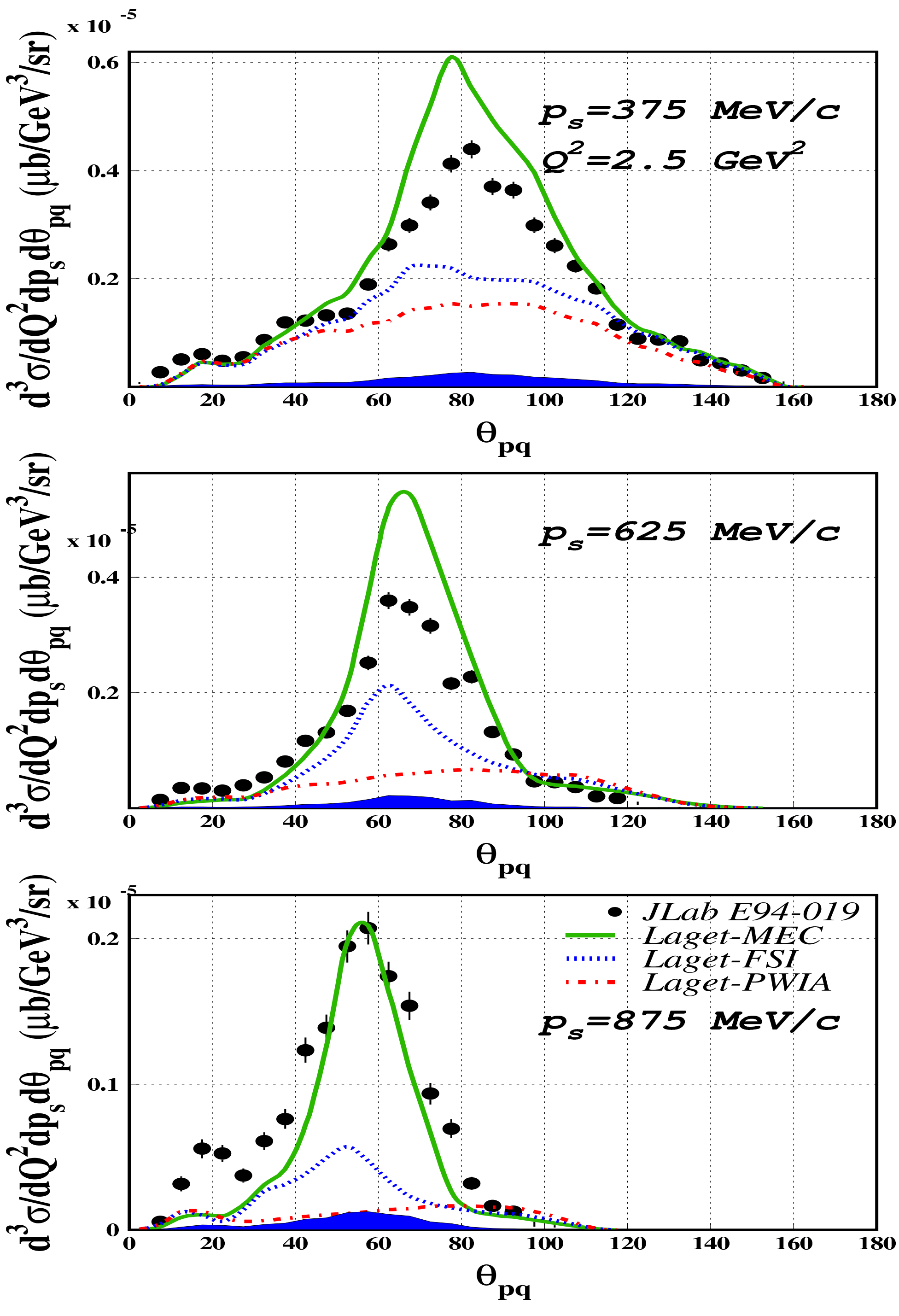

FIG. 5.11: Cross sections (circles) within the fiducial CLAS acceptance versus θ_{pq} for $p_s = 375, 625$, and 875 MeV/c and Q^2 = 2.5 GeV^2. The curves correspond to the model from Ref. [29]. Solid curves correspond to the full description of d(e,e′p)n scattering amplitude (PWIA+MEC+IC+FSI). Dot-dashed curves correspond to the PWIA and dashed curves correspond to FSIs only (PWIA+FSI). Systematic errors are represented by the solid area at the bottom of each plot.

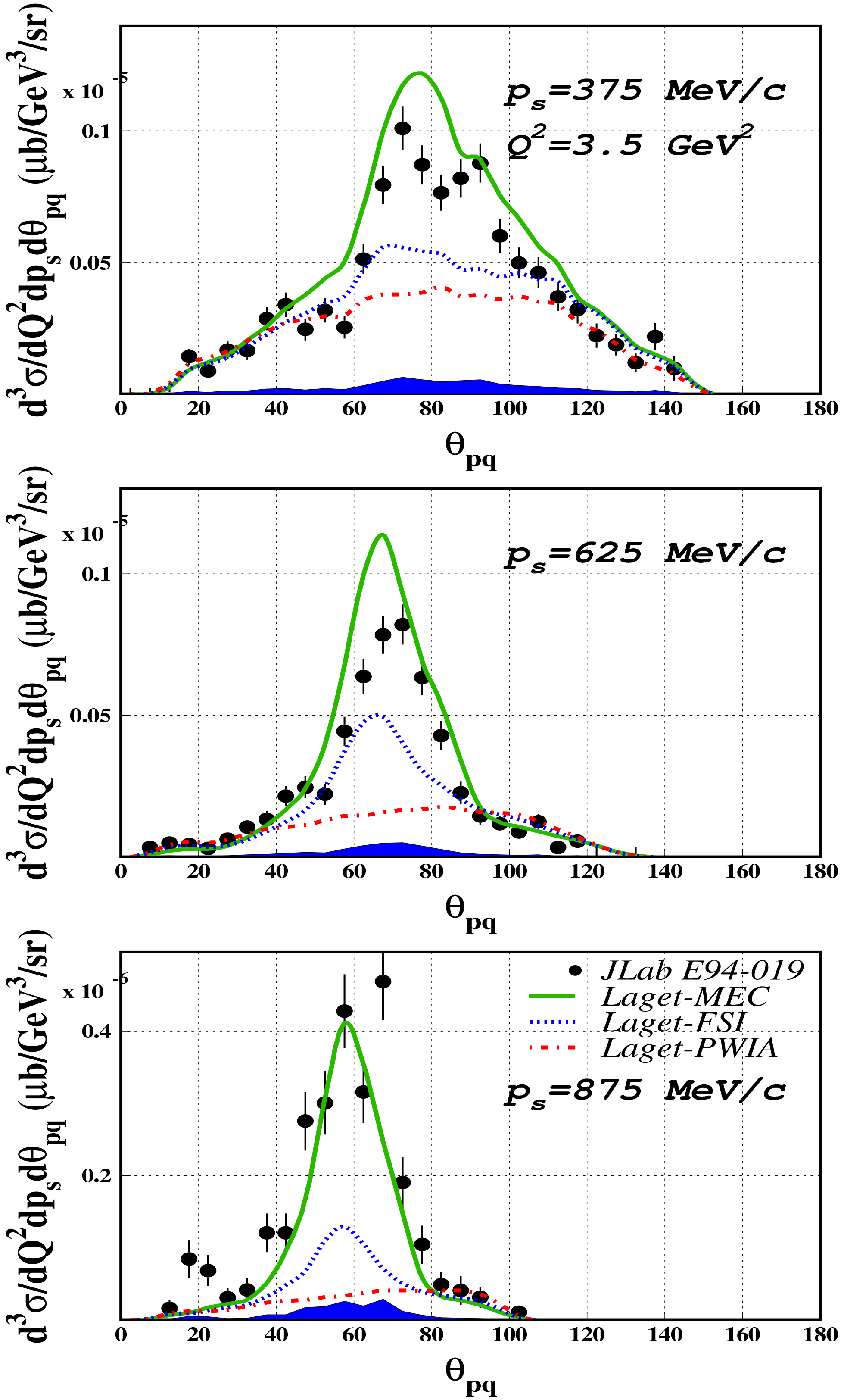

FIG. 5.12: Same as in Fig. 5.11 except for $Q^2 = 3.5$ GeV^2.

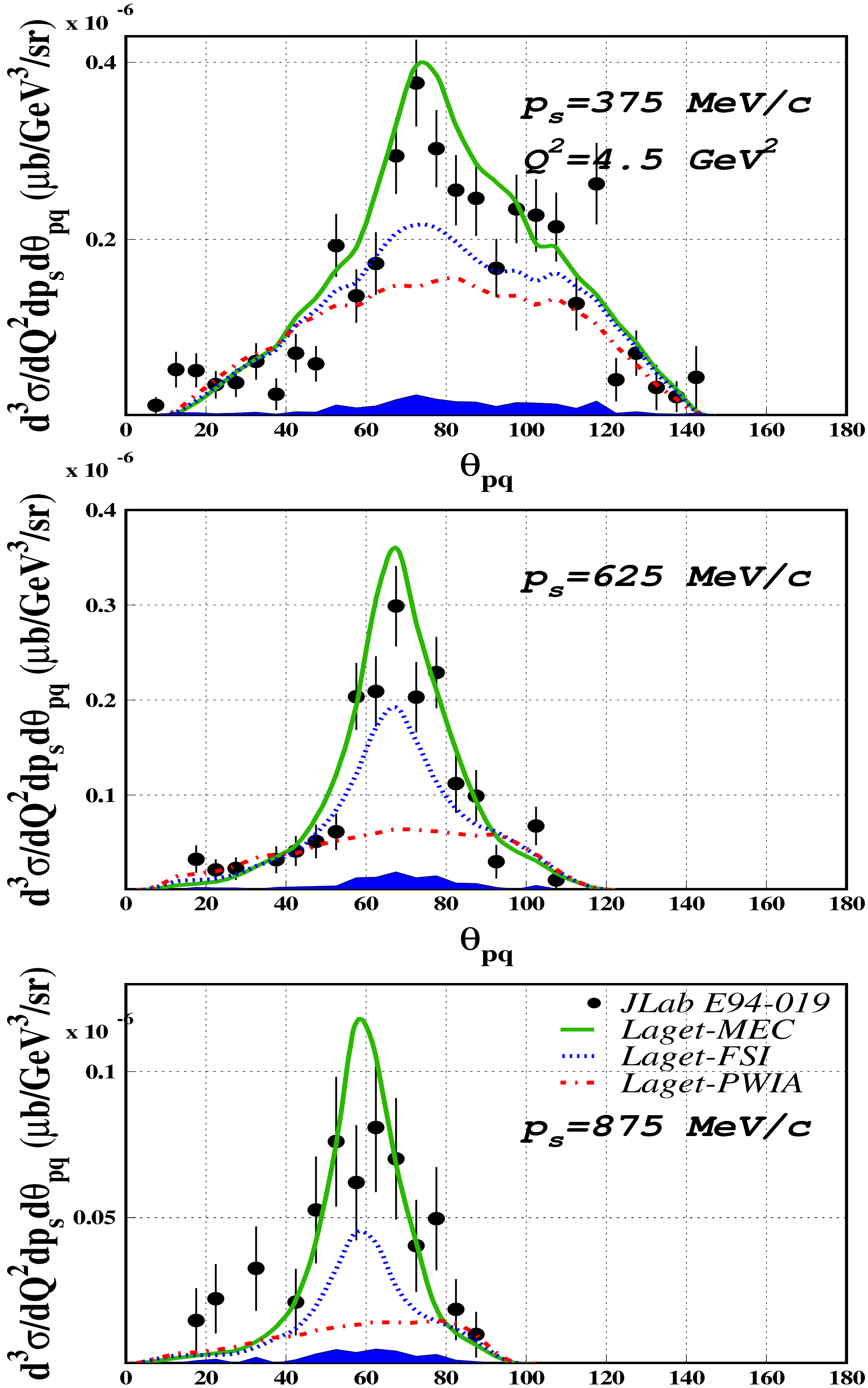

FIG. 5.13: Same as in Fig. 5.11 except for $Q^2 = 4.5$ GeV^2.

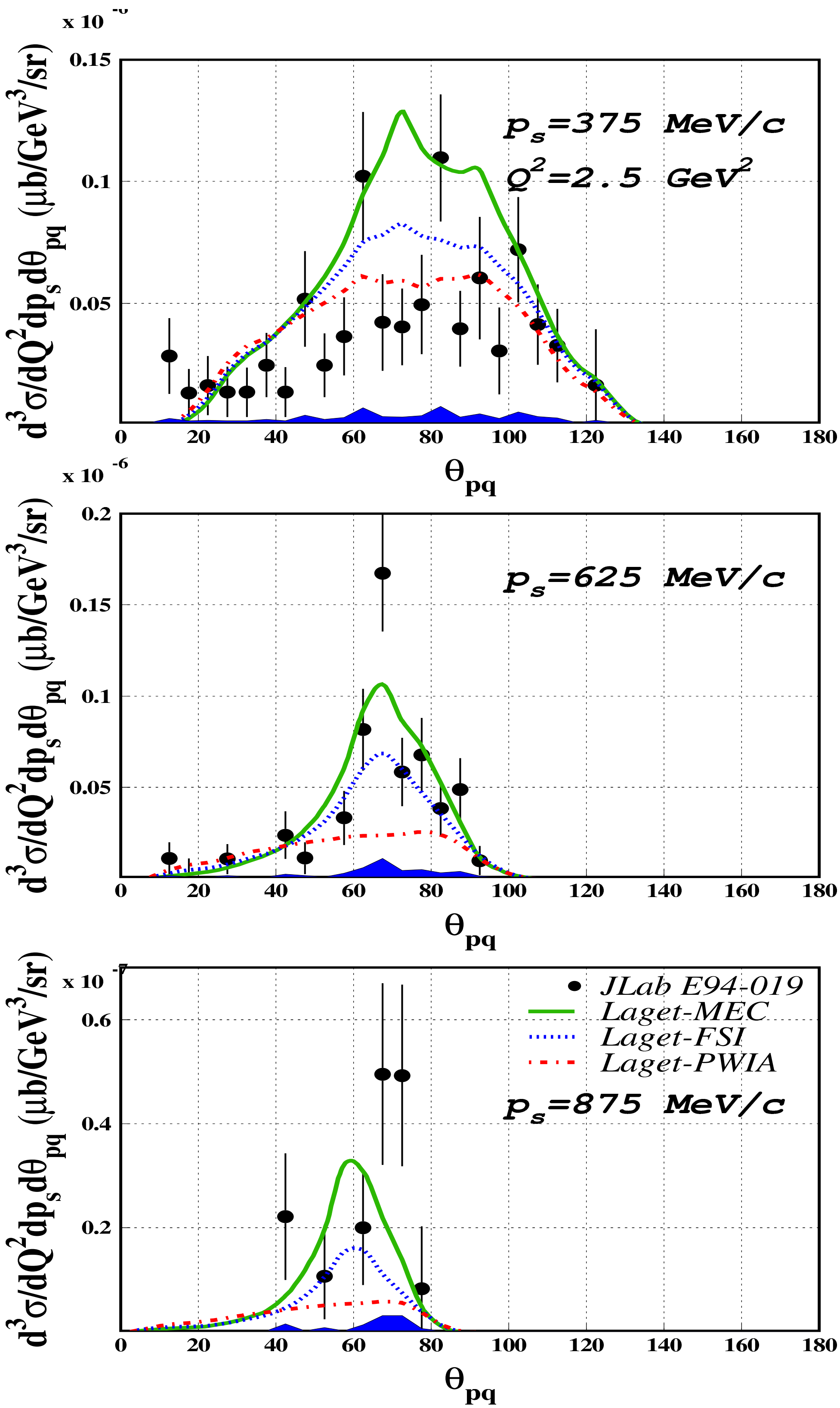

FIG. 5.14: Same as in Fig. 5.11 except for $Q^2 = 5.5$ GeV^2.

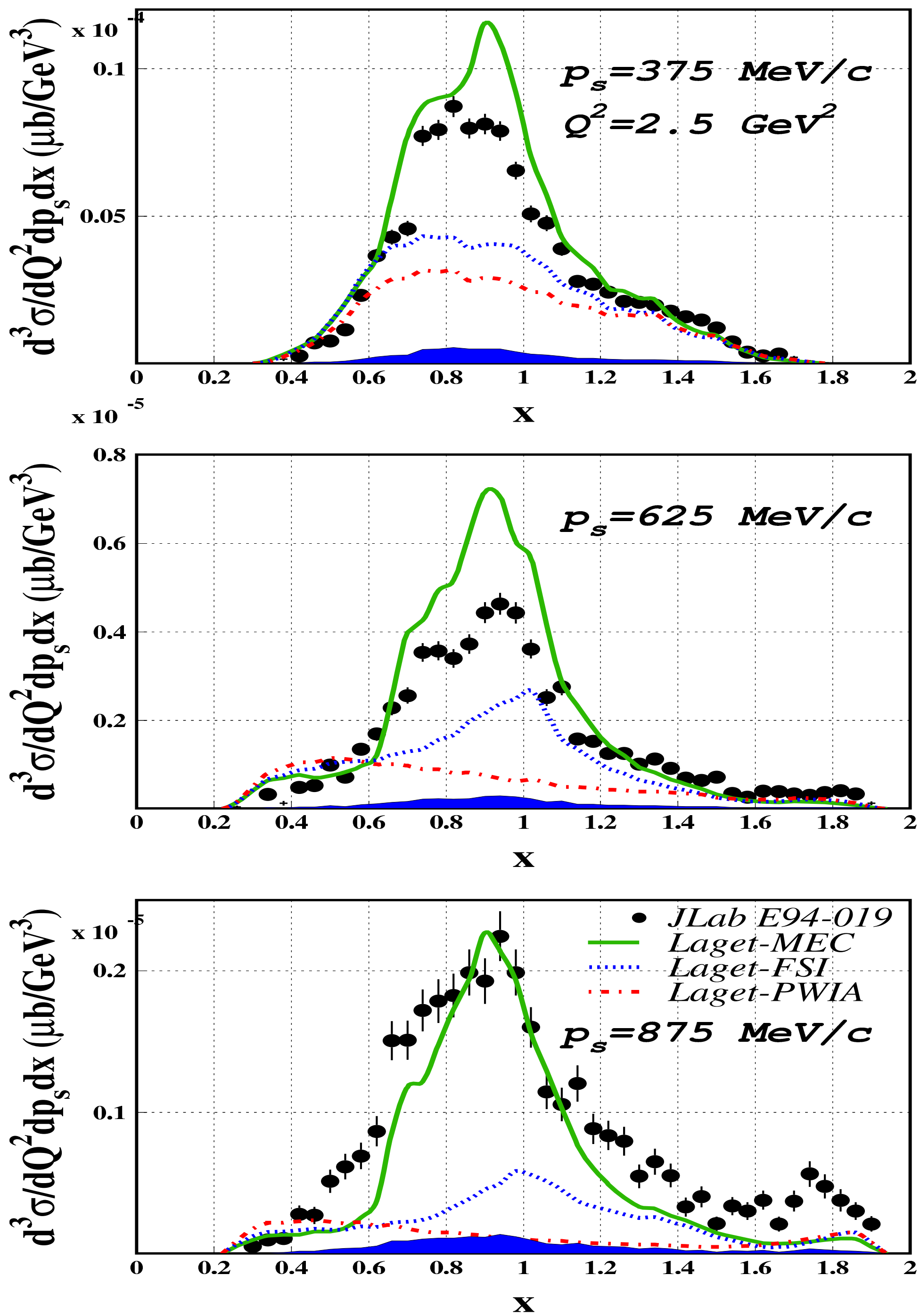

FIG. 5.15: Cross sections (circles) within the fiducial CLAS acceptance versus x for $p_s = 375, 625$, and 875 MeV/c and Q^2 = 2.5 GeV^2. The curves correspond to the model from Ref. [29]. Solid curves correspond to the full description of d(e,e$'$p)n scattering amplitude (PWIA+MEC+IC+FSI). Dot-dashed curves correspond to the PWIA and dashed curves correspond to FSIs only (PWIA+FSI). Systematic errors are represented by the solid area at the bottom of each plot.

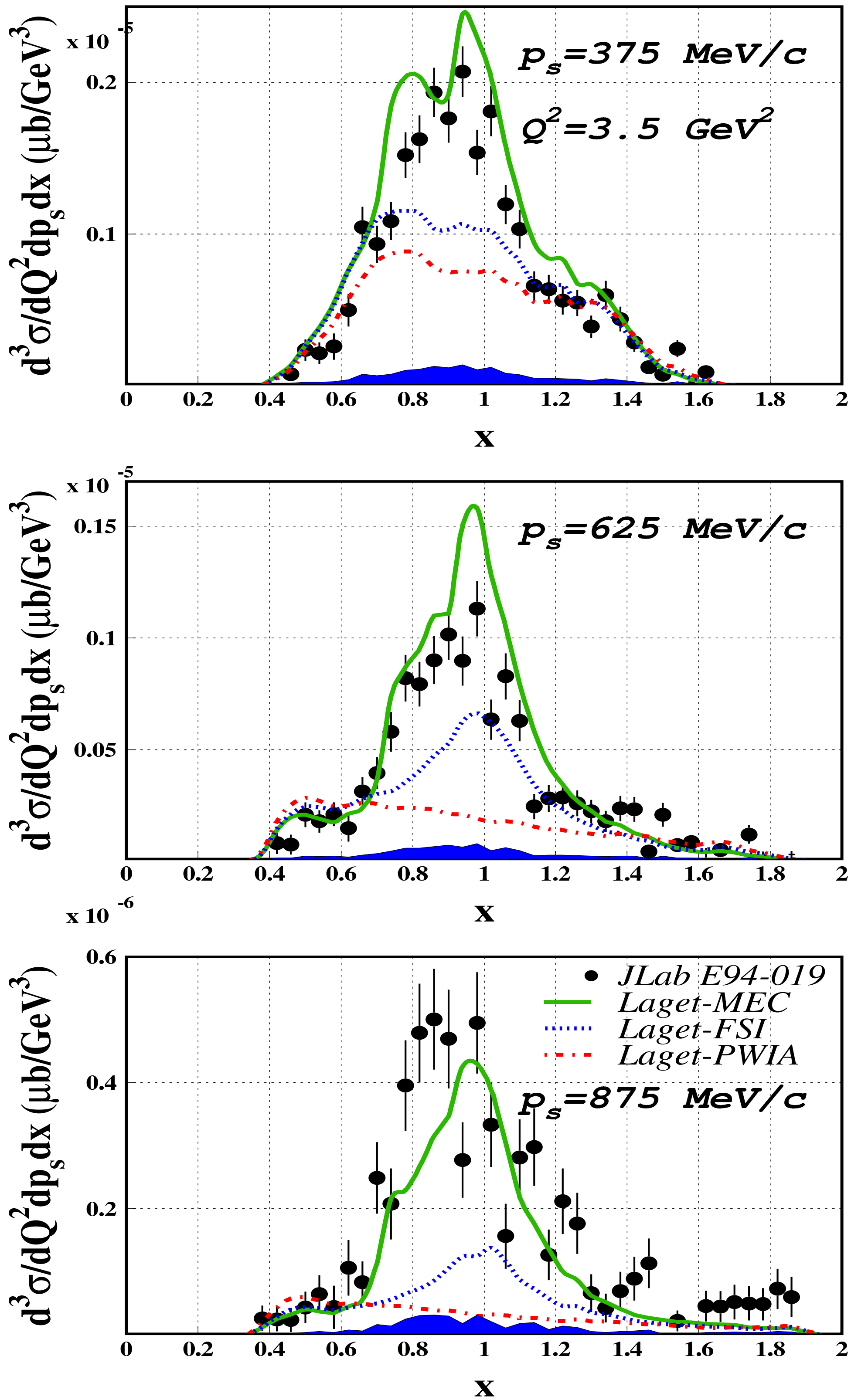

FIG. 5.16: Same as in Fig. 5.15 except for $Q^2 = 3.5$ GeV^2.

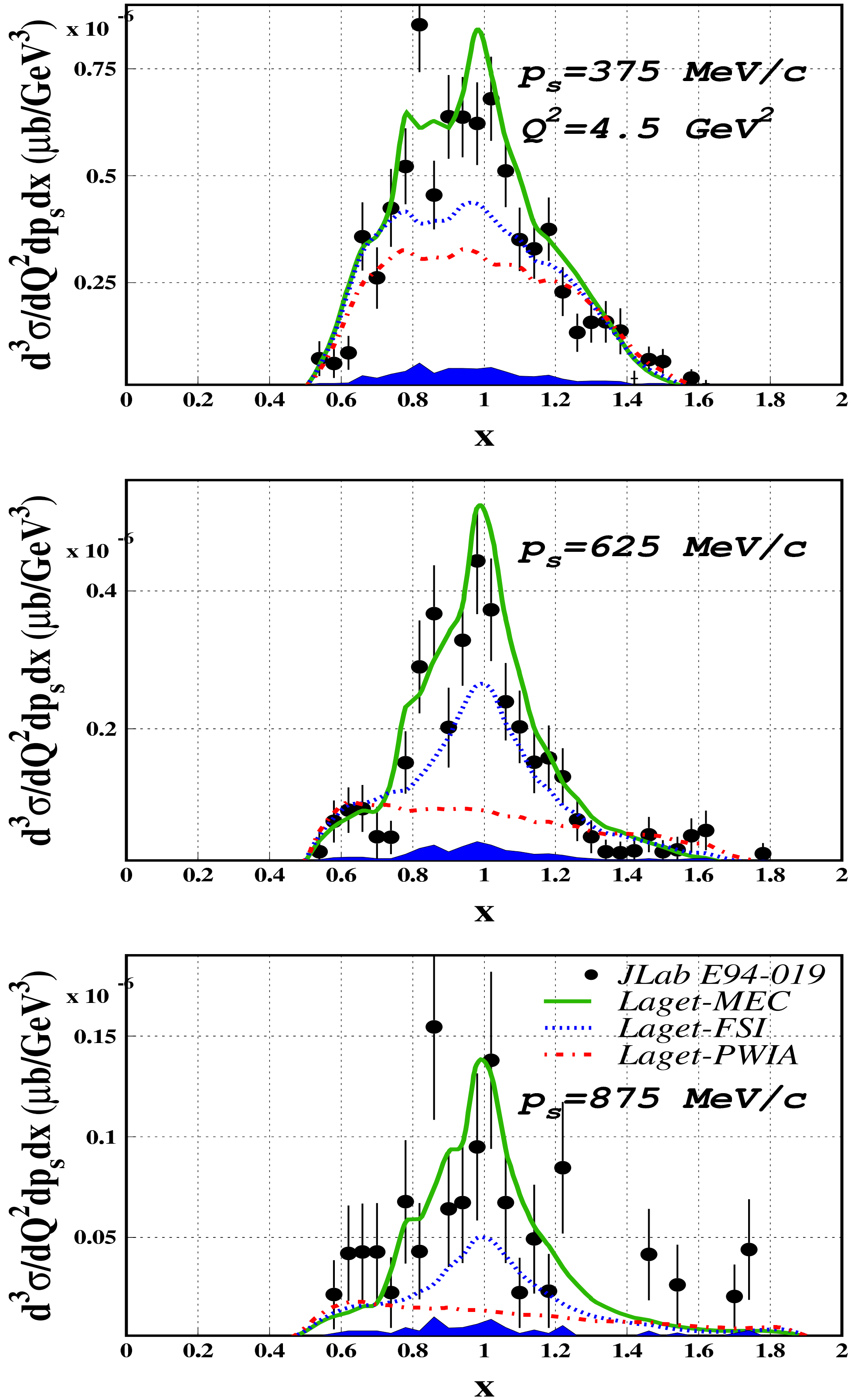

FIG. 5.17: Same as in Fig. 5.15 except for $Q^2 = 4.5$ GeV^2.

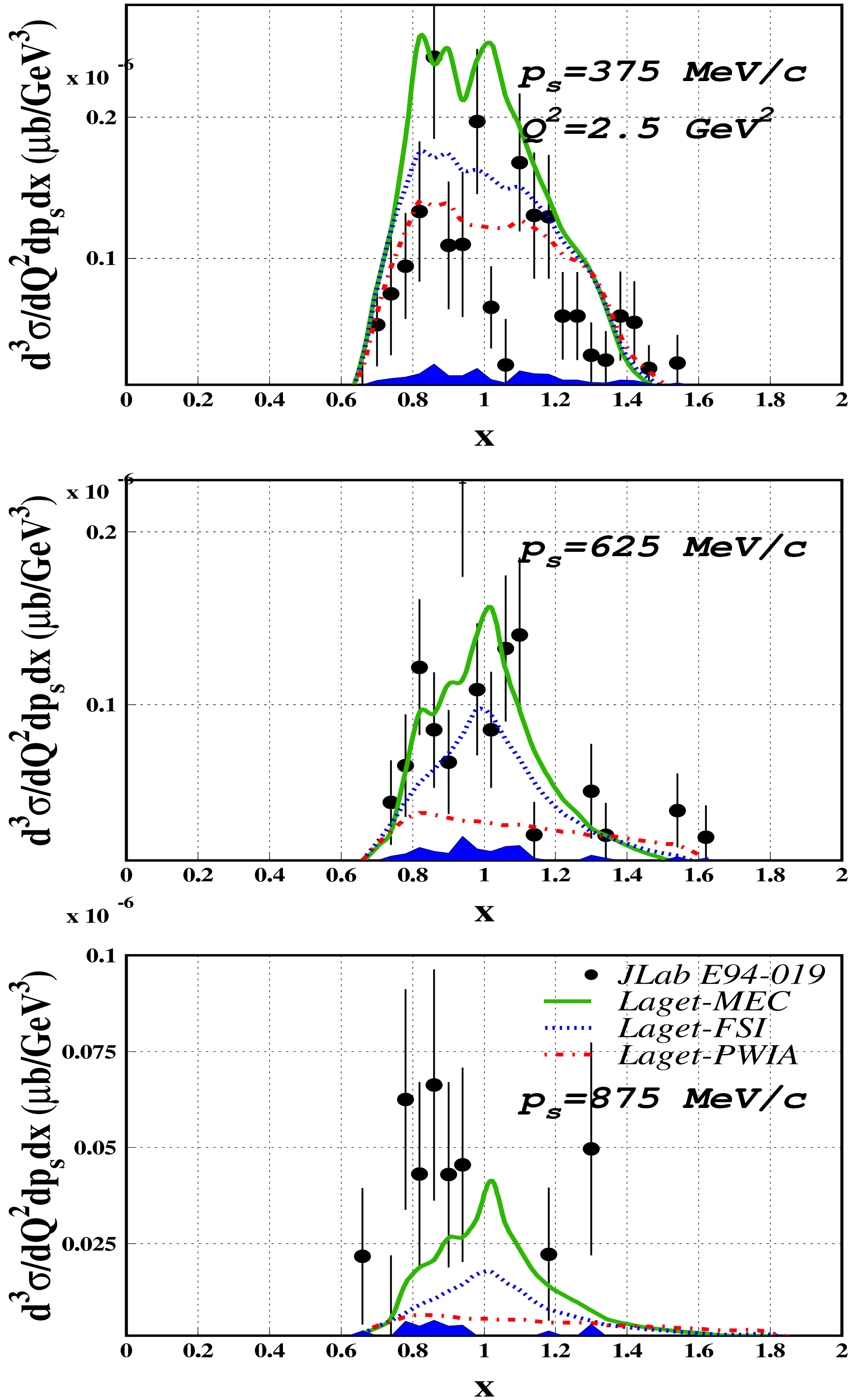

FIG. 5.18: Same as in Fig. 5.15 except for $Q^2 = 5.5$ GeV^2.

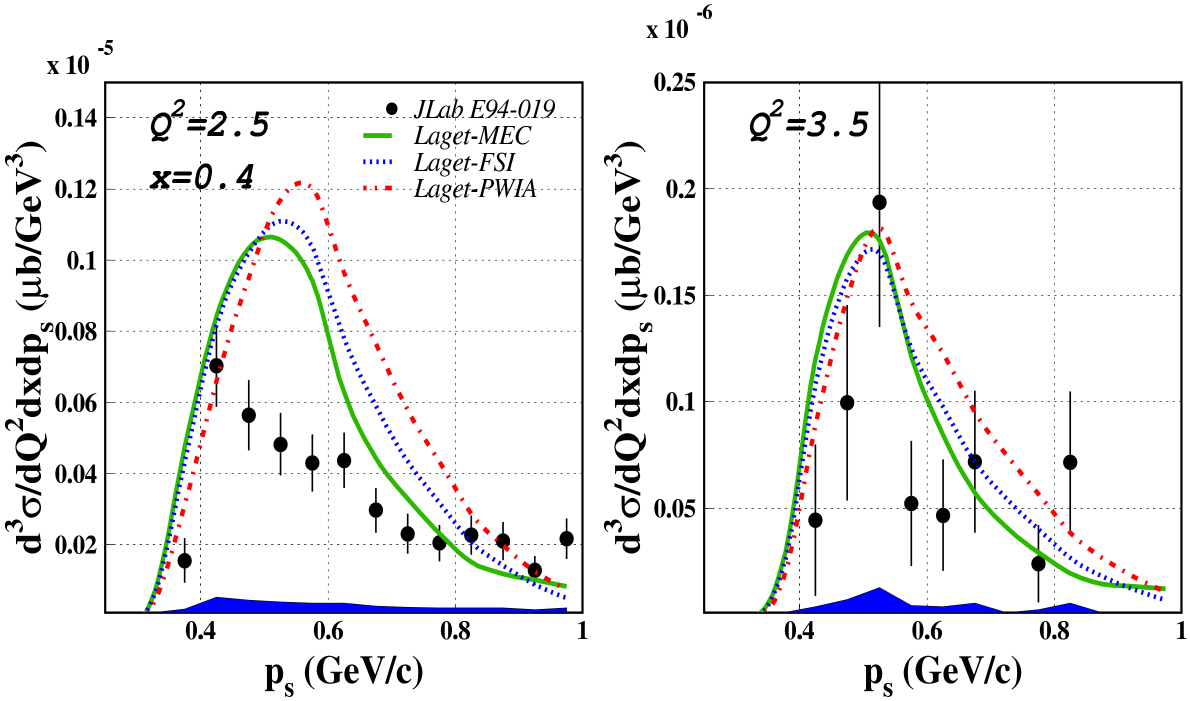

FIG. 5.19: Cross sections within the fiducial CLAS acceptance versus momentum of the scattered proton (circles) for $x = 0.4$ with $Q^2 = 2.5$ and 3.5 GeV^2. Solid curves correspond to full description of d(e,e′p)n scattering amplitude within the fiducial CLAS acceptance (PWIA+MEC+IC+FSI) [29]. Dot-dashed curves correspond to the PWIA and dashed curves correspond to the FSIs only (PWIA+FSI). Systematic errors are represented by the solid area at the bottom of each plot.

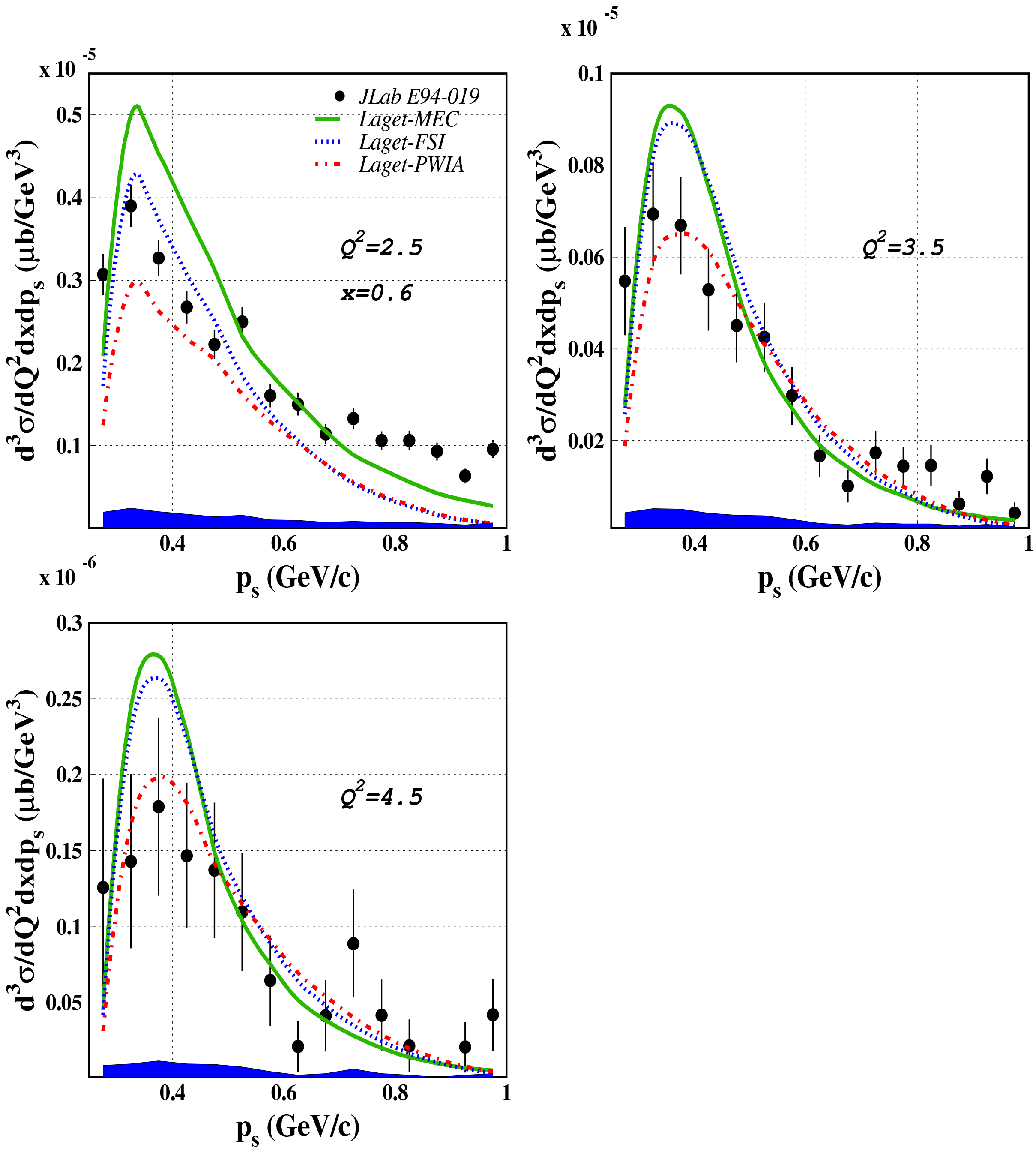

FIG. 5.20: Same as in Fig. 5.19 except with cross sections for $x = 0.6$ and $\mathrm{Q}^2 = 2.5, 3.5$ and $4.5\ \mathrm{GeV}^2$.

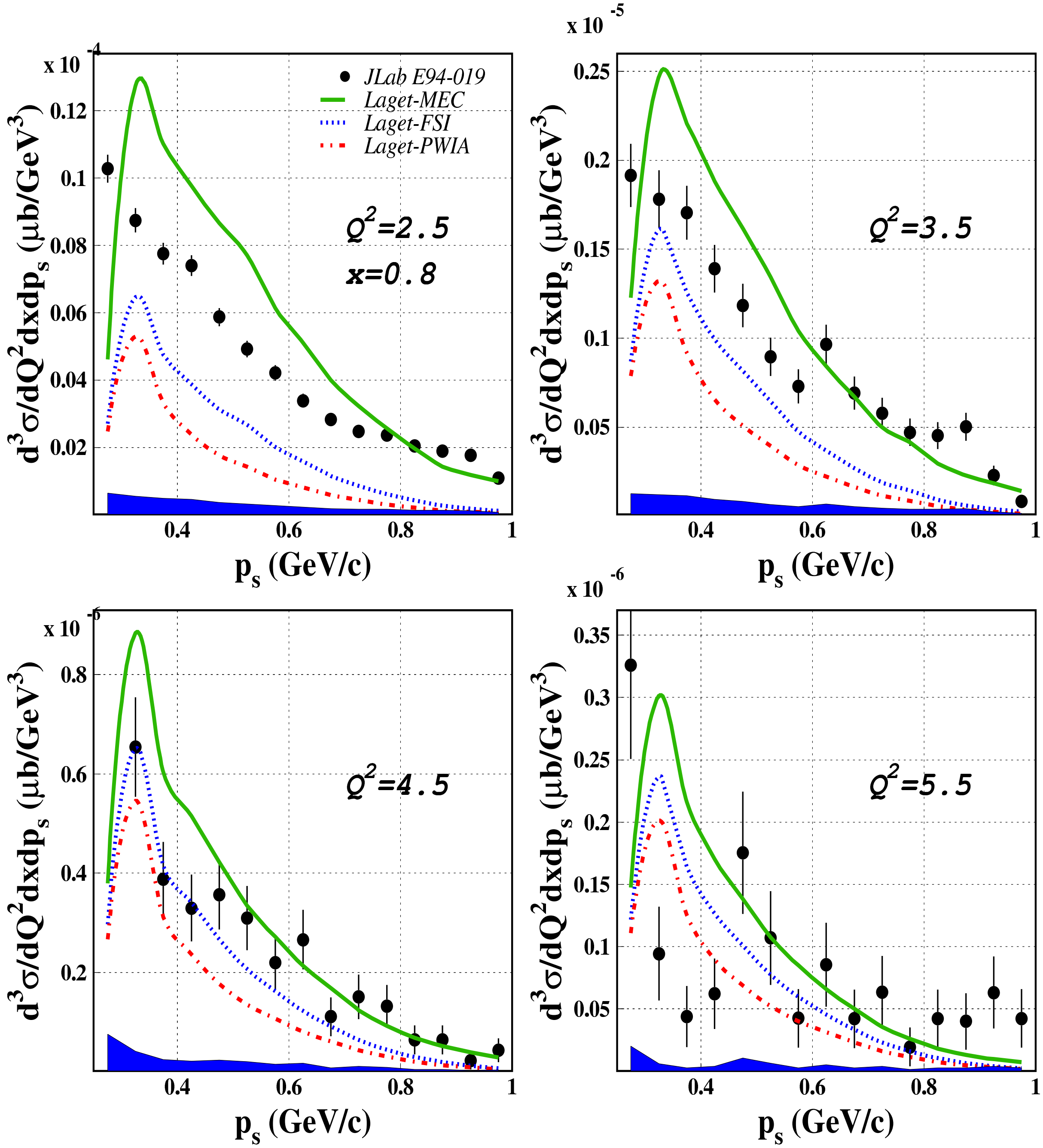

FIG. 5.21: Same as in Fig. 5.19 except with cross sections for $x = 0.8$ and $\mathrm{Q}^2 = 2.5, 3.5, 4.5$ and 5.5 GeV^2.

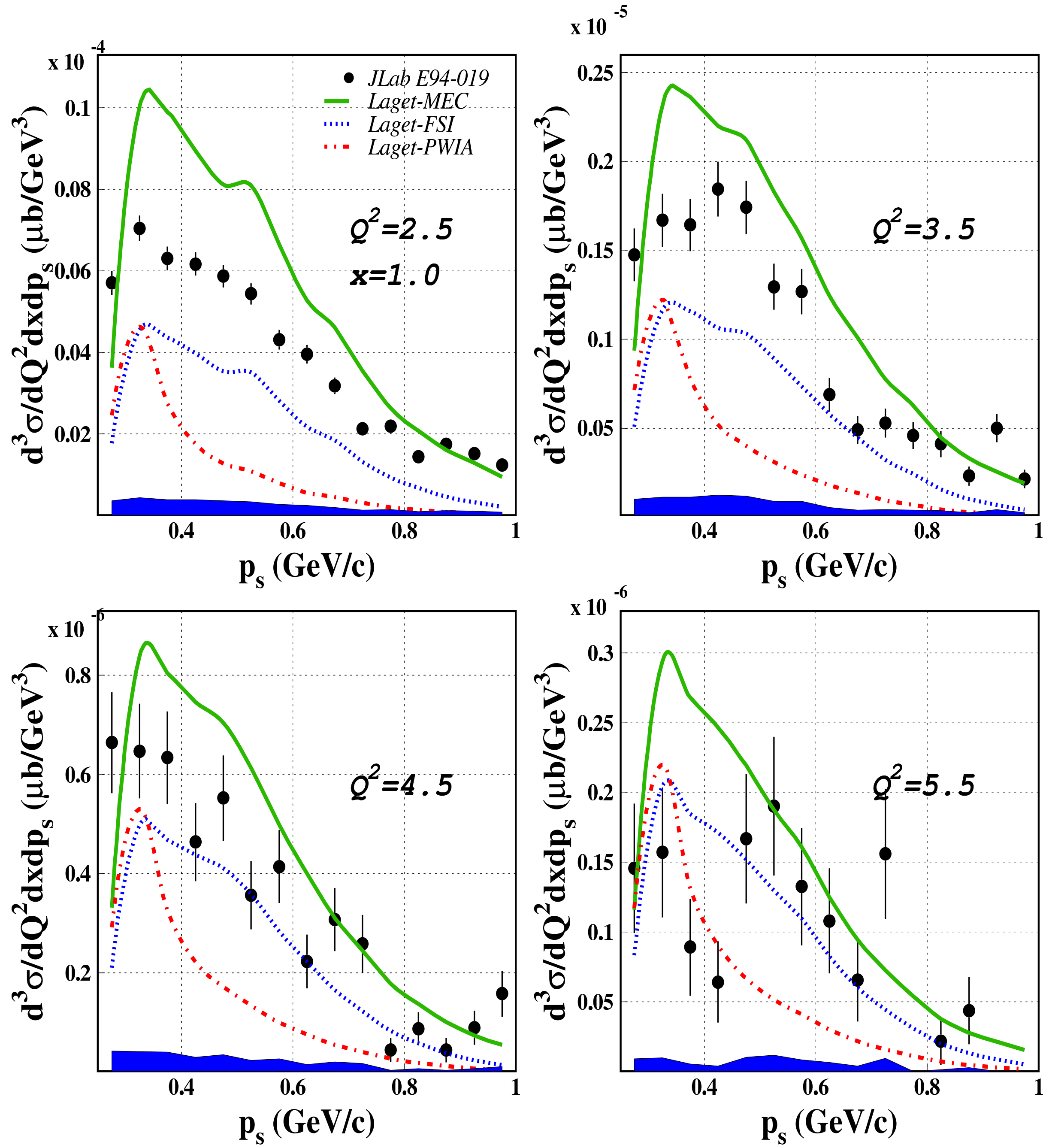

FIG. 5.22: Same as in Fig. 5.21 except with cross sections for $x = 1.0$.

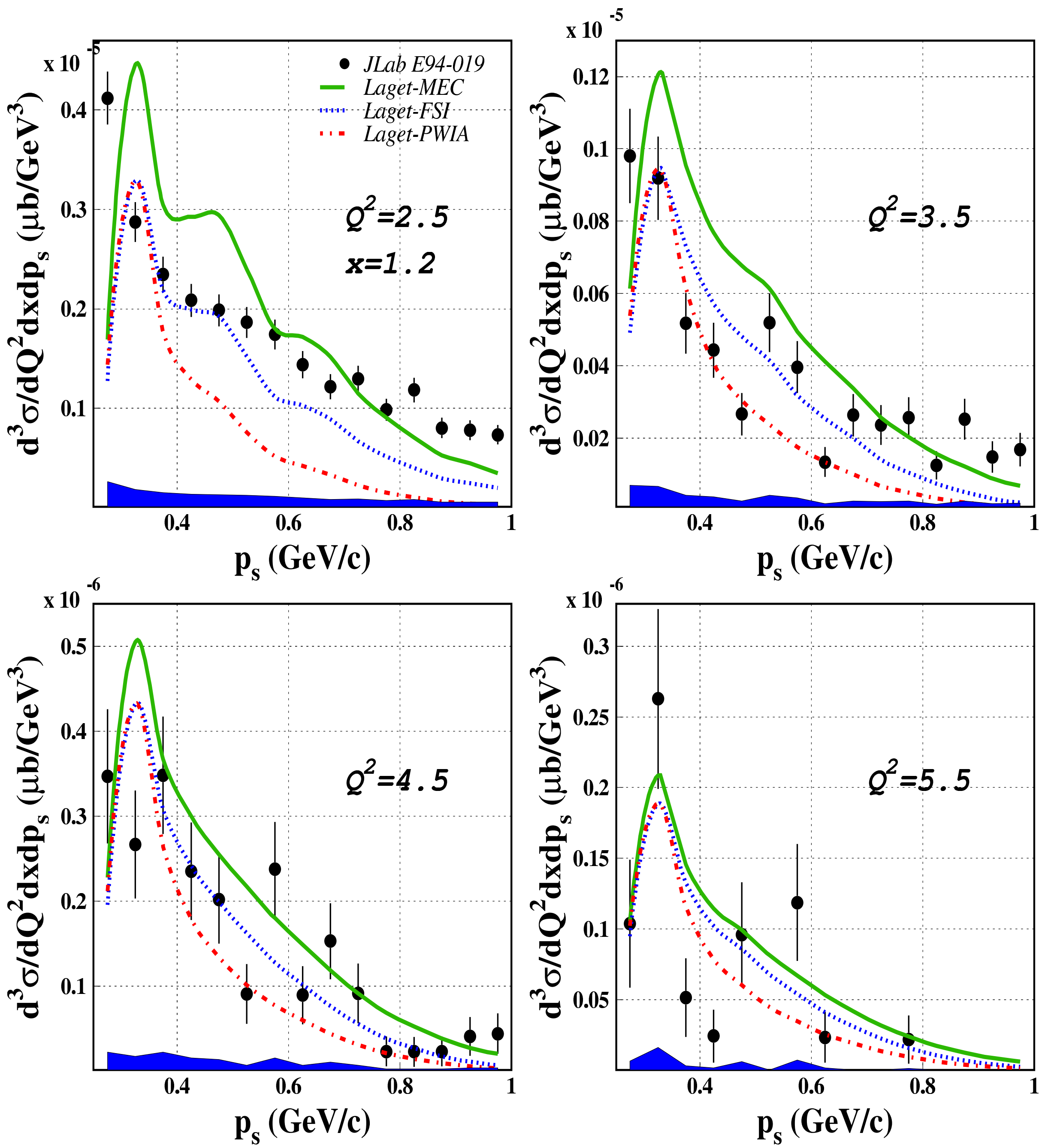

FIG. 5.23: Same as in Fig. 5.21 except with cross sections for $x = 1.2$.

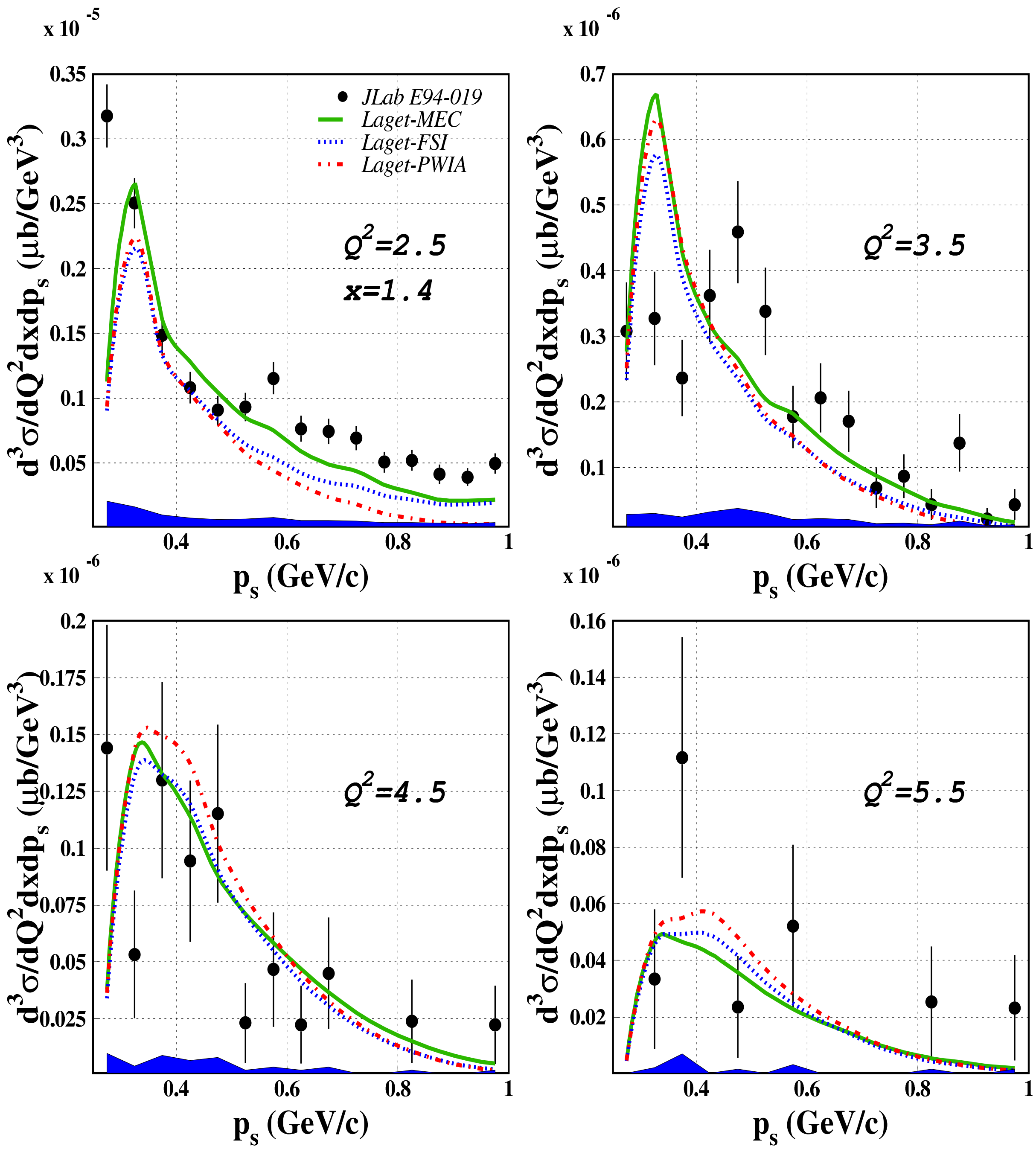

FIG. 5.24: Same as in Fig. 5.21 except with cross sections for $x = 1.4$.

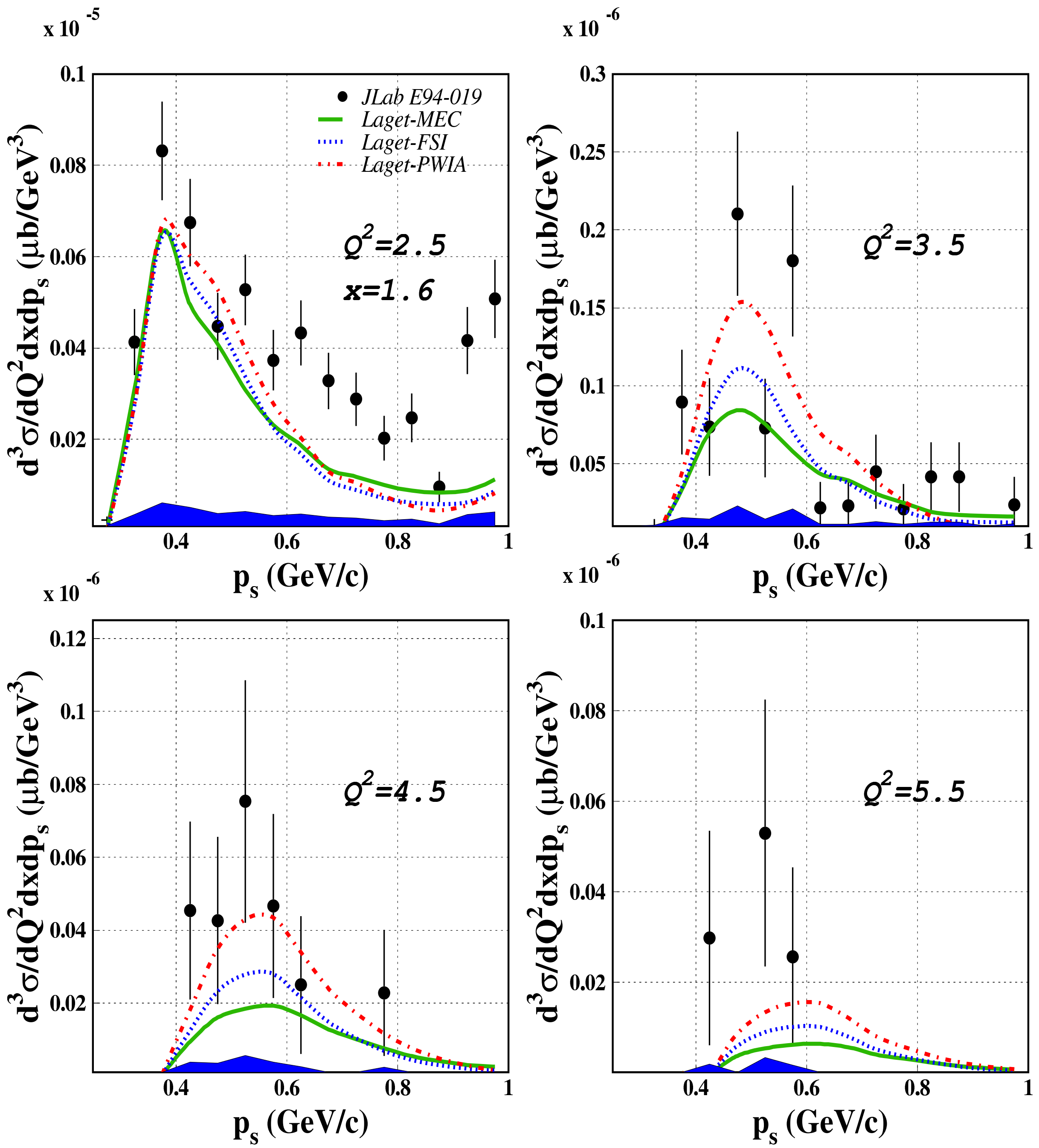

FIG. 5.25: Same as in Fig. 5.21 except with cross sections for $x = 1.6$.

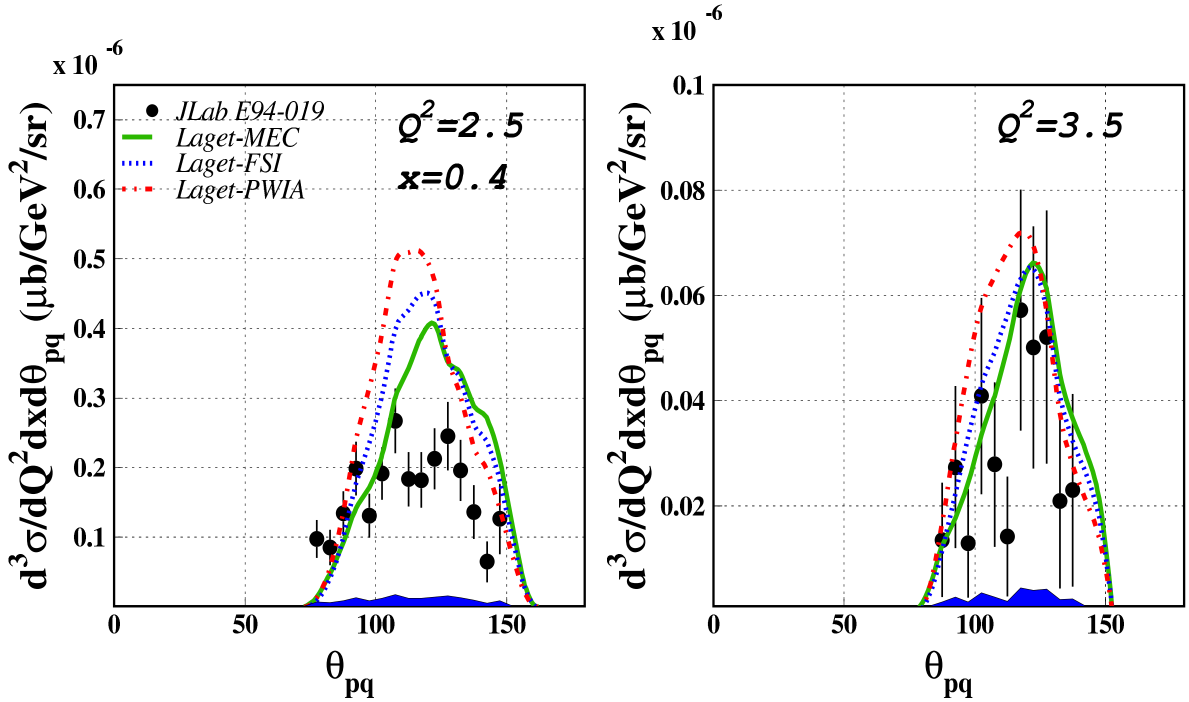

FIG. 5.26: Cross sections within the fiducial CLAS acceptance versus θ_{pq} for $x = 0.4$ with $Q^2 = 2.5$ and 3.5 GeV^2. Solid curves correspond to full description of d(e,e′p)n scattering amplitude within the fiducial CLAS acceptance (PWIA+MEC+IC+FSI) [29]. Dot-dashed curves correspond to the PWIA and dashed curves correspond to FSIs only (PWIA+FSI). Systematic errors are represented by the solid area at the bottom of each plot.

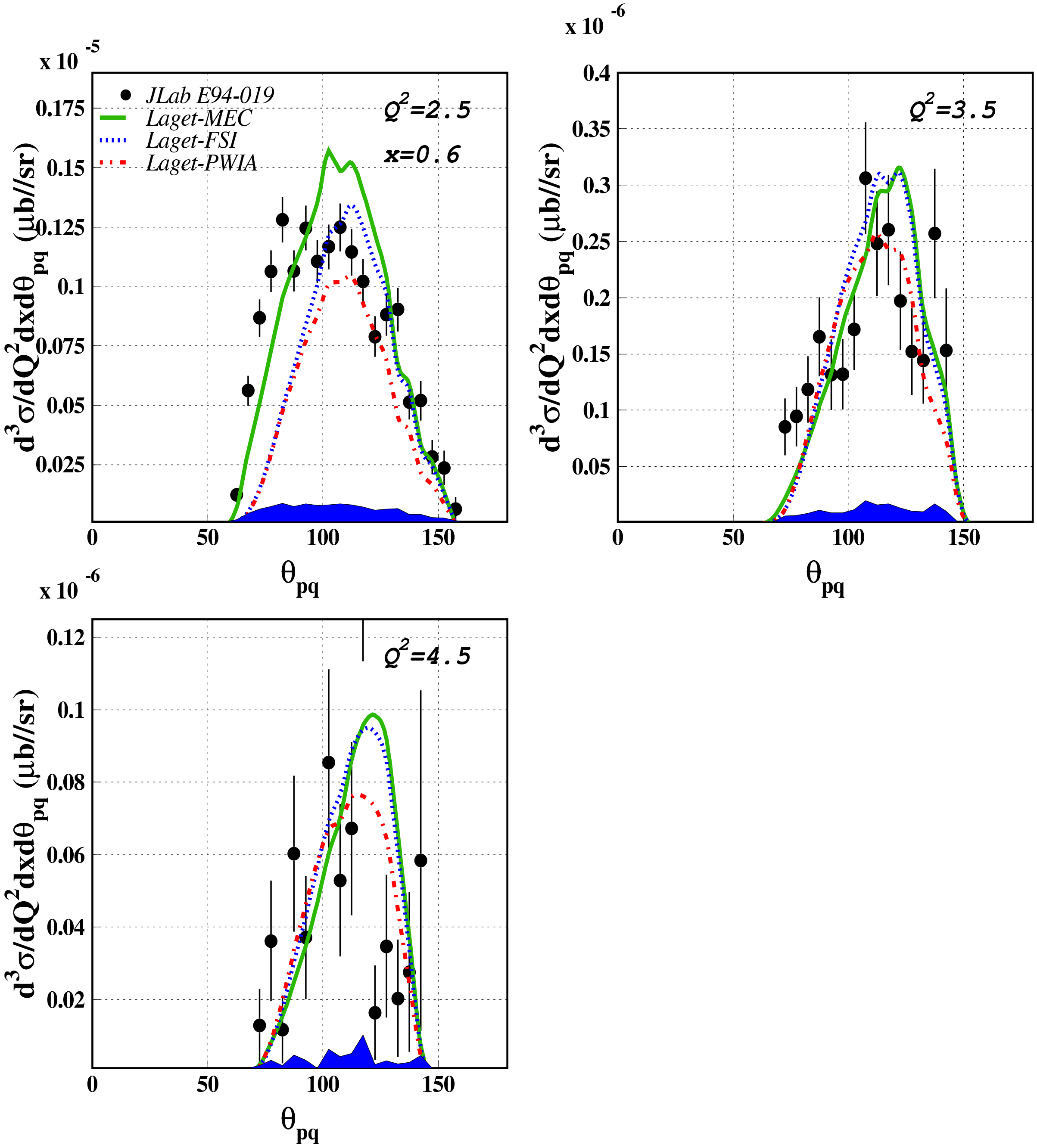

FIG. 5.27: Same as in Fig. 5.26 except with cross sections for $x = 0.6$ and $\mathrm{Q}^2 = 2.5, 3.5$, and $4.5\ \mathrm{GeV}^2$.

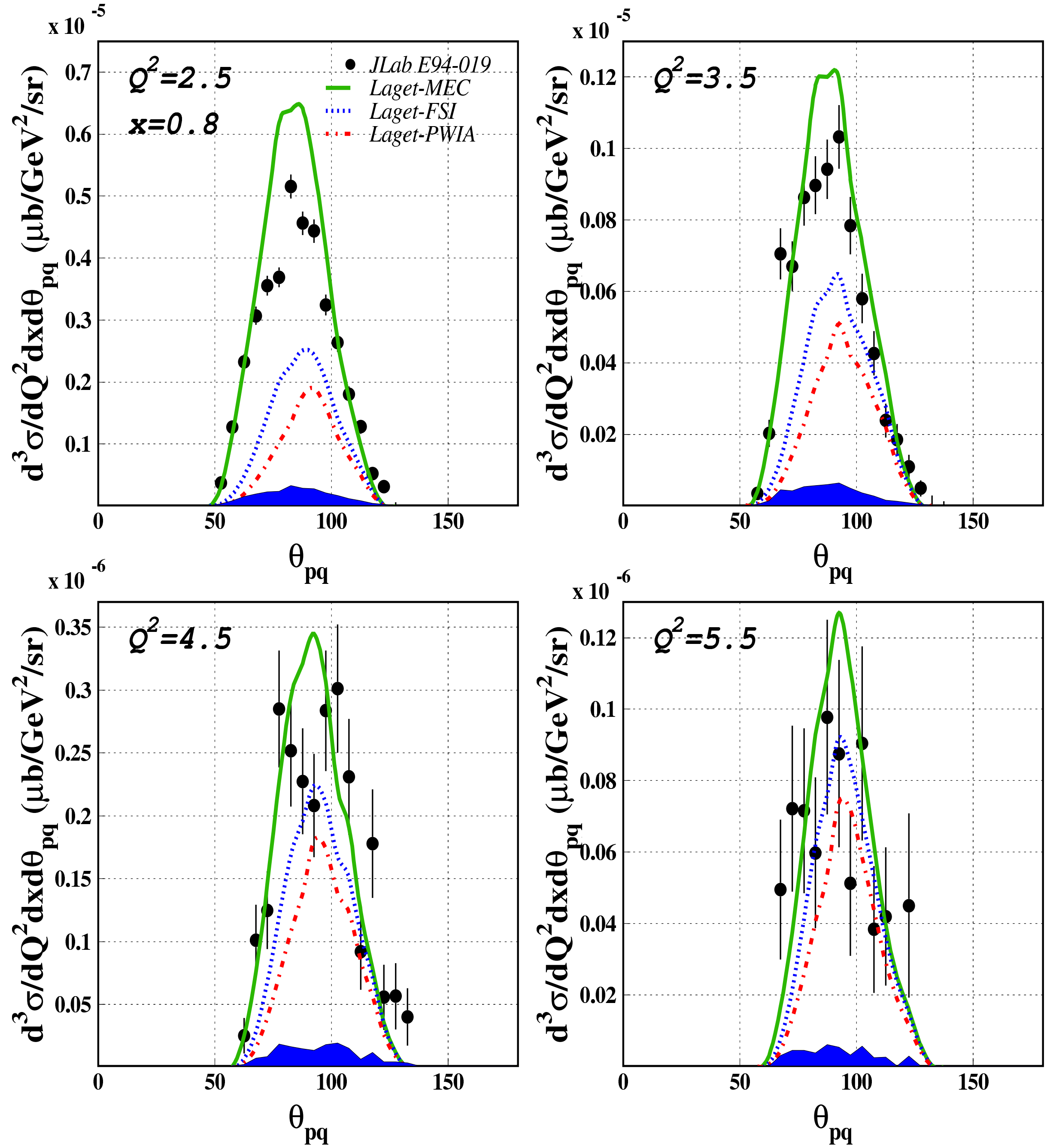

FIG. 5.28: Same as in Fig. 5.26 except with cross sections for $x = 0.8$ and $Q^2 = 2.5, 3.5, 4.5,$ and 5.5 GeV^2.

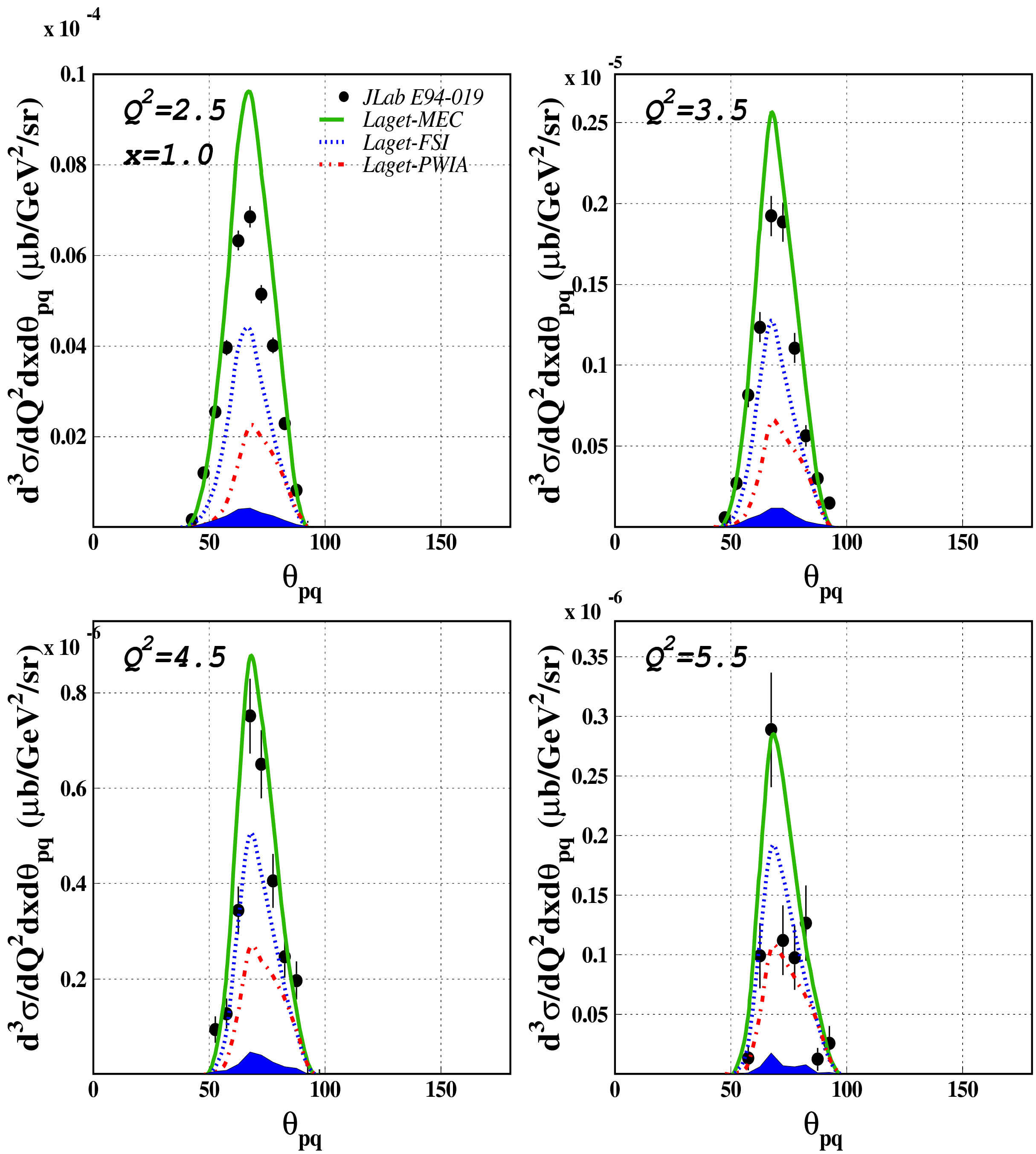

FIG. 5.29: Same as in Fig. 5.28 except with cross sections for $x = 1.0$.

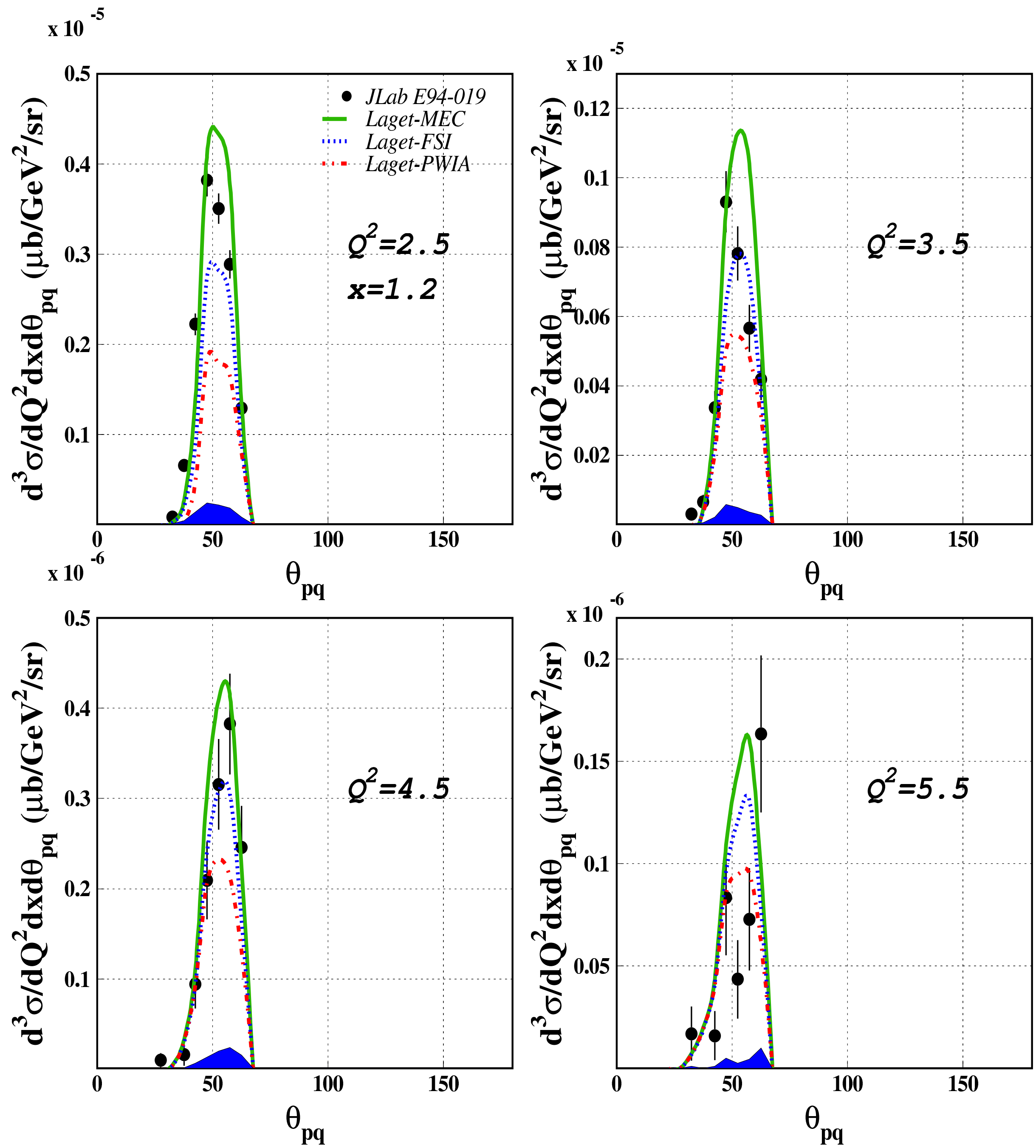

FIG. 5.30: Same as in Fig. 5.28 except with cross sections for $x = 1.2$.

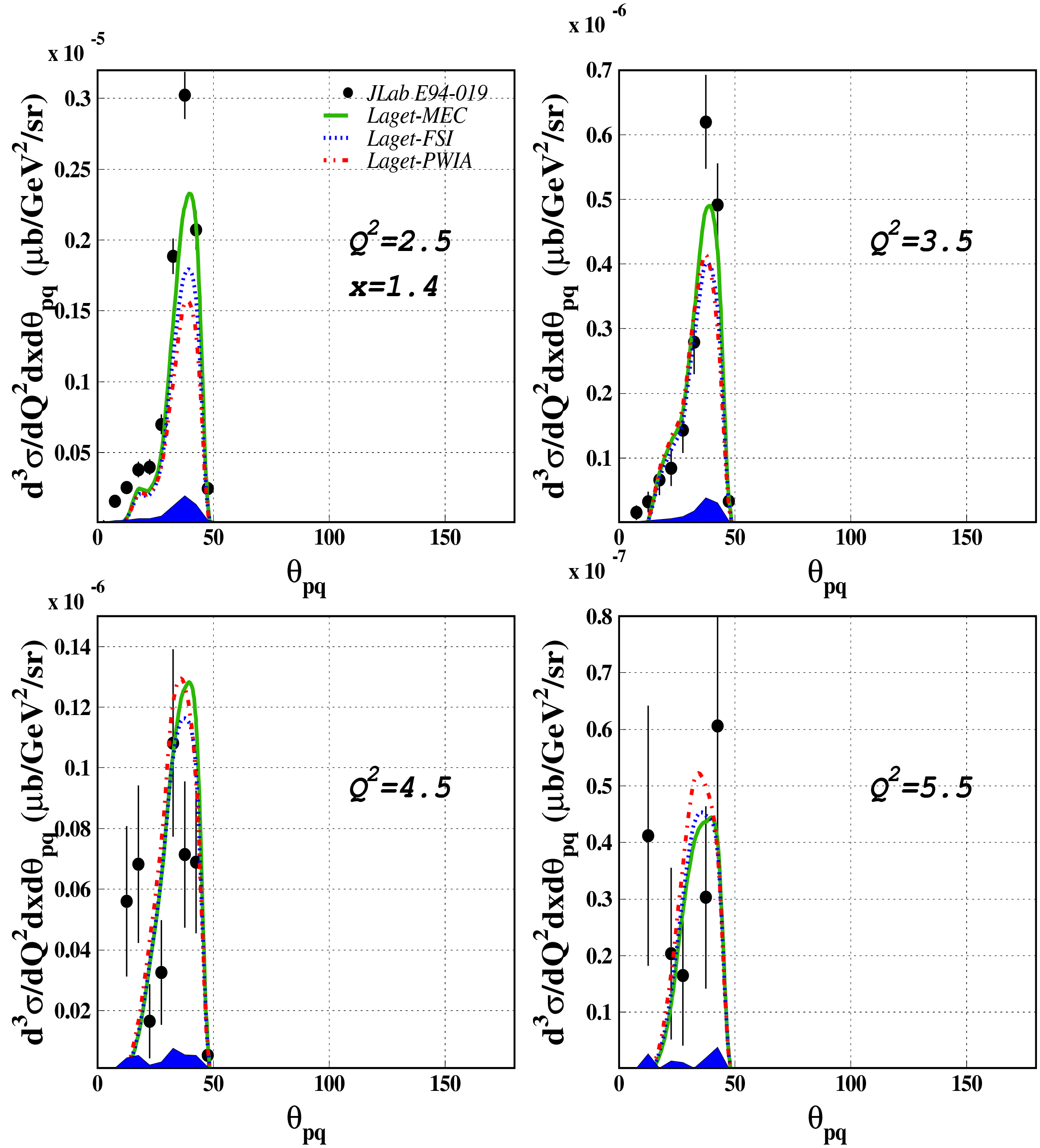

FIG. 5.31: Same as in Fig. 5.28 except with cross sections for $x = 1.4$.

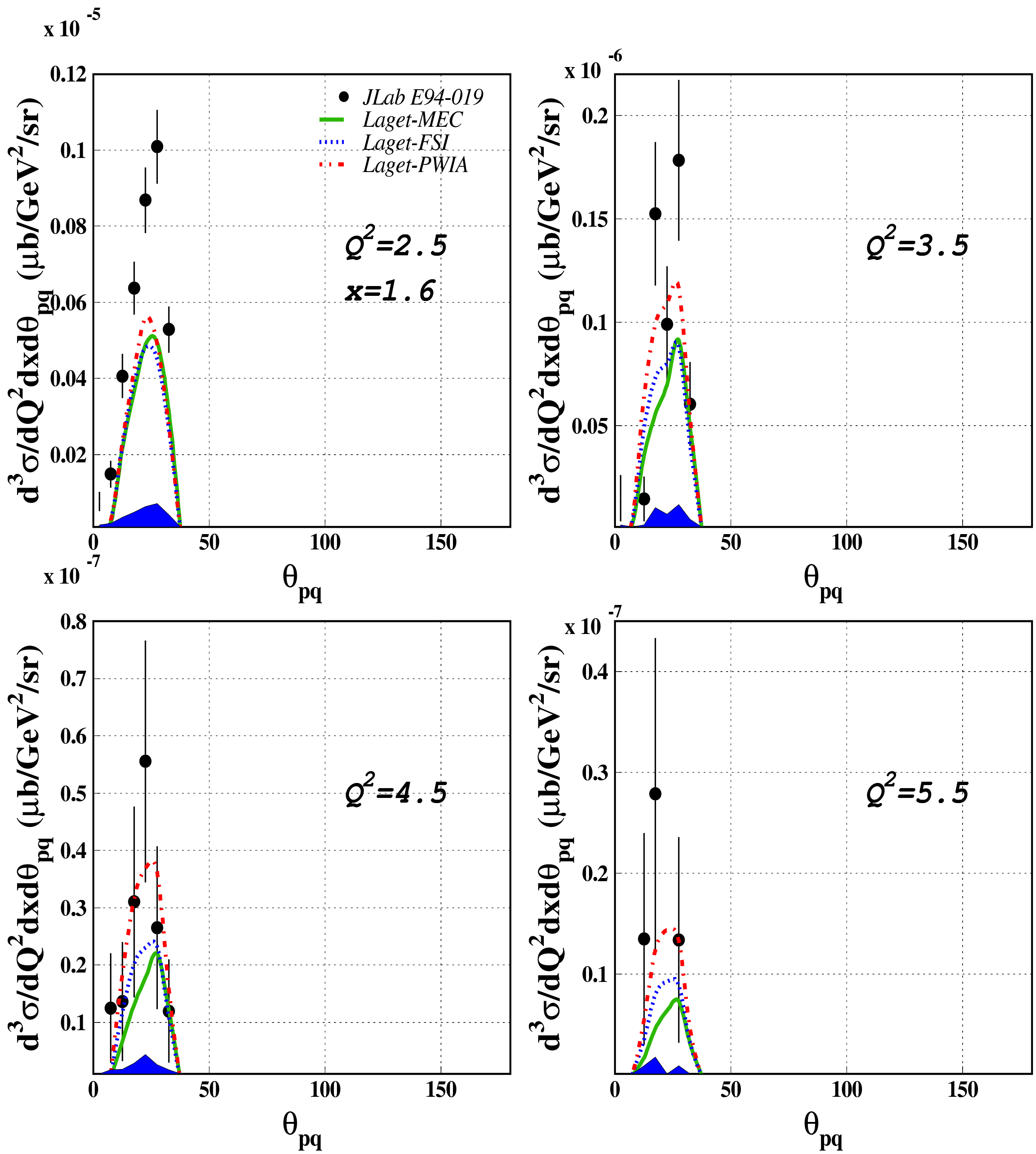

FIG. 5.32: Same as in Fig. 5.28 except with cross sections for $x = 1.6$.

5.3 Nuclear CT Signature Studies

Nuclei are in general stable systems, made up of quarks and gluons bound together by the strong force. However, the quarks and gluons are hidden, and nuclei seem rather to be composed of hadrons bound together by exchanged mesons. The hadrons are identified with color singlet states and have strong interactions very different than that of gluon (strong force carriers) exchange by colored quarks. This contradiction between the fundamental theory, quantum chromodynamics (QCD), and conventional nuclear physics could be resolved by observing nuclear matter at very small distances. This can be achieved with high energy beams at TJNAF. Electron scattering experiments at high momentum transfer in which one or two nucleons are knocked out was suggested as a new method of observation of exotic configurations such as color screening or nuclear color transparency (CT), called color coherent effects. In such a reaction, the struck nucleon must have a spatially small transverse size. A new method [102] sensitive to variation of FSIs with momentum transfer Q^2 was suggested as a signature for CT. By computing the ratio of cross sections in a region were the re-scattering effects (FSIs) are maximized, to a region were they are suppressed (screening effects) in quasi-free kinematics ($x = \frac{Q^2}{2m_p\nu} \approx 1$), we obtain a tool sensitive to re-scattering effects. In this experiment we were not able to detect spectator protons below the Fermi momentum ($<$ 65 MeV/c in the deuteron), where screening occurs. A direct comparison between cross sections dominated by re-scattering effects and the quasi-free cross section was not possible due to these kinematic restrictions. However, we computed the ratio of cross sections for two momentum ranges and for several kinematic bins around the quasi-elastic peak. As suggested earlier, a signature of color transparency will result in a strong dependence of this ratio on Q^2. In this kinematic regime where the momentum of the recoiling proton is largely transverse, the strong contribution of MEC and IC makes it difficult to observe the dissapearence of FSIs that would indicate production of a point-like constituent (PLC). Figs. 5.33 – 5.35 display the ratios of the cross section for the momentum range $p_s = 500-900$ MeV/c to the cross section for the momentum range $p_s = 250-500$ MeV/c for several bins in $x = 0.8, 1.0$ and 1.2 and light-cone variable $\alpha_s = (E_s - p_s \cos\theta_{pq})/m_p = 0.8, 1.0$ and 1.2. The ratio is nearly independent of Q^2, which indicates the absence of the signature of color coherent nucleonic states. This results in an inability to detect nucleonic PLCs under the kinematic conditions in which the Δ-nucleon and nucleon-meson re-scattering amplitudes play a major role in d(e,e′p)n. The calculations from Ref. [29] support these findings. In Figs. 5.33 – 5.35 the solid curve corresponds to the ratio R computed using cross sections containing the full description of the d(e,e′p)n scattering amplitude (PWIA+MEC+IC), dashed curve corresponds to plane wave impulse approximation (PWIA) description and dot-dashed curve corresponds to the re-scattering amplitude (FSI). This observation suggests that in the range of Q^2 up to 6 GeV^2 the formation length l_c (defined in Section 1.4) of small transverse momentum configurations is comparable to the inter-nucleon distance and much smaller than the radius of deuteron. This explains the absence of a CT signal in this data set. Further studies using double scattering reaction in the regions of high momentum transfer and parallel or antiparallel kinematics could reveal CT which should exist as a natural consequence of QCD.

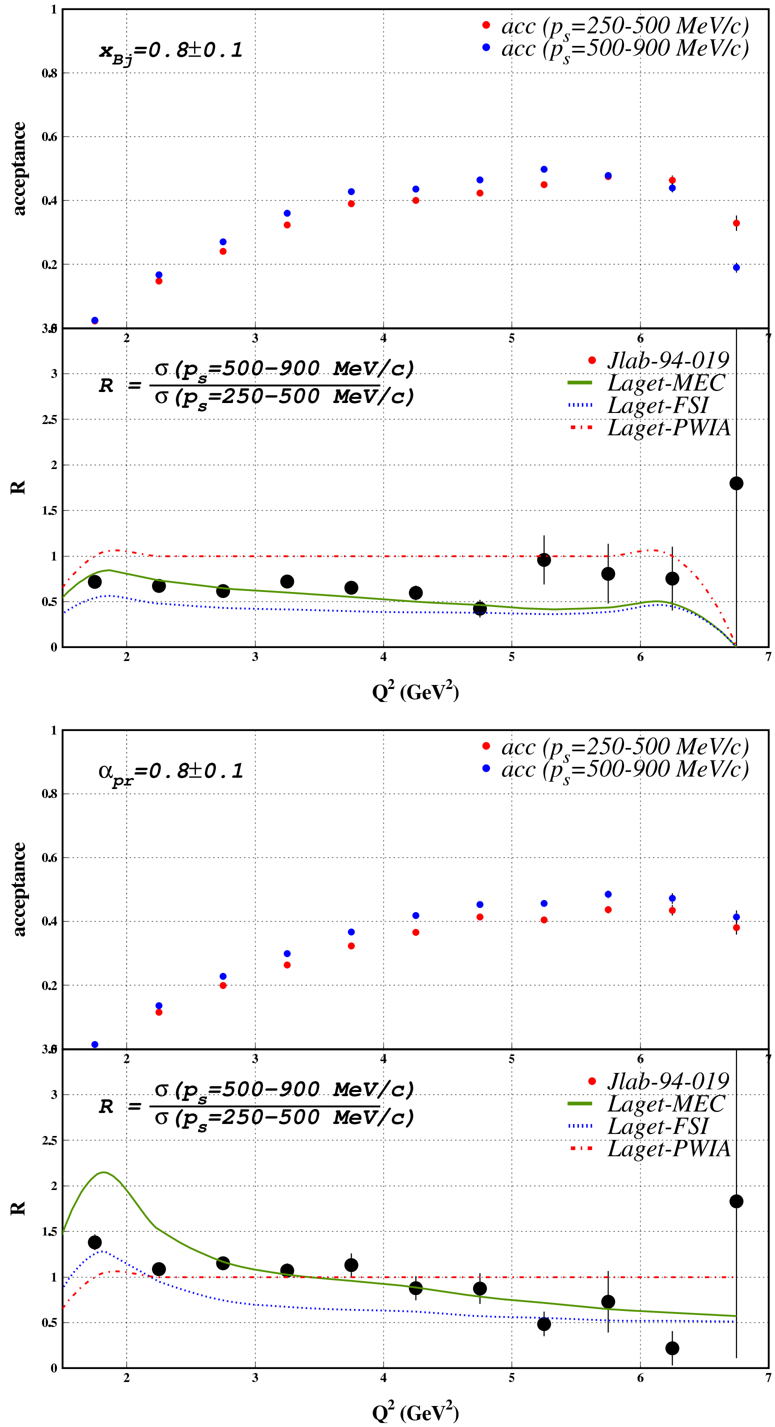

FIG. 5.33: Ratio (lower panel, circles) of cross sections for $p_s = 500 - 900$ MeV/c and $p_s = 250 - 500$ MeV/c versus Q^2 for $x = 0.8$ (upper figure) and $\alpha = 0.8$ (lower figure). The corresponding acceptances are shown in the upper panel of each figure. The curves correspond to calculations from Ref. [29]: PWIA+MEC+IC+FSI - solid curve, PWIA+FSI - dashed curve and PWIA - dot-dashed curve, respectively.

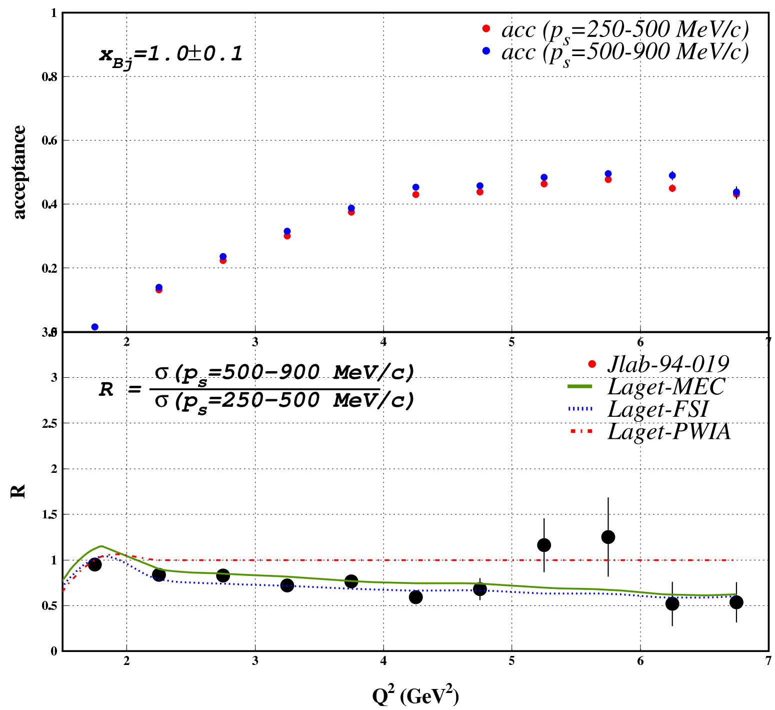

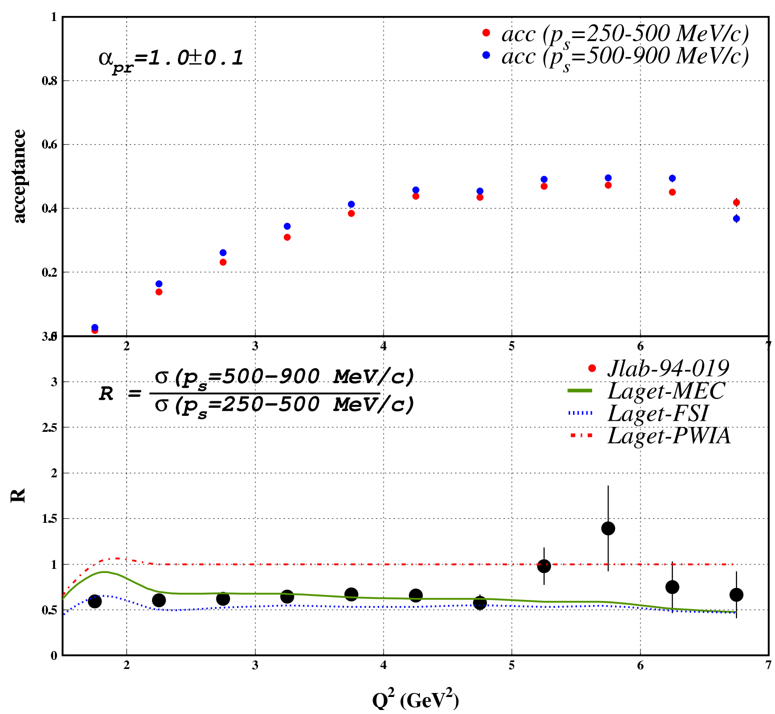

FIG. 5.34: Same as in Fig. 5.33 except for $x = 1$ (upper figure) and $\alpha = 1$ (lower figure).

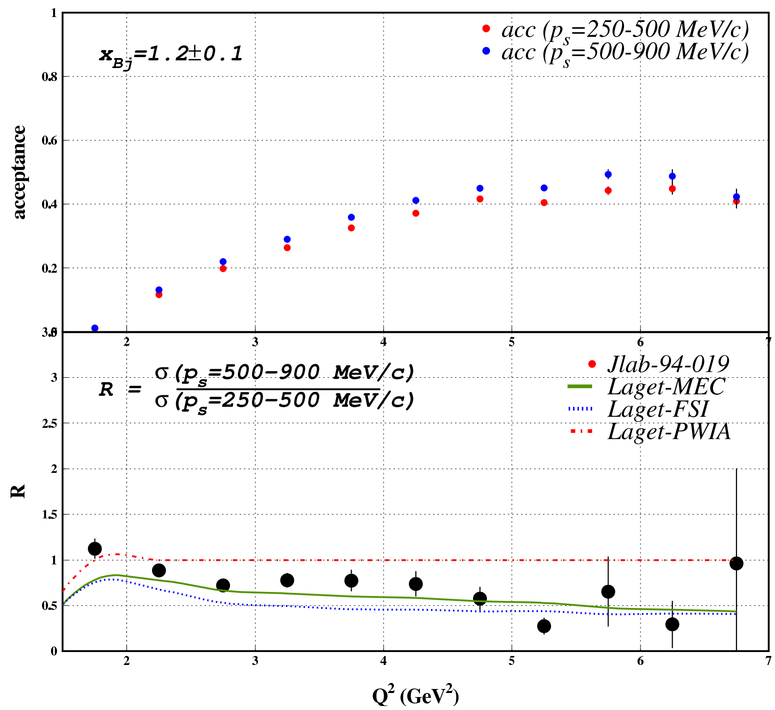

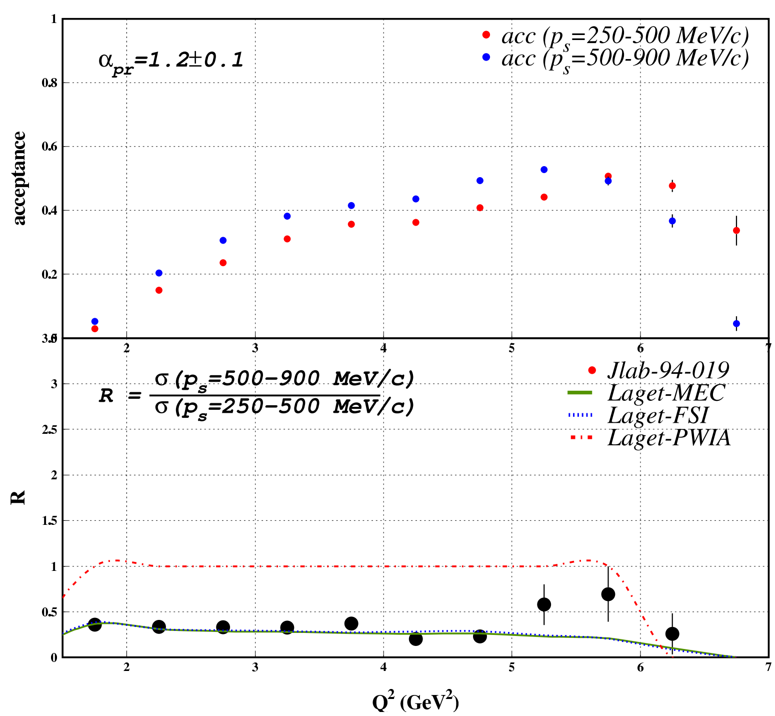

FIG. 5.35: Same as in Fig. 5.33 except for $x = 1.2$ (upper figure) and $\alpha = 1.2$ (lower figure).

5.4 Summary

Using the CEBAF Large Acceptance Spectrometer we collected data on the exclusive reaction d(e,e′p_s)n with $E_{beam} = 5.764$ GeV. Extensive simulations of the inclusive d(e,e′) reaction using a Monte Carlo event generator based on calculations from Ref. [81] were performed in order to make acceptance calculations. The technique developed for the inclusive channel was also used to calculate acceptances for the exclusive channel d(e,e′p)n. The wide kinematic range allowed us to extract inclusive cross sections for d(e,e′) for Q^2 ranging from 1.7 to 6.7 GeV^2 and with x up to 1.9. Previous data from SLAC [78, 80] and Jefferson Laboratory [73] did not cover much of this high-x region. The experimental inclusive cross sections for d(e,e′) support the theoretical calculations that include short-range correlations and described in Section 4.2.2. at a level of 5–10%. The measured inclusive d(e,e′) cross sections are tabulated in Appendix C after having been corrected for radiative effects, acceptance and bin size. The graphical representation of these cross sections for each kinematic bin are presented in Figs. 5.3 - 5.7.

We tagged quasi-elastic scattered protons in almost perpendicular kinematics with respect to the momentum transfer direction, and studied the evolution of MEC, IC, and FSIs effects with Q^2. To correct for the CLAS acceptance for d(e,e′p_s)n events, we used a model based on fits to the experimental distributions of the scattered electron and the recoil proton. This model was constrained to respect the kinematics imposed by energy and momentum conservation. The model is described in Section 4.2.3 and the parameterizations of electron and proton observables are given in Appendix F. We corrected for radiative effects and acceptance and finally extracted quasi-elastic exclusive d(e,e′p_s)n cross sections integrated over full phase space for $Q^2 = 2.5, 3.5, 4.5$ and 5.5 GeV^2 and for $p_s = 250 - 1000$ MeV/c. The experimental cross sections are in fair agreement with calculations from Ref. [29] at a level of $10-15\%$, comparable with the uncertainty level of this analysis. They are tabulated in Appendix D. The d(e,e$'$p$_s$)n cross sections within the fiducial CLAS acceptance are shown in Figs. 5.19 – 5.25 versus the recoil proton momentum p_s and in Figs. 5.26 – 5.32 versus the proton scattering angle θ_{pq} with respect to the momentum transfer direction. The theoretical predictions which are supported by these findings suggests a rather large probability of Δ-isobar on-shell rescattering overlapping with NN on-shell rescattering. In this picture, the observation of PLCs becomes difficult in the kinematics chosen in this analysis.

APPENDIX A

Feynman Diagram Rules in GEA

In this section we define the effective Feynman diagram rules, within the generalized eikonal approximation (GEA), for the knocked-out nucleon to undergo n re-scatterings off the (A-1) nucleons of the residual system. The diffractive excitation of the nucleons into an intermediate state are systematically neglected, due to small contributions in this kinematic range (energies $\leq$ 10 GeV). Figure A.1 shows

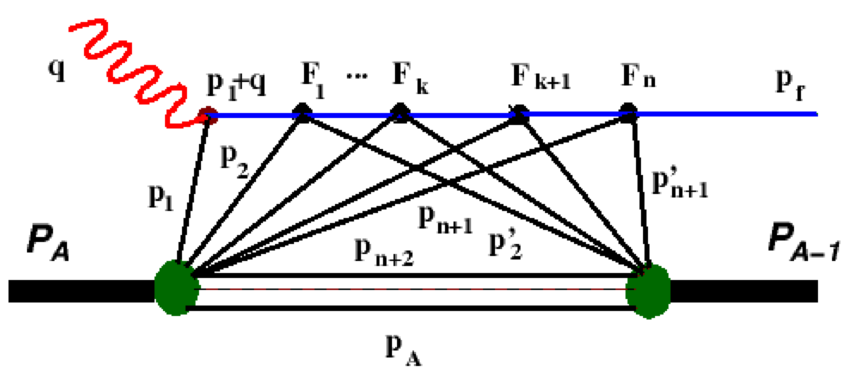

FIG. A.1: N-fold re-scattering Feynman diagram.

the Feynman diagram for n-fold re-scattering, represented through the n vertex amplitude, in which each vertex corresponding to one NN scattering. The Feynman rules for calculating the diagram in Figure A.1 are as following:

- For each vertex, the transitions between "*nucleus A*" and "*A nucleons*", and between "*(A-1) nucleons*" and the "*(A-1) nucleon final state*" are represented respectively by $\Gamma_A(p_1, ..., p_A)$ and $\Gamma_A^\dagger(p'_2, ..., p'_A)$.

- $F_N^{em,\mu}$ is assigned for the $\gamma^* N$ interaction.

- For each NN interaction a vertex function $F_k^{NN}(p_{k+1}, p'_{k+1})$ is assigned for which

$$\bar{u}(p_3)\bar{u}(p_4)F^{NN}u(p_1)u(p_2) = \sqrt{s(s-4m^2}f^{NN}(p_3,p_1)\delta_{\lambda,\lambda'} \approx sf^{NN}(p_3,p_1)\delta_{\lambda,\lambda'}, \tag{A.1}$$

  s is the total invariant energy of the two interacting nucleons with momenta p_1 and p_2

$$f^{NN} = \sigma_{tot}^{NN}(i+\alpha)e^{-\frac{B}{2}(p_3-p_1)_\perp^2}, \tag{A.2}$$

  and σ_{tot}^{NN}, α and B are known experimentally from NN scattering data. The vertex functions are normalized by the δ-function of energy-momentum conservation.

- Each nucleon in an intermediate state has a propagator $D(p)^{-1} = -(\hat{p}-m+i\epsilon)^{-1}$. The "-" sign is chosen to simplify the calculation of the overall sign for the scattering amplitude.

- Combinatorics of n- scattering's brings a factor of $n!(A-n-1)!$, and spectator nucleons are accounted as $(A-n-1)$.

- Each closed contour brings an additional factor $\frac{1}{i(2\pi)^4}$ with no additional sign.

APPENDIX B

Analytic Calculation of Scattering Amplitude

The calculation of re-scattering amplitude in Eq. 1.31 is based on the method described in Ref. [41], which uses the deuteron wave function in momentum space, defined in Ref. [99]:

$$\psi_D^\mu(p) = \frac{1}{\sqrt{4\pi}}\left(u(p) + w(p)\sqrt{\frac{1}{8}}S(p_z,p_t)\right)\chi^\mu, \tag{B.1}$$

in which χ^μ is the deuteron spin function and $S(p_z,p_t)$ is defined by the Pauli matrices, σ_p, σ_n:

$$S(p_z,p_t) = \frac{3(\vec{\sigma}_p\cdot\vec{p})(\vec{\sigma}_n\cdot\vec{p})}{p^2} - \vec{\sigma}_p\cdot\vec{\sigma}_n. \tag{B.2}$$

Here $u(p)$ and $w(p)$ are the radial S- and D- states wave functions, respectively. They can be written as [100,101]:

$$u(p) = \sum_j \frac{c_j}{p^2+m_j^2}, \quad w(p) = \sum_j \frac{d_j}{p^2+m_j}, \tag{B.3}$$

in which $\sum_j c_j = \sum_j d_j = 0$. This guarantees that $u(p)$ and $w(p) \sim \frac{1}{p^4}$ at large p and $\sum_j \frac{d_j}{m_j^2} = 0$ such that $w(p=0)=0$. By inserting Eqs. B1, B2 and B3 into the

Eq. 1.31 we obtain:

$$A_1^\mu = -\frac{(2\pi)^{\frac{2}{3}}\sqrt{eE_S}}{2}\int\frac{d^2p'_{st}}{(2\pi)^2}f^{pn}(k_t)\cdot j^\mu_{\gamma^*N}$$
$$\times \int\frac{dp'_{sz}}{(2\pi)}\left(\frac{c_j}{p'_s+m_j^2}+\frac{d_j}{p'_s+m_j^2}\sqrt{\frac{1}{8}}S(p'_{sz},p'_{st})\right)\frac{\chi^\mu}{p'_{sz}-p_{sz}+\Delta+i\epsilon}. \quad (B.4)$$

Substituting $p'^2_s + m_j^2 = \left(p'_{sz}+i\sqrt{m_j^2+p'^2_{st}}\right)\left(p'_{sz}-i\sqrt{m_j^2+p'^2_{st}}\right)$ and integrating over p'_{sz} by closing the contour in the upper p'_{sz} complex semi-plane we obtain:

$$A_1^\mu = -\frac{(2\pi)^{\frac{2}{3}}\sqrt{eE_S}}{2}\int\frac{d^2p'_{st}}{(2\pi)^2}f^{pn}(k_t)\cdot j^\mu_{\gamma^*N}\left[\frac{c_j}{2i\sqrt{p'^2_{st}+m_j^2}}+\right.$$
$$\left.+\frac{d_j}{2i\sqrt{p'^2_{st}+m_j^2}}\sqrt{\frac{1}{8}}S(i\sqrt{p'^2_{st}+m_j^2},p'_{st})\right]\frac{\chi^\mu}{i\sqrt{p'^2_{st}+m_j^2}-p_{sz}+\Delta}. \quad (B.5)$$

After regrouping of the real and imaginary parts, the above equation can be rewritten as:

$$A_1^\mu = -\frac{(2\pi)^{\frac{2}{3}}\sqrt{eE_S}}{2}\int\frac{d^2p'_{st}}{(2\pi)^2}f^{pn}(k_t)\cdot j^\mu_{\gamma^*N}(\psi^\mu(\tilde{p}_s)-i\psi'^\mu(\tilde{p}_s)), \quad (B.6)$$

in which $\tilde{p}_s(\tilde{p}_{sz},\tilde{p}_{s\perp})\equiv\vec{\tilde{p}}_s(p_{sz}-\Delta,\vec{p}_{st}-\vec{k}_t)$, ψ^μ is the wave function defined in Eq.B1 and ψ'^μ is defined as:

$$\psi'^\mu(p) = \left(u_1(p)p_z+\frac{w_1(p)p_z}{\sqrt{8}}S(p_z,p_t)+\frac{w_2(p)}{\sqrt{8}p_z}[S(p_z,p_t)-S(0,p_t)]\right)\chi^\mu. \quad (B.7)$$

Here $u_1(p)$, $w_1(p)$, and $w_2(p)$ are defined as:

$$u_1(p) = \sum_j\frac{c_j}{(p^2+m_j^2)\sqrt{p_t^2+m_j^2}}, \quad w_1(p)=\sum_j\frac{d_j}{(p^2+m_j^2)\sqrt{p_t^2+m_j^2}},$$
$$w_2(p) = \sum_j\frac{d_j}{m_j^2\sqrt{p_t^2+m_j^2}}. \quad (B.8)$$

We note that the last term in Eq. B7 does not have a singularity at $p_z=0$ since $(S(p_z,p_t)-S(0,p_t))\sim p_z$.

APPENDIX C

Inclusive d(e,e′) Cross Sections

Tabulated below are the experimental measured inclusive d(e,e′) cross sections plotted in Section 5.1 (Figs. 5.3 – 5.7) for $Q^2 = 1.7 - 7$ GeV^2 and $x = 0.7 - 1.9$. The results presented here have been corrected for radiative effects, acceptance, and bin size. The statistical and systematic errors associated with these corrections are included. The correction factor for radiative effects R.C. corresponding to each kinematic bin is given in the last column of each table.

Q^2 GeV^2	x	$d\sigma/dQ^2dx$ μb/GeV^2	R.C.
1.725	0.71	0.212E-01±0.361E-03±0.101E-02	0.855
	0.73	0.148E-01±0.293E-03±0.707E-03	0.843
	0.75	0.129E-01±0.309E-03±0.618E-03	0.839
	0.77	0.105E-01±0.303E-03±0.500E-03	0.842
	0.79	0.847E-02±0.320E-03±0.405E-03	0.855
	0.81	0.628E-02±0.305E-03±0.300E-03	0.879
	0.83	0.524E-02±0.359E-03±0.250E-03	0.902
	0.85	0.376E-02±0.384E-03±0.180E-03	0.922
	0.87	0.248E-02±0.490E-03±0.119E-03	0.919
	0.89	0.641E-02±0.236E-02±0.306E-03	0.895
1.775	0.71	0.168E-01±0.214E-03±0.803E-03	0.859
	0.73	0.134E-01±0.181E-03±0.641E-03	0.846
	0.75	0.112E-01±0.167E-03±0.537E-03	0.840
	0.77	0.923E-02±0.153E-03±0.442E-03	0.842
	0.79	0.719E-02±0.135E-03±0.345E-03	0.852
	0.81	0.606E-02±0.125E-03±0.290E-03	0.872
	0.83	0.481E-02±0.111E-03±0.231E-03	0.896
	0.85	0.411E-02±0.104E-03±0.197E-03	0.915
	0.87	0.420E-02±0.111E-03±0.201E-03	0.920
	0.89	0.431E-02±0.121E-03±0.206E-03	0.901
	0.91	0.560E-02±0.161E-03±0.268E-03	0.866
	0.93	0.722E-02±0.213E-03±0.346E-03	0.814
	0.95	0.985E-02±0.298E-03±0.472E-03	0.772
	0.97	0.118E-01±0.379E-03±0.565E-03	0.731
	0.99	0.144E-01±0.498E-03±0.689E-03	0.717
	1.01	0.124E-01±0.501E-03±0.594E-03	0.717
	1.03	0.111E-01±0.545E-03±0.531E-03	0.717
	1.05	0.817E-02±0.504E-03±0.392E-03	0.717
	1.07	0.671E-02±0.538E-03±0.322E-03	0.717
	1.09	0.465E-02±0.495E-03±0.223E-03	0.717
	1.11	0.355E-02±0.513E-03±0.170E-03	0.717
	1.13	0.274E-02±0.553E-03±0.131E-03	0.717
	1.15	0.188E-02±0.760E-03±0.901E-04	0.716
	1.17	0.152E-02±0.137E-02±0.728E-04	0.716
1.825	0.71	0.150E-01±0.169E-03±0.721E-03	0.863
	0.73	0.122E-01±0.144E-03±0.590E-03	0.850
	0.75	0.105E-01±0.134E-03±0.506E-03	0.841
	0.77	0.879E-02±0.122E-03±0.424E-03	0.840
	0.79	0.711E-02±0.110E-03±0.343E-03	0.850
	0.81	0.594E-02±0.984E-04±0.286E-03	0.868
	0.83	0.437E-02±0.822E-04±0.211E-03	0.890
	0.85	0.364E-02±0.735E-04±0.175E-03	0.911
	0.87	0.347E-02±0.727E-04±0.167E-03	0.916
	0.89	0.390E-02±0.799E-04±0.188E-03	0.903
	0.91	0.461E-02±0.939E-04±0.222E-03	0.863
	0.93	0.595E-02±0.117E-03±0.287E-03	0.817
	0.95	0.820E-02±0.153E-03±0.395E-03	0.776
	0.97	0.103E-01±0.190E-03±0.497E-03	0.733
	0.99	0.109E-01±0.210E-03±0.524E-03	0.717
	1.01	0.107E-01±0.212E-03±0.513E-03	0.717
	1.03	0.935E-02±0.201E-03±0.451E-03	0.717
	1.05	0.703E-02±0.173E-03±0.339E-03	0.717
	1.07	0.522E-02±0.147E-03±0.251E-03	0.717
	1.09	0.417E-02±0.135E-03±0.201E-03	0.717
	1.11	0.300E-02±0.115E-03±0.145E-03	0.717
	1.13	0.214E-02±0.946E-04±0.103E-03	0.717
	1.15	0.160E-02±0.878E-04±0.772E-04	0.716
	1.17	0.139E-02±0.866E-04±0.671E-04	0.716
	1.19	0.982E-03±0.742E-04±0.474E-04	0.716
	1.21	0.639E-03±0.593E-04±0.308E-04	0.716
	1.23	0.608E-03±0.648E-04±0.293E-04	0.716
	1.25	0.630E-03±0.680E-04±0.304E-04	0.716
	1.27	0.343E-03±0.484E-04±0.165E-04	0.716
	1.29	0.293E-03±0.468E-04±0.141E-04	0.716
	1.31	0.291E-03±0.479E-04±0.140E-04	0.716
	1.33	0.284E-03±0.641E-04±0.137E-04	0.716
	1.35	0.122E-03±0.451E-04±0.589E-05	0.716
	1.37	0.157E-03±0.535E-04±0.756E-05	0.716
	1.39	0.112E-03±0.454E-04±0.542E-05	0.715
	1.41	0.691E-04±0.360E-04±0.333E-05	0.715
	1.43	0.745E-04±0.388E-04±0.359E-05	0.715
	1.45	0.758E-04±0.396E-04±0.365E-05	0.715
	1.47	0.785E-04±0.409E-04±0.378E-05	0.715
	1.49	0.194E-03±0.620E-04±0.935E-05	0.715
	1.51	0.862E-04±0.450E-04±0.416E-05	0.715
1.875	0.71	0.138E-01±0.147E-03±0.667E-03	0.867
	0.73	0.104E-01±0.118E-03±0.504E-03	0.853
	0.75	0.953E-02±0.113E-03±0.460E-03	0.843
	0.77	0.791E-02±0.103E-03±0.382E-03	0.840
	0.79	0.658E-02±0.940E-04±0.318E-03	0.846
	0.81	0.536E-02±0.830E-04±0.259E-03	0.863
	0.83	0.423E-02±0.717E-04±0.204E-03	0.883
	0.85	0.357E-02±0.639E-04±0.172E-03	0.906
	0.87	0.343E-02±0.618E-04±0.166E-03	0.913
	0.89	0.367E-02±0.666E-04±0.177E-03	0.903
	0.91	0.446E-02±0.786E-04±0.215E-03	0.868
	0.93	0.557E-02±0.954E-04±0.269E-03	0.819
	0.95	0.729E-02±0.121E-03±0.352E-03	0.775
	0.97	0.890E-02±0.146E-03±0.430E-03	0.734
	0.99	0.974E-02±0.162E-03±0.470E-03	0.718
	1.01	0.916E-02±0.159E-03±0.442E-03	0.717
	1.03	0.824E-02±0.152E-03±0.398E-03	0.717
	1.05	0.672E-02±0.135E-03±0.324E-03	0.717
	1.07	0.468E-02±0.108E-03±0.226E-03	0.717
	1.09	0.370E-02±0.953E-04±0.179E-03	0.717
	1.11	0.255E-02±0.769E-04±0.123E-03	0.717
	1.13	0.189E-02±0.655E-04±0.912E-04	0.717
	1.15	0.140E-02±0.558E-04±0.674E-04	0.716
	1.17	0.102E-02±0.472E-04±0.491E-04	0.716
	1.19	0.725E-03±0.396E-04±0.350E-04	0.716
	1.21	0.557E-03±0.346E-04±0.269E-04	0.716
	1.23	0.420E-03±0.296E-04±0.203E-04	0.716
	1.25	0.339E-03±0.266E-04±0.164E-04	0.716
	1.27	0.274E-03±0.240E-04±0.132E-04	0.716
	1.29	0.215E-03±0.215E-04±0.104E-04	0.716
	1.31	0.204E-03±0.210E-04±0.986E-05	0.716
	1.33	0.129E-03±0.169E-04±0.625E-05	0.716
	1.35	0.110E-03±0.158E-04±0.533E-05	0.716
	1.37	0.955E-04±0.148E-04±0.461E-05	0.715
	1.39	0.821E-04±0.143E-04±0.397E-05	0.715
	1.41	0.761E-04±0.140E-04±0.367E-05	0.715
	1.43	0.682E-04±0.138E-04±0.330E-05	0.715
	1.45	0.356E-04±0.102E-04±0.172E-05	0.715
	1.47	0.412E-04±0.112E-04±0.199E-05	0.715
	1.49	0.534E-04±0.129E-04±0.258E-05	0.715
	1.51	0.271E-04±0.926E-05±0.131E-05	0.715
	1.53	0.277E-04±0.946E-05±0.134E-05	0.715
	1.55	0.201E-04±0.128E-04±0.971E-06	0.715
	1.57	0.349E-04±0.119E-04±0.168E-05	0.715
	1.59	0.322E-04±0.119E-04±0.156E-05	0.715
	1.61	0.376E-04±0.120E-04±0.182E-05	0.715
	1.63	0.139E-04±0.725E-05±0.672E-06	0.715
	1.65	0.225E-04±0.911E-05±0.109E-05	0.715
	1.67	0.948E-05±0.606E-05±0.458E-06	0.715
	1.69	0.275E-04±0.101E-04±0.133E-05	0.715
	1.71	0.938E-05±0.599E-05±0.453E-06	0.714
	1.73	0.933E-05±0.596E-05±0.450E-06	0.714
	1.75	0.465E-05±0.420E-05±0.225E-06	0.714

	1.77	0.146E-04±0.760E-05±0.703E-06	0.714
	1.79	0.465E-05±0.420E-05±0.225E-06	0.714
	1.81	0.876E-05±0.560E-05±0.423E-06	0.714
	1.83	0.836E-05±0.534E-05±0.404E-06	0.714
	1.85	0.429E-05±0.388E-05±0.207E-06	0.714
	1.89	0.717E-05±0.458E-05±0.346E-06	0.714
1.925	0.71	0.130E-01±0.131E-03±0.632E-03	0.870
	0.73	0.101E-01±0.107E-03±0.492E-03	0.856
	0.75	0.904E-02±0.101E-03±0.441E-03	0.845
	0.77	0.769E-02±0.932E-04±0.375E-03	0.840
	0.79	0.646E-02±0.856E-04±0.315E-03	0.845
	0.81	0.490E-02±0.725E-04±0.239E-03	0.858
	0.83	0.395E-02±0.635E-04±0.193E-03	0.878
	0.85	0.317E-02±0.544E-04±0.155E-03	0.903
	0.87	0.316E-02±0.546E-04±0.154E-03	0.915
	0.89	0.335E-02±0.587E-04±0.163E-03	0.897
	0.91	0.391E-02±0.667E-04±0.191E-03	0.863
	0.93	0.484E-02±0.794E-04±0.236E-03	0.827
	0.95	0.668E-02±0.104E-03±0.326E-03	0.778
	0.97	0.810E-02±0.124E-03±0.395E-03	0.735
	0.99	0.897E-02±0.140E-03±0.438E-03	0.718
	1.01	0.864E-02±0.139E-03±0.422E-03	0.717
	1.03	0.707E-02±0.124E-03±0.345E-03	0.717
	1.05	0.564E-02±0.110E-03±0.275E-03	0.717
	1.07	0.402E-02±0.890E-04±0.196E-03	0.717
	1.09	0.308E-02±0.767E-04±0.150E-03	0.717
	1.11	0.201E-02±0.596E-04±0.980E-04	0.717
	1.13	0.167E-02±0.546E-04±0.816E-04	0.717
	1.15	0.121E-02±0.456E-04±0.591E-04	0.717
	1.17	0.950E-03±0.400E-04±0.464E-04	0.716
	1.19	0.756E-03±0.349E-04±0.369E-04	0.716
	1.21	0.514E-03±0.287E-04±0.251E-04	0.716
	1.23	0.462E-03±0.276E-04±0.225E-04	0.716
	1.25	0.347E-03±0.229E-04±0.169E-04	0.716
	1.27	0.248E-03±0.201E-04±0.121E-04	0.716
	1.29	0.245E-03±0.198E-04±0.119E-04	0.716
	1.31	0.165E-03±0.153E-04±0.804E-05	0.716
	1.33	0.161E-03±0.168E-04±0.787E-05	0.716
	1.35	0.123E-03±0.137E-04±0.599E-05	0.716
	1.37	0.119E-03±0.140E-04±0.581E-05	0.715
	1.39	0.683E-04±0.952E-05±0.333E-05	0.715
	1.41	0.870E-04±0.126E-04±0.425E-05	0.715
	1.43	0.505E-04±0.807E-05±0.247E-05	0.715
	1.45	0.445E-04±0.788E-05±0.217E-05	0.715
	1.47	0.324E-04±0.671E-05±0.158E-05	0.715
	1.49	0.234E-04±0.585E-05±0.114E-05	0.715
	1.51	0.484E-04±0.827E-05±0.236E-05	0.715
	1.53	0.333E-04±0.708E-05±0.162E-05	0.715
	1.55	0.138E-04±0.416E-05±0.675E-06	0.715
	1.57	0.269E-04±0.589E-05±0.131E-05	0.715
	1.59	0.191E-04±0.499E-05±0.934E-06	0.715
	1.61	0.141E-04±0.368E-05±0.689E-06	0.715
	1.63	0.102E-04±0.376E-05±0.497E-06	0.715
	1.65	0.126E-04±0.508E-05±0.614E-06	0.715
	1.67	0.148E-04±0.445E-05±0.722E-06	0.715
	1.69	0.186E-04±0.687E-05±0.908E-06	0.714
	1.71	0.544E-05±0.284E-05±0.266E-06	0.714
	1.73	0.555E-05±0.289E-05±0.271E-06	0.714
	1.75	0.804E-05±0.363E-05±0.392E-06	0.714
	1.77	0.188E-05±0.170E-05±0.919E-07	0.714
	1.79	0.378E-05±0.242E-05±0.185E-06	0.714
	1.81	0.933E-05±0.377E-05±0.455E-06	0.714
	1.83	0.187E-05±0.169E-05±0.911E-07	0.714
	1.87	0.187E-05±0.169E-05±0.913E-07	0.714
1.975	0.71	0.115E-01±0.114E-03±0.559E-03	0.872
	0.73	0.904E-02±0.937E-04±0.440E-03	0.859
	0.75	0.805E-02±0.879E-04±0.392E-03	0.848
	0.77	0.730E-02±0.844E-04±0.356E-03	0.841
	0.79	0.616E-02±0.771E-04±0.300E-03	0.843
	0.81	0.467E-02±0.655E-04±0.228E-03	0.857
	0.83	0.388E-02±0.589E-04±0.189E-03	0.874
	0.85	0.316E-02±0.508E-04±0.154E-03	0.897
	0.87	0.297E-02±0.485E-04±0.144E-03	0.911
	0.89	0.313E-02±0.512E-04±0.152E-03	0.904
	0.91	0.356E-02±0.569E-04±0.173E-03	0.864
	0.93	0.466E-02±0.705E-04±0.227E-03	0.826
	0.95	0.595E-02±0.879E-04±0.290E-03	0.781
	0.97	0.715E-02±0.106E-03±0.348E-03	0.735
	0.99	0.798E-02±0.117E-03±0.389E-03	0.718
	1.01	0.725E-02±0.112E-03±0.353E-03	0.718
	1.03	0.638E-02±0.104E-03±0.310E-03	0.717
	1.05	0.481E-02±0.893E-04±0.234E-03	0.717
	1.07	0.376E-02±0.782E-04±0.183E-03	0.717
	1.09	0.268E-02±0.639E-04±0.130E-03	0.717
	1.11	0.191E-02±0.528E-04±0.928E-04	0.717
	1.13	0.140E-02±0.448E-04±0.681E-04	0.717
	1.15	0.100E-02±0.368E-04±0.488E-04	0.717
	1.17	0.777E-03±0.329E-04±0.379E-04	0.716
	1.19	0.562E-03±0.279E-04±0.274E-04	0.716
	1.21	0.438E-03±0.242E-04±0.213E-04	0.716
	1.23	0.305E-03±0.205E-04±0.148E-04	0.716
	1.25	0.285E-03±0.195E-04±0.139E-04	0.716
	1.27	0.241E-03±0.187E-04±0.117E-04	0.716
	1.29	0.159E-03±0.143E-04±0.776E-05	0.716
	1.31	0.135E-03±0.135E-04±0.656E-05	0.716
	1.33	0.117E-03±0.124E-04±0.572E-05	0.716
	1.35	0.123E-03±0.134E-04±0.600E-05	0.716
	1.37	0.764E-04±0.104E-04±0.372E-05	0.715
	1.39	0.691E-04±0.930E-05±0.336E-05	0.715
	1.41	0.531E-04±0.862E-05±0.259E-05	0.715
	1.43	0.332E-04±0.654E-05±0.161E-05	0.715
	1.45	0.374E-04±0.738E-05±0.182E-05	0.715
	1.47	0.458E-04±0.768E-05±0.223E-05	0.715
	1.49	0.329E-04±0.648E-05±0.160E-05	0.715
	1.51	0.297E-04±0.616E-05±0.145E-05	0.715
	1.53	0.455E-04±0.807E-05±0.222E-05	0.715
	1.55	0.328E-04±0.699E-05±0.160E-05	0.715
	1.57	0.197E-04±0.514E-05±0.960E-06	0.715
	1.59	0.235E-04±0.588E-05±0.114E-05	0.715
	1.61	0.184E-04±0.481E-05±0.898E-06	0.715
	1.63	0.185E-04±0.505E-05±0.903E-06	0.715
	1.65	0.151E-04±0.456E-05±0.738E-06	0.715
	1.67	0.110E-04±0.404E-05±0.534E-06	0.714
	1.69	0.169E-04±0.510E-05±0.825E-06	0.714
	1.71	0.794E-05±0.359E-05±0.387E-06	0.714
	1.73	0.760E-05±0.280E-05±0.370E-06	0.714
	1.75	0.977E-05±0.312E-05±0.476E-06	0.714
	1.77	0.633E-05±0.286E-05±0.308E-06	0.714
	1.79	0.791E-05±0.292E-05±0.385E-06	0.714
	1.81	0.728E-05±0.294E-05±0.355E-06	0.714
	1.83	0.488E-05±0.221E-05±0.238E-06	0.714
	1.85	0.346E-05±0.180E-05±0.169E-06	0.714
	1.87	0.319E-05±0.167E-05±0.156E-06	0.714
	1.89	0.372E-05±0.194E-05±0.181E-06	0.714
	1.91	0.132E-05±0.119E-05±0.642E-07	0.714
	1.93	0.620E-05±0.250E-05±0.302E-06	0.714
2.025	0.71	0.108E-01±0.103E-03±0.527E-03	0.874
	0.73	0.826E-02±0.829E-04±0.404E-03	0.862
	0.75	0.782E-02±0.822E-04±0.383E-03	0.850
	0.77	0.697E-02±0.776E-04±0.341E-03	0.842

	0.79	0.563E-02±0.700E-04±0.275E-03	0.843
	0.81	0.469E-02±0.631E-04±0.229E-03	0.852
	0.83	0.363E-02±0.537E-04±0.178E-03	0.871
	0.85	0.304E-02±0.468E-04±0.149E-03	0.891
	0.87	0.279E-02±0.451E-04±0.136E-03	0.904
	0.89	0.291E-02±0.464E-04±0.142E-03	0.898
	0.91	0.343E-02±0.531E-04±0.168E-03	0.865
	0.93	0.458E-02±0.669E-04±0.224E-03	0.825
	0.95	0.561E-02±0.797E-04±0.275E-03	0.786
	0.97	0.725E-02±0.998E-04±0.355E-03	0.736
	0.99	0.773E-02±0.108E-03±0.378E-03	0.718
	1.01	0.655E-02±0.988E-04±0.320E-03	0.718
	1.03	0.580E-02±0.935E-04±0.283E-03	0.717
	1.05	0.461E-02±0.809E-04±0.225E-03	0.717
	1.07	0.317E-02±0.645E-04±0.155E-03	0.717
	1.09	0.233E-02±0.547E-04±0.114E-03	0.717
	1.11	0.157E-02±0.430E-04±0.769E-04	0.717
	1.13	0.122E-02±0.376E-04±0.594E-04	0.717
	1.15	0.981E-03±0.346E-04±0.480E-04	0.717
	1.17	0.740E-03±0.302E-04±0.362E-04	0.716
	1.19	0.601E-03±0.271E-04±0.294E-04	0.716
	1.21	0.415E-03±0.220E-04±0.203E-04	0.716
	1.23	0.303E-03±0.182E-04±0.148E-04	0.716
	1.25	0.255E-03±0.167E-04±0.125E-04	0.716
	1.27	0.191E-03±0.144E-04±0.933E-05	0.716
	1.29	0.173E-03±0.147E-04±0.847E-05	0.716
	1.31	0.113E-03±0.110E-04±0.551E-05	0.716
	1.33	0.117E-03±0.114E-04±0.573E-05	0.716
	1.35	0.101E-03±0.109E-04±0.493E-05	0.716
	1.37	0.924E-04±0.105E-04±0.452E-05	0.715
	1.39	0.814E-04±0.983E-05±0.398E-05	0.715
	1.41	0.429E-04±0.637E-05±0.210E-05	0.715
	1.43	0.404E-04±0.678E-05±0.198E-05	0.715
	1.45	0.372E-04±0.686E-05±0.182E-05	0.715
	1.47	0.298E-04±0.561E-05±0.146E-05	0.715
	1.49	0.388E-04±0.700E-05±0.189E-05	0.715
	1.51	0.274E-04±0.568E-05±0.134E-05	0.715
	1.53	0.188E-04±0.470E-05±0.917E-06	0.715
	1.55	0.308E-04±0.695E-05±0.150E-05	0.715
	1.57	0.137E-04±0.436E-05±0.668E-06	0.715
	1.59	0.208E-04±0.566E-05±0.102E-05	0.715
	1.61	0.118E-04±0.434E-05±0.575E-06	0.715
	1.63	0.104E-04±0.354E-05±0.507E-06	0.715
	1.65	0.121E-04±0.386E-05±0.590E-06	0.715
	1.67	0.941E-05±0.380E-05±0.460E-06	0.714
	1.69	0.152E-04±0.486E-05±0.744E-06	0.714
	1.71	0.776E-05±0.313E-05±0.379E-06	0.714
	1.73	0.803E-05±0.363E-05±0.393E-06	0.714
	1.75	0.122E-04±0.451E-05±0.598E-06	0.714
	1.77	0.108E-04±0.398E-05±0.527E-06	0.714
	1.79	0.166E-05±0.150E-05±0.812E-07	0.714
	1.81	0.408E-05±0.261E-05±0.200E-06	0.714
	1.83	0.539E-05±0.281E-05±0.264E-06	0.714
	1.85	0.498E-05±0.260E-05±0.244E-06	0.714
	1.87	0.816E-05±0.369E-05±0.399E-06	0.714
	1.91	0.166E-05±0.150E-05±0.812E-07	0.714
2.075	0.71	0.996E-02±0.946E-04±0.491E-03	0.876
	0.73	0.766E-02±0.759E-04±0.378E-03	0.864
	0.75	0.709E-02±0.732E-04±0.349E-03	0.853
	0.77	0.634E-02±0.701E-04±0.313E-03	0.843
	0.79	0.537E-02±0.648E-04±0.265E-03	0.843
	0.81	0.430E-02±0.566E-04±0.212E-03	0.851
	0.83	0.347E-02±0.501E-04±0.171E-03	0.867
	0.85	0.290E-02±0.441E-04±0.143E-03	0.889
	0.87	0.263E-02±0.418E-04±0.130E-03	0.898

	0.89	0.264E-02±0.418E-04±0.130E-03	0.902
	0.91	0.306E-02±0.470E-04±0.151E-03	0.869
	0.93	0.376E-02±0.560E-04±0.185E-03	0.834
	0.95	0.509E-02±0.722E-04±0.251E-03	0.781
	0.97	0.644E-02±0.887E-04±0.317E-03	0.740
	0.99	0.693E-02±0.971E-04±0.342E-03	0.718
	1.01	0.663E-02±0.959E-04±0.327E-03	0.718
	1.03	0.504E-02±0.816E-04±0.248E-03	0.718
	1.05	0.398E-02±0.702E-04±0.196E-03	0.717
	1.07	0.273E-02±0.568E-04±0.135E-03	0.717
	1.09	0.193E-02±0.461E-04±0.953E-04	0.717
	1.11	0.133E-02±0.372E-04±0.656E-04	0.717
	1.13	0.102E-02±0.325E-04±0.503E-04	0.717
	1.15	0.745E-03±0.276E-04±0.367E-04	0.717
	1.17	0.563E-03±0.233E-04±0.277E-04	0.717
	1.19	0.403E-03±0.194E-04±0.199E-04	0.716
	1.21	0.306E-03±0.181E-04±0.151E-04	0.716
	1.23	0.223E-03±0.140E-04±0.110E-04	0.716
	1.25	0.173E-03±0.122E-04±0.853E-05	0.716
	1.27	0.173E-03±0.127E-04±0.851E-05	0.716
	1.29	0.112E-03±0.921E-05±0.551E-05	0.716
	1.31	0.110E-03±0.102E-04±0.543E-05	0.716
	1.33	0.884E-04±0.857E-05±0.436E-05	0.716
	1.35	0.546E-04±0.671E-05±0.269E-05	0.716
	1.37	0.423E-04±0.558E-05±0.209E-05	0.716
	1.39	0.409E-04±0.585E-05±0.202E-05	0.715
	1.41	0.301E-04±0.459E-05±0.148E-05	0.715
	1.43	0.454E-04±0.605E-05±0.224E-05	0.715
	1.45	0.466E-04±0.657E-05±0.230E-05	0.715
	1.47	0.264E-04±0.477E-05±0.130E-05	0.715
	1.49	0.304E-04±0.494E-05±0.150E-05	0.715
	1.51	0.207E-04±0.442E-05±0.102E-05	0.715
	1.53	0.232E-04±0.411E-05±0.114E-05	0.715
	1.55	0.172E-04±0.400E-05±0.846E-06	0.715
	1.57	0.171E-04±0.375E-05±0.843E-06	0.715
	1.59	0.115E-04±0.346E-05±0.566E-06	0.715
	1.61	0.173E-04±0.432E-05±0.851E-06	0.715
	1.63	0.117E-04±0.401E-05±0.579E-06	0.715
	1.65	0.115E-04±0.393E-05±0.567E-06	0.715
	1.67	0.109E-04±0.402E-05±0.538E-06	0.714
	1.69	0.986E-05±0.364E-05±0.486E-06	0.714
	1.71	0.135E-04±0.431E-05±0.665E-06	0.714
	1.73	0.113E-04±0.385E-05±0.556E-06	0.714
	1.75	0.179E-04±0.488E-05±0.883E-06	0.714
	1.77	0.101E-04±0.373E-05±0.499E-06	0.714
	1.79	0.161E-05±0.146E-05±0.795E-07	0.714
	1.81	0.977E-05±0.360E-05±0.482E-06	0.714
2.125	0.71	0.900E-02±0.855E-04±0.447E-03	0.877
	0.73	0.693E-02±0.683E-04±0.344E-03	0.867
	0.75	0.668E-02±0.685E-04±0.332E-03	0.855
	0.77	0.587E-02±0.642E-04±0.292E-03	0.846
	0.79	0.503E-02±0.590E-04±0.250E-03	0.842
	0.81	0.414E-02±0.537E-04±0.206E-03	0.849
	0.83	0.349E-02±0.481E-04±0.174E-03	0.863
	0.85	0.285E-02±0.431E-04±0.142E-03	0.884
	0.87	0.259E-02±0.403E-04±0.128E-03	0.896
	0.89	0.249E-02±0.392E-04±0.124E-03	0.897
	0.91	0.275E-02±0.427E-04±0.137E-03	0.875
	0.93	0.353E-02±0.519E-04±0.176E-03	0.836
	0.95	0.478E-02±0.670E-04±0.238E-03	0.787
	0.97	0.586E-02±0.810E-04±0.291E-03	0.739
	0.99	0.632E-02±0.876E-04±0.314E-03	0.718
	1.01	0.562E-02±0.826E-04±0.279E-03	0.718
	1.03	0.492E-02±0.773E-04±0.245E-03	0.718
	1.05	0.391E-02±0.681E-04±0.195E-03	0.717

	1.07	0.271E-02±0.541E-04±0.134E-03	0.717
	1.09	0.193E-02±0.443E-04±0.962E-04	0.717
	1.11	0.137E-02±0.360E-04±0.682E-04	0.717
	1.13	0.105E-02±0.320E-04±0.522E-04	0.717
	1.15	0.714E-03±0.255E-04±0.355E-04	0.717
	1.17	0.520E-03±0.219E-04±0.259E-04	0.717
	1.19	0.410E-03±0.187E-04±0.204E-04	0.716
	1.21	0.308E-03±0.162E-04±0.153E-04	0.716
	1.23	0.252E-03±0.147E-04±0.125E-04	0.716
	1.25	0.168E-03±0.118E-04±0.833E-05	0.716
	1.27	0.148E-03±0.109E-04±0.735E-05	0.716
	1.29	0.119E-03±0.983E-05±0.590E-05	0.716
	1.31	0.103E-03±0.944E-05±0.514E-05	0.716
	1.33	0.785E-04±0.831E-05±0.390E-05	0.716
	1.35	0.537E-04±0.637E-05±0.267E-05	0.716
	1.37	0.546E-04±0.653E-05±0.271E-05	0.716
	1.39	0.347E-04±0.473E-05±0.173E-05	0.715
	1.41	0.361E-04±0.503E-05±0.179E-05	0.715
	1.43	0.375E-04±0.550E-05±0.186E-05	0.715
	1.45	0.289E-04±0.477E-05±0.144E-05	0.715
	1.47	0.217E-04±0.392E-05±0.108E-05	0.715
	1.49	0.276E-04±0.490E-05±0.137E-05	0.715
	1.51	0.214E-04±0.404E-05±0.107E-05	0.715
	1.53	0.199E-04±0.384E-05±0.991E-06	0.715
	1.55	0.135E-04±0.351E-05±0.669E-06	0.715
	1.57	0.162E-04±0.377E-05±0.803E-06	0.715
	1.59	0.124E-04±0.300E-05±0.617E-06	0.715
	1.61	0.138E-04±0.323E-05±0.687E-06	0.715
	1.63	0.143E-04±0.344E-05±0.708E-06	0.715
	1.65	0.106E-04±0.287E-05±0.525E-06	0.715
	1.67	0.110E-04±0.287E-05±0.547E-06	0.714
	1.69	0.572E-05±0.211E-05±0.284E-06	0.714
	1.71	0.722E-05±0.231E-05±0.359E-06	0.714
	1.73	0.628E-05±0.215E-05±0.312E-06	0.714
	1.75	0.573E-05±0.211E-05±0.285E-06	0.714
	1.77	0.361E-05±0.163E-05±0.179E-06	0.714
	1.79	0.718E-05±0.229E-05±0.357E-06	0.714
	1.81	0.286E-05±0.149E-05±0.142E-06	0.714
2.175	0.71	0.821E-02±0.784E-04±0.412E-03	0.879
	0.73	0.636E-02±0.632E-04±0.319E-03	0.870
	0.75	0.577E-02±0.602E-04±0.290E-03	0.858
	0.77	0.541E-02±0.596E-04±0.272E-03	0.847
	0.79	0.480E-02±0.561E-04±0.241E-03	0.843
	0.81	0.392E-02±0.501E-04±0.197E-03	0.846
	0.83	0.318E-02±0.445E-04±0.160E-03	0.860
	0.85	0.270E-02±0.401E-04±0.135E-03	0.879
	0.87	0.229E-02±0.356E-04±0.115E-03	0.894
	0.89	0.224E-02±0.356E-04±0.113E-03	0.896
	0.91	0.249E-02±0.388E-04±0.125E-03	0.874
	0.93	0.318E-02±0.468E-04±0.159E-03	0.829
	0.95	0.398E-02±0.577E-04±0.200E-03	0.789
	0.97	0.528E-02±0.725E-04±0.265E-03	0.743
	0.99	0.524E-02±0.737E-04±0.263E-03	0.718
	1.01	0.517E-02±0.738E-04±0.260E-03	0.718
	1.03	0.424E-02±0.674E-04±0.213E-03	0.718
	1.05	0.328E-02±0.577E-04±0.165E-03	0.718
	1.07	0.233E-02±0.474E-04±0.117E-03	0.717
	1.09	0.160E-02±0.392E-04±0.805E-04	0.717
	1.11	0.119E-02±0.332E-04±0.596E-04	0.717
	1.13	0.919E-03±0.283E-04±0.461E-04	0.717
	1.15	0.617E-03±0.227E-04±0.310E-04	0.717
	1.17	0.504E-03±0.208E-04±0.253E-04	0.717
	1.19	0.358E-03±0.172E-04±0.180E-04	0.717
	1.21	0.293E-03±0.158E-04±0.147E-04	0.716
	1.23	0.208E-03±0.129E-04±0.104E-04	0.716

	1.25	0.197E-03±0.125E-04±0.991E-05	0.716
	1.27	0.138E-03±0.101E-04±0.691E-05	0.716
	1.29	0.129E-03±0.108E-04±0.649E-05	0.716
	1.31	0.944E-04±0.861E-05±0.474E-05	0.716
	1.33	0.923E-04±0.864E-05±0.463E-05	0.716
	1.35	0.556E-04±0.653E-05±0.279E-05	0.716
	1.37	0.481E-04±0.603E-05±0.242E-05	0.716
	1.39	0.449E-04±0.562E-05±0.225E-05	0.715
	1.41	0.281E-04±0.456E-05±0.141E-05	0.715
	1.43	0.352E-04±0.516E-05±0.177E-05	0.715
	1.45	0.287E-04±0.458E-05±0.144E-05	0.715
	1.47	0.163E-04±0.347E-05±0.819E-06	0.715
	1.49	0.890E-05±0.242E-05±0.447E-06	0.715
	1.51	0.127E-04±0.296E-05±0.637E-06	0.715
	1.53	0.136E-04±0.328E-05±0.682E-06	0.715
	1.55	0.986E-05±0.269E-05±0.495E-06	0.715
	1.57	0.164E-04±0.359E-05±0.823E-06	0.715
	1.59	0.152E-04±0.332E-05±0.761E-06	0.715
	1.61	0.691E-05±0.221E-05±0.347E-06	0.715
	1.63	0.683E-05±0.233E-05±0.343E-06	0.715
	1.65	0.359E-05±0.162E-05±0.180E-06	0.715
	1.67	0.508E-05±0.187E-05±0.255E-06	0.714
	1.69	0.181E-05±0.116E-05±0.911E-07	0.714
	1.71	0.432E-05±0.175E-05±0.217E-06	0.714
	1.73	0.879E-05±0.265E-05±0.441E-06	0.714
	1.75	0.269E-05±0.140E-05±0.135E-06	0.714
	1.77	0.339E-05±0.153E-05±0.170E-06	0.714
	1.79	0.454E-05±0.183E-05±0.228E-06	0.714
2.225	0.71	0.742E-02±0.745E-04±0.375E-03	0.880
	0.73	0.572E-02±0.580E-04±0.289E-03	0.871
	0.75	0.540E-02±0.566E-04±0.273E-03	0.860
	0.77	0.506E-02±0.560E-04±0.256E-03	0.849
	0.79	0.431E-02±0.515E-04±0.218E-03	0.844
	0.81	0.364E-02±0.472E-04±0.184E-03	0.847
	0.83	0.291E-02±0.415E-04±0.147E-03	0.858
	0.85	0.240E-02±0.363E-04±0.121E-03	0.875
	0.87	0.211E-02±0.334E-04±0.107E-03	0.891
	0.89	0.196E-02±0.322E-04±0.992E-04	0.896
	0.91	0.224E-02±0.354E-04±0.113E-03	0.873
	0.93	0.291E-02±0.433E-04±0.147E-03	0.835
	0.95	0.376E-02±0.531E-04±0.190E-03	0.791
	0.97	0.473E-02±0.657E-04±0.239E-03	0.742
	0.99	0.521E-02±0.724E-04±0.264E-03	0.718
	1.01	0.471E-02±0.691E-04±0.238E-03	0.718
	1.03	0.382E-02±0.600E-04±0.193E-03	0.718
	1.05	0.319E-02±0.545E-04±0.161E-03	0.718
	1.07	0.222E-02±0.436E-04±0.112E-03	0.718
	1.09	0.156E-02±0.357E-04±0.790E-04	0.717
	1.11	0.112E-02±0.295E-04±0.567E-04	0.717
	1.13	0.799E-03±0.247E-04±0.404E-04	0.717
	1.15	0.579E-03±0.205E-04±0.293E-04	0.717
	1.17	0.431E-03±0.179E-04±0.218E-04	0.717
	1.19	0.314E-03±0.155E-04±0.159E-04	0.717
	1.21	0.239E-03±0.133E-04±0.121E-04	0.717
	1.23	0.213E-03±0.135E-04±0.108E-04	0.716
	1.25	0.170E-03±0.111E-04±0.860E-05	0.716
	1.27	0.132E-03±0.977E-05±0.668E-05	0.716
	1.29	0.102E-03±0.841E-05±0.516E-05	0.716
	1.31	0.861E-04±0.755E-05±0.436E-05	0.716
	1.33	0.681E-04±0.684E-05±0.345E-05	0.716
	1.35	0.634E-04±0.684E-05±0.321E-05	0.716
	1.37	0.543E-04±0.639E-05±0.275E-05	0.716
	1.39	0.348E-04±0.492E-05±0.176E-05	0.716
	1.41	0.335E-04±0.498E-05±0.170E-05	0.715
	1.43	0.282E-04±0.430E-05±0.143E-05	0.715

	1.45	0.289E-04±0.477E-05±0.146E-05	0.715
	1.47	0.264E-04±0.443E-05±0.134E-05	0.715
	1.49	0.137E-04±0.311E-05±0.696E-06	0.715
	1.51	0.197E-04±0.370E-05±0.995E-06	0.715
	1.53	0.196E-04±0.378E-05±0.993E-06	0.715
	1.55	0.117E-04±0.283E-05±0.594E-06	0.715
	1.57	0.127E-04±0.318E-05±0.642E-06	0.715
	1.59	0.493E-05±0.257E-05±0.249E-06	0.715
	1.61	0.425E-05±0.172E-05±0.215E-06	0.715
	1.63	0.917E-05±0.262E-05±0.464E-06	0.715
	1.65	0.590E-05±0.201E-05±0.298E-06	0.715
	1.67	0.346E-05±0.156E-05±0.175E-06	0.714
	1.69	0.605E-05±0.207E-05±0.306E-06	0.714
	1.71	0.419E-05±0.169E-05±0.212E-06	0.714
	1.73	0.488E-05±0.197E-05±0.247E-06	0.714
	1.75	0.917E-06±0.829E-06±0.464E-07	0.714
	1.77	0.596E-05±0.204E-05±0.302E-06	0.714
	1.79	0.367E-05±0.166E-05±0.186E-06	0.714
	1.81	0.253E-05±0.132E-05±0.128E-06	0.714
	1.83	0.260E-05±0.135E-05±0.131E-06	0.714
2.275	0.71	0.700E-02±0.744E-04±0.358E-03	0.880
	0.73	0.527E-02±0.581E-04±0.269E-03	0.873
	0.75	0.490E-02±0.553E-04±0.250E-03	0.862
	0.77	0.468E-02±0.535E-04±0.239E-03	0.852
	0.79	0.407E-02±0.493E-04±0.208E-03	0.844
	0.81	0.350E-02±0.453E-04±0.179E-03	0.847
	0.83	0.284E-02±0.400E-04±0.145E-03	0.856
	0.85	0.231E-02±0.350E-04±0.118E-03	0.875
	0.87	0.201E-02±0.318E-04±0.103E-03	0.891
	0.89	0.193E-02±0.309E-04±0.988E-04	0.888
	0.91	0.217E-02±0.342E-04±0.111E-03	0.875
	0.93	0.251E-02±0.391E-04±0.128E-03	0.838
	0.95	0.325E-02±0.480E-04±0.166E-03	0.788
	0.97	0.408E-02±0.586E-04±0.208E-03	0.745
	0.99	0.427E-02±0.622E-04±0.218E-03	0.718
	1.01	0.412E-02±0.619E-04±0.210E-03	0.718
	1.03	0.335E-02±0.548E-04±0.171E-03	0.718
	1.05	0.262E-02±0.473E-04±0.134E-03	0.718
	1.07	0.190E-02±0.392E-04±0.971E-04	0.718
	1.09	0.134E-02±0.323E-04±0.683E-04	0.718
	1.11	0.987E-03±0.270E-04±0.504E-04	0.717
	1.13	0.739E-03±0.235E-04±0.378E-04	0.717
	1.15	0.582E-03±0.213E-04±0.298E-04	0.717
	1.17	0.411E-03±0.171E-04±0.210E-04	0.717
	1.19	0.321E-03±0.151E-04±0.164E-04	0.717
	1.21	0.234E-03±0.125E-04±0.120E-04	0.717
	1.23	0.185E-03±0.109E-04±0.947E-05	0.716
	1.25	0.158E-03±0.102E-04±0.809E-05	0.716
	1.27	0.116E-03±0.870E-05±0.593E-05	0.716
	1.29	0.959E-04±0.787E-05±0.490E-05	0.716
	1.31	0.754E-04±0.677E-05±0.385E-05	0.716
	1.33	0.459E-04±0.531E-05±0.235E-05	0.716
	1.35	0.583E-04±0.629E-05±0.298E-05	0.716
	1.37	0.445E-04±0.542E-05±0.227E-05	0.716
	1.39	0.421E-04±0.543E-05±0.215E-05	0.716
	1.41	0.273E-04±0.390E-05±0.139E-05	0.716
	1.43	0.238E-04±0.368E-05±0.122E-05	0.715
	1.45	0.231E-04±0.382E-05±0.118E-05	0.715
	1.47	0.222E-04±0.372E-05±0.113E-05	0.715
	1.49	0.120E-04±0.264E-05±0.616E-06	0.715
	1.51	0.163E-04±0.307E-05±0.833E-06	0.715
	1.53	0.149E-04±0.302E-05±0.764E-06	0.715
	1.55	0.153E-04±0.295E-05±0.784E-06	0.715
	1.57	0.109E-04±0.255E-05±0.558E-06	0.715
	1.59	0.851E-05±0.222E-05±0.435E-06	0.715

	1.61	0.600E-05±0.181E-05±0.306E-06	0.715
	1.63	0.476E-05±0.163E-05±0.243E-06	0.715
	1.65	0.523E-05±0.179E-05±0.267E-06	0.715
	1.67	0.279E-05±0.126E-05±0.143E-06	0.715
	1.69	0.582E-05±0.186E-05±0.298E-06	0.714
	1.71	0.568E-05±0.181E-05±0.290E-06	0.714
	1.73	0.400E-05±0.148E-05±0.204E-06	0.714
	1.75	0.476E-05±0.163E-05±0.243E-06	0.714
	1.77	0.667E-06±0.602E-06±0.341E-07	0.714
	1.79	0.340E-05±0.137E-05±0.174E-06	0.714
	1.81	0.667E-06±0.603E-06±0.341E-07	0.714
2.325	0.71	0.651E-02±0.694E-04±0.336E-03	0.879
	0.73	0.484E-02±0.540E-04±0.250E-03	0.873
	0.75	0.456E-02±0.533E-04±0.236E-03	0.863
	0.77	0.415E-02±0.514E-04±0.214E-03	0.853
	0.79	0.374E-02±0.489E-04±0.193E-03	0.846
	0.81	0.334E-02±0.466E-04±0.172E-03	0.845
	0.83	0.267E-02±0.397E-04±0.138E-03	0.856
	0.85	0.212E-02±0.338E-04±0.109E-03	0.869
	0.87	0.183E-02±0.296E-04±0.943E-04	0.886
	0.89	0.175E-02±0.288E-04±0.901E-04	0.895
	0.91	0.203E-02±0.320E-04±0.105E-03	0.871
	0.93	0.243E-02±0.370E-04±0.125E-03	0.842
	0.95	0.315E-02±0.460E-04±0.162E-03	0.792
	0.97	0.376E-02±0.537E-04±0.194E-03	0.746
	0.99	0.400E-02±0.586E-04±0.206E-03	0.719
	1.01	0.374E-02±0.578E-04±0.193E-03	0.718
	1.03	0.311E-02±0.512E-04±0.161E-03	0.718
	1.05	0.232E-02±0.433E-04±0.120E-03	0.718
	1.07	0.180E-02±0.373E-04±0.927E-04	0.718
	1.09	0.118E-02±0.295E-04±0.607E-04	0.718
	1.11	0.916E-03±0.255E-04±0.473E-04	0.717
	1.13	0.578E-03±0.200E-04±0.298E-04	0.717
	1.15	0.450E-03±0.174E-04±0.232E-04	0.717
	1.17	0.316E-03±0.143E-04±0.163E-04	0.717
	1.19	0.277E-03±0.139E-04±0.143E-04	0.717
	1.21	0.217E-03±0.121E-04±0.112E-04	0.717
	1.23	0.166E-03±0.101E-04±0.858E-05	0.717
	1.25	0.141E-03±0.986E-05±0.728E-05	0.716
	1.27	0.929E-04±0.815E-05±0.479E-05	0.716
	1.29	0.789E-04±0.747E-05±0.407E-05	0.716
	1.31	0.621E-04±0.623E-05±0.320E-05	0.716
	1.33	0.583E-04±0.608E-05±0.301E-05	0.716
	1.35	0.458E-04±0.549E-05±0.237E-05	0.716
	1.37	0.389E-04±0.497E-05±0.201E-05	0.716
	1.39	0.302E-04±0.437E-05±0.156E-05	0.716
	1.41	0.271E-04±0.408E-05±0.140E-05	0.716
	1.43	0.252E-04±0.409E-05±0.130E-05	0.715
	1.45	0.138E-04±0.303E-05±0.713E-06	0.715
	1.47	0.240E-04±0.403E-05±0.124E-05	0.715
	1.49	0.133E-04±0.269E-05±0.687E-06	0.715
	1.51	0.146E-04±0.302E-05±0.753E-06	0.715
	1.53	0.154E-04±0.304E-05±0.795E-06	0.715
	1.55	0.105E-04±0.262E-05±0.540E-06	0.715
	1.57	0.560E-05±0.179E-05±0.289E-06	0.715
	1.59	0.601E-05±0.192E-05±0.310E-06	0.715
	1.61	0.590E-05±0.188E-05±0.304E-06	0.715
	1.63	0.661E-05±0.199E-05±0.341E-06	0.715
	1.65	0.806E-05±0.230E-05±0.416E-06	0.715
	1.67	0.280E-05±0.127E-05±0.145E-06	0.715
	1.69	0.526E-05±0.180E-05±0.271E-06	0.714
	1.71	0.295E-05±0.133E-05±0.152E-06	0.714
	1.73	0.441E-05±0.163E-05±0.227E-06	0.714
	1.75	0.161E-05±0.103E-05±0.832E-07	0.714
	1.77	0.350E-05±0.142E-05±0.181E-06	0.714

	1.79	0.301E-05±0.136E-05±0.155E-06	0.714
	1.81	0.148E-05±0.943E-06±0.762E-07	0.714
2.375	0.71	0.560E-02±0.673E-04±0.292E-03	0.880
	0.73	0.429E-02±0.528E-04±0.223E-03	0.875
	0.75	0.401E-02±0.495E-04±0.209E-03	0.865
	0.77	0.385E-02±0.485E-04±0.200E-03	0.855
	0.79	0.351E-02±0.462E-04±0.183E-03	0.847
	0.81	0.321E-02±0.451E-04±0.167E-03	0.846
	0.83	0.256E-02±0.395E-04±0.133E-03	0.853
	0.85	0.211E-02±0.354E-04±0.110E-03	0.870
	0.87	0.172E-02±0.307E-04±0.894E-04	0.882
	0.89	0.167E-02±0.298E-04±0.870E-04	0.886
	0.91	0.183E-02±0.311E-04±0.956E-04	0.868
	0.93	0.219E-02±0.349E-04±0.114E-03	0.840
	0.95	0.282E-02±0.418E-04±0.147E-03	0.799
	0.97	0.348E-02±0.505E-04±0.181E-03	0.747
	0.99	0.373E-02±0.552E-04±0.194E-03	0.719
	1.01	0.335E-02±0.525E-04±0.175E-03	0.719
	1.03	0.269E-02±0.460E-04±0.140E-03	0.718
	1.05	0.205E-02±0.389E-04±0.107E-03	0.718
	1.07	0.152E-02±0.330E-04±0.792E-04	0.718
	1.09	0.106E-02±0.265E-04±0.552E-04	0.718
	1.11	0.838E-03±0.240E-04±0.437E-04	0.718
	1.13	0.533E-03±0.186E-04±0.278E-04	0.717
	1.15	0.495E-03±0.184E-04±0.258E-04	0.717
	1.17	0.316E-03±0.143E-04±0.164E-04	0.717
	1.19	0.234E-03±0.119E-04±0.122E-04	0.717
	1.21	0.175E-03±0.107E-04±0.912E-05	0.717
	1.23	0.158E-03±0.103E-04±0.824E-05	0.717
	1.25	0.114E-03±0.847E-05±0.592E-05	0.717
	1.27	0.821E-04±0.666E-05±0.428E-05	0.716
	1.29	0.881E-04±0.743E-05±0.459E-05	0.716
	1.31	0.764E-04±0.664E-05±0.398E-05	0.716
	1.33	0.449E-04±0.519E-05±0.234E-05	0.716
	1.35	0.347E-04±0.435E-05±0.181E-05	0.716
	1.37	0.394E-04±0.489E-05±0.205E-05	0.716
	1.39	0.286E-04±0.436E-05±0.149E-05	0.716
	1.41	0.271E-04±0.414E-05±0.141E-05	0.716
	1.43	0.263E-04±0.396E-05±0.137E-05	0.716
	1.45	0.130E-04±0.270E-05±0.678E-06	0.715
	1.47	0.133E-04±0.291E-05±0.693E-06	0.715
	1.49	0.142E-04±0.288E-05±0.741E-06	0.715
	1.51	0.954E-05±0.239E-05±0.497E-06	0.715
	1.53	0.141E-04±0.309E-05±0.734E-06	0.715
	1.55	0.115E-04±0.269E-05±0.600E-06	0.715
	1.57	0.815E-05±0.222E-05±0.424E-06	0.715
	1.59	0.688E-05±0.207E-05±0.358E-06	0.715
	1.61	0.754E-05±0.205E-05±0.393E-06	0.715
	1.63	0.704E-05±0.212E-05±0.367E-06	0.715
	1.65	0.427E-05±0.158E-05±0.223E-06	0.715
	1.67	0.441E-05±0.163E-05±0.230E-06	0.715
	1.69	0.332E-05±0.150E-05±0.173E-06	0.715
	1.71	0.307E-05±0.139E-05±0.160E-06	0.714
	1.73	0.445E-05±0.164E-05±0.232E-06	0.714
	1.75	0.306E-05±0.138E-05±0.159E-06	0.714
	1.77	0.294E-05±0.133E-05±0.153E-06	0.714
	1.79	0.166E-05±0.106E-05±0.865E-07	0.714
2.425	0.71	0.545E-02±0.669E-04±0.286E-03	0.879
	0.73	0.421E-02±0.539E-04±0.221E-03	0.875
	0.75	0.386E-02±0.514E-04±0.203E-03	0.867
	0.77	0.367E-02±0.511E-04±0.193E-03	0.857
	0.79	0.329E-02±0.476E-04±0.173E-03	0.848
	0.81	0.276E-02±0.422E-04±0.145E-03	0.846
	0.83	0.227E-02±0.370E-04±0.119E-03	0.851
	0.85	0.185E-02±0.325E-04±0.974E-04	0.865
	0.87	0.162E-02±0.294E-04±0.851E-04	0.883
	0.89	0.153E-02±0.279E-04±0.802E-04	0.894
	0.91	0.154E-02±0.285E-04±0.807E-04	0.876
	0.93	0.204E-02±0.352E-04±0.107E-03	0.833
	0.95	0.257E-02±0.426E-04±0.135E-03	0.791
	0.97	0.299E-02±0.488E-04±0.157E-03	0.748
	0.99	0.343E-02±0.546E-04±0.180E-03	0.719
	1.01	0.318E-02±0.526E-04±0.167E-03	0.719
	1.03	0.246E-02±0.441E-04±0.129E-03	0.719
	1.05	0.177E-02±0.359E-04±0.929E-04	0.718
	1.07	0.127E-02±0.295E-04±0.665E-04	0.718
	1.09	0.918E-03±0.244E-04±0.482E-04	0.718
	1.11	0.697E-03±0.212E-04±0.366E-04	0.718
	1.13	0.468E-03±0.164E-04±0.246E-04	0.718
	1.15	0.369E-03±0.152E-04±0.194E-04	0.717
	1.17	0.245E-03±0.119E-04±0.129E-04	0.717
	1.19	0.189E-03±0.102E-04±0.992E-05	0.717
	1.21	0.147E-03±0.901E-05±0.773E-05	0.717
	1.23	0.122E-03±0.830E-05±0.640E-05	0.717
	1.25	0.827E-04±0.653E-05±0.434E-05	0.717
	1.27	0.794E-04±0.660E-05±0.417E-05	0.717
	1.29	0.606E-04±0.581E-05±0.318E-05	0.716
	1.31	0.648E-04±0.624E-05±0.340E-05	0.716
	1.33	0.456E-04±0.532E-05±0.239E-05	0.716
	1.35	0.384E-04±0.482E-05±0.202E-05	0.716
	1.37	0.312E-04±0.470E-05±0.164E-05	0.716
	1.39	0.358E-04±0.483E-05±0.188E-05	0.716
	1.41	0.328E-04±0.475E-05±0.172E-05	0.716
	1.43	0.209E-04±0.371E-05±0.110E-05	0.716
	1.45	0.192E-04±0.339E-05±0.101E-05	0.716
	1.47	0.118E-04±0.286E-05±0.622E-06	0.715
	1.49	0.131E-04±0.295E-05±0.686E-06	0.715
	1.51	0.777E-05±0.234E-05±0.408E-06	0.715
	1.53	0.817E-05±0.233E-05±0.429E-06	0.715
	1.55	0.855E-05±0.244E-05±0.449E-06	0.715
	1.57	0.995E-05±0.260E-05±0.522E-06	0.715
	1.59	0.798E-05±0.228E-05±0.419E-06	0.715
	1.61	0.926E-05±0.252E-05±0.486E-06	0.715
	1.63	0.967E-05±0.252E-05±0.507E-06	0.715
	1.65	0.590E-05±0.188E-05±0.310E-06	0.715
	1.67	0.339E-05±0.153E-05±0.178E-06	0.715
	1.69	0.327E-05±0.148E-05±0.172E-06	0.715
	1.71	0.259E-05±0.135E-05±0.136E-06	0.714
	1.73	0.564E-05±0.193E-05±0.296E-06	0.714
	1.75	0.738E-06±0.667E-06±0.387E-07	0.714
	1.77	0.339E-05±0.153E-05±0.178E-06	0.714
	1.79	0.245E-05±0.128E-05±0.129E-06	0.714
2.475	0.71	0.536E-02±0.659E-04±0.284E-03	0.878
	0.73	0.412E-02±0.527E-04±0.218E-03	0.876
	0.75	0.348E-02±0.482E-04±0.185E-03	0.869
	0.77	0.346E-02±0.488E-04±0.183E-03	0.859
	0.79	0.313E-02±0.469E-04±0.166E-03	0.850
	0.81	0.278E-02±0.443E-04±0.147E-03	0.846
	0.83	0.214E-02±0.378E-04±0.113E-03	0.851
	0.85	0.181E-02±0.340E-04±0.957E-04	0.862
	0.87	0.153E-02±0.305E-04±0.812E-04	0.879
	0.89	0.136E-02±0.273E-04±0.721E-04	0.884
	0.91	0.142E-02±0.284E-04±0.755E-04	0.875
	0.93	0.164E-02±0.318E-04±0.869E-04	0.846
	0.95	0.214E-02±0.384E-04±0.114E-03	0.799
	0.97	0.270E-02±0.465E-04±0.143E-03	0.751
	0.99	0.297E-02±0.506E-04±0.157E-03	0.719
	1.01	0.290E-02±0.515E-04±0.154E-03	0.719
	1.03	0.216E-02±0.426E-04±0.114E-03	0.719
	1.05	0.174E-02±0.384E-04±0.924E-04	0.719

	1.07	0.115E-02±0.294E-04±0.610E-04	0.718
	1.09	0.870E-03±0.248E-04±0.461E-04	0.718
	1.11	0.602E-03±0.207E-04±0.319E-04	0.718
	1.13	0.402E-03±0.160E-04±0.213E-04	0.718
	1.15	0.303E-03±0.134E-04±0.160E-04	0.718
	1.17	0.193E-03±0.103E-04±0.102E-04	0.717
	1.19	0.167E-03±0.960E-05±0.884E-05	0.717
	1.21	0.138E-03±0.844E-05±0.733E-05	0.717
	1.23	0.116E-03±0.792E-05±0.613E-05	0.717
	1.25	0.100E-03±0.741E-05±0.533E-05	0.717
	1.27	0.651E-04±0.594E-05±0.345E-05	0.717
	1.29	0.561E-04±0.560E-05±0.297E-05	0.717
	1.31	0.547E-04±0.563E-05±0.290E-05	0.716
	1.33	0.452E-04±0.502E-05±0.239E-05	0.716
	1.35	0.327E-04±0.414E-05±0.173E-05	0.716
	1.37	0.268E-04±0.397E-05±0.142E-05	0.716
	1.39	0.240E-04±0.362E-05±0.127E-05	0.716
	1.41	0.266E-04±0.376E-05±0.141E-05	0.716
	1.43	0.235E-04±0.359E-05±0.124E-05	0.716
	1.45	0.144E-04±0.271E-05±0.762E-06	0.716
	1.47	0.151E-04±0.298E-05±0.802E-06	0.716
	1.49	0.852E-05±0.213E-05±0.451E-06	0.715
	1.51	0.594E-05±0.179E-05±0.315E-06	0.715
	1.53	0.876E-05±0.220E-05±0.464E-06	0.715
	1.55	0.597E-05±0.180E-05±0.316E-06	0.715
	1.57	0.507E-05±0.173E-05±0.269E-06	0.715
	1.59	0.268E-05±0.121E-05±0.142E-06	0.715
	1.61	0.455E-05±0.155E-05±0.241E-06	0.715
	1.63	0.403E-05±0.149E-05±0.214E-06	0.715
	1.65	0.125E-05±0.800E-06±0.664E-07	0.715
	1.67	0.216E-05±0.113E-05±0.115E-06	0.715
	1.69	0.656E-05±0.187E-05±0.348E-06	0.715
	1.71	0.132E-05±0.845E-06±0.701E-07	0.715
	1.73	0.336E-05±0.136E-05±0.178E-06	0.714
	1.75	0.125E-05±0.800E-06±0.664E-07	0.714
	1.77	0.361E-05±0.146E-05±0.191E-06	0.714
	1.79	0.131E-05±0.838E-06±0.696E-07	0.714
2.525	0.71	0.508E-02±0.628E-04±0.272E-03	0.878
	0.73	0.381E-02±0.495E-04±0.204E-03	0.876
	0.75	0.339E-02±0.465E-04±0.182E-03	0.870
	0.77	0.309E-02±0.454E-04±0.166E-03	0.860
	0.79	0.300E-02±0.455E-04±0.161E-03	0.851
	0.81	0.257E-02±0.420E-04±0.137E-03	0.846
	0.83	0.217E-02±0.385E-04±0.116E-03	0.850
	0.85	0.168E-02±0.328E-04±0.901E-04	0.861
	0.87	0.150E-02±0.305E-04±0.806E-04	0.876
	0.89	0.137E-02±0.289E-04±0.735E-04	0.882
	0.91	0.139E-02±0.289E-04±0.743E-04	0.876
	0.93	0.169E-02±0.339E-04±0.906E-04	0.844
	0.95	0.191E-02±0.377E-04±0.102E-03	0.795
	0.97	0.233E-02±0.451E-04±0.125E-03	0.748
	0.99	0.274E-02±0.508E-04±0.147E-03	0.719
	1.01	0.239E-02±0.465E-04±0.128E-03	0.719
	1.03	0.189E-02±0.406E-04±0.101E-03	0.719
	1.05	0.148E-02±0.354E-04±0.795E-04	0.719
	1.07	0.102E-02±0.277E-04±0.547E-04	0.718
	1.09	0.736E-03±0.231E-04±0.394E-04	0.718
	1.11	0.495E-03±0.185E-04±0.265E-04	0.718
	1.13	0.400E-03±0.168E-04±0.214E-04	0.718
	1.15	0.330E-03±0.156E-04±0.177E-04	0.718
	1.17	0.224E-03±0.122E-04±0.120E-04	0.718
	1.19	0.171E-03±0.107E-04±0.917E-05	0.717
	1.21	0.132E-03±0.943E-05±0.710E-05	0.717
	1.23	0.120E-03±0.898E-05±0.644E-05	0.717
	1.25	0.629E-04±0.620E-05±0.337E-05	0.717
	1.27	0.631E-04±0.618E-05±0.338E-05	0.717
	1.29	0.494E-04±0.519E-05±0.265E-05	0.717
	1.31	0.474E-04±0.501E-05±0.254E-05	0.717
	1.33	0.261E-04±0.368E-05±0.140E-05	0.716
	1.35	0.354E-04±0.466E-05±0.190E-05	0.716
	1.37	0.249E-04±0.370E-05±0.134E-05	0.716
	1.39	0.206E-04±0.310E-05±0.110E-05	0.716
	1.41	0.193E-04±0.324E-05±0.103E-05	0.716
	1.43	0.149E-04±0.293E-05±0.797E-06	0.716
	1.45	0.166E-04±0.312E-05±0.888E-06	0.716
	1.47	0.209E-04±0.357E-05±0.112E-05	0.716
	1.49	0.132E-04±0.273E-05±0.706E-06	0.716
	1.51	0.750E-05±0.204E-05±0.402E-06	0.715
	1.53	0.718E-05±0.205E-05±0.385E-06	0.715
	1.55	0.883E-05±0.221E-05±0.474E-06	0.715
	1.57	0.674E-05±0.193E-05±0.361E-06	0.715
	1.59	0.229E-05±0.103E-05±0.123E-06	0.715
	1.61	0.266E-05±0.120E-05±0.143E-06	0.715
	1.63	0.567E-05±0.181E-05±0.304E-06	0.715
	1.65	0.144E-05±0.922E-06±0.773E-07	0.715
	1.67	0.299E-05±0.135E-05±0.160E-06	0.715
	1.69	0.347E-05±0.140E-05±0.186E-06	0.715
	1.71	0.273E-05±0.123E-05±0.146E-06	0.715
	1.73	0.355E-05±0.143E-05±0.190E-06	0.715
2.575	0.71	0.482E-02±0.600E-04±0.261E-03	0.877
	0.73	0.345E-02±0.459E-04±0.187E-03	0.876
	0.75	0.316E-02±0.433E-04±0.171E-03	0.870
	0.77	0.291E-02±0.429E-04±0.158E-03	0.862
	0.79	0.273E-02±0.422E-04±0.148E-03	0.853
	0.81	0.246E-02±0.405E-04±0.133E-03	0.848
	0.83	0.212E-02±0.380E-04±0.115E-03	0.849
	0.85	0.162E-02±0.319E-04±0.879E-04	0.861
	0.87	0.131E-02±0.282E-04±0.709E-04	0.873
	0.89	0.119E-02±0.260E-04±0.646E-04	0.886
	0.91	0.135E-02±0.285E-04±0.730E-04	0.878
	0.93	0.143E-02±0.307E-04±0.775E-04	0.845
	0.95	0.199E-02±0.386E-04±0.108E-03	0.797
	0.97	0.236E-02±0.455E-04±0.128E-03	0.754
	0.99	0.274E-02±0.530E-04±0.148E-03	0.720
	1.01	0.236E-02±0.487E-04±0.128E-03	0.719
	1.03	0.205E-02±0.444E-04±0.111E-03	0.719
	1.05	0.154E-02±0.374E-04±0.834E-04	0.719
	1.07	0.996E-03±0.288E-04±0.540E-04	0.719
	1.09	0.775E-03±0.249E-04±0.420E-04	0.718
	1.11	0.555E-03±0.214E-04±0.301E-04	0.718
	1.13	0.350E-03±0.165E-04±0.190E-04	0.718
	1.15	0.240E-03±0.129E-04±0.130E-04	0.718
	1.17	0.161E-03±0.107E-04±0.872E-05	0.718
	1.19	0.152E-03±0.103E-04±0.826E-05	0.718
	1.21	0.124E-03±0.952E-05±0.673E-05	0.717
	1.23	0.110E-03±0.861E-05±0.596E-05	0.717
	1.25	0.564E-04±0.584E-05±0.306E-05	0.717
	1.27	0.460E-04±0.536E-05±0.249E-05	0.717
	1.29	0.546E-04±0.582E-05±0.296E-05	0.717
	1.31	0.469E-04±0.562E-05±0.254E-05	0.717
	1.33	0.366E-04±0.498E-05±0.198E-05	0.717
	1.35	0.201E-04±0.356E-05±0.109E-05	0.716
	1.37	0.400E-04±0.602E-05±0.217E-05	0.716
	1.39	0.183E-04±0.345E-05±0.993E-06	0.716
	1.41	0.101E-04±0.228E-05±0.548E-06	0.716
	1.43	0.128E-04±0.280E-05±0.694E-06	0.716
	1.45	0.105E-04±0.253E-05±0.569E-06	0.716
	1.47	0.146E-04±0.302E-05±0.790E-06	0.716
	1.49	0.398E-05±0.161E-05±0.216E-06	0.716
	1.51	0.592E-05±0.178E-05±0.321E-06	0.716

	1.53	0.961E-05±0.251E-05±0.521E-06	0.715
	1.55	0.619E-05±0.186E-05±0.336E-06	0.715
	1.57	0.913E-05±0.229E-05±0.495E-06	0.715
	1.59	0.468E-05±0.160E-05±0.254E-06	0.715
	1.61	0.527E-05±0.168E-05±0.285E-06	0.715
	1.63	0.350E-05±0.141E-05±0.190E-06	0.715
	1.65	0.413E-05±0.152E-05±0.224E-06	0.715
	1.67	0.562E-05±0.180E-05±0.305E-06	0.715
	1.69	0.134E-05±0.855E-06±0.725E-07	0.715
	1.71	0.395E-05±0.146E-05±0.214E-06	0.715
2.625	0.71	0.476E-02±0.579E-04±0.261E-03	0.876
	0.73	0.339E-02±0.441E-04±0.186E-03	0.875
	0.75	0.301E-02±0.421E-04±0.165E-03	0.871
	0.77	0.273E-02±0.401E-04±0.149E-03	0.863
	0.79	0.262E-02±0.403E-04±0.143E-03	0.854
	0.81	0.225E-02±0.375E-04±0.123E-03	0.848
	0.83	0.195E-02±0.350E-04±0.107E-03	0.849
	0.85	0.156E-02±0.310E-04±0.855E-04	0.858
	0.87	0.130E-02±0.277E-04±0.710E-04	0.872
	0.89	0.115E-02±0.252E-04±0.629E-04	0.884
	0.91	0.120E-02±0.261E-04±0.659E-04	0.878
	0.93	0.132E-02±0.282E-04±0.724E-04	0.848
	0.95	0.171E-02±0.349E-04±0.939E-04	0.806
	0.97	0.208E-02±0.420E-04±0.114E-03	0.753
	0.99	0.229E-02±0.462E-04±0.125E-03	0.720
	1.01	0.214E-02±0.455E-04±0.117E-03	0.720
	1.03	0.179E-02±0.417E-04±0.982E-04	0.719
	1.05	0.128E-02±0.336E-04±0.702E-04	0.719
	1.07	0.976E-03±0.294E-04±0.535E-04	0.719
	1.09	0.720E-03±0.245E-04±0.394E-04	0.719
	1.11	0.450E-03±0.185E-04±0.247E-04	0.718
	1.13	0.413E-03±0.183E-04±0.226E-04	0.718
	1.15	0.257E-03±0.133E-04±0.141E-04	0.718
	1.17	0.213E-03±0.122E-04±0.117E-04	0.718
	1.19	0.180E-03±0.116E-04±0.986E-05	0.718
	1.21	0.117E-03±0.990E-05±0.641E-05	0.718
	1.23	0.107E-03±0.961E-05±0.589E-05	0.717
	1.25	0.790E-04±0.728E-05±0.433E-05	0.717
	1.27	0.403E-04±0.470E-05±0.221E-05	0.717
	1.29	0.369E-04±0.496E-05±0.202E-05	0.717
	1.31	0.519E-04±0.723E-05±0.284E-05	0.717
	1.33	0.277E-04±0.443E-05±0.152E-05	0.717
	1.35	0.286E-04±0.443E-05±0.157E-05	0.717
	1.37	0.186E-04±0.367E-05±0.102E-05	0.716
	1.39	0.192E-04±0.369E-05±0.105E-05	0.716
	1.41	0.176E-04±0.424E-05±0.963E-06	0.716
	1.43	0.124E-04±0.312E-05±0.682E-06	0.716
	1.45	0.739E-05±0.252E-05±0.405E-06	0.716
	1.47	0.164E-04±0.349E-05±0.898E-06	0.716
	1.49	0.592E-05±0.218E-05±0.324E-06	0.716
	1.51	0.969E-05±0.277E-05±0.531E-06	0.716
	1.53	0.958E-05±0.274E-05±0.525E-06	0.716
	1.55	0.794E-05±0.254E-05±0.435E-06	0.715
	1.57	0.547E-05±0.202E-05±0.300E-06	0.715
2.675	0.71	0.432E-02±0.491E-04±0.240E-03	0.875
	0.73	0.319E-02±0.399E-04±0.177E-03	0.875
	0.75	0.291E-02±0.397E-04±0.162E-03	0.871
	0.77	0.259E-02±0.382E-04±0.144E-03	0.864
	0.79	0.240E-02±0.380E-04±0.133E-03	0.856
	0.81	0.208E-02±0.356E-04±0.115E-03	0.849
	0.83	0.180E-02±0.334E-04±0.100E-03	0.849
	0.85	0.150E-02±0.296E-04±0.834E-04	0.857
	0.87	0.124E-02±0.262E-04±0.689E-04	0.873
	0.89	0.110E-02±0.242E-04±0.609E-04	0.882
	0.91	0.109E-02±0.243E-04±0.602E-04	0.873
	0.93	0.131E-02±0.285E-04±0.726E-04	0.845
	0.95	0.162E-02±0.341E-04±0.899E-04	0.801
	0.97	0.205E-02±0.415E-04±0.114E-03	0.756
	0.99	0.208E-02±0.433E-04±0.115E-03	0.720
	1.01	0.196E-02±0.422E-04±0.109E-03	0.720
	1.03	0.162E-02±0.386E-04±0.899E-04	0.720
	1.05	0.114E-02±0.317E-04±0.634E-04	0.719
	1.07	0.816E-03±0.265E-04±0.453E-04	0.719
	1.09	0.593E-03±0.221E-04±0.329E-04	0.719
	1.11	0.376E-03±0.172E-04±0.209E-04	0.719
	1.13	0.250E-03±0.135E-04±0.139E-04	0.718
	1.15	0.242E-03±0.141E-04±0.134E-04	0.718
	1.17	0.157E-03±0.105E-04±0.874E-05	0.718
	1.19	0.128E-03±0.926E-05±0.713E-05	0.718
	1.21	0.914E-04±0.770E-05±0.507E-05	0.718
	1.23	0.720E-04±0.682E-05±0.399E-05	0.718
	1.25	0.744E-04±0.676E-05±0.413E-05	0.717
	1.27	0.620E-04±0.647E-05±0.344E-05	0.717
	1.29	0.459E-04±0.560E-05±0.255E-05	0.717
	1.31	0.385E-04±0.507E-05±0.214E-05	0.717
	1.33	0.319E-04±0.474E-05±0.177E-05	0.717
	1.35	0.304E-04±0.445E-05±0.169E-05	0.717
	1.37	0.259E-04±0.390E-05±0.144E-05	0.717
	1.39	0.175E-04±0.344E-05±0.970E-06	0.716
	1.41	0.549E-05±0.188E-05±0.305E-06	0.716
	1.43	0.951E-05±0.248E-05±0.528E-06	0.716
	1.45	0.124E-04±0.281E-05±0.691E-06	0.716
	1.47	0.742E-05±0.223E-05±0.412E-06	0.716
	1.49	0.156E-04±0.314E-05±0.863E-06	0.716
	1.51	0.314E-05±0.142E-05±0.174E-06	0.716
	1.53	0.317E-05±0.143E-05±0.176E-06	0.716
	1.55	0.389E-05±0.157E-05±0.216E-06	0.716
	1.57	0.107E-04±0.269E-05±0.595E-06	0.715
2.725	0.71	0.420E-02±0.476E-04±0.235E-03	0.875
	0.73	0.304E-02±0.367E-04±0.170E-03	0.875
	0.75	0.265E-02±0.343E-04±0.148E-03	0.872
	0.77	0.244E-02±0.337E-04±0.136E-03	0.865
	0.79	0.222E-02±0.336E-04±0.125E-03	0.857
	0.81	0.217E-02±0.351E-04±0.121E-03	0.850
	0.83	0.175E-02±0.324E-04±0.982E-04	0.849
	0.85	0.140E-02±0.281E-04±0.783E-04	0.856
	0.87	0.113E-02±0.245E-04±0.635E-04	0.868
	0.89	0.105E-02±0.236E-04±0.588E-04	0.879
	0.91	0.978E-03±0.221E-04±0.547E-04	0.873
	0.93	0.118E-02±0.260E-04±0.661E-04	0.851
	0.95	0.150E-02±0.323E-04±0.841E-04	0.806
	0.97	0.183E-02±0.377E-04±0.102E-03	0.754
	0.99	0.202E-02±0.424E-04±0.113E-03	0.720
	1.01	0.187E-02±0.408E-04±0.105E-03	0.720
	1.03	0.148E-02±0.360E-04±0.827E-04	0.720
	1.05	0.110E-02±0.307E-04±0.618E-04	0.720
	1.07	0.830E-03±0.262E-04±0.465E-04	0.719
	1.09	0.592E-03±0.221E-04±0.332E-04	0.719
	1.11	0.371E-03±0.163E-04±0.208E-04	0.719
	1.13	0.265E-03±0.138E-04±0.149E-04	0.719
	1.15	0.206E-03±0.128E-04±0.115E-04	0.718
	1.17	0.113E-03±0.879E-05±0.635E-05	0.718
	1.19	0.117E-03±0.913E-05±0.657E-05	0.718
	1.21	0.991E-04±0.818E-05±0.555E-05	0.718
	1.23	0.682E-04±0.668E-05±0.382E-05	0.718
	1.25	0.400E-04±0.505E-05±0.224E-05	0.718
	1.27	0.431E-04±0.550E-05±0.241E-05	0.717
	1.29	0.320E-04±0.426E-05±0.179E-05	0.717
	1.31	0.320E-04±0.476E-05±0.179E-05	0.717
	1.33	0.269E-04±0.411E-05±0.151E-05	0.717

	1.35	0.138E-04±0.294E-05±0.772E-06	0.717
	1.37	0.235E-04±0.425E-05±0.132E-05	0.717
	1.39	0.147E-04±0.332E-05±0.824E-06	0.717
	1.41	0.109E-04±0.274E-05±0.612E-06	0.716
	1.43	0.128E-04±0.309E-05±0.717E-06	0.716
	1.45	0.814E-05±0.245E-05±0.456E-06	0.716
	1.47	0.656E-05±0.210E-05±0.367E-06	0.716
	1.49	0.485E-05±0.179E-05±0.272E-06	0.716
	1.51	0.252E-05±0.132E-05±0.141E-06	0.716
	1.53	0.549E-05±0.203E-05±0.308E-06	0.716
2.775	0.71	0.400E-02±0.481E-04±0.227E-03	0.874
	0.73	0.269E-02±0.337E-04±0.152E-03	0.874
	0.75	0.241E-02±0.318E-04±0.137E-03	0.872
	0.77	0.227E-02±0.312E-04±0.128E-03	0.867
	0.79	0.213E-02±0.306E-04±0.121E-03	0.858
	0.81	0.195E-02±0.300E-04±0.111E-03	0.852
	0.83	0.170E-02±0.287E-04±0.965E-04	0.850
	0.85	0.139E-02±0.261E-04±0.785E-04	0.855
	0.87	0.114E-02±0.237E-04±0.646E-04	0.870
	0.89	0.982E-03±0.219E-04±0.557E-04	0.877
	0.91	0.974E-03±0.218E-04±0.552E-04	0.879
	0.93	0.111E-02±0.248E-04±0.628E-04	0.844
	0.95	0.140E-02±0.304E-04±0.793E-04	0.800
	0.97	0.166E-02±0.351E-04±0.944E-04	0.754
	0.99	0.184E-02±0.394E-04±0.104E-03	0.721
	1.01	0.163E-02±0.372E-04±0.927E-04	0.720
	1.03	0.136E-02±0.337E-04±0.770E-04	0.720
	1.05	0.101E-02±0.286E-04±0.574E-04	0.720
	1.07	0.677E-03±0.226E-04±0.384E-04	0.720
	1.09	0.462E-03±0.185E-04±0.262E-04	0.719
	1.11	0.342E-03±0.160E-04±0.194E-04	0.719
	1.13	0.276E-03±0.147E-04±0.157E-04	0.719
	1.15	0.216E-03±0.123E-04±0.122E-04	0.719
	1.17	0.145E-03±0.984E-05±0.820E-05	0.718
	1.19	0.101E-03±0.850E-05±0.575E-05	0.718
	1.21	0.886E-04±0.763E-05±0.503E-05	0.718
	1.23	0.609E-04±0.644E-05±0.345E-05	0.718
	1.25	0.719E-04±0.740E-05±0.408E-05	0.718
	1.27	0.557E-04±0.650E-05±0.316E-05	0.718
	1.29	0.278E-04±0.419E-05±0.158E-05	0.717
	1.31	0.329E-04±0.482E-05±0.187E-05	0.717
	1.33	0.232E-04±0.437E-05±0.132E-05	0.717
	1.35	0.173E-04±0.369E-05±0.982E-06	0.717
	1.37	0.251E-04±0.484E-05±0.142E-05	0.717
	1.39	0.154E-04±0.385E-05±0.871E-06	0.717
	1.41	0.125E-04±0.326E-05±0.708E-06	0.717
	1.43	0.120E-04±0.312E-05±0.679E-06	0.716
	1.45	0.134E-04±0.294E-05±0.760E-06	0.716
	1.47	0.914E-05±0.275E-05±0.518E-06	0.716
	1.49	0.710E-05±0.262E-05±0.402E-06	0.716
	1.51	0.729E-05±0.249E-05±0.413E-06	0.716
	1.53	0.798E-05±0.255E-05±0.453E-06	0.716
	1.55	0.621E-05±0.229E-05±0.352E-06	0.716
	1.57	0.508E-05±0.205E-05±0.288E-06	0.716
	1.59	0.474E-05±0.214E-05±0.269E-06	0.716
2.825	0.71	0.397E-02±0.495E-04±0.228E-03	0.873
	0.73	0.290E-02±0.386E-04±0.166E-03	0.874
	0.75	0.230E-02±0.324E-04±0.132E-03	0.873
	0.77	0.214E-02±0.306E-04±0.123E-03	0.868
	0.79	0.192E-02±0.285E-04±0.110E-03	0.860
	0.81	0.172E-02±0.278E-04±0.988E-04	0.852
	0.83	0.152E-02±0.261E-04±0.870E-04	0.849
	0.85	0.132E-02±0.242E-04±0.754E-04	0.856
	0.87	0.104E-02±0.210E-04±0.595E-04	0.865
	0.89	0.931E-03±0.200E-04±0.533E-04	0.877

	0.91	0.933E-03±0.201E-04±0.535E-04	0.871
	0.93	0.105E-02±0.225E-04±0.602E-04	0.848
	0.95	0.135E-02±0.286E-04±0.774E-04	0.803
	0.97	0.158E-02±0.329E-04±0.905E-04	0.756
	0.99	0.173E-02±0.372E-04±0.993E-04	0.721
	1.01	0.170E-02±0.381E-04±0.977E-04	0.721
	1.03	0.128E-02±0.335E-04±0.734E-04	0.720
	1.05	0.969E-03±0.274E-04±0.555E-04	0.720
	1.07	0.646E-03±0.219E-04±0.370E-04	0.720
	1.09	0.444E-03±0.179E-04±0.255E-04	0.720
	1.11	0.291E-03±0.136E-04±0.167E-04	0.719
	1.13	0.223E-03±0.126E-04±0.128E-04	0.719
	1.15	0.187E-03±0.121E-04±0.107E-04	0.719
	1.17	0.122E-03±0.929E-05±0.697E-05	0.719
	1.19	0.118E-03±0.953E-05±0.676E-05	0.718
	1.21	0.751E-04±0.696E-05±0.430E-05	0.718
	1.23	0.545E-04±0.620E-05±0.312E-05	0.718
	1.25	0.392E-04±0.522E-05±0.224E-05	0.718
	1.27	0.262E-04±0.439E-05±0.150E-05	0.718
	1.29	0.334E-04±0.483E-05±0.191E-05	0.718
	1.31	0.218E-04±0.387E-05±0.125E-05	0.717
	1.33	0.199E-04±0.339E-05±0.114E-05	0.717
	1.35	0.133E-04±0.284E-05±0.765E-06	0.717
	1.37	0.113E-04±0.294E-05±0.646E-06	0.717
	1.39	0.137E-04±0.285E-05±0.787E-06	0.717
	1.41	0.863E-05±0.235E-05±0.494E-06	0.717
	1.43	0.571E-05±0.258E-05±0.327E-06	0.717
	1.45	0.368E-05±0.235E-05±0.211E-06	0.716
	1.47	0.662E-05±0.299E-05±0.379E-06	0.716
	1.49	0.475E-05±0.175E-05±0.272E-06	0.716
	1.51	0.549E-05±0.188E-05±0.315E-06	0.716
	1.53	0.230E-05±0.120E-05±0.132E-06	0.716
2.875	0.71	0.391E-02±0.489E-04±0.226E-03	0.872
	0.73	0.262E-02±0.358E-04±0.152E-03	0.874
	0.75	0.231E-02±0.338E-04±0.134E-03	0.872
	0.77	0.205E-02±0.318E-04±0.119E-03	0.868
	0.79	0.187E-02±0.301E-04±0.108E-03	0.861
	0.81	0.171E-02±0.283E-04±0.993E-04	0.853
	0.83	0.141E-02±0.247E-04±0.817E-04	0.850
	0.85	0.112E-02±0.219E-04±0.649E-04	0.853
	0.87	0.955E-03±0.193E-04±0.553E-04	0.865
	0.89	0.850E-03±0.182E-04±0.492E-04	0.875
	0.91	0.842E-03±0.184E-04±0.487E-04	0.872
	0.93	0.975E-03±0.201E-04±0.564E-04	0.849
	0.95	0.118E-02±0.242E-04±0.682E-04	0.804
	0.97	0.148E-02±0.298E-04±0.855E-04	0.756
	0.99	0.156E-02±0.323E-04±0.901E-04	0.721
	1.01	0.141E-02±0.320E-04±0.814E-04	0.721
	1.03	0.125E-02±0.302E-04±0.725E-04	0.721
	1.05	0.906E-03±0.257E-04±0.525E-04	0.720
	1.07	0.606E-03±0.213E-04±0.351E-04	0.720
	1.09	0.389E-03±0.157E-04±0.225E-04	0.720
	1.11	0.292E-03±0.144E-04±0.169E-04	0.720
	1.13	0.221E-03±0.122E-04±0.128E-04	0.719
	1.15	0.134E-03±0.959E-05±0.775E-05	0.719
	1.17	0.111E-03±0.844E-05±0.640E-05	0.719
	1.19	0.964E-04±0.802E-05±0.558E-05	0.719
	1.21	0.645E-04±0.643E-05±0.373E-05	0.718
	1.23	0.522E-04±0.631E-05±0.302E-05	0.718
	1.25	0.481E-04±0.571E-05±0.279E-05	0.718
	1.27	0.257E-04±0.410E-05±0.149E-05	0.718
	1.29	0.279E-04±0.409E-05±0.162E-05	0.718
	1.31	0.205E-04±0.338E-05±0.119E-05	0.718
	1.33	0.215E-04±0.381E-05±0.124E-05	0.717
	1.35	0.144E-04±0.308E-05±0.837E-06	0.717

	1.37	0.137E-04±0.301E-05±0.794E-06	0.717
	1.39	0.110E-04±0.266E-05±0.639E-06	0.717
	1.41	0.111E-04±0.269E-05±0.645E-06	0.717
	1.43	0.843E-05±0.230E-05±0.488E-06	0.717
	1.45	0.443E-05±0.164E-05±0.257E-06	0.717
	1.47	0.888E-05±0.242E-05±0.514E-06	0.716
	1.49	0.315E-05±0.142E-05±0.183E-06	0.716
	1.51	0.318E-05±0.144E-05±0.184E-06	0.716
2.925	0.71	0.357E-02±0.459E-04±0.209E-03	0.872
	0.73	0.253E-02±0.349E-04±0.148E-03	0.873
	0.75	0.214E-02±0.319E-04±0.125E-03	0.872
	0.77	0.184E-02±0.295E-04±0.108E-03	0.868
	0.79	0.178E-02±0.297E-04±0.104E-03	0.862
	0.81	0.163E-02±0.288E-04±0.951E-04	0.854
	0.83	0.136E-02±0.264E-04±0.797E-04	0.850
	0.85	0.110E-02±0.223E-04±0.640E-04	0.852
	0.87	0.878E-03±0.191E-04±0.513E-04	0.865
	0.89	0.809E-03±0.177E-04±0.472E-04	0.877
	0.91	0.767E-03±0.174E-04±0.448E-04	0.873
	0.93	0.816E-03±0.181E-04±0.476E-04	0.850
	0.95	0.112E-02±0.233E-04±0.653E-04	0.806
	0.97	0.123E-02±0.251E-04±0.719E-04	0.761
	0.99	0.150E-02±0.303E-04±0.877E-04	0.721
	1.01	0.136E-02±0.292E-04±0.795E-04	0.721
	1.03	0.109E-02±0.262E-04±0.639E-04	0.721
	1.05	0.788E-03±0.218E-04±0.460E-04	0.721
	1.07	0.497E-03±0.164E-04±0.290E-04	0.720
	1.09	0.439E-03±0.166E-04±0.256E-04	0.720
	1.11	0.277E-03±0.128E-04±0.162E-04	0.720
	1.13	0.211E-03±0.115E-04±0.123E-04	0.719
	1.15	0.126E-03±0.856E-05±0.734E-05	0.719
	1.17	0.894E-04±0.678E-05±0.522E-05	0.719
	1.19	0.707E-04±0.633E-05±0.413E-05	0.719
	1.21	0.895E-04±0.825E-05±0.523E-05	0.719
	1.23	0.523E-04±0.595E-05±0.305E-05	0.718
	1.25	0.396E-04±0.522E-05±0.231E-05	0.718
	1.27	0.408E-04±0.569E-05±0.238E-05	0.718
	1.29	0.283E-04±0.467E-05±0.165E-05	0.718
	1.31	0.296E-04±0.458E-05±0.173E-05	0.718
	1.33	0.240E-04±0.497E-05±0.140E-05	0.718
	1.35	0.213E-04±0.467E-05±0.124E-05	0.717
	1.37	0.114E-04±0.285E-05±0.664E-06	0.717
	1.39	0.107E-04±0.291E-05±0.625E-06	0.717
	1.41	0.119E-04±0.298E-05±0.694E-06	0.717
	1.43	0.919E-05±0.277E-05±0.537E-06	0.717
	1.45	0.105E-04±0.273E-05±0.610E-06	0.717
	1.47	0.658E-05±0.243E-05±0.384E-06	0.717
	1.49	0.376E-05±0.196E-05±0.220E-06	0.716
2.975	0.71	0.322E-02±0.404E-04±0.190E-03	0.871
	0.73	0.238E-02±0.333E-04±0.141E-03	0.873
	0.75	0.203E-02±0.305E-04±0.120E-03	0.872
	0.77	0.186E-02±0.297E-04±0.110E-03	0.869
	0.79	0.170E-02±0.285E-04±0.100E-03	0.864
	0.81	0.149E-02±0.269E-04±0.882E-04	0.855
	0.83	0.127E-02±0.248E-04±0.753E-04	0.851
	0.85	0.107E-02±0.228E-04±0.634E-04	0.855
	0.87	0.937E-03±0.212E-04±0.554E-04	0.863
	0.89	0.797E-03±0.195E-04±0.471E-04	0.869
	0.91	0.666E-03±0.163E-04±0.393E-04	0.874
	0.93	0.768E-03±0.178E-04±0.454E-04	0.850
	0.95	0.930E-03±0.204E-04±0.550E-04	0.805
	0.97	0.115E-02±0.245E-04±0.682E-04	0.762
	0.99	0.135E-02±0.286E-04±0.797E-04	0.722
	1.01	0.120E-02±0.270E-04±0.712E-04	0.721
	1.03	0.948E-03±0.237E-04±0.560E-04	0.721

	1.05	0.722E-03±0.206E-04±0.427E-04	0.721
	1.07	0.515E-03±0.166E-04±0.304E-04	0.720
	1.09	0.357E-03±0.138E-04±0.211E-04	0.720
	1.11	0.296E-03±0.129E-04±0.175E-04	0.720
	1.13	0.204E-03±0.107E-04±0.120E-04	0.720
	1.15	0.117E-03±0.744E-05±0.689E-05	0.719
	1.17	0.925E-04±0.699E-05±0.547E-05	0.719
	1.19	0.990E-04±0.745E-05±0.585E-05	0.719
	1.21	0.614E-04±0.542E-05±0.363E-05	0.719
	1.23	0.489E-04±0.532E-05±0.289E-05	0.719
	1.25	0.259E-04±0.384E-05±0.153E-05	0.718
	1.27	0.245E-04±0.359E-05±0.145E-05	0.718
	1.29	0.197E-04±0.331E-05±0.116E-05	0.718
	1.31	0.233E-04±0.439E-05±0.138E-05	0.718
	1.33	0.190E-04±0.374E-05±0.112E-05	0.718
	1.35	0.161E-04±0.352E-05±0.949E-06	0.718
	1.37	0.155E-04±0.314E-05±0.917E-06	0.717
	1.39	0.715E-05±0.215E-05±0.423E-06	0.717
	1.41	0.124E-04±0.281E-05±0.734E-06	0.717
	1.43	0.484E-05±0.179E-05±0.286E-06	0.717
	1.45	0.557E-05±0.190E-05±0.329E-06	0.717
	1.47	0.699E-05±0.211E-05±0.413E-06	0.717
	1.49	0.323E-05±0.146E-05±0.191E-06	0.717
3.025	0.71	0.311E-02±0.408E-04±0.186E-03	0.871
	0.73	0.213E-02±0.292E-04±0.127E-03	0.872
	0.75	0.187E-02±0.282E-04±0.112E-03	0.872
	0.77	0.171E-02±0.279E-04±0.102E-03	0.870
	0.79	0.157E-02±0.274E-04±0.937E-04	0.864
	0.81	0.143E-02±0.264E-04±0.858E-04	0.856
	0.83	0.131E-02±0.255E-04±0.784E-04	0.851
	0.85	0.105E-02±0.224E-04±0.625E-04	0.853
	0.87	0.925E-03±0.211E-04±0.553E-04	0.860
	0.89	0.772E-03±0.190E-04±0.462E-04	0.872
	0.91	0.723E-03±0.184E-04±0.432E-04	0.874
	0.93	0.742E-03±0.188E-04±0.444E-04	0.852
	0.95	0.905E-03±0.219E-04±0.541E-04	0.815
	0.97	0.113E-02±0.254E-04±0.673E-04	0.762
	0.99	0.117E-02±0.263E-04±0.698E-04	0.722
	1.01	0.108E-02±0.254E-04±0.647E-04	0.722
	1.03	0.954E-03±0.240E-04±0.571E-04	0.721
	1.05	0.668E-03±0.194E-04±0.399E-04	0.721
	1.07	0.456E-03±0.157E-04±0.273E-04	0.721
	1.09	0.325E-03±0.129E-04±0.195E-04	0.720
	1.11	0.214E-03±0.102E-04±0.128E-04	0.720
	1.13	0.146E-03±0.829E-05±0.871E-05	0.720
	1.15	0.115E-03±0.746E-05±0.688E-05	0.720
	1.17	0.805E-04±0.600E-05±0.481E-05	0.720
	1.19	0.748E-04±0.600E-05±0.447E-05	0.719
	1.21	0.696E-04±0.597E-05±0.416E-05	0.719
	1.23	0.408E-04±0.454E-05±0.244E-05	0.719
	1.25	0.375E-04±0.427E-05±0.224E-05	0.719
	1.27	0.359E-04±0.458E-05±0.215E-05	0.718
	1.29	0.198E-04±0.332E-05±0.118E-05	0.718
	1.31	0.212E-04±0.345E-05±0.127E-05	0.718
	1.33	0.880E-05±0.221E-05±0.526E-06	0.718
	1.35	0.135E-04±0.272E-05±0.807E-06	0.718
	1.37	0.633E-05±0.191E-05±0.379E-06	0.718
	1.39	0.996E-05±0.232E-05±0.595E-06	0.717
	1.41	0.766E-05±0.200E-05±0.458E-06	0.717
	1.43	0.678E-05±0.194E-05±0.405E-06	0.717
	1.45	0.338E-05±0.136E-05±0.202E-06	0.717
	1.47	0.422E-05±0.156E-05±0.253E-06	0.717
	1.49	0.133E-05±0.849E-06±0.795E-07	0.717
3.075	0.71	0.304E-02±0.407E-04±0.184E-03	0.871
	0.73	0.210E-02±0.305E-04±0.127E-03	0.871

	0.75	0.173E-02±0.264E-04±0.104E-03	0.872
	0.77	0.149E-02±0.239E-04±0.902E-04	0.869
	0.79	0.135E-02±0.237E-04±0.816E-04	0.866
	0.81	0.127E-02±0.240E-04±0.764E-04	0.857
	0.83	0.117E-02±0.239E-04±0.709E-04	0.852
	0.85	0.968E-03±0.213E-04±0.585E-04	0.852
	0.87	0.820E-03±0.193E-04±0.496E-04	0.860
	0.89	0.709E-03±0.176E-04±0.428E-04	0.870
	0.91	0.688E-03±0.176E-04±0.416E-04	0.872
	0.93	0.734E-03±0.184E-04±0.443E-04	0.853
	0.95	0.836E-03±0.208E-04±0.505E-04	0.815
	0.97	0.107E-02±0.259E-04±0.643E-04	0.762
	0.99	0.118E-02±0.289E-04±0.715E-04	0.722
	1.01	0.113E-02±0.289E-04±0.680E-04	0.722
	1.03	0.798E-03±0.223E-04±0.482E-04	0.722
	1.05	0.626E-03±0.197E-04±0.378E-04	0.721
	1.07	0.466E-03±0.162E-04±0.281E-04	0.721
	1.09	0.287E-03±0.119E-04±0.173E-04	0.721
	1.11	0.212E-03±0.105E-04±0.128E-04	0.720
	1.13	0.136E-03±0.792E-05±0.820E-05	0.720
	1.15	0.107E-03±0.699E-05±0.648E-05	0.720
	1.17	0.856E-04±0.643E-05±0.517E-05	0.720
	1.19	0.488E-04±0.457E-05±0.295E-05	0.720
	1.21	0.433E-04±0.461E-05±0.262E-05	0.719
	1.23	0.457E-04±0.451E-05±0.276E-05	0.719
	1.25	0.154E-04±0.239E-05±0.931E-06	0.719
	1.27	0.199E-04±0.287E-05±0.120E-05	0.719
	1.29	0.151E-04±0.246E-05±0.914E-06	0.718
	1.31	0.186E-04±0.313E-05±0.113E-05	0.718
	1.33	0.135E-04±0.245E-05±0.818E-06	0.718
	1.35	0.767E-05±0.209E-05±0.463E-06	0.718
	1.37	0.131E-04±0.259E-05±0.794E-06	0.718
	1.39	0.631E-05±0.180E-05±0.381E-06	0.718
	1.41	0.908E-05±0.219E-05±0.548E-06	0.717
	1.43	0.726E-05±0.219E-05±0.438E-06	0.717
	1.45	0.977E-05±0.236E-05±0.590E-06	0.717
	1.47	0.439E-05±0.150E-05±0.265E-06	0.717
	1.49	0.316E-05±0.128E-05±0.191E-06	0.717
3.125	0.71	0.286E-02±0.385E-04±0.175E-03	0.871
	0.73	0.192E-02±0.286E-04±0.118E-03	0.871
	0.75	0.176E-02±0.278E-04±0.107E-03	0.871
	0.77	0.145E-02±0.248E-04±0.887E-04	0.869
	0.79	0.133E-02±0.235E-04±0.813E-04	0.866
	0.81	0.114E-02±0.212E-04±0.694E-04	0.858
	0.83	0.104E-02±0.211E-04±0.636E-04	0.853
	0.85	0.927E-03±0.206E-04±0.566E-04	0.853
	0.87	0.773E-03±0.190E-04±0.472E-04	0.861
	0.89	0.638E-03±0.164E-04±0.390E-04	0.868
	0.91	0.624E-03±0.163E-04±0.381E-04	0.876
	0.93	0.711E-03±0.182E-04±0.435E-04	0.852
	0.95	0.829E-03±0.206E-04±0.506E-04	0.808
	0.97	0.104E-02±0.254E-04±0.633E-04	0.763
	0.99	0.109E-02±0.268E-04±0.664E-04	0.723
	1.01	0.101E-02±0.268E-04±0.614E-04	0.722
	1.03	0.832E-03±0.237E-04±0.509E-04	0.722
	1.05	0.577E-03±0.191E-04±0.353E-04	0.722
	1.07	0.406E-03±0.162E-04±0.248E-04	0.721
	1.09	0.287E-03±0.132E-04±0.175E-04	0.721
	1.11	0.198E-03±0.106E-04±0.121E-04	0.721
	1.13	0.143E-03±0.832E-05±0.872E-05	0.720
	1.15	0.103E-03±0.777E-05±0.628E-05	0.720
	1.17	0.711E-04±0.565E-05±0.434E-05	0.720
	1.19	0.540E-04±0.506E-05±0.330E-05	0.720
	1.21	0.397E-04±0.423E-05±0.243E-05	0.720
	1.23	0.387E-04±0.463E-05±0.236E-05	0.719

	1.25	0.272E-04±0.362E-05±0.166E-05	0.719
	1.27	0.216E-04±0.317E-05±0.132E-05	0.719
	1.29	0.193E-04±0.299E-05±0.118E-05	0.719
	1.31	0.191E-04±0.306E-05±0.117E-05	0.719
	1.33	0.152E-04±0.280E-05±0.928E-06	0.718
	1.35	0.114E-04±0.236E-05±0.697E-06	0.718
	1.37	0.713E-05±0.179E-05±0.436E-06	0.718
	1.39	0.657E-05±0.171E-05±0.401E-06	0.718
	1.41	0.594E-05±0.162E-05±0.363E-06	0.718
	1.43	0.531E-05±0.152E-05±0.325E-06	0.718
	1.45	0.356E-05±0.122E-05±0.218E-06	0.717
	1.47	0.439E-05±0.140E-05±0.269E-06	0.717
3.175	0.71	0.284E-02±0.382E-04±0.176E-03	0.872
	0.73	0.196E-02±0.289E-04±0.121E-03	0.871
	0.75	0.159E-02±0.256E-04±0.983E-04	0.871
	0.77	0.143E-02±0.245E-04±0.885E-04	0.870
	0.79	0.131E-02±0.241E-04±0.813E-04	0.866
	0.81	0.112E-02±0.222E-04±0.695E-04	0.860
	0.83	0.997E-03±0.205E-04±0.616E-04	0.854
	0.85	0.823E-03±0.184E-04±0.509E-04	0.852
	0.87	0.699E-03±0.171E-04±0.432E-04	0.860
	0.89	0.600E-03±0.159E-04±0.371E-04	0.869
	0.91	0.568E-03±0.151E-04±0.351E-04	0.868
	0.93	0.577E-03±0.158E-04±0.356E-04	0.855
	0.95	0.699E-03±0.186E-04±0.432E-04	0.810
	0.97	0.880E-03±0.225E-04±0.544E-04	0.765
	0.99	0.990E-03±0.253E-04±0.612E-04	0.723
	1.01	0.940E-03±0.255E-04±0.581E-04	0.723
	1.03	0.730E-03±0.218E-04±0.451E-04	0.722
	1.05	0.559E-03±0.189E-04±0.346E-04	0.722
	1.07	0.372E-03±0.152E-04±0.230E-04	0.722
	1.09	0.262E-03±0.122E-04±0.162E-04	0.721
	1.11	0.194E-03±0.107E-04±0.120E-04	0.721
	1.13	0.109E-03±0.765E-05±0.677E-05	0.721
	1.15	0.946E-04±0.747E-05±0.585E-05	0.720
	1.17	0.849E-04±0.715E-05±0.525E-05	0.720
	1.19	0.592E-04±0.591E-05±0.366E-05	0.720
	1.21	0.348E-04±0.402E-05±0.215E-05	0.720
	1.23	0.248E-04±0.338E-05±0.154E-05	0.720
	1.25	0.295E-04±0.366E-05±0.182E-05	0.719
	1.27	0.237E-04±0.367E-05±0.146E-05	0.719
	1.29	0.134E-04±0.252E-05±0.826E-06	0.719
	1.31	0.875E-05±0.177E-05±0.541E-06	0.719
	1.33	0.124E-04±0.212E-05±0.766E-06	0.719
	1.35	0.977E-05±0.197E-05±0.604E-06	0.718
	1.37	0.859E-05±0.183E-05±0.531E-06	0.718
	1.39	0.705E-05±0.170E-05±0.436E-06	0.718
	1.41	0.405E-05±0.122E-05±0.250E-06	0.718
	1.43	0.281E-05±0.104E-05±0.174E-06	0.718
	1.45	0.215E-05±0.970E-06±0.133E-06	0.718
	1.47	0.216E-05±0.976E-06±0.134E-06	0.717
3.225	0.71	0.267E-02±0.362E-04±0.167E-03	0.873
	0.73	0.190E-02±0.281E-04±0.119E-03	0.871
	0.75	0.153E-02±0.252E-04±0.954E-04	0.871
	0.77	0.135E-02±0.235E-04±0.846E-04	0.870
	0.79	0.121E-02±0.226E-04±0.756E-04	0.866
	0.81	0.110E-02±0.220E-04±0.687E-04	0.861
	0.83	0.876E-03±0.193E-04±0.547E-04	0.855
	0.85	0.716E-03±0.175E-04±0.448E-04	0.853
	0.87	0.652E-03±0.161E-04±0.408E-04	0.857
	0.89	0.576E-03±0.149E-04±0.360E-04	0.869
	0.91	0.515E-03±0.143E-04±0.322E-04	0.870
	0.93	0.574E-03±0.160E-04±0.359E-04	0.853
	0.95	0.671E-03±0.181E-04±0.420E-04	0.813
	0.97	0.839E-03±0.217E-04±0.524E-04	0.767

	0.99	0.951E-03±0.250E-04±0.594E-04	0.723
	1.01	0.814E-03±0.232E-04±0.509E-04	0.723
	1.03	0.702E-03±0.210E-04±0.439E-04	0.723
	1.05	0.459E-03±0.162E-04±0.287E-04	0.722
	1.07	0.366E-03±0.149E-04±0.229E-04	0.722
	1.09	0.248E-03±0.119E-04±0.155E-04	0.722
	1.11	0.163E-03±0.961E-05±0.102E-04	0.721
	1.13	0.121E-03±0.834E-05±0.755E-05	0.721
	1.15	0.791E-04±0.613E-05±0.494E-05	0.721
	1.17	0.482E-04±0.490E-05±0.301E-05	0.720
	1.19	0.387E-04±0.413E-05±0.242E-05	0.720
	1.21	0.399E-04±0.454E-05±0.249E-05	0.720
	1.23	0.356E-04±0.474E-05±0.222E-05	0.720
	1.25	0.228E-04±0.382E-05±0.142E-05	0.720
	1.27	0.190E-04±0.318E-05±0.119E-05	0.719
	1.29	0.244E-04±0.378E-05±0.152E-05	0.719
	1.31	0.114E-04±0.237E-05±0.715E-06	0.719
	1.33	0.907E-05±0.205E-05±0.567E-06	0.719
	1.35	0.112E-04±0.245E-05±0.699E-06	0.719
	1.37	0.514E-05±0.164E-05±0.321E-06	0.718
	1.39	0.862E-05±0.225E-05±0.538E-06	0.718
	1.41	0.543E-05±0.163E-05±0.339E-06	0.718
	1.43	0.511E-05±0.154E-05±0.319E-06	0.718
3.275	0.71	0.247E-02±0.342E-04±0.156E-03	0.874
	0.73	0.179E-02±0.268E-04±0.113E-03	0.871
	0.75	0.145E-02±0.239E-04±0.917E-04	0.871
	0.77	0.134E-02±0.236E-04±0.847E-04	0.870
	0.79	0.115E-02±0.216E-04±0.729E-04	0.867
	0.81	0.101E-02±0.206E-04±0.636E-04	0.861
	0.83	0.946E-03±0.204E-04±0.597E-04	0.855
	0.85	0.754E-03±0.179E-04±0.476E-04	0.855
	0.87	0.629E-03±0.163E-04±0.397E-04	0.859
	0.89	0.516E-03±0.145E-04±0.326E-04	0.868
	0.91	0.464E-03±0.134E-04±0.293E-04	0.872
	0.93	0.499E-03±0.138E-04±0.315E-04	0.855
	0.95	0.548E-03±0.152E-04±0.346E-04	0.819
	0.97	0.750E-03±0.204E-04±0.474E-04	0.764
	0.99	0.821E-03±0.228E-04±0.518E-04	0.724
	1.01	0.765E-03±0.218E-04±0.483E-04	0.723
	1.03	0.579E-03±0.189E-04±0.365E-04	0.723
	1.05	0.449E-03±0.167E-04±0.283E-04	0.723
	1.07	0.322E-03±0.141E-04±0.203E-04	0.722
	1.09	0.204E-03±0.106E-04±0.129E-04	0.722
	1.11	0.136E-03±0.824E-05±0.855E-05	0.722
	1.13	0.948E-04±0.673E-05±0.598E-05	0.721
	1.15	0.878E-04±0.704E-05±0.554E-05	0.721
	1.17	0.545E-04±0.510E-05±0.344E-05	0.721
	1.19	0.585E-04±0.587E-05±0.369E-05	0.720
	1.21	0.425E-04±0.523E-05±0.268E-05	0.720
	1.23	0.218E-04±0.315E-05±0.137E-05	0.720
	1.25	0.257E-04±0.411E-05±0.162E-05	0.720
	1.27	0.261E-04±0.394E-05±0.165E-05	0.720
	1.29	0.125E-04±0.241E-05±0.789E-06	0.719
	1.31	0.126E-04±0.293E-05±0.792E-06	0.719
	1.33	0.128E-04±0.308E-05±0.805E-06	0.719
	1.35	0.971E-05±0.277E-05±0.612E-06	0.719
	1.37	0.116E-04±0.291E-05±0.732E-06	0.719
	1.39	0.104E-04±0.272E-05±0.658E-06	0.718
	1.41	0.526E-05±0.212E-05±0.332E-06	0.718
	1.43	0.513E-05±0.207E-05±0.324E-06	0.718
	1.45	0.680E-05±0.232E-05±0.429E-06	0.718
	1.47	0.179E-05±0.114E-05±0.113E-06	0.718
3.325	0.71	0.238E-02±0.304E-04±0.152E-03	0.874
	0.73	0.170E-02±0.256E-04±0.108E-03	0.871
	0.75	0.139E-02±0.229E-04±0.885E-04	0.871
	0.77	0.120E-02±0.214E-04±0.768E-04	0.870
	0.79	0.107E-02±0.206E-04±0.681E-04	0.867
	0.81	0.980E-03±0.203E-04±0.626E-04	0.862
	0.83	0.861E-03±0.191E-04±0.550E-04	0.857
	0.85	0.765E-03±0.179E-04±0.489E-04	0.853
	0.87	0.596E-03±0.156E-04±0.381E-04	0.857
	0.89	0.510E-03±0.144E-04±0.326E-04	0.864
	0.91	0.449E-03±0.130E-04±0.287E-04	0.869
	0.93	0.465E-03±0.140E-04±0.297E-04	0.851
	0.95	0.572E-03±0.166E-04±0.366E-04	0.814
	0.97	0.672E-03±0.186E-04±0.429E-04	0.769
	0.99	0.770E-03±0.211E-04±0.492E-04	0.724
	1.01	0.680E-03±0.202E-04±0.435E-04	0.724
	1.03	0.554E-03±0.182E-04±0.354E-04	0.723
	1.05	0.357E-03±0.143E-04±0.228E-04	0.723
	1.07	0.267E-03±0.123E-04±0.171E-04	0.723
	1.09	0.184E-03±0.995E-05±0.118E-04	0.722
	1.11	0.140E-03±0.877E-05±0.895E-05	0.722
	1.13	0.844E-04±0.664E-05±0.540E-05	0.722
	1.15	0.623E-04±0.546E-05±0.398E-05	0.721
	1.17	0.614E-04±0.595E-05±0.393E-05	0.721
	1.19	0.332E-04±0.408E-05±0.212E-05	0.721
	1.21	0.266E-04±0.385E-05±0.170E-05	0.721
	1.23	0.188E-04±0.326E-05±0.120E-05	0.720
	1.25	0.167E-04±0.296E-05±0.107E-05	0.720
	1.27	0.150E-04±0.271E-05±0.957E-06	0.720
	1.29	0.999E-05±0.226E-05±0.638E-06	0.720
	1.31	0.849E-05±0.205E-05±0.542E-06	0.719
	1.33	0.103E-04±0.233E-05±0.659E-06	0.719
	1.35	0.862E-05±0.208E-05±0.551E-06	0.719
	1.37	0.756E-05±0.197E-05±0.483E-06	0.719
	1.39	0.563E-05±0.169E-05±0.360E-06	0.719
	1.41	0.728E-05±0.190E-05±0.465E-06	0.718
	1.43	0.322E-05±0.130E-05±0.206E-06	0.718
3.375	0.71	0.232E-02±0.305E-04±0.150E-03	0.875
	0.73	0.161E-02±0.222E-04±0.104E-03	0.871
	0.75	0.136E-02±0.216E-04±0.875E-04	0.870
	0.77	0.111E-02±0.203E-04±0.718E-04	0.870
	0.79	0.103E-02±0.196E-04±0.662E-04	0.868
	0.81	0.914E-03±0.192E-04±0.589E-04	0.863
	0.83	0.800E-03±0.183E-04±0.516E-04	0.857
	0.85	0.671E-03±0.165E-04±0.433E-04	0.855
	0.87	0.594E-03±0.155E-04±0.383E-04	0.860
	0.89	0.503E-03±0.142E-04±0.324E-04	0.863
	0.91	0.413E-03±0.123E-04±0.266E-04	0.871
	0.93	0.474E-03±0.140E-04±0.306E-04	0.856
	0.95	0.547E-03±0.161E-04±0.353E-04	0.811
	0.97	0.669E-03±0.189E-04±0.431E-04	0.769
	0.99	0.721E-03±0.209E-04±0.465E-04	0.724
	1.01	0.666E-03±0.204E-04±0.430E-04	0.724
	1.03	0.502E-03±0.168E-04±0.324E-04	0.724
	1.05	0.362E-03±0.135E-04±0.233E-04	0.723
	1.07	0.244E-03±0.115E-04±0.157E-04	0.723
	1.09	0.182E-03±0.996E-05±0.118E-04	0.722
	1.11	0.113E-03±0.788E-05±0.729E-05	0.722
	1.13	0.847E-04±0.658E-05±0.546E-05	0.722
	1.15	0.685E-04±0.604E-05±0.442E-05	0.722
	1.17	0.468E-04±0.498E-05±0.302E-05	0.721
	1.19	0.390E-04±0.437E-05±0.252E-05	0.721
	1.21	0.298E-04±0.397E-05±0.192E-05	0.721
	1.23	0.154E-04±0.283E-05±0.992E-06	0.721
	1.25	0.139E-04±0.261E-05±0.895E-06	0.720
	1.27	0.189E-04±0.312E-05±0.122E-05	0.720
	1.29	0.114E-04±0.231E-05±0.738E-06	0.720
	1.31	0.722E-05±0.188E-05±0.466E-06	0.720

	1.33	0.109E-04±0.255E-05±0.706E-06	0.719
	1.35	0.670E-05±0.192E-05±0.432E-06	0.719
	1.37	0.506E-05±0.161E-05±0.326E-06	0.719
	1.39	0.308E-05±0.124E-05±0.199E-06	0.719
	1.41	0.130E-05±0.830E-06±0.838E-07	0.719
	1.43	0.210E-05±0.109E-05±0.135E-06	0.718
3.425	0.71	0.224E-02±0.316E-04±0.146E-03	0.877
	0.73	0.159E-02±0.233E-04±0.104E-03	0.871
	0.75	0.128E-02±0.196E-04±0.834E-04	0.870
	0.77	0.116E-02±0.195E-04±0.755E-04	0.870
	0.79	0.960E-03±0.188E-04±0.626E-04	0.868
	0.81	0.882E-03±0.187E-04±0.575E-04	0.863
	0.83	0.795E-03±0.177E-04±0.518E-04	0.858
	0.85	0.666E-03±0.163E-04±0.434E-04	0.855
	0.87	0.536E-03±0.143E-04±0.349E-04	0.858
	0.89	0.433E-03±0.128E-04±0.282E-04	0.867
	0.91	0.427E-03±0.129E-04±0.278E-04	0.869
	0.93	0.456E-03±0.135E-04±0.297E-04	0.856
	0.95	0.468E-03±0.141E-04±0.305E-04	0.823
	0.97	0.624E-03±0.182E-04±0.407E-04	0.768
	0.99	0.689E-03±0.197E-04±0.449E-04	0.725
	1.01	0.676E-03±0.205E-04±0.441E-04	0.724
	1.03	0.496E-03±0.169E-04±0.323E-04	0.724
	1.05	0.317E-03±0.132E-04±0.207E-04	0.724
	1.07	0.227E-03±0.110E-04±0.148E-04	0.723
	1.09	0.173E-03±0.916E-05±0.113E-04	0.723
	1.11	0.109E-03±0.700E-05±0.713E-05	0.722
	1.13	0.919E-04±0.687E-05±0.599E-05	0.722
	1.15	0.577E-04±0.543E-05±0.376E-05	0.722
	1.17	0.368E-04±0.391E-05±0.240E-05	0.722
	1.19	0.368E-04±0.409E-05±0.240E-05	0.721
	1.21	0.222E-04±0.330E-05±0.145E-05	0.721
	1.23	0.200E-04±0.296E-05±0.130E-05	0.721
	1.25	0.226E-04±0.308E-05±0.148E-05	0.721
	1.27	0.867E-05±0.209E-05±0.565E-06	0.720
	1.29	0.110E-04±0.248E-05±0.716E-06	0.720
	1.31	0.926E-05±0.224E-05±0.604E-06	0.720
	1.33	0.112E-04±0.253E-05±0.732E-06	0.720
	1.35	0.711E-05±0.203E-05±0.463E-06	0.719
	1.37	0.709E-05±0.193E-05±0.462E-06	0.719
	1.39	0.344E-05±0.139E-05±0.224E-06	0.719
	1.41	0.133E-05±0.847E-06±0.864E-07	0.719
3.475	0.71	0.220E-02±0.310E-04±0.145E-03	0.878
	0.73	0.155E-02±0.237E-04±0.102E-03	0.871
	0.75	0.131E-02±0.216E-04±0.868E-04	0.870
	0.77	0.105E-02±0.180E-04±0.692E-04	0.870
	0.79	0.909E-03±0.164E-04±0.600E-04	0.868
	0.81	0.838E-03±0.171E-04±0.553E-04	0.864
	0.83	0.691E-03±0.158E-04±0.456E-04	0.859
	0.85	0.573E-03±0.149E-04±0.378E-04	0.855
	0.87	0.543E-03±0.147E-04±0.359E-04	0.858
	0.89	0.437E-03±0.128E-04±0.288E-04	0.864
	0.91	0.389E-03±0.120E-04±0.256E-04	0.870
	0.93	0.386E-03±0.123E-04±0.255E-04	0.859
	0.95	0.432E-03±0.136E-04±0.285E-04	0.817
	0.97	0.560E-03±0.168E-04±0.370E-04	0.770
	0.99	0.589E-03±0.178E-04±0.389E-04	0.725
	1.01	0.617E-03±0.193E-04±0.407E-04	0.725
	1.03	0.419E-03±0.157E-04±0.276E-04	0.724
	1.05	0.326E-03±0.132E-04±0.215E-04	0.724
	1.07	0.253E-03±0.120E-04±0.167E-04	0.723
	1.09	0.168E-03±0.992E-05±0.111E-04	0.723
	1.11	0.102E-03±0.695E-05±0.672E-05	0.723
	1.13	0.869E-04±0.649E-05±0.573E-05	0.722
	1.15	0.524E-04±0.523E-05±0.346E-05	0.722

	1.17	0.357E-04±0.400E-05±0.236E-05	0.722
	1.19	0.323E-04±0.397E-05±0.213E-05	0.722
	1.21	0.241E-04±0.315E-05±0.159E-05	0.721
	1.23	0.115E-04±0.216E-05±0.757E-06	0.721
	1.25	0.171E-04±0.265E-05±0.113E-05	0.721
	1.27	0.103E-04±0.214E-05±0.681E-06	0.721
	1.29	0.608E-05±0.159E-05±0.401E-06	0.720
	1.31	0.368E-05±0.126E-05±0.243E-06	0.720
	1.33	0.493E-05±0.148E-05±0.325E-06	0.720
	1.35	0.424E-05±0.135E-05±0.280E-06	0.720
	1.37	0.435E-05±0.139E-05±0.287E-06	0.719
	1.39	0.203E-05±0.917E-06±0.134E-06	0.719
3.525	0.71	0.197E-02±0.266E-04±0.131E-03	0.879
	0.73	0.153E-02±0.234E-04±0.102E-03	0.872
	0.75	0.127E-02±0.213E-04±0.847E-04	0.870
	0.77	0.106E-02±0.194E-04±0.708E-04	0.870
	0.79	0.868E-03±0.166E-04±0.578E-04	0.868
	0.81	0.769E-03±0.152E-04±0.512E-04	0.864
	0.83	0.656E-03±0.144E-04±0.437E-04	0.858
	0.85	0.586E-03±0.146E-04±0.390E-04	0.856
	0.87	0.502E-03±0.139E-04±0.334E-04	0.858
	0.89	0.420E-03±0.122E-04±0.280E-04	0.863
	0.91	0.406E-03±0.126E-04±0.271E-04	0.865
	0.93	0.385E-03±0.123E-04±0.256E-04	0.853
	0.95	0.433E-03±0.134E-04±0.288E-04	0.818
	0.97	0.543E-03±0.166E-04±0.362E-04	0.774
	0.99	0.532E-03±0.168E-04±0.354E-04	0.725
	1.01	0.523E-03±0.173E-04±0.348E-04	0.725
	1.03	0.403E-03±0.149E-04±0.268E-04	0.725
	1.05	0.307E-03±0.127E-04±0.204E-04	0.724
	1.07	0.219E-03±0.109E-04±0.146E-04	0.724
	1.09	0.155E-03±0.884E-05±0.103E-04	0.723
	1.11	0.972E-04±0.694E-05±0.647E-05	0.723
	1.13	0.540E-04±0.472E-05±0.360E-05	0.723
	1.15	0.494E-04±0.496E-05±0.329E-05	0.722
	1.17	0.474E-04±0.488E-05±0.315E-05	0.722
	1.19	0.250E-04±0.341E-05±0.167E-05	0.722
	1.21	0.218E-04±0.315E-05±0.145E-05	0.722
	1.23	0.255E-04±0.364E-05±0.170E-05	0.721
	1.25	0.124E-04±0.244E-05±0.825E-06	0.721
	1.27	0.136E-04±0.256E-05±0.903E-06	0.721
	1.29	0.932E-05±0.198E-05±0.621E-06	0.721
	1.31	0.736E-05±0.184E-05±0.490E-06	0.720
	1.33	0.105E-04±0.237E-05±0.699E-06	0.720
	1.35	0.354E-05±0.131E-05±0.236E-06	0.720
	1.37	0.827E-05±0.200E-05±0.551E-06	0.720
3.575	0.71	0.202E-02±0.262E-04±0.136E-03	0.881
	0.73	0.142E-02±0.202E-04±0.957E-04	0.873
	0.75	0.121E-02±0.203E-04±0.817E-04	0.870
	0.77	0.103E-02±0.192E-04±0.697E-04	0.870
	0.79	0.858E-03±0.175E-04±0.578E-04	0.869
	0.81	0.776E-03±0.163E-04±0.523E-04	0.865
	0.83	0.639E-03±0.141E-04±0.431E-04	0.860
	0.85	0.526E-03±0.125E-04±0.355E-04	0.855
	0.87	0.433E-03±0.116E-04±0.292E-04	0.857
	0.89	0.395E-03±0.118E-04±0.266E-04	0.865
	0.91	0.338E-03±0.109E-04±0.228E-04	0.868
	0.93	0.358E-03±0.118E-04±0.242E-04	0.855
	0.95	0.424E-03±0.134E-04±0.286E-04	0.814
	0.97	0.508E-03±0.156E-04±0.343E-04	0.771
	0.99	0.576E-03±0.180E-04±0.388E-04	0.726
	1.01	0.487E-03±0.166E-04±0.328E-04	0.725
	1.03	0.423E-03±0.154E-04±0.285E-04	0.725
	1.05	0.273E-03±0.123E-04±0.184E-04	0.725
	1.07	0.206E-03±0.104E-04±0.139E-04	0.724

	1.09	0.137E-03±0.828E-05±0.923E-05	0.724
	1.11	0.903E-04±0.651E-05±0.609E-05	0.723
	1.13	0.625E-04±0.533E-05±0.421E-05	0.723
	1.15	0.298E-04±0.360E-05±0.201E-05	0.723
	1.17	0.465E-04±0.491E-05±0.313E-05	0.722
	1.19	0.179E-04±0.286E-05±0.121E-05	0.722
	1.21	0.167E-04±0.259E-05±0.113E-05	0.722
	1.23	0.171E-04±0.273E-05±0.115E-05	0.722
	1.25	0.432E-05±0.123E-05±0.291E-06	0.721
	1.27	0.962E-05±0.185E-05±0.649E-06	0.721
	1.29	0.851E-05±0.199E-05±0.574E-06	0.721
	1.31	0.490E-05±0.156E-05±0.330E-06	0.721
	1.33	0.390E-05±0.158E-05±0.263E-06	0.720
3.625	0.71	0.193E-02±0.259E-04±0.132E-03	0.882
	0.73	0.138E-02±0.197E-04±0.938E-04	0.874
	0.75	0.111E-02±0.174E-04±0.755E-04	0.870
	0.77	0.952E-03±0.172E-04±0.648E-04	0.870
	0.79	0.832E-03±0.170E-04±0.566E-04	0.869
	0.81	0.702E-03±0.157E-04±0.478E-04	0.866
	0.83	0.599E-03±0.146E-04±0.408E-04	0.860
	0.85	0.534E-03±0.131E-04±0.364E-04	0.856
	0.87	0.455E-03±0.117E-04±0.310E-04	0.857
	0.89	0.363E-03±0.102E-04±0.247E-04	0.862
	0.91	0.329E-03±0.991E-05±0.224E-04	0.866
	0.93	0.370E-03±0.119E-04±0.252E-04	0.855
	0.95	0.365E-03±0.122E-04±0.249E-04	0.826
	0.97	0.471E-03±0.150E-04±0.321E-04	0.772
	0.99	0.478E-03±0.159E-04±0.325E-04	0.726
	1.01	0.505E-03±0.171E-04±0.344E-04	0.726
	1.03	0.325E-03±0.128E-04±0.221E-04	0.725
	1.05	0.287E-03±0.125E-04±0.195E-04	0.725
	1.07	0.184E-03±0.952E-05±0.125E-04	0.725
	1.09	0.128E-03±0.783E-05±0.872E-05	0.724
	1.11	0.751E-04±0.580E-05±0.511E-05	0.724
	1.13	0.579E-04±0.537E-05±0.394E-05	0.723
	1.15	0.525E-04±0.503E-05±0.358E-05	0.723
	1.17	0.356E-04±0.393E-05±0.242E-05	0.723
	1.19	0.228E-04±0.330E-05±0.155E-05	0.722
	1.21	0.253E-04±0.361E-05±0.172E-05	0.722
	1.23	0.190E-04±0.286E-05±0.130E-05	0.722
	1.25	0.601E-05±0.140E-05±0.410E-06	0.722
	1.27	0.599E-05±0.180E-05±0.408E-06	0.721
	1.29	0.587E-05±0.201E-05±0.400E-06	0.721
	1.31	0.122E-04±0.305E-05±0.828E-06	0.721
	1.33	0.442E-05±0.179E-05±0.301E-06	0.721
3.675	0.71	0.170E-02±0.246E-04±0.117E-03	0.884
	0.73	0.128E-02±0.185E-04±0.880E-04	0.875
	0.75	0.109E-02±0.173E-04±0.752E-04	0.870
	0.77	0.945E-03±0.163E-04±0.651E-04	0.870
	0.79	0.773E-03±0.150E-04±0.533E-04	0.869
	0.81	0.728E-03±0.159E-04±0.501E-04	0.866
	0.83	0.615E-03±0.148E-04±0.424E-04	0.860
	0.85	0.542E-03±0.141E-04±0.374E-04	0.857
	0.87	0.455E-03±0.125E-04±0.313E-04	0.858
	0.89	0.365E-03±0.104E-04±0.252E-04	0.861
	0.91	0.317E-03±0.928E-05±0.219E-04	0.866
	0.93	0.308E-03±0.938E-05±0.212E-04	0.857
	0.95	0.381E-03±0.116E-04±0.263E-04	0.820
	0.97	0.423E-03±0.137E-04±0.291E-04	0.776
	0.99	0.473E-03±0.154E-04±0.326E-04	0.727
	1.01	0.427E-03±0.147E-04±0.294E-04	0.726
	1.03	0.328E-03±0.127E-04±0.226E-04	0.726
	1.05	0.237E-03±0.105E-04±0.163E-04	0.725
	1.07	0.173E-03±0.921E-05±0.119E-04	0.725
	1.09	0.997E-04±0.662E-05±0.687E-05	0.724

	1.11	0.840E-04±0.598E-05±0.579E-05	0.724
	1.13	0.604E-04±0.525E-05±0.416E-05	0.724
	1.15	0.463E-04±0.480E-05±0.319E-05	0.723
	1.17	0.316E-04±0.392E-05±0.218E-05	0.723
	1.19	0.356E-04±0.430E-05±0.245E-05	0.723
	1.21	0.170E-04±0.301E-05±0.117E-05	0.722
	1.23	0.143E-04±0.275E-05±0.984E-06	0.722
	1.25	0.129E-04±0.243E-05±0.889E-06	0.722
	1.27	0.921E-05±0.231E-05±0.635E-06	0.722
	1.29	0.106E-04±0.240E-05±0.731E-06	0.721
	1.31	0.751E-05±0.196E-05±0.517E-06	0.721
3.725	0.71	0.174E-02±0.282E-04±0.121E-03	0.885
	0.73	0.129E-02±0.193E-04±0.897E-04	0.875
	0.75	0.105E-02±0.167E-04±0.728E-04	0.871
	0.77	0.871E-03±0.154E-04±0.606E-04	0.869
	0.79	0.769E-03±0.146E-04±0.535E-04	0.869
	0.81	0.684E-03±0.139E-04±0.476E-04	0.867
	0.83	0.552E-03±0.130E-04±0.384E-04	0.863
	0.85	0.500E-03±0.133E-04±0.348E-04	0.858
	0.87	0.447E-03±0.128E-04±0.311E-04	0.857
	0.89	0.367E-03±0.115E-04±0.255E-04	0.863
	0.91	0.294E-03±0.952E-05±0.204E-04	0.866
	0.93	0.273E-03±0.880E-05±0.190E-04	0.853
	0.95	0.325E-03±0.100E-04±0.226E-04	0.824
	0.97	0.391E-03±0.120E-04±0.272E-04	0.773
	0.99	0.454E-03±0.144E-04±0.316E-04	0.727
	1.01	0.395E-03±0.139E-04±0.275E-04	0.727
	1.03	0.328E-03±0.127E-04±0.228E-04	0.726
	1.05	0.213E-03±0.101E-04±0.148E-04	0.726
	1.07	0.160E-03±0.860E-05±0.112E-04	0.725
	1.09	0.117E-03±0.743E-05±0.813E-05	0.725
	1.11	0.896E-04±0.719E-05±0.624E-05	0.724
	1.13	0.496E-04±0.467E-05±0.345E-05	0.724
	1.15	0.408E-04±0.432E-05±0.284E-05	0.724
	1.17	0.250E-04±0.310E-05±0.174E-05	0.723
	1.19	0.139E-04±0.229E-05±0.965E-06	0.723
	1.21	0.113E-04±0.197E-05±0.789E-06	0.723
	1.23	0.120E-04±0.231E-05±0.835E-06	0.722
	1.25	0.969E-05±0.201E-05±0.675E-06	0.722
	1.27	0.786E-05±0.225E-05±0.547E-06	0.722
	1.29	0.786E-05±0.214E-05±0.547E-06	0.722
	1.31	0.708E-05±0.213E-05±0.493E-06	0.721
	1.33	0.630E-05±0.201E-05±0.438E-06	0.721
3.775	0.71	0.170E-02±0.285E-04±0.119E-03	0.886
	0.73	0.123E-02±0.209E-04±0.867E-04	0.876
	0.75	0.944E-03±0.158E-04±0.664E-04	0.871
	0.77	0.839E-03±0.148E-04±0.590E-04	0.870
	0.79	0.725E-03±0.141E-04±0.510E-04	0.869
	0.81	0.608E-03±0.128E-04±0.427E-04	0.867
	0.83	0.521E-03±0.119E-04±0.366E-04	0.862
	0.85	0.507E-03±0.126E-04±0.357E-04	0.858
	0.87	0.436E-03±0.124E-04±0.306E-04	0.858
	0.89	0.335E-03±0.109E-04±0.236E-04	0.863
	0.91	0.312E-03±0.103E-04±0.219E-04	0.865
	0.93	0.301E-03±0.101E-04±0.211E-04	0.860
	0.95	0.330E-03±0.104E-04±0.232E-04	0.823
	0.97	0.338E-03±0.108E-04±0.238E-04	0.773
	0.99	0.402E-03±0.127E-04±0.282E-04	0.728
	1.01	0.349E-03±0.116E-04±0.245E-04	0.727
	1.03	0.293E-03±0.110E-04±0.206E-04	0.727
	1.05	0.199E-03±0.930E-05±0.140E-04	0.726
	1.07	0.158E-03±0.833E-05±0.111E-04	0.726
	1.09	0.948E-04±0.655E-05±0.667E-05	0.725
	1.11	0.816E-04±0.590E-05±0.574E-05	0.725
	1.13	0.491E-04±0.446E-05±0.345E-05	0.724

	1.15	0.302E-04±0.347E-05±0.213E-05	0.724
	1.17	0.258E-04±0.333E-05±0.182E-05	0.724
	1.19	0.150E-04±0.247E-05±0.105E-05	0.723
	1.21	0.171E-04±0.302E-05±0.120E-05	0.723
	1.23	0.907E-05±0.183E-05±0.637E-06	0.723
	1.25	0.111E-04±0.200E-05±0.780E-06	0.722
	1.27	0.510E-05±0.139E-05±0.359E-06	0.722
	1.29	0.834E-05±0.183E-05±0.586E-06	0.722
	1.31	0.307E-05±0.105E-05±0.216E-06	0.722
	1.33	0.242E-05±0.827E-06±0.170E-06	0.721
3.825	0.71	0.157E-02±0.266E-04±0.111E-03	0.888
	0.73	0.121E-02±0.215E-04±0.857E-04	0.878
	0.75	0.980E-03±0.176E-04±0.696E-04	0.872
	0.77	0.838E-03±0.154E-04±0.595E-04	0.869
	0.79	0.676E-03±0.132E-04±0.480E-04	0.869
	0.81	0.610E-03±0.129E-04±0.433E-04	0.867
	0.83	0.527E-03±0.120E-04±0.374E-04	0.863
	0.85	0.474E-03±0.114E-04±0.336E-04	0.859
	0.87	0.370E-03±0.100E-04±0.263E-04	0.858
	0.89	0.312E-03±0.971E-05±0.221E-04	0.861
	0.91	0.285E-03±0.964E-05±0.202E-04	0.867
	0.93	0.270E-03±0.959E-05±0.191E-04	0.862
	0.95	0.313E-03±0.110E-04±0.222E-04	0.827
	0.97	0.347E-03±0.119E-04±0.246E-04	0.776
	0.99	0.378E-03±0.124E-04±0.268E-04	0.728
	1.01	0.340E-03±0.119E-04±0.241E-04	0.727
	1.03	0.271E-03±0.104E-04±0.192E-04	0.727
	1.05	0.203E-03±0.872E-05±0.144E-04	0.726
	1.07	0.129E-03±0.677E-05±0.916E-05	0.726
	1.09	0.105E-03±0.653E-05±0.743E-05	0.726
	1.11	0.727E-04±0.565E-05±0.516E-05	0.725
	1.13	0.513E-04±0.476E-05±0.364E-05	0.725
	1.15	0.385E-04±0.415E-05±0.273E-05	0.724
	1.17	0.259E-04±0.324E-05±0.184E-05	0.724
	1.19	0.161E-04±0.262E-05±0.115E-05	0.724
	1.21	0.133E-04±0.269E-05±0.947E-06	0.723
	1.23	0.138E-04±0.273E-05±0.982E-06	0.723
	1.25	0.815E-05±0.197E-05±0.579E-06	0.723
	1.27	0.144E-04±0.324E-05±0.102E-05	0.722
	1.29	0.766E-05±0.231E-05±0.544E-06	0.722
	1.31	0.681E-05±0.218E-05±0.484E-06	0.722
3.875	0.71	0.155E-02±0.243E-04±0.112E-03	0.890
	0.73	0.111E-02±0.205E-04±0.797E-04	0.879
	0.75	0.991E-03±0.184E-04±0.712E-04	0.872
	0.77	0.843E-03±0.165E-04±0.606E-04	0.870
	0.79	0.688E-03±0.145E-04±0.495E-04	0.869
	0.81	0.531E-03±0.118E-04±0.382E-04	0.867
	0.83	0.475E-03±0.114E-04±0.341E-04	0.863
	0.85	0.420E-03±0.106E-04±0.302E-04	0.859
	0.87	0.365E-03±0.982E-05±0.263E-04	0.857
	0.89	0.322E-03±0.933E-05±0.232E-04	0.863
	0.91	0.279E-03±0.875E-05±0.201E-04	0.867
	0.93	0.253E-03±0.897E-05±0.182E-04	0.856
	0.95	0.268E-03±0.100E-04±0.192E-04	0.822
	0.97	0.363E-03±0.128E-04±0.261E-04	0.781
	0.99	0.389E-03±0.140E-04±0.279E-04	0.728
	1.01	0.338E-03±0.130E-04±0.243E-04	0.728
	1.03	0.247E-03±0.998E-05±0.178E-04	0.727
	1.05	0.192E-03±0.847E-05±0.138E-04	0.727
	1.07	0.128E-03±0.674E-05±0.917E-05	0.726
	1.09	0.714E-04±0.490E-05±0.513E-05	0.726
	1.11	0.652E-04±0.469E-05±0.469E-05	0.726
	1.13	0.344E-04±0.357E-05±0.248E-05	0.725
	1.15	0.312E-04±0.364E-05±0.224E-05	0.725
	1.17	0.303E-04±0.372E-05±0.218E-05	0.724
	1.19	0.276E-04±0.349E-05±0.198E-05	0.724
	1.21	0.166E-04±0.294E-05±0.119E-05	0.724
	1.23	0.210E-04±0.330E-05±0.151E-05	0.723
	1.25	0.770E-05±0.174E-05±0.553E-06	0.723
	1.27	0.746E-05±0.187E-05±0.536E-06	0.723
	1.29	0.533E-05±0.152E-05±0.383E-06	0.723
	1.31	0.465E-05±0.140E-05±0.334E-06	0.722
3.925	0.71	0.144E-02±0.225E-04±0.104E-03	0.891
	0.73	0.109E-02±0.186E-04±0.788E-04	0.881
	0.75	0.948E-03±0.186E-04±0.687E-04	0.873
	0.77	0.766E-03±0.155E-04±0.555E-04	0.870
	0.79	0.643E-03±0.141E-04±0.466E-04	0.869
	0.81	0.549E-03±0.129E-04±0.398E-04	0.868
	0.83	0.474E-03±0.113E-04±0.344E-04	0.865
	0.85	0.366E-03±0.954E-05±0.266E-04	0.860
	0.87	0.350E-03±0.981E-05±0.254E-04	0.859
	0.89	0.280E-03±0.869E-05±0.203E-04	0.861
	0.91	0.258E-03±0.829E-05±0.187E-04	0.863
	0.93	0.256E-03±0.832E-05±0.186E-04	0.854
	0.95	0.260E-03±0.899E-05±0.189E-04	0.821
	0.97	0.340E-03±0.122E-04±0.247E-04	0.780
	0.99	0.361E-03±0.133E-04±0.261E-04	0.729
	1.01	0.347E-03±0.131E-04±0.252E-04	0.728
	1.03	0.259E-03±0.109E-04±0.188E-04	0.728
	1.05	0.173E-03±0.816E-05±0.126E-04	0.727
	1.07	0.141E-03±0.750E-05±0.102E-04	0.727
	1.09	0.791E-04±0.547E-05±0.574E-05	0.726
	1.11	0.548E-04±0.435E-05±0.397E-05	0.726
	1.13	0.541E-04±0.444E-05±0.392E-05	0.725
	1.15	0.336E-04±0.348E-05±0.244E-05	0.725
	1.17	0.180E-04±0.254E-05±0.130E-05	0.725
	1.19	0.121E-04±0.200E-05±0.880E-06	0.724
	1.21	0.188E-04±0.296E-05±0.137E-05	0.724
	1.23	0.979E-05±0.198E-05±0.710E-06	0.724
	1.25	0.544E-05±0.131E-05±0.394E-06	0.723
	1.27	0.746E-05±0.180E-05±0.541E-06	0.723
	1.29	0.416E-05±0.125E-05±0.302E-06	0.723
3.975	0.71	0.133E-02±0.220E-04±0.972E-04	0.892
	0.73	0.106E-02±0.180E-04±0.780E-04	0.882
	0.75	0.940E-03±0.172E-04±0.689E-04	0.874
	0.77	0.794E-03±0.160E-04±0.582E-04	0.871
	0.79	0.666E-03±0.147E-04±0.488E-04	0.869
	0.81	0.542E-03±0.131E-04±0.397E-04	0.867
	0.83	0.464E-03±0.122E-04±0.340E-04	0.864
	0.85	0.388E-03±0.104E-04±0.284E-04	0.861
	0.87	0.337E-03±0.943E-05±0.247E-04	0.859
	0.89	0.278E-03±0.863E-05±0.204E-04	0.861
	0.91	0.233E-03±0.759E-05±0.171E-04	0.865
	0.93	0.246E-03±0.830E-05±0.180E-04	0.855
	0.95	0.273E-03±0.903E-05±0.200E-04	0.826
	0.97	0.272E-03±0.932E-05±0.199E-04	0.776
	0.99	0.300E-03±0.108E-04±0.220E-04	0.729
	1.01	0.310E-03±0.118E-04±0.227E-04	0.729
	1.03	0.236E-03±0.103E-04±0.173E-04	0.728
	1.05	0.170E-03±0.858E-05±0.125E-04	0.728
	1.07	0.111E-03±0.677E-05±0.814E-05	0.727
	1.09	0.725E-04±0.532E-05±0.532E-05	0.727
	1.11	0.636E-04±0.496E-05±0.466E-05	0.726
	1.13	0.379E-04±0.355E-05±0.278E-05	0.726
	1.15	0.292E-04±0.306E-05±0.214E-05	0.725
	1.17	0.167E-04±0.213E-05±0.122E-05	0.725
	1.19	0.161E-04±0.243E-05±0.118E-05	0.725
	1.21	0.117E-04±0.193E-05±0.857E-06	0.724
	1.23	0.517E-05±0.125E-05±0.379E-06	0.724
	1.25	0.668E-05±0.167E-05±0.490E-06	0.724

	1.27	0.391E-05±0.118E-05±0.287E-06	0.723
	1.29	0.375E-05±0.128E-05±0.275E-06	0.723
	1.31	0.613E-05±0.154E-05±0.449E-06	0.723
4.025	0.71	0.128E-02±0.224E-04±0.945E-04	0.893
	0.73	0.941E-03±0.170E-04±0.697E-04	0.883
	0.75	0.842E-03±0.158E-04±0.624E-04	0.875
	0.77	0.747E-03±0.149E-04±0.554E-04	0.871
	0.79	0.603E-03±0.133E-04±0.447E-04	0.869
	0.81	0.564E-03±0.133E-04±0.418E-04	0.868
	0.83	0.468E-03±0.123E-04±0.347E-04	0.864
	0.85	0.411E-03±0.116E-04±0.305E-04	0.861
	0.87	0.333E-03±0.101E-04±0.247E-04	0.859
	0.89	0.274E-03±0.866E-05±0.203E-04	0.861
	0.91	0.219E-03±0.740E-05±0.162E-04	0.867
	0.93	0.203E-03±0.701E-05±0.150E-04	0.859
	0.95	0.233E-03±0.807E-05±0.172E-04	0.830
	0.97	0.293E-03±0.100E-04±0.217E-04	0.784
	0.99	0.307E-03±0.107E-04±0.227E-04	0.730
	1.01	0.255E-03±0.965E-05±0.189E-04	0.729
	1.03	0.220E-03±0.951E-05±0.163E-04	0.729
	1.05	0.155E-03±0.802E-05±0.115E-04	0.728
	1.07	0.929E-04±0.588E-05±0.688E-05	0.728
	1.09	0.836E-04±0.586E-05±0.619E-05	0.727
	1.11	0.496E-04±0.441E-05±0.368E-05	0.727
	1.13	0.415E-04±0.395E-05±0.308E-05	0.726
	1.15	0.230E-04±0.264E-05±0.170E-05	0.726
	1.17	0.174E-04±0.242E-05±0.129E-05	0.725
	1.19	0.159E-04±0.230E-05±0.118E-05	0.725
	1.21	0.101E-04±0.166E-05±0.746E-06	0.725
	1.23	0.112E-04±0.202E-05±0.827E-06	0.724
	1.25	0.732E-05±0.183E-05±0.542E-06	0.724
	1.27	0.715E-05±0.173E-05±0.530E-06	0.724
	1.29	0.766E-05±0.179E-05±0.568E-06	0.723
	1.31	0.204E-05±0.923E-06±0.151E-06	0.723
4.075	0.71	0.127E-02±0.227E-04±0.949E-04	0.894
	0.73	0.882E-03±0.172E-04±0.661E-04	0.885
	0.75	0.802E-03±0.158E-04±0.601E-04	0.876
	0.77	0.678E-03±0.140E-04±0.508E-04	0.871
	0.79	0.590E-03±0.124E-04±0.442E-04	0.870
	0.81	0.522E-03±0.124E-04±0.391E-04	0.869
	0.83	0.479E-03±0.124E-04±0.359E-04	0.866
	0.85	0.377E-03±0.108E-04±0.282E-04	0.862
	0.87	0.344E-03±0.107E-04±0.257E-04	0.858
	0.89	0.265E-03±0.917E-05±0.199E-04	0.861
	0.91	0.221E-03±0.762E-05±0.165E-04	0.866
	0.93	0.195E-03±0.705E-05±0.146E-04	0.860
	0.95	0.220E-03±0.787E-05±0.165E-04	0.823
	0.97	0.260E-03±0.930E-05±0.195E-04	0.777
	0.99	0.308E-03±0.110E-04±0.231E-04	0.730
	1.01	0.257E-03±0.984E-05±0.192E-04	0.730
	1.03	0.217E-03±0.892E-05±0.163E-04	0.729
	1.05	0.140E-03±0.700E-05±0.105E-04	0.729
	1.07	0.881E-04±0.564E-05±0.660E-05	0.728
	1.09	0.647E-04±0.511E-05±0.485E-05	0.728
	1.11	0.514E-04±0.447E-05±0.385E-05	0.727
	1.13	0.331E-04±0.376E-05±0.248E-05	0.727
	1.15	0.297E-04±0.365E-05±0.222E-05	0.726
	1.17	0.209E-04±0.288E-05±0.157E-05	0.726
	1.19	0.113E-04±0.229E-05±0.848E-06	0.725
	1.21	0.115E-04±0.212E-05±0.862E-06	0.725
	1.23	0.750E-05±0.160E-05±0.561E-06	0.725
	1.25	0.812E-05±0.173E-05±0.608E-06	0.724
	1.27	0.477E-05±0.130E-05±0.357E-06	0.724
	1.29	0.304E-05±0.104E-05±0.227E-06	0.724
4.125	0.71	0.118E-02±0.222E-04±0.893E-04	0.895
	0.73	0.865E-03±0.173E-04±0.654E-04	0.885
	0.75	0.778E-03±0.162E-04±0.588E-04	0.876
	0.77	0.642E-03±0.142E-04±0.486E-04	0.871
	0.79	0.575E-03±0.128E-04±0.435E-04	0.870
	0.81	0.479E-03±0.108E-04±0.362E-04	0.869
	0.83	0.425E-03±0.108E-04±0.321E-04	0.866
	0.85	0.362E-03±0.106E-04±0.274E-04	0.862
	0.87	0.302E-03±0.951E-05±0.229E-04	0.858
	0.89	0.262E-03±0.906E-05±0.198E-04	0.861
	0.91	0.207E-03±0.788E-05±0.156E-04	0.866
	0.93	0.200E-03±0.742E-05±0.151E-04	0.860
	0.95	0.185E-03±0.710E-05±0.140E-04	0.823
	0.97	0.240E-03±0.861E-05±0.181E-04	0.777
	0.99	0.254E-03±0.965E-05±0.192E-04	0.730
	1.01	0.224E-03±0.880E-05±0.170E-04	0.730
	1.03	0.186E-03±0.800E-05±0.141E-04	0.729
	1.05	0.158E-03±0.763E-05±0.120E-04	0.729
	1.07	0.106E-03±0.613E-05±0.800E-05	0.728
	1.09	0.592E-04±0.422E-05±0.448E-05	0.728
	1.11	0.540E-04±0.476E-05±0.408E-05	0.727
	1.13	0.323E-04±0.339E-05±0.244E-05	0.727
	1.15	0.255E-04±0.303E-05±0.193E-05	0.726
	1.17	0.174E-04±0.246E-05±0.132E-05	0.726
	1.19	0.160E-04±0.269E-05±0.121E-05	0.725
	1.21	0.155E-04±0.274E-05±0.117E-05	0.725
	1.23	0.799E-05±0.175E-05±0.604E-06	0.725
	1.25	0.100E-04±0.208E-05±0.758E-06	0.724
	1.27	0.605E-05±0.146E-05±0.457E-06	0.724
	1.29	0.346E-05±0.110E-05±0.261E-06	0.724
4.175	0.71	0.122E-02±0.221E-04±0.931E-04	0.896
	0.73	0.833E-03±0.169E-04±0.636E-04	0.885
	0.75	0.792E-03±0.169E-04±0.605E-04	0.876
	0.77	0.671E-03±0.153E-04±0.513E-04	0.871
	0.79	0.561E-03±0.134E-04±0.429E-04	0.870
	0.81	0.483E-03±0.110E-04±0.369E-04	0.869
	0.83	0.412E-03±0.997E-05±0.315E-04	0.866
	0.85	0.340E-03±0.965E-05±0.260E-04	0.862
	0.87	0.297E-03±0.946E-05±0.227E-04	0.858
	0.89	0.236E-03±0.844E-05±0.180E-04	0.861
	0.91	0.202E-03±0.777E-05±0.155E-04	0.866
	0.93	0.202E-03±0.788E-05±0.155E-04	0.860
	0.95	0.214E-03±0.840E-05±0.164E-04	0.823
	0.97	0.207E-03±0.831E-05±0.158E-04	0.777
	0.99	0.273E-03±0.101E-04±0.209E-04	0.730
	1.01	0.243E-03±0.937E-05±0.185E-04	0.730
	1.03	0.191E-03±0.828E-05±0.146E-04	0.729
	1.05	0.128E-03±0.655E-05±0.975E-05	0.729
	1.07	0.876E-04±0.511E-05±0.669E-05	0.728
	1.09	0.650E-04±0.450E-05±0.497E-05	0.728
	1.11	0.421E-04±0.345E-05±0.322E-05	0.727
	1.13	0.302E-04±0.326E-05±0.231E-05	0.727
	1.15	0.199E-04±0.236E-05±0.152E-05	0.726
	1.17	0.144E-04±0.206E-05±0.110E-05	0.726
	1.19	0.987E-05±0.166E-05±0.754E-06	0.725
	1.21	0.706E-05±0.171E-05±0.540E-06	0.725
	1.23	0.103E-04±0.208E-05±0.786E-06	0.725
	1.25	0.569E-05±0.142E-05±0.434E-06	0.724
	1.27	0.232E-05±0.937E-06±0.177E-06	0.724
	1.29	0.325E-05±0.111E-05±0.248E-06	0.724
4.225	0.71	0.110E-02±0.201E-04±0.851E-04	0.897
	0.73	0.813E-03±0.166E-04±0.628E-04	0.888
	0.75	0.708E-03±0.158E-04±0.547E-04	0.879
	0.77	0.606E-03±0.145E-04±0.468E-04	0.872
	0.79	0.538E-03±0.137E-04±0.415E-04	0.871
	0.81	0.448E-03±0.117E-04±0.346E-04	0.869

	0.83	0.391E-03±0.985E-05±0.302E-04	0.867
	0.85	0.312E-03±0.839E-05±0.241E-04	0.864
	0.87	0.283E-03±0.880E-05±0.219E-04	0.860
	0.89	0.240E-03±0.849E-05±0.185E-04	0.860
	0.91	0.197E-03±0.760E-05±0.152E-04	0.867
	0.93	0.170E-03±0.703E-05±0.131E-04	0.859
	0.95	0.181E-03±0.767E-05±0.140E-04	0.836
	0.97	0.213E-03±0.904E-05±0.165E-04	0.781
	0.99	0.239E-03±0.100E-04±0.185E-04	0.732
	1.01	0.229E-03±0.930E-05±0.177E-04	0.731
	1.03	0.162E-03±0.746E-05±0.125E-04	0.730
	1.05	0.122E-03±0.631E-05±0.944E-05	0.730
	1.07	0.787E-04±0.508E-05±0.608E-05	0.729
	1.09	0.560E-04±0.427E-05±0.432E-05	0.729
	1.11	0.417E-04±0.347E-05±0.322E-05	0.728
	1.13	0.318E-04±0.332E-05±0.246E-05	0.728
	1.15	0.184E-04±0.229E-05±0.142E-05	0.727
	1.17	0.145E-04±0.208E-05±0.112E-05	0.727
	1.19	0.912E-05±0.143E-05±0.704E-06	0.727
	1.21	0.749E-05±0.148E-05±0.578E-06	0.726
	1.23	0.783E-05±0.177E-05±0.604E-06	0.726
	1.25	0.261E-05±0.962E-06±0.201E-06	0.725
	1.27	0.491E-05±0.128E-05±0.379E-06	0.725
4.275	0.71	0.105E-02±0.187E-04±0.820E-04	0.898
	0.73	0.799E-03±0.158E-04±0.623E-04	0.890
	0.75	0.695E-03±0.154E-04±0.542E-04	0.880
	0.77	0.581E-03±0.145E-04±0.453E-04	0.873
	0.79	0.505E-03±0.135E-04±0.394E-04	0.870
	0.81	0.413E-03±0.118E-04±0.322E-04	0.869
	0.83	0.327E-03±0.930E-05±0.255E-04	0.868
	0.85	0.318E-03±0.888E-05±0.248E-04	0.864
	0.87	0.275E-03±0.825E-05±0.215E-04	0.861
	0.89	0.231E-03±0.773E-05±0.180E-04	0.863
	0.91	0.183E-03±0.725E-05±0.143E-04	0.865
	0.93	0.185E-03±0.767E-05±0.144E-04	0.854
	0.95	0.183E-03±0.759E-05±0.143E-04	0.832
	0.97	0.211E-03±0.896E-05±0.164E-04	0.782
	0.99	0.192E-03±0.856E-05±0.150E-04	0.732
	1.01	0.198E-03±0.903E-05±0.155E-04	0.732
	1.03	0.166E-03±0.803E-05±0.129E-04	0.731
	1.05	0.116E-03±0.631E-05±0.901E-05	0.730
	1.07	0.754E-04±0.462E-05±0.588E-05	0.730
	1.09	0.539E-04±0.410E-05±0.420E-05	0.729
	1.11	0.343E-04±0.310E-05±0.268E-05	0.729
	1.13	0.257E-04±0.267E-05±0.201E-05	0.728
	1.15	0.184E-04±0.222E-05±0.144E-05	0.728
	1.17	0.139E-04±0.199E-05±0.109E-05	0.727
	1.19	0.104E-04±0.169E-05±0.814E-06	0.727
	1.21	0.940E-05±0.163E-05±0.733E-06	0.726
	1.23	0.100E-04±0.184E-05±0.780E-06	0.726
	1.25	0.533E-05±0.139E-05±0.416E-06	0.726
	1.27	0.822E-05±0.175E-05±0.641E-06	0.725
4.325	0.71	0.101E-02±0.177E-04±0.791E-04	0.899
	0.73	0.698E-03±0.142E-04±0.549E-04	0.891
	0.75	0.654E-03±0.141E-04±0.514E-04	0.882
	0.77	0.535E-03±0.133E-04±0.421E-04	0.874
	0.79	0.460E-03±0.125E-04±0.362E-04	0.871
	0.81	0.368E-03±0.109E-04±0.290E-04	0.870
	0.83	0.348E-03±0.106E-04±0.274E-04	0.868
	0.85	0.312E-03±0.911E-05±0.246E-04	0.864
	0.87	0.269E-03±0.822E-05±0.212E-04	0.863
	0.89	0.185E-03±0.641E-05±0.146E-04	0.863
	0.91	0.174E-03±0.650E-05±0.137E-04	0.865
	0.93	0.164E-03±0.676E-05±0.129E-04	0.857
	0.95	0.165E-03±0.723E-05±0.130E-04	0.829
	0.97	0.217E-03±0.887E-05±0.171E-04	0.787
	0.99	0.207E-03±0.907E-05±0.163E-04	0.733
	1.01	0.188E-03±0.881E-05±0.148E-04	0.732
	1.03	0.168E-03±0.829E-05±0.132E-04	0.731
	1.05	0.102E-03±0.629E-05±0.803E-05	0.731
	1.07	0.732E-04±0.502E-05±0.576E-05	0.730
	1.09	0.459E-04±0.358E-05±0.361E-05	0.730
	1.11	0.359E-04±0.326E-05±0.282E-05	0.729
	1.13	0.190E-04±0.221E-05±0.149E-05	0.729
	1.15	0.148E-04±0.195E-05±0.116E-05	0.728
	1.17	0.147E-04±0.218E-05±0.115E-05	0.728
	1.19	0.934E-05±0.172E-05±0.735E-06	0.727
	1.21	0.113E-04±0.189E-05±0.887E-06	0.727
	1.23	0.653E-05±0.158E-05±0.514E-06	0.726
	1.25	0.432E-05±0.123E-05±0.340E-06	0.726
	1.27	0.421E-05±0.120E-05±0.332E-06	0.726
4.375	0.71	0.934E-03±0.168E-04±0.743E-04	0.900
	0.73	0.697E-03±0.134E-04±0.554E-04	0.893
	0.75	0.611E-03±0.133E-04±0.486E-04	0.882
	0.77	0.569E-03±0.133E-04±0.452E-04	0.875
	0.79	0.443E-03±0.121E-04±0.352E-04	0.871
	0.81	0.357E-03±0.110E-04±0.284E-04	0.869
	0.83	0.335E-03±0.111E-04±0.267E-04	0.869
	0.85	0.293E-03±0.925E-05±0.233E-04	0.865
	0.87	0.250E-03±0.816E-05±0.199E-04	0.862
	0.89	0.180E-03±0.631E-05±0.143E-04	0.863
	0.91	0.170E-03±0.640E-05±0.135E-04	0.865
	0.93	0.146E-03±0.576E-05±0.116E-04	0.862
	0.95	0.172E-03±0.726E-05±0.137E-04	0.836
	0.97	0.173E-03±0.786E-05±0.137E-04	0.784
	0.99	0.195E-03±0.866E-05±0.155E-04	0.733
	1.01	0.203E-03±0.932E-05±0.161E-04	0.733
	1.03	0.151E-03±0.774E-05±0.120E-04	0.732
	1.05	0.105E-03±0.650E-05±0.837E-05	0.731
	1.07	0.886E-04±0.587E-05±0.704E-05	0.731
	1.09	0.400E-04±0.374E-05±0.318E-05	0.730
	1.11	0.402E-04±0.367E-05±0.320E-05	0.730
	1.13	0.189E-04±0.228E-05±0.150E-05	0.729
	1.15	0.166E-04±0.226E-05±0.132E-05	0.729
	1.17	0.129E-04±0.200E-05±0.103E-05	0.728
	1.19	0.101E-04±0.172E-05±0.799E-06	0.728
	1.21	0.953E-05±0.166E-05±0.758E-06	0.727
	1.23	0.686E-05±0.139E-05±0.545E-06	0.727
	1.25	0.261E-05±0.834E-06±0.208E-06	0.726
	1.27	0.196E-05±0.723E-06±0.156E-06	0.726
	1.29	0.229E-05±0.781E-06±0.182E-06	0.726
4.425	0.71	0.977E-03±0.181E-04±0.784E-04	0.901
	0.73	0.664E-03±0.130E-04±0.532E-04	0.893
	0.75	0.579E-03±0.124E-04±0.465E-04	0.884
	0.77	0.499E-03±0.120E-04±0.400E-04	0.876
	0.79	0.430E-03±0.116E-04±0.345E-04	0.872
	0.81	0.395E-03±0.118E-04±0.317E-04	0.870
	0.83	0.332E-03±0.110E-04±0.266E-04	0.868
	0.85	0.267E-03±0.929E-05±0.214E-04	0.866
	0.87	0.248E-03±0.847E-05±0.199E-04	0.862
	0.89	0.215E-03±0.762E-05±0.172E-04	0.864
	0.91	0.159E-03±0.642E-05±0.128E-04	0.868
	0.93	0.143E-03±0.584E-05±0.115E-04	0.855
	0.95	0.173E-03±0.688E-05±0.138E-04	0.826
	0.97	0.188E-03±0.761E-05±0.151E-04	0.790
	0.99	0.193E-03±0.847E-05±0.155E-04	0.734
	1.01	0.177E-03±0.852E-05±0.142E-04	0.733
	1.03	0.135E-03±0.742E-05±0.108E-04	0.732
	1.05	0.112E-03±0.677E-05±0.899E-05	0.732
	1.07	0.591E-04±0.448E-05±0.474E-05	0.731

	1.09	0.377E-04±0.342E-05±0.302E-05	0.731
	1.11	0.434E-04±0.436E-05±0.348E-05	0.730
	1.13	0.276E-04±0.309E-05±0.221E-05	0.729
	1.15	0.196E-04±0.246E-05±0.157E-05	0.729
	1.17	0.134E-04±0.237E-05±0.107E-05	0.728
	1.19	0.145E-04±0.252E-05±0.116E-05	0.728
	1.21	0.852E-05±0.193E-05±0.684E-06	0.728
	1.23	0.624E-05±0.151E-05±0.500E-06	0.727
	1.25	0.356E-05±0.114E-05±0.285E-06	0.727
	1.27	0.368E-05±0.136E-05±0.295E-06	0.726
	1.29	0.367E-05±0.135E-05±0.294E-06	0.726
4.475	0.71	0.939E-03±0.166E-04±0.760E-04	0.902
	0.73	0.643E-03±0.131E-04±0.521E-04	0.894
	0.75	0.534E-03±0.115E-04±0.433E-04	0.885
	0.77	0.456E-03±0.110E-04±0.369E-04	0.877
	0.79	0.428E-03±0.113E-04±0.346E-04	0.872
	0.81	0.375E-03±0.110E-04±0.304E-04	0.871
	0.83	0.323E-03±0.107E-04±0.262E-04	0.868
	0.85	0.236E-03±0.876E-05±0.191E-04	0.866
	0.87	0.228E-03±0.830E-05±0.185E-04	0.863
	0.89	0.182E-03±0.713E-05±0.147E-04	0.863
	0.91	0.167E-03±0.662E-05±0.136E-04	0.864
	0.93	0.140E-03±0.595E-05±0.114E-04	0.859
	0.95	0.163E-03±0.639E-05±0.132E-04	0.838
	0.97	0.157E-03±0.646E-05±0.127E-04	0.790
	0.99	0.200E-03±0.835E-05±0.162E-04	0.734
	1.01	0.192E-03±0.902E-05±0.156E-04	0.734
	1.03	0.125E-03±0.715E-05±0.102E-04	0.733
	1.05	0.930E-04±0.608E-05±0.753E-05	0.732
	1.07	0.615E-04±0.484E-05±0.498E-05	0.732
	1.09	0.475E-04±0.429E-05±0.384E-05	0.731
	1.11	0.328E-04±0.370E-05±0.266E-05	0.730
	1.13	0.146E-04±0.194E-05±0.118E-05	0.730
	1.15	0.106E-04±0.159E-05±0.855E-06	0.729
	1.17	0.125E-04±0.203E-05±0.101E-05	0.729
	1.19	0.793E-05±0.156E-05±0.643E-06	0.728
	1.21	0.633E-05±0.135E-05±0.513E-06	0.728
	1.23	0.558E-05±0.130E-05±0.452E-06	0.728
	1.25	0.334E-05±0.953E-06±0.270E-06	0.727
	1.27	0.278E-05±0.889E-06±0.226E-06	0.727
4.525	0.71	0.899E-03±0.159E-04±0.735E-04	0.903
	0.73	0.665E-03±0.129E-04±0.544E-04	0.896
	0.75	0.547E-03±0.120E-04±0.447E-04	0.886
	0.77	0.465E-03±0.110E-04±0.380E-04	0.877
	0.79	0.380E-03±0.101E-04±0.311E-04	0.873
	0.81	0.357E-03±0.101E-04±0.292E-04	0.870
	0.83	0.276E-03±0.907E-05±0.226E-04	0.869
	0.85	0.262E-03±0.948E-05±0.215E-04	0.866
	0.87	0.218E-03±0.836E-05±0.178E-04	0.863
	0.89	0.176E-03±0.719E-05±0.144E-04	0.864
	0.91	0.147E-03±0.642E-05±0.120E-04	0.866
	0.93	0.131E-03±0.578E-05±0.107E-04	0.862
	0.95	0.145E-03±0.635E-05±0.118E-04	0.831
	0.97	0.144E-03±0.644E-05±0.118E-04	0.786
	0.99	0.176E-03±0.740E-05±0.144E-04	0.735
	1.01	0.171E-03±0.768E-05±0.140E-04	0.734
	1.03	0.114E-03±0.611E-05±0.934E-05	0.733
	1.05	0.848E-04±0.557E-05±0.694E-05	0.733
	1.07	0.552E-04±0.446E-05±0.452E-05	0.732
	1.09	0.381E-04±0.390E-05±0.312E-05	0.731
	1.11	0.233E-04±0.269E-05±0.191E-05	0.731
	1.13	0.145E-04±0.221E-05±0.118E-05	0.730
	1.15	0.165E-04±0.238E-05±0.135E-05	0.730
	1.17	0.116E-04±0.205E-05±0.948E-06	0.729
	1.19	0.110E-04±0.211E-05±0.896E-06	0.729
	1.21	0.440E-05±0.110E-05±0.360E-06	0.728
	1.23	0.556E-05±0.130E-05±0.454E-06	0.728
	1.25	0.344E-05±0.110E-05±0.282E-06	0.728
	1.27	0.260E-05±0.886E-06±0.212E-06	0.727
4.575	0.71	0.915E-03±0.159E-04±0.757E-04	0.904
	0.73	0.640E-03±0.123E-04±0.529E-04	0.897
	0.75	0.573E-03±0.125E-04±0.474E-04	0.888
	0.77	0.460E-03±0.111E-04±0.381E-04	0.878
	0.79	0.379E-03±0.986E-05±0.313E-04	0.873
	0.81	0.316E-03±0.911E-05±0.261E-04	0.871
	0.83	0.267E-03±0.884E-05±0.221E-04	0.869
	0.85	0.246E-03±0.911E-05±0.203E-04	0.866
	0.87	0.190E-03±0.790E-05±0.157E-04	0.864
	0.89	0.162E-03±0.687E-05±0.134E-04	0.862
	0.91	0.143E-03±0.633E-05±0.118E-04	0.867
	0.93	0.118E-03±0.556E-05±0.973E-05	0.859
	0.95	0.119E-03±0.562E-05±0.980E-05	0.830
	0.97	0.154E-03±0.707E-05±0.128E-04	0.786
	0.99	0.173E-03±0.761E-05±0.143E-04	0.735
	1.01	0.147E-03±0.694E-05±0.122E-04	0.735
	1.03	0.987E-04±0.525E-05±0.816E-05	0.734
	1.05	0.940E-04±0.539E-05±0.777E-05	0.733
	1.07	0.628E-04±0.486E-05±0.519E-05	0.733
	1.09	0.326E-04±0.302E-05±0.270E-05	0.732
	1.11	0.332E-04±0.361E-05±0.275E-05	0.731
	1.13	0.207E-04±0.276E-05±0.172E-05	0.731
	1.15	0.278E-04±0.366E-05±0.230E-05	0.730
	1.17	0.109E-04±0.177E-05±0.900E-06	0.730
	1.19	0.834E-05±0.178E-05±0.690E-06	0.729
	1.21	0.461E-05±0.104E-05±0.381E-06	0.729
	1.23	0.278E-05±0.794E-06±0.230E-06	0.728
4.625	0.71	0.882E-03±0.151E-04±0.736E-04	0.905
	0.73	0.649E-03±0.124E-04±0.542E-04	0.898
	0.75	0.521E-03±0.110E-04±0.435E-04	0.889
	0.77	0.469E-03±0.115E-04±0.391E-04	0.879
	0.79	0.365E-03±0.968E-05±0.305E-04	0.874
	0.81	0.292E-03±0.856E-05±0.243E-04	0.871
	0.83	0.244E-03±0.819E-05±0.204E-04	0.869
	0.85	0.218E-03±0.793E-05±0.182E-04	0.867
	0.87	0.191E-03±0.764E-05±0.160E-04	0.864
	0.89	0.171E-03±0.748E-05±0.143E-04	0.863
	0.91	0.148E-03±0.688E-05±0.124E-04	0.867
	0.93	0.115E-03±0.558E-05±0.956E-05	0.863
	0.95	0.116E-03±0.582E-05±0.971E-05	0.836
	0.97	0.162E-03±0.732E-05±0.135E-04	0.791
	0.99	0.160E-03±0.749E-05±0.134E-04	0.736
	1.01	0.122E-03±0.620E-05±0.102E-04	0.735
	1.03	0.109E-03±0.601E-05±0.908E-05	0.734
	1.05	0.840E-04±0.517E-05±0.701E-05	0.734
	1.07	0.515E-04±0.377E-05±0.430E-05	0.733
	1.09	0.405E-04±0.350E-05±0.338E-05	0.732
	1.11	0.282E-04±0.306E-05±0.235E-05	0.732
	1.13	0.184E-04±0.239E-05±0.153E-05	0.731
	1.15	0.113E-04±0.187E-05±0.946E-06	0.731
	1.17	0.965E-05±0.178E-05±0.806E-06	0.730
	1.19	0.596E-05±0.131E-05±0.497E-06	0.730
	1.21	0.791E-05±0.164E-05±0.660E-06	0.729
	1.23	0.516E-05±0.116E-05±0.431E-06	0.729
4.675	0.71	0.800E-03±0.134E-04±0.673E-04	0.907
	0.73	0.593E-03±0.114E-04±0.499E-04	0.899
	0.75	0.531E-03±0.111E-04±0.446E-04	0.890
	0.77	0.464E-03±0.108E-04±0.390E-04	0.880
	0.79	0.358E-03±0.101E-04±0.301E-04	0.874
	0.81	0.297E-03±0.865E-05±0.250E-04	0.872
	0.83	0.235E-03±0.766E-05±0.198E-04	0.870

	0.85	0.217E-03±0.808E-05±0.183E-04	0.867
	0.87	0.170E-03±0.698E-05±0.143E-04	0.866
	0.89	0.150E-03±0.688E-05±0.127E-04	0.863
	0.91	0.120E-03±0.594E-05±0.101E-04	0.864
	0.93	0.109E-03±0.545E-05±0.920E-05	0.862
	0.95	0.126E-03±0.614E-05±0.106E-04	0.835
	0.97	0.135E-03±0.677E-05±0.114E-04	0.791
	0.99	0.157E-03±0.794E-05±0.132E-04	0.736
	1.01	0.145E-03±0.733E-05±0.122E-04	0.736
	1.03	0.105E-03±0.595E-05±0.881E-05	0.735
	1.05	0.860E-04±0.537E-05±0.723E-05	0.734
	1.07	0.512E-04±0.385E-05±0.431E-05	0.734
	1.09	0.312E-04±0.267E-05±0.262E-05	0.733
	1.11	0.248E-04±0.257E-05±0.208E-05	0.732
	1.13	0.204E-04±0.251E-05±0.172E-05	0.732
	1.15	0.103E-04±0.179E-05±0.867E-06	0.731
	1.17	0.171E-04±0.265E-05±0.144E-05	0.731
	1.19	0.524E-05±0.158E-05±0.441E-06	0.730
	1.21	0.105E-04±0.237E-05±0.882E-06	0.730
	1.23	0.340E-05±0.109E-05±0.286E-06	0.729
4.725	0.71	0.788E-03±0.135E-04±0.670E-04	0.908
	0.73	0.589E-03±0.108E-04±0.501E-04	0.900
	0.75	0.506E-03±0.108E-04±0.430E-04	0.891
	0.77	0.442E-03±0.103E-04±0.375E-04	0.882
	0.79	0.381E-03±0.100E-04±0.324E-04	0.876
	0.81	0.299E-03±0.920E-05±0.254E-04	0.873
	0.83	0.234E-03±0.792E-05±0.199E-04	0.871
	0.85	0.188E-03±0.684E-05±0.160E-04	0.868
	0.87	0.176E-03±0.699E-05±0.149E-04	0.866
	0.89	0.153E-03±0.668E-05±0.130E-04	0.864
	0.91	0.128E-03±0.602E-05±0.108E-04	0.866
	0.93	0.112E-03±0.564E-05±0.950E-05	0.861
	0.95	0.111E-03±0.582E-05±0.940E-05	0.838
	0.97	0.129E-03±0.684E-05±0.109E-04	0.790
	0.99	0.141E-03±0.731E-05±0.120E-04	0.737
	1.01	0.118E-03±0.660E-05±0.101E-04	0.736
	1.03	0.916E-04±0.554E-05±0.778E-05	0.735
	1.05	0.758E-04±0.497E-05±0.644E-05	0.735
	1.07	0.492E-04±0.396E-05±0.418E-05	0.734
	1.09	0.286E-04±0.270E-05±0.243E-05	0.733
	1.11	0.214E-04±0.249E-05±0.182E-05	0.733
	1.13	0.207E-04±0.244E-05±0.176E-05	0.732
	1.15	0.109E-04±0.177E-05±0.927E-06	0.732
	1.17	0.139E-04±0.215E-05±0.118E-05	0.731
	1.19	0.501E-05±0.131E-05±0.426E-06	0.730
	1.21	0.823E-05±0.171E-05±0.700E-06	0.730
	1.23	0.641E-05±0.145E-05±0.545E-06	0.730
4.775	0.71	0.761E-03±0.131E-04±0.654E-04	0.910
	0.73	0.561E-03±0.103E-04±0.482E-04	0.901
	0.75	0.477E-03±0.100E-04±0.410E-04	0.893
	0.77	0.430E-03±0.100E-04±0.369E-04	0.883
	0.79	0.358E-03±0.921E-05±0.307E-04	0.876
	0.81	0.290E-03±0.863E-05±0.249E-04	0.872
	0.83	0.228E-03±0.789E-05±0.196E-04	0.871
	0.85	0.205E-03±0.750E-05±0.176E-04	0.869
	0.87	0.150E-03±0.613E-05±0.129E-04	0.866
	0.89	0.133E-03±0.606E-05±0.114E-04	0.864
	0.91	0.129E-03±0.630E-05±0.111E-04	0.864
	0.93	0.947E-04±0.486E-05±0.813E-05	0.862
	0.95	0.106E-03±0.561E-05±0.913E-05	0.837
	0.97	0.109E-03±0.589E-05±0.939E-05	0.791
	0.99	0.121E-03±0.664E-05±0.104E-04	0.738
	1.01	0.131E-03±0.720E-05±0.113E-04	0.737
	1.03	0.995E-04±0.603E-05±0.854E-05	0.736
	1.05	0.672E-04±0.497E-05±0.577E-05	0.735
	1.07	0.432E-04±0.362E-05±0.371E-05	0.735
	1.09	0.291E-04±0.288E-05±0.250E-05	0.734
	1.11	0.252E-04±0.283E-05±0.217E-05	0.733
	1.13	0.149E-04±0.198E-05±0.128E-05	0.733
	1.15	0.101E-04±0.142E-05±0.866E-06	0.732
	1.17	0.122E-04±0.208E-05±0.105E-05	0.731
	1.19	0.586E-05±0.132E-05±0.504E-06	0.731
	1.21	0.902E-05±0.198E-05±0.775E-06	0.730
	1.23	0.428E-05±0.129E-05±0.367E-06	0.730
4.825	0.71	0.742E-03±0.130E-04±0.643E-04	0.910
	0.73	0.540E-03±0.103E-04±0.467E-04	0.902
	0.75	0.470E-03±0.945E-05±0.407E-04	0.894
	0.77	0.398E-03±0.935E-05±0.345E-04	0.884
	0.79	0.347E-03±0.906E-05±0.301E-04	0.876
	0.81	0.282E-03±0.821E-05±0.245E-04	0.874
	0.83	0.239E-03±0.818E-05±0.207E-04	0.871
	0.85	0.180E-03±0.702E-05±0.156E-04	0.869
	0.87	0.155E-03±0.623E-05±0.134E-04	0.867
	0.89	0.123E-03±0.556E-05±0.107E-04	0.866
	0.91	0.106E-03±0.521E-05±0.921E-05	0.865
	0.93	0.108E-03±0.536E-05±0.939E-05	0.857
	0.95	0.106E-03±0.550E-05±0.917E-05	0.835
	0.97	0.127E-03±0.688E-05±0.110E-04	0.789
	0.99	0.122E-03±0.668E-05±0.105E-04	0.738
	1.01	0.101E-03±0.619E-05±0.873E-05	0.737
	1.03	0.870E-04±0.568E-05±0.753E-05	0.737
	1.05	0.581E-04±0.455E-05±0.504E-05	0.736
	1.07	0.392E-04±0.367E-05±0.340E-05	0.735
	1.09	0.363E-04±0.376E-05±0.315E-05	0.734
	1.11	0.245E-04±0.277E-05±0.212E-05	0.734
	1.13	0.186E-04±0.266E-05±0.161E-05	0.733
	1.15	0.884E-05±0.174E-05±0.765E-06	0.732
	1.17	0.990E-05±0.205E-05±0.858E-06	0.732
	1.19	0.778E-05±0.157E-05±0.674E-06	0.731
	1.21	0.745E-05±0.180E-05±0.645E-06	0.731
	1.23	0.382E-05±0.115E-05±0.331E-06	0.730
	1.25	0.337E-05±0.961E-06±0.291E-06	0.730
4.875	0.71	0.709E-03±0.126E-04±0.620E-04	0.912
	0.73	0.507E-03±0.990E-05±0.444E-04	0.903
	0.75	0.473E-03±0.954E-05±0.414E-04	0.895
	0.77	0.386E-03±0.872E-05±0.338E-04	0.885
	0.79	0.333E-03±0.876E-05±0.291E-04	0.877
	0.81	0.268E-03±0.785E-05±0.235E-04	0.874
	0.83	0.234E-03±0.752E-05±0.205E-04	0.871
	0.85	0.184E-03±0.705E-05±0.161E-04	0.869
	0.87	0.173E-03±0.734E-05±0.151E-04	0.867
	0.89	0.121E-03±0.547E-05±0.106E-04	0.867
	0.91	0.104E-03±0.498E-05±0.909E-05	0.866
	0.93	0.943E-04±0.511E-05±0.825E-05	0.858
	0.95	0.958E-04±0.506E-05±0.838E-05	0.841
	0.97	0.101E-03±0.532E-05±0.880E-05	0.794
	0.99	0.983E-04±0.587E-05±0.860E-05	0.739
	1.01	0.928E-04±0.594E-05±0.812E-05	0.738
	1.03	0.739E-04±0.524E-05±0.647E-05	0.737
	1.05	0.631E-04±0.504E-05±0.552E-05	0.736
	1.07	0.547E-04±0.491E-05±0.479E-05	0.736
	1.09	0.245E-04±0.279E-05±0.215E-05	0.735
	1.11	0.205E-04±0.265E-05±0.180E-05	0.734
	1.13	0.942E-05±0.181E-05±0.824E-06	0.734
	1.15	0.981E-05±0.167E-05±0.859E-06	0.733
	1.17	0.539E-05±0.115E-05±0.472E-06	0.732
	1.19	0.382E-05±0.957E-06±0.334E-06	0.732
	1.21	0.504E-05±0.107E-05±0.441E-06	0.731
	1.23	0.289E-05±0.922E-06±0.253E-06	0.731
4.925	0.71	0.673E-03±0.125E-04±0.594E-04	0.914

	0.73	0.530E-03±0.102E-04±0.468E-04	0.904
	0.75	0.455E-03±0.939E-05±0.402E-04	0.896
	0.77	0.378E-03±0.862E-05±0.334E-04	0.886
	0.79	0.318E-03±0.803E-05±0.281E-04	0.878
	0.81	0.277E-03±0.805E-05±0.244E-04	0.874
	0.83	0.232E-03±0.749E-05±0.204E-04	0.872
	0.85	0.177E-03±0.645E-05±0.157E-04	0.869
	0.87	0.150E-03±0.650E-05±0.132E-04	0.867
	0.89	0.110E-03±0.533E-05±0.972E-05	0.865
	0.91	0.104E-03±0.508E-05±0.917E-05	0.867
	0.93	0.958E-04±0.509E-05±0.846E-05	0.861
	0.95	0.776E-04±0.439E-05±0.685E-05	0.837
	0.97	0.890E-04±0.502E-05±0.786E-05	0.795
	0.99	0.105E-03±0.575E-05±0.926E-05	0.739
	1.01	0.957E-04±0.565E-05±0.845E-05	0.739
	1.03	0.690E-04±0.498E-05±0.610E-05	0.738
	1.05	0.568E-04±0.441E-05±0.501E-05	0.737
	1.07	0.402E-04±0.381E-05±0.355E-05	0.736
	1.09	0.250E-04±0.289E-05±0.221E-05	0.735
	1.11	0.135E-04±0.219E-05±0.119E-05	0.735
	1.13	0.114E-04±0.184E-05±0.100E-05	0.734
	1.15	0.882E-05±0.178E-05±0.779E-06	0.733
	1.17	0.117E-04±0.212E-05±0.104E-05	0.733
	1.19	0.700E-05±0.163E-05±0.618E-06	0.732
	1.21	0.387E-05±0.124E-05±0.342E-06	0.732
	1.23	0.649E-05±0.163E-05±0.573E-06	0.731
4.975	0.71	0.640E-03±0.131E-04±0.570E-04	0.915
	0.73	0.503E-03±0.988E-05±0.448E-04	0.906
	0.75	0.436E-03±0.918E-05±0.389E-04	0.897
	0.77	0.365E-03±0.837E-05±0.326E-04	0.888
	0.79	0.307E-03±0.767E-05±0.273E-04	0.880
	0.81	0.255E-03±0.729E-05±0.227E-04	0.874
	0.83	0.223E-03±0.725E-05±0.199E-04	0.872
	0.85	0.168E-03±0.623E-05±0.149E-04	0.869
	0.87	0.152E-03±0.623E-05±0.135E-04	0.868
	0.89	0.109E-03±0.554E-05±0.972E-05	0.867
	0.91	0.889E-04±0.477E-05±0.792E-05	0.868
	0.93	0.806E-04±0.431E-05±0.718E-05	0.863
	0.95	0.847E-04±0.471E-05±0.755E-05	0.840
	0.97	0.923E-04±0.503E-05±0.822E-05	0.798
	0.99	0.107E-03±0.603E-05±0.956E-05	0.740
	1.01	0.970E-04±0.574E-05±0.864E-05	0.739
	1.03	0.798E-04±0.527E-05±0.711E-05	0.738
	1.05	0.531E-04±0.414E-05±0.473E-05	0.737
	1.07	0.283E-04±0.303E-05±0.252E-05	0.737
	1.09	0.277E-04±0.295E-05±0.247E-05	0.736
	1.11	0.200E-04±0.258E-05±0.178E-05	0.735
	1.13	0.144E-04±0.211E-05±0.128E-05	0.735
	1.15	0.842E-05±0.170E-05±0.750E-06	0.734
	1.17	0.709E-05±0.151E-05±0.631E-06	0.733
	1.19	0.745E-05±0.154E-05±0.664E-06	0.733
	1.21	0.285E-05±0.973E-06±0.254E-06	0.732
5.025	0.71	0.661E-03±0.144E-04±0.595E-04	0.917
	0.73	0.464E-03±0.974E-05±0.418E-04	0.907
	0.75	0.392E-03±0.855E-05±0.353E-04	0.898
	0.77	0.338E-03±0.799E-05±0.304E-04	0.889
	0.79	0.289E-03±0.746E-05±0.260E-04	0.880
	0.81	0.280E-03±0.753E-05±0.252E-04	0.876
	0.83	0.217E-03±0.689E-05±0.195E-04	0.873
	0.85	0.175E-03±0.655E-05±0.157E-04	0.870
	0.87	0.152E-03±0.613E-05±0.137E-04	0.868
	0.89	0.122E-03±0.554E-05±0.110E-04	0.866
	0.91	0.101E-03±0.555E-05±0.909E-05	0.866
	0.93	0.870E-04±0.487E-05±0.783E-05	0.862
	0.95	0.817E-04±0.465E-05±0.735E-05	0.837
	0.97	0.807E-04±0.468E-05±0.727E-05	0.799
	0.99	0.933E-04±0.532E-05±0.839E-05	0.741
	1.01	0.679E-04±0.431E-05±0.611E-05	0.740
	1.03	0.778E-04±0.518E-05±0.700E-05	0.739
	1.05	0.500E-04±0.387E-05±0.450E-05	0.738
	1.07	0.337E-04±0.314E-05±0.303E-05	0.737
	1.09	0.293E-04±0.344E-05±0.263E-05	0.736
	1.11	0.161E-04±0.233E-05±0.145E-05	0.736
	1.13	0.794E-05±0.156E-05±0.715E-06	0.735
	1.15	0.146E-04±0.241E-05±0.131E-05	0.734
	1.17	0.108E-04±0.218E-05±0.970E-06	0.734
	1.19	0.106E-04±0.225E-05±0.950E-06	0.733
	1.21	0.229E-05±0.103E-05±0.206E-06	0.733
	1.23	0.387E-05±0.132E-05±0.348E-06	0.732
5.075	0.71	0.631E-03±0.142E-04±0.573E-04	0.919
	0.73	0.426E-03±0.100E-04±0.388E-04	0.909
	0.75	0.399E-03±0.890E-05±0.363E-04	0.900
	0.77	0.344E-03±0.811E-05±0.313E-04	0.890
	0.79	0.293E-03±0.758E-05±0.266E-04	0.881
	0.81	0.241E-03±0.688E-05±0.219E-04	0.875
	0.83	0.219E-03±0.668E-05±0.199E-04	0.873
	0.85	0.171E-03±0.628E-05±0.155E-04	0.871
	0.87	0.142E-03±0.573E-05±0.129E-04	0.869
	0.89	0.109E-03±0.496E-05±0.991E-05	0.867
	0.91	0.882E-04±0.460E-05±0.802E-05	0.866
	0.93	0.651E-04±0.431E-05±0.592E-05	0.865
	0.95	0.811E-04±0.468E-05±0.737E-05	0.845
	0.97	0.873E-04±0.514E-05±0.794E-05	0.798
	0.99	0.881E-04±0.514E-05±0.800E-05	0.741
	1.01	0.768E-04±0.478E-05±0.698E-05	0.740
	1.03	0.534E-04±0.381E-05±0.486E-05	0.739
	1.05	0.373E-04±0.318E-05±0.339E-05	0.739
	1.07	0.302E-04±0.299E-05±0.274E-05	0.738
	1.09	0.147E-04±0.186E-05±0.134E-05	0.737
	1.11	0.168E-04±0.226E-05±0.152E-05	0.736
	1.13	0.791E-05±0.152E-05±0.719E-06	0.736
	1.15	0.686E-05±0.138E-05±0.623E-06	0.735
	1.17	0.490E-05±0.114E-05±0.445E-06	0.734
	1.19	0.205E-05±0.755E-06±0.186E-06	0.734
	1.21	0.174E-05±0.703E-06±0.158E-06	0.733
	1.23	0.313E-05±0.944E-06±0.285E-06	0.732
5.125	0.71	0.647E-03±0.132E-04±0.593E-04	0.920
	0.73	0.425E-03±0.107E-04±0.390E-04	0.910
	0.75	0.339E-03±0.838E-05±0.311E-04	0.901
	0.77	0.319E-03±0.781E-05±0.293E-04	0.891
	0.79	0.273E-03±0.724E-05±0.250E-04	0.882
	0.81	0.250E-03±0.712E-05±0.230E-04	0.876
	0.83	0.196E-03±0.614E-05±0.180E-04	0.874
	0.85	0.175E-03±0.601E-05±0.161E-04	0.871
	0.87	0.135E-03±0.551E-05±0.124E-04	0.869
	0.89	0.112E-03±0.499E-05±0.103E-04	0.869
	0.91	0.965E-04±0.475E-05±0.885E-05	0.866
	0.93	0.777E-04±0.432E-05±0.712E-05	0.862
	0.95	0.796E-04±0.485E-05±0.730E-05	0.837
	0.97	0.734E-04±0.461E-05±0.673E-05	0.800
	0.99	0.771E-04±0.480E-05±0.707E-05	0.742
	1.01	0.644E-04±0.433E-05±0.591E-05	0.741
	1.03	0.628E-04±0.440E-05±0.576E-05	0.740
	1.05	0.358E-04±0.311E-05±0.328E-05	0.739
	1.07	0.380E-04±0.345E-05±0.348E-05	0.738
	1.09	0.181E-04±0.223E-05±0.166E-05	0.738
	1.11	0.138E-04±0.200E-05±0.127E-05	0.737
	1.13	0.120E-04±0.216E-05±0.110E-05	0.736
	1.15	0.836E-05±0.169E-05±0.767E-06	0.735
	1.17	0.496E-05±0.129E-05±0.455E-06	0.735

	1.19	0.573E-05±0.138E-05±0.525E-06	0.734
	1.21	0.375E-05±0.113E-05±0.344E-06	0.733
	1.23	0.250E-05±0.923E-06±0.230E-06	0.733
5.175	0.71	0.615E-03±0.120E-04±0.570E-04	0.922
	0.73	0.437E-03±0.106E-04±0.405E-04	0.911
	0.75	0.368E-03±0.959E-05±0.341E-04	0.902
	0.77	0.310E-03±0.791E-05±0.287E-04	0.893
	0.79	0.255E-03±0.677E-05±0.236E-04	0.883
	0.81	0.224E-03±0.650E-05±0.208E-04	0.877
	0.83	0.198E-03±0.624E-05±0.183E-04	0.874
	0.85	0.148E-03±0.527E-05±0.137E-04	0.873
	0.87	0.126E-03±0.508E-05±0.116E-04	0.870
	0.89	0.110E-03±0.502E-05±0.102E-04	0.868
	0.91	0.835E-04±0.445E-05±0.773E-05	0.866
	0.93	0.793E-04±0.451E-05±0.734E-05	0.862
	0.95	0.741E-04±0.445E-05±0.686E-05	0.845
	0.97	0.755E-04±0.508E-05±0.699E-05	0.802
	0.99	0.774E-04±0.504E-05±0.717E-05	0.743
	1.01	0.747E-04±0.501E-05±0.692E-05	0.742
	1.03	0.446E-04±0.337E-05±0.413E-05	0.741
	1.05	0.364E-04±0.311E-05±0.337E-05	0.740
	1.07	0.292E-04±0.281E-05±0.271E-05	0.739
	1.09	0.162E-04±0.209E-05±0.150E-05	0.738
	1.11	0.171E-04±0.261E-05±0.158E-05	0.737
	1.13	0.911E-05±0.161E-05±0.843E-06	0.737
	1.15	0.101E-04±0.191E-05±0.939E-06	0.736
	1.17	0.558E-05±0.146E-05±0.517E-06	0.735
	1.19	0.718E-05±0.173E-05±0.665E-06	0.735
	1.21	0.485E-05±0.139E-05±0.450E-06	0.734
5.225	0.71	0.582E-03±0.114E-04±0.544E-04	0.924
	0.73	0.457E-03±0.103E-04±0.428E-04	0.912
	0.75	0.368E-03±0.992E-05±0.344E-04	0.903
	0.77	0.326E-03±0.884E-05±0.305E-04	0.894
	0.79	0.275E-03±0.745E-05±0.257E-04	0.885
	0.81	0.214E-03±0.642E-05±0.200E-04	0.878
	0.83	0.176E-03±0.582E-05±0.165E-04	0.875
	0.85	0.152E-03±0.537E-05±0.142E-04	0.872
	0.87	0.125E-03±0.475E-05±0.117E-04	0.869
	0.89	0.117E-03±0.509E-05±0.109E-04	0.868
	0.91	0.870E-04±0.434E-05±0.813E-05	0.867
	0.93	0.770E-04±0.433E-05±0.720E-05	0.863
	0.95	0.763E-04±0.444E-05±0.714E-05	0.839
	0.97	0.818E-04±0.506E-05±0.765E-05	0.799
	0.99	0.818E-04±0.534E-05±0.765E-05	0.743
	1.01	0.780E-04±0.537E-05±0.729E-05	0.742
	1.03	0.445E-04±0.331E-05±0.416E-05	0.741
	1.05	0.379E-04±0.336E-05±0.355E-05	0.740
	1.07	0.254E-04±0.274E-05±0.237E-05	0.739
	1.09	0.159E-04±0.207E-05±0.148E-05	0.739
	1.11	0.115E-04±0.183E-05±0.107E-05	0.738
	1.13	0.111E-04±0.192E-05±0.103E-05	0.737
	1.15	0.663E-05±0.150E-05±0.620E-06	0.736
	1.17	0.459E-05±0.125E-05±0.429E-06	0.736
	1.19	0.345E-05±0.110E-05±0.323E-06	0.735
	1.21	0.405E-05±0.129E-05±0.379E-06	0.734
5.275	0.71	0.552E-03±0.108E-04±0.521E-04	0.926
	0.73	0.426E-03±0.929E-05±0.402E-04	0.914
	0.75	0.363E-03±0.967E-05±0.342E-04	0.905
	0.77	0.302E-03±0.890E-05±0.285E-04	0.895
	0.79	0.254E-03±0.760E-05±0.239E-04	0.885
	0.81	0.217E-03±0.658E-05±0.204E-04	0.878
	0.83	0.177E-03±0.579E-05±0.167E-04	0.875
	0.85	0.160E-03±0.550E-05±0.151E-04	0.872
	0.87	0.123E-03±0.502E-05±0.116E-04	0.870
	0.89	0.102E-03±0.443E-05±0.960E-05	0.868
	0.91	0.876E-04±0.423E-05±0.826E-05	0.867
	0.93	0.753E-04±0.413E-05±0.710E-05	0.864
	0.95	0.675E-04±0.408E-05±0.636E-05	0.840
	0.97	0.632E-04±0.415E-05±0.596E-05	0.800
	0.99	0.719E-04±0.471E-05±0.678E-05	0.744
	1.01	0.733E-04±0.542E-05±0.691E-05	0.743
	1.03	0.523E-04±0.399E-05±0.493E-05	0.742
	1.05	0.379E-04±0.338E-05±0.357E-05	0.741
	1.07	0.247E-04±0.257E-05±0.233E-05	0.740
	1.09	0.228E-04±0.264E-05±0.215E-05	0.739
	1.11	0.106E-04±0.163E-05±0.995E-06	0.738
	1.13	0.942E-05±0.181E-05±0.888E-06	0.738
	1.15	0.792E-05±0.169E-05±0.747E-06	0.737
	1.17	0.445E-05±0.127E-05±0.420E-06	0.736
	1.19	0.468E-05±0.141E-05±0.442E-06	0.736
	1.21	0.323E-05±0.119E-05±0.305E-06	0.735
5.325	0.71	0.521E-03±0.105E-04±0.496E-04	0.927
	0.73	0.397E-03±0.871E-05±0.378E-04	0.915
	0.75	0.337E-03±0.837E-05±0.321E-04	0.906
	0.77	0.294E-03±0.899E-05±0.280E-04	0.897
	0.79	0.241E-03±0.774E-05±0.229E-04	0.887
	0.81	0.207E-03±0.663E-05±0.197E-04	0.879
	0.83	0.165E-03±0.560E-05±0.157E-04	0.876
	0.85	0.130E-03±0.488E-05±0.124E-04	0.873
	0.87	0.118E-03±0.478E-05±0.113E-04	0.872
	0.89	0.101E-03±0.445E-05±0.958E-05	0.869
	0.91	0.841E-04±0.402E-05±0.801E-05	0.869
	0.93	0.686E-04±0.395E-05±0.653E-05	0.866
	0.95	0.698E-04±0.420E-05±0.664E-05	0.846
	0.97	0.685E-04±0.410E-05±0.652E-05	0.800
	0.99	0.726E-04±0.471E-05±0.691E-05	0.745
	1.01	0.583E-04±0.428E-05±0.555E-05	0.744
	1.03	0.596E-04±0.472E-05±0.567E-05	0.743
	1.05	0.351E-04±0.321E-05±0.334E-05	0.742
	1.07	0.231E-04±0.239E-05±0.220E-05	0.741
	1.09	0.183E-04±0.219E-05±0.174E-05	0.740
	1.11	0.133E-04±0.173E-05±0.126E-05	0.739
	1.13	0.875E-05±0.155E-05±0.833E-06	0.738
	1.15	0.706E-05±0.159E-05±0.672E-06	0.737
	1.17	0.214E-05±0.729E-06±0.203E-06	0.737
	1.19	0.286E-05±0.913E-06±0.272E-06	0.736
	1.21	0.225E-05±0.828E-06±0.214E-06	0.735
5.375	0.71	0.501E-03±0.109E-04±0.480E-04	0.930
	0.73	0.386E-03±0.845E-05±0.370E-04	0.917
	0.75	0.350E-03±0.828E-05±0.336E-04	0.907
	0.77	0.292E-03±0.822E-05±0.281E-04	0.898
	0.79	0.235E-03±0.801E-05±0.225E-04	0.888
	0.81	0.185E-03±0.652E-05±0.177E-04	0.881
	0.83	0.166E-03±0.573E-05±0.159E-04	0.877
	0.85	0.146E-03±0.549E-05±0.140E-04	0.874
	0.87	0.109E-03±0.465E-05±0.104E-04	0.871
	0.89	0.912E-04±0.399E-05±0.875E-05	0.869
	0.91	0.801E-04±0.386E-05±0.769E-05	0.868
	0.93	0.695E-04±0.376E-05±0.667E-05	0.862
	0.95	0.490E-04±0.326E-05±0.471E-05	0.840
	0.97	0.683E-04±0.432E-05±0.656E-05	0.806
	0.99	0.705E-04±0.473E-05±0.677E-05	0.745
	1.01	0.646E-04±0.439E-05±0.620E-05	0.744
	1.03	0.445E-04±0.362E-05±0.427E-05	0.743
	1.05	0.394E-04±0.384E-05±0.378E-05	0.742
	1.07	0.217E-04±0.267E-05±0.209E-05	0.741
	1.09	0.181E-04±0.243E-05±0.174E-05	0.740
	1.11	0.105E-04±0.170E-05±0.101E-05	0.739
	1.13	0.734E-05±0.145E-05±0.704E-06	0.739
	1.15	0.472E-05±0.110E-05±0.453E-06	0.738

	1.17	0.333E-05±0.106E-05±0.320E-06	0.737
	1.19	0.348E-05±0.948E-06±0.334E-06	0.737
5.425	0.71	0.509E-03±0.119E-04±0.494E-04	0.932
	0.73	0.398E-03±0.876E-05±0.386E-04	0.918
	0.75	0.341E-03±0.820E-05±0.331E-04	0.909
	0.77	0.300E-03±0.811E-05±0.291E-04	0.899
	0.79	0.275E-03±0.883E-05±0.266E-04	0.889
	0.81	0.189E-03±0.706E-05±0.183E-04	0.881
	0.83	0.155E-03±0.582E-05±0.151E-04	0.877
	0.85	0.124E-03±0.484E-05±0.121E-04	0.874
	0.87	0.110E-03±0.470E-05±0.107E-04	0.873
	0.89	0.100E-03±0.450E-05±0.970E-05	0.871
	0.91	0.747E-04±0.370E-05±0.724E-05	0.867
	0.93	0.626E-04±0.345E-05±0.607E-05	0.866
	0.95	0.626E-04±0.367E-05±0.607E-05	0.842
	0.97	0.682E-04±0.424E-05±0.662E-05	0.799
	0.99	0.702E-04±0.468E-05±0.681E-05	0.746
	1.01	0.538E-04±0.407E-05±0.522E-05	0.745
	1.03	0.420E-04±0.348E-05±0.408E-05	0.744
	1.05	0.243E-04±0.262E-05±0.235E-05	0.743
	1.07	0.226E-04±0.277E-05±0.219E-05	0.742
	1.09	0.101E-04±0.169E-05±0.980E-06	0.741
	1.11	0.118E-04±0.182E-05±0.114E-05	0.740
	1.13	0.109E-04±0.171E-05±0.105E-05	0.739
	1.15	0.357E-05±0.108E-05±0.347E-06	0.738
	1.17	0.509E-05±0.127E-05±0.494E-06	0.738
	1.19	0.227E-05±0.836E-06±0.220E-06	0.737
5.475	0.71	0.529E-03±0.129E-04±0.518E-04	0.934
	0.73	0.338E-03±0.820E-05±0.331E-04	0.921
	0.75	0.324E-03±0.793E-05±0.317E-04	0.910
	0.77	0.276E-03±0.742E-05±0.270E-04	0.901
	0.79	0.234E-03±0.733E-05±0.229E-04	0.890
	0.81	0.183E-03±0.707E-05±0.179E-04	0.882
	0.83	0.149E-03±0.613E-05±0.146E-04	0.878
	0.85	0.133E-03±0.543E-05±0.131E-04	0.875
	0.87	0.103E-03±0.436E-05±0.101E-04	0.873
	0.89	0.985E-04±0.439E-05±0.964E-05	0.872
	0.91	0.724E-04±0.368E-05±0.708E-05	0.868
	0.93	0.728E-04±0.398E-05±0.712E-05	0.863
	0.95	0.474E-04±0.287E-05±0.464E-05	0.848
	0.97	0.614E-04±0.358E-05±0.601E-05	0.806
	0.99	0.658E-04±0.429E-05±0.644E-05	0.747
	1.01	0.558E-04±0.398E-05±0.546E-05	0.746
	1.03	0.355E-04±0.305E-05±0.347E-05	0.745
	1.05	0.265E-04±0.280E-05±0.259E-05	0.743
	1.07	0.195E-04±0.220E-05±0.191E-05	0.742
	1.09	0.103E-04±0.155E-05±0.101E-05	0.742
	1.11	0.960E-05±0.181E-05±0.940E-06	0.741
	1.13	0.933E-05±0.188E-05±0.914E-06	0.740
	1.15	0.550E-05±0.120E-05±0.538E-06	0.739
	1.17	0.558E-05±0.130E-05±0.547E-06	0.738
	1.19	0.252E-05±0.804E-06±0.247E-06	0.738
5.525	0.71	0.508E-03±0.123E-04±0.501E-04	0.937
	0.73	0.357E-03±0.934E-05±0.352E-04	0.922
	0.75	0.315E-03±0.785E-05±0.311E-04	0.911
	0.77	0.251E-03±0.683E-05±0.248E-04	0.902
	0.79	0.246E-03±0.717E-05±0.243E-04	0.892
	0.81	0.185E-03±0.690E-05±0.183E-04	0.883
	0.83	0.179E-03±0.736E-05±0.176E-04	0.879
	0.85	0.117E-03±0.520E-05±0.115E-04	0.876
	0.87	0.870E-04±0.388E-05±0.859E-05	0.874
	0.89	0.844E-04±0.397E-05±0.833E-05	0.871
	0.91	0.581E-04±0.313E-05±0.573E-05	0.869
	0.93	0.540E-04±0.310E-05±0.533E-05	0.864
	0.95	0.548E-04±0.343E-05±0.541E-05	0.841
	0.97	0.598E-04±0.370E-05±0.590E-05	0.803
	0.99	0.610E-04±0.396E-05±0.602E-05	0.748
	1.01	0.632E-04±0.429E-05±0.623E-05	0.746
	1.03	0.353E-04±0.304E-05±0.349E-05	0.745
	1.05	0.319E-04±0.309E-05±0.315E-05	0.744
	1.07	0.276E-04±0.268E-05±0.273E-05	0.743
	1.09	0.107E-04±0.177E-05±0.106E-05	0.742
	1.11	0.859E-05±0.152E-05±0.847E-06	0.741
	1.13	0.727E-05±0.159E-05±0.718E-06	0.740
	1.15	0.492E-05±0.123E-05±0.486E-06	0.740
	1.17	0.389E-05±0.117E-05±0.384E-06	0.739
	1.19	0.366E-05±0.110E-05±0.362E-06	0.738
5.575	0.71	0.486E-03±0.114E-04±0.483E-04	0.938
	0.73	0.371E-03±0.101E-04±0.368E-04	0.923
	0.75	0.302E-03±0.784E-05±0.299E-04	0.912
	0.77	0.248E-03±0.685E-05±0.247E-04	0.903
	0.79	0.210E-03±0.628E-05±0.208E-04	0.892
	0.81	0.200E-03±0.691E-05±0.199E-04	0.885
	0.83	0.153E-03±0.656E-05±0.152E-04	0.879
	0.85	0.117E-03±0.550E-05±0.116E-04	0.877
	0.87	0.978E-04±0.460E-05±0.971E-05	0.874
	0.89	0.803E-04±0.412E-05±0.797E-05	0.872
	0.91	0.621E-04±0.333E-05±0.617E-05	0.871
	0.93	0.595E-04±0.332E-05±0.591E-05	0.863
	0.95	0.478E-04±0.297E-05±0.475E-05	0.845
	0.97	0.559E-04±0.343E-05±0.555E-05	0.803
	0.99	0.527E-04±0.358E-05±0.523E-05	0.748
	1.01	0.447E-04±0.314E-05±0.444E-05	0.747
	1.03	0.430E-04±0.376E-05±0.427E-05	0.746
	1.05	0.322E-04±0.315E-05±0.320E-05	0.745
	1.07	0.169E-04±0.208E-05±0.168E-05	0.744
	1.09	0.173E-04±0.223E-05±0.171E-05	0.743
	1.11	0.103E-04±0.173E-05±0.102E-05	0.742
	1.13	0.660E-05±0.130E-05±0.655E-06	0.741
	1.15	0.442E-05±0.115E-05±0.439E-06	0.740
	1.17	0.306E-05±0.833E-06±0.304E-06	0.739
	1.19	0.298E-05±0.896E-06±0.296E-06	0.739
5.625	0.71	0.483E-03±0.106E-04±0.481E-04	0.940
	0.73	0.361E-03±0.963E-05±0.359E-04	0.925
	0.75	0.293E-03±0.865E-05±0.292E-04	0.914
	0.77	0.220E-03±0.632E-05±0.220E-04	0.904
	0.79	0.226E-03±0.664E-05±0.225E-04	0.894
	0.81	0.184E-03±0.619E-05±0.183E-04	0.885
	0.83	0.147E-03±0.589E-05±0.147E-04	0.880
	0.85	0.109E-03±0.559E-05±0.108E-04	0.878
	0.87	0.980E-04±0.507E-05±0.976E-05	0.874
	0.89	0.788E-04±0.417E-05±0.785E-05	0.872
	0.91	0.675E-04±0.364E-05±0.672E-05	0.870
	0.93	0.515E-04±0.313E-05±0.513E-05	0.865
	0.95	0.525E-04±0.328E-05±0.523E-05	0.849
	0.97	0.594E-04±0.359E-05±0.591E-05	0.802
	0.99	0.440E-04±0.309E-05±0.438E-05	0.749
	1.01	0.463E-04±0.323E-05±0.461E-05	0.748
	1.03	0.350E-04±0.294E-05±0.348E-05	0.747
	1.05	0.254E-04±0.263E-05±0.253E-05	0.745
	1.07	0.212E-04±0.270E-05±0.211E-05	0.744
	1.09	0.128E-04±0.178E-05±0.127E-05	0.743
	1.11	0.109E-04±0.172E-05±0.109E-05	0.742
	1.13	0.793E-05±0.138E-05±0.790E-06	0.742
	1.15	0.673E-05±0.152E-05±0.670E-06	0.741
	1.17	0.385E-05±0.110E-05±0.383E-06	0.740
	1.19	0.181E-05±0.730E-06±0.180E-06	0.739
5.675	0.71	0.482E-03±0.107E-04±0.483E-04	0.943
	0.73	0.328E-03±0.862E-05±0.329E-04	0.928
	0.75	0.294E-03±0.897E-05±0.295E-04	0.915

	0.77	0.239E-03±0.711E-05±0.240E-04	0.906
	0.79	0.187E-03±0.589E-05±0.188E-04	0.895
	0.83	0.134E-03±0.518E-05±0.135E-04	0.887
	0.85	0.138E-03±0.613E-05±0.139E-04	0.881
	0.87	0.943E-04±0.531E-05±0.947E-05	0.878
	0.89	0.793E-04±0.445E-05±0.796E-05	0.875
	0.91	0.637E-04±0.353E-05±0.640E-05	0.873
	0.93	0.483E-04±0.288E-05±0.485E-05	0.871
	0.95	0.512E-04±0.328E-05±0.514E-05	0.865
	0.97	0.468E-04±0.319E-05±0.470E-05	0.844
	0.99	0.496E-04±0.355E-05±0.498E-05	0.808
	1.01	0.456E-04±0.338E-05±0.458E-05	0.750
	1.03	0.374E-04±0.302E-05±0.376E-05	0.748
	1.05	0.242E-04±0.240E-05±0.243E-05	0.747
	1.07	0.159E-04±0.192E-05±0.160E-05	0.746
	1.09	0.114E-04±0.169E-05±0.114E-05	0.745
	1.11	0.798E-05±0.136E-05±0.801E-06	0.744
	1.13	0.526E-05±0.119E-05±0.528E-06	0.743
	1.15	0.434E-05±0.113E-05±0.436E-06	0.742
	1.17	0.222E-05±0.819E-06±0.223E-06	0.741
	1.19	0.264E-05±0.902E-06±0.265E-06	0.740
5.725	0.71	0.577E-03±0.136E-04±0.582E-04	0.945
	0.73	0.349E-03±0.855E-05±0.352E-04	0.930
	0.75	0.271E-03±0.837E-05±0.274E-04	0.917
	0.77	0.255E-03±0.827E-05±0.257E-04	0.907
	0.79	0.194E-03±0.620E-05±0.195E-04	0.897
	0.81	0.160E-03±0.552E-05±0.162E-04	0.887
	0.83	0.151E-03±0.559E-05±0.152E-04	0.881
	0.85	0.132E-03±0.566E-05±0.133E-04	0.878
	0.87	0.943E-04±0.497E-05±0.951E-05	0.875
	0.89	0.681E-04±0.421E-05±0.686E-05	0.875
	0.91	0.548E-04±0.333E-05±0.552E-05	0.870
	0.93	0.453E-04±0.297E-05±0.457E-05	0.867
	0.95	0.405E-04±0.281E-05±0.408E-05	0.843
	0.97	0.486E-04±0.312E-05±0.490E-05	0.812
	0.99	0.470E-04±0.324E-05±0.474E-05	0.751
	1.01	0.488E-04±0.346E-05±0.492E-05	0.749
	1.03	0.417E-04±0.337E-05±0.420E-05	0.748
	1.05	0.264E-04±0.241E-05±0.266E-05	0.747
	1.07	0.128E-04±0.162E-05±0.129E-05	0.746
	1.09	0.111E-04±0.161E-05±0.112E-05	0.745
	1.11	0.800E-05±0.147E-05±0.807E-06	0.744
	1.13	0.741E-05±0.126E-05±0.747E-06	0.743
	1.15	0.399E-05±0.931E-06±0.403E-06	0.742
	1.17	0.445E-05±0.121E-05±0.449E-06	0.741
	1.19	0.344E-05±0.127E-05±0.346E-06	0.740
5.775	0.71	0.827E-03±0.246E-04±0.835E-04	0.948
	0.73	0.323E-03±0.800E-05±0.327E-04	0.932
	0.75	0.270E-03±0.802E-05±0.272E-04	0.919
	0.77	0.243E-03±0.832E-05±0.246E-04	0.909
	0.79	0.193E-03±0.645E-05±0.195E-04	0.898
	0.81	0.160E-03±0.555E-05±0.162E-04	0.888
	0.83	0.151E-03±0.546E-05±0.152E-04	0.883
	0.85	0.120E-03±0.505E-05±0.121E-04	0.879
	0.87	0.941E-04±0.487E-05±0.950E-05	0.877
	0.89	0.789E-04±0.468E-05±0.797E-05	0.874
	0.91	0.585E-04±0.397E-05±0.591E-05	0.874
	0.93	0.410E-04±0.295E-05±0.414E-05	0.868
	0.95	0.438E-04±0.297E-05±0.442E-05	0.849
	0.97	0.410E-04±0.301E-05±0.414E-05	0.808
	0.99	0.401E-04±0.303E-05±0.405E-05	0.751
	1.01	0.425E-04±0.308E-05±0.430E-05	0.750
	1.03	0.321E-04±0.269E-05±0.324E-05	0.749
	1.05	0.353E-04±0.294E-05±0.356E-05	0.747
	1.07	0.204E-04±0.214E-05±0.206E-05	0.746

	1.09	0.183E-04±0.225E-05±0.185E-05	0.745
	1.11	0.104E-04±0.169E-05±0.105E-05	0.744
	1.13	0.598E-05±0.127E-05±0.604E-06	0.743
	1.15	0.603E-05±0.136E-05±0.609E-06	0.742
	1.17	0.379E-05±0.108E-05±0.383E-06	0.742
5.825	0.71	0.170E-02±0.818E-04±0.173E-03	0.951
	0.73	0.378E-03±0.968E-05±0.383E-04	0.934
	0.75	0.255E-03±0.728E-05±0.258E-04	0.920
	0.77	0.231E-03±0.787E-05±0.234E-04	0.910
	0.79	0.181E-03±0.665E-05±0.183E-04	0.899
	0.81	0.151E-03±0.542E-05±0.153E-04	0.890
	0.83	0.142E-03±0.533E-05±0.143E-04	0.883
	0.85	0.115E-03±0.482E-05±0.116E-04	0.880
	0.87	0.924E-04±0.460E-05±0.936E-05	0.877
	0.89	0.747E-04±0.441E-05±0.757E-05	0.875
	0.91	0.508E-04±0.364E-05±0.515E-05	0.874
	0.93	0.471E-04±0.344E-05±0.477E-05	0.865
	0.95	0.452E-04±0.308E-05±0.457E-05	0.846
	0.97	0.422E-04±0.301E-05±0.427E-05	0.806
	0.99	0.474E-04±0.332E-05±0.480E-05	0.752
	1.01	0.394E-04±0.313E-05±0.399E-05	0.751
	1.03	0.299E-04±0.261E-05±0.302E-05	0.749
	1.05	0.249E-04±0.232E-05±0.252E-05	0.748
	1.07	0.184E-04±0.213E-05±0.186E-05	0.747
	1.09	0.119E-04±0.165E-05±0.120E-05	0.746
	1.11	0.670E-05±0.121E-05±0.679E-06	0.745
	1.13	0.659E-05±0.124E-05±0.668E-06	0.744
	1.15	0.421E-05±0.982E-06±0.427E-06	0.743
	1.17	0.241E-05±0.769E-06±0.244E-06	0.742
5.875	0.71	0.110E-01±0.139E-02±0.112E-02	0.953
	0.73	0.557E-03±0.165E-04±0.566E-04	0.937
	0.75	0.259E-03±0.704E-05±0.263E-04	0.922
	0.77	0.209E-03±0.705E-05±0.212E-04	0.912
	0.79	0.180E-03±0.721E-05±0.183E-04	0.901
	0.81	0.155E-03±0.592E-05±0.157E-04	0.891
	0.83	0.139E-03±0.522E-05±0.141E-04	0.884
	0.85	0.101E-03±0.435E-05±0.103E-04	0.881
	0.87	0.847E-04±0.415E-05±0.860E-05	0.877
	0.89	0.801E-04±0.435E-05±0.813E-05	0.875
	0.91	0.589E-04±0.393E-05±0.598E-05	0.872
	0.93	0.376E-04±0.315E-05±0.381E-05	0.867
	0.95	0.392E-04±0.320E-05±0.398E-05	0.848
	0.97	0.462E-04±0.333E-05±0.469E-05	0.810
	0.99	0.479E-04±0.342E-05±0.486E-05	0.753
	1.01	0.393E-04±0.313E-05±0.399E-05	0.752
	1.03	0.277E-04±0.242E-05±0.281E-05	0.750
	1.05	0.225E-04±0.226E-05±0.229E-05	0.749
	1.07	0.139E-04±0.158E-05±0.141E-05	0.748
	1.09	0.798E-05±0.127E-05±0.810E-06	0.747
	1.11	0.651E-05±0.109E-05±0.660E-06	0.746
	1.13	0.498E-05±0.100E-05±0.505E-06	0.745
	1.15	0.330E-05±0.770E-06±0.335E-06	0.744
	1.17	0.196E-05±0.589E-06±0.199E-06	0.743
5.925	0.75	0.299E-03±0.834E-05±0.304E-04	0.924
	0.77	0.213E-03±0.673E-05±0.216E-04	0.913
	0.79	0.181E-03±0.693E-05±0.184E-04	0.903
	0.81	0.168E-03±0.678E-05±0.170E-04	0.892
	0.83	0.108E-03±0.458E-05±0.110E-04	0.885
	0.85	0.116E-04±0.485E-05±0.118E-04	0.881
	0.87	0.814E-04±0.410E-05±0.828E-05	0.878
	0.89	0.694E-04±0.395E-05±0.706E-05	0.877
	0.91	0.622E-04±0.393E-05±0.632E-05	0.874
	0.93	0.507E-04±0.383E-05±0.515E-05	0.868
	0.95	0.339E-04±0.293E-05±0.345E-05	0.847
	0.97	0.310E-04±0.261E-05±0.316E-05	0.811

	0.99	0.472E-04±0.336E-05±0.480E-05	0.754
	1.01	0.347E-04±0.304E-05±0.353E-05	0.752
	1.03	0.256E-04±0.241E-05±0.260E-05	0.751
	1.05	0.191E-04±0.202E-05±0.195E-05	0.750
	1.07	0.152E-04±0.190E-05±0.155E-05	0.748
	1.09	0.130E-05±0.174E-05±0.132E-06	0.747
	1.11	0.531E-05±0.105E-05±0.540E-06	0.746
	1.13	0.814E-05±0.139E-06±0.828E-06	0.745
	1.15	0.305E-05±0.830E-06±0.310E-06	0.744
	1.17	0.280E-05±0.842E-06±0.284E-06	0.743
5.975	0.75	0.228E-03±0.715E-05±0.233E-04	0.926
	0.77	0.217E-03±0.664E-05±0.222E-04	0.914
	0.79	0.183E-03±0.664E-05±0.187E-04	0.904
	0.81	0.158E-03±0.668E-05±0.162E-04	0.894
	0.83	0.114E-03±0.499E-05±0.117E-04	0.886
	0.85	0.996E-04±0.443E-05±0.102E-04	0.883
	0.87	0.751E-04±0.392E-05±0.769E-05	0.879
	0.89	0.673E-04±0.356E-05±0.690E-05	0.875
	0.91	0.560E-04±0.345E-05±0.573E-05	0.874
	0.93	0.432E-04±0.329E-05±0.442E-05	0.870
	0.95	0.389E-04±0.332E-05±0.399E-05	0.850
	0.97	0.338E-04±0.320E-05±0.346E-05	0.809
	0.99	0.369E-04±0.311E-05±0.378E-05	0.755
	1.01	0.383E-04±0.313E-05±0.392E-05	0.753
	1.03	0.328E-04±0.290E-05±0.336E-05	0.752
	1.05	0.203E-04±0.213E-05±0.207E-05	0.750
	1.07	0.123E-04±0.169E-05±0.126E-05	0.749
	1.09	0.641E-05±0.111E-05±0.656E-06	0.748
	1.11	0.888E-05±0.137E-05±0.909E-06	0.747
	1.13	0.383E-05±0.863E-06±0.392E-06	0.746
	1.15	0.365E-05±0.880E-06±0.373E-06	0.745
	1.17	0.384E-05±0.867E-06±0.393E-06	0.744
6.025	0.77	0.225E-03±0.688E-05±0.232E-04	0.916
	0.79	0.151E-03±0.573E-05±0.155E-04	0.906
	0.81	0.145E-03±0.630E-05±0.149E-04	0.895
	0.83	0.120E-03±0.562E-05±0.123E-04	0.887
	0.85	0.867E-04±0.411E-05±0.893E-05	0.883
	0.87	0.734E-04±0.381E-05±0.756E-05	0.879
	0.89	0.691E-04±0.366E-05±0.712E-05	0.876
	0.91	0.524E-04±0.317E-05±0.540E-05	0.875
	0.93	0.322E-04±0.241E-05±0.332E-05	0.871
	0.95	0.361E-04±0.305E-05±0.372E-05	0.855
	0.97	0.332E-04±0.308E-05±0.342E-05	0.812
	0.99	0.408E-04±0.340E-05±0.420E-05	0.755
	1.01	0.331E-04±0.317E-05±0.341E-05	0.754
	1.03	0.239E-04±0.224E-05±0.246E-05	0.752
	1.05	0.231E-04±0.248E-05±0.238E-05	0.751
	1.07	0.140E-04±0.170E-05±0.144E-05	0.750
	1.09	0.119E-04±0.187E-05±0.122E-05	0.749
	1.11	0.689E-05±0.139E-05±0.710E-06	0.747
	1.13	0.619E-05±0.136E-05±0.638E-06	0.746
	1.15	0.395E-05±0.113E-05±0.407E-06	0.745
	1.17	0.168E-05±0.677E-06±0.173E-06	0.744
6.075	0.77	0.233E-03±0.785E-05±0.242E-04	0.918
	0.79	0.175E-03±0.592E-05±0.182E-04	0.907
	0.81	0.145E-03±0.606E-05±0.151E-04	0.896
	0.83	0.117E-03±0.574E-05±0.121E-04	0.889
	0.85	0.871E-04±0.466E-05±0.903E-05	0.883
	0.87	0.768E-04±0.399E-05±0.797E-05	0.881
	0.89	0.553E-04±0.309E-05±0.573E-05	0.878
	0.91	0.484E-04±0.300E-05±0.502E-05	0.874
	0.93	0.476E-04±0.312E-05±0.493E-05	0.869
	0.95	0.338E-04±0.285E-05±0.351E-05	0.854
	0.97	0.411E-04±0.337E-05±0.426E-05	0.815
	0.99	0.377E-04±0.383E-05±0.391E-05	0.756

	1.01	0.304E-04±0.315E-05±0.315E-05	0.755
	1.03	0.199E-04±0.215E-05±0.207E-05	0.753
	1.05	0.181E-04±0.198E-05±0.187E-05	0.752
	1.07	0.122E-04±0.166E-05±0.126E-05	0.751
	1.09	0.966E-05±0.147E-05±0.100E-05	0.749
	1.11	0.479E-05±0.102E-05±0.496E-06	0.748
	1.13	0.475E-05±0.101E-05±0.492E-06	0.747
	1.15	0.296E-05±0.846E-06±0.307E-06	0.746
	1.17	0.195E-05±0.718E-06±0.202E-06	0.745
6.125	0.79	0.182E-03±0.616E-05±0.190E-04	0.909
	0.81	0.152E-03±0.589E-05±0.159E-04	0.898
	0.83	0.111E-03±0.549E-05±0.116E-04	0.889
	0.85	0.958E-04±0.523E-05±0.100E-04	0.884
	0.87	0.671E-04±0.369E-05±0.702E-05	0.882
	0.89	0.578E-04±0.321E-05±0.605E-05	0.879
	0.91	0.566E-04±0.342E-05±0.593E-05	0.875
	0.93	0.395E-04±0.268E-05±0.413E-05	0.869
	0.95	0.363E-04±0.295E-05±0.379E-05	0.852
	0.97	0.392E-04±0.351E-05±0.410E-05	0.815
	0.99	0.387E-04±0.348E-05±0.405E-05	0.757
	1.01	0.239E-04±0.236E-05±0.250E-05	0.756
	1.03	0.147E-04±0.178E-05±0.154E-05	0.754
	1.05	0.185E-04±0.219E-05±0.193E-05	0.753
	1.07	0.841E-05±0.128E-05±0.879E-06	0.751
	1.09	0.880E-05±0.156E-05±0.920E-06	0.750
	1.11	0.562E-05±0.114E-05±0.588E-06	0.749
	1.13	0.353E-05±0.884E-06±0.369E-06	0.748
	1.15	0.327E-05±0.852E-06±0.342E-06	0.747
	1.17	0.243E-05±0.776E-06±0.254E-06	0.746
6.175	0.79	0.220E-03±0.827E-05±0.233E-04	0.910
	0.81	0.137E-03±0.528E-05±0.146E-04	0.898
	0.83	0.116E-03±0.546E-05±0.123E-04	0.889
	0.85	0.107E-03±0.582E-05±0.114E-04	0.884
	0.87	0.792E-04±0.445E-05±0.839E-05	0.882
	0.89	0.437E-04±0.271E-05±0.463E-05	0.879
	0.91	0.454E-04±0.309E-05±0.482E-05	0.875
	0.93	0.335E-04±0.253E-05±0.355E-05	0.869
	0.95	0.420E-04±0.315E-05±0.446E-05	0.852
	0.97	0.338E-04±0.301E-05±0.358E-05	0.815
	0.99	0.374E-04±0.362E-05±0.397E-05	0.757
	1.01	0.321E-04±0.354E-05±0.340E-05	0.756
	1.03	0.236E-04±0.263E-05±0.251E-05	0.754
	1.05	0.148E-04±0.195E-05±0.157E-05	0.753
	1.07	0.957E-05±0.153E-05±0.101E-05	0.751
	1.09	0.834E-05±0.131E-05±0.884E-06	0.750
	1.11	0.563E-05±0.117E-05±0.597E-06	0.749
	1.13	0.538E-05±0.114E-05±0.570E-06	0.748
	1.15	0.400E-05±0.100E-05±0.424E-06	0.747
	1.17	0.167E-05±0.673E-06±0.177E-06	0.746
6.225	0.79	0.147E-03±0.714E-05±0.157E-04	0.911
	0.81	0.139E-03±0.539E-05±0.149E-04	0.900
	0.83	0.124E-03±0.534E-05±0.133E-04	0.892
	0.85	0.921E-04±0.518E-05±0.983E-05	0.887
	0.87	0.735E-04±0.459E-05±0.784E-05	0.883
	0.89	0.562E-04±0.350E-05±0.600E-05	0.880
	0.91	0.439E-04±0.289E-05±0.468E-05	0.876
	0.93	0.393E-04±0.283E-05±0.420E-05	0.872
	0.95	0.291E-04±0.244E-05±0.311E-05	0.857
	0.97	0.341E-04±0.274E-05±0.363E-05	0.812
	0.99	0.323E-04±0.275E-05±0.344E-05	0.759
	1.01	0.287E-04±0.319E-05±0.306E-05	0.757
	1.03	0.140E-04±0.214E-05±0.149E-05	0.756
	1.05	0.123E-04±0.203E-05±0.132E-05	0.754
	1.07	0.113E-04±0.187E-05±0.121E-05	0.753
	1.09	0.783E-05±0.151E-05±0.835E-06	0.751

	1.11	0.660E-05±0.154E-05±0.704E-06	0.750
	1.13	0.479E-05±0.125E-05±0.511E-06	0.749
	1.15	0.405E-05±0.122E-05±0.432E-06	0.748
	1.17	0.226E-05±0.912E-06±0.241E-06	0.747
6.275	0.81	0.162E-03±0.686E-05±0.174E-04	0.902
	0.83	0.104E-03±0.462E-05±0.111E-04	0.892
	0.85	0.949E-04±0.493E-05±0.102E-04	0.887
	0.87	0.558E-04±0.378E-05±0.598E-05	0.884
	0.89	0.556E-04±0.381E-05±0.597E-05	0.879
	0.91	0.379E-04±0.278E-05±0.407E-05	0.876
	0.93	0.330E-04±0.244E-05±0.354E-05	0.873
	0.95	0.348E-04±0.265E-05±0.374E-05	0.858
	0.97	0.387E-04±0.309E-05±0.415E-05	0.816
	0.99	0.305E-04±0.274E-05±0.327E-05	0.760
	1.01	0.286E-04±0.285E-05±0.307E-05	0.758
	1.03	0.205E-04±0.271E-05±0.220E-05	0.756
	1.05	0.132E-04±0.201E-05±0.142E-05	0.755
	1.07	0.124E-04±0.192E-05±0.133E-05	0.754
	1.09	0.582E-05±0.175E-05±0.625E-06	0.752
	1.11	0.457E-05±0.119E-05±0.491E-06	0.751
	1.13	0.472E-05±0.118E-05±0.507E-06	0.750
	1.15	0.291E-05±0.992E-06±0.312E-06	0.749
	1.17	0.175E-05±0.790E-06±0.188E-06	0.748
6.325	0.81	0.129E-03±0.613E-05±0.140E-04	0.903
	0.83	0.108E-03±0.488E-05±0.117E-04	0.894
	0.85	0.791E-04±0.413E-05±0.856E-05	0.888
	0.87	0.635E-04±0.422E-05±0.686E-05	0.884
	0.89	0.579E-04±0.424E-05±0.625E-05	0.881
	0.91	0.483E-04±0.349E-05±0.522E-05	0.877
	0.93	0.349E-04±0.252E-05±0.378E-05	0.872
	0.95	0.321E-04±0.249E-05±0.346E-05	0.851
	0.97	0.292E-04±0.250E-05±0.315E-05	0.815
	0.99	0.305E-04±0.290E-05±0.329E-05	0.761
	1.01	0.278E-04±0.271E-05±0.300E-05	0.759
	1.03	0.231E-04±0.279E-05±0.250E-05	0.757
	1.05	0.163E-04±0.225E-05±0.176E-05	0.756
	1.07	0.908E-05±0.164E-05±0.982E-06	0.754
	1.09	0.619E-05±0.128E-05±0.669E-06	0.753
	1.11	0.481E-05±0.116E-05±0.520E-06	0.752
	1.13	0.393E-05±0.102E-05±0.425E-06	0.750
	1.15	0.233E-05±0.857E-06±0.251E-06	0.749
6.375	0.83	0.128E-03±0.605E-05±0.139E-04	0.896
	0.85	0.882E-04±0.441E-05±0.960E-05	0.889
	0.87	0.630E-04±0.395E-05±0.685E-05	0.885
	0.89	0.488E-04±0.379E-05±0.531E-05	0.881
	0.91	0.437E-04±0.349E-05±0.475E-05	0.879
	0.93	0.315E-04±0.249E-05±0.343E-05	0.871
	0.95	0.306E-04±0.243E-05±0.333E-05	0.855
	0.97	0.314E-04±0.265E-05±0.341E-05	0.811
	0.99	0.263E-04±0.250E-05±0.286E-05	0.762
	1.01	0.238E-04±0.237E-05±0.259E-05	0.760
	1.03	0.223E-04±0.255E-05±0.242E-05	0.758
	1.05	0.153E-04±0.211E-05±0.166E-05	0.757
	1.07	0.810E-05±0.164E-05±0.881E-06	0.755
	1.09	0.669E-05±0.142E-05±0.728E-06	0.754
	1.11	0.549E-05±0.111E-05±0.597E-06	0.752
	1.13	0.289E-05±0.924E-06±0.315E-06	0.751
	1.15	0.301E-05±0.784E-06±0.327E-06	0.750
6.425	0.83	0.938E-04±0.505E-05±0.102E-04	0.896
	0.85	0.812E-04±0.405E-05±0.886E-05	0.890
	0.87	0.608E-04±0.370E-05±0.663E-05	0.886
	0.89	0.522E-04±0.394E-05±0.570E-05	0.882
	0.91	0.454E-04±0.382E-05±0.496E-05	0.879
	0.93	0.378E-04±0.290E-05±0.413E-05	0.874
	0.95	0.296E-04±0.254E-05±0.323E-05	0.859

	0.97	0.354E-04±0.286E-05±0.387E-05	0.816
	0.99	0.320E-04±0.276E-05±0.350E-05	0.763
	1.01	0.211E-04±0.227E-05±0.230E-05	0.761
	1.03	0.185E-04±0.213E-05±0.202E-05	0.759
	1.05	0.158E-04±0.208E-05±0.172E-05	0.757
	1.07	0.754E-05±0.145E-05±0.824E-06	0.756
	1.09	0.407E-05±0.116E-05±0.444E-06	0.754
	1.11	0.472E-05±0.110E-05±0.515E-06	0.753
	1.13	0.396E-05±0.893E-06±0.432E-06	0.752
	1.15	0.257E-05±0.772E-06±0.280E-06	0.751
6.475	0.85	0.888E-04±0.442E-05±0.976E-05	0.891
	0.87	0.748E-04±0.405E-05±0.822E-05	0.887
	0.89	0.417E-04±0.293E-05±0.458E-05	0.885
	0.91	0.416E-04±0.364E-05±0.457E-05	0.882
	0.93	0.287E-04±0.284E-05±0.315E-05	0.874
	0.95	0.251E-04±0.229E-05±0.276E-05	0.857
	0.97	0.256E-04±0.229E-05±0.281E-05	0.817
	0.99	0.252E-04±0.227E-05±0.277E-05	0.764
	1.01	0.270E-04±0.262E-05±0.297E-05	0.762
	1.03	0.240E-04±0.263E-05±0.263E-05	0.760
	1.05	0.116E-04±0.183E-05±0.127E-05	0.758
	1.07	0.945E-05±0.182E-05±0.104E-05	0.757
	1.09	0.771E-05±0.145E-05±0.846E-06	0.755
	1.11	0.542E-05±0.136E-05±0.595E-06	0.754
	1.13	0.319E-05±0.118E-05±0.350E-06	0.753
	1.15	0.293E-05±0.883E-06±0.322E-06	0.751
6.525	0.85	0.607E-04±0.382E-05±0.669E-05	0.893
	0.87	0.659E-04±0.372E-05±0.727E-05	0.888
	0.89	0.535E-04±0.339E-05±0.590E-05	0.885
	0.91	0.473E-04±0.399E-05±0.521E-05	0.882
	0.93	0.281E-04±0.263E-05±0.310E-05	0.876
	0.95	0.254E-04±0.246E-05±0.280E-05	0.856
	0.97	0.274E-04±0.261E-05±0.302E-05	0.815
	0.99	0.222E-04±0.214E-05±0.245E-05	0.765
	1.01	0.194E-04±0.197E-05±0.214E-05	0.763
	1.03	0.170E-04±0.207E-05±0.187E-05	0.761
	1.05	0.109E-04±0.169E-05±0.121E-05	0.759
	1.07	0.827E-05±0.156E-05±0.911E-06	0.757
	1.09	0.500E-05±0.986E-06±0.551E-06	0.756
	1.11	0.285E-05±0.858E-06±0.314E-06	0.755
	1.13	0.292E-05±0.932E-06±0.322E-06	0.753
	1.15	0.259E-05±0.828E-06±0.286E-06	0.752
6.575	0.87	0.686E-04±0.422E-05±0.761E-05	0.888
	0.89	0.478E-04±0.312E-05±0.531E-05	0.884
	0.91	0.357E-04±0.286E-05±0.396E-05	0.882
	0.93	0.324E-04±0.315E-05±0.359E-05	0.876
	0.95	0.260E-04±0.260E-05±0.288E-05	0.859
	0.97	0.216E-04±0.221E-05±0.240E-05	0.822
	0.99	0.235E-04±0.244E-05±0.261E-05	0.766
	1.01	0.266E-04±0.253E-05±0.295E-05	0.764
	1.03	0.196E-04±0.225E-05±0.217E-05	0.762
	1.05	0.111E-04±0.160E-05±0.123E-05	0.760
	1.07	0.854E-05±0.132E-05±0.947E-06	0.758
	1.09	0.446E-05±0.924E-06±0.495E-06	0.757
	1.11	0.339E-05±0.791E-06±0.376E-06	0.755
	1.13	0.294E-05±0.885E-06±0.326E-06	0.754
	1.15	0.253E-05±0.862E-06±0.280E-06	0.753
6.625	0.87	0.517E-04±0.355E-05±0.577E-05	0.889
	0.89	0.530E-04±0.335E-05±0.590E-05	0.887
	0.91	0.295E-04±0.241E-05±0.329E-05	0.883
	0.93	0.353E-04±0.310E-05±0.393E-05	0.878
	0.95	0.302E-04±0.291E-05±0.337E-05	0.859
	0.97	0.234E-04±0.238E-05±0.261E-05	0.817
	0.99	0.275E-04±0.270E-05±0.306E-05	0.767
	1.01	0.198E-04±0.220E-05±0.221E-05	0.765

	1.03	0.163E-04±0.197E-05±0.182E-05	0.763
	1.05	0.129E-04±0.184E-05±0.144E-05	0.761
	1.07	0.875E-05±0.142E-05±0.976E-06	0.759
	1.09	0.632E-05±0.124E-05±0.704E-06	0.758
	1.11	0.517E-05±0.121E-05±0.577E-06	0.756
	1.13	0.319E-05±0.102E-05±0.355E-06	0.755
	1.15	0.131E-05±0.835E-06±0.146E-06	0.753
6.675	0.89	0.471E-04±0.343E-05±0.529E-05	0.887
	0.91	0.395E-04±0.301E-05±0.443E-05	0.881
	0.93	0.332E-04±0.291E-05±0.373E-05	0.878
	0.95	0.186E-04±0.218E-05±0.208E-05	0.861
	0.97	0.219E-04±0.255E-05±0.246E-05	0.817
	0.99	0.165E-04±0.213E-05±0.185E-05	0.768
	1.01	0.131E-04±0.168E-05±0.147E-05	0.766
	1.03	0.121E-04±0.158E-05±0.136E-05	0.764
	1.05	0.782E-05±0.113E-05±0.878E-06	0.762
	1.07	0.748E-05±0.128E-05±0.839E-06	0.760
	1.09	0.380E-05±0.748E-06±0.426E-06	0.758
	1.11	0.253E-05±0.809E-06±0.284E-06	0.757
	1.13	0.330E-05±0.113E-05±0.371E-06	0.755
	1.15	0.138E-05±0.882E-06±0.155E-06	0.754
6.725	0.89	0.445E-04±0.353E-05±0.504E-05	0.886
	0.91	0.316E-04±0.250E-05±0.357E-05	0.883
	0.93	0.338E-04±0.268E-05±0.382E-05	0.879
	0.95	0.207E-04±0.222E-05±0.235E-05	0.858
	0.97	0.207E-04±0.237E-05±0.234E-05	0.819
	0.99	0.195E-04±0.236E-05±0.221E-05	0.769
	1.01	0.154E-04±0.209E-05±0.174E-05	0.767
	1.03	0.136E-04±0.183E-05±0.154E-05	0.765
	1.05	0.888E-05±0.152E-05±0.100E-05	0.763
	1.07	0.719E-05±0.142E-05±0.813E-06	0.761
	1.09	0.448E-05±0.112E-05±0.506E-06	0.759
	1.11	0.171E-05±0.691E-06±0.193E-06	0.758
	1.13	0.294E-05±0.886E-06±0.333E-06	0.756
	1.15	0.200E-05±0.682E-06±0.226E-06	0.755
6.775	0.91	0.358E-04±0.284E-05±0.408E-05	0.885
	0.93	0.258E-04±0.229E-05±0.294E-05	0.878
	0.95	0.218E-04±0.218E-05±0.248E-05	0.861
	0.97	0.224E-04±0.271E-05±0.255E-05	0.822
	0.99	0.193E-04±0.233E-05±0.220E-05	0.770
	1.01	0.146E-04±0.208E-05±0.166E-05	0.768
	1.03	0.113E-04±0.155E-05±0.128E-05	0.765
	1.05	0.109E-04±0.160E-05±0.124E-05	0.764
	1.07	0.563E-05±0.102E-05±0.641E-06	0.762
	1.09	0.326E-05±0.982E-06±0.371E-06	0.760
	1.11	0.411E-05±0.875E-06±0.468E-06	0.758
	1.13	0.185E-05±0.966E-06±0.211E-06	0.757
	1.15	0.195E-05±0.789E-06±0.222E-06	0.756
6.825	0.91	0.288E-04±0.278E-05±0.330E-05	0.886
	0.93	0.290E-04±0.237E-05±0.332E-05	0.878
	0.95	0.208E-04±0.201E-05±0.238E-05	0.858
	0.97	0.175E-04±0.209E-05±0.200E-05	0.820
	0.99	0.168E-04±0.221E-05±0.192E-05	0.771
	1.01	0.149E-04±0.215E-05±0.170E-05	0.769
	1.03	0.169E-04±0.230E-05±0.193E-05	0.766
	1.05	0.809E-05±0.136E-05±0.926E-06	0.764
	1.07	0.559E-05±0.108E-05±0.640E-06	0.763
	1.09	0.400E-05±0.966E-06±0.458E-06	0.761
	1.11	0.351E-05±0.100E-05±0.401E-06	0.759
	1.13	0.200E-05±0.683E-06±0.229E-06	0.758
	1.15	0.146E-05±0.659E-06±0.167E-06	0.756
6.875	0.93	0.304E-04±0.272E-05±0.349E-05	0.881
	0.95	0.209E-04±0.202E-05±0.241E-05	0.861
	0.97	0.258E-04±0.274E-05±0.297E-05	0.821
	0.99	0.215E-04±0.264E-05±0.247E-05	0.772
	1.01	0.158E-04±0.248E-05±0.182E-05	0.770
	1.03	0.161E-04±0.249E-05±0.185E-05	0.767
	1.05	0.879E-05±0.165E-05±0.101E-05	0.765
	1.07	0.794E-05±0.153E-05±0.914E-06	0.763
	1.09	0.455E-05±0.968E-06±0.523E-06	0.762
	1.11	0.286E-05±0.815E-06±0.329E-06	0.760
	1.13	0.226E-05±0.646E-06±0.260E-06	0.759
	1.15	0.157E-05±0.578E-06±0.180E-06	0.757
6.925	0.93	0.286E-04±0.301E-05±0.331E-05	0.882
	0.95	0.282E-04±0.323E-05±0.327E-05	0.861
	0.97	0.225E-04±0.239E-05±0.261E-05	0.821
	0.99	0.239E-04±0.288E-05±0.277E-05	0.772
	1.01	0.164E-04±0.240E-05±0.190E-05	0.770
	1.03	0.126E-04±0.242E-05±0.146E-05	0.767
	1.05	0.935E-05±0.194E-05±0.108E-05	0.765
	1.07	0.527E-05±0.119E-05±0.610E-06	0.763
	1.09	0.385E-05±0.100E-05±0.446E-06	0.762
	1.11	0.287E-05±0.819E-06±0.332E-06	0.760
	1.13	0.181E-05±0.578E-06±0.210E-06	0.759
	1.15	0.120E-05±0.542E-06±0.139E-06	0.757
6.975	0.93	0.743E-04±0.124E-04±0.866E-05	0.882
	0.95	0.437E-04±0.512E-05±0.509E-05	0.861
	0.97	0.340E-04±0.349E-05±0.396E-05	0.821
	0.99	0.400E-04±0.469E-05±0.465E-05	0.774
	1.01	0.261E-04±0.378E-05±0.304E-05	0.772
	1.03	0.227E-04±0.332E-05±0.264E-05	0.769
	1.05	0.136E-04±0.262E-05±0.159E-05	0.767
	1.07	0.526E-05±0.137E-05±0.613E-06	0.765
	1.09	0.686E-05±0.160E-05±0.799E-06	0.763
	1.11	0.298E-05±0.952E-06±0.348E-06	0.762
	1.13	0.346E-05±0.104E-05±0.403E-06	0.760
	1.15	0.131E-05±0.682E-06±0.152E-06	0.759

APPENDIX D

Exclusive d(e,e$'$p$_S$)n Cross Sections

Tabulated below are the experimental measured exclusive d(e,e$'p_s$)n cross sections similar to those plotted in Section 5.2 (shown in Figs. 5.19 – 5.25) for $p_s = 0.25 - 1$ GeV/c and Q$^2 = 2 - 6$ GeV^2. In this case unobserved variables are integrated over their full range and not limited to the experimentally dependent cross sections within CLAS fiducial cuts. The results presented here have been corrected for radiative effects, acceptance and bin size. The statistical and systematic errors associated with these corrections are included. The correction factor for radiative effects R.C. for each kinematic bin is given in the last column of each table.

Q^2 [GeV^2]	x	p [GeV/c]	$d\sigma/dQ^2dxdp$ [μb/GeV^3]	R.C.
2.5	0.4	0.375	0.215E-05 $\pm$ 0.858E-06 $\pm$ 0.131E-06	0.858
		0.425	0.549E-05 $\pm$ 0.978E-06 $\pm$ 0.335E-06	0.828
		0.475	0.390E-05 $\pm$ 0.694E-06 $\pm$ 0.238E-06	0.898
		0.525	0.245E-05 $\pm$ 0.472E-06 $\pm$ 0.149E-06	0.956
		0.575	0.205E-05 $\pm$ 0.394E-06 $\pm$ 0.125E-06	0.900
		0.625	0.218E-05 $\pm$ 0.388E-06 $\pm$ 0.133E-06	0.857
		0.675	0.150E-05 $\pm$ 0.319E-06 $\pm$ 0.915E-07	0.860
		0.725	0.113E-05 $\pm$ 0.273E-06 $\pm$ 0.692E-07	0.863
		0.775	0.104E-05 $\pm$ 0.262E-06 $\pm$ 0.634E-07	0.857
		0.825	0.911E-06 $\pm$ 0.243E-06 $\pm$ 0.556E-07	0.859
		0.875	0.105E-05 $\pm$ 0.264E-06 $\pm$ 0.638E-07	0.870
		0.925	0.527E-06 $\pm$ 0.187E-06 $\pm$ 0.321E-07	0.833
		0.975	0.948E-06 $\pm$ 0.248E-06 $\pm$ 0.578E-07	0.834
2.5	0.6	0.275	0.254E-04 $\pm$ 0.210E-05 $\pm$ 0.155E-05	0.926
		0.325	0.286E-04 $\pm$ 0.189E-05 $\pm$ 0.174E-05	0.908
		0.375	0.202E-04 $\pm$ 0.140E-05 $\pm$ 0.123E-05	0.904
		0.425	0.145E-04 $\pm$ 0.110E-05 $\pm$ 0.884E-06	0.925
		0.475	0.116E-04 $\pm$ 0.939E-06 $\pm$ 0.708E-06	0.909
		0.525	0.132E-04 $\pm$ 0.978E-06 $\pm$ 0.806E-06	0.885
		0.575	0.878E-05 $\pm$ 0.786E-06 $\pm$ 0.536E-06	0.852
		0.625	0.810E-05 $\pm$ 0.754E-06 $\pm$ 0.494E-06	0.864
		0.675	0.582E-05 $\pm$ 0.635E-06 $\pm$ 0.355E-06	0.915
		0.725	0.744E-05 $\pm$ 0.721E-06 $\pm$ 0.454E-06	0.848
		0.775	0.568E-05 $\pm$ 0.633E-06 $\pm$ 0.346E-06	0.888
		0.825	0.560E-05 $\pm$ 0.625E-06 $\pm$ 0.341E-06	0.908
		0.875	0.487E-05 $\pm$ 0.587E-06 $\pm$ 0.297E-06	0.920
		0.925	0.352E-05 $\pm$ 0.500E-06 $\pm$ 0.215E-06	0.867
		0.975	0.523E-05 $\pm$ 0.604E-06 $\pm$ 0.319E-06	0.862
2.5	0.8	0.275	0.661E-04 $\pm$ 0.273E-05 $\pm$ 0.403E-05	0.911
		0.325	0.538E-04 $\pm$ 0.226E-05 $\pm$ 0.328E-05	0.903
		0.375	0.472E-04 $\pm$ 0.204E-05 $\pm$ 0.288E-05	0.888
		0.425	0.441E-04 $\pm$ 0.192E-05 $\pm$ 0.269E-05	0.895
		0.475	0.348E-04 $\pm$ 0.168E-05 $\pm$ 0.213E-05	0.887
		0.525	0.304E-04 $\pm$ 0.157E-05 $\pm$ 0.185E-05	0.857
		0.575	0.249E-04 $\pm$ 0.142E-05 $\pm$ 0.152E-05	0.896
		0.625	0.211E-04 $\pm$ 0.130E-05 $\pm$ 0.129E-05	0.845
		0.675	0.170E-04 $\pm$ 0.118E-05 $\pm$ 0.103E-05	0.882
		0.725	0.156E-04 $\pm$ 0.113E-05 $\pm$ 0.952E-06	0.859
		0.775	0.145E-04 $\pm$ 0.109E-05 $\pm$ 0.887E-06	0.885
		0.825	0.131E-04 $\pm$ 0.105E-05 $\pm$ 0.797E-06	0.872

Q^2 [GeV^2]	x	p [GeV/c]	$d\sigma/dQ^2dxdp$ [μb/GeV^3]	R.C.
		0.875	0.119E-04 $\pm$ 0.101E-05 $\pm$ 0.726E-06	0.878
		0.925	0.115E-04 $\pm$ 0.994E-06 $\pm$ 0.704E-06	0.860
		0.975	0.675E-05 $\pm$ 0.768E-06 $\pm$ 0.412E-06	0.926
2.5	1.0	0.275	0.379E-04 $\pm$ 0.208E-05 $\pm$ 0.231E-05	0.876
		0.325	0.474E-04 $\pm$ 0.218E-05 $\pm$ 0.289E-05	0.876
		0.375	0.425E-04 $\pm$ 0.203E-05 $\pm$ 0.259E-05	0.883
		0.425	0.425E-04 $\pm$ 0.201E-05 $\pm$ 0.259E-05	0.864
		0.475	0.417E-04 $\pm$ 0.198E-05 $\pm$ 0.254E-05	0.843
		0.525	0.384E-04 $\pm$ 0.191E-05 $\pm$ 0.234E-05	0.846
		0.575	0.297E-04 $\pm$ 0.169E-05 $\pm$ 0.181E-05	0.874
		0.625	0.291E-04 $\pm$ 0.169E-05 $\pm$ 0.178E-05	0.829
		0.675	0.227E-04 $\pm$ 0.150E-05 $\pm$ 0.138E-05	0.865
		0.725	0.154E-04 $\pm$ 0.125E-05 $\pm$ 0.938E-06	0.867
		0.775	0.164E-04 $\pm$ 0.131E-05 $\pm$ 0.100E-05	0.861
		0.825	0.106E-04 $\pm$ 0.105E-05 $\pm$ 0.646E-06	0.907
		0.875	0.134E-04 $\pm$ 0.119E-05 $\pm$ 0.820E-06	0.872
		0.925	0.109E-04 $\pm$ 0.108E-05 $\pm$ 0.667E-06	0.940
		0.975	0.920E-05 $\pm$ 0.962E-06 $\pm$ 0.561E-06	0.870
2.5	1.2	0.275	0.337E-04 $\pm$ 0.220E-05 $\pm$ 0.205E-05	0.767
		0.325	0.236E-04 $\pm$ 0.171E-05 $\pm$ 0.144E-05	0.801
		0.375	0.194E-04 $\pm$ 0.151E-05 $\pm$ 0.118E-05	0.824
		0.425	0.180E-04 $\pm$ 0.144E-05 $\pm$ 0.110E-05	0.806
		0.475	0.171E-04 $\pm$ 0.141E-05 $\pm$ 0.105E-05	0.820
		0.525	0.163E-04 $\pm$ 0.137E-05 $\pm$ 0.991E-06	0.813
		0.575	0.147E-04 $\pm$ 0.130E-05 $\pm$ 0.899E-06	0.834
		0.625	0.119E-04 $\pm$ 0.118E-05 $\pm$ 0.727E-06	0.856
		0.675	0.100E-04 $\pm$ 0.107E-05 $\pm$ 0.613E-06	0.849
		0.725	0.110E-04 $\pm$ 0.111E-05 $\pm$ 0.669E-06	0.823
		0.775	0.799E-05 $\pm$ 0.930E-06 $\pm$ 0.487E-06	0.857
		0.825	0.964E-05 $\pm$ 0.102E-05 $\pm$ 0.588E-06	0.839
		0.875	0.613E-05 $\pm$ 0.805E-06 $\pm$ 0.374E-06	0.882
		0.925	0.639E-05 $\pm$ 0.814E-06 $\pm$ 0.390E-06	0.807
		0.975	0.612E-05 $\pm$ 0.816E-06 $\pm$ 0.373E-06	0.839
2.5	1.4	0.275	0.282E-04 $\pm$ 0.220E-05 $\pm$ 0.172E-05	0.716
		0.325	0.226E-04 $\pm$ 0.176E-05 $\pm$ 0.138E-05	0.717
		0.375	0.126E-04 $\pm$ 0.125E-05 $\pm$ 0.767E-06	0.759
		0.425	0.943E-05 $\pm$ 0.106E-05 $\pm$ 0.575E-06	0.746
		0.475	0.768E-05 $\pm$ 0.940E-06 $\pm$ 0.469E-06	0.765
		0.525	0.673E-05 $\pm$ 0.865E-06 $\pm$ 0.410E-06	0.913
		0.575	0.941E-05 $\pm$ 0.102E-05 $\pm$ 0.574E-06	0.813

Q^2 [GeV^2]	x	p [GeV/c]	$d\sigma/dQ^2dxdp$ [μb/GeV^3]	R.C.
		0.625	0.630E-05 $\pm$ 0.833E-06 $\pm$ 0.384E-06	0.800
		0.675	0.554E-05 $\pm$ 0.770E-06 $\pm$ 0.338E-06	0.883
		0.725	0.590E-05 $\pm$ 0.797E-06 $\pm$ 0.360E-06	0.786
		0.775	0.452E-05 $\pm$ 0.710E-06 $\pm$ 0.276E-06	0.797
		0.825	0.465E-05 $\pm$ 0.721E-06 $\pm$ 0.283E-06	0.810
		0.875	0.345E-05 $\pm$ 0.629E-06 $\pm$ 0.210E-06	0.851
		0.925	0.344E-05 $\pm$ 0.631E-06 $\pm$ 0.210E-06	0.860
		0.975	0.427E-05 $\pm$ 0.708E-06 $\pm$ 0.261E-06	0.886
2.5	1.6	0.275	0.228E-06 $\pm$ 0.761E-07 $\pm$ 0.139E-07	0.752
		0.325	0.323E-05 $\pm$ 0.581E-06 $\pm$ 0.197E-06	0.782
		0.375	0.776E-05 $\pm$ 0.999E-06 $\pm$ 0.473E-06	0.715
		0.425	0.571E-05 $\pm$ 0.869E-06 $\pm$ 0.349E-06	0.841
		0.475	0.435E-05 $\pm$ 0.752E-06 $\pm$ 0.265E-06	0.804
		0.525	0.574E-05 $\pm$ 0.857E-06 $\pm$ 0.350E-06	0.782
		0.575	0.424E-05 $\pm$ 0.750E-06 $\pm$ 0.259E-06	0.757
		0.625	0.495E-05 $\pm$ 0.808E-06 $\pm$ 0.302E-06	0.754
		0.675	0.385E-05 $\pm$ 0.722E-06 $\pm$ 0.235E-06	0.758
		0.725	0.334E-05 $\pm$ 0.675E-06 $\pm$ 0.204E-06	0.769
		0.775	0.214E-05 $\pm$ 0.546E-06 $\pm$ 0.130E-06	0.879
		0.825	0.249E-05 $\pm$ 0.581E-06 $\pm$ 0.152E-06	0.951
		0.875	0.122E-05 $\pm$ 0.419E-06 $\pm$ 0.742E-07	0.800
		0.925	0.490E-05 $\pm$ 0.849E-06 $\pm$ 0.299E-06	0.808
		0.975	0.524E-05 $\pm$ 0.870E-06 $\pm$ 0.319E-06	0.817
3.5	0.4	0.425	0.226E-06 $\pm$ 0.180E-06 $\pm$ 0.138E-07	0.862
		0.475	0.287E-06 $\pm$ 0.132E-06 $\pm$ 0.175E-07	0.859
		0.525	0.430E-06 $\pm$ 0.129E-06 $\pm$ 0.262E-07	0.863
		0.575	0.109E-06 $\pm$ 0.613E-07 $\pm$ 0.666E-08	0.865
		0.625	0.995E-07 $\pm$ 0.556E-07 $\pm$ 0.607E-08	0.853
		0.675	0.153E-06 $\pm$ 0.704E-07 $\pm$ 0.931E-08	0.868
		0.775	0.544E-07 $\pm$ 0.415E-07 $\pm$ 0.332E-08	0.887
		0.825	0.158E-06 $\pm$ 0.727E-07 $\pm$ 0.965E-08	0.870
3.5	0.6	0.275	0.364E-05 $\pm$ 0.779E-06 $\pm$ 0.222E-06	0.864
		0.325	0.361E-05 $\pm$ 0.589E-06 $\pm$ 0.220E-06	0.860
		0.375	0.260E-05 $\pm$ 0.423E-06 $\pm$ 0.159E-06	0.892
		0.425	0.187E-05 $\pm$ 0.324E-06 $\pm$ 0.114E-06	0.890
		0.475	0.156E-05 $\pm$ 0.277E-06 $\pm$ 0.953E-07	0.847
		0.525	0.146E-05 $\pm$ 0.257E-06 $\pm$ 0.888E-07	0.842
		0.575	0.102E-05 $\pm$ 0.214E-06 $\pm$ 0.620E-07	0.837
		0.625	0.572E-06 $\pm$ 0.159E-06 $\pm$ 0.349E-07	0.840
		0.675	0.350E-06 $\pm$ 0.124E-06 $\pm$ 0.213E-07	0.846

Q^2 [GeV^2]	x	p [GeV/c]	$d\sigma/dQ^2dxdp$ [μb/GeV^3]	R.C.
		0.725	0.598E-06 $\pm$ 0.167E-06 $\pm$ 0.365E-07	0.840
		0.775	0.502E-06 $\pm$ 0.150E-06 $\pm$ 0.306E-07	0.847
		0.825	0.498E-06 $\pm$ 0.150E-06 $\pm$ 0.304E-07	0.855
		0.875	0.213E-06 $\pm$ 0.975E-07 $\pm$ 0.130E-07	0.848
		0.925	0.429E-06 $\pm$ 0.137E-06 $\pm$ 0.262E-07	0.826
		0.975	0.148E-06 $\pm$ 0.813E-07 $\pm$ 0.901E-08	0.818
3.5	0.8	0.275	0.773E-05 $\pm$ 0.719E-06 $\pm$ 0.472E-06	0.852
		0.325	0.690E-05 $\pm$ 0.622E-06 $\pm$ 0.421E-06	0.845
		0.375	0.653E-05 $\pm$ 0.580E-06 $\pm$ 0.398E-06	0.839
		0.425	0.529E-05 $\pm$ 0.511E-06 $\pm$ 0.323E-06	0.830
		0.475	0.453E-05 $\pm$ 0.470E-06 $\pm$ 0.276E-06	0.826
		0.525	0.344E-05 $\pm$ 0.409E-06 $\pm$ 0.210E-06	0.819
		0.575	0.282E-05 $\pm$ 0.372E-06 $\pm$ 0.172E-06	0.822
		0.625	0.370E-05 $\pm$ 0.425E-06 $\pm$ 0.226E-06	0.815
		0.675	0.268E-05 $\pm$ 0.364E-06 $\pm$ 0.163E-06	0.822
		0.725	0.221E-05 $\pm$ 0.326E-06 $\pm$ 0.135E-06	0.823
		0.775	0.183E-05 $\pm$ 0.298E-06 $\pm$ 0.112E-06	0.822
		0.825	0.177E-05 $\pm$ 0.296E-06 $\pm$ 0.108E-06	0.828
		0.875	0.196E-05 $\pm$ 0.306E-06 $\pm$ 0.119E-06	0.823
		0.925	0.886E-06 $\pm$ 0.209E-06 $\pm$ 0.541E-07	0.826
		0.975	0.328E-06 $\pm$ 0.129E-06 $\pm$ 0.200E-07	0.828
3.5	1.0	0.275	0.645E-05 $\pm$ 0.651E-06 $\pm$ 0.393E-06	0.811
		0.325	0.728E-05 $\pm$ 0.653E-06 $\pm$ 0.444E-06	0.815
		0.375	0.727E-05 $\pm$ 0.648E-06 $\pm$ 0.444E-06	0.813
		0.425	0.813E-05 $\pm$ 0.680E-06 $\pm$ 0.496E-06	0.811
		0.475	0.781E-05 $\pm$ 0.669E-06 $\pm$ 0.476E-06	0.810
		0.525	0.578E-05 $\pm$ 0.573E-06 $\pm$ 0.352E-06	0.809
		0.575	0.569E-05 $\pm$ 0.572E-06 $\pm$ 0.347E-06	0.804
		0.625	0.308E-05 $\pm$ 0.420E-06 $\pm$ 0.188E-06	0.802
		0.675	0.223E-05 $\pm$ 0.359E-06 $\pm$ 0.136E-06	0.804
		0.725	0.240E-05 $\pm$ 0.371E-06 $\pm$ 0.146E-06	0.805
		0.775	0.211E-05 $\pm$ 0.350E-06 $\pm$ 0.129E-06	0.815
		0.825	0.181E-05 $\pm$ 0.322E-06 $\pm$ 0.110E-06	0.810
		0.875	0.108E-05 $\pm$ 0.253E-06 $\pm$ 0.656E-07	0.820
		0.925	0.223E-05 $\pm$ 0.360E-06 $\pm$ 0.136E-06	0.806
		0.975	0.960E-06 $\pm$ 0.236E-06 $\pm$ 0.586E-07	0.811
3.5	1.2	0.275	0.506E-05 $\pm$ 0.670E-06 $\pm$ 0.309E-06	0.731
		0.325	0.473E-05 $\pm$ 0.590E-06 $\pm$ 0.288E-06	0.756
		0.375	0.258E-05 $\pm$ 0.418E-06 $\pm$ 0.158E-06	0.777
		0.425	0.224E-05 $\pm$ 0.384E-06 $\pm$ 0.137E-06	0.789

Q^2 [GeV^2]	x	p [GeV/c]	$d\sigma/dQ^2dxdp$ [μb/GeV^3]	R.C.
		0.475	0.137E-05 ± 0.303E-06 ± 0.834E-07	0.791
		0.525	0.268E-05 ± 0.420E-06 ± 0.163E-06	0.795
		0.575	0.205E-05 ± 0.371E-06 ± 0.125E-06	0.794
		0.625	0.694E-06 ± 0.216E-06 ± 0.423E-07	0.786
		0.675	0.139E-05 ± 0.307E-06 ± 0.846E-07	0.789
		0.725	0.128E-05 ± 0.295E-06 ± 0.778E-07	0.792
		0.775	0.137E-05 ± 0.304E-06 ± 0.834E-07	0.798
		0.825	0.672E-06 ± 0.212E-06 ± 0.410E-07	0.801
		0.875	0.136E-05 ± 0.303E-06 ± 0.832E-07	0.797
		0.925	0.795E-06 ± 0.233E-06 ± 0.485E-07	0.813
		0.975	0.905E-06 ± 0.248E-06 ± 0.552E-07	0.806
3.5	1.4	0.275	0.171E-05 ± 0.410E-06 ± 0.104E-06	0.702
		0.325	0.187E-05 ± 0.407E-06 ± 0.114E-06	0.702
		0.375	0.131E-05 ± 0.320E-06 ± 0.799E-07	0.722
		0.425	0.196E-05 ± 0.378E-06 ± 0.119E-06	0.751
		0.475	0.250E-05 ± 0.423E-06 ± 0.153E-06	0.769
		0.525	0.182E-05 ± 0.356E-06 ± 0.111E-06	0.775
		0.575	0.923E-06 ± 0.248E-06 ± 0.563E-07	0.777
		0.625	0.104E-05 ± 0.263E-06 ± 0.632E-07	0.780
		0.675	0.959E-06 ± 0.259E-06 ± 0.585E-07	0.783
		0.725	0.357E-06 ± 0.157E-06 ± 0.218E-07	0.785
		0.775	0.452E-06 ± 0.173E-06 ± 0.276E-07	0.792
		0.825	0.227E-06 ± 0.124E-06 ± 0.139E-07	0.801
		0.875	0.695E-06 ± 0.218E-06 ± 0.424E-07	0.798
		0.925	0.115E-06 ± 0.893E-07 ± 0.704E-08	0.807
		0.975	0.238E-06 ± 0.130E-06 ± 0.145E-07	0.808
3.5	1.6	0.325	0.302E-07 ± 0.227E-07 ± 0.184E-08	0.761
		0.375	0.444E-06 ± 0.165E-06 ± 0.271E-07	0.743
		0.425	0.416E-06 ± 0.177E-06 ± 0.254E-07	0.726
		0.475	0.113E-05 ± 0.295E-06 ± 0.687E-07	0.835
		0.525	0.424E-06 ± 0.183E-06 ± 0.258E-07	0.755
		0.575	0.117E-05 ± 0.309E-06 ± 0.712E-07	0.758
		0.625	0.137E-06 ± 0.103E-06 ± 0.834E-08	0.767
		0.675	0.138E-06 ± 0.104E-06 ± 0.842E-08	0.763
		0.725	0.295E-06 ± 0.157E-06 ± 0.180E-07	0.758
		0.775	0.146E-06 ± 0.112E-06 ± 0.891E-08	0.786
		0.825	0.293E-06 ± 0.155E-06 ± 0.179E-07	0.749
		0.875	0.285E-06 ± 0.153E-06 ± 0.174E-07	0.770
		0.975	0.143E-06 ± 0.109E-06 ± 0.873E-08	0.779
4.5	0.6	0.275	0.666E-06 ± 0.376E-06 ± 0.406E-07	0.863

Q^2 [GeV^2]	x	p [GeV/c]	$d\sigma/dQ^2dxdp$ [μb/GeV^3]	R.C.
4.5	0.6	0.325	0.501E-06 $\pm$ 0.200E-06 $\pm$ 0.306E-07	0.864
		0.375	0.443E-06 $\pm$ 0.144E-06 $\pm$ 0.270E-07	0.861
		0.425	0.351E-06 $\pm$ 0.114E-06 $\pm$ 0.214E-07	0.857
		0.475	0.307E-06 $\pm$ 0.994E-07 $\pm$ 0.187E-07	0.857
		0.525	0.148E-06 $\pm$ 0.680E-07 $\pm$ 0.906E-08	0.850
		0.575	0.145E-06 $\pm$ 0.664E-07 $\pm$ 0.884E-08	0.853
		0.625	0.469E-07 $\pm$ 0.371E-07 $\pm$ 0.286E-08	0.848
		0.675	0.953E-07 $\pm$ 0.539E-07 $\pm$ 0.581E-08	0.879
		0.725	0.202E-06 $\pm$ 0.799E-07 $\pm$ 0.123E-07	0.854
		0.775	0.102E-06 $\pm$ 0.576E-07 $\pm$ 0.622E-08	0.868
		0.825	0.513E-07 $\pm$ 0.411E-07 $\pm$ 0.313E-08	0.865
		0.925	0.490E-07 $\pm$ 0.390E-07 $\pm$ 0.299E-08	0.859
		0.975	0.997E-07 $\pm$ 0.560E-07 $\pm$ 0.608E-08	0.860
4.5	0.8	0.275	0.353E-05 $\pm$ 0.423E-06 $\pm$ 0.215E-06	0.851
		0.325	0.176E-05 $\pm$ 0.268E-06 $\pm$ 0.107E-06	0.845
		0.375	0.104E-05 $\pm$ 0.200E-06 $\pm$ 0.636E-07	0.840
		0.425	0.883E-06 $\pm$ 0.179E-06 $\pm$ 0.538E-07	0.836
		0.475	0.938E-06 $\pm$ 0.184E-06 $\pm$ 0.572E-07	0.827
		0.525	0.819E-06 $\pm$ 0.171E-06 $\pm$ 0.500E-07	0.826
		0.575	0.595E-06 $\pm$ 0.147E-06 $\pm$ 0.363E-07	0.825
		0.625	0.702E-06 $\pm$ 0.158E-06 $\pm$ 0.428E-07	0.824
		0.675	0.238E-06 $\pm$ 0.928E-07 $\pm$ 0.145E-07	0.823
		0.725	0.413E-06 $\pm$ 0.122E-06 $\pm$ 0.252E-07	0.827
		0.775	0.358E-06 $\pm$ 0.115E-06 $\pm$ 0.218E-07	0.832
		0.825	0.170E-06 $\pm$ 0.776E-07 $\pm$ 0.104E-07	0.844
		0.875	0.175E-06 $\pm$ 0.794E-07 $\pm$ 0.107E-07	0.833
		0.925	0.605E-07 $\pm$ 0.471E-07 $\pm$ 0.369E-08	0.816
		0.975	0.119E-06 $\pm$ 0.659E-07 $\pm$ 0.727E-08	0.826
4.5	1.0	0.275	0.185E-05 $\pm$ 0.282E-06 $\pm$ 0.113E-06	0.815
		0.325	0.179E-05 $\pm$ 0.262E-06 $\pm$ 0.109E-06	0.812
		0.375	0.177E-05 $\pm$ 0.260E-06 $\pm$ 0.108E-06	0.814
		0.425	0.129E-05 $\pm$ 0.219E-06 $\pm$ 0.789E-07	0.815
		0.475	0.158E-05 $\pm$ 0.245E-06 $\pm$ 0.962E-07	0.811
		0.525	0.991E-06 $\pm$ 0.192E-06 $\pm$ 0.605E-07	0.809
		0.575	0.118E-05 $\pm$ 0.209E-06 $\pm$ 0.717E-07	0.806
		0.625	0.630E-06 $\pm$ 0.154E-06 $\pm$ 0.385E-07	0.800
		0.675	0.882E-06 $\pm$ 0.182E-06 $\pm$ 0.538E-07	0.803
		0.725	0.761E-06 $\pm$ 0.170E-06 $\pm$ 0.464E-07	0.810
		0.775	0.126E-06 $\pm$ 0.684E-07 $\pm$ 0.766E-08	0.800
		0.825	0.253E-06 $\pm$ 0.976E-07 $\pm$ 0.154E-07	0.804

Q^2 [GeV^2]	x	p [GeV/c]	$d\sigma/dQ^2dxdp$ [μb/GeV^3]	R.C.
		0.875	0.130E-06 $\pm$ 0.723E-07 $\pm$ 0.796E-08	0.828
		0.925	0.259E-06 $\pm$ 0.101E-06 $\pm$ 0.158E-07	0.810
		0.975	0.461E-06 $\pm$ 0.135E-06 $\pm$ 0.281E-07	0.807
4.5	1.2	0.275	0.121E-05 $\pm$ 0.274E-06 $\pm$ 0.741E-07	0.755
		0.325	0.898E-06 $\pm$ 0.213E-06 $\pm$ 0.548E-07	0.760
		0.375	0.118E-05 $\pm$ 0.232E-06 $\pm$ 0.720E-07	0.780
		0.425	0.762E-06 $\pm$ 0.184E-06 $\pm$ 0.465E-07	0.790
		0.475	0.687E-06 $\pm$ 0.176E-06 $\pm$ 0.419E-07	0.795
		0.525	0.301E-06 $\pm$ 0.116E-06 $\pm$ 0.183E-07	0.796
		0.575	0.781E-06 $\pm$ 0.181E-06 $\pm$ 0.477E-07	0.797
		0.625	0.306E-06 $\pm$ 0.117E-06 $\pm$ 0.187E-07	0.790
		0.675	0.522E-06 $\pm$ 0.152E-06 $\pm$ 0.319E-07	0.796
		0.725	0.321E-06 $\pm$ 0.124E-06 $\pm$ 0.196E-07	0.799
		0.775	0.794E-07 $\pm$ 0.609E-07 $\pm$ 0.484E-08	0.793
		0.825	0.787E-07 $\pm$ 0.616E-07 $\pm$ 0.480E-08	0.826
		0.875	0.797E-07 $\pm$ 0.607E-07 $\pm$ 0.486E-08	0.781
		0.925	0.149E-06 $\pm$ 0.829E-07 $\pm$ 0.912E-08	0.830
		0.975	0.161E-06 $\pm$ 0.869E-07 $\pm$ 0.983E-08	0.783
4.5	1.4	0.275	0.541E-06 $\pm$ 0.199E-06 $\pm$ 0.330E-07	0.731
		0.325	0.200E-06 $\pm$ 0.105E-06 $\pm$ 0.122E-07	0.744
		0.375	0.534E-06 $\pm$ 0.176E-06 $\pm$ 0.326E-07	0.731
		0.425	0.377E-06 $\pm$ 0.141E-06 $\pm$ 0.230E-07	0.750
		0.475	0.437E-06 $\pm$ 0.147E-06 $\pm$ 0.266E-07	0.765
		0.525	0.938E-07 $\pm$ 0.712E-07 $\pm$ 0.572E-08	0.776
		0.575	0.186E-06 $\pm$ 0.100E-06 $\pm$ 0.113E-07	0.780
		0.625	0.868E-07 $\pm$ 0.659E-07 $\pm$ 0.530E-08	0.775
		0.675	0.170E-06 $\pm$ 0.922E-07 $\pm$ 0.104E-07	0.788
		0.825	0.884E-07 $\pm$ 0.675E-07 $\pm$ 0.539E-08	0.785
		0.975	0.866E-07 $\pm$ 0.664E-07 $\pm$ 0.528E-08	0.791
4.5	1.6	0.425	0.182E-06 $\pm$ 0.957E-07 $\pm$ 0.111E-07	0.748
		0.475	0.167E-06 $\pm$ 0.887E-07 $\pm$ 0.102E-07	0.764
		0.525	0.316E-06 $\pm$ 0.137E-06 $\pm$ 0.193E-07	0.756
		0.575	0.213E-06 $\pm$ 0.114E-06 $\pm$ 0.130E-07	0.767
		0.625	0.112E-06 $\pm$ 0.844E-07 $\pm$ 0.686E-08	0.760
		0.775	0.987E-07 $\pm$ 0.741E-07 $\pm$ 0.602E-08	0.758
5.5	0.8	0.275	0.702E-06 $\pm$ 0.168E-06 $\pm$ 0.428E-07	0.929
		0.325	0.216E-06 $\pm$ 0.859E-07 $\pm$ 0.132E-07	0.852
		0.375	0.101E-06 $\pm$ 0.564E-07 $\pm$ 0.615E-08	0.845
		0.425	0.143E-06 $\pm$ 0.651E-07 $\pm$ 0.874E-08	0.837
		0.475	0.408E-06 $\pm$ 0.113E-06 $\pm$ 0.249E-07	0.832

Q^2 [GeV^2]	x	p [GeV/c]	$d\sigma/dQ^2dxdp$ [μb/GeV^3]	R.C.
		0.525	0.249E-06 ± 0.877E-07 ± 0.152E-07	0.836
		0.575	0.980E-07 ± 0.542E-07 ± 0.598E-08	0.827
		0.625	0.196E-06 ± 0.766E-07 ± 0.119E-07	0.829
		0.675	0.966E-07 ± 0.537E-07 ± 0.589E-08	0.833
		0.725	0.144E-06 ± 0.656E-07 ± 0.881E-08	0.837
		0.775	0.456E-07 ± 0.364E-07 ± 0.278E-08	0.864
		0.825	0.989E-07 ± 0.548E-07 ± 0.603E-08	0.832
		0.875	0.989E-07 ± 0.560E-07 ± 0.603E-08	0.867
		0.925	0.154E-06 ± 0.701E-07 ± 0.942E-08	0.835
		0.975	0.104E-06 ± 0.571E-07 ± 0.632E-08	0.822
5.5	1.0	0.275	0.347E-06 ± 0.110E-06 ± 0.212E-07	0.810
		0.325	0.368E-06 ± 0.109E-06 ± 0.224E-07	0.822
		0.375	0.210E-06 ± 0.814E-07 ± 0.128E-07	0.813
		0.425	0.155E-06 ± 0.699E-07 ± 0.945E-08	0.825
		0.475	0.410E-06 ± 0.113E-06 ± 0.250E-07	0.821
		0.525	0.450E-06 ± 0.117E-06 ± 0.275E-07	0.816
		0.575	0.307E-06 ± 0.969E-07 ± 0.187E-07	0.807
		0.625	0.273E-06 ± 0.946E-07 ± 0.166E-07	0.811
		0.675	0.157E-06 ± 0.703E-07 ± 0.959E-08	0.808
		0.725	0.359E-06 ± 0.106E-06 ± 0.219E-07	0.828
		0.825	0.529E-07 ± 0.416E-07 ± 0.323E-08	0.833
		0.875	0.117E-06 ± 0.649E-07 ± 0.715E-08	0.826
5.5	1.2	0.275	0.279E-06 ± 0.120E-06 ± 0.170E-07	0.756
		0.325	0.720E-06 ± 0.171E-06 ± 0.439E-07	0.763
		0.375	0.137E-06 ± 0.741E-07 ± 0.833E-08	0.793
		0.425	0.668E-07 ± 0.516E-07 ± 0.407E-08	0.804
		0.475	0.187E-06 ± 0.831E-07 ± 0.114E-07	0.800
		0.575	0.294E-06 ± 0.101E-06 ± 0.179E-07	0.798
		0.625	0.618E-07 ± 0.477E-07 ± 0.377E-08	0.801
		0.775	0.616E-07 ± 0.477E-07 ± 0.376E-08	0.808
5.5	1.4	0.325	0.954E-07 ± 0.698E-07 ± 0.582E-08	0.721
		0.375	0.352E-06 ± 0.131E-06 ± 0.215E-07	0.741
		0.475	0.738E-07 ± 0.560E-07 ± 0.450E-08	0.776
		0.575	0.148E-06 ± 0.802E-07 ± 0.901E-08	0.794
		0.825	0.806E-07 ± 0.613E-07 ± 0.492E-08	0.779
		0.975	0.699E-07 ± 0.545E-07 ± 0.426E-08	0.820
5.5	1.6	0.425	0.906E-07 ± 0.673E-07 ± 0.552E-08	0.743
		0.525	0.178E-06 ± 0.947E-07 ± 0.109E-07	0.763
		0.575	0.715E-07 ± 0.539E-07 ± 0.436E-08	0.765

APPENDIX E

GSIM FFREAD Card Settings

MLIST

CUTS 5.e-3 5.e-3 5.e-3 5.e-3 5.e-3

CCCUTS 1.e-3 1.e-3 1.e-3 1.e-3 1.e-3

DCCUTS 1.e-4 1.e-4 1.e-4 1.e-4 1.e-4

ECCUTS 1.e-4 1.e-4 1.e-4 1.e-4 1.e-4

SCCUTS 1.e-4 1.e-4 1.e-4 1.e-4 1.e-4

MAGTYPE 3

MAGSCALE .5829 0.75

TARGET 'e6a'

TGTP 2 1

RUNG 10

NOSEC 'TORU" 'MINI'

NOGEOM 'PTG ' 'ST'

AUTO 1

STOP

APPENDIX F

Parameterization of p_S, Q^2, x and ϕ_{pq}

For extraction of acceptances for d(e,e′p)n reaction we simulated events based on a realistic model build to fit experimental data and kinematic corrected to respect the energy and momentum conservation. We fitted the acceptance corrected data distributions for scattered proton momentum p_s, momentum transfer Q^2, Bjorken scaling variable x and proton azimuthal scattering angle ϕ_{pq} and extracted parameterization functions for each distribution individually. This factorization assumption fit the differential cross sections well. We used combinations of uniform, Gaussian $f(x) \propto \sigma^{-(x-x_0)^2/2\sigma^2}$, exponential $f(x) \propto e^{bx}$ and sinusoidal probability distributions in the model.

p_s (GeV/c) was picked:

- 38% from a uniform distribution on the interval [0.2,1.0].
- 62% from a gaussian distribution on the interval [0.2,1.0], with $\sigma = 0.345$ and $x_0 = 0.195$.

Q^2 (GeV^2) was picked:

- 13.45% from an exponential distribution on the interval [1.5, 5.5] with $b = -2.848$.
- 86.55% from an exponential distribution on the interval [1.5, 5.5] with $b = -1.284$.

x was picked:

- 66% from a gaussian distribution on the interval [0,2] with $\sigma = 0.174$ and $x_0 = 0.877$.
- 34% from a gaussian distribution on the interval [0,2] with $\sigma = 0.326$ and $x_0 = 1.059$.

ϕ_{pq} was picked from a distribution:

- $1 - f \cos \phi_{pq}$ on the interval $[0,2\pi]$ with $f = 0.274$.

ϕ_{el} was picked from a uniform distribution on the interval $[0,2\pi]$

The virtual photon azimuthal angle is then $\phi_q = \phi_{el} - \pi$. The proton polar angle θ_{pq} is given by Eq. 4.7.

BIBLIOGRAPHY

[1] H. Yukawa, "Models and Methods in the Meson Theory", Rev. Mod. Phys. **21**, 474-479 (1949).

[2] C. M. G. Lattes, H. Muirhead, G. p. S. Occhialini and C. F. Powell, "Processes Involving Charged Mesons", Nature **159**, 694-7 (1947).

[3] J. I. Friedman and H. W. Kendall, Ann. Rev. Nucl. Sci. **22**, 203 (1972).

[4] J. J. Drake *et al.*, Astrophys. J. **572**, 996 (2002).

[5] F. Halzen and A. D. Martin, Quarks and Leptons, John Wiley and Sons, (1984).

[6] W. E. Burcham and M. Jobes, Nuclear and Particle Physics, Longman House, Burnt Mill, Harlow, Essex CM20 2JE, England, (1995).

[7] N. Makins *et al.*, [NE18 Collaboration], Phys. Rev. Lett. **72**, 1986 (1994).

[8] T. G. O'Neill *et al.*, [NE18 Collaboration], Phys. Lett. **B 351**, 87 (1995).

[9] D. Abbott *et al.*, Phys. Rev. Lett. **80**, 5072 (1998).

[10] K. Garrow *et al.*, Phys Rev. **C 66**, 044613 (2002).

[11] N. Liyanage *et al.*, Phys. Rev. Lett. **86**, 5670 (2001).

[12] H. Arenhövel, W. Leidemann and E. L. Tomusiak, Phys. Rev. **C 52**, 1232 (1995).

[13] C. D. Epp and T. A. Griffy, Phys. Rev. **C1**, 1633 (1970);F. Cannata, J. P. Dedonder and F. Lenz, Ann. Phys. (N.Y.)**143**, 84 (1982).

[14] R. J. Glauber, Phys.Rev. **100**,242 (1955); Lectures in Theoretical Physics, **v.1**, ed. W. Brittain and L. G. Dunham, Interscience Publ., N.Y. (1959).

[15] M. M. Sargsian, “Selected Topics in High Energy Semi-Exclusive Electro-Nuclear Reactions”, nucl-th/0110053 (2005).

[16] K. I. Blomqvist *et al.*, Phys. Lett. **B 424**, 33 (1998).

[17] V. R. Pandharihande and S. C. Pieper, Phys. Rev. **C 45**, 791 (1992).

[18] M. M. Sargsian, Int. J. Mod. Phys. **E 10**,p405-458 (2001).

[19] L. L. Frankfurt, M. I. Strikman. Phys. Rep. **76**, 215 (1981).

[20] Y. Surya and F. Gross, Phys. Rev. **C 53**, 2422 (1996).

[21] V. N. Gribov, JETP, **30**, 709 (1970).

[22] L. Bertuchi and A. Capella Il Nuovo Cimento, **A 51**, 369 (1967).

[23] L. Frankfurt, G. A. Miller and M. I. Strikman, Nucl. Phys. **A 555**, 752 (1993).

[24] D. R. Yennie, “Hadronic Interactions of Electrons and Photons”, edited by J. Cummings and D. Osborn (Academic, New York, 1971), p.321.

[25] D. E. Groom *et al.*, [Particle Data Group Collaboration], Eur. Phys. J. **C 15**, 1 (2000).

[26] M. Frodyma *et al.*, Phys Rev. **C 47**, 1599 (1993).

[27] G. Goggi *et al.*, Phys. Lett., **B 72** 265 (1977).

[28] P. Stoler, Phys. Rept. **226** 103 (1993).

[29] J. M. Laget, Phys. Lett. **B 49**, 609 (2005).

[30] J. M. Laget, Phys. Rep. **69**, 1 (1981).

[31] S. Galster *et. al.*, Nucl. Phys. **B 32**, 221 (1971).

[32] O. Gayou *et al.*, Phys. Rev. Lett. **88**, 092301 (2002).

[33] J. M. Laget, Nucl. Phys. **A 579**, 333 (1994).

[34] M. Ungaro, Ph. D. Thesis, RPI (2004).

[35] D. Higinbotham, in *International Symposium on Electromagnetic Interactions in Nuclear and Hadron Physics*, 4-7 December 2001, Osaka, Japan. Eds. M Fujiwara and T. Shima. World Scientific, p. 291 (2002).

[36] M. M. Rvachev, Ph. D. Thesis, MIT (2003); M.M.Rvachev *et al.*, nucl-ex/049005.

[37] S. J. Brodsky and G. R. Farrar, Phys. Rev. Lett **31**, 1153 (1973).

[38] A. H. Muller, Phys. Rept. **73**,237 (1981).

[39] S. J. Brodsky, L. L. Frankfurt, J. F. Gunion, A. H. Mueller and M. I. Strikman, Phys. Rev. **D 50**, 3134 (1994).

[40] E. M. Aitala *et al.* [E791 Collaboration], Phys. Rev. Lett. **86**, 4773 (2001).

[41] L. L. Frankfurt, W. R. Greenberg, G. A. Miller, M. M. Sargsian and M. I. Strikman, Z. Phys. **A 352**, 97 (1995).

[42] L. L. Frankfurt, W.R. Greenberg, G. A. Miller, M. M. Sargsian and M. I. Strikman, Phys. Lett. **B 369**, 201 (1996).

[43] G. R. Farrar, H. Liu, L. L. Frankfurt and M. I. Strikman, Phys. Rev. **C 46**, 2547 (1992).

[44] M. A. Braun, C. Ciofi degli Atti and D. Treleani, Phys. Rev. **C 62**, 034606 (2000).

[45] K. Sh. Egiyan, K. A. Griffioen and M. I. Strikman, E94-019 CLAS Proposal (1994)

[46] S. J. Brodsky, L. L. Frankfurt, J. F. Gunion, A. H. Mueller and M. I. Strikman, Phys. Rev. **D 50**, 3134 (1994).

[47] J. C. Collins, L. L. Frankfurt and M. I. Strikman, Phys. Rev. **D 56**, 2982 (1997).

[48] M. R. Adams *et al.* (E665 Collaboration), Phys Rev. Lett.**86**, 4773 (1995).

[49] J. Aclander *et al.*, Phys Rev. **C 70**, 015208 (2004).

[50] Y. Mardor *et al.*, Phys. Rev. Lett. **81**, 5085 (1998).

[51] S. A. Caroll *et al.*,Phys. Rev. Lett **61**, 1698 (1988).

[52] A. Leksanov *et al.*, Phys. Rev. Lett. **87**, 212301 (2001).

[53] J. P. Ralston and B. Pire, Phys. Rev. Lett. **61**, 1823 (1988).

[54] S. J. Brodsky and G. F. de Teramond, Phys. Rev. Lett. **60**, 1924 (1988).

[55] G. Garino *et al.*, Phys. Rev. **C 45**, 780 (1992).

[56] H. Gao, V. R. Pandharipande, and S. C. Pieper (private communication); V. R. Pandharipande and S. C. Pieper, Phys. Rev. **C 45**, 791 (1982).

[57] L. L. Frankfurt and M. I. Strikman, Prog. in Part. and Nucl. Phys. **27**, 135 (1991).

[58] K. S. Egiyan *et al.*, Nucl. Phys. **A 580**, 365 (1994).

[59] L. L. Frankfurt *et al.*, Phys. Rev. **A 352**, 97 (1997).

[60] T. de Forest, Nucl. Phys. **A 392**, 232 (1983).

[61] C. Ciofi degli Atti, S. Simula, L. L. Frankfurt, M. I. Strikman, Phys. Rev. **C 44**, R7 (1991).

[62] M. M. Sargsian, J. Phys. **G 29**, R1-R45 (2003).

[63] J. Arrington *et al.*, Phys. Rev. Lett. **82**, 2056 (1999).

[64] M.D. Mestayer *et al.*, "The CLAS Drift Chamber System", Nucl.Inst.and Meth. **A 449**, 81 (2000).

[65] E. Smith *et al.*, "Calibration of Time-of-Flight System", CLAS-NOTE 1999-011.

[66] M. Amarian *et al.*, "The CLAS Forward Electromagnetic Calorimeter", Nucl.Inst.and Meth. **A460**, 239 (2001).

[67] D. Lawrence *et al.*, "CLAS Drift Chamber Calibration Procedure", CLAS-NOTE 1999-018.

[68] A. Vlasov *et al.*, "CLAS Cherenkov Detector Calibration", CLAS-NOTE 1999-005.

[69] E. Smith and R. Nasseripour, “Systematic study of Time-walk Corrections for the TOF counters”, CLAS-NOTE 2002-007.

[70] A. V. Klimenko, Ph. D. Thesis (2004).

[71] P. Bosted, “Pair-Symetric and Pion Backgrounds for Eg1b”, CLAS-NOTE 2004-005.

[72] S. E. Kuhn, A. V. Klimenko, “Momentum Corrections for E6”, CLAS-NOTE 2003-005.

[73] I. Niculescu, Ph. D. Thesis, Hampton University (1999).

[74] A. Bodek, Phys. Rev. Lett. **51** 534 (1983); A. Bodek *et al.*, Phys. Rev. Lett. **50**, 1431 (1983); A. Bodek *et al.*, Phys. Rev, **D 20**, 1471 (1979).

[75] L. M. Stuart *et al.*, Phys. Rev. **D 58**, 032003 (1998).

[76] S. Rock *et al.*, Phys. Rev. **D 46**, 24 (1992).

[77] S. Dasu *et al.*, Phys. Rev. **D 49**, 5641 (1994).

[78] W. B. Atwood, G. West, Phys. Rev. **D 7**, 773, (1973).

[79] M. Osipenko, G. Ricco, S. Simula, M. Battaglieri, M. Ripani, hep-ex/0506004. (2005).

[80] M. D. Mestayer, SLAC-214 (1978).

[81] M. M. Sargsian, Preprint YERPHI-1331-26-91, (1991).

[82] L. L. Frankfurt, M. I. Strikman. Phys. Rep. **160**, 236 (1988).

[83] J. Schwinger, “Radiative Corrections in β decays”, Phys. Rev. Lett. **19**, 1501-1503 (1967).

[84] L. W. Mo and Y. Tsai, “Radiative Corrections to Elastic and Inelastic ep and μp Scattering”, Rev. Mod. Phys. **41**, 205 (1969); Y. S. Tsai, Preprint SLAC, PUB-848 (1971).

[85] M. M. Sargsian, “Event Generator of Electron-Nucleus Reactions”, CLAS-NOTE 92-018.

[86] M. M. Sargsian, “Computer Code for Inclusive (e,e′) Electro-Production Reactions and Radiative Corrections”, CLAS-NOTE 90-007.

[87] D. Y. Bardin and N. M. Shumeiko, Nucl Phys. **B 127**, 242 (1977).

[88] A. Afanasev, I. Akushevich, V. Burkert, and K. Joo, “QED radiative corrections in processes of exclusive pion electro-production”, Phys. Rev. **D 66**, 074004 (2002).

[89] G. P. Gilfoyle and A. Afanasev, CLAS-NOTE 2005-022.

[90] C. Ciofi degli Atti and S. Simula, Phys. Rev. **C 53**, 1689 (1996).

[91] S. C. Pieper, R. B. Wiringa, and V. P. Pandharipande, Phys. Rev. **C 46**, 1741 (1992).

[92] L. L. Frankfurt and M. I. Strikman, in *Electromagnetic Interactions with Nuclei*, edited by B. Frois and I. Sick (World Scientific, Singapore, 1991).

[93] L. L. Frankfurt, M. I. Strikman, D. B. Day, and M. M. Sargsian, Phys. Rev. **C 48**, 2451 (1993).

[94] K. Sh. Egiyan *et al*, Phys. Rev. **C 68**, 014313 (2003).

[95] D. Day *et al* , Phys. Rev. Lett. **59**, 427 (1979).

[96] K. Sh. Egiyan *et al*, Phys. Rev. **C 68**, 014313 (2005).

[97] M. Osipenko *et al.*, “The deuteron structure function F2 with CLAS”, CLAS-NOTE 2005-013.

[98] K. Sh. Egiyan *et al.*, CLAS-NOTE 2005, unpublished.

[99] G. E. Brown and A. D. Jackson, The Nucleon-Nucleon Interactions, North-Holland Publishing Company (1976).

[100] M. Lacombe, B. Loiseau, R. Vinh Mau, J. Cote, P. Pires and R. de Tourreil, Phys. Lett. **B 101**, 139 (1981).

[101] R. Machleidt, K. Holinde, and C. Elster, Phys. Rep. **149**, 1 (1987).

[102] L. L. Frankfurt, G. A. Miller and M. Strikman, Phys. Lett. B **303**, 1 (1993).

VITA

Cornel Butuceanu

Cornel Butuceanu was born in Medias, Romania on May 15, 1969. He received a Bachelor of Science degree in physics in "Babes-Bolyai" University in Cluj-Napoca, Romania. Following several years of teaching in Romanian public schools, he entered the physics graduate program at The College of William and Mary in 1999 and received a Master of Science degree in Physics in May of 2001. This dissertation was defended on November 29, 2005 at The College of William and Mary.